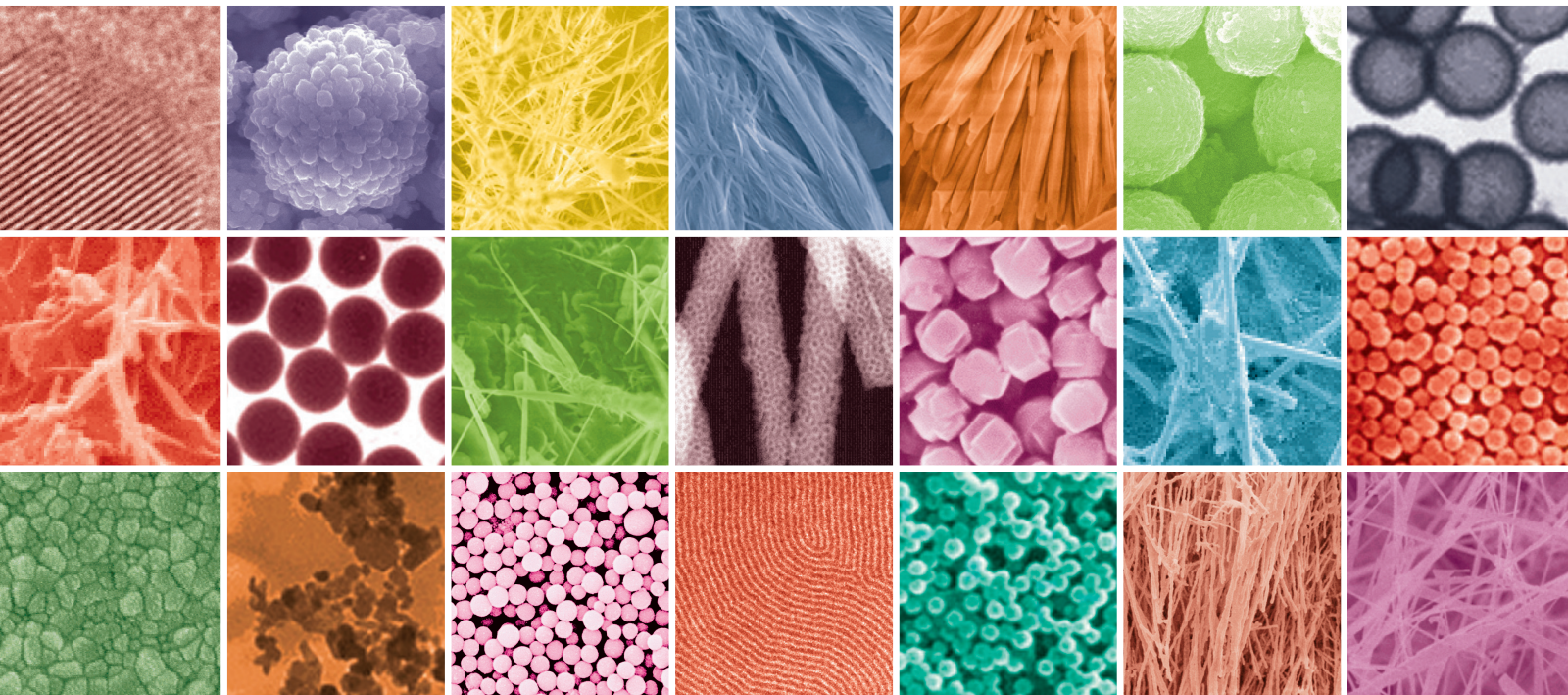


Nanostructured Surfaces, Coatings, and Films: Fabrication, Characterization, and Application

Guest Editors: Mengnan Qu, Jiamin Wu, Guangyu Zhao, and Yuan Zhang





Nanostructured Surfaces, Coatings, and Films: Fabrication, Characterization, and Application

Journal of Nanomaterials

Nanostructured Surfaces, Coatings, and Films: Fabrication, Characterization, and Application

Guest Editors: Mengnan Qu, Jiamin Wu, Guangyu Zhao,
and Yuan Zhang



Copyright © 2013 Hindawi Publishing Corporation. All rights reserved.

This is a special issue published in "Journal of Nanomaterials." All articles are open access articles distributed under the Creative Commons Attribution License, which permits unrestricted use, distribution, and reproduction in any medium, provided the original work is properly cited.

Editorial Board

Katerina E. Aifantis, Greece
Nageh K. Allam, USA
Margarida Amaral, Portugal
Xuedong Bai, China
Lavinia Balan, France
Enrico Bergamaschi, Italy
Theodorian Borca-Tasciuc, USA
C. Jeffrey Brinker, USA
Christian Brosseau, France
Xuebo Cao, China
Shafiq Chowdhury, USA
Kwang-Leong Choy, UK
Cui Chunxiang, China
Miguel A. Correa-Duarte, Spain
Shadi A. Dayeh, USA
Claude Estourns, France
Alan Fuchs, USA
Lian Gao, China
Russell E. Gorga, USA
Hongchen Chen Gu, China
Mustafa O. Guler, Turkey
John Zhanhu Guo, USA
Smrati Gupta, Germany
Michael Harris, USA
Zhongkui Hong, China
Michael Z. Hu, USA
David Hui, USA
Y.-K. Jeong, Republic of Korea
Sheng-Rui Jian, Taiwan
Wanqin Jin, China
Rakesh K. Joshi, UK
Zhenhui Kang, China
Fathallah Karimzadeh, Iran
Alireza Khataee, Iran

Do Kyung Kim, Korea
Alan K. T. Lau, Hong Kong
Burtrand Lee, USA
Jun Li, Singapore
Benxia Li, China
Xing-Jie Liang, China
Shijun Liao, China
Gong Ru Lin, Taiwan
J.-Y. Liu, USA
Tianxi Liu, China
Jue Lu, USA
Songwei Lu, USA
Daniel Lu, China
Ed Ma, USA
Gaurav Mago, USA
Santanu K. Maiti, India
Sanjay R. Mathur, Germany
Vikas Mittal, UAE
Weihai Ni, Germany
Sherine Obare, USA
Atsuto Okamoto, Japan
Abdelwahab Omri, Canada
Edward Andrew Payzant, USA
Kui-Qing Peng, China
Anukorn Phuruangrat, Thailand
Suprakas Sinha Ray, South Africa
Ugur Serincan, Turkey
Huaiyu Shao, Japan
Donglu Shi, USA
Vladimir Sivakov, Germany
Marinella Striccoli, Italy
Bohua Sun, South Africa
Saikat Talapatra, USA
Nairong Tao, China

Titipun Thongtem, Thailand
Somchai Thongtem, Thailand
Alexander Tolmachev, Ukraine
Valeri P. Tolstoy, Russia
Tsung-Yen Tsai, Taiwan
Takuya Tsuzuki, Australia
Raquel Verdejo, Spain
Mat U. Wahit, Malaysia
Zhenbo Wang, China
Ruiping Wang, Canada
Shiren Wang, USA
Cheng Wang, China
Yong Wang, USA
Jinquan Wei, China
Ching-Ping Wong, Hong Kong
Xingcai Wu, China
Guodong Xia, Hong Kong
Zhi Li Xiao, USA
Ping Xiao, UK
Yangchuan Xing, USA
Shuangxi Xing, China
N. Xu, China
Doron Yadlovker, Israel
Yingkui Yang, China
Khaled Youssef, USA
Kui Yu, Canada
William W. Yu, USA
Haibo Zeng, China
Tianyou Zhai, Japan
Renyun Zhang, Sweden
Bin Zhang, China
Yanbao Zhao, China
Lianxi Zheng, Singapore
Chunyi Zhi, Hong Kong

Contents

Nanostructured Surfaces, Coatings, and Films: Fabrication, Characterization, and Application, Mengnan Qu, Jiamin Wu, Guangyu Zhao, and Yuan Zhang
Volume 2013, Article ID 492646, 2 pages

Fabrication of Orderly Copper Particle Arrays on a Multi-Electrolyte-Step Anodic Aluminum Oxide Template, Chun-Ko Chen, Der-Sheng Chan, Cheng-Chung Lee, and Sheng-Hui Chen
Volume 2013, Article ID 784927, 7 pages

Evaluation of the Antitumor Activity by Ni Nanoparticles with Verbascoside, Mingyue Chen, Yaqin Zhang, Bin Huang, Xueming Yang, Yunong Wu, Bin Liu, Yi Yuan, and Gen Zhang
Volume 2013, Article ID 623497, 6 pages

Influence of Annealing on Properties of Spray Deposited ZnO Thin Films, Kalyani Nadarajah, Ching Yern Chee, and Chou Yong Tan
Volume 2013, Article ID 146382, 8 pages

Effect of a Polymeric Protective Coating on Optical and Electrical Properties of Poly(*p*-phenylene vinylene) Derivatives, V. C. Gonçalves, C. A. Olivati, A. J. F. Carvalho, and D. T. Balogh
Volume 2013, Article ID 160464, 5 pages

Liquid Phase Deposition of Silica on the Hexagonally Close-Packed Monolayer of Silica Spheres, Seo Young Yoon, Sung-Eun Choi, and Jin Seok Lee
Volume 2013, Article ID 510524, 7 pages

Facile Fabrication of a Hierarchical Superhydrophobic Coating with Aluminate Coupling Agent Modified Kaolin, Hui Li, Mengnan Qu, Zhe Sun, Jinmei He, and Anning Zhou
Volume 2013, Article ID 497216, 5 pages

Effect of Nanosilica Filled Polyurethane Composite Coating on Polypropylene Substrate, Yern Chee Ching and Nurehan Syamimie
Volume 2013, Article ID 567908, 8 pages

Fluoroalkylsilane versus Alkylsilane as Hydrophobic Agents for Silica and Silicates, Damian Ambroźewicz, Filip Ciesielczyk, Magdalena Nowacka, Joanna Karasiewicz, Adam Piasecki, Hieronim Maciejewski, and Teofil Jesionowski
Volume 2013, Article ID 631938, 13 pages

Formation of Porous Structure with Subspot Size under the Irradiation of Picosecond Laser Pulses, Bin Liu, Wenjun Wang, Gedong Jiang, Xuesong Mei, Kedian Wang, and JiuHong Wang
Volume 2013, Article ID 301301, 9 pages

Fabrication of TiO₂@Yeast-Carbon Hybrid Composites with the Raspberry-Like Structure and Their Synergistic Adsorption-Photocatalysis Performance, Dang Yu, Bai Bo, and He Yunhua
Volume 2013, Article ID 851417, 8 pages

TiO₂-SiO₂/Ph-POSS Functional Hybrids: Preparation and Characterisation, Magdalena Nowacka, Damian Ambroźewicz, and Teofil Jesionowski
Volume 2013, Article ID 680821, 10 pages

Preparation and Characterization of Multifunctional Chitin/Lignin Materials, Lukasz Klapiszewski, Marcin Wysokowski, Izabela Majchrzak, Tomasz Szatkowski, Magdalena Nowacka, Katarzyna Siwińska-Stefańska, Karolina Szwarc-Rzepka, Przemyslaw Bartczak, Hermann Ehrlich, and Teofil Jesionowski
Volume 2013, Article ID 425726, 13 pages

Magnetic Properties and Microstructure of FeO₂/Fe/FePt and FeO₂/FePt Films, Jai-Lin Tsai, Po-Ran Chen, Yi-Hsiu Chen, and Qi-Shao Luo
Volume 2013, Article ID 954621, 8 pages

Cytocompatibility of Plasma and Thermally Treated Biopolymers, Petr Slepíčka, Iva Michaljaničová, Nikola Slepíčková Kasálková, Petr Sajdl, Zdeňka Kolská, and Václav Švorčík
Volume 2013, Article ID 238742, 10 pages

Heterogeneous Deposition of Cu₂O Nanoparticles on TiO₂ Nanotube Array Films in Organic Solvent, Xinwen Huang and Zongjian Liu
Volume 2013, Article ID 517648, 8 pages

Molecular Design and Applications of Self-Assembling Surfactant-Like Peptides, Chengkang Tang, Feng Qiu, and Xiaojun Zhao
Volume 2013, Article ID 469261, 9 pages

Upconversion Luminescence and Photodegradation Performances of Pr Doped Y₂SiO₅ Nanomaterials, Yi Yang, Cheng Liu, Ping Mao, and Lian-Jun Wang
Volume 2013, Article ID 427370, 6 pages

Interaction of Silver Nanoparticles and Chitin Powder with Different Sizes and Surface Structures: The Correlation with Antimicrobial Activities, Vinh Quang Nguyen, Masayuki Ishihara, Shingo Nakamura, Hidemi Hattori, Takeshi Ono, Yasushi Miyahira, and Takemi Matsui
Volume 2013, Article ID 467534, 9 pages

Fabrication of Polystyrene/Detonation Nanographite Composite Microspheres with the Core/Shell Structure via Pickering Emulsion Polymerization, Hou Xuemei and Ying Hao
Volume 2013, Article ID 751497, 8 pages

I-V Characteristics of Pt_xCo_{1-x} (x = 0.2, 0.5, and 0.7) Thin Films, M. Erkovan, E. Şentürk, Y. Şahin, and M. Okutan
Volume 2013, Article ID 579131, 6 pages

Effect of RGD Peptide-Coated TiO₂ Nanotubes on the Attachment, Proliferation, and Functionality of Bone-Related Cells, Seunghan Oh, Kyung Suk Moon, and Seoung Hoon Lee
Volume 2013, Article ID 965864, 11 pages

Formation of Various Pyramidal Structures on Monocrystalline Silicon Surface and Their Influence on the Solar Cells, Yangang Han, Xuegong Yu, Dong Wang, and Deren Yang
Volume 2013, Article ID 716012, 5 pages

Synthesis of Coral-Like, Straw-Tied-Like, and Flower-Like Antimony Sulfides by a Facile Wet-Chemical Method, Jutarat Kavinchan, Titipun Thongtem, Somchai Thongtem, and Eksuree Saksornchai
Volume 2013, Article ID 719679, 5 pages

Structure and Properties of Nanostructured (Ti-Hf-Zr-V-Nb)N Coatings, Alexander D. Pogrebnjak
Volume 2013, Article ID 780125, 12 pages

Photocatalytic and Magnetic Behaviors Observed in BiFeO₃ Nanofibers by Electrospinning, Xuehui Zhang, Haiyang Liu, Bin Zheng, Yuanhua Lin, Deping Liu, and Ce-Wen Nan
Volume 2013, Article ID 917948, 7 pages

Cobalt Xanthate Thin Film with Chemical Bath Deposition, İ. A. Kariper and T. Özpozan
Volume 2013, Article ID 139864, 9 pages

Nanocomposite Coatings Codeposited with Nanoparticles Using Aerosol-Assisted Chemical Vapour Deposition, Xianghui Hou, Kwang-Leong Choy, Nathalie Brun, and Virginie Serin
Volume 2013, Article ID 219039, 8 pages

Editorial

Nanostructured Surfaces, Coatings, and Films: Fabrication, Characterization, and Application

Mengnan Qu,¹ Jiamin Wu,² Guangyu Zhao,³ and Yuan Zhang⁴

¹ College of Chemistry and Chemical Engineering, Xi'an University of Science and Technology, Xi'an, China

² Department of Chemical and Petroleum Engineering, University of Pittsburgh, Pittsburgh, PA, USA

³ Academy of Fundamental and Interdisciplinary Sciences, Harbin Institute of Technology, Harbin, China

⁴ State Key Laboratory of Applied Organic Chemistry, Lanzhou University, Lanzhou, China

Correspondence should be addressed to Mengnan Qu; mnanqu@gmail.com

Received 10 December 2013; Accepted 10 December 2013

Copyright © 2013 Mengnan Qu et al. This is an open access article distributed under the Creative Commons Attribution License, which permits unrestricted use, distribution, and reproduction in any medium, provided the original work is properly cited.

A number of promising approaches to fabricate nanostructured surfaces, coatings, and films have been stimulated by opportunities to enhance the properties of surfaces and interfaces via the combination of surface structure, morphology, and physical and chemical properties. Such functional nanostructured surfaces, coatings, and films are playing an increasingly important part in a broad range of novel applications, such as energy, electronics, advanced materials, and biomedical applications. This special issue features one review article and twenty-seven research articles that cover a wide range of recent progress in design, fabrication, and characterization of innovative nanostructured surfaces with the aim of improving their surface properties and functional performance, as well as new insights on physical principles underlying their properties and enormous potential applications. Highlighted below are important contributions from this special issue.

In this issue, the review paper presented by C. Tang et al. thoroughly overviews recent advances in molecular design and potential applications of self-assembling surfactant-like peptides. A. Pogrebñjak reports structures and properties of nanostructured (Ti-Hf-Zr-V-Nb)N coatings. X. Hou et al. report nanocomposite coatings co-deposited with nanoparticles using aerosol-assisted chemical vapour deposition. Y. C. Ching and N. Syaminie prepare nanosilica filled polyurethane composite coatings on polypropylene substrates. H. Li et al. fabricate a hierarchical superhydrophobic coating with aluminate coupling agent modified kaolin. V. C. Gonçalves et al. report effects of polymeric protective coatings on

the optical and electrical properties of poly(p-phenylene-vinylene) derivatives.

J. L. Tsai et al. report microstructures and magnetic properties of FeOx/Fe/FePt and FeOx/FePt films. K. Nadarajah et al. investigate the influence of annealing on properties of spray deposited ZnO thin films. M. Erkovan et al. study the resistivity of platinum and cobalt alloy thin films. İ. Kariper and Z. Liu deposit cobalt xanthate thin films by chemical bath deposition method. X. Huang and Z. J. Liu report a method to prepare TiO₂ nanotube array films (NAFs) decorated with Cu₂O nanoparticles, which shows more the photoactive than the undecorated TiO₂.

D. Yu et al. report preparation and photocatalytic properties of raspberry-like TiO₂/yeast-carbon hybrid composites. X. Zhang et al. study the photocatalytic and magnetic behaviors of BiFeO₃ nanofibers fabricated by electrospinning. Y. Yang et al. report the upconversion luminescence and photodegradation performances of Pr(III)-doped Y₂SiO₅ nanomaterials. B. Huang et al. evaluate the antitumor activities of verbascoside-coated Ni nanoparticles. S. Oh et al. investigate effects of RGD-peptide coated TiO₂ nanotubes on the cell attachment and proliferation. P. Slepíčka et al. report the cytocompatibility of plasma and thermally treated biopolymers. V. Q. Nguyen et al. develop a method to synthesize chitin/Ag NP composites, which exhibit antibacterial and antifungal activities.

C. K. Chen et al. fabricate free-standing ordered copper particles using an anodic aluminum oxide (AAO) template by a multielectrolyte-step process. S. Y. Yoon et al. present the

liquid-phase-deposition (LPD) of silica onto the hexagonally close-packed silica sphere monolayers. B. Liu et al. fabricate porous structures with subspot-size under the irradiation of picosecond laser pulses. Y. Han et al. report the fabrication of various pyramidal structures on monocrystalline silicon surface by wet etching techniques and investigated their applications to the solar cells. D. Ambrożewicz et al. prepare hydrophobic powders via surface modification of silica or magnesium silicate with selected fluoroalkylsilanes and alkylsilanes. X. Hou et al. synthesize polystyrene/detonation nanographite composite microspheres with the core/shell structure via Pickering emulsion polymerization. L. Klapiszewski et al. report the preparation and characterization of multifunctional chitin/lignin materials. J. Kavinchan et al. prepare antimony sulfide (Sb_2S_3) with different morphologies by a wet chemical method. M. Nowacka et al. prepare and characterize TiO_2 - SiO_2 /Ph-POSS functional hybrids.

As guest editors for this special issue, we hope that this special issue will stimulate further developments in the field of nanostructured surfaces, coatings, and films.

Acknowledgments

The editors gratefully thank the authors for their contributions to this special issue and the reviewers for their constructive comments.

*Mengnan Qu
Jiamin Wu
Guangyu Zhao
Yuan Zhang*

Research Article

Fabrication of Orderly Copper Particle Arrays on a Multi-Electrolyte-Step Anodic Aluminum Oxide Template

Chun-Ko Chen,¹ Der-Sheng Chan,² Cheng-Chung Lee,¹ and Sheng-Hui Chen¹

¹ Department of Optics and Photonics, National Central University, 300 Chung-Da Road, Chung-Li 32001, Taiwan

² Department of Chemical and Materials Engineering, Lee-Ming Institute of Technology, Lizhuan Road, New Taipei City 24305, Taiwan

Correspondence should be addressed to Sheng-Hui Chen; ericchen@dop.ncu.edu.tw

Received 4 September 2013; Revised 4 November 2013; Accepted 6 November 2013

Academic Editor: Guangyu Zhao

Copyright © 2013 Chun-Ko Chen et al. This is an open access article distributed under the Creative Commons Attribution License, which permits unrestricted use, distribution, and reproduction in any medium, provided the original work is properly cited.

A multi-electrolyte-step (MES) anodic aluminum oxide (AAO) method was used to achieve nanochannel arrays with good circularity and periodic structure. The nano-channel array fabrication process included immersion in a phosphoric acid solution with a 120–150 bias voltage. Bowl-shaped structures were then formed by removing the walls of the nano-channel arrays. The nano-channel arrays were grown from the bottom of the bowl structure in an oxalic solution using a 50 V bias voltage. A comparison of this new MES process with the one-step and five-step AAO process showed a 50% improvement in the circularity over the one-step process. The standard deviation of the average period in the MES array was 25 nm which is less than that of one-step process. This MES method also took 1/4 of the growing time of the five-step process. The orderliness of the nano-channel arrays for the five-step and MES process was similar. Finally, Cu nanoparticle arrays with a 200 nm period were grown using an electroplating process inside the MES nano-channel arrays on fluorine doped tin oxide glass. Stronger surface plasmon resonance absorption from 550 nm to 750 nm was achieved with the MES process than was possible with the one-step process.

1. Introduction

In recent years, surface plasmon resonance (SPR) in nanoparticle array has attracted a lot of attention because of the adjustable absorption band [1, 2]. SPR assisted energy conversion in dye-sensitized solar cell has also been studied [3]. The SPR effect is dependent on the shape and the arrangement of the nanoparticles but it is not easy to achieve good circularity and periodicity in metallic nanoparticle arrays. It has been shown that carbon nanotubes, nanoparticles, quantum dots, and nanopillars can be grown in nanochannel arrays utilizing various methods for their fabrication [4]. The use of the anodic aluminum oxide (AAO) method for the fabrication of nanochannel arrays to nanoparticle arrays has matured [5]. However, the positioning of the nanochannel arrays grown using the AAO method is random making it very difficult to control the hole quality and to form orderly arrays. There have been some methods for growing good quality AAO nanochannel arrays developed. They require either an increase in circularity or improvement in the period of

the channels, so it becomes a long process [6]. For example, in the multistep AAO process [7], channels are repeatedly grown and removed to achieve periodic arrays. The problem is the thickness of the raw material, Al, has to be greater than 1 μm , which is too thick for the deposition of a good quality of film. Another method involves using mixed electrolytes to improve the circularity of the nanochannel arrays. The limitations of this method are that the period of the arrays that can be grown is less than 150 nm and the arrangement of the arrays is irregular [8, 9]. A nanoimprinting method can be applied to control and regularize the positions of the nanochannel arrays [10], but the imprinting mold is easily broken during the imprinting process. The use of an atomic force microscope (AFM) for prepatterning [11] is good, but the working area is very small. In this study a multi-electrolyte-step (MES) method was applied to improve the circularity and period of the arrays. The goal was to grow orderly nanochannel arrays in a simpler and more useful fashion. A nanochannel template was applied for the masking of antireflectance structures on a large area [12]

for the production of omnidirectional reflectors [13]. Finally, periodic copper particles with larger periods were grown in the MES nanochannel arrays on fluorine doped tin oxide (FTO) glass and the absorption of the spectrum was in the visible region due to SPR.

2. Definition and Simulation

Nanochannel arrays for periodic structure applications have to be precisely ordered with a regular period and good circularity [14, 15]. The circularity f_{circ} of the nanochannel arrays can be defined as follows:

$$f_{\text{circ}} = \frac{4\pi A}{P^2}, \quad (1)$$

where P is the perimeter of a hole and A is its area. When the circularity is 1, the hole is a perfect circle. When the hole flattens, the circularity approaches 0. In the past, AAO nanochannel arrays were grown in phosphoric or oxalic acid. The results of analysis of the circularities of the holes produced from one-step AAO processes [16–27] are shown in Figure 1. It can be seen that it is difficult to grow good quality arrays with a period in the range from 150 to 300 nm in phosphoric acid using the traditional AAO method. It has also been proven that better quality arrays can be produced using an AAO process with oxalic acid, with most holes being in the upper 0.8 range in circularity. We devise an MES method designed to grow orderly nanochannel arrays in a simpler and more useful fashion, which produces arrays with improved circularity and periodicity. We first simulated a 200 nm bowl structure and applied an added bias of 50 V to see if the AAO process could be applied theoretically. The simulation results obtained by finite element analysis are shown in Figure 2. Parkhutik and Shershulsky [28] and Houser and Hebert [29] proposed a model that can suitably describe the charge characteristics of an AAO electrode. This model [30] was also used to analyze the potential distribution inside the anode. The results in Figure 2 show the distribution of the potential and gradient of the potential, where A indicates the position at the top of curve S, B at the middle, and C at the bottom. The value of the gradient of the potential at A is higher than that at B or C. The results indicate that the maximum oxidation reaction rate occurs at A, due to the geometrical symmetry effect. According to the simulation results, the highest bias occurred at the central position of the bowl structure, with a new channel growing there due to the electrochemical reaction. Thus, we could design a process for the growth of large-period nanochannel arrays at lower voltages.

3. Experiments

In the experimental process, 99.5% aluminum foils were used as the substrates which were electropolished in an $\text{H}_3\text{PO}_4/\text{H}_2\text{SO}_4/\text{di water}$ (2:2:1) solution; the roughness of the substrate surface could range from 30 to 13.1 nm. After substrate cleaning, the MES process was used to grow large-period nanochannel arrays in a 10 wt% phosphoric acid at

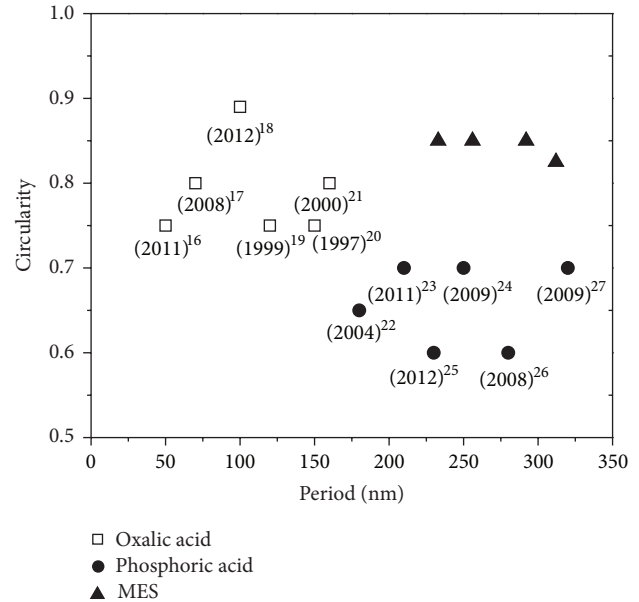


FIGURE 1: The analysis of circularity produced by AAO processes in oxalic acid and phosphoric acid.

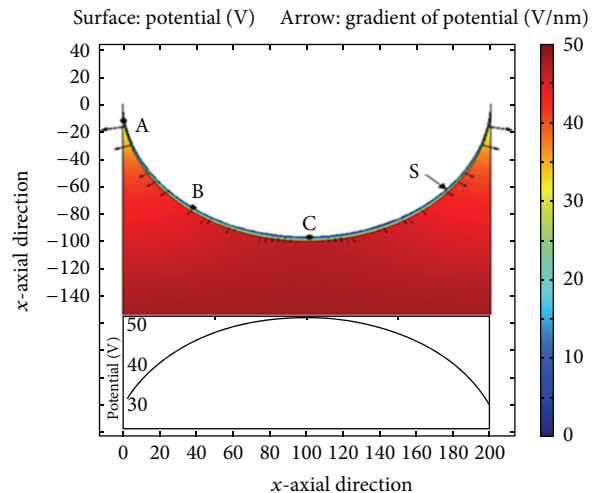


FIGURE 2: Distribution profiles of the potential with an applied voltage of 50 V.

4°C with the application of a bias voltage of 120–150 V for 10 minutes. The process design and its images are illustrated in Figure 3. The size of the holes was increased by chemical dissolution in a 0.5 M NaOH solution until the walls of the nanochannels were very thin, and bowl-shaped structures were formed by removing the walls of the nanochannel arrays. Nanochannel arrays were grown from the bottom of the bowl structure using a 50 V bias voltage in an oxalic acid solution for 30 minutes. It was easier to obtain nanochannels similar in shape to the circular holes in the oxalic acid solution than in the phosphoric acid solution. The results of the one-step AAO process were compared with the MES AAO

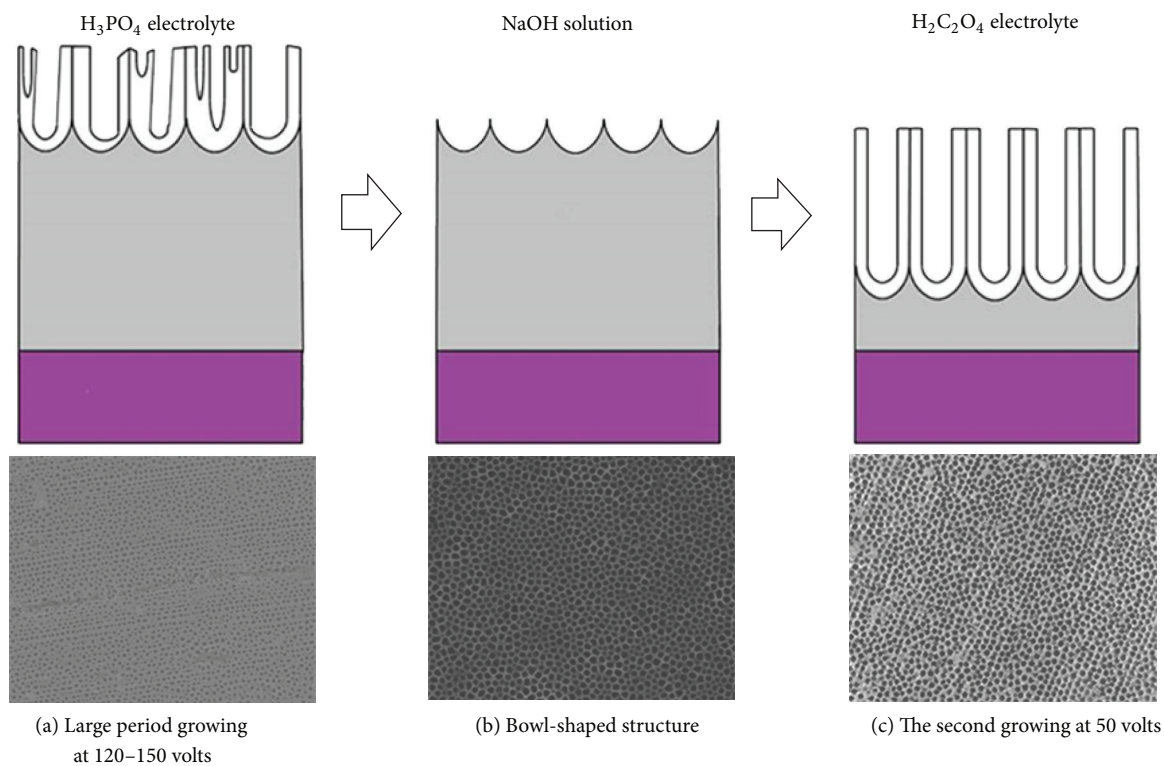


FIGURE 3: Nanochannel arrays with a large period growing at 120–150 volts and the second growing at 50 volts.

results. The one-step process involved growth in a 10 wt% phosphoric acid with a voltage of 120–150 V for 30 minutes. The holes increased in size to 0.5 μm when the NaOH solution was used. The one-step process was repeated five times (five-step process); the results are also discussed in our study. It should be noted that these are the usual methods that have been used for the orderly growth of arrays in other studies. After this comparison, 300 nm Al films were coated onto FTO glass after cleaning it with alcohol and acetone, and nanochannel arrays were grown using the one-step and MES process. Cu particles with a 200 nm period were grown at a bias voltage 1V in the 0.05 M CuSO_4 solution utilizing an electroplating process, after which the AAO nanochannel arrays were removed by chemical dissolution. Finally, the spectra of the Cu nanoparticle arrays were measured by an integrating sphere spectrometer, where the scattered light could be collected by the integrating sphere. Then the absorption would be calculated. All of the chemicals used in the experiments were obtained from the Echo Chemical Co.

4. Results and Discussion

Analysis of the scanning electron microscope (SEM) images of nanochannel arrays grown through the traditional one-step and five-step processes and the MES AAO process was carried out. Figures 4(a)–4(d) show the nanochannel arrays produced after only 30 minutes of growth with the one-step process, with voltages of 120 V to 150 V. The positions

of the channels in the arrays thus grown are nonuniform, and the hole sizes are not orderly. It can be seen in Figures 4(e)–4(h) that the nanochannel arrays grown by the five-step process are more orderly than those grown with the one-step process, but the process took about 3 hours. Figures 4(i)–4(l) show the nanochannel arrays grown with the MES process at voltages of 120–150 V. The interpore distance of the nanochannel arrays increased following an increase in the bias voltage from 120 to 150 V. The hole sizes of the nanochannels produced during the five-step and MES processes were larger than those produced in the one-step AAO process. The interpore distance also increased slower with the MES process than with the five-step process, being similar to that obtained from the one-step AAO process, as can be seen in Figure 4. We compared the circularity obtained with the MES, one-step, and five-step AAO methods, as determined by (1). The distribution curves for the circularity are shown in Figure 5. Analysis shows that the highest peak in Figure 5 is obtained for a circularity of 0.85–0.9 obtained with 120–150 volts in MES. It was found that the circularity in the nanochannel arrays grown using the one-step AAO process (120–140 V) was less than 50% (ranging from 0.8 to 1.0) of that obtained with the five-step or MES methods. Using the MES AAO process, we were able to produce larger numbers of nanochannel arrays with good circularity at 120–150 V. Furthermore, the MES AAO process could grow more passable nanochannel arrays than with the one-step AAO process at 120–140 V. As a result, we could achieve a high ratio of circularity and uniform nanochannel arrays with

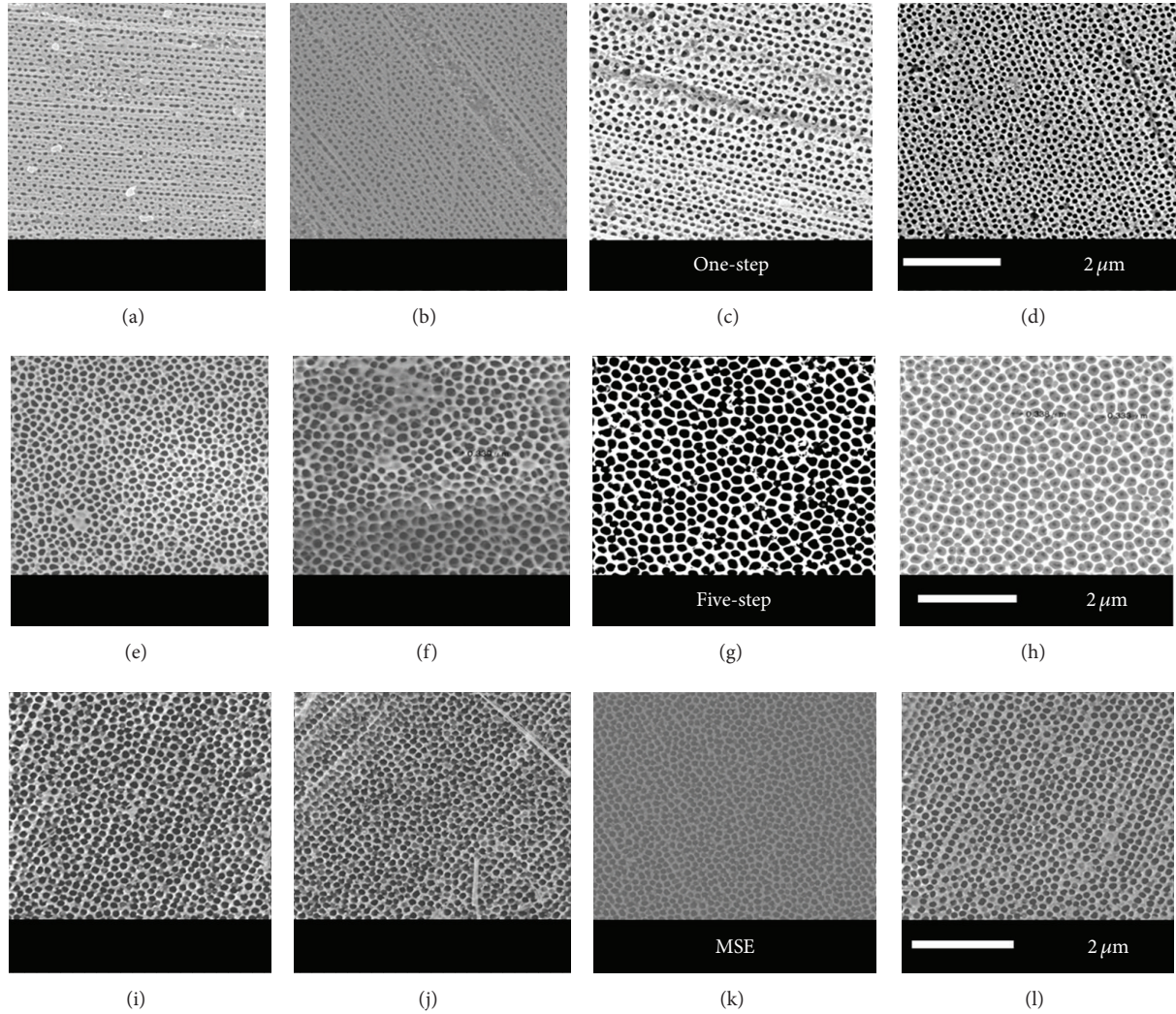


FIGURE 4: Nanochannel arrays grown with the one-step process at voltages of (a) 120, (b) 130, (c) 140, and (d) 150 V; five-step at voltages of (e) 120, (f) 130, (g) 140, and (h) 150 V; and the MES process at voltages of (i) 120, (j) 130, (k) 140, and (l) 150 V.

TABLE 1: The standard deviations and periods of nano-channel arrays produced at 120–150 V by the one-step, five-step, and MES processes.

Bias	One-step	Five-step	MES
120 V	202 ± 92 nm	213 ± 22 nm	233 ± 18 nm
130 V	232 ± 54 nm	282 ± 25 nm	256 ± 17 nm
140 V	261 ± 84 nm	332 ± 15 nm	292 ± 15 nm
150 V	280 ± 31 nm	358 ± 19 nm	312 ± 23 nm

the MES AAO process. In addition, the MES arrays had good circularity with a larger period compared to those obtained with the other methods, as can be seen (triangle dots) in Figure 1.

The Fast Fourier Transform (FFT) method was used to analyze the average period and the standard deviation of period which is the distance between the interpore centers. The positional shift for the one-step process was larger than

50 nm at 120–140 V, but less than 25 nm at 120–150 V for the five-step and MES processes, as shown in Figure 6. The results prove that the MES method was able to produce better periodic nanochannel arrays than the one-step method with a shorter growing time, allowing for a large-period design; see Figure 6. The average period for the one-step, five-step, and MES processes was also analyzed. In the five-step AAO process, the period increased slowly from 202 to 280 nm, then more quickly from 213 to 358 nm, while in the MES process the period increased from 233 to 312 nm, as shown in Table 1. This method had the advantage of increasing the period by repeating the growth steps. Figures 7(a) and 7(b) show Cu nanoparticle arrays with a 200 nm period grown on FTO glass by the electroplating process with the one-step and MES nanochannel processes. The diameters of the copper particles were between 100 and 150 nm with 120–150 volts in one-step and between 150 and 225 nm in MES process. We can find that the Cu nanoparticle array has better period and circularity in Figure 7(b) than in Figure 7(a). Figure 8

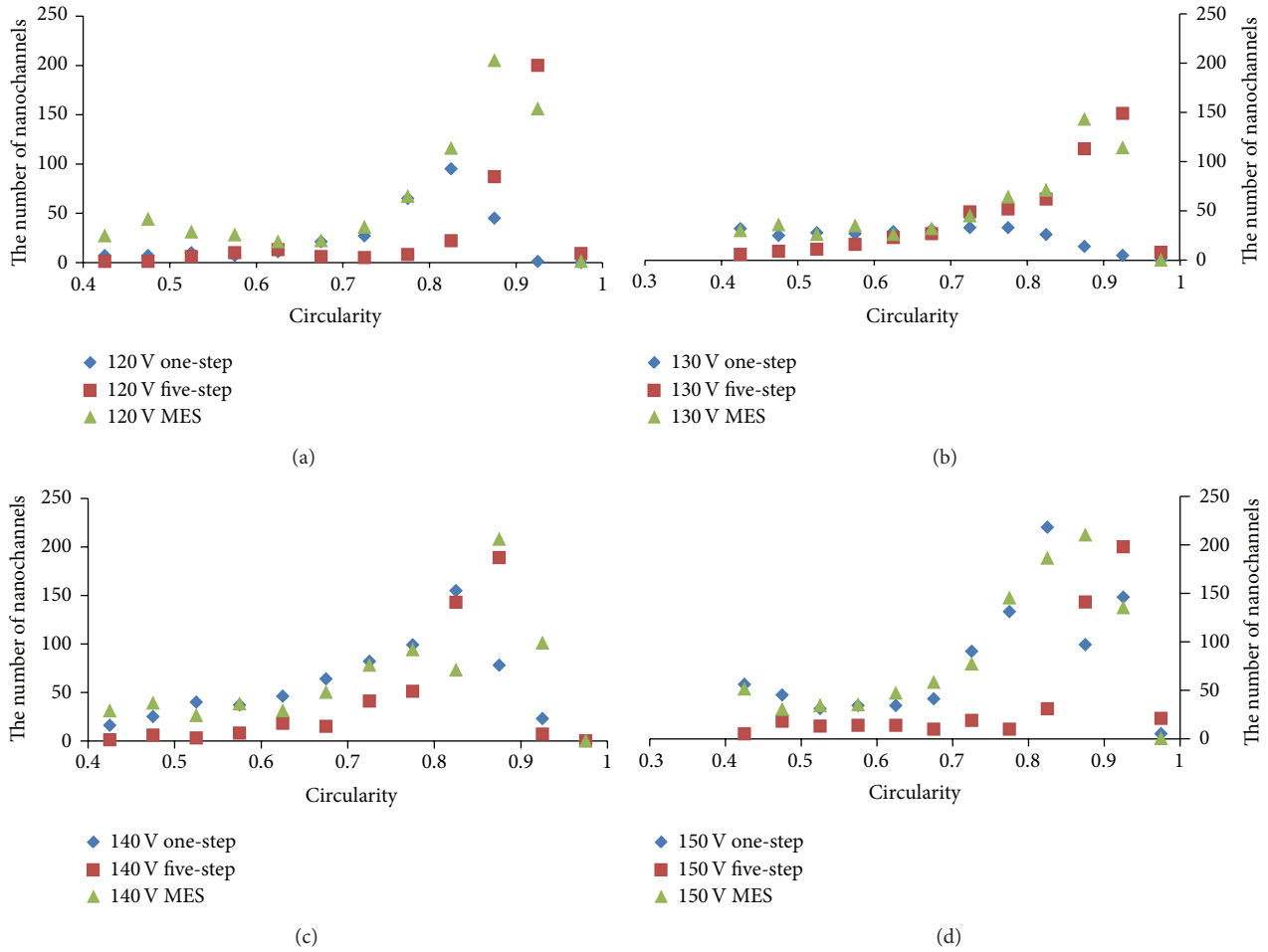


FIGURE 5: Circularity analysis for the one-step, five-step, and MES processes with 120–150 V.

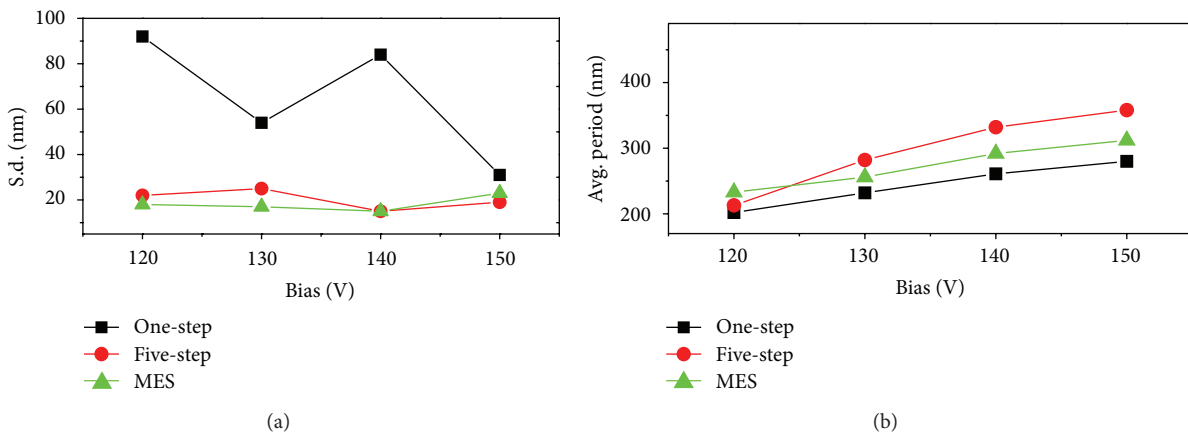


FIGURE 6: Average periods of AAO nanochannel arrays with a standard deviation (s.d.) at 120–150 V for the one-step, five-step, and MES AAO processes.

shows the absorption spectra of the Cu nanoparticle arrays grown with the one-step and the MES AAO processes. The results show that the SPR absorption from 550 nm to 750 nm is stronger for the arrays produced with the MES process than with the one-step process.

5. Conclusion

This study proves that more orderly periodic nanochannel arrays can be produced with an MES process combining two electrolytes of phosphoric acid and oxalic acid. The analysis

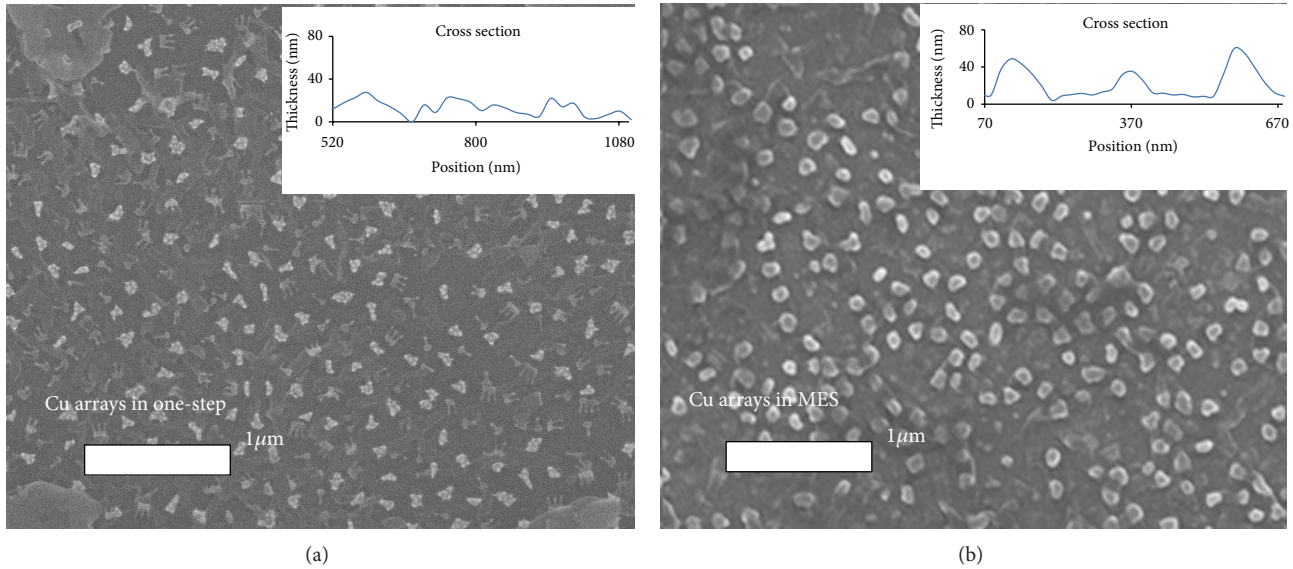


FIGURE 7: Cu nanoparticle arrays with a 200 nm period produced with (a) the one-step and (b) with MES AAO processes.

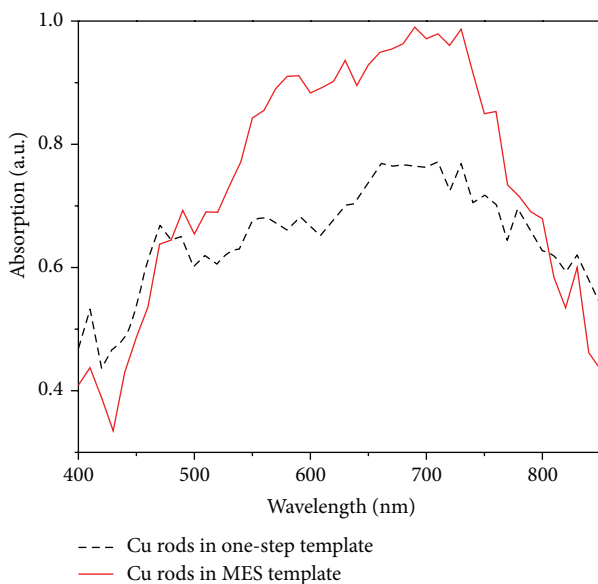


FIGURE 8: Absorption spectra for the Cu nanoparticle arrays produced by the MES and one-step AAO processes.

shows better circularity of 0.85–0.9 with 120–150 V in the MES process, with a standard deviation of the average period of less than 25 nm. The advance in the development of orderly nanochannel arrays with the MES method is similar to that achieved with the longer five-step process. Finally, Cu nanoparticle arrays with a period of 200 nm were grown in AAO templates on FTO glass using the MES process. The SPR absorption ranged from 550 nm to 750 nm, stronger than with the one-step process.

Acknowledgment

The authors would like to thank the National Science Council of Taiwan for their financial support of this research under

Contract nos. NSC 101-2221-E-008-052 and 101-3113-P-008-009.

References

- [1] S. Linic, P. Christopher, and D. B. Ingram, "Plasmonic-metal nanostructures for efficient conversion of solar to chemical energy," *Nature Materials*, vol. 10, no. 12, pp. 911–921, 2011.
- [2] J. F. Sanchez-Ramírez, "Preparation and optical absorption of colloidal dispersion of Au/Cu nanoparticles," *Superficies Y Vacio*, vol. 15, pp. 16–18, 2002.
- [3] B. Ding, B. J. Lee, M. Yang, H. S. Jung, and J. K. Lee, "Surface-Plasmon Assisted Energy Conversion in Dye-Sensitized Solar Cells," *Advanced Energy Materials*, vol. 1, no. 3, pp. 415–421, 2011.
- [4] R.-L. Zong, J. Zhou, B. Li, M. Fu, S.-K. Shi, and L.-T. Li, "Optical properties of transparent copper nanorod and nanowire arrays embedded in anodic alumina oxide," *Journal of Chemical Physics*, vol. 123, no. 9, Article ID 094710, 2005.
- [5] Y. Zhang, W. Xu, S. Xu, G. Fei, Y. Xiao, and J. Hu, "Optical properties of Ni and Cu nanowire arrays and Ni/Cu superlattice nanowire arrays," *Nanoscale Research Letters*, vol. 7, no. 1, p. 569, 2012.
- [6] C.-K. Chung, T. Y. Liu, and W. T. Chang, "Effect of oxalic acid concentration on the formation of anodic aluminum oxide using pulse anodization at room temperature," *Microsystem Technologies*, vol. 16, no. 8-9, pp. 1451–1456, 2010.
- [7] C. Y. Han, G. A. Willing, Z. Xiao, and H. H. Wang, "Control of the anodic aluminum oxide barrier layer opening process by wet chemical etching," *Langmuir*, vol. 23, no. 3, pp. 1564–1568, 2007.
- [8] Y. Jia, H. Zhou, P. Luo, S. Luo, J. Chen, and Y. Kuang, "Preparation and characteristics of well-aligned macroporous films on aluminum by high voltage anodization in mixed acid," *Surface and Coatings Technology*, vol. 201, no. 3-4, pp. 513–518, 2006.
- [9] S. Shingubara, K. Morimoto, H. Sakaue, and T. Takahagi, "Self-organization of a porous alumina nanohole array using a sulfuric/oxalic acid mixture as electrolyte," *Electrochemical and Solid-State Letters*, vol. 7, no. 3, pp. E15–E17, 2004.

- [10] C. Y. Liu, A. Datta, and Y. L. Wang, "Ordered anodic alumina nanochannels on focused-ion-beam-prepatterned aluminum surfaces," *Applied Physics Letters*, vol. 78, no. 1, pp. 120–122, 2001.
- [11] S. Shingubara, Y. Murakami, K. Morimoto, and T. Takahagi, "Formation of aluminum nanodot array by combination of nanoindentation and anodic oxidation of aluminum," *Surface Science*, vol. 532–535, pp. 317–323, 2003.
- [12] S. H. Chan, C. K. Chen, S. Z. Tseng, C. H. Hsu, and W. H. Cho, "Atomic layer deposition of aluminum-doped zinc oxide films for the light harvesting enhancement of a nanostructured silicon solar cell," *The Journal of Vacuum Science and Technology A*, vol. 31, no. 1, pp. 01A125–01A128, 2013.
- [13] C. K. Chen, Y. C. Huang, C. C. Lee, and S. H. Chen, "Omnidirectional reflectors for UV LED using symmetric autocloning method," *Optical Review*, vol. 20, no. 2, pp. 141–144, 2013.
- [14] I. Cavarretta, C. O'Sullivan, and M. R. Coop, "Applying 2D shape analysis techniques to granular materials with 3D particle geometries," in *Proceedings of the 6th International Conference on Micromechanics of Granular Media, Powders and Grains 2009*, pp. 833–836, July 2009.
- [15] A. P. Z. Stevenson, D. B. Bea, S. Civit, S. A. Contera, A. I. Cerveto, and S. Trigueros, "Three strategies to stabilise nearly monodispersed silver nanoparticles in aqueous solution," *Nanoscale Research Letters*, vol. 7, pp. 151–158, 2012.
- [16] O. Sanz, F. J. Echave, J. A. Odriozola, and M. Montes, "Aluminum anodization in oxalic acid: controlling the texture of $\text{Al}_2\text{O}_3/\text{Al}$ monoliths for catalytic applications," *Industrial and Engineering Chemistry Research*, vol. 50, no. 4, pp. 2117–2125, 2011.
- [17] A. Belwalkar, E. Grasing, W. Van Geertruyden, Z. Huang, and W. Z. Misiolek, "Effect of processing parameters on pore structure and thickness of anodic aluminum oxide (AAO) tubular membranes," *Journal of Membrane Science*, vol. 319, no. 1–2, pp. 192–198, 2008.
- [18] K. Ersching, E. Dorico, R. C. da Silva et al., "Surface and interface characterization of nanoporous alumina templates produced in oxalic acid and submitted to etching procedures," *Materials Chemistry and Physics*, vol. 137, pp. 140–146, 2012.
- [19] A. P. Li, F. Muller, A. Birner, K. Nielsch, and U. Gösele, "Fabrication and microstructuring of hexagonally ordered two-dimensional nanopore arrays in anodic alumina," *Advanced Materials*, vol. 11, no. 6, pp. 483–487, 1999.
- [20] H. Masuda, H. Yamada, M. Satoh, H. Asoh, M. Nakao, and T. Tamamura, "Highly ordered nanochannel-array architecture in anodic alumina," *Applied Physics Letters*, vol. 71, no. 19, pp. 10–12, 1997.
- [21] A. P. Li, F. Müller, and U. Gösele, "Polycrystalline and monocrystalline pore arrays with large interpore distance in anodic alumina," *Electrochemical and Solid-State Letters*, vol. 3, no. 3, pp. 131–134, 2000.
- [22] B. Yu, Y. Gao, and H. Li, "Fabrication and optical characterization of poly(2,5-di-n-butoxyphenylene) nanofibril arrays," *Journal of Applied Polymer Science*, vol. 91, no. 1, pp. 425–430, 2004.
- [23] K.-L. Lai, M.-H. Hon, and I.-C. Leu, "Fabrication of ordered nanoporous anodic alumina prepatterened by mold-assisted chemical etching," *Nanoscale Research Letters*, vol. 6, pp. 157–162, 2011.
- [24] A. Nourmohammadi, S. J. Asadabadi, M. H. Yousefi, and M. Ghasemzadeh, "Photoluminescence mission of nanoporous anodic aluminum oxide films prepared in phosphoric acid," *Nanoscale Research Letters*, vol. 7, pp. 689–695, 2012.
- [25] C.-G. Kuo and C.-C. Chen, "Technique for self-assembly of tin nano-particles on anodic aluminum oxide (AAO) templates," *Materials Transactions*, vol. 50, no. 5, pp. 1102–1104, 2009.
- [26] W. Chen, J.-S. Wu, and X.-H. Xia, "Porous anodic alumina with continuously manipulated pore/cell size," *ACS Nano*, vol. 2, no. 5, pp. 959–965, 2008.
- [27] L. Zaraska, G. D. Sulka, and M. Jaskua, "Properties of nanostructures obtained by anodization of aluminum in phosphoric acid at moderate potentials," *Journal of Physics: Conference Series*, vol. 146, Article ID 012020, pp. 012020–012026, 2009.
- [28] V. P. Parkhutik and V. I. Shershulsky, "Theoretical modelling of porous oxide growth on aluminum," *Journal of Physics D*, vol. 25, pp. 1258–1263, 1992.
- [29] J. E. Houser and K. R. Hebert, "Modeling the potential distribution in porous anodic alumina films during steady-state growth," *Journal of the Electrochemical Society*, vol. 153, no. 12, Article ID 078612JES, pp. B566–B573, 2006.
- [30] H. Chen, D. S. Chan, C. K. Chen, T. H. Chang, Y. H. Lai, and C. C. Lee, "Nanoimprinting pre-patterned effects on anodic aluminum oxide," *Japanese Journal of Applied Physics*, vol. 49, no. 1, pp. 015201–015204, 2010.

Research Article

Evaluation of the Antitumor Activity by Ni Nanoparticles with Verbascoside

Mingyue Chen,¹ Yaqin Zhang,² Bin Huang,³ Xueming Yang,⁴ Yunong Wu,⁴ Bin Liu,⁵ Yi Yuan,⁴ and Gen Zhang⁶

¹ Department of Biomedical Engineering, School of Kangda, Nanjing Medical University, Nanjing 210029, China

² Department of Biochemical Molecular, School of Basic Medical Sciences, Nanjing Medical University, Nanjing 210029, China

³ Department of Radiology, Nanjing Brain Hospital, Nanjing Medical University, Nanjing 210009, China

⁴ Institute of Stomatology, Nanjing Medical University, Nanjing 210029, China

⁵ Department of Biomedical Engineering, School of Basic Medical Sciences, Nanjing Medical University, Nanjing 210029, China

⁶ Department of Cell Biology, School of Basic Medical Sciences, Nanjing Medical University, Nanjing 210029, China

Correspondence should be addressed to Yi Yuan; xpywyw@126.com and Gen Zhang; zhanggen123@126.com

Received 1 September 2013; Revised 25 October 2013; Accepted 4 November 2013

Academic Editor: Mengnan Qu

Copyright © 2013 Mingyue Chen et al. This is an open access article distributed under the Creative Commons Attribution License, which permits unrestricted use, distribution, and reproduction in any medium, provided the original work is properly cited.

Verbascoside (VB) has attracted a great deal of attention due to ITS pharmacological properties. In our study, we synthesized a multifunctional verbascoside coated Ni nanoparticles (VB-Ni). Transmission electron microscopy (TEM) and high performance liquid chromatography (HPLC) display the characteristics of VB-Ni nanoparticles. Compared with VB, VB-Ni has been proven to induce apoptosis and resist the growth of doxorubicin-resistant K562 cells *in vitro* and *in vivo*. Thus, VB-Ni nanoparticles can be thought of as an ideal mode of cancer treatment.

1. Introduction

Cancer is quickly becoming the leading cause of death worldwide [1]. Nickel nanoparticles (Ni NPs) have been applied in a wide range of fields due to their unique structure and properties [2–6]. Over the past decades, nanoparticles have been increasingly applied in clinical diagnoses and cancer therapy with promising and far-ranging prospects in the medical fields. Increasing interest in the application of nanotechnology for cancer therapy has been noted [7–10]. Previous phytochemical studies have demonstrated that flavonoids and phenylpropanoid glycosides are major bioactive constituents of the Tsoong herb (Chinese name: Banchunmaxianhao, BCM) [11]. Among these constituents, VB has attracted a great deal of attention due to its pharmacological properties [12–17]. Its properties include hepatoprotective, anti-inflammatory, antitumor, cytotoxic, and antioxidant activities [18–20].

In recent years, many studies on the therapeutic effect of drug-loaded nanoparticles have become a hot spot

[21, 22]. Based on the above considerations, we have verified the biological effects of VB-Ni nanoparticles on treating cancer cells [23, 24]. These observations indicate their great potential in clinical and biomedical applications.

2. Materials and Methods

2.1. Materials. BCM were collected from Gangcha, Qinghai, China, and identified by Professor Li-Juan Mei (Northwest Institute of Plateau Biology, Chinese Academy of Sciences). Materials used for HPLC analysis were of analytical grade.

2.2. Cell Culture. K562 cells were purchased from Tianjin Institute of Hematology and cultured in Dulbecco's Modification of Eagle's Medium (DMEM) supplemented with 10% FBS (GIBCO) and penicillin (100 U/mL)/streptomycin (100 mg/mL) at 37°C in a 5% CO₂, water-saturated atmosphere. To test the function of VB-Ni, VB-Ni, or VB was added to K562 cells in the same concentration. Cells were

observed by microscope after 48 or 72 h treatment, using DNA Ladder to detect the apoptosis of cells.

2.3. Extract VB from BCM Plant. BCM (500 g) were powdered and extracted three times with 70% EtOH under reflux. After concentration under vacuum, the residues were suspended in distilled water and extracted with light petroleum, EtOAc, and n-butanol, respectively. The n-butanol solutions were evaporated to dryness under vacuum at 70 °C to generate n-butanol extract, which was loaded on silica gel column and eluted with various proportions of a mixture of chloroform : methanol. The chloroform : methanol (3 : 1) fraction was concentrated to produce crude sample for subsequent high-speed counter-current chromatography (HSCCC) isolation and purification. With a two-phase solvent system composed of chloroform : n-butanol : methanol : water (4 : 3 : 4 : 5, v/v), the crude sample was separated to yield VB.

2.4. Preparation of Drug-Loaded Ni Nanoparticle. We mixed 2 mg VB and 30 mg Ni nanoparticles with ddH₂O in nitrogen environment. Then, we separated the final product from the mixture solution by magnet, washed them for three times, and added 300 mL distilled water to suspend. Finally, VB-Ni nanoparticles were measured by transmission electron microscope (TEM).

2.5. DNA Fragmentation Assay. K562 cells were incubated with VB, Ni, or VB-Ni for 24 h, 48 h, and 72 h, respectively. The untreated cells served as controls. DNA was extracted from K562 cells using Apoptotic DNA ladder isolation kit (Yuan Ping Hao Biotechnology Co., Ltd, Beijing, China), and then loaded onto 1% agarose gel. The DNA ladders stained with ethidium bromide were visualized under UV light.

2.6. Acridine Orange/Ethidium Bromide (AO/EB) Staining to Detect Apoptosis. K562 cells were incubated with VB-Ni for 48 h or 72 h. To stain apoptotic cells, the cells were trypsinized for 5 min before adding 1 μ L of AO/EB dye mixture (100 μ g/mL acridine orange and 100 μ g/mL ethidium bromide) to each well. Then, cells were viewed under the fluorescent light microscope.

2.7. Experimental Animals. The female mice (6-week old) were purchased from the Animal Feeding Farm of National Institute for the Control of Pharmaceutical and Biological Products (China). All K562 tumor C57 mice were housed in the animal facility, and animal experiments, (1) control ($n = 3$), (2) VB ($n = 5$), (3) VB-Ni plus a magnet fixed under skin close to the tumor site ($n = 5$), that were conducted followed the guidelines by the Animal Research Ethics Board of Nanjing Medical University. Animals were kept in the facility with free access to food and water. Injection was intravenously administered by tail vein at days 0, 2, 4, 6, 8, 10, 12, 14, 16, and 18. The tumor volume of mice was measured and calculated at the 20th day after treatment. The tumor volume

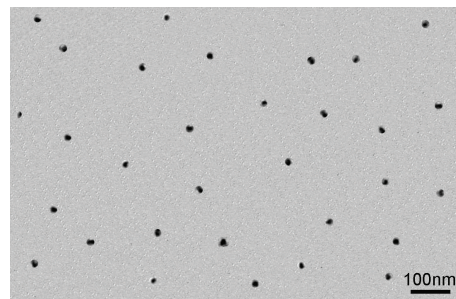


FIGURE 1: TEM images of VB-Ni nanoparticle. TEM image of an individual nanocrystal of VB-Ni.

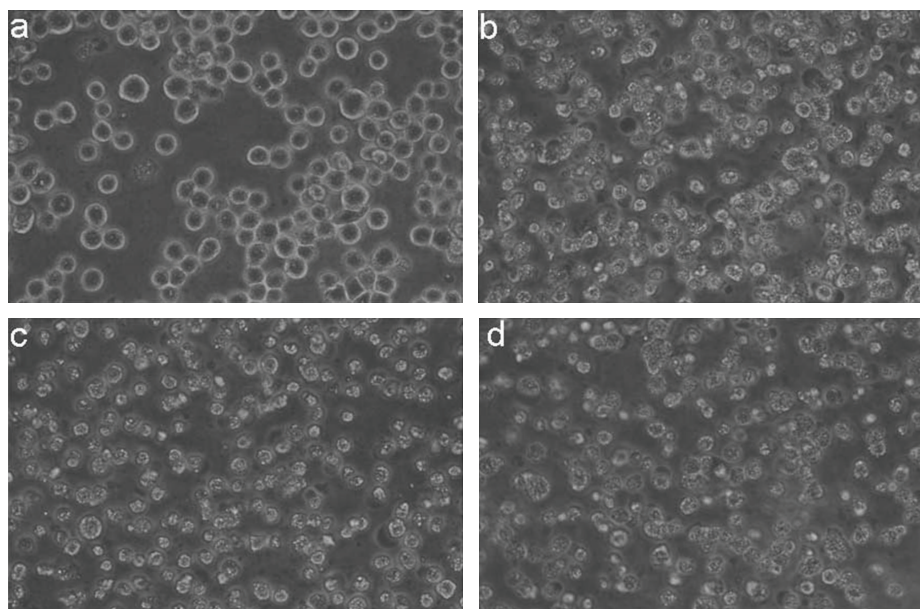
calculation was performed using the formula $(\pi \times \text{long axis} \times \text{short axis} \times \text{short axis})/6$.

3. Results

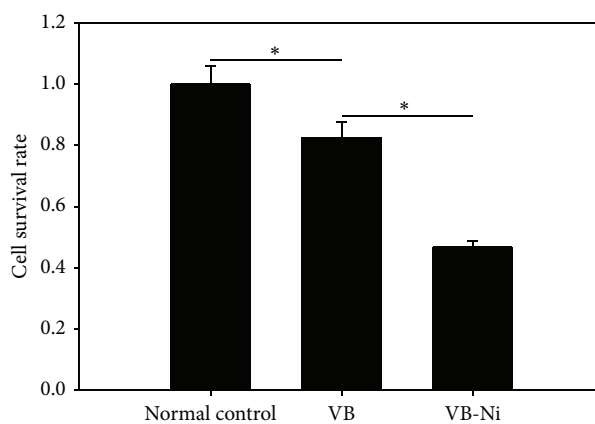
3.1. Synthesis and Characterization of VB-Ni Nanoparticles. In our previous study, the structure of VB has been identified and synthesized through HPLC analysis. And the NMR data of VB was in agreement with published data [25]. Herein, we further measured the size of VB-Ni nanoparticle, which was synthesized successfully by mixed 2 mg VB with 30 mg Ni in solution. As shown in Figure 1, the average diameter of VB-Ni nanoparticle was about 10 nm in TEM image. The size of VB-Ni nanoparticles was about 15 nm in cell culture medium through particle sizer analysis, which was relatively uniform and stable (unpublished data).

3.2. The Effects of VB-Ni in Recipient K562 Cells. Many researchers including us have reported that VB components can increase the apoptosis and inhibit the growth of cancer cells *in vitro* and *in vivo* [26]. As a new nanoparticle, we also determined the effect of VB-Ni in doxorubicin-resistant K562 cells. Firstly, K562 cells were incubated for 24 hours with the same concentration of VB and VB-Ni. We found that the apoptosis level was higher in VB-Ni group than VB group (Figures 2(A), 2(b), and (c)). However, to study the relationship between time and the enhanced effect of apoptosis in K562 cells, we treated the cells with VB-Ni at different time points. We further detected the apoptosis level of K562 cells after treatment of VB-Ni. The result demonstrated that the apoptosis rate of K562 cells was further enhanced after 72 h treatment than 24 h (Figures 2(A) and (d)). Consistent with our hypothesis, VB-Ni was effective to increase the apoptosis of cancer cells. Besides, we observed a similar inhibitory effect of VB-Ni on viability or survival in K562 cells through MTT assay (Figure 2(B)).

3.3. Fluorescence Microscopic Assay of Apoptosis in K562 Cells. In order to further determine the apoptosis effect of VB-Ni, next, we treated K562 cells with VB-Ni. Using AO/EB staining for apoptotic cells, apoptotic nuclei were identified by their characteristic features such as chromosomal condensation, distinctively margined, and fragmented under fluorescence



(A)



(B)

FIGURE 2: The effects of VB-Ni in recipient K562 cells. (A) K562 cells were treated with or without VB-Ni, VB for 48 h or 72 h, and then observed under microscopy. (a) Microscopy image of normal K562 cells. (b) K562 cells were treated with VB for 48 h. (c) K562 cells were treated with VB-Ni for 48 h. (d) K562 cells were treated with VB-Ni for 72 h. (scale bar = 100 nm). (B) MTT measurement of cellular survival in K562 cells treated with VB or VB-Ni.

microscope. We found that the apoptotic nuclei in K562 cells treatment with VB-Ni (Figures 3(c) and 3(d)) were emerged compared with normal control (Figures 3(a) and 3(b)).

3.4. DNA Fragmentation Experiments. To figure out whether the cell growth inhibition was caused by the apoptotic response, the DNA fragmentations were examined by agarose gel electrophoresis. When K562 cells were treated with VB-Ni or VB (Figure 4), the intensity of fragmented chromosomal DNA bands was much higher than that observed from cells untreated (Figure 4, lanes 1 and 2, resp.) in a fixed time interval (i.e., 24 h (a), 48 h (b), and 72 h (c)). The formation of DNA ladders was clearly present after treatment with VB-Ni (Figure 4, lane 1) but was only weakly discernible when the cells were treated with VB (Figure 4, lane 2). Our

observations support the hypothesis that the remarkable enhancement of apoptosis was induced by the synergistic effect of VB-Ni nanoparticles on K562 cells.

3.5. VB-Ni Inhibits the Tumor Growth In Vivo. We next tested whether delivery of VB-Ni can efficiently suppress the implanted tumor growth in mice. In this experiment, C57 mice were subcutaneously implanted with K562 tumor cells. Mice were intravenously injected with different reagents every other day. After 20 days, the treatment with VB-Ni effectively reduced the volume (Figures 5(a) and 5(b)) or weight (Figure 5(c)) of the implanted tumors compared with VB-treated control. These data strongly suggest that the VB-Ni can transfer Ni into the mouse implanted tumor cells, in

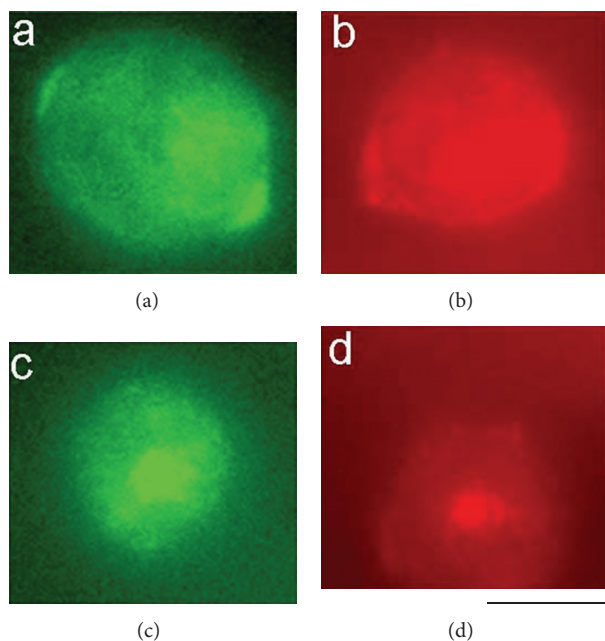


FIGURE 3: Fluorescence detection of the apoptosis of K562 cell. Detect the normal and apoptotic K562 cells by Acridine orange/ethidium bromide (AO/EB) staining. (a) Early apoptotic nuclei of normal control K562 cells were observed. (b) Later apoptotic nuclei of normal control K562 cells were observed. (c) Early apoptotic nuclei of treatment K562 cells with VB-Ni were observed. (d) Later apoptotic nuclei of treatment K562 cells with VB-Ni were observed (400x). (bar = 10 μm).

which Ni with VB suppresses the tumor cell growth (plus a magnet fixed under skin close to the tumor site).

4. Discussion

In this study, we demonstrated that a combination of verbascoiside (VB) and Ni where the VB is bound to Ni surface by electrostatic interaction will suppress the growth of tumor cells. Compared with VB-Ni, the same or even higher concentration of VB did not cause a significant reduction in cell viability in K562 cells. However, when K562 cells were treated with VB-Ni, we observed a remarkable enhancement of cell growth inhibition (Figure 2). The results strongly suggest that the VB-Ni nanoparticles can induce cell growth inhibition of K562 cell *in vitro*.

Two major types of cell death are recognized: apoptosis and necrosis [27]. Apoptosis is a regulated process that can be triggered by different stimuli and is mediated by a cascade of enzymes. Necrosis is a catastrophic form of cell death which does not involve the regulated action of enzymes. Studies have demonstrated that the presence of smaller DNA fragments is believed to reflect the release of nucleosomes from apoptotic cells and higher molecular weight DNA molecules are believed to reflect release from necrotic cells. Apoptosis results in fragmentation of cells into apoptotic bodies which are engulfed by neighboring cells and macrophages. However, uptake of necrotic cells

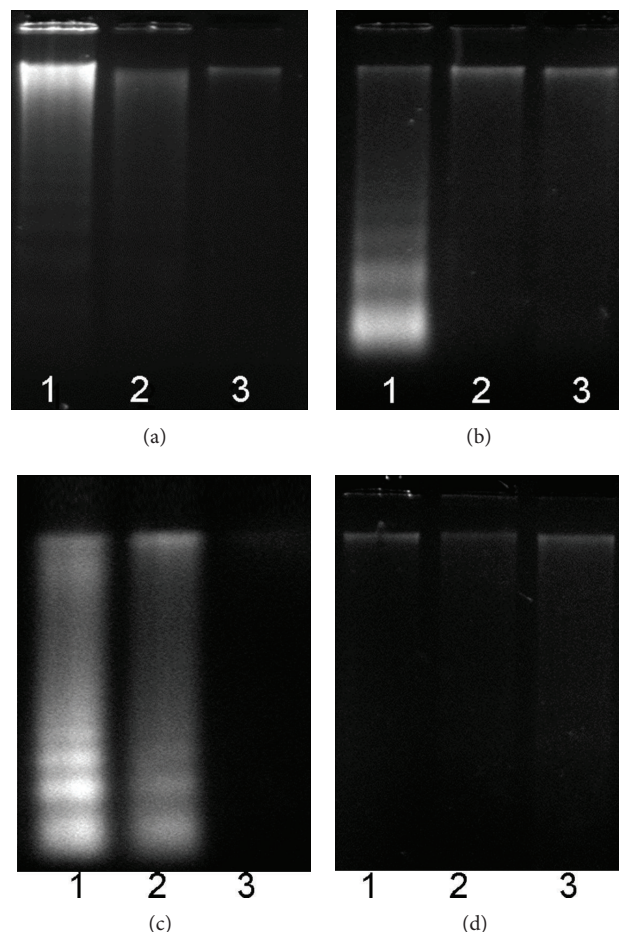
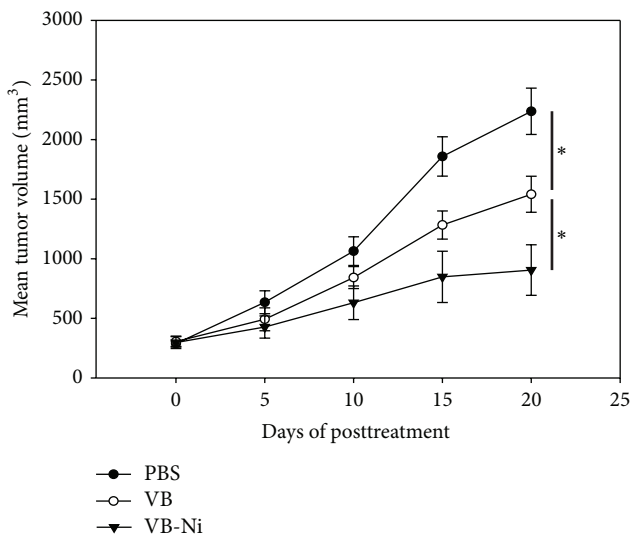


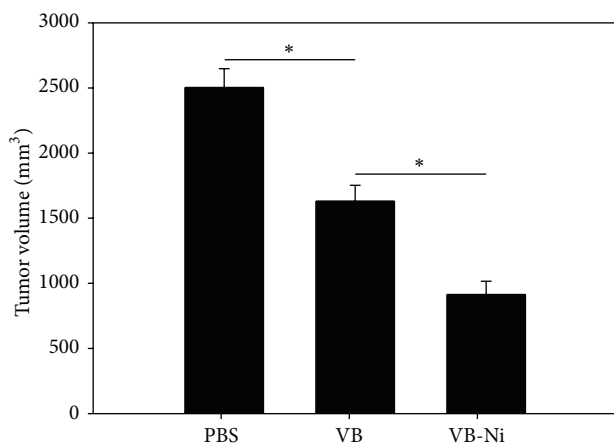
FIGURE 4: DNA fragmentation in K562 cells after different treatments. Genomic DNA was extracted from K562 cells treated with various reagents using Apoptotic DNA ladder isolation kit and then loaded onto 1% agarose gel. Then, DNA ladders were visualized under UV light with ethidium bromide staining. (a) K562 cells were treated with VB-Ni (lane 1), VB (lane 2), or control (lane 3) treatment for 24 h. (b) K562 cells were treated with VB-Ni (lane 1), VB (lane 2), or control (lane 3) treatment for 48 h. (c) K562 cells were treated with VB-Ni (lane 1), VB (lane 2), or control (lane 3) treatment for 72 h. (d) Normal K562 cells.

has been reported to be less efficient than phagocytosis of apoptotic cells. So active anticancer drugs which induce apoptosis in malignant cells should be a main way to clinical antitumor. Interestingly, we found that VB-Ni can induce K562 cell apoptosis with a rate significantly higher than that of VB, or Ni alone treatment *in vitro*. Moreover, we analyzed the cells apoptosis morphology from various assays, nuclei staining. When cells were treated with VB-Ni, they exhibited characteristic morphological features of apoptosis, such as chromosomal condensation and DNA fragment.

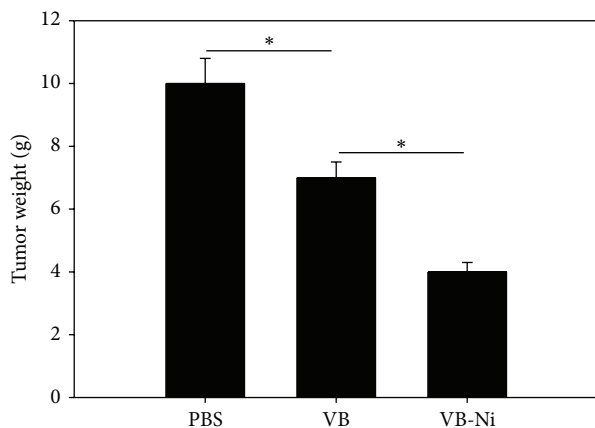
As the above results illustrated, we recognized the evidence of apoptosis of cancer cells *in vitro*. It is possible that VB-Ni could play a critical role in inducing apoptosis *in vivo*. The tumor growth in group 3 mice (treated with VB-Ni) (Figure 5(b)) was suppressed most efficiently.



(a)



(b)



(c)

FIGURE 5: Inhibit the tumor growth in K652/ADM mice with VB-Ni treatments. (a) and (b) Tumor volumes in mice treated with various reagents. Cancer cells were injected into the abdominal area of mice (plus a magnet fixed under skin close to the tumor site). When the tumors reached a minimal size of 300 mm³, mice were divided to 3 groups with 3–5 mice in each group. The mouse groups received various reagents every other day by tail-vein injections. (c) The weight of tumor in (a).

5. Conclusion

In summary, in the current study, we have investigated the synergistic effect of Ni with the anticancer drug verbascoide (VB) on the induction of apoptosis of K562 cell. Our observations demonstrate that Ni readily facilitated the uptake of the VB into K562 cells by electrochemical assay. Apoptotic staining and DNA fragmentation further demonstrate that treatment of VB-Ni can clearly activate apoptosis in K562 cells. Moreover, our *in vivo* study indicates that the treatment of VB-Ni effectively inhibited the mice tumor growth. The increased cell apoptosis rate was closely correlated with the enhanced inhibition of tumor growth in the studied animals (plus a magnet fixed under skin close to the tumor site). Thus, VB-Ni may serve as a novel strategy to sensitively track the respective cancer cells for efficient cancer chemotherapy.

Authors' Contribution

Mingyue Chen, Yaqin Zhang, and Bin Huang contributed equally to this work.

Acknowledgments

This research was financially supported by the Priority Academic Program for the Development of Jiangsu Higher Education Institutions (JX10531801/005), Medical Science and Technology Foundation of Jiangsu, Department of Health (Z201008), NSFC (31201003), Funding from the State Key Laboratory of Bioelectronics of Southeast University, Nanjing Medical University Science and Technology Development Fund (KY1011431121612218 and KY1011431121612230), and Science and Technology Innovation Supporting Fund (JX10131801147, JX10131801149, and JX10131801154).

References

- [1] G. Zhang, X. Zeng, H. L. Yue, P. Li, and X. H. Zhao, "Evaluation of the antitumor activity by cdte qds with verbascoide," *Nano*, vol. 08, no. 03, Article ID 1350031, 2013.
- [2] S. Yu, G. Wu, X. Gu et al., "Magnetic and pH-sensitive nanoparticles for antitumor drug delivery," *Colloids and Surfaces B*, vol. 103, pp. 15–22, 2013.
- [3] M. Bououdina, S. Rashdan, J. L. Bobet, and Y. Ichiyanagi, "Nanomaterials for biomedical applications: synthesis, characterization, and applications," *Journal of Nanomaterials*, vol. 2013, Article ID 962384, 4 pages, 2013.
- [4] S. Li, Z. Niu, X. Zhong et al., "Fabrication of magnetic Ni nanoparticles functionalized water-soluble graphene sheets nanocomposites as sorbent for aromatic compounds removal," *Journal of Hazardous Materials*, vol. 229–230, pp. 42–47, 2012.
- [5] S. Larumbe, C. Gomez-Polo, J. I. Perez-Landazabal et al., "Ni doped Fe₃O₄ magnetic nanoparticles," *Journal of Nanoscience and Nanotechnology*, vol. 12, no. 3, pp. 2652–2660, 2012.
- [6] G. Zhang, X. Zeng, and P. Li, "Nanomaterials in cancer-therapy drug delivery system," *Journal of Biomedical Nanotechnology*, vol. 9, no. 5, pp. 741–750, 2013.
- [7] D. Guo, C. Wu, X. Li, H. Jiang, X. Wang, and B. Chen, "In vitro cellular uptake and cytotoxic effect of functionalized nickel

- nanoparticles on leukemia cancer cells," *Journal of Nanoscience and Nanotechnology*, vol. 8, no. 5, pp. 2301–2307, 2008.
- [8] J. Li, C. Wu, Y. Dai et al., "Doxorubicin-CdS nanoparticles: a potential anticancer agent for enhancing the drug uptake of cancer cells," *Journal of Nanoscience and Nanotechnology*, vol. 7, no. 2, pp. 435–439, 2007.
- [9] I. Brigger, C. Dubernet, and P. Couvreur, "Nanoparticles in cancer therapy and diagnosis," *Advanced Drug Delivery Reviews*, vol. 54, no. 5, pp. 631–651, 2002.
- [10] Z. Q. Yu, R. M. Schmaltz, T. C. Bozeman et al., "Selective tumor cell targeting by the disaccharide moiety of bleomycin," *Journal of the American Chemical Society*, vol. 135, no. 8, pp. 2883–2886, 2013.
- [11] Y. Cui, Q. Wei, H. Park, and C. M. Lieber, "Nanowire nanosensors for highly sensitive and selective detection of biological and chemical species," *Science*, vol. 293, no. 5533, pp. 1289–1292, 2001.
- [12] S. A. Schonbichler, L. K. Bittner, J. D. Pallua et al., "Simultaneous quantification of verbenalin and verbascoside in *Verbena officinalis* by ATR-IR and NIR spectroscopy," *Journal of Pharmaceutical and Biomedical Analysis*, vol. 84, pp. 97–102, 2013.
- [13] L. Speranza, S. Franceschelli, M. Pesce et al., "Antiinflammatory effects in THP-1 cells treated with verbascoside," *Phytotherapy Research*, vol. 24, no. 9, pp. 1398–1404, 2010.
- [14] L. Funes, O. Laporta, M. Cerdán-Calero, and V. Micol, "Effects of verbascoside, a phenylpropanoid glycoside from lemon verbena, on phospholipid model membranes," *Chemistry and Physics of Lipids*, vol. 163, no. 2, pp. 190–199, 2010.
- [15] A. Santoro, G. Bianco, P. Picerno et al., "Verminoside- and verbascoside-induced genotoxicity on human lymphocytes: involvement of PARP-1 and p53 proteins," *Toxicology Letters*, vol. 178, no. 2, pp. 71–76, 2008.
- [16] C. Zhao, G. Dodin, C. Yuan et al., "'In vitro' protection of DNA from Fenton reaction by plant polyphenol verbascoside," *Biochimica et Biophysica Acta*, vol. 1723, no. 1–3, pp. 114–123, 2005.
- [17] Y. Shi, W. Wang, Y. Shi et al., "Fast repair of dAMP hydroxyl radical adduct by verbascoside via electron transfer," *Science in China C*, vol. 42, no. 6, pp. 626–627, 1999.
- [18] C. Zhang, N. Awasthi, M. A. Schwarz, S. Hinz, and R. E. Schwarz, "Superior antitumor activity of nanoparticle albumin-bound paclitaxel in experimental gastric cancer," *PLoS ONE*, vol. 8, no. 2, Article ID e58037, 2013.
- [19] S. Xin, X. Li, Y. Zhu et al., "Nanofibrous mats coated by homocharged biopolymer-layered silicate nanoparticles and their antitumor activity," *Colloids and Surfaces B*, vol. 105, pp. 137–143, 2013.
- [20] A. F. Ourique, S. Azoubel, C. V. Ferreira et al., "Lipid-core nanocapsules as a nanomedicine for parenteral administration of tretinoin: development and in vitro antitumor activity on human myeloid leukaemia cells," *Journal of biomedical nanotechnology*, vol. 6, no. 3, pp. 214–223, 2010.
- [21] M. H. El-Dakdouki, E. Pure, and X. Huang, "Development of drug loaded nanoparticles for tumor targeting. Part 2: enhancement of tumor penetration through receptor mediated transcytosis in 3D tumor models," *Nanoscale*, vol. 5, no. 9, pp. 3904–3911, 2013.
- [22] B. Auffinger, R. Morshed, A. Tobias, Y. Cheng, A. U. Ahmed, and M. S. Lesniak, "Drug-loaded nanoparticle systems and adult stem cells: a potential marriage for the treatment of malignant glioma?" *Oncotarget*, vol. 4, no. 3, pp. 378–396, 2013.
- [23] B. Behl, I. Papageorgiou, C. Brown et al., "Biological effects of cobalt-chromium nanoparticles and ions on dural fibroblasts and dural epithelial cells," *Biomaterials*, vol. 34, no. 14, pp. 3547–3558, 2013.
- [24] D. Fourches, D. Pu, and A. Tropsha, "Exploring quantitative nanostructure-activity relationships (QNAR) modeling as a tool for predicting biological effects of manufactured nanoparticles," *Combinatorial Chemistry and High Throughput Screening*, vol. 14, no. 3, pp. 217–225, 2011.
- [25] C. Andary, R. Wylde, C. Laffite, G. Privat, and F. Winternitz, "Structures of verbascoside and orobanchoside, caffeic acid sugar esters from *Orobancha rapum-genistae*," *Phytochemistry*, vol. 21, no. 5, pp. 1123–1127, 1982.
- [26] L. Ji, Z. Yun, Z. Hong, S. Baoning, and Z. Rongliang, "Differentiation of human gastric adenocarcinoma cell line MGc80-3 induced by verbascoside," *Planta Medica*, vol. 63, no. 6, pp. 499–502, 1997.
- [27] T. A. Taton, C. A. Mirkin, and R. L. Letsinger, "Scanometric DNA array detection with nanoparticle probes," *Science*, vol. 289, no. 5485, pp. 1757–1760, 2000.

Research Article

Influence of Annealing on Properties of Spray Deposited ZnO Thin Films

Kalyani Nadarajah, Ching Yern Chee, and Chou Yong Tan

Department of Mechanical Engineering, Faculty of Engineering, University of Malaya, Lembah Pantai, 50603 Kuala Lumpur, Malaysia

Correspondence should be addressed to Ching Yern Chee; chingyc@um.edu.my

Received 8 August 2013; Revised 18 October 2013; Accepted 21 October 2013

Academic Editor: Mengnan Qu

Copyright © 2013 Kalyani Nadarajah et al. This is an open access article distributed under the Creative Commons Attribution License, which permits unrestricted use, distribution, and reproduction in any medium, provided the original work is properly cited.

Zinc Oxide (ZnO) thin films were deposited on glass substrates via the spray pyrolysis technique. The films were subsequently annealed in ambient air from 300°C to 500°C. The morphology and structural properties of the thin films were studied by field emission scanning electron microscope (FESEM), atomic force microscopy (AFM), and X-ray diffractometry (XRD) techniques. Electrical resistivity of the thin films was measured using a data acquisition unit. The optical properties of the films were characterized by UV-vis spectroscopy and photoluminescence (PL) technique. X-ray diffraction data showed that the films were grown in the (002) direction with a hexagonal wurtzite structure. The average grain size ranged from 15 to 27 nm. Increasing annealing temperatures resulted in larger grain sizes and higher crystallinity, with the surface roughness of annealed films being more than twice if compared to unannealed film. The electrical resistivity of the films decreased with the increasing annealing temperature. The UV and visible band emissions were observed in the photoluminescence spectra, due to exciton and defect-related emissions, respectively. The transmission values of the films were as high as 90% within the visible range (400–700 nm).

1. Introduction

Currently, ZnO nanomaterials are being applied in electronics, photonics, catalysis, lighting, and chemical sensing. It is well known that ZnO exhibits many favorable properties, such as high chemical stability, wide bandgap of 3.37 eV, high exciton binding energy of 60 meV, and abundance in nature, and is also regarded as nontoxic [1, 2]. High-quality ZnO films are mainly fabricated by using physical and chemical methods. The physical methods include sputtering [3], molecular beam epitaxy [4], and laser ablation [5], while the chemical method includes spray pyrolysis [6], chemical vapor deposition (CVD) [7], sol-gel [8], spin coating [9], dip coating [10], and electrodeposition [11]. Most of the methods mentioned in the literature are not ideally suited for large area coatings. However, the spray pyrolysis method is one of the best methods to produce large area coatings based on the previous studies [3–11]. Additionally, it is simple, has low temperature deposition, is cost-effective, has good adhesion between films and substrate, and demonstrates

uniform particle distribution, high purity, and excellent optical properties [12]. Some of the main factors affecting the properties of the film that uses spray pyrolysis technique are chemical solution (chemical composition, concentration), the distance between the substrate and atomizer interaction during film deposition, spray temperatures, substrate homogeneity, annealing conditions, and spray rates [13]. The spray pyrolysis method is efficient in producing thin film, multilayer film, thick film, and porous film on an inexpensive substrate [12]. Several oxides, such as ZnO [14], CdO [15], TiO₂ [16], SnO₂ [17], NiO [18], and Bi₂O₃ [19], have been deposited using a spray pyrolysis method. This technique involves a water/alcohol solution of metal salts sprayed onto a heated substrate, followed by allowing it to decompose into an oxide film. The formation of oxide due to the decomposition reaction is thermodynamically feasible and leaves no residue on other reactants. The substrate temperature strongly affects film morphology. By increasing the temperature, the film's morphology can be changed from a cracked to a porous structure [20]. The types and

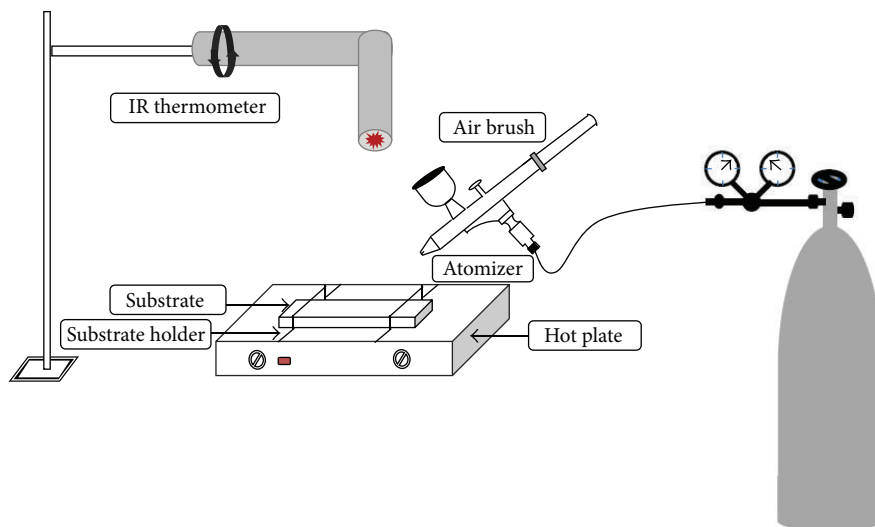


FIGURE 1: Schematic diagram of spray pyrolysis experimental setup.

concentrations of precursor and additive elements are other vital variables that influence the properties and structure [21]. The unannealed spray deposited film has high resistivity, low roughness, and less transparency due to its low crystallinity and the presence of organic residues [22–24]. The properties of the unannealed film can be enhanced due to the thermal annealing, plasma treatment, and laser treatment [25, 26]. Of these options, the thermal annealing is one of the simplest and effective ways to treat the spray deposited films. The thermal annealing temperatures, time, and various gaseous environments influence films and structural defects in the materials. During the thermal annealing process, dislocations and other structural defects in the material, adsorption, or decomposition are retained on the surface; therefore, the structure and the stoichiometric ratio of the material are altered [27]. Oxygen interstitials, zinc interstitials, oxygen vacancies, zinc vacancies, and excess oxygen are common defects found in deposited ZnO films. Zinc interstitial and oxygen vacancies are the most common defects [28, 29].

Nunes et al. [30, 31] reported the deposition of ZnO thin films using zinc acetate as a precursor. Their work reported the structural, optical, and electrical properties of undoped and doped ZnO thin films under different conditions. Yoon and Cho [32] demonstrated the synthesis of ZnO thin films using a zinc acetate dihydrate as a precursor. Their work reported on the effects of different substrate temperatures and heat treatments on the luminescence properties of ZnO film. Ayouchi et al. [33] also synthesized ZnO thin films using zinc acetate precursor and described the effects of substrate temperature and the physical properties of ZnO thin films. Despite our knowledge of various influences on film structure, the effects of annealing temperature on the ZnO films prepared by spray pyrolysis are unknown. In this study, the effects of annealing on the structural, morphological, electrical, optical, and photoluminescence behavior of ZnO films are investigated.

2. Experimental

2.1. Sample Preparation. The ZnO thin films were deposited on glass and Si substrates using spray pyrolysis techniques. The substrates were ultrasonically cleaned in methanol and acetone for 20 minutes and then immersed into 0.1 M HCl for 12 hours to remove the ionic contamination and metal residues. These substrates were rinsed with deionized water and dried in ambient air prior to the deposition. 0.1 M zinc acetate ($\text{Zn}(\text{C}_2\text{H}_3\text{O}_2)_2$ 99.9% purity Sigma Aldrich) was used as a precursor. A 2 mL acetic acid was added to the ethanol to assist in the complete dissolution of the zinc acetate. A schematic diagram of the spray pyrolysis system is illustrated in Figure 1. The precursor solution was atomized into fine uniform droplets on the heated substrate using the spray gun which is connected with nitrogen gas. The substrate was heated to 250°C during the deposition process. The outlet gas pressure was kept constant at 30 psi. The distance between the substrate and target was kept at 100 mm, and spray rate was 30 sec. After spraying, the deposited films were annealed in ambient air from 300°C to 500°C for 120 minutes. The annealing temperature was conducted until 500°C in this study since further increase of the temperature would cause the bending of the soda-lime glass substrate.

2.2. Characterization of Film. The morphologies of the film and grain size were studied with a Zeiss Ultra-60 field emission scanning electron microscopy (FESEM). The roughness and surface morphology were evaluated using an Ambios 4500 model atomic force microscope (AFM). Film crystallinity was characterized by Bruker X-ray diffraction (XRD) with $\text{CuK}\alpha$ radiation. The electrical resistivity of the film was measured using data acquisition unit. The film thickness was measured using KLA Tencor surface profile. The crystalline quality of the film was studied using *Renishaw inVia Raman* spectroscope with a He-Cd laser at 325 nm.

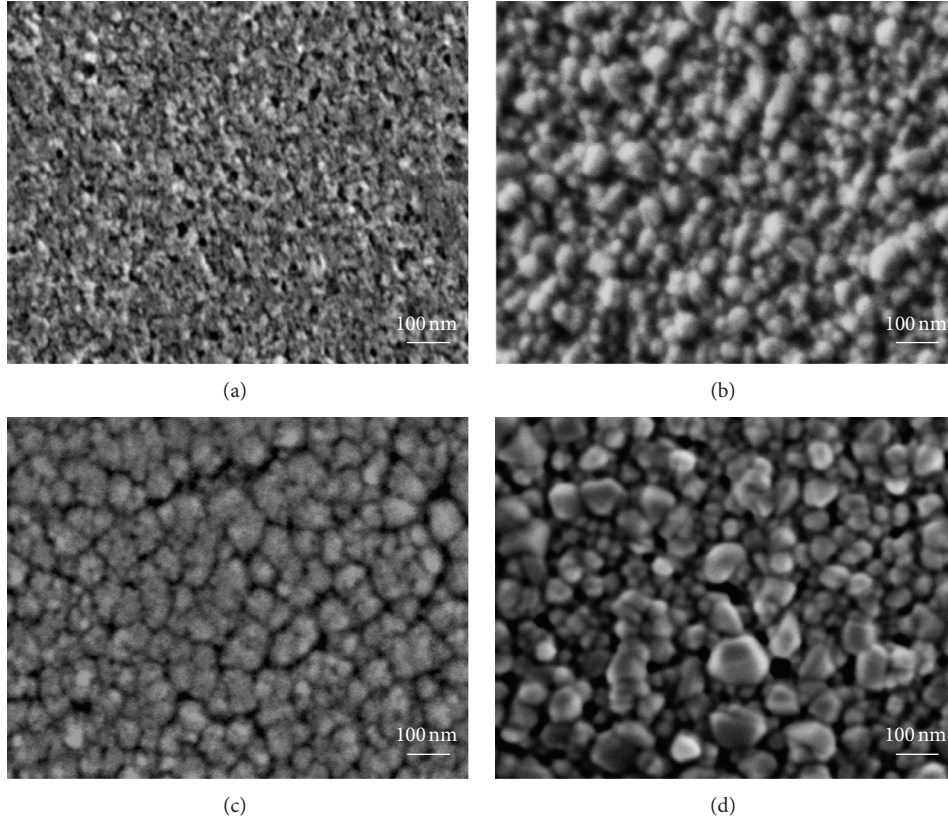


FIGURE 2: FESEM images of ZnO thin film deposited on Si substrate (a) unannealed, (b) annealed at 300°C, (c) annealed at 400°C, and (d) annealed at 500°C.

Optical transmission spectra were characterized using a double beam UV-vis spectrophotometer (Cary 50) in the wavelength range of 300–800 nm.

3. Results and Discussion

3.1. Surface Morphology Study of Films by FESEM. Figure 2 illustrates the surface morphologies of the films before and after annealing (300°C and 500°C) process. It appears that the grain size and morphology of the films improved with the increasing annealing temperatures. The FESEM micrograph shows that the unannealed films are not compact and have very small crystallites on Si substrate, which occur due to incomplete intermediate products from the spray pyrolysis technique. The well-defined round shapes of the grains are observed in the film at an annealing temperature of 300°C. A 30 nm average grain size of ZnO films is achieved when the annealing temperature reaches 500°C. The grain size increases with the increase in the annealing temperatures, due to reduction of grain boundaries in ZnO thin film [34].

3.2. AFM Morphology Study of Films. Figures 3(a) to 3(c) show the AFM images with the corresponding rms value of unannealed and annealed ZnO thin films grown on Si substrates. For the unannealed films (Figure 3(a)), the result exhibits less elongated grains over the surface. Figures 3(b)

and 3(c) display fine grains that exhibit greatly improved vertical alignment (nanotips-like morphology) than the unannealed films, which is consistent with the FESEM results. The surface roughness of the ZnO film is determined using AFM software. The rms roughness value can be estimated using the following formula [35]:

$$R(\text{rms}) = \left(\frac{\sum_{i=1}^N (Z_i - Z_{\text{avg}})^2}{N} \right)^{1/2}, \quad (1)$$

where N is the number of points, Z_i is the i th point of Z , and Z_{avg} is the average value of the Z . The unannealed film roughness is 2.1 nm. After being annealed at 300°C, 400°C, and 500°C, the film's roughness increased to 4.3 nm, 5.4 nm, and 5.6 nm, respectively. The measurements of samples revealed that the average roughness of annealed films increased compared to that of the unannealed film. As a result of this, the annealing temperature enhances elongated grains over the surface of the film, which leads to the slight increase of surface roughness. Tong et al. [36] have reported that an increase of roughness is suitable for the growth of ZnO nanowires on ZnO thin films.

3.3. Structural Studies of Films. The phase composition of ZnO thin films is determined using XRD at room temperature, with monochromatic $\text{CuK}\alpha$ ($\lambda = 0.15406$ nm). The

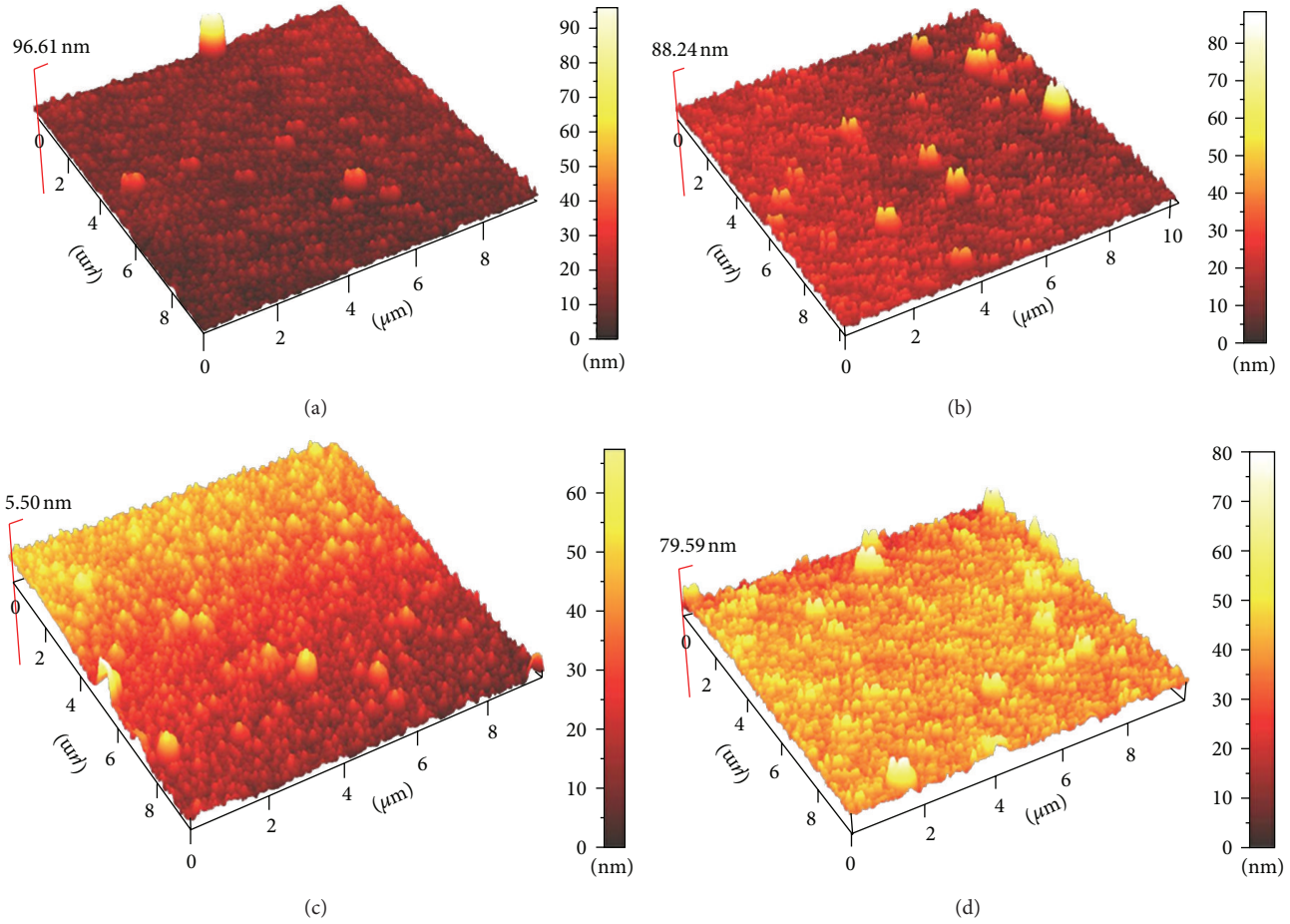


FIGURE 3: AFM images of ZnO thin film deposited on Si substrate (a) unannealed, (b) annealed at 300°C, (c) annealed at 400°C, and (d) annealed at 500°C.

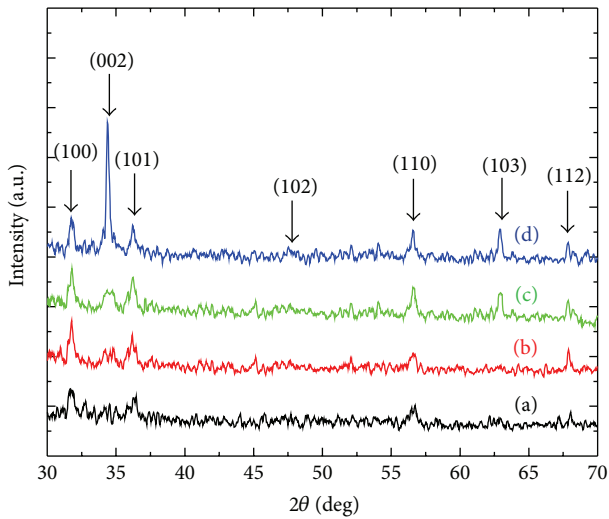


FIGURE 4: XRD pattern of ZnO thin film on Si substrate (a) unannealed, (b) annealed at 300°C, (c) annealed at 400°C, and (d) annealed at 500°C.

intensity data is collected over a range of 2θ , from 30° to 70° , with a scan rate of 0.03 deg/s. The XRD spectra of the spray pyrolysis deposited unannealed and annealed ZnO films on Si substrate are illustrated in Figure 4. ZnO diffraction peaks are indexed as (100), (101), (002), (102), (110), (103), and (112) for corresponding peak positions of 31.766° , 34.419° , 36.251° , 47.536° , 56.591° , 62.852° , and 67.942° . These diffraction peaks' position and intensities quantities are well matched with the Joint Committee on Powder Diffraction Standards (JCPDS) card no. 067454. The patterns observed from the XRD measurements show that the films possess the hexagonal wurtzite structure and a space group $P6_3mc$. The unannealed film shows lower diffraction peak intensities compared to that of the annealed film. The diffraction peaks intensities increase with the increasing annealing temperatures. Thus, the 500°C annealed film shows a strong preferential growth orientation along the (002) plane. The diffraction peaks of the film become more intense when the annealing temperature increases, which in turn leads to increase in the grain size, as well as the enhancement of crystallinity. The full width half maxima (FWHM) values decrease with increasing annealing

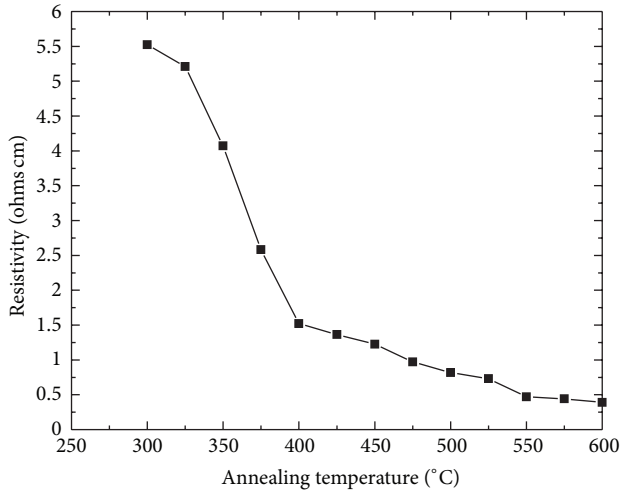


FIGURE 5: Electrical resistivity variation of ZnO thin film on glass substrate as a function of annealing temperatures.

temperatures. The grain size (D) can be computed using the following Scherrer's formula [37]:

$$D = \frac{0.94\lambda}{\beta \cos \theta}, \quad (2)$$

where β is FWHM, λ is wavelength of X-ray, and θ is Bragg's diffraction angle. Furthermore, the average grain sizes are estimated to be around 15, 20, 22, and 27 nm for unannealed and 300°C, 400°C, and 500°C annealed films, respectively. The decrease of FWHM with the increase of annealing temperature can be attributed to the increase of grain sizes. This correlates with the findings reported by previous researchers [24, 38].

3.4. Electrical Resistivity Study of Films. Figure 5 illustrates the electrical resistivity of ZnO thin films as a function of annealing temperatures. The electrical resistivity is greatly influenced by the annealing temperatures. It is observed that the resistivity of the film decreases dramatically up to 400°C and again decreases slowly afterward. This might be due to either an increase in the mobility and/or increase of the carriers. The increase of annealing temperature is attributed to larger grain sizes, thus leading to the increase of mobility change that has been reported in the literature [39]. At room temperature, there are very small numbers of charge carriers that are available in ZnO. The electronically active carriers increase when the temperature increases, thereby leading to an excess carrier in the conduction band. This increase in carriers occurs due to thermal excitation giving rise to the conductivity of the films. Similar results have been reported in the literature [40]. The resistivity of the 500°C annealed film is measured to be 0.81 Ω cm.

3.5. Photoluminescence Studies of Films. The room temperature photoluminescence (PL) spectra of unannealed and annealed ZnO thin films on glass substrate are illustrated in Figure 6. There are three peaks positions that are observed

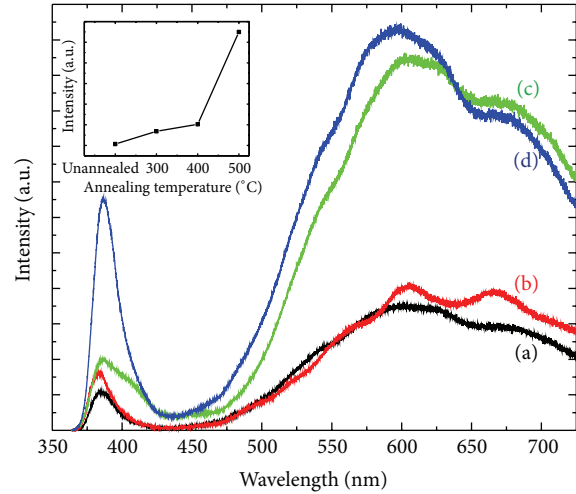


FIGURE 6: The photoluminescence spectra of ZnO thin film on glass substrate (a) unannealed, (b) annealed at 300°C, (c) annealed at 400°C, and (d) annealed at 500°C. The inset shows the intensity variation of near band edge emission at different annealed temperatures.

from the spectra. For unannealed films, the PL spectrum consists of three emission bands: a strong UV emission band at ~ 382 nm (3.25 eV), yellow band at ~ 603 nm (2.06 eV), and orange-red band at ~ 672 nm (1.85 eV), respectively. The band emission occurring in the UV range is due to excitonic recombination, while the band emission existing at the visible emission band is due to the recombination of deep-level holes and electrons [41]. All of the deep-level emissions are correlated to the defects arising during the growth of crystallites and are related to the change of crystallinity due to zinc interstitials, zinc vacancies, oxygen interstitials, oxygen vacancies, and dislocations [42]. Previous works [43, 44] reported that the yellow-orange emission originated from oxygen interstitials in ZnO, while the orange-red emission could be related to excess oxygen on the ZnO surface. From the spectra, it is observed that the PL peak intensity increases with the increasing annealing temperature. The increase of the visible emissions of the ZnO film is due to the increase of the oxygen interstitials and excess oxygen concentrations [45] by the increase of annealing temperature. The UV peak position is red shifted from 3.25 eV (for unannealed film) to 3.22 eV (for 500°C annealed film). The red shift can be explained by the quantum confinement theory, which states that the energy bandgap of a semiconductor decreases with increasing grain sizes [46]. However, after annealing, the yellow emission is improved with a blue shift towards a wavelength of 594 nm. Fujihara et al. [47] and Chen et al. [48] have also reported a blue shift in their studies.

The inset of Figure 6 shows the UV portion of the PL emission centered at 385 nm as a function of annealing temperatures. The intensity of UV-PL peak increases with the increasing annealing temperature, as shown in the inset of Figure 6. The increase in the UV portion of the PL emission is due to the removal of microstructural defects and homogenization of the films.

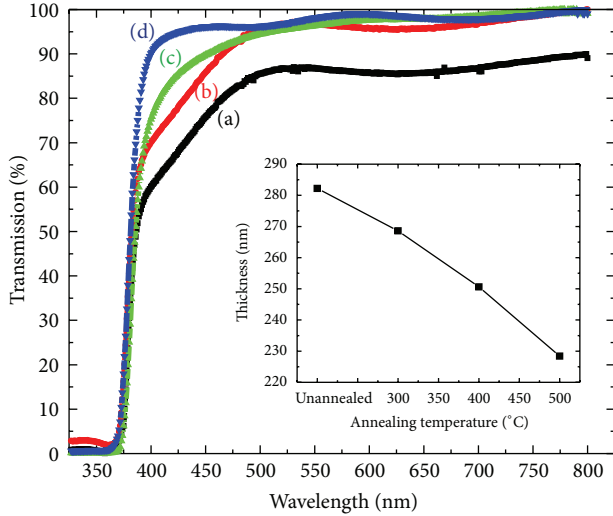


FIGURE 7: The transmission spectra of ZnO thin film on glass substrate (a) unannealed, (b) annealed at 300°C, (c) annealed at 400°C, and (d) annealed at 500°C. The inset shows the films thickness variation of different annealed temperatures.

3.6. Transmission Studies of ZnO Thin Films. The optical transmission of ZnO films is carried out using a double beam spectrophotometer in the wavelength range from 300 to 800 nm. Figure 7 shows optical transmission spectra of both unannealed and annealed ZnO thin films. The average transmittance values are directly related to the thickness of films. The inset in Figure 7 illustrates the average thickness variation of the films with the increase of annealing temperatures. The thickness of unannealed film is 282.2 nm. After annealing at 300°C, 400°C, and 500°C, the film thickness decreases to 268.6 nm, 250.6 nm, and 228.4 nm, respectively. The relationship between the optical transmission and thickness is given by the Beer-Lambert equation as follows [49]:

$$T = \frac{I}{I_0} = e^{-\alpha t}, \quad (3)$$

where I is the transmitted intensity at a particular wavelength, I_0 is the incident light intensity, α is the absorption coefficient, and t is the film thickness. The equation shows that the optical transmission of the ZnO films will decrease inversely proportional to the film thickness. The optical transmission is inversely proportional to the thickness of the films. The transmission in the visible region of the unannealed film is approximately 80%. The visible transmission of the ZnO films increases from 90% to 92% when annealing temperature increased from 300°C to 400°C. The transmission film approaches to 96% when the annealing temperature reached 500°C. A very steep absorption edge near 370 nm is observed for both unannealed and annealed films indicating high crystal quality, which could enhance luminescent efficiency. The transmission of films increases in tandem with annealing temperatures due to the increase in grain sizes, structural homogeneity, and crystallinity. The same observation has been reported by previous researchers [50, 51]. Jayatissa et al. [52] have demonstrated that the transmission of ZnO

films can be improved by annealing, which could lead to the reaction of oxygen with ZnO. It suggests that ambient conditions annealing would greatly influence the optical transmission of ZnO films. This is especially valuable for the applications as a front electrode and window materials in solar cell.

4. Conclusions

ZnO thin films were prepared by spray pyrolysis method, and it was thermally annealed at different temperatures. The structural, electrical, and optical properties of the ZnO thin films were characterized using XRD, AFM, data acquisition unit, and UV-vis spectrophotometer. The grain size of the films increases with the increase of annealing temperatures. The XRD diffractogram revealed that the thermal annealed film at 500°C possesses good crystalline hexagonal wurtzite structure, with a preferred plane orientation along (002). The grain size estimated from FESEM analysis is in good agreement with XRD data. The PL emission of the samples shows a narrow emission centered at 385 nm and a broad peak emission located at 594 nm and 672 nm. The ZnO films show an increase of transmission with the increase of annealing temperature. In particular, ZnO film annealed at 500°C achieves high light transmission of 96% in the visible range with low electrical resistivity of 0.82 Ω cm. These properties render that the ZnO film is attractive to optoelectronic device applications.

Acknowledgment

The authors acknowledge financial support from the University Malaya Postgraduate Research Grant of nos. PV033-2012A, CG013-2013, CG07-2013, RP011A-13AET, FP030-2013A, and ER014-2012A.

References

- [1] J.-H. Lee, K.-H. Ko, and B.-O. Park, "Electrical and optical properties of ZnO transparent conducting films by the sol-gel method," *Journal of Crystal Growth*, vol. 247, no. 1-2, pp. 119–125, 2003.
- [2] R. Könenkamp, K. Boedecker, M. C. Lux-Steiner et al., "Thin film semiconductor deposition on free-standing ZnO columns," *Applied Physics Letters*, vol. 77, no. 16, pp. 2575–2577, 2000.
- [3] S. Eisermann, J. Sann, A. Polity, and B. K. Meyer, "Sputter deposition of ZnO thin films at high substrate temperatures," *Thin Solid Films*, vol. 517, no. 20, pp. 5805–5807, 2009.
- [4] D. C. Look, D. C. Reynolds, C. W. Litton, R. L. Jones, D. B. Eason, and G. Cantwell, "Characterization of homoepitaxial p-type ZnO grown by molecular beam epitaxy," *Applied Physics Letters*, vol. 81, no. 10, pp. 1830–1832, 2002.
- [5] M. Hiramatsu, K. Imaeda, N. Horio, and M. Nawata, "Transparent conducting ZnO thin films prepared by XeCl excimer laser ablation," *Journal of Vacuum Science and Technology A*, vol. 16, no. 2, pp. 669–673, 1998.
- [6] R. Ayouchi, D. Leinen, F. Martín, M. Gabas, E. Dalchiele, and J. R. Ramos-Barrado, "Preparation and characterization of transparent ZnO thin films obtained by spray pyrolysis," *Thin Solid Films*, vol. 426, no. 1-2, pp. 68–77, 2003.

- [7] S. Fay, U. Kroll, C. Bucher, E. Vallat-Sauvain, and A. Shah, "Low pressure chemical vapour deposition of ZnO layers for thin-film solar cells: temperature-induced morphological changes," *Solar Energy Materials and Solar Cells*, vol. 86, no. 3, pp. 385–397, 2005.
- [8] D. Bao, H. Gu, and A. Kuang, "Sol-gel-derived c-axis oriented ZnO thin films," *Thin Solid Films*, vol. 312, no. 1-2, pp. 37–39, 1998.
- [9] G. Srinivasan, N. Gopalakrishnan, Y. S. Yu, R. Kesavamoorthy, and J. Kumar, "Influence of post-deposition annealing on the structural and optical properties of ZnO thin films prepared by sol-gel and spin-coating method," *Superlattices and Microstructures*, vol. 43, no. 2, pp. 112–119, 2008.
- [10] C. J. Brinker, G. C. Frye, A. J. Hurd, and C. S. Ashley, "Fundamentals of sol-gel dip coating," *Thin Solid Films*, vol. 201, no. 1, pp. 97–108, 1991.
- [11] E. A. Dalchiale, P. Giorgi, R. E. Marotti et al., "Electrodeposition of ZnO thin films on n-Si(100)," *Solar Energy Materials and Solar Cells*, vol. 70, no. 3, pp. 245–254, 2001.
- [12] D. Perednis and L. J. Gauckler, "Thin film deposition using spray pyrolysis," *Journal of Electroceramics*, vol. 14, no. 2, pp. 103–111, 2005.
- [13] G. Korotcenkov, V. Brinzari, J. Schwank, and A. Cerneavski, "Possibilities of aerosol technology for deposition of SnO₂-based films with improved gas sensing characteristics," *Materials Science and Engineering C*, vol. 19, no. 1-2, pp. 73–77, 2002.
- [14] M. Krunks and E. Melnikov, "Zinc oxide thin films by the spray pyrolysis method," *Thin Solid Films*, vol. 270, no. 1-2, pp. 33–36, 1995.
- [15] O. Vigil, F. Cruz, A. Morales-Acevedo, G. Contreras-Puente, L. Vaillant, and G. Santana, "Structural and optical properties of annealed CdO thin films prepared by spray pyrolysis," *Materials Chemistry and Physics*, vol. 68, no. 1–3, pp. 249–252, 2001.
- [16] C. Natarajan, N. Fukunaga, and G. Nogami, "Titanium dioxide thin film deposited by spray pyrolysis of aqueous solution," *Thin Solid Films*, vol. 322, no. 1-2, pp. 6–8, 1998.
- [17] V. Brinzari, G. Korotcenkov, and V. Golovanov, "Factors influencing the gas sensing characteristics of tin dioxide films deposited by spray pyrolysis: understanding and possibilities of control," *Thin Solid Films*, vol. 391, no. 2, pp. 167–175, 2001.
- [18] P. S. Patil and L. D. Kadam, "Preparation and characterization of spray pyrolyzed nickel oxide (NiO) thin films," *Applied Surface Science*, vol. 199, no. 1–4, pp. 211–221, 2002.
- [19] T. P. Gujar, V. R. Shinde, and C. D. Lokhande, "Spray pyrolysed bismuth oxide thin films and their characterization," *Materials Research Bulletin*, vol. 41, no. 8, pp. 1558–1564, 2006.
- [20] C. Chen, E. M. Kelder, P. J. J. M. van der Put, and J. Schoonman, "Morphology control of thin LiCoO₂ films fabricated using the electrostatic spray deposition (ESD) technique," *Journal of Materials Chemistry*, vol. 6, no. 5, pp. 765–771, 1996.
- [21] S. Golshahi, S. M. Rozati, R. Martins, and E. Fortunato, "P-type ZnO thin film deposited by spray pyrolysis technique: the effect of solution concentration," *Thin Solid Films*, vol. 518, no. 4, pp. 1149–1152, 2009.
- [22] S. Salam, M. Islam, M. Alam et al., "The effect of processing conditions on the structural morphology and physical properties of ZnO and CdS thin films produced via sol-gel synthesis and chemical bath deposition techniques," *Advances in Natural Sciences: Nanoscience and Nanotechnology*, vol. 2, no. 4, Article ID 045001, 2011.
- [23] X. Zhu, E. Defay, M. Aid et al., "Preferential growth and enhanced dielectric properties of Ba_{0.7}Sr_{0.3}TiO₃ thin films with pre annealed Pt bottom electrode," *Journal of Applied Physics D*, vol. 46, Article ID 105301, 2013.
- [24] J. Karamdel, C. F. Dee, and B. Y. Majlis, "Effects of annealing conditions on the surface morphology and crystallinity of sputtered ZnO nano films," *Sains Malaysiana*, vol. 40, no. 3, pp. 209–213, 2011.
- [25] J. Yang, J. Bei, and S. Wang, "Enhanced cell affinity of poly (D,L-lactide) by combining plasma treatment with collagen anchorage," *Biomaterials*, vol. 23, no. 12, pp. 2607–2614, 2002.
- [26] B. D. Ahn, S. H. Oh, C. H. Lee, G. H. Kim, H. J. Kim, and S. Y. Lee, "Influence of thermal annealing ambient on Ga-doped ZnO thin films," *Journal of Crystal Growth*, vol. 309, no. 2, pp. 128–133, 2007.
- [27] L. Wang, Y. Pu, W. Fang et al., "Effect of high-temperature annealing on the structural and optical properties of ZnO films," *Thin Solid Films*, vol. 491, no. 1-2, pp. 323–327, 2005.
- [28] H. S. Kang, J. S. Kang, J. W. Kim, and S. Y. Lee, "Annealing effect on the property of ultraviolet and green emissions of ZnO thin films," *Journal of Applied Physics*, vol. 95, no. 3, pp. 1246–1250, 2004.
- [29] P. Sagar, P. K. Shishodia, R. M. Mehra, H. Okada, A. Wakahara, and A. Yoshida, "Photoluminescence and absorption in sol-gel-derived ZnO films," *Journal of Luminescence*, vol. 126, no. 2, pp. 800–806, 2007.
- [30] P. Nunes, E. Fortunato, and R. Martins, "Influence of the post-treatment on the properties of ZnO thin films," *Thin Solid Films*, vol. 383, no. 1-2, pp. 277–280, 2001.
- [31] P. Nunes, B. Fernandes, E. Fortunato, P. Vilarinho, and R. Martins, "Performances presented by zinc oxide thin films deposited by spray pyrolysis," *Thin Solid Films*, vol. 337, no. 1-2, pp. 176–179, 1999.
- [32] K. H. Yoon and J. Y. Cho, "Photoluminescence characteristics of zinc oxide thin films prepared by spray pyrolysis technique," *Materials Research Bulletin*, vol. 35, no. 1, pp. 39–46, 2000.
- [33] R. Ayouchi, F. Martin, D. Leinen, and J. R. Ramos-Barrado, "Growth of pure ZnO thin films prepared by chemical spray pyrolysis on silicon," *Journal of Crystal Growth*, vol. 247, no. 3–4, pp. 497–504, 2003.
- [34] P. Uthirakumar and C.-H. Hong, "Effect of annealing temperature and pH on morphology and optical property of highly dispersible ZnO nanoparticles," *Materials Characterization*, vol. 60, no. 11, pp. 1305–1310, 2009.
- [35] C. Periasamy, R. Prakash, and P. Chakrabarti, "Effect of post annealing on structural and optical properties of ZnO thin films deposited by vacuum coating technique," *Journal of Materials Science: Materials in Electronics*, vol. 21, no. 3, pp. 309–315, 2010.
- [36] Y. Tong, Y. Liu, L. Dong et al., "Growth of ZnO nanostructures with different morphologies by using hydrothermal technique," *Journal of Physical Chemistry B*, vol. 110, no. 41, pp. 20263–20267, 2006.
- [37] Q. Humayun, M. Kashif, and U. Hashim, "Area-selective ZnO thin film deposition on variable microgap electrodes and their impact on UV sensing," *Journal of Nanomaterials*, vol. 2013, Article ID 301674, 5 pages, 2013.
- [38] Z. B. Fang, Z. J. Yan, Y. S. Tan, X. Q. Liu, and Y. Y. Wang, "Influence of post-annealing treatment on the structure properties of ZnO films," *Applied Surface Science*, vol. 241, no. 3–4, pp. 303–308, 2005.

- [39] M. Rusop, K. Uma, T. Soga, and T. Jimbo, "Post-growth annealing of zinc oxide thin films pulsed laser deposited under enhanced oxygen pressure on quartz and silicon substrates," *Materials Science and Engineering B*, vol. 127, no. 2-3, pp. 150–153, 2006.
- [40] N. H. Al-Hardan, M. J. Abdullah, A. Abdul Aziz, H. Ahmad, and L. Y. Low, "ZnO thin films for VOC sensing applications," *Vacuum*, vol. 85, no. 1, pp. 101–106, 2010.
- [41] R. Hong, H. Qi, J. Huang, H. He, Z. Fan, and J. Shao, "Influence of oxygen partial pressure on the structure and photoluminescence of direct current reactive magnetron sputtering ZnO thin films," *Thin Solid Films*, vol. 473, no. 1, pp. 58–62, 2005.
- [42] A. B. Djurišić, W. C. H. Choy, V. A. L. Roy et al., "Photoluminescence and electron paramagnetic resonance of ZnO tetrapod structures," *Advanced Functional Materials*, vol. 14, no. 9, pp. 856–864, 2004.
- [43] W. Q. Peng, S. C. Qu, G. W. Cong, and Z. G. Wang, "Structure and visible luminescence of ZnO nanoparticles," *Materials Science in Semiconductor Processing*, vol. 9, no. 1–3, pp. 156–159, 2006.
- [44] B. Panigrahy, M. Aslam, D. S. Misra, M. Ghosh, and D. Bahadur, "Defect-related emissions and magnetization properties of ZnO Nanorods," *Advanced Functional Materials*, vol. 20, no. 7, pp. 1161–1165, 2010.
- [45] A. B. Djurišić, Y. H. Leung, K. H. Tam et al., "Defect emissions in ZnO nanostructures," *Nanotechnology*, vol. 18, no. 9, Article ID 095702, 2007.
- [46] S. Cho, J. Ma, Y. Kim, Y. Sun, G. K. L. Wong, and J. B. Ketterson, "Photoluminescence and ultraviolet lasing of polycrystalline ZnO thin films prepared by the oxidation of the metallic Zn," *Applied Physics Letters*, vol. 75, no. 18, pp. 2761–2763, 1999.
- [47] S. Fujihara, Y. Ogawa, and A. Kasai, "Tunable visible photoluminescence from ZnO thin films through Mg-doping and annealing," *Chemistry of Materials*, vol. 16, no. 15, pp. 2965–2968, 2004.
- [48] S. Chen, Z. Zhao, B. Z. Tang, and H. S. Kwok, "Growth methods, enhanced photoluminescence, high hydrophobicity and light scattering of 4, 4'-bis(1, 2, 2-triphenylvinyl)biphenyl nanowires," *Organic Electronics*, vol. 13, pp. 1996–2002, 2012.
- [49] V. S. Reddy, K. Das, A. Dhar, and S. K. Ray, "The effect of substrate temperature on the properties of ITO thin films for OLED applications," *Semiconductor Science and Technology*, vol. 21, no. 12, pp. 1747–1752, 2006.
- [50] A. L. Mercado, C. E. Allmond, J. G. Hoekstra, and J. M. Fitzgerald, "Pulsed laser deposition vs. matrix assisted pulsed laser evaporation for growth of biodegradable polymer thin films," *Applied Physics A*, vol. 81, no. 3, pp. 591–599, 2005.
- [51] R. Jones and D. Fried, "Attenuation of 1310-nm and 1550-nm laser light through sound dental enamel," in *Lasers in Dentistry VIII*, vol. 4610 of *Proceedings of SPIE*, pp. 187–190, San Jose, Calif, USA, January 2002.
- [52] A. H. Jayatissa, S.-T. Cheng, and T. Gupta, "Annealing effect on the formation of nanocrystals in thermally evaporated tungsten oxide thin films," *Materials Science and Engineering B*, vol. 109, no. 1–3, pp. 269–275, 2004.

Research Article

Effect of a Polymeric Protective Coating on Optical and Electrical Properties of Poly(*p*-phenylene vinylene) Derivatives

V. C. Gonçalves,¹ C. A. Olivati,² A. J. F. Carvalho,³ and D. T. Balogh¹

¹ Instituto de Física de São Carlos (IFSC), USP, CP 369, CEP 13566-590 São Carlos, SP, Brazil

² Faculdade de Ciência e Tecnologia (FCT), Unesp Presidente Prudente, CP 467, CEP 19060-900 Presidente Prudente, SP, Brazil

³ Departamento de Engenharia de Materiais, Escola de Engenharia de São Carlos (EESC), USP, CP 359, CEP 13566-590 São Carlos, SP, Brazil

Correspondence should be addressed to C. A. Olivati; olivati@fct.unesp.br

Received 14 August 2013; Revised 26 September 2013; Accepted 29 September 2013

Academic Editor: Jiamin Wu

Copyright © 2013 V. C. Gonçalves et al. This is an open access article distributed under the Creative Commons Attribution License, which permits unrestricted use, distribution, and reproduction in any medium, provided the original work is properly cited.

The resistance to photodegradation of poly[(2-methoxy-5-n-hexyloxy)-*p*-phenylene vinylene] (OC₁OC₆-PPV) films was significantly enhanced by the use of poly(vinyl alcohol) 99% hydrolyzed as protective coating. The deposition of poly(vinyl alcohol) onto OC₁OC₆-PPV films did not affect the absorption and the emission spectra of the luminescent polymer. The protected film showed 5% drop on the absorbance at 500 nm after 270 hours of light exposure while the unprotected film completely degraded in the same conditions. The conductivity of the protected film remained stable (around 7×10^{-10} S/m) while the value for the unprotected one dropped around two orders of magnitude after 100 hours of light exposure.

1. Introduction

Poly(*p*-phenylene vinylene), PPV, derivatives have been widely explored for applications in optoelectronics such as photoluminescent devices, light-emitting diodes, and sensors [1–3]. Despite their wide range of possible applications, the PPV derivatives are highly susceptible to photodegradation, by the combined action of light and oxygen. The photodegradation reaction involves mainly the vinyl group, leading to the formation of carbonyl groups, reducing the conjugation length and, in further stages, leading to chain scission [4–14]. The photodegradation occurs in solution or in the solid state, causing a decay in the absorbance intensity and a blue shift in the absorbance and, consequently, in the emission spectrum of the polymer. In solid state, the photodegradation is thickness dependent due to mainly two factors. The first factor is the difference in the light intensity through the thickness of the material due to the light absorption. The light intensity should be maximum at the surface and decrease exponentially with the increase in thickness (Lambert's law) [15]. The second factor is

the oxygen concentration throughout the material, which depends on the oxygen diffusion through the film [11]. Some approaches have been used in order to prevent or at least try to minimize the photodegradation in the PPV derivatives. An alternative is the use of different encapsulations [16–21]. In a previous paper [16], we presented some results on the use of polymer protective layers aiming to reduce the effects of the photodegradation PPV derivatives. We observed that, among the several polymers tested, poly(vinyl alcohol) (PVA) which is 99% hydrolyzed and deposited onto films of poly(2-methoxy-5-hexyloxy-*p*-phenylene vinylene) (OC₁OC₆-PPV) remarkably reduced the photodegradation of these films. However, PVA is water soluble and can absorb water at room conditions. Then, the effect of this protective layer on the electrical properties of OC₁OC₆-PPV has to be explored prior to its use in conductivity-based devices. In this paper, thin films and single layer devices fabricated with OC₁OC₆-PPV and coated with PVA were submitted to continuous white light exposure and their optical and electrical properties, such as conductivity and electroluminescence, were explored.

2. Experimental

Cast films of $\text{OC}_1\text{OC}_6\text{-PPV}$ (ca. 300–400 nm thickness) were deposited onto glass substrates, indium tin oxide (ITO) or interdigitated chromium-gold array at room temperature in the dark [22] from chloroform solutions (0.3 mg/mL). The PVA coatings were prepared by dipping the samples into a 2 wt% solution of PVA 99% hydrolyzed in ethanol-water mixture and drying them under reduced pressure at 40°C, yielding $a \approx 1 \mu\text{m}$ layer. The gold array was prepared by lift-off lithography with 100 lines of 5 mm length electrodes with 100 nm of thickness, separated by 10 μm of distance. Photodegradation experiments were performed with a white light from a halogen lamp (50 W, 12 V-Osram) placed at a fixed distance from the samples, yielding 17 mW/cm² of power at the sample surface. These irradiations were performed at room atmosphere at 25°C. UV-Vis absorption measurements were carried out in a HITACHI U-2001 spectrophotometer in the range between 400 and 650 nm. The emission spectra of the film ($\lambda_{\text{exc}} = 490 \text{ nm}$) and the emission spectra of the device (current applied = 6 mA) were recorded in a Shimadzu 5301 PC spectrofluorimeter. All films used in the photodegradation measurements presented the same optical density in order to avoid the effect of film thicknesses on photodegradation. The device used to record the electroluminescence spectra was ITO/ $\text{OC}_1\text{OC}_6\text{-PPV}$ /Al; the $\text{OC}_1\text{OC}_6\text{-PPV}$ active layer was made of cast film from 0.25 mg/mL chloroform solution (ca. 300 nm). In this case, the PVA layer was applied over the aluminum layer. A 90 nm thick Al cathode was vacuum evaporated (10^{-6} Torr) and with an active area for the devices of 0.12 cm². The electrical behavior was carried out by measuring the current versus voltage at room conditions with a Keithley238 high voltage source-measure unit.

3. Results

The characteristic current versus electrical field curves do not show significant differences with the use of PVA as coating, as shown in Figure 1. The onset voltage of the device coated with PVA was around 5 V, which is similar to other devices of $\text{OC}_1\text{OC}_6\text{-PPV}$ made from cast films and the same configuration [23–25].

The absorption in the visible region of the cast films with and without the PVA coating showed no significant differences, and the maximum wavelengths of absorption are at 500 nm (Figure 2). The same result was obtained for the photoluminescence (PL) and electroluminescence (EL) spectra of these films, as also shown in Figure 2 and its inset. The emission wavelength of the zero-phonon transition was about 590 nm for all samples. It is worth to note that the values of absorbance, PL and EL, of protected film are nearly the same of the neat film since the protective coating is completely transparent and does not absorb or have emission on the visible range and all the film production and the coating processes are performed in dark. Extreme care should be taken to reproduce intensity values of the photo- and electroluminescence spectra of $\text{OC}_1\text{OC}_6\text{-PPV}$ because even

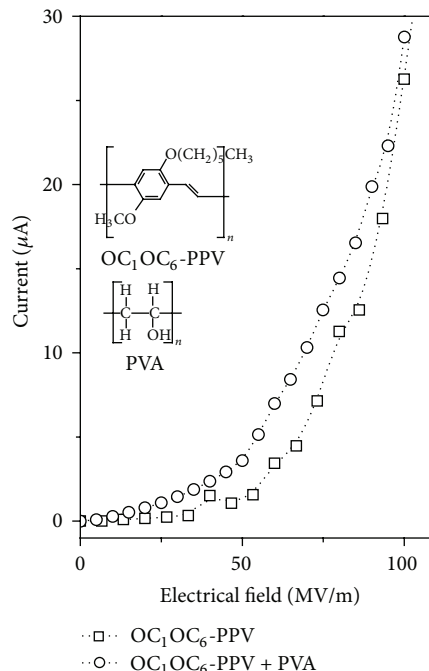


FIGURE 1: Current versus electrical field of ITO/ $\text{OC}_1\text{OC}_6\text{-PPV}$ /Al, neat and coated with PVA.

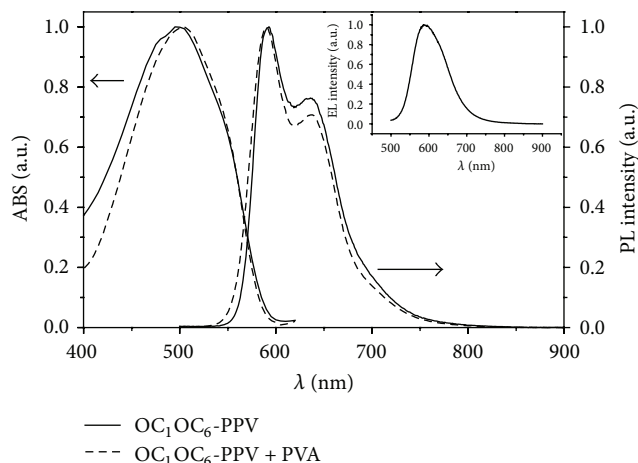


FIGURE 2: Visible, photoluminescence, and electroluminescence spectra of $\text{OC}_1\text{OC}_6\text{-PPV}$ films with and without a PVA coating. The electroluminescence spectra were carried out onto ITO/ $\text{OC}_1\text{OC}_6\text{-PPV}$ /Al (neat and coated with PVA).

the ambient light degrades the neat film. Also, very short exposures to the excitation light have to be used to record the photoluminescence spectra of these films in ambient conditions.

The electroluminescence of two single layer devices of $\text{OC}_1\text{OC}_6\text{-PPV}$ (ITO/ $\text{OC}_1\text{OC}_6\text{-PPV}$ /Al), neat and coated with poly(vinyl alcohol) over the aluminum layer (as in inset of Figure 3), was recorded continuously for 300 seconds at ambient conditions as shown in Figure 3. After the turn-on, the devices presented some instability due to the electrical

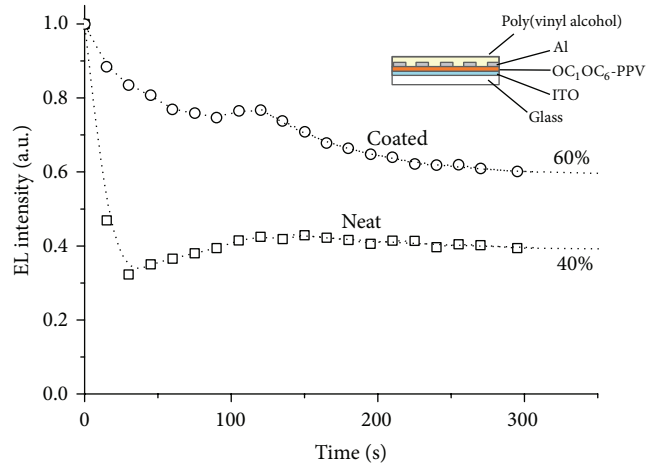


FIGURE 3: Normalized electroluminescence decay for the ITO/OC₁OC₆-PPV/Al cast film and ITO/OC₁OC₆-PPV/Al cast film coated with PVA. The lines are only to guide the eyes.

contacts. After 150 seconds of stabilization, the coated device presented 60% of the initial emission intensity while the neat one presented just 40%. Studies on the effects of the luminance and lifetime of the devices are subject of future works. For single layer devices, interface and Joule effects are more pronounced in long-term experiments which is required for lifetime studies, turning the results more complicated to analyze properly. Build-up of multilayer devices can introduce more variables in the analysis turning the system even more complicated to reach a clear conclusion. Therefore, long-term experiments of light exposure were performed only with optical and conductivity measurements and not with the devices.

The absorption spectra of OC₁OC₆-PPV cast film without the poly(vinyl alcohol) coating, taken after several periods of exposure to the white light, showed a behavior similar to the one observed in earlier reports [13, 14]. The absorbance initially decreases without changing the line shape of the spectra or the wavelength of maximum absorbance and, in a further step of the degradation, the spectra are blue shifted while continuously decreasing the maximum absorbance values [14]. However, when the cast film is coated with poly(vinyl alcohol), the changes in the spectra are drastically reduced, and, in the same period of irradiation, the decrease in the absorbance values was about 5%, while in the same period the nonprotected OC₁OC₆-PPV film was completely degraded. This effect is clearly seen by plotting the normalized absorbance values at 500 nm (wavelength of maximum absorption of the nondegraded OC₁OC₆-PPV) in function of the irradiation time as shown in Figure 4. This figure shows the results of the film coated with poly(vinyl alcohol) in function of the continuous exposure of the film to the white light till 620 hours, showing a total decrease of ca. 12% of the absorbance values. The inset of Figure 4 shows the kinetic plot from which the photodegradation rates could be estimated, being two orders of magnitude lower for the coated film: ca. $4 \times 10^{-2} \text{ h}^{-1}$ and $2 \times 10^{-4} \text{ h}^{-1}$, respectively, for the neat film and the film coated with PVA. It is very important

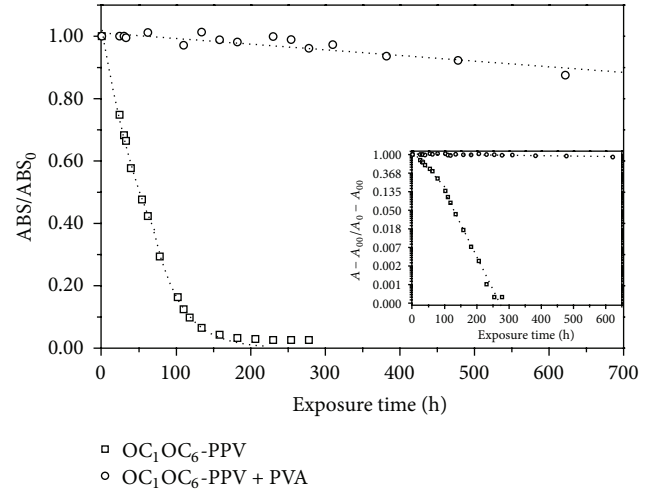


FIGURE 4: Normalized absorbance decay for the OC₁OC₆-PPV cast film and OC₁OC₆-PPV cast film coated with PVA, irradiated with white light. The inset shows the kinetic plot (y -axis in log scale) for the same samples. The lines are only to guide the eyes.

to emphasize that these estimated values are only valid for samples with thicknesses of ca. 300–400 nm since there is a strong dependence between the absorbance decay rates and the film thickness.

Similar protecting effect of the PVA coating against OC₁OC₆-PPV photodegradation can also be seen in the photoluminescence characterization. The PL intensity of the pure film drops 50% in the first 40 minutes of exposure, while the intensity for the coated one remains the same.

For the conductivity measurements, a constant voltage of 6 V was applied for several hours at room conditions while exposing the films under the electrodes to the white light and measuring the current at different time intervals. The conductivity measurements showed that the cast films coated with PVA presented a more stable conductivity than that observed for neat OC₁OC₆-PPV films (Figure 5). The conductivity values obtained for the PVA-protected OC₁OC₆-PPV film deposited onto an interdigitated chromium-gold array under the illumination remain constant (around $7 \times 10^{-10} \text{ S/m}$) for at least 100 hours of continuous light exposure. For the unprotected OC₁OC₆-PPV, the conductivity decreased two orders of magnitude in the same exposure period (from $4.5 \times 10^{-10} \text{ S/m}$ to $2.5 \times 10^{-12} \text{ S/m}$).

4. Conclusions

In conclusion, the use of coatings of poly(vinyl alcohol) onto OC₁OC₆-PPV films was successful in minimizing the photodegradation, probably due to its low oxygen permeation, showing only 12% of absorbance decay after 30 days of continuous exposure to a 50 W halogen lamp. The coating did not affect the optical properties, such as emission and absorption spectra, of the OC₁OC₆-PPV. The conductivity of the protected OC₁OC₆-PPV film showed remarkable stability under the exposure to light. This method of coating allows fabrication of stable devices which, after the proper

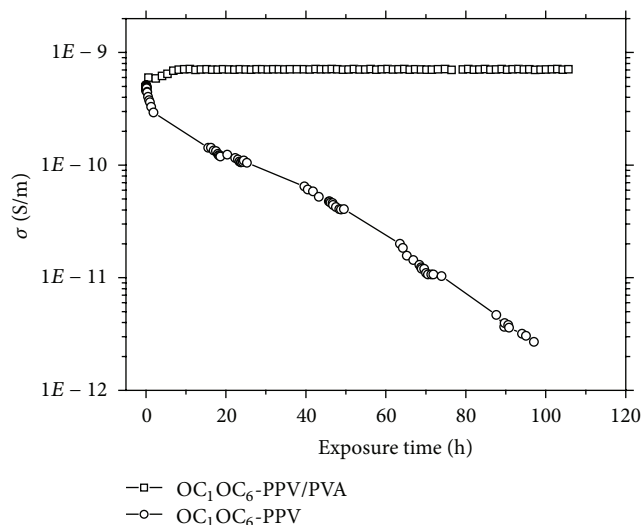


FIGURE 5: Conductivity values of the OC_1OC_6 -PPV cast film and OC_1OC_6 -PPV cast film coated with PVA, measured in an interdigitated electrode and irradiated with white light. The lines are only to guide the eyes.

optimization of fabrication, can be used in applications such as sensors and FETs, among others.

Acknowledgments

The financial support of Conselho Nacional de Desenvolvimento Científico e Tecnológico (CNPq), Fundação de Amparo à Pesquisa do Estado de São Paulo (FAPESP), Coordenação de Aperfeiçoamento de Pessoal de Nível Superior (CAPES), and Instituto Nacional de Eletrônica Orgânica, Brazil is acknowledged.

References

- [1] J. H. Burroughes, D. D. C. Bradley, A. R. Brown et al., "Light-emitting diodes based on conjugated polymers," *Nature*, vol. 347, pp. 539–541, 1990.
- [2] N. C. Greenham, S. C. Moratti, D. D. C. Bradley, R. H. Friend, and A. B. Holmes, "Efficient light-emitting diodes based on polymers with high electron affinities," *Nature*, vol. 365, no. 6447, pp. 628–630, 1993.
- [3] F. Hide, M. A. Díaz-García, B. J. Schwartz, M. R. Andersson, Q. Pei, and A. J. Heeger, "Semiconducting polymers: a new class of solid-state laser materials," *Science*, vol. 273, no. 5283, pp. 1833–1836, 1996.
- [4] B. H. Cumpston and K. F. Jensen, "Photo-oxidation of electroluminescent polymers," *Trends in Polymer Science*, vol. 4, no. 5, pp. 151–157, 1996.
- [5] G. H. Gelinck and J. M. Warman, "The effect of photo-oxidation on the photo-conductivity of isolated polyphenylenevinylene chains," *Chemical Physics Letters*, vol. 277, no. 4, pp. 361–366, 1997.
- [6] F. J. J. Janssen, L. J. Van IJzendoorn, H. F. M. Schoo et al., "Degradation effects in poly para-phenylene vinylene derivatives due to controlled oxygen exposure," *Synthetic Metals*, vol. 131, no. 1–3, pp. 167–174, 2002.
- [7] W. Holzer, A. Penzkofer, M. Pichlmaier, D. D. C. Bradley, and W. J. Blau, "Photodegradation of some luminescent polymers," *Chemical Physics*, vol. 248, no. 2-3, pp. 273–284, 1999.
- [8] H. Y. Low, "Photo and photo-oxidative degradations of poly(phenylene vinylene) derivatives," *Thin Solid Films*, vol. 413, no. 1-2, pp. 160–166, 2002.
- [9] B. H. Cumpston and K. F. Jensen, "Photo-oxidation of polymers used in electroluminescent devices," *Synthetic Metals*, vol. 73, no. 3, pp. 195–199, 1995.
- [10] G. D. Hale, S. J. Oldenburg, and N. J. Halas, "Effects of photo-oxidation on conjugated polymer films," *Applied Physics Letters*, vol. 71, no. 11, pp. 1483–1485, 1997.
- [11] A. Alba García, H. Schut, L. D. A. Siebbeles, and A. Van Veen, "Depth profiling of the degradation of OC1OC10-PPV monitored by positron beam analysis," *Synthetic Metals*, vol. 138, no. 1-2, pp. 43–47, 2003.
- [12] R. F. Bianchi, D. T. Balogh, M. Tinani, R. M. Faria, and E. A. Irene, "Ellipsometry study of the photo-oxidation of Poly[(2-methoxy-5-hexyloxy)-p-phenylenevinylene]," *Journal of Polymer Science, Part B*, vol. 42, no. 6, pp. 1033–1041, 2004.
- [13] F. M. Marconi, R. F. Bianchi, R. M. Faria, and D. T. Balogh, "Solvent effects on the photodegradation of a PPV derivative," *Molecular Crystals and Liquid Crystals Science and Technology Section A*, vol. 374, pp. 475–480, 2002.
- [14] C. A. Olivati, M. Ferreira, R. F. Bianchi, R. M. Faria, O. N. Oliveira Jr., and D. T. Balogh, "The influence of preparation method of OC1OC6-PPV films on the photo-oxidation process," *Polymer Degradation and Stability*, vol. 91, no. 10, pp. 2342–2346, 2006.
- [15] F. H. Lohman, "The mathematical combination of Lambert's law and Beer's law," *Journal of Chemical Education*, vol. 32, no. 3, p. 155, 1955.
- [16] V. C. Gonçalves, A. J. F. Carvalho, and D. T. Balogh, "Polymeric coatings for photostability enhancement of poly(p-phenylene vinylene) derivative films," *Polymer International*, vol. 59, no. 5, pp. 637–641, 2010.
- [17] H.-C. Lee, T.-W. Lee, Y. T. Lim, and O. O. Park, "Improved environmental stability in poly(p-phenylene vinylene)/layered silicate nanocomposite," *Applied Clay Science*, vol. 21, no. 5-6, pp. 287–293, 2002.
- [18] B. H. Cumpston and K. F. Jensen, "Photooxidative stability of substituted poly(phenylene vinylene) (PPV) and poly(phenylene acetylene) (PPA)," *Journal of Applied Polymer Science*, vol. 69, no. 12, pp. 2451–2458, 1998.
- [19] P. Le Rendu, T. P. Nguyen, and L. Carrois, "Cellulose acetate and PVDC used as protective layers for organic diodes," *Synthetic Metals*, vol. 138, no. 1-2, pp. 285–288, 2003.
- [20] J. S. Lewis and M. S. Weaver, "Thin-film permeation-barrier technology for flexible organic light-emitting devices," *IEEE Journal on Selected Topics in Quantum Electronics*, vol. 10, no. 1, pp. 45–57, 2004.
- [21] G. H. Kim, J. Oh, Y. S. Yang, L.-M. Do, and K. S. Suh, "Encapsulation of organic light-emitting devices by means of photopolymerized polyacrylate films," *Polymer*, vol. 45, no. 6, pp. 1879–1883, 2004.
- [22] C. De Almeida Olivati, R. F. Bianchi, F. M. Marconi, D. T. Balogh, and R. M. Faria, "Photoconduction effect on PPV and MH-PPV structures," *Molecular Crystals and Liquid Crystals Science and Technology Section A*, vol. 374, pp. 451–456, 2002.
- [23] C. A. Olivati, M. Ferreira, A. J. F. Carvalho et al., "Polymer light emitting devices with Langmuir-Blodgett (LB) films: enhanced

- performance due to an electron-injecting layer of ionomers,” *Chemical Physics Letters*, vol. 408, no. 1–3, pp. 31–36, 2005.
- [24] C. A. Olivati, A. J. F. Carvalho, D. T. Balogh, and R. M. Faria, “Electrical properties of polymer/metal interface in polymer light-emitting devices: electron injection barrier suppression,” *Journal of Materials Science*, vol. 41, no. 10, pp. 2767–2770, 2006.
- [25] C. A. Olivati, A. J. F. Carvalho, D. T. Balogh, H. von Seggern, and R. M. Faria, “Effect of ion concentration of ionomer in electron injection layer of polymer light-emitting devices,” *Journal of Non-Crystalline Solids*, vol. 352, no. 9–20, pp. 1686–1690, 2006.

Research Article

Liquid Phase Deposition of Silica on the Hexagonally Close-Packed Monolayer of Silica Spheres

Seo Young Yoon, Sung-Eun Choi, and Jin Seok Lee

Department of Chemistry, Sookmyung Women's University, Seoul 140-742, Republic of Korea

Correspondence should be addressed to Jin Seok Lee; jinslee@sookmyung.ac.kr

Received 19 July 2013; Accepted 12 September 2013

Academic Editor: Guangyu Zhao

Copyright © 2013 Seo Young Yoon et al. This is an open access article distributed under the Creative Commons Attribution License, which permits unrestricted use, distribution, and reproduction in any medium, provided the original work is properly cited.

Liquid phase deposition is a method used for the nonelectrochemical production of polycrystalline ceramic films at low temperatures, most commonly silicon dioxide films. Herein, we report that silica spheres are organized in a hexagonal close-packed array using a patterned substrate. On this monolayer of silica spheres, we could fabricate new nanostructures in which deposition and etching compete through a modified LPD reaction. In the early stage, silica spheres began to undergo etching, and then, silica bridges between the silica spheres appeared by the local deposition reaction. Finally, the silica spheres and bridges disappeared completely. We propose the mechanism for the formation of nanostructure.

1. Introduction

Silicon dioxide (SiO_2) films are widely useful in various fields. These films act as interlayer dielectrics and gate oxides in transistors and in the fabrication of integrated circuits and ultralarge-scale integration (ULSI) technologies [1–7]. In addition, SiO_2 films play an important role in semiconductor devices as electrical insulators preventing the motion of carriers from [8] and could be universally applicable as one of the chief components of optical antireflection coatings and liquid crystal display (LCD) substrates as a mask to prevent alkali ions from diffusing to the ITO films [9]. Many techniques to produce SiO_2 films have been researched, such as thermal oxidation, chemical vapor deposition (CVD), and sputtering [7, 9, 10]. However, these techniques have several drawbacks, mainly the need for specific equipments such as vacuum systems or glove boxes as well as expensive and sensitive organometallic precursors [11]. Furthermore, some techniques require a high reaction temperature of around several hundred degrees centigrade.

Recently, among various techniques, the liquid phase deposition (LPD) has been focused on as a useful method for the deposition of oxide films at low temperatures in aqueous solutions. LPD can overcome the abovementioned drawbacks of conventional methods because it does not require the use of

vacuum systems and sensitive reagents. LPD progresses easily at room temperature, demands low production costs, and has minimal environmental impact. LPD is especially useful in coating not only flat substrates but also nonplanar substrates [11].

Up until now, research regarding LPD has investigated the formation and kinetics of films on planar substrates. In 1998, Nagayama et al. reported that SiO_2 films could be deposited on glass in an H_2SiF_6 solution supersaturated with silica, after H_3BO_3 was added to the H_2SiF_6 solution which was saturated with SiO_2 [12]. Whitsitt and Barron found that SiO_2 films could be formed on substrates in an H_2SiF_6 solution supersaturated with SiO_2 by dissolving aluminum instead of H_3BO_3 [11]. Further, Tsukuma et al. researched other silicic acid solutions having the unique ability to deposit films on a substrate and described the processing and properties of the silica film with some organic groups, deposited in the liquid phase [13]. However, most of the LPD research has been focused on flat substrates, and research on nanostructured substrates remains to be investigated. Kim and Roh fabricated isolated nanostructure by using the selective LPD on silicon substrates with grooves formed through etching [14]. Whitsitt and Barron researched different morphology of silica particles by LPD method with different surfactant [15]. Here, we investigated LPD on nanostructured surfaces

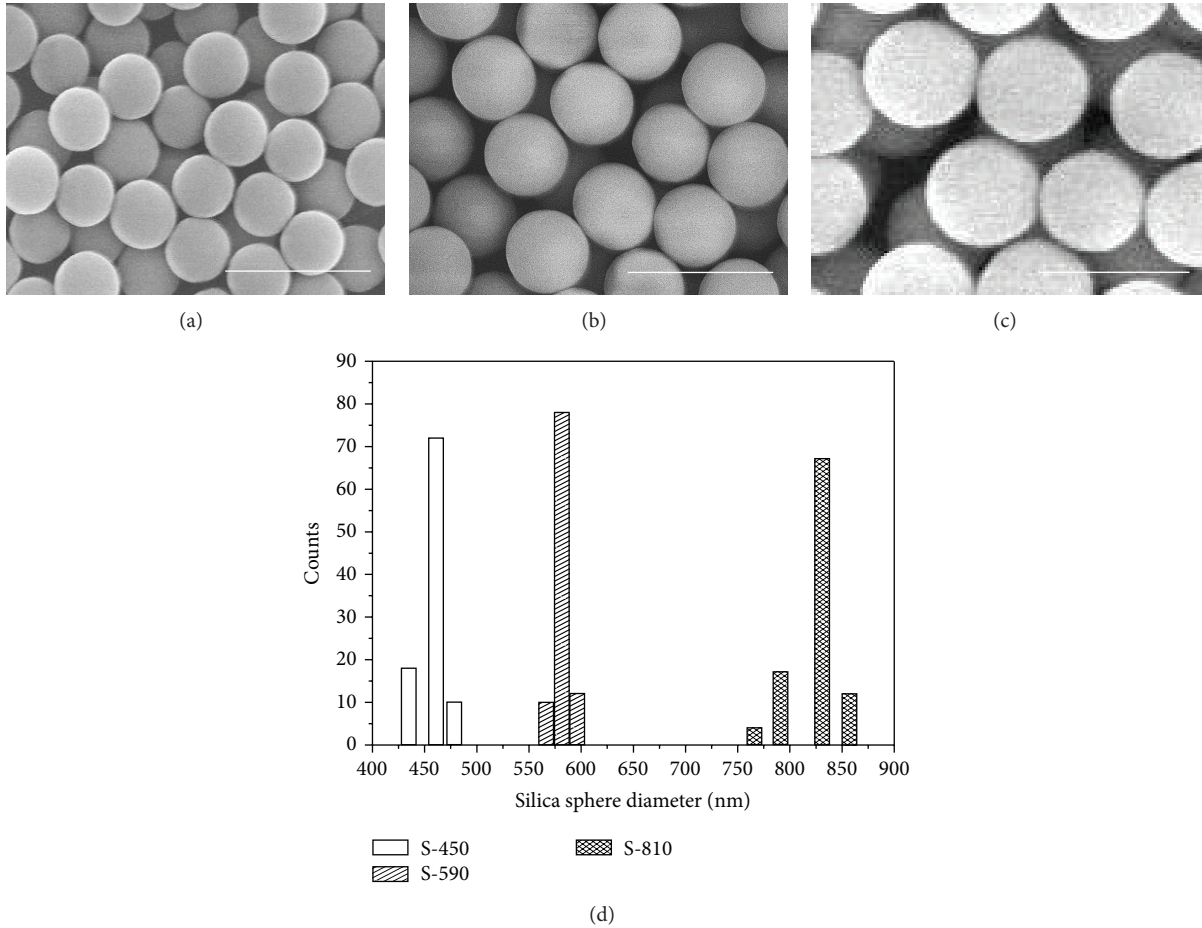


FIGURE 1: SEM images of silica spheres synthesized by the Stöber method. The average diameter of the silica spheres is 450 nm (a), 590 nm (b), and 810 nm (c), denoted by S-450, S-590, and S-810, respectively. The distribution of the diameters of silica spheres is shown in (d). Scale bars are $1\ \mu\text{m}$.

formed by the manual-assembled building blocks, which are different from previous research. For more effective production of oxide films, it is possible to either increase the concentration of water or decrease the concentration of hydrofluoric acid based on Le Chatelier's principle. To decrease the concentration of hydrofluoric acid, boric acid or aluminum metals are commonly used to function as fluoride (F^-) scavengers [10]. Boric acid or aluminum metals could be used to produce more silicon dioxide; however, the use of these supplementary additives affects the film properties because other materials might be doped into SiO_2 film and increase the impurity level. Consequently, the quality and insulating properties of the SiO_2 film are degraded.

In this study, we assembled silica spheres with hexagonally close-packing by using a patterned substrate. Then, we performed a modified LPD reaction on the nanostructure, which meant the silica sphere array, without additives but by changing the saturation of hydrofluorosilicic acid (H_2SiF_6). As a result, we fabricated a new nanostructure showing local deposition and etching reaction at the same time and proposed the mechanism of formation of the new nanostructure.

2. Experiments

2.1. Synthesis of Silica Spheres. Silica spheres were synthesized using the Stöber method, which involves the hydrolysis of tetraethyl orthosilicate (TEOS) in ethanol in the presence of ammonia (NH_3) as a catalyst [16, 17]. By controlling the concentration of reactants, we changed the size of the silica spheres. Ammonia and ethanol adjusted to the proper concentrations were placed in a glass flask and stirred. After stabilizing the solution, TEOS was added and stirred to induce hydrolysis and condensation process. Finally, the silica suspension was centrifuged and washed by repeated redispersion in pure ethanol several times.

2.2. Assembly of Silica Spheres. The silicon wafer with a 300 nm thick SiO_2 layer was coated with poly(methyl methacrylate) (PMMA) C2 by spin coating. The patterned Si substrates were immersed in piranha solution for 30 min and washed with deionized (DI) water. To prepare the poly(dimethylsiloxane) (PDMS) stamp, PDMS was poured onto the cleaned, patterned Si substrates and baked at 70°C for a few hours. Then, a small amount of the silica spheres

powder was placed on the PDMS stamp and rubbed repeatedly in the same direction using a PDMS slab. After rubbing, the randomly aggregated upper layers of silica spheres were removed from the bottom layer with hexagonally close-packing (HCP) by using a fresh sticky PDMS slab for a few seconds on top of the silica sphere array and subsequently removing the PDMS slab. Finally, this monolayer of the HCP silica spheres on the PDMS stamp was transferred to the precoated silicon wafer with a 300 nm thick SiO₂ layer with PMMA [18].

2.3. Liquid Phase Deposition of Nanostructure. As mentioned in the previous section, HCP silica spheres were heated at 200°C for 2 min to soften PMMA, which immobilized the silica spheres on PMMA layer. On the other hand, the liquid phase deposition solution was prepared as follows. First, 110 mL of hydrofluorosilicic acid (H₂SiF₆, 35%) and 2 g of fumed silica (SiO₂) powder were mixed and stirred at 400 rpm overnight. After stirring, this solution was filtered using a vacuum filtration, and DI water was added to the filtered solution at a ratio of 1 : 2 to allow for supersaturation with silicic acid. Immediately after preparing the solution, the samples were immersed in the solution for various times from 5 to 30 min. After the reaction, the sample was rinsed with DI water and dried with nitrogen blowing.

3. Results and Discussion

We synthesized silica spheres with various sizes by controlling the concentrations of the reactants (Figure 1). Among them, S-590 was the most uniform. Narrow size distribution is an important factor in forming a uniform nanostructure consisting of silica spheres with a low density of defects using patterned substrates. We used the silica spheres with a diameter of around 600 nm. The assembly process of silica spheres using patterned substrates is described in Figure 2. We fabricated a patterned Si substrate with hexagonal arrays of spherical protrusions. PDMS was poured and hardened on this patterned Si substrate, and then, a patterned PDMS stamp with hexagonal array of wells, contrary to the patterned Si substrate, was created (see the Supplementary Material for SEM images of patterned substrate available online at <http://dx.doi.org/10.1155/2013/510524>). After rubbing the silica spheres on the PDMS stamp, the monolayer of silica spheres was transferred onto the precoated silicon wafer with a 300 nm thick SiO₂ layer with PMMA. One advantage of this method is the utilization of silica sphere powder rather than a dispersion solution of silica spheres. When the Langmuir-Blodgett assembly method is used, a diluted dispersion solution of silica spheres that can suspend and spread along the interface between air and water is required [19, 20]. As the silica sphere array dries after the Langmuir-Blodgett assembly, water evaporates from them. This evaporation may influence the assembly of the silica spheres, which may crack because of particle shrinkage, but eventually, grain formation occurs. Although it is possible to rub silica sphere powder on glass, this method may lead to crack formation, as in the case of the Langmuir-Blodgett assembly. However, when the silica

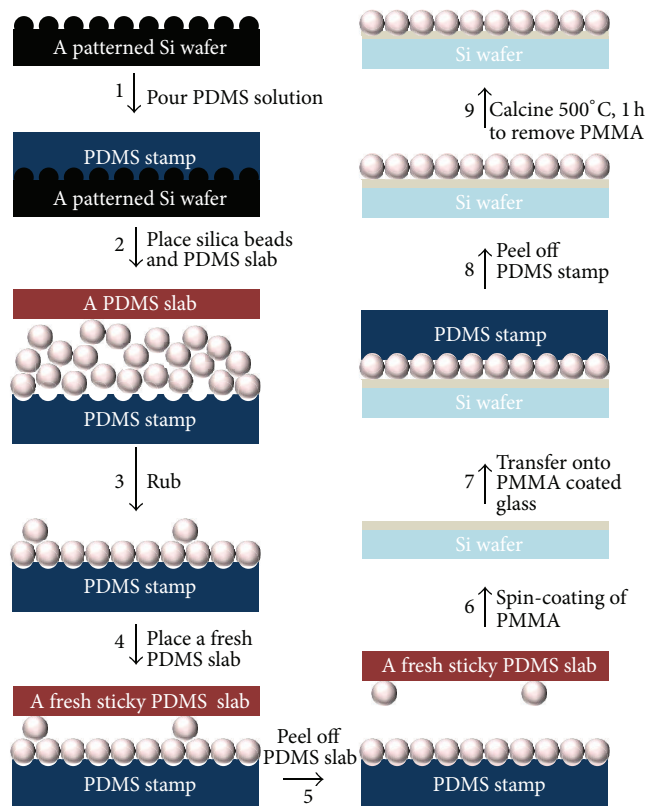


FIGURE 2: Schematic diagram of the general procedure to prepare perfect hexagonally close-packed arrays of silica spheres.

sphere powder is rubbed on the patterned Si wafer substrate, a perfect hexagonally close-packed assembly is formed over a very large area. Thus, this process is highly rapid and simple.

We conducted the LPD of silica on the hexagonally close-packed monolayer of silica spheres. The general LPD reaction, hydrofluorosilicic acid supersaturated with silicon dioxide is used to make the LPD solution. In this study, we experimented with LPD solutions consisting of unsaturated hydrofluorosilicic acid with 2 g of fumed silica powder, as the source of silicon dioxide. When supersaturated hydrofluorosilicic acid is filtered, undissolved silica substances are commonly sieved from the solution. However, our solution was not supersaturated because of insufficient silicon dioxide, and hence, there were no filtered substances. The experiment progressed using this LPD solution, and the results according to time are shown in Figure 3. In the general LPD reaction, silicon dioxide is homogeneously precipitated onto the substrate; however, we obtained surprising outcomes. Before the LPD reaction (0 min), the silica spheres were hexagonally close-packed (Figure 3(a)). After the LPD reaction for 5 min, the silica sphere size was reduced. It should be emphasized that at this point, short and fine bridges between silica spheres started appearing (Figure 3(b)). The average length of the bridges and the standard deviation were 32.59 nm and 6.32 nm, respectively. After another 5 min, the silica spheres were continuously reduced, and the bridges became more elongated to 108.18 nm ± 14.82 nm (Figure 3(c)). The

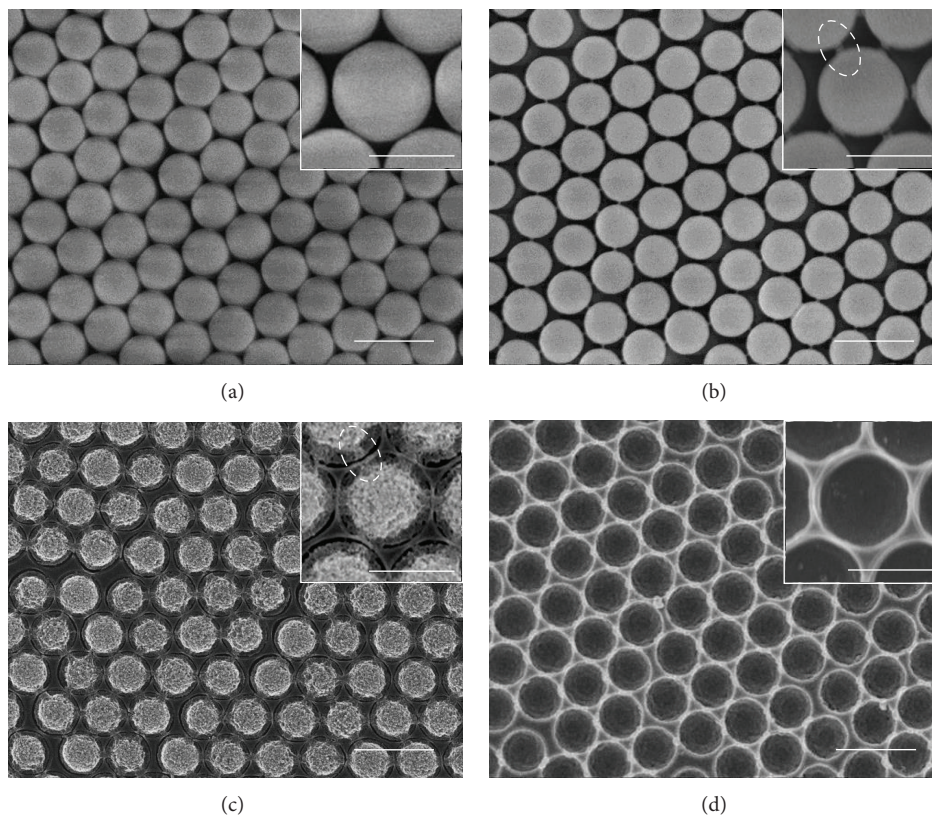


FIGURE 3: SEM images of liquid phase deposition according to the deposition time: (a) 0 min, (b) 5 min, (c) 10 min, and (d) 30 min. The dashed circle represents the bridge between silica spheres. Scale bars are $1\ \mu\text{m}$, and inset scale bars are $500\ \text{nm}$.

surface of the silica spheres and the bridges after 10 min were different from those observed after 5 min. Commonly, bridge formation is observed in both assemblies, which is the result of deposition. However, in Figure 3(c), the silica spheres seem to be very rough, which is an evidence of the etching reaction. Therefore, both reactions, that is, deposition and etching, occur simultaneously in one solution and compete with each other. After the LPD reaction in 30 min, all the silica spheres and bridges were etched and eventually disappeared. Only a trace of the embedded silica spheres was discovered (Figure 3(d)). We reported a similar nanostructure in our previous work using the same processes: first, isotropic etching of silica spheres, formation of a sphere-bridge networks (SB-NWs), and eventual disappearance of the silica spheres and SB-NWs structure [21].

The changes in silica sphere size during the LPD reaction with time are shown in Figure 4(a). Once the reaction commenced, the silica spheres were etched and their size showed a consistent decrease. During the etching reaction, the silica spheres size decreased, and the bridge length between the silica spheres increased. Finally, the bridges disappeared after 30 min because of perfect etching. In our previous work, while the etching reaction was progressed, the etching rate of the silica sphere array decreased because the amount of hydrofluoric acid decreased. On the other hand, while the current LPD reaction progressed, silicon dioxides were formed in hydrofluorosilicic acid from the silica spheres by

etching themselves. In accordance with this reaction, a large amount of hydrofluoric acid was produced because of the reaction between silicon dioxide and hydrofluorosilicic acid. For this reason, the reaction rate increased, in contrast to our previous work, and was probed throughout the slope of the graph. The slope tended to increase with time. Energy dispersive X-ray spectrometry (EDS) analysis of the silica spheres and networks are shown in Figures 4(b) and 4(c). The EDS spectra measured at the centers of the silica spheres and bridges confirmed the existence of Si and O. The Si/O atomic ratio in the silica sphere was estimated to be 1:1.17, which is quite similar to that of the bridge (1:1.20) and close to the stoichiometric composition of SiO_2 . Thus, this analysis confirms that the bridges are composed of SiO_2 in a ratio essentially equal to that in the case of the silica spheres.

In our previous work, the sphere-bridge network structure was formed by etching using a neutral solution of 1:30 (v/v) mixture of 49% HF acid and 40% NH_4F , and a mechanism for the formation of SB-NW structures was proposed. This work demonstrates an increased ammonium hexafluorosilicate (AHFS) concentration in the formed droplets at the interstitial sites of three adjacent silica spheres, and it indicates where the three materials, that is, AHFS, silica sphere, and aqueous silicic acid, are in contact, that is, the bridges formed between the silica spheres through the precipitation of silicic acids. As opposed to our previous work, in the present case, we used an LPD solution

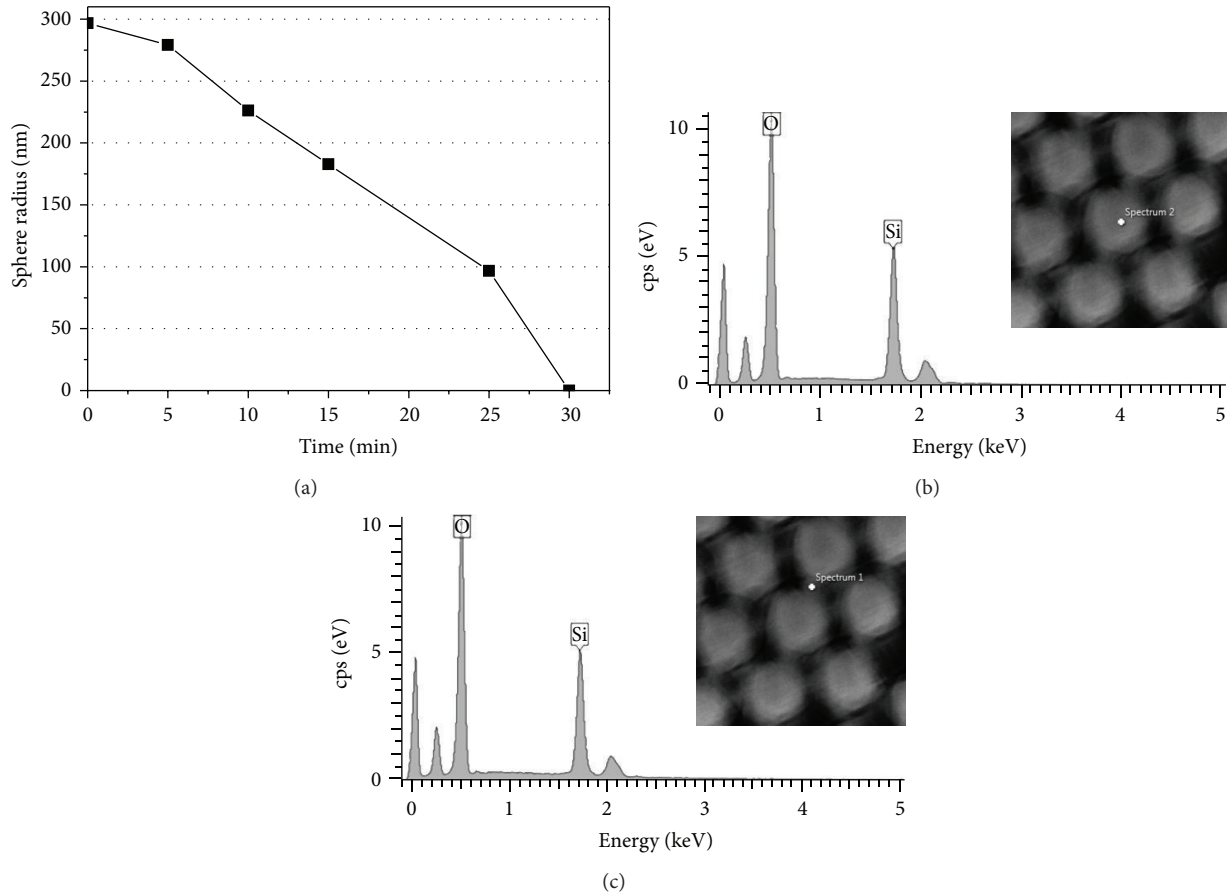
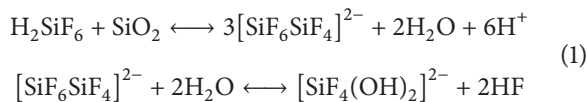
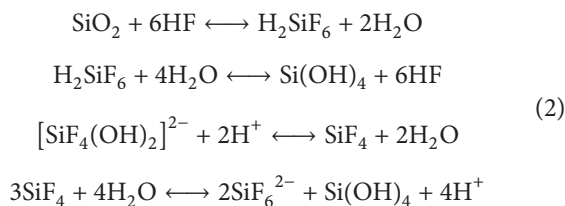


FIGURE 4: (a) Graph of the reaction rate of liquid phase deposition with respect to time. EDS analysis of the center of a silica sphere (b) and a bridge (c).

containing 2 g of fumed silica instead of a near neutral solution. In our LPD solution, the following reaction occurred [1]:



In these reactions, hydrofluoric acid could start etching the silica spheres, which were composed of silicon dioxide; accordingly, the size of the spheres was reduced. Meanwhile, silicic acid was produced at the same time as the etching reaction, as per the following reactions [1, 21]:



The concentration of silicic acid was much higher at the point of contact between the silica spheres than at any other site. At that contact point, therefore, polymerization of silicic acid could progress, leading to the formation of bridges between the silica spheres. In other words, the formation of

bridges indicates a deposition reaction in the local region which the silica spheres contacted. Concurrently, the etching reaction occurs in the region of uncontacted silica spheres. Therefore, two reactions, deposition and etching, competed with each other. After lapse of time, according to the abovementioned process, the concentration of hydrofluoric acid increased, and hence, the etching reaction became more predominant. After the silica sphere size decreased and the bridges between silica spheres elongated, the bridges were also etched. Thus, all the silica spheres and bridges were etched and eventually disappeared. This final etching result is explained by (1) the equilibrium reaction of silicic acid and silicon dioxide and (2) the change in the reaction rate according to the acidic conditions. First, the equilibrium reaction of silicic acid and silicon dioxide occurs as follows:



In accordance with this reaction, the equilibrium constant is dependent on the concentration of silicic acid. While the LPD reaction progressed, the amount of silicic acids was insufficient. Therefore, the abovementioned reaction accelerated toward the formation of silicic acid and silicon dioxide, consistently supplied by the self-etching of the

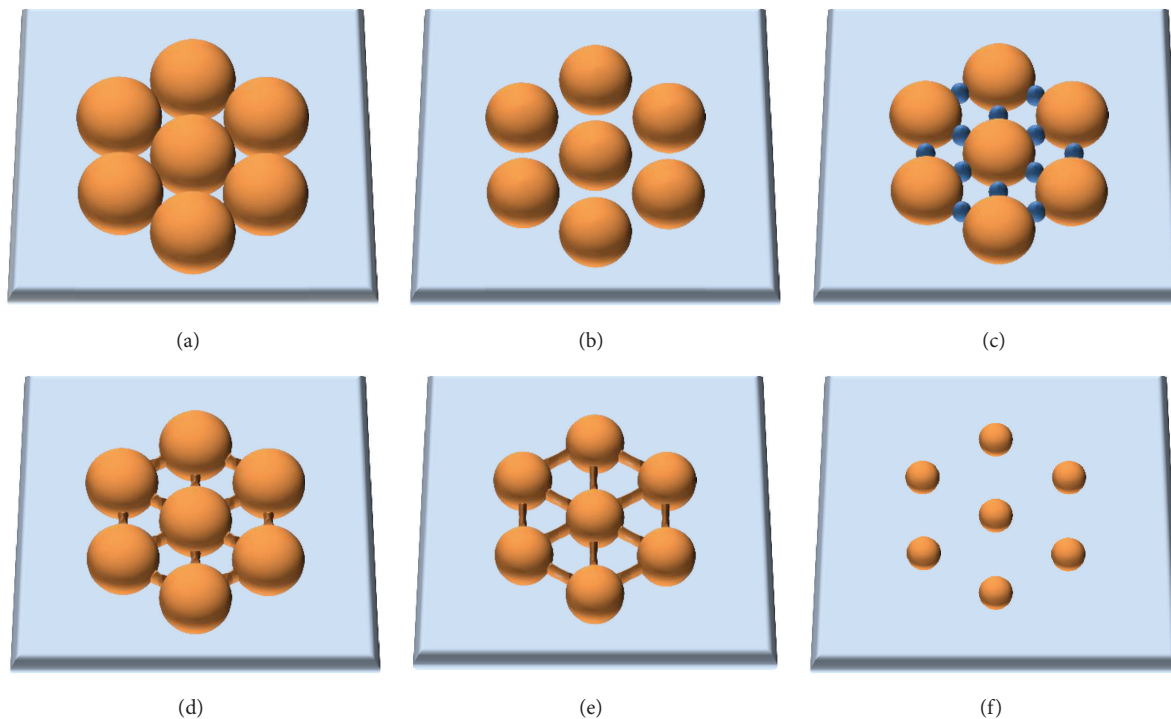


FIGURE 5: Schematic illustration depicting the mechanism of formation of nanostructure. (a) Hexagonally close-packed spheres in an aqueous solution. (b) Decrease in the size of silica spheres through homogeneous etching. (c) High concentration of silicic acid (blue) between the silica spheres. (d) Deposition of silica bridges between silica spheres. (e) Reduction of the nanostructure size due to etching. (f) Disappearance of the bridges.

silica spheres. Moreover, in the conditions under pH 7, the rate of the condensation reaction rapidly decreases, but the rate of hydrolysis sharply increases [22]. Because this reaction progresses in acidic solutions, the hydrolysis reaction occurs more easily than the condensation reaction does. Through this mechanism, we can fabricate nanostructures that have not been traditionally obtained by general methods such as synthesis and growth. Figure 5 depicts in brief the mechanism for the formation of the nanostructure.

4. Conclusions

In this work, we fabricated an array of perfect hexagonally close-packed silica spheres over a large area of a patterned substrate. Then, we experimented with a modified LPD reaction on this nanostructured substrate and demonstrated a new nanostructure that certified simultaneous deposition and etching, that is, between these two processes; then, we proposed the mechanism for the formation of this nanostructure. This nanostructure could be useful in the biointerface field as a substrate that influences biological systems such as cell and bacteria. Because biological behaviors are dependent on the external environment, the unique surface topography of the nanostructure could trigger new biological responses such as cellular adhesion, development, differentiation, proliferation, and so on.

Acknowledgment

This work was supported by the SRC Research Center for Women's Diseases of Sookmyung Women's University (2010).

References

- [1] S. E. Babayan, J. Y. Jeong, A. Schütze et al., "Deposition of silicon dioxide films with a non-equilibrium atmospheric-pressure plasma jet," *Plasma Sources Science and Technology*, vol. 10, no. 4, pp. 573–578, 2001.
- [2] M. F. Ceiler Jr., P. A. Kohl, and S. A. Bidstrup, "Plasma-enhanced chemical vapor deposition of silicon dioxide deposited at low temperatures," *Journal of the Electrochemical Society*, vol. 142, no. 6, pp. 2067–2071, 1995.
- [3] K. Ikeda, S. Nakayama, and M. Maeda, "Characteristics of silicon dioxide films on patterned substrates prepared by atmospheric-pressure chemical vapor deposition using tetraethoxysilane and ozone," *Journal of the Electrochemical Society*, vol. 143, no. 5, pp. 1715–1718, 1996.
- [4] K. Murase, "Dielectric constant of silicon dioxide deposited by atmospheric-pressure chemical vapor deposition using tetraethylorthosilicate and ozone," *Japanese Journal of Applied Physics*, vol. 33, no. 3, pp. 1385–1389, 1994.
- [5] W. J. Patrick, G. C. Schwartz, J. D. Chapple-Sokol, R. Carruthers, and K. Olsen, "Plasma-enhanced chemical vapor deposition of silicon dioxide films using tetraethoxysilane and oxygen: characterization and properties of films," *Journal of the Electrochemical Society*, vol. 139, no. 9, pp. 2604–2613, 1992.

- [6] S. K. Ray, C. K. Maiti, S. K. Lahiri, and N. B. Chakrabarti, "TEOS-based PECVD of silicon dioxide for VLSI applications," *Advanced Materials for Optics and Electronics*, vol. 6, no. 2, pp. 73–82, 1996.
- [7] K. S. Kim and Y. Roh, "Silicon dioxide deposited by using liquid phase deposition at room temperature for nanometer-scaled isolation technology," *Journal of the Korean Physical Society*, vol. 51, no. 3, pp. 1191–1194, 2007.
- [8] A. I. Kingon, J.-P. Maria, and S. K. Streiffer, "Alternative dielectrics to silicon dioxide for memory and logic devices," *Nature*, vol. 406, no. 6799, pp. 1032–1038, 2000.
- [9] A. Hishinuma, T. Goda, M. Kitaoka, S. Hayashi, and H. Kawahara, "Formation of silicon dioxide films in acidic solutions," *Applied Surface Science*, vol. 48–49, pp. 405–408, 1991.
- [10] A. V. Valiulis and P. Silickas, "Liquid phase deposition methods monitoring techniques influence for solid substrates and thin metal oxide films properties," *Journal of Achievements in Materials and Manufacturing Engineering*, vol. 24, pp. 188–192, 2007.
- [11] E. A. Whitsitt and A. R. Barron, *Liquid phase deposition of silica: thin films, colloids and fullerenes [Ph.D. thesis]*, 2004.
- [12] H. Nagayama, H. Honda, and H. Kawahara, "New process for silica coating solid-state science and technology," *Journal of the Electrochemical Society*, vol. 135, no. 8, pp. 2013–2016, 1988.
- [13] K. Tsukuma, T. Akiyama, N. Yamada, and H. Imai, "Liquid phase deposition of a film of silica with an organic functional group," *Journal of Non-Crystalline Solids*, vol. 231, no. 1–2, pp. 161–168, 1998.
- [14] K. S. Kim and Y. Roh, "Silicon dioxide deposited by using liquid phase deposition at room temperature for nanometer-scaled isolation technology," *Journal of the Korean Physical Society*, vol. 51, no. 3, pp. 1191–1194, 2007.
- [15] E. A. Whitsitt and A. R. Barron, "Effect of surfactant on particle morphology for liquid phase deposition of submicron silica," *Journal of Colloid and Interface Science*, vol. 287, no. 1, pp. 318–325, 2005.
- [16] W. Stöber, A. Fink, and E. Bohn, "Controlled growth of monodisperse silica spheres in the micron size range," *Journal of Colloid And Interface Science*, vol. 26, no. 1, pp. 62–69, 1968.
- [17] K. Nozawa, H. Gailhanou, L. Raison et al., "Smart control of monodisperse stöber silica particles: effect of reactant addition rate on growth process," *Langmuir*, vol. 21, no. 4, pp. 1516–1523, 2005.
- [18] N. N. Khanh and B. Y. Kyung, "Facile organization of colloidal particles into large, perfect one-and two-dimensional arrays by dry manual assembly on patterned substrates," *Journal of the American Chemical Society*, vol. 131, no. 40, pp. 14228–14230, 2009.
- [19] S. Reculosa and S. Ravaine, "Synthesis of colloidal crystals of controllable thickness through the Langmuir-Blodgett technique," *Chemistry of Materials*, vol. 15, no. 2, pp. 598–605, 2003.
- [20] J. Zhu, Z. Yu, G. F. Burkhardt et al., "Optical absorption enhancement in amorphous silicon nanowire and nanocone arrays," *Nano Letters*, vol. 9, no. 1, pp. 279–282, 2009.
- [21] J. Yi, H. S. Jang, J. S. Lee, and W. I. Park, "Bioinspired morphogenesis of highly intricate and symmetric silica nanostructures," *Nano Letters*, vol. 12, pp. 743–748, 2012.
- [22] C. J. Brinker and G. W. Scherer, *Sol-Gel Science: the Physics and Chemistry of Sol-Gel Processing*, Academic Press, San Diego, Calif, USA, 1990.

Research Article

Facile Fabrication of a Hierarchical Superhydrophobic Coating with Aluminate Coupling Agent Modified Kaolin

Hui Li, Mengnan Qu, Zhe Sun, Jinmei He, and Anning Zhou

College of Chemistry and Chemical Engineering, Xi'an University of Science and Technology, Xi'an 710054, China

Correspondence should be addressed to Jinmei He; jinmhe@gmail.com and Anning Zhou; zhouan@xust.edu.cn

Received 18 July 2013; Revised 9 September 2013; Accepted 11 September 2013

Academic Editor: Jiamin Wu

Copyright © 2013 Hui Li et al. This is an open access article distributed under the Creative Commons Attribution License, which permits unrestricted use, distribution, and reproduction in any medium, provided the original work is properly cited.

A superhydrophobic coating was fabricated from the dispersion of unmodified kaolin particles and aluminate coupling agent in anhydrous ethanol. Through surface modification, water contact angle of the coating prepared by modified kaolin particles increased dramatically from 0° to 152° , and the sliding angle decreased from 90° to 3° . Scanning electron microscopy was used to examine the surface morphology. A structure composed of micro-nano hierarchical component, combined with the surface modification by aluminate coupling agent which reduced the surface energy greatly, was found to be responsible for the superhydrophobicity. The method adopted is relatively simple, facile, and cost-effective and can potentially be applied to large water-repellent surface coatings.

1. Introduction

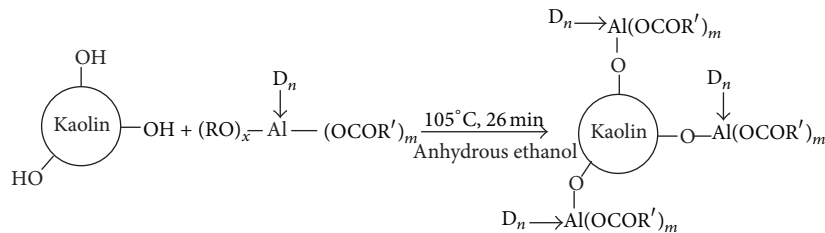
Recently, superhydrophobic surfaces have drawn much attention because of the potentials for both academic research and industrial applications [1, 2]. The criteria for a superhydrophobic surface are having a water contact angle (WCA) higher than 150° and a sliding angle (SA) lower than 10° [1, 3, 4]. They show many particular properties, such as biomimicking anti-sticking, contamination prevention, water repellency, self-cleaning, anti-fogging, and anti-reflection, and so forth [2, 5, 6]. Lots of relevant reports have emerged, including oil-water separation [7–9], industrial metal cleaning [10], tunable wettability surfaces [6, 11–14], self-repairing surfaces [15], fluidic drag reduction [5], electronic devices protection [16], and biomedical instruments [17]. Despite the intense research, these surfaces are still restricted by the following problems: limited hydrophobicity with high contact angle hysteresis, failure upon physical friction, weak environment stability, substrate limitation, and high production cost, which means a significant restriction of applications [15, 18].

Kaolin is a type of clay mineral consisting mainly of hydrated aluminum silicate or kaolinite [19], which is commercially available and low in cost [20]. Kaolin is also an important industrial material, and because of its high

whiteness, it was once used as the leading white pigment—in point of tonnage-consumed by North American industry [21]. Lots of applications of kaolin have emerged, such as paper coating, plastic and rubber filling, refractory, and ceramic and paint industries [19, 21–23]. Clay-polymer composites have drawn much attention because the incorporation of clay particles can lead to desirable changes in the material properties [24].

Herein, we present a very facile and simple method to fabricate a hierarchical superhydrophobic material by surface modifying kaolin particles of size 100–400 nm with aluminate coupling agent (ACA). ACA is an important surfactant. Usually, their colors show faint yellow to white, which is near to kaolin's color. It also has high activity in surface reactions and a high decomposition temperature and is environmental-friendly. The structural formula is $(\text{RO})_x\text{Al}(\text{OCR}')_m \cdot \text{D}_n$. There are two different kinds of functional groups in ACA, in which $(\text{RO})_x$ are hydrophilic and $(\text{OCR}')_m$ are hydrophobic. And D_n represent coordinating groups, such as N and O. The hydrophilic groups can make chemical reactions with the polar groups on the kaolin particles, making the particles coated with hydrophobic groups, which can reduce the surface energy greatly.

In this study, ACA modified kaolin was coated on commercially available glass slides to fabricate superhydrophobic



SCHEME 1: Illustration of chemical reaction between kaolin and ACA.

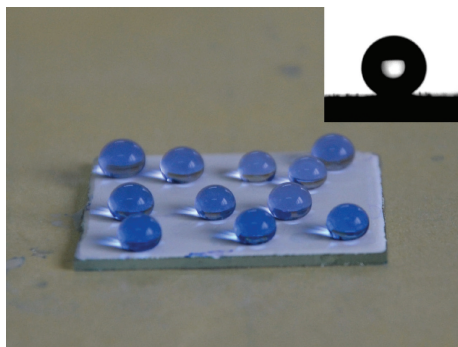


FIGURE 1: Images of water droplets dyed by methylene blue with different sizes on the ACA modified kaolin particles coating. Insets: profiles of water droplets on the surface have the contact angles of 152° .

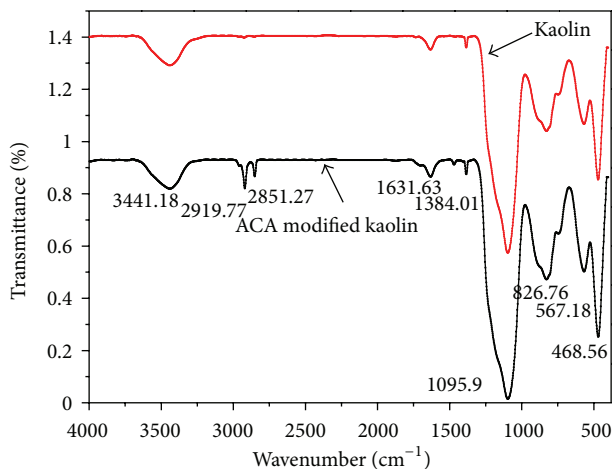


FIGURE 2: IR spectra of kaolin and aluminate coupling agent modified kaolin.

surfaces. This technique has no tedious procedures or expensive instruments and the resulting superhydrophobic material shows an excellent environment stability [25]. Because the fabricated particles were superhydrophobic, this can dramatically improve the application convenience. Furthermore, the material can be used on a variety of substrates, which can greatly expand the scope of applications. To examine the material's environmental stability, it was put outside; after three months of environmental exposure, it still shows excellent superhydrophobicity. For all the reasons above,

both for academic and industrial aspects, the as-prepared superhydrophobic material is expected to be of great value.

2. Materials and Methods

2.1. Materials. Kaolin particles of size 100–400 nm were purchased from Sinopharm Chemical Reagent Co., Ltd. and before used, they were dried at 120°C for 5 h to remove water. Aluminate coupling agent purchased from Nanjing Daoning Chemical Co., Ltd. was used as received. All other reagents were of AR grade and used as received.

2.2. Substrate Treatment. Glass slides were ultrasonically cleaned with water for 10 min and then immersed in ethanol for about 15 min, followed by rinsing with a copious amount of water prior to use.

2.3. Fabrication of the Superhydrophobic Material. 0.16 g ACA was dissolved in 11 mL anhydrous ethanol at 30°C for 20 min, and then 5.0 g kaolin particles were ultrasonically dispersed in the mixture for 15 min. Then, they were heated at 106°C for 26 min. Scheme 1 showed the reaction equation. At last, the mixture was drop-coated on glass slides. Samples were dried at room temperature, covered with a culture dish to slow down ethanol evaporation, and then cured at 120°C for 1 h. Another, for the convenience of use, ACA modified kaolin particles can also be obtained. The mixture was centrifugally separated for 5 min, and then the particles were collected by suction filtration using a sand core funnel. Finally, they were dried at 100°C for 1 h. ACA modified kaolin particles (500 mg) were suspended in 1.2 mL anhydrous ethanol, subsequently, by heating for 25 min at 100°C to make a suspension. The preparation of the samples and the following treatments are the same as the stated above.

2.4. Characterization and Instruments. Infrared (IR) spectra were recorded on a Bruker Tensor 27 IR spectrometer (Bruker, Germany) with KBr as the background in the range of $4000\text{--}400\text{ cm}^{-1}$. Samples were prepared by pressing the particles into KBr pellets. Water contact angle (WCA) and sliding angle measurements were performed using a SL200B instrument (Solon Tech., Shanghai, China) at ambient temperature. The volumes of probing liquids in the measurements were approximately $5\ \mu\text{L}$ for the contact angle measurement and $10\ \mu\text{L}$ for the sliding angle measurement. Each contact angle reported was an average value of at least

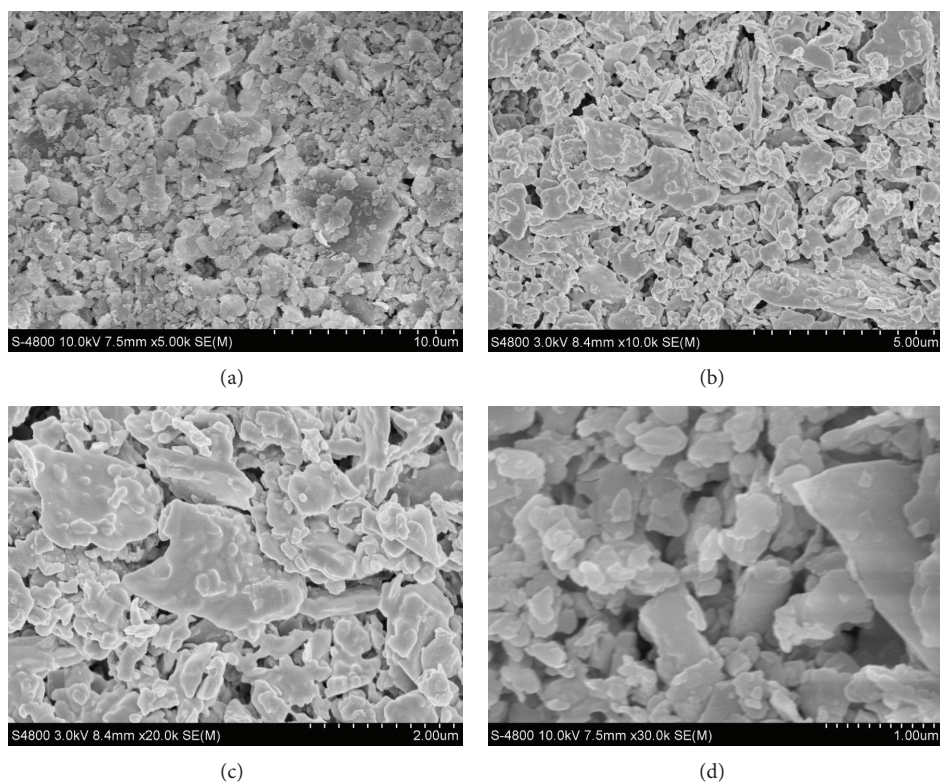


FIGURE 3: SEM micrographs of the as-prepared superhydrophobic surface. The scale bars represent (a) 10 μm , (b) 5 μm , (c) 2 μm , and (d) 1 μm , respectively.

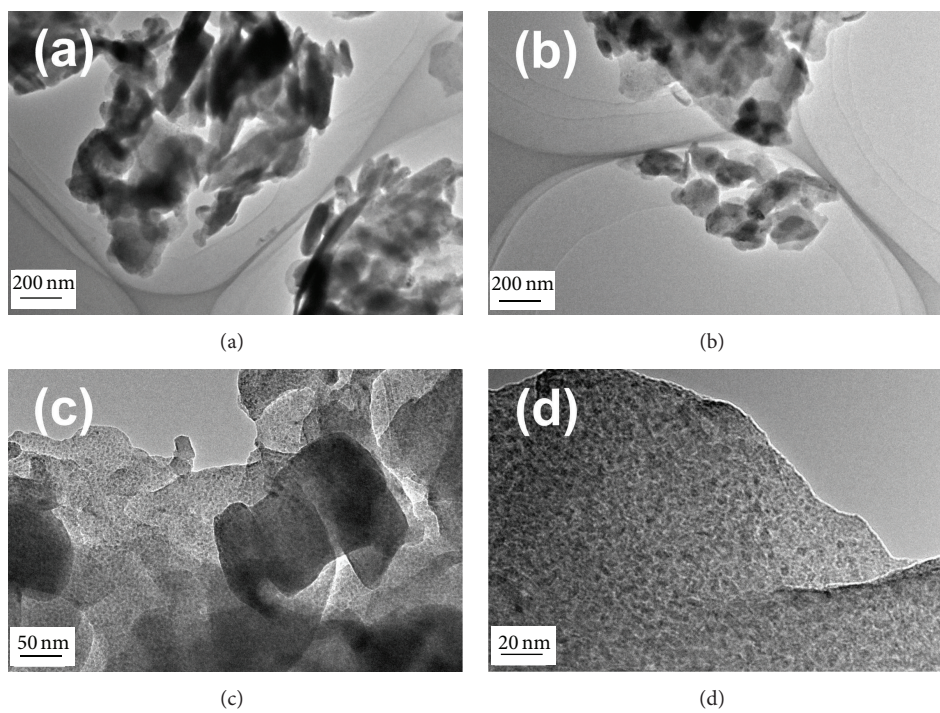


FIGURE 4: TEM micrographs of kaolin particles. The scale bars represent (a) 200 nm, (b) 200 nm, (c) 50 nm, and (d) 20 nm, respectively.



FIGURE 5: Images of water droplets dyed by methylene blue with different sizes on the ACA modified kaolin particles coating after three months of exposure to outdoor conditions.

five independent measurements on different positions. A scanning electron microscopy (SEM) (Hitachi S-4800) was used for examining the sample surface morphology in top-view or in cross-sections. Before the SEM investigations, all the samples were coated with gold cluster. Transmission electron microscopy (TEM) measurements were carried out using a JSM-1200EX transmission electron microscopy.

3. Results and Discussion

As noted above, the application of superhydrophobic surfaces is greatly hampered for the problem of high contact angle hysteresis, failure upon physical friction, weak environment stability, substrate limitation, and high production cost. Our work is to prepare a coating, which is superhydrophobic, using a very facile and cost-effective method, and can be applied on various substrates. Such a superhydrophobic coating was obtained by surface modification of kaolin particles using ACA as a surfactant. After the samples were cured in the oven, the as-prepared ACA modified kaolin particles surface had a static WCA of 152° , as shown in Figure 1; compared to the WCA of the unmodified kaolin, which was almost 0° , it had demonstrated an outstanding superhydrophobicity. The SA was only 3° and water droplets on this superhydrophobic coating surface easily rolled off even when there is only little tilt of the surfaces and made it very difficult to measure the WCA.

The coupling reaction was confirmed by IR analyses of ACA modified kaolin. In Figure 2, the dark and red lines are the modified and unmodified kaolin particles, respectively. For the ACA modified kaolin particles, the characteristic peaks of the asymmetric and symmetric CH_2 stretching vibration at 2919.77 and 2851.27 cm^{-1} , respectively, suggested a complete alkylation reaction between ACA and kaolin.

To further analyze the morphology of the surface, SEM was applied. The SEM images in Figure 3 showed the morphology of the coating surface. In Figures 3(a) and 3(b), it can be seen that the kaolin particles of different sizes were distributed evenly in the coating. Figures 3(c) and 3(d) revealed that the particles formed a micro-nano hierarchical structure, which, combined with the hydrophobic groups introduced by ACA modification, is supposed to be

essential for superhydrophobicity [26–29]. All these features endowed the coating superhydrophobicity. The images exhibited an evident morphology of the surface roughness, which explained the prominent superhydrophobicity.

The modified kaolin particles were also analyzed by TEM (Figure 4). The TEM images revealed that the size of kaolin particles was in a range of $100\text{--}400 \text{ nm}$ and that the surfaces of the particles were not smooth, which were composed of many overhang and re-entrant structures. Both the different particle sizes and the rough surface were contributed to the construction of hierarchical structures, so as to potentially render the particle coating superhydrophobic.

To estimate the durability of the superhydrophobic coatings, an environmental stability experiment was carried out. The coatings were exposed to environmental conditions by keeping them outdoor. The results indicated that, after three months of exposure to outdoor conditions, no superhydrophobicity decrease was found. Water drops still kept a spherical shape in the surface with a WCA of 151° and were also easily rolling off, taking dusts away in their paths (see Figure 5). We also coated the material on a variety of other substrates, such as commercial marble, limestone, plank, and plasterboard, and all the samples showed good superhydrophobicity. The results indicated that the coating can be applied on a variety of substrates.

4. Conclusions

In the present work, a coating from ACA modified kaolin was fabricated to render the surface with superhydrophobicity. The superhydrophobic surface exhibited a highly rugged structure with micro-nano hierarchical particles randomly distributed all through the coating. Both the hierarchical structure and the ACA modified kaolin furnished the surface with superhydrophobicity. Furthermore, the as-prepared superhydrophobic material showed very good environmental durability and practicability. The technique utilized here is cost-effective, environmental-friendly, and the coating can be prepared easily on various substrates; we expect that this technique can considerably expand the range for various applications, examples of which may include fabricating large water-repellent surface coatings.

Acknowledgments

The authors thank the National Natural Science Foundation of China (Grant nos. 21003099; 21102113) and the Natural Science Research Project of Science and Technology Agency of Shaanxi Province, China (Grant no. 2013KJXX-41) for continuing financial support.

References

- [1] T. Sun, L. Feng, X. Gao, and L. Jiang, "Bioinspired surfaces with special wettability," *Accounts of Chemical Research*, vol. 38, no. 8, pp. 644–652, 2005.
- [2] H. Zhou, H. Wang, H. Niu, A. Gestos, X. Wang, and T. Lin, "Fluoroalkyl silane modified silicone rubber/nanoparticle composite: a super durable, robust superhydrophobic fabric

- coating," *Advanced Materials*, vol. 24, no. 18, pp. 2409–2412, 2012.
- [3] C. P. Hsu, L. Y. Chang, C. W. Chiu, P. T. Lee, and J. J. Lin, "Facile fabrication of robust superhydrophobic epoxy film with polyamine dispersed carbon nanotubes," *ACS Applied Materials & Interfaces*, vol. 5, no. 3, pp. 538–545, 2013.
- [4] M. Liu, Y. Zheng, J. Zhai, and L. Jiang, "Bioinspired superantiwetting interfaces with special liquid–solid adhesion," *Accounts of Chemical Research*, vol. 43, no. 3, pp. 368–377, 2010.
- [5] X. Yao, J. Gao, Y. Song, and L. Jiang, "Superoleophobic surfaces with controllable oil adhesion and their application in oil transportation," *Advanced Functional Materials*, vol. 21, no. 22, pp. 4270–4276, 2011.
- [6] J. Yang, Z. Zhang, X. Men, X. Xu, X. Zhu, and X. Zhou, "Counterion exchange to achieve reversibly switchable hydrophobicity and oleophobicity on fabrics," *Langmuir*, vol. 27, no. 12, pp. 7357–7360, 2011.
- [7] R. W. Field, "Surface science: separation by reconfiguration," *Nature*, vol. 489, pp. 41–42, 2012.
- [8] L. Zhang, Z. Zhang, and P. Wang, "Smart surfaces with switchable superoleophilicity and superoleophobicity in aqueous media: toward controllable oil/water separation," *NPG Asia Materials*, vol. 4, no. 2, p. e8, 2012.
- [9] G. Kwon, A. K. Kota, Y. Li, A. Sohani, J. M. Mabry, and A. Tuteja, "On-demand separation of oil-water mixtures," *Advanced Materials*, vol. 24, no. 27, pp. 3666–3671, 2012.
- [10] Z. Guo, F. Zhou, J. Hao, and W. Liu, "Stable biomimetic super-hydrophobic engineering materials," *The Journal of the American Chemical Society*, vol. 127, no. 45, pp. 15670–15671, 2005.
- [11] L. Wang, Y. Lin, B. Peng, and Z. Su, "Tunable wettability by counterion exchange at the surface of electrostatic self-assembled multilayers," *Chemical Communications*, no. 45, pp. 5972–5974, 2008.
- [12] L. Wang, Y. Lin, and Z. Su, "Counterion exchange at the surface of polyelectrolyte multilayer film for wettability modulation," *Soft Matter*, vol. 5, no. 10, pp. 2072–2078, 2009.
- [13] L. Wang, B. Peng, and Z. Su, "Tunable wettability and rewritable wettability gradient from superhydrophilicity to superhydrophobicity," *Langmuir*, vol. 26, no. 14, pp. 12203–12208, 2010.
- [14] H. Wang, Y. Xue, J. Ding, L. Feng, X. Wang, and T. Lin, "Durable, self-healing superhydrophobic and superoleophobic surfaces from fluorinated-decyl polyhedral oligomeric silsesquioxane and hydrolyzed fluorinated alkyl silane," *Angewandte Chemie*, vol. 50, no. 48, pp. 11433–11436, 2011.
- [15] T.-S. Wong, S. H. Kang, S. K. Y. Tang et al., "Bioinspired self-repairing slippery surfaces with pressure-stable omniphobicity," *Nature*, vol. 477, no. 7365, pp. 443–447, 2011.
- [16] S. Lee, W. Kim, and K. Yong, "Overcoming the water vulnerability of electronic devices: a highly water-resistant ZnO nanodevice with multifunctionality," *Advanced Materials*, vol. 23, no. 38, pp. 4398–4402, 2011.
- [17] A. M. Shanmugharaj, J. H. Yoon, W. J. Yang, and S. H. Ryu, "Synthesis, characterization, and surface wettability properties of amine functionalized graphene oxide films with varying amine chain lengths," *Journal of Colloid and Interface Science*, vol. 401, pp. 148–154, 2013.
- [18] J. Zhang and S. Seeger, "Superoleophobic coatings with ultralow sliding angles based on silicone nanofilaments," *Angewandte Chemie*, vol. 50, no. 29, pp. 6652–6656, 2011.
- [19] S. Solihin, Q. Zhang, W. Tongamp, and F. Saito, "Mechanochemical synthesis of kaolin-KH₂PO₄ and kaolin-NH₄H₂PO₄ complexes for application as slow release fertilizer," *Powder Technology*, vol. 212, no. 2, pp. 354–358, 2011.
- [20] Z. Lu, M. Ren, H. Yin et al., "Preparation of nanosized anatase TiO₂-coated kaolin composites and their pigmentary properties," *Powder Technology*, vol. 196, no. 2, pp. 122–125, 2009.
- [21] L. A. Agnello, H. H. Morris, and F. A. Gunn, "Kaolin," *Industrial & Engineering Chemistry Research*, vol. 52, no. 5, pp. 370–376, 1960.
- [22] M. Özdemir and H. Çetişli, "Sulfate removal from alunitic kaolin by chemical method," *Industrial & Engineering Chemistry Research*, vol. 44, no. 9, pp. 3213–3219, 2005.
- [23] Y. M. Liew, H. Kamarudin, A. M. Mustafa Al Bakri et al., "Processing and characterization of calcined kaolin cement powder," *Construction and Building Materials*, vol. 30, pp. 794–802, 2012.
- [24] Y. Zhang, D. I. Gittins, D. Skuse, T. Cosgrove, and J. S. van Duijneveldt, "Composites of kaolin and polydimethylsiloxane," *Langmuir*, vol. 24, no. 20, pp. 12032–12039, 2008.
- [25] B. B. J. Basu and A. K. Paranthaman, "A simple method for the preparation of superhydrophobic PVDF-HMFS hybrid composite coatings," *Applied Surface Science*, vol. 255, no. 8, pp. 4479–4483, 2009.
- [26] M. Qu, B. Zhang, S. Song, L. Chen, J. Zhang, and X. Cao, "Fabrication of superhydrophobic surfaces on engineering materials by a solution-immersion process," *Advanced Functional Materials*, vol. 17, no. 4, pp. 593–596, 2007.
- [27] M. Qu, G. Zhao, X. Cao, and J. Zhang, "Biomimetic fabrication of lotus-leaf-like structured polyaniline film with stable superhydrophobic and conductive properties," *Langmuir*, vol. 24, no. 8, pp. 4185–4189, 2008.
- [28] W. Ye, J. Yan, Q. Ye, and F. Zhou, "Template-free and direct electrochemical deposition of hierarchical dendritic gold microstructures: growth and their multiple applications," *The Journal of Physical Chemistry C*, vol. 114, no. 37, pp. 15617–15624, 2010.
- [29] H. Bellanger, T. Darmanin, and F. Guittard, "Surface structuration (micro and/or nano) governed by the fluorinated tail lengths toward superoleophobic surfaces," *Langmuir*, vol. 28, no. 1, pp. 186–192, 2012.

Research Article

Effect of Nanosilica Filled Polyurethane Composite Coating on Polypropylene Substrate

Yern Chee Ching and Nurehan Syamimie

Department of Mechanical Engineering, Faculty of Engineering, University of Malaya, Lembah Pantai, 50603 Kuala Lumpur, Malaysia

Correspondence should be addressed to Yern Chee Ching; chingyc@um.edu.my

Received 19 July 2013; Revised 16 September 2013; Accepted 20 September 2013

Academic Editor: Mengnan Qu

Copyright © 2013 Y. C. Ching and N. Syamimie. This is an open access article distributed under the Creative Commons Attribution License, which permits unrestricted use, distribution, and reproduction in any medium, provided the original work is properly cited.

Acrylic based polyurethane (PU) coatings with various amounts of nanosilica contents were prepared using solution casting method. The nanosilica (SiO_2) particles used are around 16 nm in diameter. The friction and wear test was conducted using the reciprocating wear testing machine. The tests were performed at rotary speed of 100 rpm and 200 rpm with load of 0.1 kg to 0.4 kg under 1 N interval. The effect of the PU/nano- SiO_2 composite coating on friction and wear behavior of polypropylene substrate was investigated and compared. The worn surface of coating film layer after testing was investigated by using an optical microscope. The introduction of PU/nanosilica composite coating containing 3 wt% of nano- SiO_2 content gives the lowest friction coefficient and wear rate to PP substrate. Both the friction and wear rate of PP substrate coated with >3 wt% of nano- SiO_2 filled PU coating would increase with the increasing of applied load and sliding time.

1. Introduction

Polypropylene (PP) is an attractive engineering material due to its low cost, ease of processability, good mechanical properties, resistance to organic solvents, and favorable environmental aspects. However, the disadvantages of polypropylene are the lack of adhesion and poor scratch resistance [1, 2]. Current technologies applied to improve scratch resistance of PP included coating, lamination, additives, and altering the nature of the PP resin. Incorporating metal-oxide nanoparticles such as nanoalumina and nanosilica into polymer coatings to enhance mechanical durability has been widely utilized in the current antiscratch and mar technologies [1]. Generally, hydrophobic surface type nanomaterials will be more attractive for polymer coating due to their unique properties such as self-cleaning, antisticking, water repellence and anticontamination [3, 4]. From the recent research studies in nanoparticles field, hydrophobic nano- SiO_2 particles have been widely introduced into coatings to improve the heat resistance, wear resistance, hardness, antisticking, and optical properties of the polymer materials [1, 2].

In polymeric coatings, the use of nanoparticles is more towards upgrading the level of resistance to wear and friction. The presence of nanoparticle in the surface layer of film

enhances the scratch hardness and hence protects both the coating film and substrate against marring, cracking, wear, and mild abrasions [2]. Blees et al. [1] have studied the adhesion of the sol gel coating on polypropylene by using scratch test method that focuses on the effect of friction between indenter and coating on the critical load. The critical load (normal to the surface) showed a pronounced decrease of more than the order of magnitude with increasing of friction coefficient. Zhou et al. [2] have reported that the addition of nano- SiO_2 can improve the hardness, abrasion resistance, scratch resistance, tensile strength, modulus, and weatherability of the polymer based coating lacquer. Despite using nano- SiO_2 particles, the other nanoparticles such as TiO_2 , SiC , ZnO , ZrO_2 , and Al_2O_3 were also chosen to improve tribological properties [5–14]. Song et al. [5] have studied the tribological behaviours of the phenolic composite coating filled with modified nano- TiO_2 . The addition of small amounts of TiO_2 or TF- TiO_2 can improve the friction-reduction and antiwear abilities of phenolic coating, and TF- TiO_2 as a filler is superior to TiO_2 in terms of ability to decrease the friction coefficient and wear rate of phenolic coating [6].

Recently, the gradual replacement of metal parts into polymeric components takes place in several industries

especially in automotive and aerospace manufacture. Thus, the need for understanding the tribological behaviour of polymers substrate and polymer base coating materials becomes important. The polymer matrix composites (PMCs) are subjected to abrasive wear in many applications especially plowing effect from counterface hard asperities during coal handling, and the mining process has resulted in material removal and groves. Previous studies [15–18] have reported the effect of inorganic fillers to the friction and wear behavior of polyurethane coating; however, the tribological studies related to the performance of these polymers composite coatings onto various substrates are limited. Thus, this study was mainly focused on the effect of acrylic based polyurethane coating embedded with nanosilica to the wear and friction resistance of polypropylene substrate.

2. Experimental

2.1. Materials. In this work, acrylic based polyurethane, PU340, was supplied from Worldtex Specialty Chemical. PU 340 is a one-pack translucent solventborne polyurethane based on aliphatic urethane with approximately 30% solid content (viscosity at 25°C: 80 MPa). Meanwhile, nanosilica, Aerosil R972, supplied by Degussa Huls, was used for the preparation of the nanocomposites. Aerosil R972 is one type of hydrophobic fumed silica treated with dimethyldichlorosilane (DDS) based on hydrophilic fumed silica. The average primary particle size of Aerosil R972 was 16 nm in average diameter with the specific surface area of 130 m²/g. The mixture of toluene/isopropanol/ethyl acetate in a fixed volume fraction of 6:3:1 was employed in the present work as a solvent. Polypropylene (PP) substrate with a size of 110 mm × 25 mm × 1 mm was used as a substrate for PU/nanosilica composite coating. Various amounts of nanosilica powders ranging from 0 to 10 wt% were added to the polyurethane (PU) resin. The mixture was vigorously stirred using magnetic stirring at ambient temperature for at least 1 hour until clear dispersion and homogeneous mixture were obtained. To obtain the same coating thickness of around 3 micrometers for all samples, 1 g of the mixed suspensions was then directly coated on each PP substrate using Rod Mayer technique. The coating thickness is mainly determined by the withdrawal speed, by the solid content, and by the viscosity of the liquid [19]. The consistency of the coating thickness was controlled by monitoring the three factors above. Only the sample with the consistent thickness will be used for the further characterization study.

2.2. Preparation of PU/Nanosilica Composite Coating on PP Substrate. Nanosilica particles were directly embedded into the acrylic resin solution at 60°C under vigorous stirring for an hour. Polyurethane/nanosilica composite was deposited on polypropylene substrate using a Rod Mayer bar. The Rod Mayer technique was used to deposit the polyurethane/nanosilica composite material on the surface of the polyethylene substrate. Wire-wound rod 0.5 inch in diameter and 12 inches in length was used to spread the nanocomposite materials on the surface of the ceramic

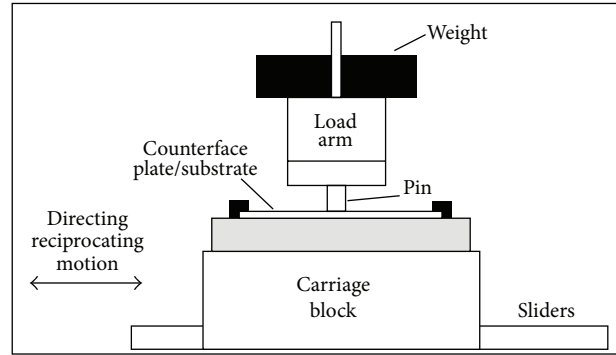


FIGURE 1: Schematic diagram of reciprocating wear machine.

substrate. The wire-wound rod used has wire of 20 mils. The PU/nanocomposite coating passes through the grooves between the wires and then levels off to a uniform thickness on the substrate. All the samples were cured in the laboratory with relative humidity of 40–60% and temperature of 25°C. After solvent evaporation, a thin film around 3 μm was obtained on the substrate.

2.3. Characterization. The nanocomposite coating thickness was measured by using optical microscope DM750P. The microstructure of PU coating and PU/nanosilica composite coatings was examined with a Field Emission Scanning Electron Microscope (FESEM, Hitachi Corporation, Japan) with accelerating voltage of 0.8 kV. For SEM study, a 1 cm × 1 cm size piece was cut from the middle part of the sample. In order to increase the resolution for the SEM observation, the tested polymeric samples were plated with gold coating to render them electrically conductive. The friction and wear test was conducted under a dry and clean condition using Reciprocating Wear Testing Machine (BICERI). This apparatus consists of a stationary pin sliding on a reciprocating plate with its axis perpendicular to the direction of motion as illustrated schematically in Figure 1. The sizes of samples used are 110 mm × 25 mm with the thickness of 2 mm. The sliding performs at a rotary speed of 100 rpm and 200 rpm with the load varying from 0.1 kg to 0.4 kg. The reciprocal sliding tests were run at a sliding distance of 80 mm/revolution with an interval of 0.1 kg and duration time of 10 minutes. The worn surface after testing was then observed using light optical microscope. All the friction and wear tests were carried out at ambient temperature, 20°C to 25°C, with the relative humidity of 60%. A computer program periodically records the amount of linear wear, which is equal to the decrease in pin height plus the depth of the groove worn in the plate.

3. Results and Discussion

FESEM was used to investigate the dispersion of nano-SiO₂ particle and surface morphological changes of the nano-SiO₂ filled PU coating. The FESEM micrograph in Figure 2 reveals the dispersion condition of 3 wt% and 7 wt% of nano-SiO₂ contents in polyurethane coating. From Figure 2(a), the dispersion of 3 wt% of nanosilica particles in PU matrix

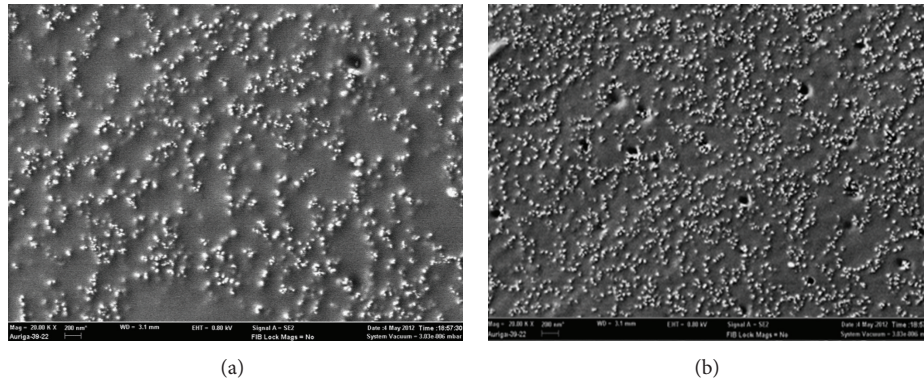


FIGURE 2: FESEM micrographs of PP substrate coated with (a) 3 wt% and (b) 7 wt% nano-SiO₂ filled PU coating.

can be concluded to be well distributed with numerous clusters. However, there were higher agglomerates and aggregates found in polyurethane filled with 7 wt% of nano-SiO₂ (Figure 2(b)). This microstructure had caused the increase of surface roughness for polyurethane films containing 7 wt% of nano-SiO₂ content. The strong tendency of nano-SiO₂ to agglomerate has caused difficulty to achieve homogenous dispersion in PU/nano-SiO₂ composite coating especially filled with high content of nano-SiO₂ particles. It was also found that there were some cavities or pores on the surfaces of PU/nano-SiO₂ composite coating containing 7 wt% of nano-SiO₂ that might be caused by the trapped air bubbles generated during the mixing and stirring process [6–11]. According to Kansy et al. [20], nanoparticles dispersion and surface roughness have considerable impact on the friction and wear behaviors of the nanocomposite coating. Higher roughness increases the asperities slope angle which in turn increases friction coefficient [21].

Figure 3 illustrates that the neat polypropylene achieves the highest friction coefficient with a value of 0.6 under 0.2 kg load. When neat polyurethane coating was introduced to PP substrate, it shows that there was a slight decrease in the coefficient of friction. The introduction of 3 wt% of nano-SiO₂ into the PU coating layer has successfully reduced the friction coefficient of the nanocomposite coated PP from 0.56 to 0.30. This might be due to the thin layer of PU/nano-SiO₂ coating with low amount of nanomaterials which has provided a form of self-lubrication during sliding. The same observation was found in the research on titanium-containing amorphous hydrocarbon coatings [22, 23] and titanium carbide amorphous composite coating [24]. However, there was a sharp increase of friction coefficient of PP coated with PU/nano-SiO₂ composite film when 7 wt% and 10 wt% nano-SiO₂ particles were introduced to the composite. This may be closely related to the amount and distribution state of nanosilica particulates on coating surfaces, that is, the coating surface roughness. The polyurethane nanocomposite coatings with lower content of nanosilica may have smaller surface roughness thus lower friction coefficient, and for polyurethane nanocomposite coating with higher content of nanosilica, they may have larger surface roughness which leads to higher coefficient of friction. This is possibly due to

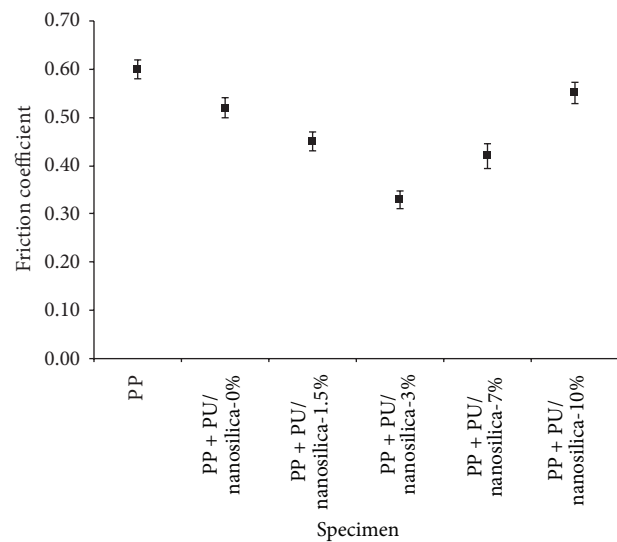


FIGURE 3: The friction coefficient of PU/nano-SiO₂ composite coated PP substrates under load of 0.2 kg with a speed of 100 rpm in 10 min sliding time.

the different extent of abrasion action of nanosilica aggregates [22]. Hence, it can be concluded that the addition of small amounts of nano-SiO₂ content can exhibit the improvement of friction coefficient of the polyurethane coated PP matrix.

Figure 4 shows the effect of applied load on the friction coefficient of nano-SiO₂ filled PU coating under the speed of 100 rpm in 10 min sliding time. It can be seen that PP, PP coated with a neat PU coating, and PP coated with PU filled with high amount of nano-SiO₂ would increase with increasing applied load from 0.1 kg to 0.4 kg. However, the friction coefficient of PP coated with 3 wt% of nano-SiO₂ filled PU coating dropped when applied load increases from 0.1 kg to 0.2 kg. This might be with the incorporation of small amounts of nanosilica; the effect of load on friction coefficient was caused by the elastic deformation of surface asperities under relatively lower load and the plastic deformation under relatively higher load [25, 26]. At low load of 0.1 kg to 0.2 kg, the particle-shaped or flaky debris on the surface of PP coated with PU/nano-SiO₂-3% composite would be crashed, staved,

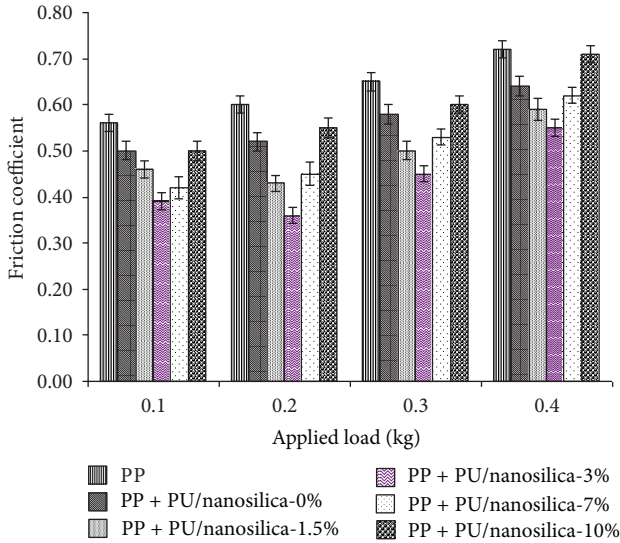


FIGURE 4: Effect of applied load on the friction coefficient of PU/nano-SiO₂ composite coated PP under speed of 100 rpm.

or sheared into thinner flakes or small particles accordingly, thus reducing the surface roughness [27]. The newly formed debris would become more integrated, and concurrently, the film on the worn surface would be thinner. Consequently, the more integrated smaller debris but the thinner film on the worn surface would bring smaller friction coefficient due to the decrease in the degree of the two-body abrasive wear [28]. Therefore, the minimal friction coefficient was observed on PP coated with PU containing 3 wt% of nano-SiO₂ particles under the applied load of 0.2 kg. At higher loads, the plastic deformation occurs at the asperities in contact. Increasing applied load on nanocomposite layer with 3 wt% of nano-SiO₂ content would result in more nano-SiO₂ dropping out from the polyurethane matrix during the friction process, which led to severe abrasive wear and resulted in a higher friction coefficient. With the high amount of >3 wt% of nano-SiO₂ in PU coating, the friction coefficient increased with the increasing of applied load due to the combination of both high amounts of nanosilica aggregates, and applied load would lead to severe plastic deformation of polyurethane coating, owing to mechanical incompatibility between the coating and substrate.

Since 3 wt% of nano-SiO₂ filled PU composite coated on PP substrates shows the lowest friction coefficient, hence it appears as the optimal nanosilica content in PU. This proportion was further investigated for the effect in terms of applied load and speed on the friction behavior. Figure 5 illustrates the friction coefficient of PP coated with 3 wt% of nano-SiO₂ filled PU under sliding speeds of 100 rpm and 200 rpm at different applied loads. The friction coefficient of all composite coated samples increases as sliding speed goes up from 100 rpm to 200 rpm. The increase of friction coefficient with sliding speed is closely related to the friction-induced heat. At higher speed, the friction-induced heat will pay a significant role at the frictional interface sliding compared to that at lower speed. This accelerated the degradation

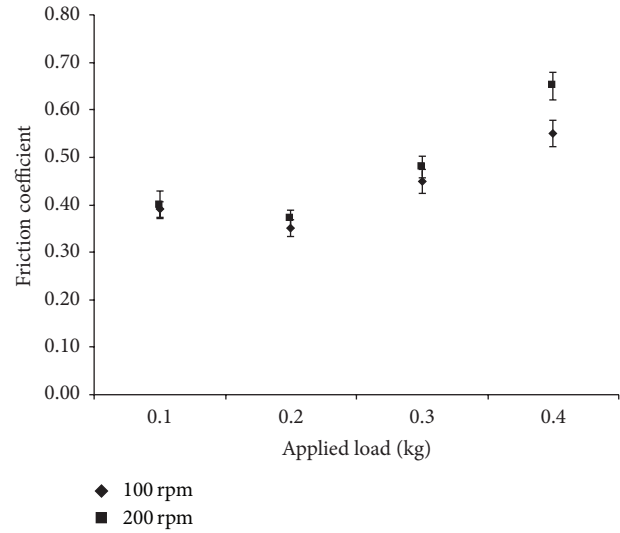


FIGURE 5: Effect of speed rate on friction coefficient of 3 wt% nano-SiO₂ filled PU coated PP substrate with different applied loads.

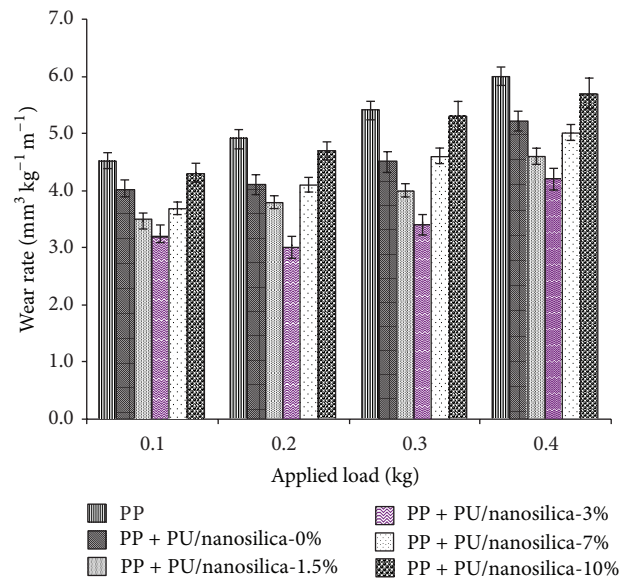


FIGURE 6: Effect of applied load on the wear rate of various compositions of PU/nano-SiO₂ composite coated PP under speed of 100 rpm.

and decomposition of the polyurethane resin matrix and nanosilica, thus causing the increase of friction coefficient of the composite, and substrates became more severe at high sliding speed [29].

The effect of applied load on the wear rate of various compositions of PU/nano-SiO₂ composite coated PP substrate under speed of 100 rpm and 10 min sliding time is shown in Figure 6. The neat PP without composite coating layer shows the highest wear rate throughout the applied load ranges. The wear rate of PP substrate decreases significantly with the introduction of neat PU coating and PU/nanosilica composite coating modified with small amount of nano-SiO₂

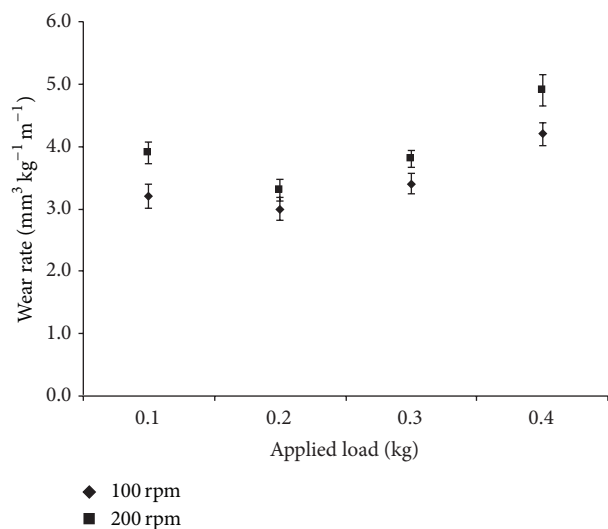


FIGURE 7: Effect of speed rate on the wear rate of 3 wt% nano-SiO₂ filled PU coated PP substrate with different applied load.

particles. However, with addition of >3 wt% of nano-SiO₂ to the PU coating layer would increase the wear rate of the samples significantly. Hence, it can be concluded that the addition of small amounts of nano-SiO₂ content at 3 wt% would lead to the improvement of wear rate of polyurethane coated PP substrate.

Same as the effect of friction coefficient, 3 wt% of nano-SiO₂ filled PU coating provides the lowest wear rate to PP substrate for all the applied loads from 0.1 kg to 0.4 kg. The wear rate increases with the increasing of applied load for uncoated PP and PP coated with PU containing high amount of nano-SiO₂ fillers (e.g., 7–10 wt%). The increase in wear rate as a result of increasing load may be due to the failure of the coatings to protect the surface of the substrate as high applied load can lead to severe plastic deformation of the polyurethane coating. The plastic deformation is due to the mechanical incompatibility between the polyurethane coating and the substrate under high applied load. Higher amount of nano-SiO₂ fillers also means a more severe aggregation of the fillers, thereby hindering the friction-reducing behavior of the filled composite coating, due to the abrasion action of the filler aggregates [2, 30, 31]. On the other hand, small amount of nano-SiO₂ filler aggregates on composite coating surfaces may function to resist abrasion by the counterface asperities, thereby resulting in improved wear resistance of the composite coating [2, 30].

Figure 7 illustrates that the wear rate of 3 wt% nano-SiO₂ filled PU coated PP substrate increases with the rising of applied loads of >0.2 kg for both sliding speeds of 100 rpm and 200 rpm. This indicates that the addition of nanosilica has helped in improving the ability of carrying loads in the polyurethane coating. The better antiwear behavior of nano-SiO₂ coating under different applied loads mainly dominated by the elastic deformation of surface asperities under relatively lower load and plastic deformation under relatively higher load as has been described before [25, 30].

Hence, it can be concluded that the optimal amount of nano-SiO₂ at 3 wt% filler aggregates on composite coating surfaces may function to resist abrasion by the counterface asperities, thereby resulting in improved wear resistance of the composite coating.

Figure 8 shows the optical micrographs of the worn surface of PU/nano-SiO₂ composite coated PP substrate with various content of nano-SiO₂ tested under the applied load of 0.2 kg and a speed of 100 rpm. The worn surface after wear test for PP coated with a neat PU coating shows signs of adhesion and abrasive wear (Figure 8(a)). The surface was very rough, displaying plucked and ploughed marks indicative of adhesive wear and ploughing. This might be due to fatigue-delamination generated under repeated loading during sliding [32]. Fatigue wear has been regarded as a main mechanism responsible for the sliding of the unfilled PU coating against a hard counterpart.

With the introduction of 3 wt% of nano-SiO₂ contents in the PU coating layer, it can be seen that the worn surface of the nanocomposite coated PP substrate was smooth and showed only fine scratches as shown in Figure 8(b). It can be inferred that a polymer film layer can be transferred to the steel counterpart, and this results in a new counter surface producing primarily an adhesive wear mechanism. For polymer coating sliding surface, this mechanism is less harmful if compared to abrasive wear as this mechanism will result in a lower coefficient of friction and wear rate. This smooth, uniform, and compact worn surface leads to the good influence in increasing the wear resistance of PU/nano-SiO₂ coating layer. This is proven from the previous friction and wear behaviors study. However, the worn surface appeared with severe plastic deformation and microcracking as the nano-SiO₂ content in PU/nano-SiO₂ composite was increased to 7 wt% (Figure 8(c)).

The worn surfaces of PP substrate coated with 3 wt% nano-SiO₂ filled PU coating under different applied loads are shown in Figures 9(a)–9(c). Figure 9(a) shows that the worn surface of the coating was smooth under 0.1 kg load with speed of 100 rpm. When the applied load was increased to 0.2 kg, there are some adhesion marks and cracks on the worn surfaces as shown in Figure 9(b). With further increase of applied load, there are some large amounts of cracks or flaky debris in the worn surface that would be crushed or sheared into smaller particles or thinner flakes and act as lubricants (Figure 9(c)). At the same time, the newly formed debris would come into being a more integrated layer on the worn surface and reduced the “direct contact” between the fabric composite and the counterpart.

The effect of speed on the worn surface of 3 wt% nano-SiO₂ filled PU coated PP substrate is shown in Figure 10. Mild wear occurred on the worn surface of the sample tested with the speed of 100 rpm (Figure 10(a)). In Figure 10(b), the wear became severe under speed 200 rpm indicating that the serious fatigue wear is the main wear mechanism of the filled PU coating when sliding under higher speed. It can be inferred that large area of frictional surface of the filled PU coating would flake away if the speed increases further and the coating would be seriously damaged.

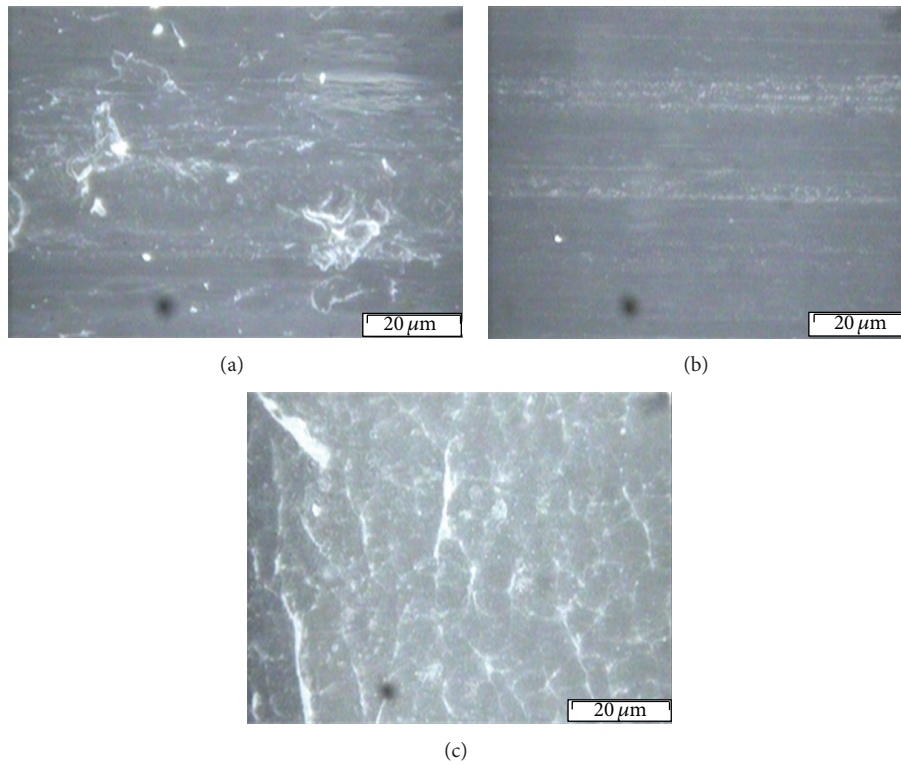


FIGURE 8: Optical micrographs of the worn surface of PU/nano-SiO₂ composite coated PP with various content of nano-SiO₂ (a) 0 wt%, (b) 3 wt%, and (c) 7 wt% (0.2 kg, 100 rpm, 10 min).

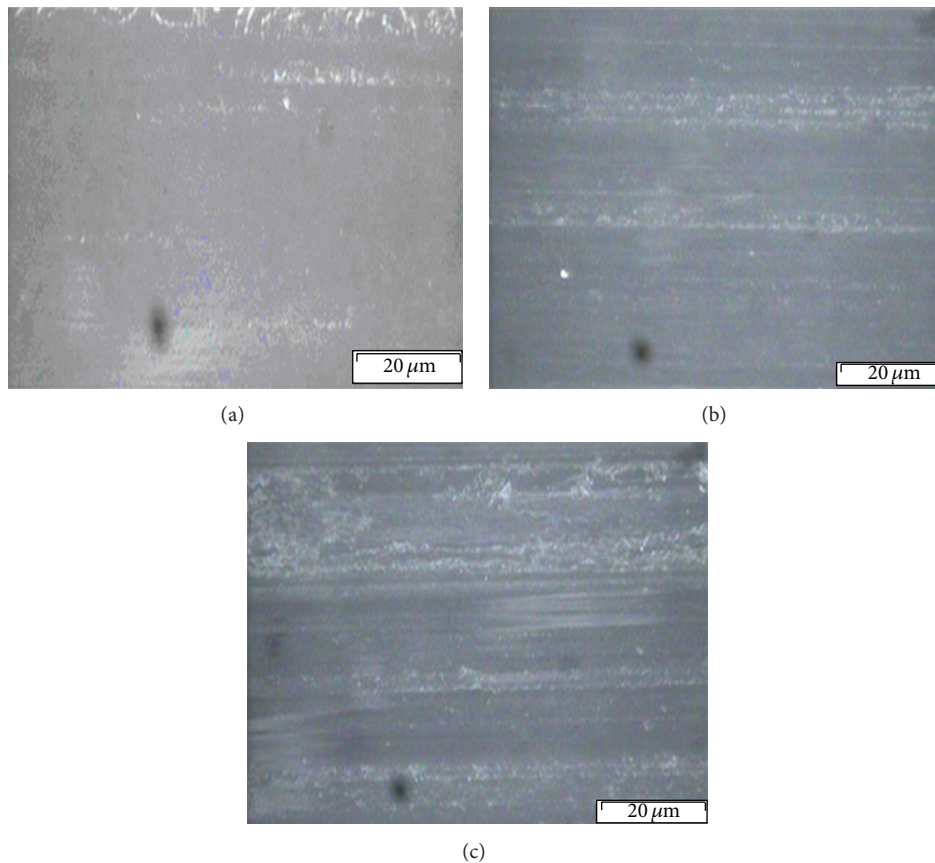


FIGURE 9: Optical micrographs of the worn surfaces of PP coated with 3 wt% nanosilica filled PU coating under different applied loads (a) 0.1 kg, (b) 0.2 kg, and (c) 0.4 kg (100 rpm, 10 min).

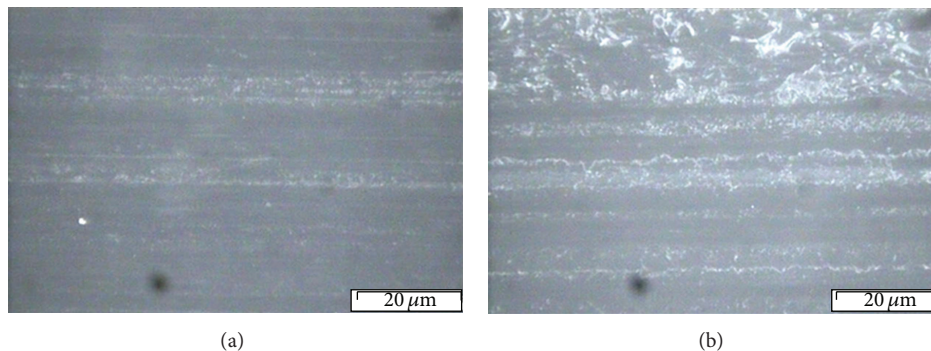


FIGURE 10: Optical micrographs of the worn surfaces of 3 wt% nanosilica filled polyurethane coating under 0.2 kg load, with different speeds of (a) 100 rpm and (b) 200 rpm (10 min).

4. Conclusions

PU/nano-SiO₂ composite coating without agglomeration was successfully prepared by using a magnetic stirring technique. Introduction of small quantities of nano-SiO₂ into PU coating would resist the abrasion by counterface asperities and hence can improve the wear resistance of composite coating. The friction and wear behavior of PU/nano-SiO₂ composite coating was closely related to the sliding condition, such as sliding speed and applied load. The sliding speed and applied load have influenced the wear process and the worn surface. The low load and speed combination has made the matrix tend to adhere to nanoparticles and give the lesser degree of debris formation. The wear resistance behavior of PU/nano-SiO₂ composite coating under different applied loads was mainly dominated by both the elastic and plastic deformation. In this study, PU/nano-SiO₂ composite coating with 3 wt% of nano-SiO₂ content exhibits a strengthened filler-matrix bonding has successfully protected the polypropylene substrate against wearing and mild abrasions.

Acknowledgments

The authors would like to thank the financial support provided by UMRG RP011A-13AET, PG079-2012B, FP030-2013A, and ER014-2012A.

References

- [1] M. H. Bles, G. B. Winkelman, A. R. Balkenende, and J. M. J. Den Toonder, "Effect of friction on scratch adhesion testing: application to a sol-gel coating on polypropylene," *Thin Solid Films*, vol. 359, no. 1, pp. 1–13, 2000.
- [2] S. Zhou, L. Wu, J. Sun, and W. Shen, "The change of the properties of acrylic-based polyurethane via addition of nanosilica," *Progress in Organic Coatings*, vol. 45, no. 1, pp. 33–42, 2002.
- [3] H.-J. Song, Z.-Z. Zhang, and X.-H. Men, "Superhydrophobic PEEK/PTFE composite coating," *Applied Physics A*, vol. 91, no. 1, pp. 73–76, 2008.
- [4] J. B. Bharathibai and D. Kumar, "Fabrication of superhydrophobic nanocomposite coatings using polytetrafluoroethylene and silica nanoparticles," *ISRN Nanotechnology*, vol. 2011, Article ID 10.5402/2011/803910, 6 pages, 2011.
- [5] H.-J. Song, Z.-Z. Zhang, and X.-H. Men, "Surface-modified carbon nanotubes and the effect of their addition on the tribological behavior of a polyurethane coating," *European Polymer Journal*, vol. 43, no. 10, pp. 4092–4102, 2007.
- [6] D. Lingaraju, K. Ramji, M. P. Devi, and U. R. Lakshmi, "Mechanical and tribological studies of polymer hybrid nanocomposites with nano reinforcements," *Bulletin of Materials Science*, vol. 34, no. 4, pp. 705–712, 2011.
- [7] Y. C. Ching, Y. C. Ching, and I. I. Yaacob, "Weathering effect on virgin PE & PE coated with polyamide/nanosilica composite coating," *Journal of Computational and Theoretical Nanoscience*, vol. 9, no. 9, pp. 1161–1164, 2012.
- [8] Y. C. Ching, Y. C. Ching, and I. Yaacob, "Effect of polyurethane/nanosilica composite coating on thermomechanical properties of polyethylene film," *Materials Technology*, vol. 27, no. 1, pp. 113–115, 2012.
- [9] Y. C. Ching, Y. C. Ching, and I. Yaacob, "Weathering resistance of solventborne polyurethane/nanosilica composite," *Advanced Science Letters*, vol. 27, pp. 165–169, 2012.
- [10] Y. C. Ching and I. I. Yaacob, "Weathering effect on PE coated with thin layer of PU/nanosilica composite," *Advanced Materials Research*, vol. 181–182, pp. 697–701, 2011.
- [11] Q.-H. Wang, X.-R. Zhang, and X.-Q. Pei, "Study on the friction and wear behavior of basalt fabric composites filled with graphite and nano-SiO₂," *Materials and Design*, vol. 31, no. 3, pp. 1403–1409, 2010.
- [12] H.-J. Song, Z.-Z. Zhang, and X.-H. Men, "Tribological behavior of polyurethane-based composite coating reinforced with TiO₂ nanotubes," *European Polymer Journal*, vol. 44, no. 4, pp. 1012–1022, 2008.
- [13] Y. C. Ching and I. I. Yaacob, "Influence of nanosilica/polyurethane composite coating on IR effectiveness and visible light transmission properties of polyethylene," *Advanced Materials Research*, vol. 97–101, pp. 1669–1672, 2010.
- [14] Y. C. Ching and I. I. Yaacob, "Influence of nano-sio₂/polyamide composites coating on thermic effect and optical properties of polyethylene film," *International Journal of Modern Physics B*, vol. 23, no. 6–7, pp. 1395–1400, 2009.
- [15] Q.-H. Wang, X.-R. Zhang, and X.-Q. Pei, "Study on the friction and wear behavior of basalt fabric composites filled with graphite and nano-SiO₂," *Materials and Design*, vol. 31, no. 3, pp. 1403–1409, 2010.

- [16] F. Bauer, R. Flyunt, K. Czihal et al., "UV curing and matting of acrylate coatings reinforced by nano-silica and micro-corundum particles," *Progress in Organic Coatings*, vol. 60, no. 2, pp. 121–126, 2007.
- [17] F. Dolatzadeh, S. Moradian, and M. M. Jalili, "Effect of nanosilica on moisture absorption of polyurethane clear coats as studied by EIS and gravimetric methods," *Progress in Color Colorants Coating*, vol. 3, pp. 92–100, 2010.
- [18] X. Gao, Y. Zhu, X. Zhao et al., "Synthesis and characterization of polyurethane/SiO₂ nanocomposites," *Applied Surface Science*, vol. 257, no. 10, pp. 4719–4724, 2011.
- [19] S. K. Dhoke, N. Rajgopalan, and A. S. Khanna, "Effect of nanoalumina on the electrochemical and mechanical properties of waterborne polyurethane composite coatings," *Journal of Nanoparticles*, vol. 2013, Article ID 527432, 11 pages, 2013.
- [20] J. Kansy, G. Consolati, and C. Dauwe, "Positronium trapping in free volume of polymers," *Radiation Physics and Chemistry*, vol. 58, no. 5-6, pp. 427–431, 2000.
- [21] S. J. Bull, P. R. Chalker, C. Johnston, and V. Moore, "The effect of roughness on the friction and wear of diamond thin films," *Surface and Coatings Technology*, vol. 68-69, pp. 603–610, 1994.
- [22] Y. Kang, X. Chen, S. Song, L. Yu, and P. Zhang, "Friction and wear behavior of nanosilica-filled epoxy resin composite coatings," *Applied Surface Science*, vol. 258, no. 17, pp. 6384–6390, 2012.
- [23] M. M. Nikje, M. R. Khanmohammadi, and A. B. Garmarudi, "Nanosilica reinforced epoxy floor coating composites: preparation and thermophysical characterization," *Current Chemistry Letter*, vol. 1, pp. 1–8, 2012.
- [24] D. M. Cao, B. Feng, W. J. Meng, L. E. Rehn, P. M. Baldo, and M. M. Khonsari, "Friction and wear characteristics of ceramic nanocomposite coatings: titanium carbide/amorphous hydrocarbon," *Applied Physics Letters*, vol. 79, no. 3, pp. 329–331, 2001.
- [25] M. Rostami, Z. Ranjbar, and M. Mohseni, "Investigating the interfacial interaction of different aminosilane treated nano silicas with a polyurethane coating," *Applied Surface Science*, vol. 257, no. 3, pp. 899–904, 2010.
- [26] D. K. Chattopadhyay and K. V. S. N. Raju, "Structural engineering of polyurethane coatings for high performance applications," *Progress in Polymer Science*, vol. 32, no. 3, pp. 352–418, 2007.
- [27] K. Friedrich, J. Flöck, K. Váradi, and Z. Néder, "Experimental and numerical evaluation of the mechanical properties of compacted wear debris layers formed between composite and steel surfaces in sliding contact," *Wear*, vol. 250-251, no. 2, pp. 1202–1212, 2001.
- [28] G. Zhao, T. Wang, and Q. Wang, "Studies on wettability, mechanical and tribological properties of the polyurethane composites filled with talc," *Applied Surface Science*, vol. 258, no. 8, pp. 3557–3564, 2012.
- [29] H.-J. Song, Z.-Z. Zhang, X.-H. Men, and Z.-Z. Luo, "A study of the tribological behavior of nano-ZnO-filled polyurethane composite coatings," *Wear*, vol. 269, no. 1-2, pp. 79–85, 2010.
- [30] M. M. A. Nikje, A. B. Garmarudia, and M. Haghshena, "Nanosilica reinforced epoxy floor coating composites: preparation and thermophysical characterization," *Current Chemistry Letters*, vol. 1, pp. 13–20, 2012.
- [31] Y. C. Ching, C. Y. Chen, and I. I. Yaacob, "Mechanical properties changes of nanosilica filled solventborne polyamide binder after accelerated weathering exposure weathering," *Advanced Science Letters*, vol. 13, pp. 575–578, 2012.
- [32] R. O. Ritchie, "Mechanisms of fatigue-crack propagation in ductile and brittle solids," *International Journal of Fracture*, vol. 100, no. 1, pp. 55–83, 1999.

Research Article

Fluoroalkylsilane versus Alkylsilane as Hydrophobic Agents for Silica and Silicates

Damian Ambrożewicz,¹ Filip Ciesielczyk,¹ Magdalena Nowacka,¹ Joanna Karasiewicz,² Adam Piasecki,³ Hieronim Maciejewski,^{2,4} and Teofil Jesionowski¹

¹ Institute of Chemical Technology and Engineering, Faculty of Chemical Technology, Poznan University of Technology, M. Skłodowskiej-Curie 2, 60965 Poznan, Poland

² Department of Organometallic Chemistry, Faculty of Chemistry, Adam Mickiewicz University, Grunwaldzka 6, 60780 Poznan, Poland

³ Institute of Materials Science and Engineering, Faculty of Mechanical Engineering and Management, Poznan University of Technology, Jana Pawła II 24, 60965 Poznan, Poland

⁴ Poznan Science & Technology Park, AMU Foundation, Rubież 46, 61612 Poznan, Poland

Correspondence should be addressed to Teofil Jesionowski; teofil.jesionowski@put.poznan.pl

Received 3 July 2013; Revised 23 August 2013; Accepted 28 August 2013

Academic Editor: Mengnan Qu

Copyright © 2013 Damian Ambrożewicz et al. This is an open access article distributed under the Creative Commons Attribution License, which permits unrestricted use, distribution, and reproduction in any medium, provided the original work is properly cited.

Hydrophobic powders were obtained via surface modification of silica or magnesium silicate with selected silanes. A modified precipitation method, carried out in an emulsion system, was used for monodisperse silica synthesis, while magnesium silicate was precipitated in a traditional water system. Functionalization of the obtained inorganic supports was performed with selected alkylsilanes: one newly synthesized, 3-(2,2,3,3,4,4,5,5-octafluoropentyloxy)propyltriethoxysilane (OPF), and two commercial, octadecylsilane (ODS) and octyltriethoxysilane $C_{14}H_{32}O_3Si$ (OCS), in amounts of 3, 5, or 10 weight parts by mass of SiO_2 . It was determined how the chemical modification of the silica or magnesium silicate surface affected its physicochemical properties. The dispersive characteristics of both unmodified and functionalized silica-based systems were evaluated. The morphology and microstructure of the samples obtained were analyzed using scanning electron microscopy. The parameters of porous structure of the prepared systems were evaluated on the basis of BET equation as well as nitrogen adsorption/desorption isotherms. Wettability tests as well as elemental analysis of the obtained inorganic oxide hybrids were also performed. In order to verify the effectiveness of silica and magnesium silicate surface functionalization with selected silanes, FTIR spectra were investigated. The resulting experimental data allowed calculation of the degree of coverage of the silica-based systems with modifying agents.

1. Introduction

Many methods for chemical surface modification of silica and silicate fillers have been proposed. The selection of a specific method depends on the scale of the process (laboratory, industrial), the thickness of the target layer, and the degree of modification [1].

Since the activity of silica fillers depends mainly on their structure, much attention has been paid to the chemical character of surface and possibilities of its modification. An important problem is the modification of their surface by chemical reactions. First of all, the surface of silica and silicate is modified to improve their affinity to organic compounds, polymers in particular. This can be achieved by reduction

of surface hydrophilicity and its energy as well as by the introduction of appropriate functional groups [2].

Many methods have been proposed to perform the surface modification of fillers, including the sol-gel method (in which organofunctional groups are introduced onto, e.g., silica during its synthesis) [3, 4], a method based on the use of water solvents (modification is carried out in a polar environment of water-methanol or water-acetone type) [5], a method based on the use of organic solvents (carried out in anhydrous conditions, anhydrous organic solvent, and dehydrated surface, and the stage of silane hydrolysis being omitted) [6–10], the method of self-organized monolayers (a variation of adsorption from liquid phase) [11–13], the intermediate hybrid method (developed by Sandoval et

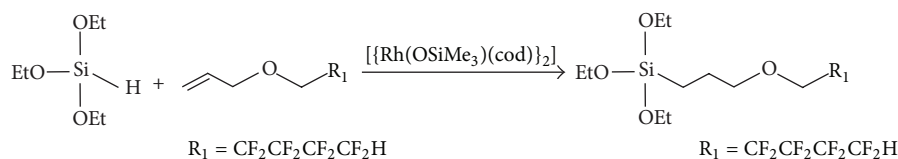


FIGURE 1: Synthesis of 3-(2,2,3,3,4,4,5,5-octafluoropentyloxy)propyltriethoxysilane.

al., employing a two-stage silanization-alkylation procedure instead of alkylsilylation [14–16], and the gas phase method (fluidal bed) [17–19].

Modification is a complex process depending on many parameters, including the type of solvent, the type and concentration of modifying substance, pH, duration, and the catalysts used. The process involving surface wetting of the substrate is performed in a reactor that should ensure minimum consumption of the modifying agent (the solvent) and the modifier (the proadhesive compound). In the process, the silane coupling agents are attached to the functional silanol groups of the powder substance via the mechanism of electrophilic substitution [20–24].

An addition of a small amount of an organofunctional silane to a certain filler significantly improves its binding ability with organic and/or bioorganic compounds and thus improves the physicochemical properties of final polymer products. Apart from the above application, silane coupling agents are used to enable bonding of metal complexes (catalysis) or enzymes (biochemistry) and to permit the separation of mixtures of hydrocarbons (chromatography).

In the process of modification, organofunctional silanes are deposited from a solution, emulsion, or water suspension. In water media, two processes take place: hydrolysis and condensation. The rate of hydrolysis depends on the concentration of silane, the pH of the solution (pH > 10 and pH < 5 give a high rate, pH near 7 gives the slowest rate), and the character of the functional groups of silanes and alkoxy groups [20–22]. Hydrolysis is catalyzed by hydronium ions H_3O^+ , hydroxyl ions OH^- , Lewis bases, and some metals. Hydrolysis is followed by silane condensation, which is slowest at a pH of 4–5, so this is the optimum pH of the reaction environment, ensuring fast hydrolysis and slow condensation.

Surfactants (anionic, cationic, and non-ionic) [24–29] and proadhesive compounds (silanes: titanates, borates, phosphates, zirconates, and hafnates) [30–36] are commonly used modifiers. Modification significantly extends the range of application of a given silica-based filler. Modified silicates with reduced wettability are used in the construction of sunlight collectors, elements of touch panels for optical and other devices used in industry, and motor vehicles and household utensils and also in the production of new types of textile products [37, 38].

The aim of this study was to obtain silica-based systems characterized by well-defined physicochemical properties including high degree of dispersion and high hydrophobicity, by means of surface functionalization with selected alkylsilanes.

2. Experimental

2.1. Materials. Highly dispersed silica was obtained in a process of precipitation, carried out in an emulsion system, using 5% solutions of sodium silicate (Na_2O 8.50%, SiO_2 27.18%, density 1.39 g/cm^3 , modulus 3.3, Vitrosilicon SA) and hydrochloric acid (analytical grade, density 1.19 g/cm^3 , POCh SA) as the initial substrates. Cyclohexane (analytical grade, density 0.779 g/cm^3 , POCh SA) as the organic phase and nonylphenylpolyoxyethyleneglycol ethers NP3 and NP6 ($\text{C}_9\text{H}_{19}\text{Ph}(\text{CH}_2\text{CH}_2\text{O})_n\text{H}$, purchased from Sigma-Aldrich) as emulsifying agents determining the stability of the emulsion were also used.

On the other hand, magnesium silicate was precipitated from 5% aqueous solutions of sodium silicate and magnesium sulfate ($\text{MgSO}_4 \cdot 7\text{H}_2\text{O}$, analytical grade, density 2.66 g/dm^3 , purchased from Chempur).

The surface of those inorganic supports was grafted with selected silanes: one newly synthesized, 3-(2,2,3,3,4,4,5,5-octafluoropentyloxy)propyl-triethoxysilane $\text{C}_{14}\text{H}_{24}\text{F}_8\text{O}_4\text{Si}$ (OPF), and two commercial, octadecylsilane $\text{C}_{18}\text{H}_{40}\text{Si}$ (ODS) and octyltriethoxysilane $\text{C}_{14}\text{H}_{32}\text{O}_3\text{Si}$ (OCS), both with 97% purity, purchased from Sigma-Aldrich (Table I).

2.1.1. Synthesis of Fluorocarbofunctional Triethoxysilane (OPF). Synthesis of OPF was carried out in a two-stage process. In the first stage, allyl-fluoroalkyl ether was obtained via the Williamson reaction, using fluoroalkyl alcohol and allyl chloride. Then the allyl-fluoroalkyl ether was subjected to hydrosilylation with triethoxysilane in the presence of siloxide rhodium complex as catalyst [39] (Figure 1).

1,1,2,2,3,3,4,4-octafluoropentyl allyl ether in a quantity of 20.4 g (75 mmol) and rhodium catalyst in a quantity of $0.22 \mu\text{g}$ ($10^{-5} \text{ mol Rh/1 mol } \equiv\text{Si-H}$) $[\{\text{Rh}(\text{OSiMe}_3)(\text{cod})\}_2]$ were placed in a three-neck round-bottom flask equipped with a thermometer, condenser, and magnetic bar. Then 11.5 g of triethoxysilane (70 mmol) was introduced, and the solution was heated up to 60°C and kept at that temperature for 1 h. After the reaction was completed, the solvent and excess of olefin were evaporated under vacuum to give the product in a quantity of 29.9 g (98% of the theoretical yield).

The product structure was confirmed by NMR analysis.

^1H NMR. (C_6D_6 , 298 K, 300 MHz) δ (ppm): 0.6 (2H, $-\text{SiCH}_2-$); 1.13 (9H, CH_3-); 1.67 (2H, $-\text{CH}_2-$); 3.17 (2H, $-\text{CH}_2\text{O}-$); 3.47 (2H, $-\text{OCH}_2-\text{CF}_2-$); 3.72 (6H, $\text{CH}_3-\text{CH}_2\text{O}-$); 5.59 (1H, $-\text{CF}_2\text{H}$).

^{13}C NMR. (C_6D_6 , 298 K, 75.5 MHz) δ (ppm): 6.73 ($-\text{SiCH}_2-$); 18.38 ($-\text{CH}_3$); 23.34 ($-\text{CH}_2-$); 58.47 ($-\text{OCH}_2\text{CH}_3$); 67.52

TABLE I: Alkylsilanes' characteristics.

Name	Acronym	Chemical formula	Structure
3-(2,2,3,3,4,4,5,5-octafluoropentyloxy)propyltriethoxysilane	OPF	$C_{14}H_{24}F_8O_4Si$	
Octadecylsilane	ODS	$C_{18}H_{40}Si$	
Octyltriethoxysilane	OCS	$C_{14}H_{32}O_3Si$	

($-OCH_2CF_2-$); 75.03 ($-CH_2O-$); 108.17, 111.53, 116.00 ($-CF_2-$); 119.39 ($-CF_2H$).

^{29}Si NMR. (C_6D_6 , 298 K, 59.6 MHz) δ (ppm): -46.14 ($(EtO)_3SiCH_2-$).

2.2. Procedures and Methods

2.2.1. Precipitation of Silica. Precipitation of the silica support took place in a two-emulsion system. The first emulsion, E1, was formed using 5% solution of sodium silicate (as silica precursor), cyclohexane (as organic phase), and nonionic surfactants NP3 and NP6 in quantities of 2.3 g and 2.5 g, respectively (as emulsifiers). Emulsion E2 was formed with a 5% solution of hydrochloric acid, cyclohexane, and a mixture of the same emulsifiers but in quantities of 1.5 g and 1.3 g, respectively. Before the precipitation process, emulsion E2 was placed in a special reactor equipped with a high-speed homogenizer, to which homogenized E1 was added at a constant rate of $10\text{ cm}^3/\text{min}$. As a result of the reaction, an emulsion containing silica was obtained. Then the reaction system was heated up to 80°C , in order to destabilize the emulsion, and after that it was possible to separate the organic phase using a vacuum evaporator made by Büchi Labortechnik GmbH. The mixture was filtered off under reduced pressure and the filtrate was washed with hot water and then with acetone in order to remove surfactant residues. Finally, the sample was dried by a convection method at 105°C for 48 h, using a MEMMERT dryer.

2.2.2. Precipitation of Magnesium Silicate. Highly dispersed magnesium silicate was precipitated in a reactor of 10 dm^3 in capacity (made by QVF MiniPlant PILO-TEC) equipped with

a high-speed stirrer (1000 rpm). The precipitation reaction was carried out at room temperature. At the beginning of the process, a certain volume of a 5% solution of magnesium silicate was placed in the reactor, to which a 5% solution of sodium silicate was introduced using a peristaltic pump at a constant rate of $20\text{ cm}^3/\text{min}$. The process lasted for about 5 h.

The precipitate was separated from the postreaction mixture by filtration, and then the filtrate was washed a few times with hot, distilled water to remove residues of unreacted salts. Then the samples were dried at 105°C and classified.

The silica and the magnesium silicate obtained were subjected to a comprehensive range of tests to evaluate their physicochemical properties.

2.2.3. Surface Modification of Silica and Magnesium Silicate by Chemical Method. The inorganic powders obtained were subjected to surface modification with selected silanes (see Table I) used in quantities of 3, 5, and 10 weight parts by mass of SiO_2 . Modifying agents were first hydrolyzed in a methanol/water system (4/1, v/v) with a controlled pH value being maintained in the range of 4-5. After that, the modifying mixture was sprayed onto the surface of the filler. Modification was performed using a vacuum evaporator, to which the mixture of obtained silica or silicate together with the modifying agent was introduced. In this way, it was possible to remove the organic solvent (methanol) from the reaction mixture. The process lasted for 1 hour.

2.2.4. Physicochemical Properties of the Obtained Hybrids. The dispersive characteristics (particle size distributions) of the fillers obtained were evaluated with a Zetasizer Nano

ZS and a Mastersizer 2000, both made by Malvern Instruments Ltd., using the noninvasive backscattering (NIBS) method and laser diffraction technique, respectively. These two devices enable the measurement of particle sizes in different ranges: 0.6–6000 nm and 0.2–2000 μm , respectively. Mastersizer 2000 allowed to obtain characteristic dispersion parameters such as $d(0.1)$, $d(0.5)$, $d(0.9)$, and $D[4.3]$. The terms $d(0.1)$, $d(0.5)$, and $d(0.9)$ correspond, respectively, to the frequencies of 10%, 50%, and 90%. For instance, $d(0.5)$ means that 50% of the particles possess a diameter less than a given value. Thus, the term $D[4.3]$ is described as mean particle diameter calculated from the whole sample volume. The morphology and microstructure of the samples were determined using a scanning electron microscope (Zeiss EVO40). The observations permitted evaluation of the degree of dispersion, the structure of particles, and the nature of agglomerations. The effectiveness of the functionalization process was also evaluated on the basis of zeta potential measurements. Zeta potential was measured by the electrophoretic light scattering method using a Zetasizer Nano ZS instrument equipped with an autotitrator made by Malvern Instruments Ltd. The electrokinetic potential was measured in the presence of a 0.001 M NaCl electrolyte. Measurements were performed in the pH range from 1.5 to 11, which enabled the determination of the electrokinetic curves. The standard deviation of the zeta potential at a given pH was ± 1.5 mV or less, and the error in the pH was estimated to be 0.05 pH units or lower. The degree of modification of the inorganic supports with selected alkylsilanes was determined using a FTIR EQUINOX 55 spectrophotometer made by Bruker. The obtained fillers were subjected to FTIR analysis after tableting using KBr. The chemical composition of the modified fillers was determined using a Vario EL Cube apparatus made by Elementar Analysensysteme GmbH and using a Specs Phoibos-100 spectrophotometer operating based on the XPS (X-ray photoelectron spectroscopy) method. Parameters of porous structure (surface area and pore size distribution) were also evaluated for selected samples. Measurements were made using an ASAP 2020 instrument made by Micromeritics Instrument Co. operating on the basis of low-temperature nitrogen adsorption.

In order to characterize the hydrophilic/hydrophobic character of the obtained fillers, they were subjected to wettability tests, performed by the sorption method using a K100 tensiometer (Krüss). Measurements were performed for about 600 s, until the sample attained a constant mass.

3. Results and Discussion

In the first stage of the research, a comparative analysis was carried out on the dispersive and morphological properties (SEM observations) of unmodified silica and SiO_2 functionalized with 5 weight parts by mass of 3-(2,2,3,3,4,4,5,5-octafluoropentyl)propyltriethoxysilane (OPF), octadecylsilane (ODS), and octyltriethoxysilane (OCS) (Figures 2 and 3).

Figure 2 presents the particle size distributions, according to volume contribution, determined for both unmodified and silica modified with 5 weight parts by mass of OPF (Figure 2(b)), ODS (Figure 2(c)), or OCS (Figure 2(d)). Monodisperse particle size distribution was obtained only for unmodified silica, and the dominant volume contribution of 38.3% was recorded for particles of 531 nm in diameter. Modification of the silica surface resulted in an increase in the particles' tendency to agglomerate (presence of secondary agglomerates). The sample modified with 5 weight parts by mass of ODS is characterized by bimodal particle size distribution; the two bands correspond to particle diameters in the range of 91–295 nm and 1480–6440 nm, respectively. Similarly, the particle size distribution of the sample modified with 5 weight parts by mass of OPF is also bimodal, with the two bands covering the particle diameter ranges of 142–255 nm and 2670–6440 nm (Figure 2(b)). The SEM image of unmodified silica (Figure 3(a)) confirms the high homogeneity and spherical shape of the particles, with low tendency towards agglomerate formation, which is also confirmed by the low polydispersity index of 0.289. The SEM image of silica modified with 5 weight parts by mass of OPF also confirms the presence of spherically shaped particles, but they are less regular and tend to form agglomerates (Figures 3(b)–3(d)). The polydispersity index of this sample is 0.460.

As follows from the literature [40–42], the alkoxy silanes, especially those containing =NH or $-\text{NH}_2$ groups, have been mostly used for surface modification of emulsion silicas and induce a considerable increase in the tendency towards formation of primary and secondary agglomerates. The SEM images presented in Figures 3(e)–3(f) also confirm that the particles' tendency to form agglomerates in the sample of silica modified with applied silanes is greater than in the unmodified SiO_2 . Microscopic observations are in agreement with particle size measurement results.

Figure 4 allows a comparison of the particle size distributions obtained for both unmodified and magnesium silicate modified with 5 weight parts by mass of the three different silane coupling agents. Table 2 gives the dispersive characteristics of magnesium silicate-based fillers. As follows from these data, the modification process of $\text{MgO}\cdot\text{SiO}_2$ causes small changes in the particle sizes of the obtained fillers. The unmodified magnesium silicate is composed of particles with diameters ranging from 1 to 100 μm . The dominant volume contribution of 5.01% is recorded for particles 39.8 μm in diameter (Figure 4 and Table 2). Analysis of the results shows that in this sample 10% of particles have diameters not greater than 3.8 μm , 50% have diameters not greater than 22.5 μm , and 90% have diameters smaller than 73.6 μm . The mean diameter of particles $D[4.3]$ in the sample of unmodified $\text{MgO}\cdot\text{SiO}_2$ is 31.5 μm . Modification of magnesium silicate with 5 weight parts by mass of OPF, ODS, or OCS resulted in increased particle size. The sample modified with 5 weight parts by mass of OPF contained 10% of particles with diameters below 8.7 μm , 50% with diameters not greater than 35.6 μm , and 90% with diameters smaller than 94.0 μm . In turn, the inorganic support modified with 5 weight parts by mass of ODS is characterized by a 10% volume contribution of particles with diameters below 6.6 μm , while 50% have

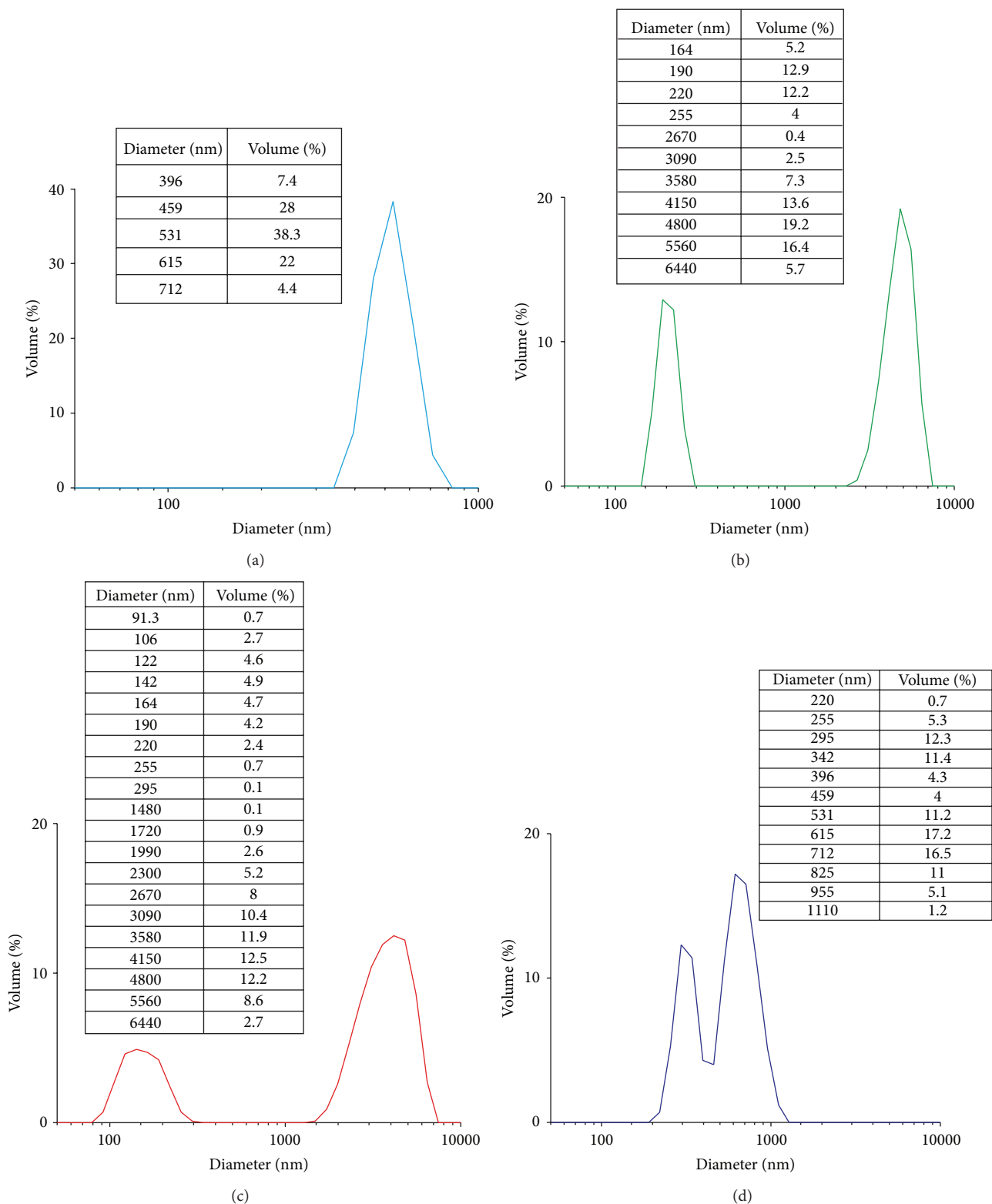


FIGURE 2: Particle size distributions of unmodified silica (a) and silica modified with 5 weight parts by mass of OPF (b), ODS (c), and OCS (d).

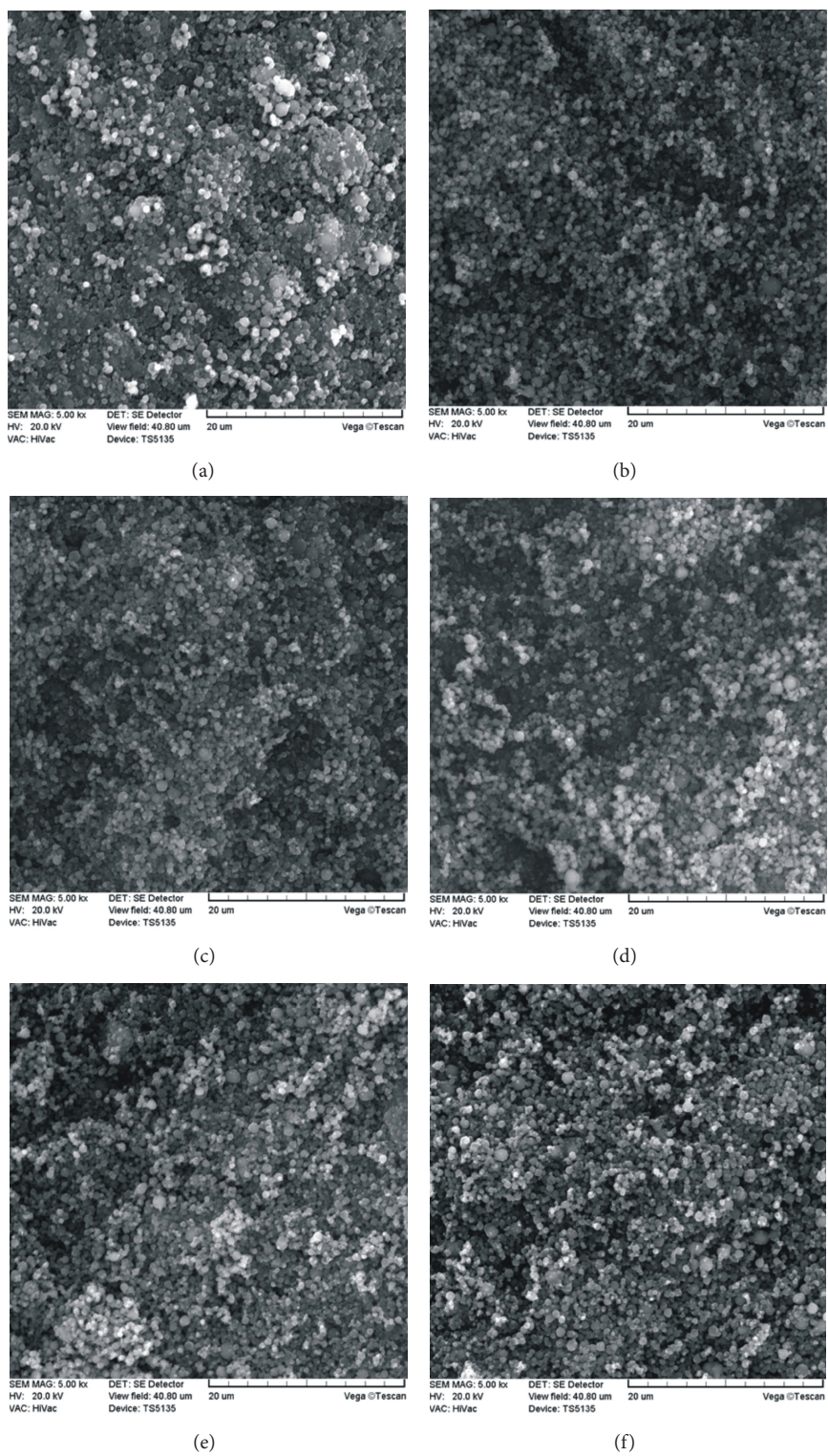
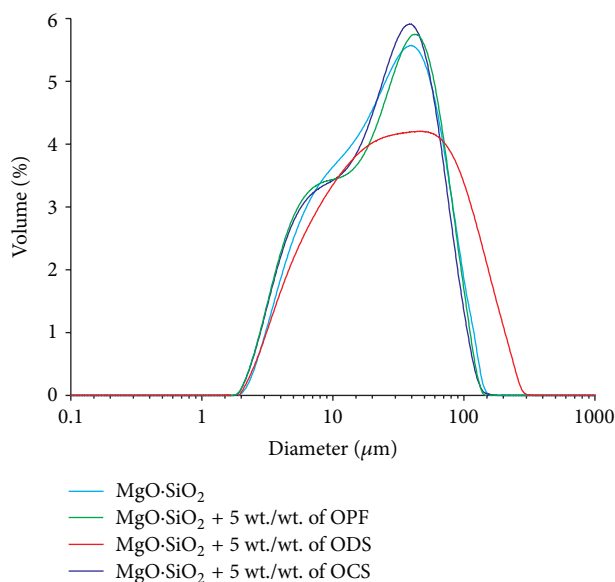


FIGURE 3: SEM images of unmodified silica, (a) silica functionalized with 3, 5, and 10 weight parts by mass of OPF ((b), (c), and (d)), respectively, and 5 weight parts by mass of ODS (e) and OCS (f).

TABLE 2: Dispersive parameters of unmodified MgO-SiO₂ and magnesium silicate modified with different alkylsilanes.

Sample	Diameter (μm)			Mean diameter $D(4.3)$ (μm)
	$d(0.1)$	$d(0.5)$	$d(0.9)$	
MgO-SiO ₂	3.8	22.5	73.6	31.5
MgO-SiO ₂ + 5 weight parts by mass of OPF	8.7	35.6	94.0	42.0
MgO-SiO ₂ + 5 weight parts by mass of ODS	6.6	30.8	91.0	46.0
MgO-SiO ₂ + 5 weight parts by mass of OCS	8.2	37.0	96.0	44.0

FIGURE 4: Comparison of particle size distributions of unmodified MgO-SiO₂ and magnesium silicate modified with 5 weight parts by mass of different silanes.

diameters below 30.8 μm and 90% have diameters below 91.0 μm . Moreover, the dispersive parameters $d(0.1) = 8.2 \mu\text{m}$, $d(0.5) = 37.0 \mu\text{m}$, and $d(0.9) = 96.0 \mu\text{m}$ are found for the magnesium silicate sample modified with 5 weight parts by mass of OCS. The particle diameter ranges are confirmed by the SEM images presented in Figure 5.

Figure 6(a) presents a comparison of the dependencies of zeta potential on pH for unmodified silica and for the samples modified with 5 weight parts by mass of selected silanes. Modification with silanes leads to the introduction of new chemical groups on the silica surface, which changes its initial properties and also the surface charge, manifested by the values of zeta potential.

Electrokinetic potential of unmodified silica is negative in the entire pH range studied and the isoelectric point (IEP) was reached at pH close to 1.7. The unmodified silica is characterized by high electrokinetic stability for pH values ranging from 4 to 11, which is manifested by zeta potential values from -30mV to -52mV . The most pronounced changes in the electrokinetic properties were noted as a result of silica modification with 5 weight parts by mass of OPF, while the changes caused by modification with 5 weight parts by mass of OCS and ODS with respect to the curve obtained for the unmodified silica sample were insignificant. Modification of

the SiO₂ surface with OPF results in a significant shift of the electrokinetic curve towards higher pH, relative to that for the unmodified sample. Sample modified with OPF is stable at pH from 6 to 11 and its zeta potential values vary from -2 to -33mV over the pH range analyzed.

The character of electrokinetic curves is an indirect confirmation of the effectiveness of the proposed method of surface modification.

In the case of magnesium silicate grafted with different silanes, changes in the electrokinetic properties was not much significant. Magnesium silicate-based samples are characterized with zeta potential range of 10 – $(-48)\text{mV}$. In the pH range of 3–12 all samples have negative zeta potential values with the highest negative value of -48mV obtained for the sample modified with 5 weight parts by mass of OPF silane. In comparison to the silica-based fillers, all samples of MgO-SiO₂ grafted with silanes exhibit IEP (isoelectric point—pH at which zeta potential is 0) which value is determined by its higher base surface character and the surface charge changes caused by modification process. Unmodified magnesium silicate has IEP at pH = 3; on the other hand, sample modified with 5 weight parts by mass of ODS—pH = 3.3 and samples modified with 5 weight parts by of OPF and OCS—pH = 3.6.

The effectiveness and chemical nature of the modification process were evaluated on the basis of FTIR spectra. Figure 7(a) shows the FTIR spectra of raw silica and SiO₂ functionalized with 5 weight parts by mass of three different alkylsilanes. The FTIR spectra show common bands assigned to various vibrations in the solid network. The analysis of those spectra revealed the broad band centered at around 3470 – 3450cm^{-1} which corresponds to the overlapping of the $-\text{OH}$ stretching bands of hydrogen-bonded water molecules as well as Si-OH stretching of surface silanols hydrogen-bonded to molecular water. Furthermore, the Si-O in-plane stretching vibrations of the silanol Si-OH groups appear at around 960cm^{-1} , and the absorption bands corresponding to the adsorbed water molecules deformation vibrations appear at 1653 – 1634cm^{-1} which is in agreement with [43]. The absorption of water molecules on the surface of such powders is due to the existence of the surface silanol groups and therefore to the hydrophilic nature of those materials. The intense silicon-oxygen covalent bonds vibrations appear mainly in the 1200 – 1000cm^{-1} range, revealing the existence of a dense silica network, where oxygen atoms play the role of bridges between each two silicon sites. The very intense and broad band appearing at 1095 – 1089cm^{-1} and the shoulder at around 1200cm^{-1} are assigned, respectively, to the transversal optical and longitudinal optical modes of the Si-O-Si asymmetric

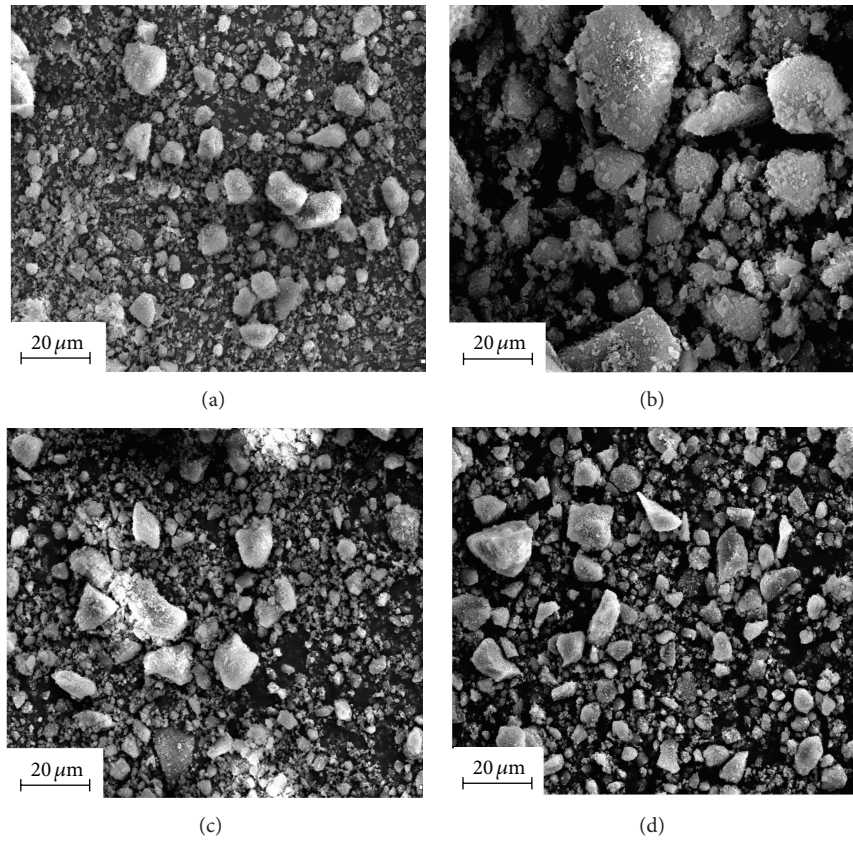


FIGURE 5: SEM images of unmodified magnesium silicate (a) and MgO-SiO₂ modified with 5 weight parts by mass of OPF (b), ODS (c), and OCS (d).

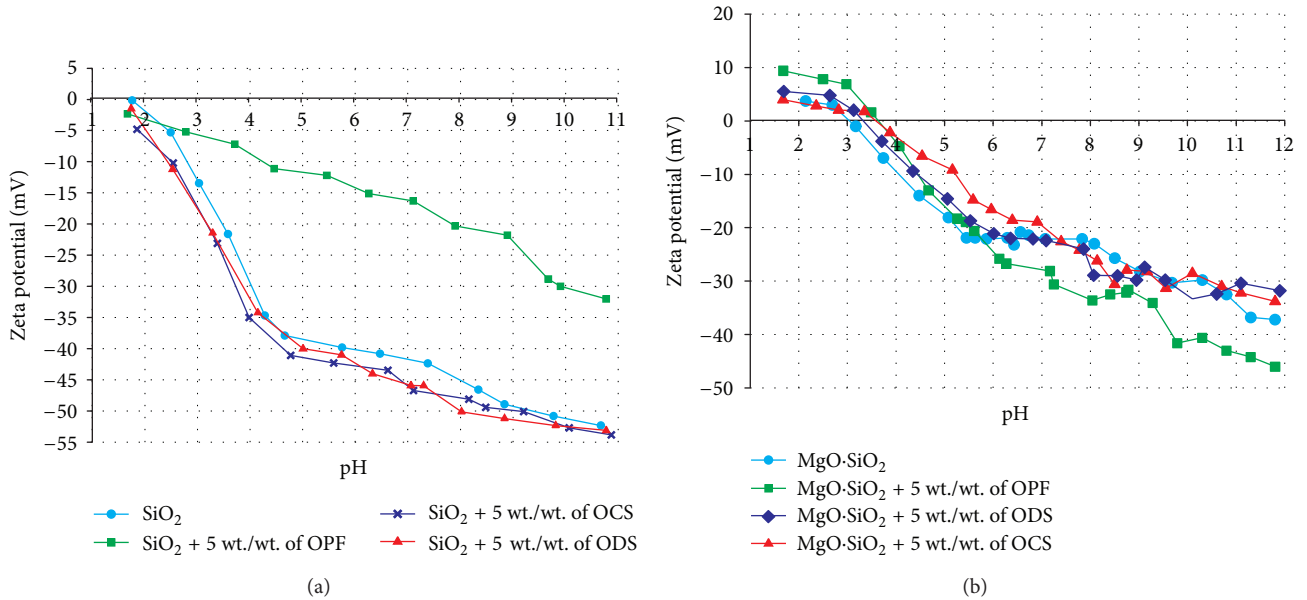


FIGURE 6: Zeta potential versus pH for SiO₂ (a) and magnesium silicate (b) grafted with 5 weight parts by mass of tested silanes.

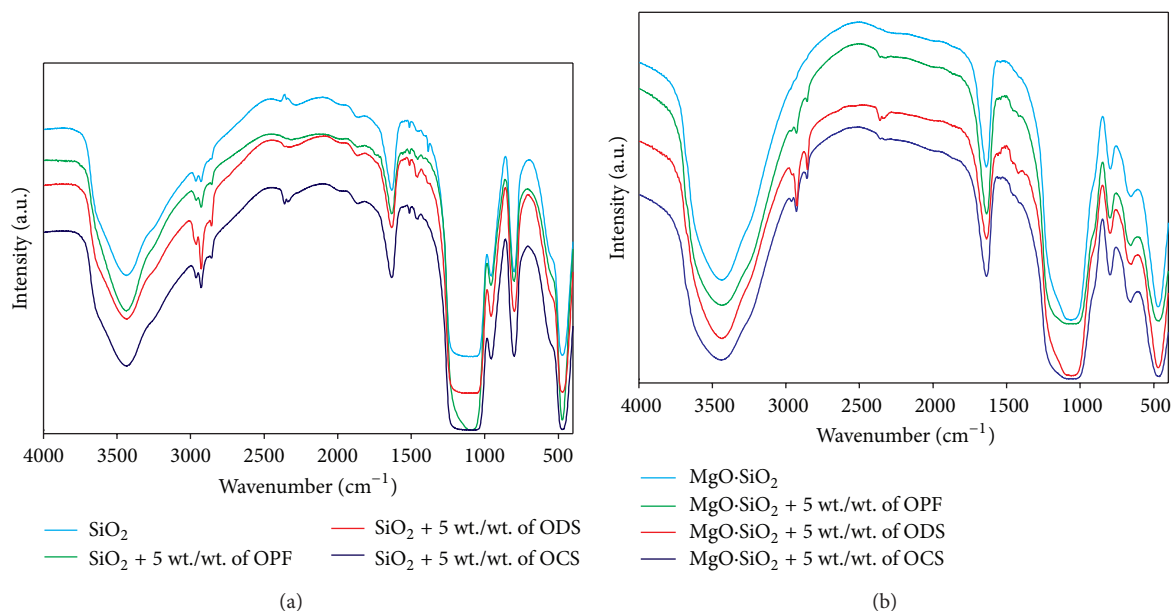


FIGURE 7: Comparison of the FTIR spectra of silica (a) and MgO-SiO₂ (b) modified with 5 weight parts by mass of silanes.

stretching vibrations as also presented in [44]. On the other hand, the symmetric stretching vibrations of Si–O–Si appear at 800 cm⁻¹ and its bending mode appears at 469–467 cm⁻¹ which is in agreement with [43]. The FT-IR spectrum of silica modified with 5 weight parts by mass of OPF shows that the bands attributed to the stretching vibrations of –CH groups (2965–2850 cm⁻¹) as well as of –CH₃ groups become much more intensive. The increase in the intensities of these peaks is coupled to the increase of the intensities of the C–H deformation peaks appearing between 1466 and 1379 cm⁻¹. This spectrum also shows peak at 1341 cm⁻¹ that could be assigned to the –CH₂– deformation vibrations of the propyl group. Thus, the spectrum of silica modified with 5 weight parts by mass of OCS shows very intense asymmetric and symmetric C–H stretching vibrations between 2930 and 2858 cm⁻¹. The existence of these intense bands is due to the large number of –CH₂ groups in the octyl-modified silica material, showing their rocking vibrations at 723 cm⁻¹. The existence of these octyl-surface groups is coupled with an increase of the hydrophobicity of the samples shown by the decrease of the intensities of the surface-absorbed water at 3450 and 1635 cm⁻¹. FT-IR spectrum for sample modified with 5 weight parts by mass of ODS shows an increase in the intensities of the CH₃ (from ν(C–H)) 2956 cm⁻¹, –CH₂ 2913 and 2848 cm⁻¹, and C–H deformation peaks appearing between 1466 and 1379 cm⁻¹. The spectra showed peaks at 1341 cm⁻¹ that could be assigned to the –CH₂– deformation vibrations of the silane group which is in agreement with [45, 46].

Figure 7 shows IR spectra of unmodified silicate and powder modified with 5 weight parts by mass of different silanes. The FTIR spectra confirm the hydrophilic surface character of the magnesium silicate result from the process of its precipitation in a polar medium. They show a clear

character with the principal Si–O stretching bands at 1000–1080 cm⁻¹, a Si–OH deformation band at 895 cm⁻¹, a single Si–O–Mg bending vibration at 450 cm⁻¹ (with a shoulder at 400 cm⁻¹), and perpendicular Mg vibrations at 555 cm⁻¹, which is in agreement with [47, 48]. The absorption band covering the range of 3850–3150 cm⁻¹ is attributed to water adsorbed on the surface of silicate, the same as in the case of silica (Figure 7(a)). Modification of magnesium silicate with different silanes results in the same changes in the FTIR spectra and presence of the same groups characteristic for modifier molecules as compared to silica spectra, but less intensive.

The effectiveness of modification and the degree of coverage of the inorganic support with the applied modifiers were estimated on the basis of elemental analysis and X-ray photoelectron spectroscopy (XPS). The content of carbon, hydrogen, oxygen, fluorine, silicon, and magnesium in the structure of the samples was determined. Percentage contributions of the above-mentioned elements are given in Tables 3 and 4. According to the data collected, the content of fluorine on the surface of both fillers (silica and magnesium silicate) increases with increasing quantity of alkylsilane applied in the process of modification. The quantity of fluorine in the silica sample modified with 10 weight parts by mass of OPF was 23.10% atm., while in the magnesium silicate sample modified with the same amount of the same modifier it was 8.07% atm. An increasing amount of modifier also caused an increase in the content of carbon, from 1.72% for unmodified silica to 6.27% for silica modified with 10 weight parts by mass of ODS and from 0.00% to 3.59% for unmodified and ODS-grafted magnesium silicate, respectively. The degree of coverage of the support surface with selected modifier also increases with increasing amount of silane used, reaching a maximum value of 7.61 μmol/m² for

TABLE 3: Chemical composition and degree of coverage of both unmodified and grafted silica.

Sample	Content					
	Elemental analysis			XPS		Degree of coverage ($\mu\text{mol}/\text{m}^2$)
	C (%)	H (%)	O (% atm.)	F (% atm.)	Si (% atm.)	
SiO ₂	1.72	1.46	54.21	—	24.98	—
SiO ₂ + 3 wt./wt. of OPF	2.17	1.57	48.51	11.12	22.91	4.53
SiO ₂ + 5 wt./wt. of OPF	2.57	1.67	42.97	17.85	19.64	5.24
SiO ₂ + 10 wt./wt. of OPF	3.27	1.67	39.25	23.10	18.81	7.61
SiO ₂ + 3 wt./wt. of ODS	2.80	1.54	38.98		19.87	3.74
SiO ₂ + 5 wt./wt. of ODS	4.30	1.85	42.83		21.59	4.14
SiO ₂ + 10 wt./wt. of ODS	6.27	2.36	45.79	Not determined	24.65	4.78
SiO ₂ + 3 wt./wt. of OCS	2.25	1.87	48.78		22.68	4.48
SiO ₂ + 5 wt./wt. of OCS	2.59	1.98	50.57		24.82	4.65
SiO ₂ + 10 wt./wt. of OCS	3.08	2.00	53.78		27.98	5.20

TABLE 4: Chemical composition and degree of coverage of both unmodified and grafted magnesium silicate.

Sample	Content						
	Elemental analysis			XPS		Degree of coverage ($\mu\text{mol}/\text{m}^2$)	
	C (%)	H (%)	O (% atm.)	F (% atm.)	Si (% atm.)		Mg (% atm.)
MgO·SiO ₂	—	3.03	63.29	—	21.90	8.00	—
MgO·SiO ₂ + 3 wt./wt. of OPF	1.57	2.78	59.88	3.12	19.67	7.09	0.21
MgO·SiO ₂ + 5 wt./wt. of OPF	1.95	2.86	57.82	4.51	17.35	7.42	0.25
MgO·SiO ₂ + 10 wt./wt. of OPF	2.29	2.98	50.34	8.07	19.31	7.21	0.30
MgO·SiO ₂ + 3 wt./wt. of ODS	1.90	3.06	56.78		19.10	7.11	0.17
MgO·SiO ₂ + 5 wt./wt. of ODS	2.14	3.13	58.35		20.50	7.71	0.17
MgO·SiO ₂ + 10 wt./wt. of ODS	3.59	3.29	59.98	Not determined	22.05	7.99	0.21
MgO·SiO ₂ + 3 wt./wt. of OCS	1.02	2.46	59.78		19.87	7.10	0.20
MgO·SiO ₂ + 5 wt./wt. of OCS	1.25	2.73	62.10		21.33	8.45	0.22
MgO·SiO ₂ + 10 wt./wt. of OCS	1.58	2.97	65.34		24.56	9.98	0.26

silica modified with 10 weight parts by mass OPF, while for magnesium silicate modified with the same alkylsilane in the same amount the degree of coverage is $0.30 \mu\text{mol}/\text{m}^2$.

To verify the possibility of using the silicas and magnesium silicate as adsorbents and polymer fillers, their parameters of porous structure were characterized, based on BET equation as well as nitrogen adsorption/desorption isotherms. Table 5 presents the parameters of porous structure of functionalized silica and silicate fillers. Irrespective of the modifier used, a decrease in the values for the surface area of functionalized hybrid fillers was observed, which indirectly testifies to the effectiveness of modification process. For silica-based fillers the highest value of surface area was found for unmodified silica ($48 \text{ m}^2/\text{g}$), and the lowest one ($17 \text{ m}^2/\text{g}$) for silica modified with 10 weight parts by mass of ODS. The surface area of unmodified magnesium silicate is $480 \text{ m}^2/\text{g}$, which is much higher than that obtained for the hydrophobized samples. In turn, the lowest surface area of $310 \text{ m}^2/\text{g}$ was obtained for the sample of MgO·SiO₂ functionalized with 10 weight parts by mass of OCS.

Besides the introduction of functional groups, the functionalization process is also intended to enhance the

hydrophobicity of the samples relative to that of the raw silica or magnesium silicate. The hydrophilic/hydrophobic properties of the samples were evaluated on the basis of wettability profiles (Figure 8). Analysing the experimental data, an increase in the hydrophobicity of the modified samples was noted. The smallest mass increase, and thus the weakest affinity to water, was established for the silica and magnesium silicate samples modified with 5 weight parts by mass of OPF (Figures 8(a) and 8(b)).

Many previously published papers have been focused on the silane-functionalization of inorganic fillers, but the novelty of the present work is the application of newly synthesized fluorosilane for this purpose. Using this silane for modification of fillers will probably extend the range of their functionality and utility.

4. Conclusions

Modification of silica and magnesium silicate carried out with 3-(2,2,3,3,4,4,5,5-octafluoropentyloxy)propyltriethoxysilane (OPF), octadecylsilane (ODS), or octyltriethoxysilane (OCS), used in amounts of 3, 5, and 10 weight parts by mass,

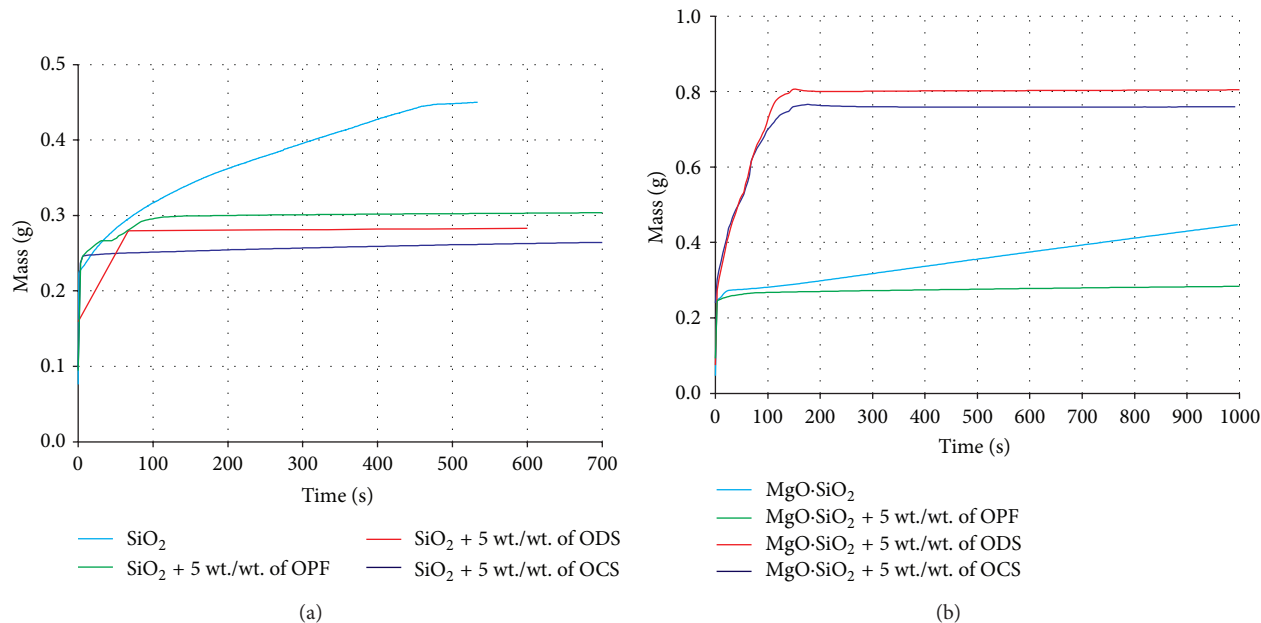


FIGURE 8: Wettability profiles of (a) silica- and (b) magnesium silicate-based fillers.

TABLE 5: Parameters of porous structure of the obtained fillers.

Filler type	Modifying agent type	Amount of modifying agent (wt./wt.)	A_{BET} (m^2/g)
SiO ₂	—	—	48
	OPF	3	32
		5	31
		10	28
	ODS	3	37
		5	22
		10	17
	OCS	3	38
		5	37
		10	24
MgO-SiO ₂	—	—	480
	OPF	3	471
		5	367
		10	362
	ODS	3	392
		5	369
		10	341
	OCS	3	360
		5	324
		10	310

resulted in increased hydrophobicity of the hybrid fillers and pronounced agglomeration of the products' particles. The products with optimal physicochemical parameters (relatively high homogeneity and hydrophobicity) proved to be those modified with 3-(2,2,3,3,4,4,5,5-octafluoropentyl)propyltriethoxysilane. Based on electrokinetic properties evaluation, it was confirmed that this kind of oxide systems is characterized by high electrokinetic stability,

especially in alkaline pH range. Moreover, functionalization of oxides surface with selected silanes (especially with OPF) significantly affect the measured values of the zeta potential and the electrokinetic stability.

Performed FTIR and XPS spectral investigations as well as elemental analysis results proved the chemical nature of interactions and the effectiveness of the modification process.

Surface modification of silica-based fillers with 3-(2,2,3,3,4,4,5,5-octafluoropentyl)propyltriethoxysilane caused the smallest decrease in the surface area, even when used in the amount of 10 weight parts by mass. Due to obtained results, it is expected that inorganic powders modified with OPF will be successfully applied as functional fillers in selected polymer composites, as an alternative for commonly used silanes.

Acknowledgments

This work was supported by the following research grants: Poznan University of Technology (32-375/2013-DS) and Ministry of Science and Higher Education (N N209 765640).

References

- [1] M. W. Daniels and L. F. Francis, "Silane adsorption behavior, microstructure, and properties of glycidoxypolytrimethoxysilane-modified colloidal silica coatings," *Journal of Colloid and Interface Science*, vol. 1, no. 1, pp. 191–200, 1998.
- [2] C. Gellermann, W. Storch, and H. Wolter, "Synthesis and characterization of the organic surface modifications of monodisperse colloidal silica," *Journal of Sol-Gel Science and Technology*, vol. 8, no. 1–3, pp. 173–176, 1997.
- [3] V. M. Sglavo, S. Diré, and M. Ferrari, "Structure-property behavior during aging of sol-gel-derived silica modified with

- Si-H and Si-CH₃ groups," *Journal of Materials Research*, vol. 14, no. 5, pp. 2100–2106, 1999.
- [4] H. Zhang and C. G. Pantano, "Synthesis and characterization of silicon oxycarbide glasses," *Journal of the American Ceramic Society*, vol. 73, no. 4, pp. 958–963, 1990.
- [5] N. Nishiyama, R. Shick, and H. Ishida, "Adsorption behavior of a silane coupling agent on colloidal silica studied by gel permeation chromatography," *Journal of Colloid and Interface Science*, vol. 143, no. 1, pp. 146–156, 1991.
- [6] J. P. Blitz, R. S. S. Murthy, and D. E. Leyden, "Studies of silylation of Cab-O-Sil with methoxymethylsilanes by diffuse reflectance FTIR spectroscopy," *Journal of Colloid and Interface Science*, vol. 121, no. 1, pp. 63–69, 1988.
- [7] J. P. Blitz, R. S. S. Murthy, and D. E. Leyden, "The role of amine structure on catalytic activity for silylation reactions with Cab-O-Sil," *Journal of Colloid and Interface Science*, vol. 126, no. 2, pp. 387–392, 1988.
- [8] J. P. Blitz, R. S. S. Murthy, and D. E. Leyden, "Ammonia-catalyzed silylation reactions of Cab-O-Sil with methoxymethylsilanes," *Journal of the American Chemical Society*, vol. 109, no. 23, pp. 7141–7145, 1987.
- [9] K. M. R. Kallury, P. M. Macdonald, and M. Thompson, "Effect of surface water and base catalysis on the silanization of silica by (aminopropyl)alkoxysilanes studied by X-ray photoelectron spectroscopy and ¹³C cross-polarization/magic angle spinning nuclear magnetic resonance," *Langmuir*, vol. 10, no. 2, pp. 492–499, 1994.
- [10] M. E. McGovern, K. M. R. Kallury, and M. Thompson, "Role of solvent on the silanization of glass with octadecyltrichlorosilane," *Langmuir*, vol. 10, no. 2, pp. 3607–3614, 1994.
- [11] R. Maoz and J. Sagiv, "On the formation and structure of self-assembling monolayers. I. A comparative atr-wettability study of Langmuir-Blodgett and adsorbed films on flat substrates and glass microbeads," *Journal of Colloid and Interface Science*, vol. 100, no. 2, pp. 465–496, 1984.
- [12] D. A. Offord and J. H. Griffin, "Kinetic control in the formation of self-assembled mixed monolayers on planar silica substrates," *Langmuir*, vol. 9, no. 11, pp. 3015–3025, 1993.
- [13] J. D. Le Grange, J. L. Markham, and C. R. Kurkjian, "Effects of surface hydration on the deposition of silane monolayers on silica," *Langmuir*, vol. 9, no. 11, pp. 1749–1753, 1993.
- [14] J. E. Sandoval and J. J. Pesek, "Synthesis and characterization of a hydride-modified porous silica material as an intermediate in the preparation of chemically bonded chromatographic stationary phases," *Analytical Chemistry*, vol. 61, no. 18, pp. 2067–2075, 1989.
- [15] J. J. Pesek, J. E. Sandoval, and M. Su, "New alumina-based stationary phases for high-performance liquid chromatography. Synthesis by olefin hydrosilation on a silicon hydride-modified alumina intermediate," *Journal of Chromatography*, vol. 630, no. 1-2, pp. 95–103, 1993.
- [16] C. Chu, E. Jonsson, M. Auvinen, J. J. Pesek, and J. E. Sandoval, "A new approach for the preparation of a hydride-modified substrate used as an intermediate in the synthesis of surface-bonded materials," *Analytical Chemistry*, vol. 65, no. 6, pp. 808–816, 1993.
- [17] J. B. Danner and J. M. Vohs, "The chemistry of organosilane/metal oxide interfaces: reaction of trimethoxysilane on MgO and SiO₂ surfaces," *Applied Surface Science*, vol. 62, no. 4, pp. 255–262, 1992.
- [18] D. W. Sindorf and G. E. Maciel, "Cross-polarization/magic-angle-spinning silicon-29 nuclear magnetic resonance study of silica gel using trimethylsilane bonding as a probe of surface geometry and reactivity," *Journal of Physical Chemistry*, vol. 86, no. 26, pp. 5208–5219, 1982.
- [19] D. G. Kurth and T. Bein, "Monomolecular layers and thin films of silane coupling agents by vapor-phase adsorption on oxidized aluminum," *Journal of Physical Chemistry*, vol. 96, no. 16, pp. 6707–6712, 1992.
- [20] V. A. Basyuk, "Reactions of gaseous organic compounds on silica surface. Spectral studies and synthetic aspects," *Reaction Kinetics & Catalysis Letters*, vol. 50, no. 1-2, pp. 83–88, 1993.
- [21] K. L. Mittal, *Silane and other Coupling Agents*, VSP, Utrecht, The Netherlands, 1992.
- [22] T. Jesionowski and A. Krysztafkiewicz, "Comparison of the techniques used to modify amorphous hydrated silicas," *Journal of Non-Crystalline Solids*, vol. 277, no. 1, pp. 45–57, 2000.
- [23] E. P. Pluddemann, *Silane Coupling Agents*, Academic Press, New York, NY, USA, 1982.
- [24] A. Krysztafkiewicz, B. Rager, and T. Jesionowski, "The effect of surface modification on physicochemical properties of precipitated silica," *Journal of Materials Science*, vol. 32, no. 5, pp. 1333–1339, 1997.
- [25] L. Sierra, B. Lopez, and J. Guth, "Preparation of mesoporous silica particles with controlled morphology from sodium silicate solutions and a non-ionic surfactant at pH values between 2 and 6," *Microporous and Mesoporous Materials*, vol. 39, no. 3, pp. 519–527, 2000.
- [26] T. Suhara, H. Fukui, and M. Yamaguchi, "Fine silica powder modified with quaternary ammonium groups 2. The influence of electrolyte and pH," *Colloids and Surfaces A*, vol. 101, no. 1, pp. 29–37, 1995.
- [27] T. Suhara, H. Fukui, M. Yamaguchi, and F. Suzuki, "Fine silica powder modified with quaternary ammonium group. 3. the adsorption behavior of anionic surfactants," *Colloids and Surfaces A*, vol. 119, no. 1-2, pp. 15–21, 1996.
- [28] T. Suhara, F. Shimano, Y. Sato, H. Fukui, and M. Yamaguchi, "Fine silica powder modified with quaternary ammonium group 4. Bactericidal activity," *Colloids and Surfaces A*, vol. 119, no. 2-3, pp. 105–114, 1996.
- [29] J. Zajac, "Adsorption microcalorimetry used to study interfacial aggregation of quaternary ammonium surfactants (zwitterionic and cationic) on powdered silica supports in dilute aqueous solutions," *Colloids and Surfaces A*, vol. 167, no. 1-2, pp. 3–19, 2000.
- [30] M. Drach, Ł. Łajtar, J. Narkiewicz-Michałek, W. Rudziński, and J. Zając, "Adsorption of cationic surfactants on hydrophobic silica: effect of surface energetic heterogeneity," *Colloids and Surfaces A*, vol. 145, no. 1-3, pp. 243–261, 1998.
- [31] I. Rachas, T. F. Tadros, and P. Taylor, "The displacement of adsorbed polymer from silica surfaces by the addition of a nonionic surfactant," *Colloids and Surfaces A*, vol. 161, no. 2, pp. 307–319, 2000.
- [32] S. Lagerge, E. Keh, S. Partyka, and M. Lindheimer, "On the behavior of nonionic surfactants at the N-heptane/silica gel interface: Influence of the presence of interfacial water inferred from adsorption isotherms and calorimetric data," *Journal of Colloid and Interface Science*, vol. 227, no. 2, pp. 412–420, 2000.
- [33] Y. Cheng, H. Lin, and C. Mou, "Control of mesostructure and morphology of surfactant-templated silica in a mixed surfactant system," *Physical Chemistry Chemical Physics*, vol. 1, no. 21, pp. 5051–5058, 1999.

- [34] A. Y. Fadeev and Y. V. Kazakevich, "Covalently attached monolayers of oligo(dimethylsiloxane)s on silica: a siloxane chemistry approach for surface modification," *Langmuir*, vol. 18, no. 7, pp. 2665–2672, 2002.
- [35] T. I. Suratwala, M. L. Hanna, E. L. Miller et al., "Surface chemistry and trimethylsilyl functionalization of Stöber silica sols," *Journal of Non-Crystalline Solids*, vol. 316, no. 2-3, pp. 349–363, 2003.
- [36] M. C. Capel-Sanchez, L. Barrio, J. M. Campos-Martin, and J. L. G. Fierro, "Silylation and surface properties of chemically grafted hydrophobic silica," *Journal of Colloid and Interface Science*, vol. 277, no. 1, pp. 146–153, 2004.
- [37] E. Loste, J. Fraile, M. A. Fanovich, G. F. Woerlee, and C. Domingo, "Anhydrous supercritical carbon dioxide method for the controlled silanization of inorganic nanoparticles," *Advanced Materials*, vol. 16, no. 8, pp. 739–744, 2004.
- [38] N. Ardès-Guisot, J. Durand, M. Granier et al., "Trichlorosilane isocyanate as coupling agent for mild conditions functionalization of silica-coated surfaces," *Langmuir*, vol. 21, no. 21, pp. 9406–9408, 2005.
- [39] H. Maciejewski, B. Marciniak, I. Dąbek, and J. Karasiewicz, Polish patent application P-388 929.
- [40] T. G. Waddell, D. E. Leyden, and M. T. DeBello, "The nature of organosilane to silica-surface bonding," *Journal of the American Chemical Society*, vol. 103, no. 18, pp. 5303–5307, 1981.
- [41] X. Liu, Z. Ma, J. Xing, and H. Liu, "Preparation and characterization of amino-silane modified superparamagnetic silica nanospheres," *Journal of Magnetism and Magnetic Materials*, vol. 270, no. 1-2, pp. 1–6, 2004.
- [42] B. I. Lee and U. Paik, "Effect of aminosilane adsorption on rheology of silica powders in nonaqueous media," *Journal of Materials Science*, vol. 27, no. 21, pp. 5692–5700, 1992.
- [43] R. S. McDonald, "Surface functionality of amorphous silica by infrared spectroscopy," *Journal of Physical Chemistry*, vol. 62, no. 10, pp. 1168–1178, 1958.
- [44] R. Al-Oweini and H. El-Rassy, "Synthesis and characterization by FTIR spectroscopy of silica aerogels prepared using several $\text{Si}(\text{OR})_4$ and $\text{R}'\text{Si}(\text{OR}')_3$ precursors," *Journal of Molecular Structure*, vol. 919, no. 1–3, pp. 140–145, 2009.
- [45] R. Brambilla, G. P. Pires, J. H. Z. dos Santos, M. S. L. Miranda, and B. Chornik, "Octadecylsilane-modified silicas prepared by grafting and sol-gel methods," *Journal of Electron Spectroscopy and Related Phenomena*, vol. 156–158, pp. 413–420, 2007.
- [46] T. Jesionowski, M. Nowacka, and F. Ciesielczyk, "Electrokinetic properties of hybrid pigments obtained via adsorption of organic dyes on the silica support," *Pigment and Resin Technology*, vol. 41, no. 1, pp. 9–19, 2012.
- [47] V. C. Farmer, "The layer silicates," in *The Infrared Spectra of Minerals*, Mineralogical Society Monograph, London, UK, 1974.
- [48] J. D. Russel, "Infrared methods," in *A Handbook of Determinative Methods in Clay Mineralogy*, M. J. Wilson, Ed., Blackie Academic and Professional, London, UK, 1987.

Research Article

Formation of Porous Structure with Subspot Size under the Irradiation of Picosecond Laser Pulses

Bin Liu, Wenjun Wang, Gedong Jiang, Xuesong Mei, Kedian Wang, and JiuHong Wang

State Key Laboratory for Manufacturing System Engineering, Xi'an Jiaotong University, Xi'an 710054, China

Correspondence should be addressed to Wenjun Wang; wenjunwang@mail.xjtu.edu.cn

Received 17 July 2013; Revised 6 September 2013; Accepted 8 September 2013

Academic Editor: Guangyu Zhao

Copyright © 2013 Bin Liu et al. This is an open access article distributed under the Creative Commons Attribution License, which permits unrestricted use, distribution, and reproduction in any medium, provided the original work is properly cited.

A study was presented in this paper on porous structure with microsize holes significantly smaller than laser spot on the stainless steel 304 target surface induced by a picosecond Nd:van regenerative amplified laser, operating at 1064 nm. The target surface variations were studied in air ambience. The estimated surface damage threshold was 0.15 J/cm^2 . The target specific surface changes and phenomena observed supported a complementary study on the formation and growth of the subspot size pit holes on metal surface with dependence of laser pulse number of 50–1000 and fluences of 0.8 and 1.6 J/cm^2 . Two kinds of porous structures were presented: periodic holes are formed from Coulomb Explosion during locally spatial modulated ablation, and random holes are formed from the burst of bubbles in overheated liquid during phase explosion. It can be concluded that it is effective to fabricate a large metal surface area of porous structure by laser scanning regime. Generally, it is also difficult for ultrashort laser to fabricate the microporous structures compared with traditional methods. These porous structures potentially have a number of important applications in nanotechnology, industry, nuclear complex, and so forth.

1. Introduction

The application of lasers surface structure fabrication to different materials including metal is of great interest. With the appearance of ultrashort laser in 1990s, material/metal surface texturing gained a whole new dimension. From that moment, it became possible to touch three time regimes from fs, ps, to ns [1]. Surface structure fabrications by ultrashort laser have been paid serious attention because it can manufacture structures with sub-spot size and can provide greater flexibility in fixing the position of ablated areas [2, 3]. They have widely potential applications in the fields of physics, chemistry, and materials, such as enhancing light absorption [4], improving catalytic action [5], and strengthening tribological and hydrophilic properties [6].

In the recent years, the fabrication of the micro- and nanosized periodical structures on the surface of materials by laser radiation with intensity exceeding the melt threshold has been intensively studied [7–9]. Periodic patterns of the ripples are often referred to as one of the most common laser-induced periodic surface structures (LIPSS). Some pit holes with diameters significantly smaller than laser spot are often observed during LIPSS fabrication on material surface

[10, 11]. So far, many studies have been carried out on LIPSS formed by laser pulses [7–9]. However, a detailed study on the origin and development of these pit holes is rare, but some underlying physical effects have been preliminarily investigated by pump-probe microscopy on a $\text{Ta}_2\text{O}_5/\text{Pt}$ layer system on glass substrate [12]. Fan and Zhong found that specific porous coral-like structures on Cu by picosecond can enhance broadband absorption [13], and Zhao and Zhang found that the porous structure on MoO_3 films can be used for supercapacitors [14].

In this work, a complementary study was presented on the influence of the laser pulse number and fluence on the formation and growth of these subspot size pit holes on metal surface. Nano/micrometer-sized holes were found to be formed under specific irradiation conditions. A comparison of these experimental results based on the currently accepted mechanism revealed the evolution of the holes.

2. Experimental

The laser system (High-Q IC-1500) based on a regenerative Nd:van amplifier using chirped pulse amplification technique

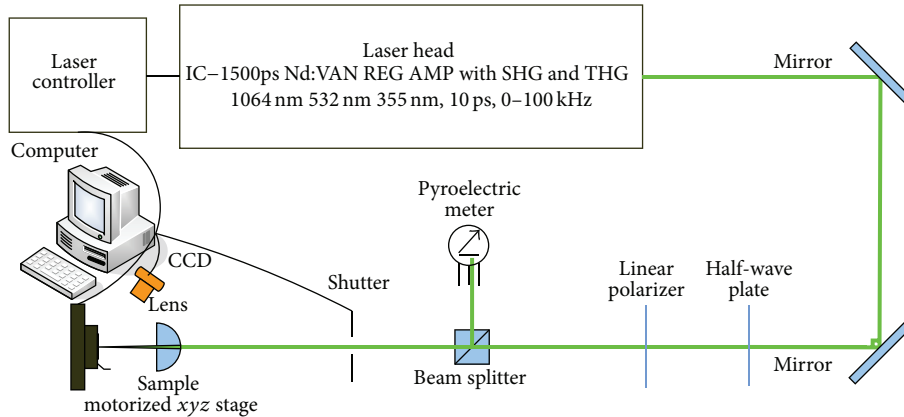


FIGURE 1: Experimental device.

provides high-intensity picosecond laser pulses for the experiment. The pulse duration of the output beam from amplifier is 10 ps with nominal wavelength at 1064 nm. The laser system delivers ~ 0.3 mJ per pulse at 1 kHz repetition rate and $\lambda = 1064$ nm, 10 ps pulse length, and observed bandwidth $\Delta\lambda \sim 5.5$ nm. The power density distribution of the laser beam is Gaussian with a measured 3D Gaussian fit parameter of ~ 0.87 . The IR (1064 nm) radiation can be converted into green (532 nm) by a Second Harmonic Generator (SHG) unit. The experimental setup is depicted in Figure 1. The laser power is adjusted by using a combination of a half-wave plate and a linear polarizer. A pyroelectric detector is used to inspect the laser power in real time with a beam splitter. The number of pulses is programmable using an electromechanical shutter control. The laser beam are focused and normally irradiated onto the surface of sample using f -theta lens ($f' = 150$ mm). A motorized xyz stage controlled by computer is used to get a precise positioning of the samples.

The experiment was performed on the stainless steel 304 which is widely used in industry. Firstly, the surface of the steel sample was mechanically polished with sandpaper with a grit size of 2500 grooves/mm and subsequently fine polished with the Alumina powder with an average particle size of ~ 500 nm. After the polishing process, the sample was cleaned in an ultrasonic bath firstly by acetone to remove oily contaminants for 10 minutes and subsequently by alcohol for 10 minutes. Finally, the sample was rinsed with distilled water and dried by nitrogen.

In experiments, all the laser ablation experiments were performed in air. The samples were irradiated by a series of laser pulses with the different fluence and pulse number at wavelength 1064 nm and 1 kHz repetition rate. After laser irradiation, the ablated surfaces of the samples were inspected with a Scanning Electron Microscope (SEM: Hitachi SU-8010) and Energy Dispersive X-ray (EDX) which is the component of SEM. For a detailed 3D characterization of multi-pulse laser ablated craters, Laser Confocal Scanning Microscopy (LCSM: Olympus OLS-400) imaging was used.

3. Results and Discussions

The surface of the stainless steel 304 had a typical silver-grey metallic color before irradiation. The investigation of

the effect of picosecond laser on target morphological changes was started with a series of the spot irradiated by different pulse numbers N and fluences F . It was interesting to find that some sub-spot holes are formed at the bottom of some ablated crater under the certain situations.

3.1. Generation of Holes Depended on Laser Fluence. Figure 2 shows SEM images of craters ablated by picosecond laser with fluences $F = 0.8$ and 1.6 J/cm² and the pulse number $N = 500$. The specific surface morphology of the ablated craters can be observed in SEM images.

Figure 3 shows LCSM images of ablated craters for laser fluences of 0.8 and 1.6 J/cm² with 500 pulses. 3D feature is shown in the LCSM images with typical cross-sectional graphs taken along the crater centre at the right-hand side of each image.

For the fluence of 0.8 J/cm², microholes on the irradiated surface are shown in Figures 2(a) and 3(a). These pit holes varied in dimension with the dependence of the Gaussian laser energy distribution field. Holes with the average diameters of ~ 1.5 μm are observed in the center of ablated crater (left-hand inset SEM images in Figure 2(a)); while near the edge of ablated crater, pit holes with the average diameter of ~ 0.9 μm also appear among the ripples (right-hand inset SEM images in Figure 2(a)). All holes seem to be regularly lying along lines which are directed almost perpendicular to the ripples, and the average distance between two adjacent holes ~ 3.6 μm led to hole-lying lines with period ~ 3.6 μm . These periodic holes were also observed in previous report while in-depth analysis was absent [11]. At the outer edge of ablated crater, ripples just remain because of the lower fluence. The depth of ablated crater reaches ~ 7 μm , but the depth of pit holes in the center of ablated crater bottom is very small.

When the fluence increased to 1.6 J/cm², morphology of the microholes had a significant change as shown in Figures 2(b) and 3(b); the maximum size of holes in center of ablated crater reaches ~ 5 μm (left-hand inset SEM images in Figure 2(b)). Holes are nonperiodic in the center of ablated crater, which can be called as random holes. The dimension of random holes decreases to ~ 2 μm near the edge of ablated crater, with dependence of the Gaussian laser energy distribution field. A few periodic holes ~ 1 μm are still observed near the edge of ablated crater (right-hand inset SEM images in

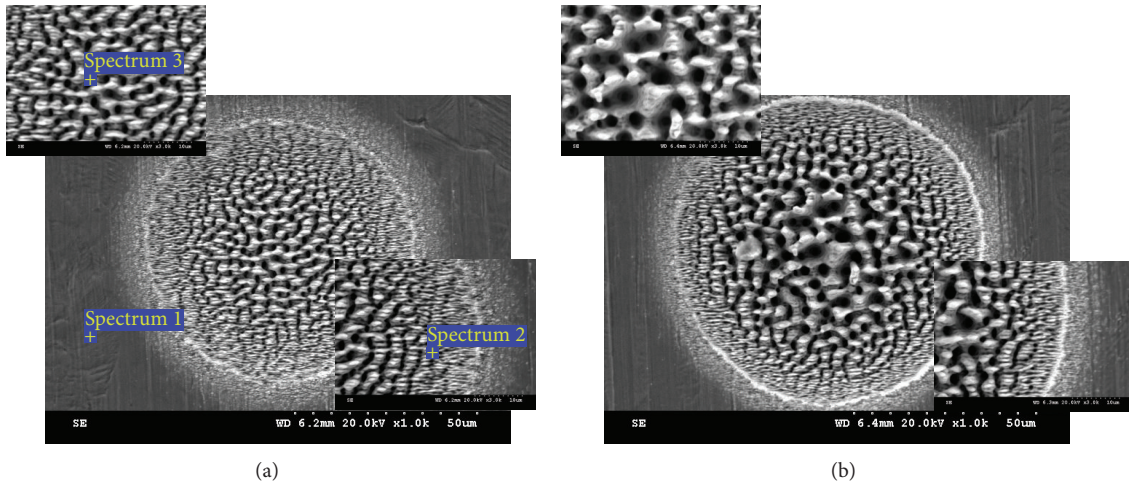


FIGURE 2: SEM images of 500 pulse ablated craters using fluences of 0.8 J/cm^2 (a) and 1.6 J/cm^2 (b), respectively. The location where pointed spectral analysis was conducted is marked.

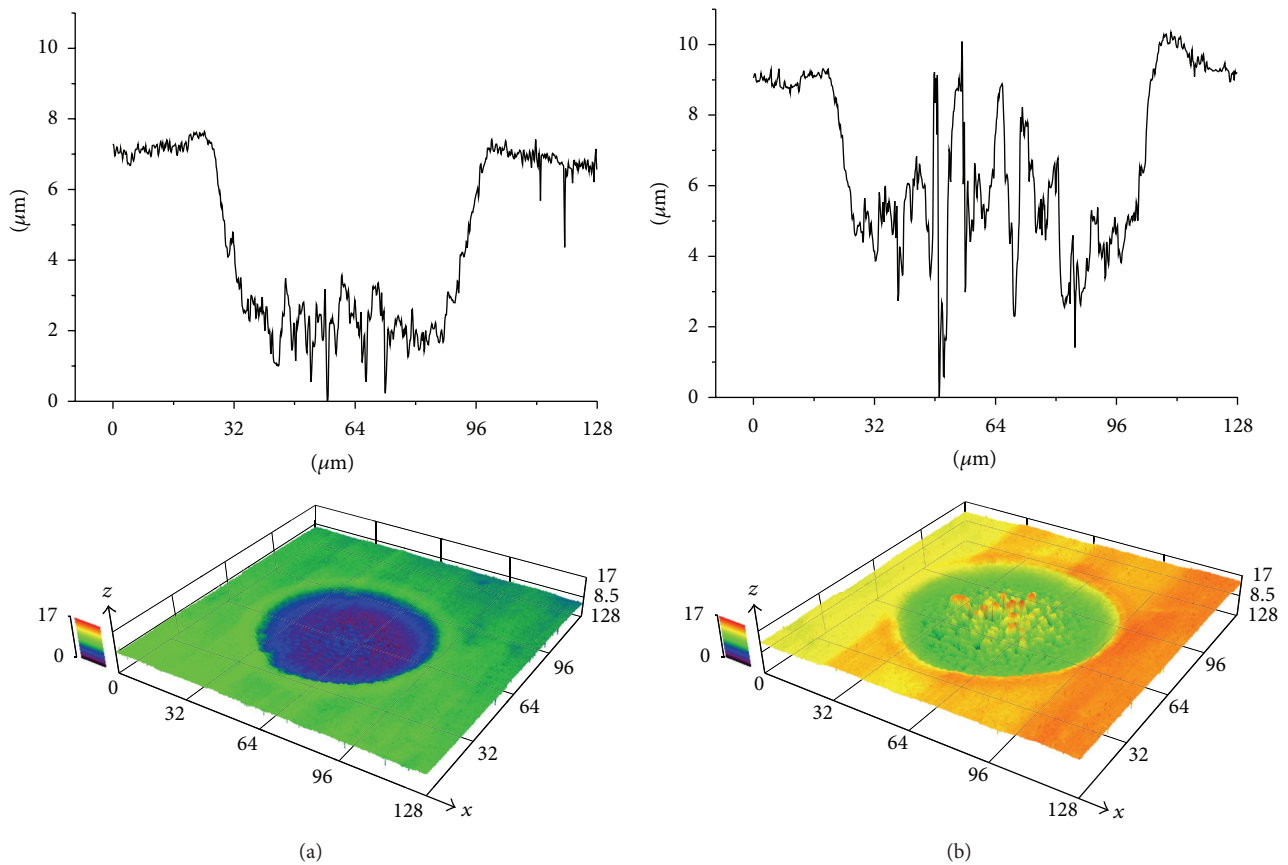


FIGURE 3: LCSM images of 500 pulse ablated craters using fluences of 0.8 J/cm^2 (a) and 1.6 J/cm^2 (b), respectively.

Figure 2(b)). Compared with Figure 3(a), the average depth of ablated crater seems to be decreasing obviously; however, the depth of microholes on the crater bottom reaches $\sim 9 \mu\text{m}$. A lot of microholes with large depth and diameter make the quality of the crater bottom worse in roughness, as shown in Figure 3(b). It is also inferred that formation of holes in

center of ablated crater in Figure 3(b) may be explained by a mechanism that the rapid cooling and resolidification after overheated liquid explosion which differs from the moderate characterization in Figure 3(a).

Irradiation on the target sample was performed in air atmosphere; therefore, the oxygen content in the irradiated

region is expected to increase. For monitoring of the target constituents, including oxygen, before and after the irradiation of laser pulses, EDX method was used; and the elemental analysis was carried out along the ablated crater at 3 points in Figure 2(a). The results obtained are given in Table 1. Generally, irradiation of the sample laser resulted in the increase of oxygen content and the decrease of carbon content from the periphery towards the center (Table 1, Figure 2(a)). This result implies a relatively efficient removal of carbon from the steel surface.

As shown in Figures 2 and 3, morphologies of the different pit holes in different laser irradiated regions indicate that the hole-formation significantly depends on laser fluence. So it is necessary to understand the effect of laser fluence.

Damage threshold is defined as the minimum laser energy/fluence necessary for creating detectable damage on the material surface. Based on the micrographs of craters ablated by different numbers of pulses (1–500) and fluences (0.2–1.7 J/cm²), the damage thresholds of the target were determined for different numbers of pulses, as shown in Figure 4. These damage thresholds and focused beam radius can be evaluated using the method given in references [10, 15, 16]. The focused beam radius ω_0 was calculated to be $\sim 45 \mu\text{m}$.

The region of holes did not obviously increase with the increase of the number of pulses. The surface morphology ablated by 500 pulses was used to predict the formation of pit holes dependence of a Gaussian spatial beam fluence profile, which is schematically presented in Figure 5. The fluence of each ablate crater has a Gaussian profile, shown in Figure 5(a). $F_{\text{th}2}$ is the threshold for random pit holes and $F_{\text{th}1}$ is the threshold for periodic pit holes. $F_{\text{th}1}$ or $F_{\text{th}2}$ can be calculated by the following equations:

$$F(r) = F_0^{\text{pk}} \exp\left(-\frac{2r^2}{\omega_0^2}\right) \quad (1)$$

$$F_0^{\text{pk}} = \frac{2E_p}{\pi\omega_0^2},$$

where F_0^{pk} is the peak laser fluence (the fluence at the center for $r = 0$), E_p is laser pulse energy. Based on the surface morphologies in Figures 2(a) and 2(b), $F_{\text{th}1}$ and $F_{\text{th}2}$ are $\sim 0.76 \text{ J/cm}^2$ and $\sim 1.2 \text{ J/cm}^2$, respectively.

During laser interaction with metals, when the laser fluence is significantly higher than multipulse damage threshold, the thermal diffusivity cannot be neglected [17, 18], and a series of thermal effects such as melting, vaporization of molten material, and dissociation, can be generated on the target [19]. Here a calculation for thermal effects based on two temperatures in ablation process is presented [1]. Considering the following set of parameters for the stainless steel 304 (density $\rho = 7.93 \text{ g/cm}^3$, heat capacity $C_p = 605 \text{ J kg}^{-1} \text{ K}^{-1}$ calculated at an average temperature of $T = 1005 \text{ K}$ between room temperature $T_0 = 298 \text{ K}$ and the melting temperature $T_m = 1713 \text{ K}$ [20], and the thickness $d_{\text{abs}1}$ equaled to the laser optical energy penetration depth of $\alpha^{-1} = 20 \text{ nm}$ [21]), the relationship between the temperature and the pulse fluence can be obtained using the equation of $\Delta T = F/(\rho C_p d_{\text{abs}})$ [10]. During laser acting on the thick material surface layer, only

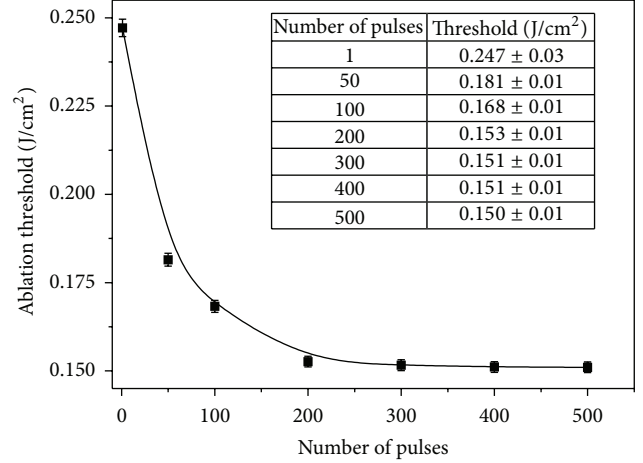


FIGURE 4: Ablation thresholds versus number of pulses.

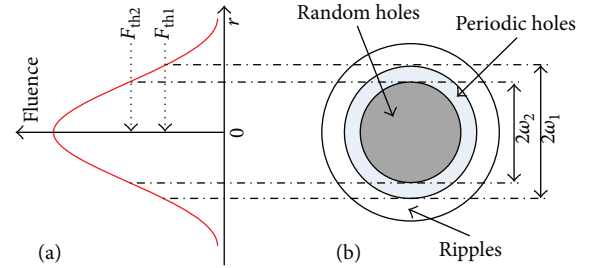


FIGURE 5: Illustration of laser ablation: (a) the profile of Gaussian beam intensity in r -axis and (b) the exposure area of ps-laser.

about 10% of the incidence energy fluence is absorbed [22], and the rest is used for the expanding plasma to move into the ambient air with a small part lost in radiation [23, 24]. Thus, it is easily calculated that the pulse fluence of 0.147 J/cm^2 can cause surface melting and the fluence of 0.283 J/cm^2 can cause surface vaporizing. The theoretically calculated threshold 0.147 J/cm^2 agrees with the experimentally calculated threshold 0.150 J/cm^2 well. According to the above analysis, the laser fluences 0.80 and 1.6 J/cm^2 used in Figures 2 and 3 are enough to vaporize the material in skin surface and conduct heat into the bulk of material. Thermal diffusivity indeed occurs.

As the fluence increases from 0.8 to 1.6 J/cm^2 , the depth and dimension of pit holes increase. However, the formation of pit holes can be obviously divided into two phases based on the characteristics of pit holes and adopted laser fluences. In phase I, for low fluences ($0.76 < F < 1.2 \text{ J/cm}^2$), more laser energy irradiation makes a growth of periodic pit holes from ~ 0.9 to $\sim 1.5 \mu\text{m}$. The formation of these periodic holes may be resulted from Coulomb Explosion [5] during locally spatial modulated ablation. Compared with ripples, the holes have a superiority in absorbing laser energy, which promotes an increasing size of pit holes for prompted dissolution of bubbles of materials after irradiation. In phase II, for high fluences ($F > 1.29 \text{ J/cm}^2$), the random pit holes present a characteristic of overheated liquid explosion, which differs from phase I. So the creation of holes in phase II may be explained by the phase explosion [25, 26].

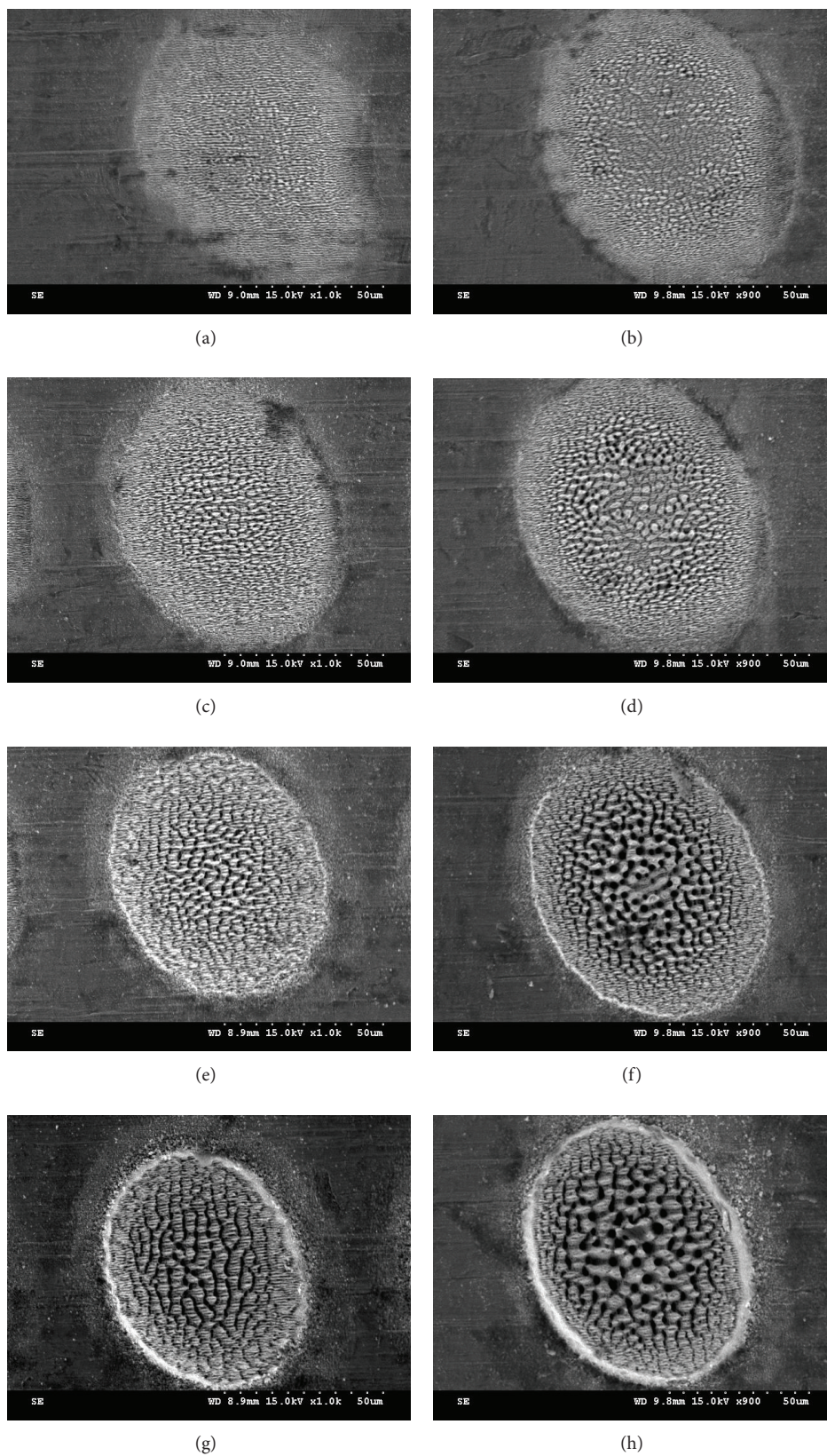


FIGURE 6: SEM images of an array of craters ablated on the surface of stainless steel 304 with fluence 0.8 J/cm^2 and pulse number of 100 (a), 200 (c), 500 (e), and 1000 (g) and fluence 1.6 J/cm^2 and pulse number of 100 (b), 200 (d), 500 (f), and 1000 (h), respectively.

TABLE 1: EDX elemental analysis of the stainless steel 304 surface. Measuring locations are given in Figure 2(a).

Spectrum (wt.%)	C	O	Si	Cr	Mn	Fe	Ni	Total
Spectrum 1	8.28	2.77	0.51	16.72	1.11	62.81	7.80	
Spectrum 2	5.37	5.25	0.40	17.24	1.88	62.90	6.96	~100
Spectrum 3	2.26	7.97	0.48	18.07	2.33	62.70	6.18	

(SEM SU-8010, voltage: 15.0 Kv, magnification: 10.0 Kx, count rate: 1434 cts).

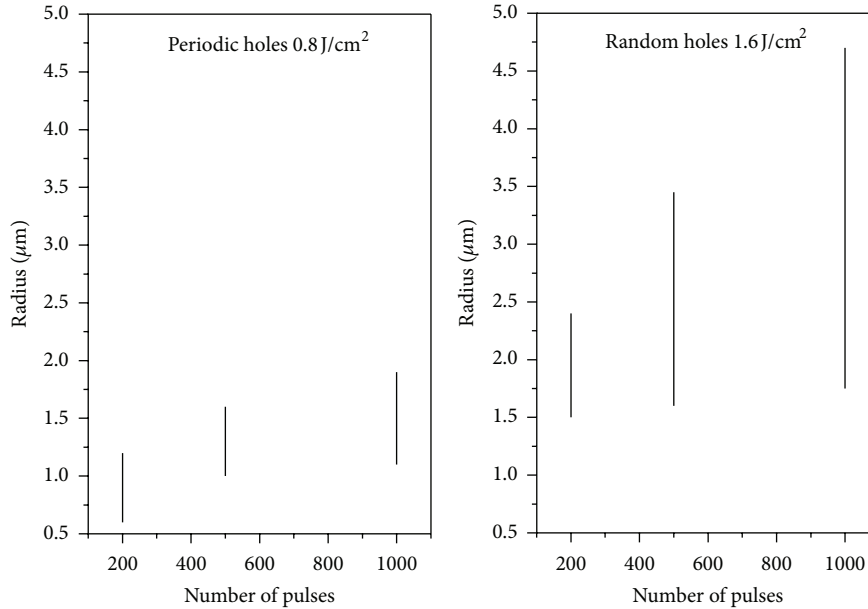


FIGURE 7: Radius of periodic/random holes versus the number of pulses.

3.2. Surface Morphology of Ablated Craters Evolution with Number of Pulses. The section above has discussed two kinds of pit holes, the periodic and random ones, and their causes under the action of different fluences. The following content mainly discusses the role of the pulse number during the formation of pit holes. Figure 6 shows an analysis of the surface morphology of ablated craters irradiated by multiple ($N = 50-1000$) laser pulses with two fluences (0.8 and 1.6 J/cm^2). It is found that two kinds of pit hole formation both depend on the number of pulses. As the number of pulses increases from 50 to 500, a transition of main surface structures occurs from ripples (Figures 6(a) and 6(b)) to pit holes (Figures 6(e) and 6(f)). However, due to different mechanisms in two kinds of pit hole formation (discussed in Section 3.1), for $F = 0.826 \text{ J/cm}^2$ and $N = 1000$, the size of periodic holes increases, and eventually they join together and form channels (Figure 6(g)). These channels also can be deemed a type of periodic surface structure. For $F = 1.650 \text{ J/cm}^2$ and $N = 200-500$, from Figures 6(d) and 6(f), holes start to form between the center and edge of the ablated crater, whose resolidification is obviously presented in the center; laser with the highest intensity in the center of the beam spot can be mainly used for material removal in the effective penetration depth, which causes less mix of gas-liquid and burst of bubbles in the molten bottom of ablated crater. When N reaches 1000, the size of random holes also increases and the surface of ablated crater presents

porous with resolidification. Images in Figure 6 show that the depth of ablated crater increases obviously but the distribution area of pit holes does not obviously increase with the increasing number of the pulses. Figure 7 shows that the diameter of periodic/random holes increases with the increasing number of the pulses from 200 to 1000. It is interesting that both of the periodic pit holes and the random pit holes begin to appear at 200 pulses; likewise the ablation threshold tends asymptotically to a constant value at 200 pulses, as shown in Figure 4. It is inferred that the first 200 pulses results in a stable ablated material status and then subsequent pulses have excess energy to reinforce the formation of pit holes.

During laser interaction with metals, the laser energy is absorbed primarily by free electrons [18]. The absorbed radiation energy in the skin layer involves thermalization of electrons. Part of the electron energy is transferred into the bulk in the form of heat, while the later part is transferred to the lattice subsystem. In the first case, the electron diffusion process is essential. Finally, if the initial laser fluence is sufficient, surface damage/ablation will take place. In our experiments, for laser pulses with fluence higher than 0.283 J/cm^2 , a single pulse could generate the afterheat, which made a rise of temperature in skin layer of ablated crater. However, the afterheat from a single pulse was not enough for the burst of bubbles in molten material. Seen in Figure 5, the most dramatic decrease of the ablation threshold presents the most dramatic decrease during the first 200 laser pulses: the single

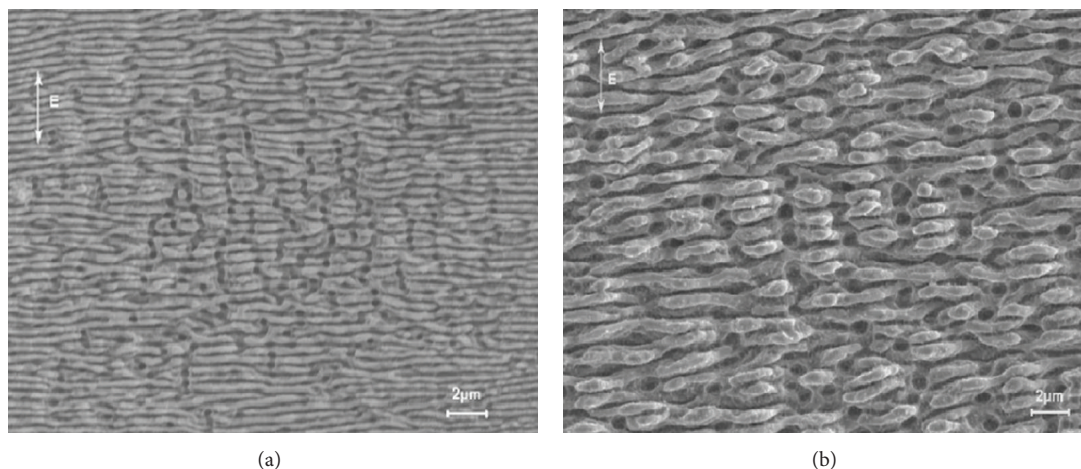


FIGURE 8: SEM images of surface irradiated by laser pulses of 532 nm (a) and 1064 nm (b), with 0.8 J/cm^2 and 250 pulses.

pulse ablation threshold of 0.247 J/cm^2 is reduced to 0.151 J/cm^2 , which is an almost 38% decrease, when 200 laser pulses are applied. As the number of pulses exceeds 200, the threshold fluence tends asymptotically to a constant value of $\sim 0.150 \text{ J/cm}^2$ in this case. After first 200 pulses, the subsequent pulses do not have to use most energy to ablate surface material so that afterheat accumulated promotes the generation of pit holes. So 200 pulses irradiated are necessary for the generation of pit holes. From the different cases among Figures 6(c)–6(f), the optimal number of pulses to form holes for the corresponding fluence needs further study.

3.3. Porous Structures of Ablated Craters Affected by Other Experimental Conditions. The morphological changes induced by picosecond laser on the stainless steel 304 target primarily have shown their dependence on the laser fluence and the number of accumulated pulses, and they are also affected by other factors, such as laser beam characteristics (wavelength, pulse length) and laser irradiation environment (in air atmosphere or in vacuum).

Metals are surface absorbers, with low ionization potential, high electron number density, and higher absorption coefficient for shorter wavelength laser [27]. It means that the morphology of subspot size holes will change with the varying laser wavelength. In order to confirm this inference, the sample surface characteristics are compared after the irradiation of 532 nm and 1064 nm wavelength laser, as shown in Figure 8. The experimental result shows the close dependence of the spacing of these periodic holes and the wavelength of incident laser pulses: subspot size holes produced by 532 nm laser pulses have a period $\sim 1.8 \mu\text{m}$, which is about half of the ones produced by 1064 nm laser pulses.

In pulsed laser ablation, depending on the respective pulse length range, different beam-matter interaction mechanisms become dominant [1]. For laser pulses in the micro- and nanosecond range, the ablation process is dominated by heat conduction, melting, evaporation, and plasma formation [19]. Ultrashort pico- and femtosecond laser pulses (where thermal diffusion into the material is small) were used, the generated vapor becomes rapidly ionized [19], and due

to the short interaction time, the material cannot evaporate continuously but can be transferred into a state of overheated liquid for the phase explosion [25, 26]. From above, long pulse length may lead to bubbling in molten liquid for mild random holes.

Irradiation of the target sample in this paper was performed in air atmosphere; if in vacuum, the oxidation reaction on the surface can be neglected with absence of the oxide [28]. Ultrafast laser ablation in vacuum leads to the bubbles of materials directly produced from the irradiated material through phase explosion and their flying away from the target surface ahead of the plume with a characteristic velocity of $\sim 10^4 \text{ m/s}$ [29]. Therefore, it is inferred that subspot size holes with larger size will be obtained.

3.4. Preparation of Large-Area Porous Structures. In order to explore the effect of porous structures as a kind of functional modified surface structure, the preparation of large-area porous structure is presented. According to the processing parameters discussed above, we choose $F = 1.1 \text{ J/cm}^2$ and $V = 0.174 \text{ mm/s}$ (the effective number of pulses in a fixed position during laser scan $N_f = 500$) for a large scanned area of porous structure, as shown in Figure 8. Pit holes are formed on the surface of the scanned area, which have the average diameter of $\sim 5 \mu\text{m}$ (as shown in inset SEM image of Figure 9). And the processing technology for laser scan forming porous structure in large area remains need to be further optimized.

After preparing large-area porous structures, the surface is modified for the hydrophobic surface by fluoroalkyl silane. It is seen that the surface has a contact angle of 151.3° , as shown in Figure 10. Therefore, the porous structure surface has wettability. In addition, porous structure may have many other important applications such as lighting absorption and abrasion resistance, which will be the focus of the future research.

4. Conclusion

A study was presented about local morphological changes on the stainless steel 304 target surface induced by a picosecond Nd:van regenerative amplified laser, operating at 1064 nm.

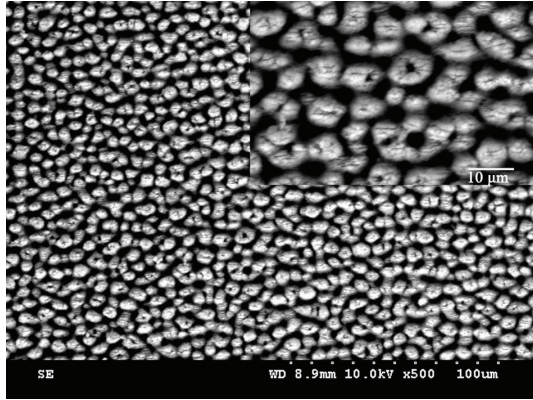


FIGURE 9: SEM image of large-area porous structure fabricated on the surface of stainless steel 304.

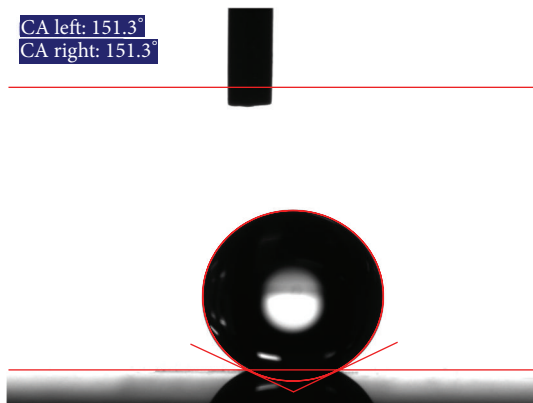


FIGURE 10: Image of contact angle measurements of a water drop on the large-area porous structure surface of stainless steel 304.

It was shown that laser pulses in the fluences of ~ 0.8 and 1.6 J/cm^2 and the numbers of pulses $N = 100\text{--}1000$, in air, induced specific morphological changes at the stainless steel 304 target. High energy treatment (1.65 J/cm^2 , 500 pulses) resulted in the formation of sub-spot hole with the size of $\sim 5\text{--}3 \mu\text{m}$, while the reduced energy (0.824 J/cm^2 , 500 pulses) led to the creation of sub-spot periodic holes with the size of $\sim 1.5\text{--}1 \mu\text{m}$. The experimental results prove that the formation of sub-spot holes on the target depends not only on the number of pulses but also on laser fluence. Although 200 pulse irradiation can cause an initial to form these sub-spot holes, the formation of holes can be obviously divided into 2 phases based on characteristics of holes and energy conditions for their formation. For fluences ($0.76 < F < 1.2 \text{ J/cm}^2$), more irradiating laser energy makes a growth of periodic structures from pits $\sim 300 \text{ nm}$ to holes $\sim 1.5 \mu\text{m}$, finally to periodic groove; for fluences ($F > 1.2 \text{ J/cm}^2$), the holes present a characteristic of overheated liquid explosion without period and have a larger size.

Generally, it can be deduced that the sub-spot holes with a homogeneous distribution across the whole modified area can have a number of important applications in nanotechnology, industry, nuclear complex, and so forth. Thus, preparation of sub-spot porous structure homogeneously distributed

across the whole modified area in large area will be the main direction of our future study.

Acknowledgments

This work was supported by National Natural Science Foundation of China (Grant no. 91123024), Program for Changjiang Scholars and Innovative Research Team in University (Grant no. IRT1172), and the Fundamental Research Funds for the Central Universities (Grant no. xjj2012113).

References

- [1] B. N. Chichkov, C. Momma, S. Nolte, F. Von Alvensleben, and A. Tünnermann, "Femtosecond, picosecond and nanosecond laser ablation of solids," *Applied Physics A*, vol. 63, no. 2, pp. 109–115, 1997.
- [2] W. Wang, X. Mei, and G. Jiang, "Control of microstructure shape and morphology in femtosecond laser ablation of imprint rollers," *International Journal of Advanced Manufacturing Technology*, vol. 41, no. 5-6, pp. 504–512, 2009.
- [3] Y. Ding, J. Shao, X. Li, H. Tian, L. Miao, and H. Liu, "Controllable formation of nanogaps in thin metallic film by rear side irradiation with ultrashort pulsed laser," *Physica E*, vol. 44, no. 2, pp. 430–434, 2011.
- [4] K. Paivasaari, J. J. J. Kaakkunen, M. Kuittinen, and T. Jaaskelainen, "Enhanced optical absorptance of metals using interferometric femtosecond ablation," *Optics Express*, vol. 15, no. 21, pp. 13838–13843, 2007.
- [5] W.-Q. Han, L. Wu, R. F. Klie, and Y. Zhu, "Enhanced optical absorption induced by dense nanocavities inside titania nanorods," *Advanced Materials*, vol. 19, no. 18, pp. 2525–2529, 2007.
- [6] Y. B. Gerbig, S. I.-U. Ahmed, D. G. Chetwynd, and H. Haefke, "Topography-related effects on the lubrication of nanostructured hard surfaces," *Tribology International*, vol. 39, no. 9, pp. 945–952, 2006.
- [7] J. Bonse, A. Rosenfeld, and J. Krüger, "Implications of transient changes of optical and surface properties of solids during femtosecond laser pulse irradiation to the formation of laser-induced periodic surface structures," *Applied Surface Science*, vol. 257, no. 12, pp. 5420–5423, 2011.
- [8] A. Borowiec and H. K. Haugen, "Subwavelength ripple formation on the surfaces of compound semiconductors irradiated with femtosecond laser pulses," *Applied Physics Letters*, vol. 82, no. 25, pp. 4462–4464, 2003.
- [9] G. A. Martsinovskii and G. D. Shandybina, "Ultrashort excitations of surface polaritons and waveguide modes in semiconductors," *Optics and Spectroscopy*, vol. 105, pp. 67–72, 2008.
- [10] N. G. Semaltianos, W. Perrie, P. French et al., "Femtosecond laser ablation characteristics of nickel-based superalloy C263," *Applied Physics A*, vol. 94, no. 4, pp. 999–1009, 2009.
- [11] M. Guillermin, F. Garrelie, N. Sanner, E. Audouard, and H. Soder, "Single- and multi-pulse formation of surface structures under static femtosecond irradiation," *Applied Surface Science*, vol. 253, no. 19, pp. 8075–8079, 2007.
- [12] S. Rapp and J. Rosenberger, "Pump-probe microscopy investigations on fs-laser ablation of thin $\text{Ta}_2\text{O}_5/\text{Pt}$ layer systems," *Journal of Applied Physics*, vol. 112, Article ID 013110, 2012.
- [13] P. Fan and M. Zhong, "Rapid fabrication of surface micro/nano structures with enhanced broadband absorption on Cu by picosecond laser," *Optics Express*, vol. 21, pp. 11628–11637, 2013.

- [14] G. Zhao and N. Zhang, "Porous MoO₃ films with ultra-short relaxation time used for supercapacitors," *Materials Research Bulletin*, vol. 48, no. 3, pp. 1328–1332, 2013.
- [15] J. M. Liu, "Simple technique for measurements of pulsed Gaussian-beam spot sizes," *Optics Letters*, vol. 7, pp. 196–198, 1982.
- [16] W. Wang, X. Mei, and G. Jiang, "Control of microstructure shape and morphology in femtosecond laser ablation of imprint rollers," *International Journal of Advanced Manufacturing Technology*, vol. 41, no. 5-6, pp. 504–512, 2009.
- [17] A. Ben-Yakar, A. Harkin, J. Ashmore, R. L. Byer, and H. A. Stone, "Thermal and fluid processes of a thin melt zone during femtosecond laser ablation of glass: the formation of rims by single laser pulses," *Journal of Physics D*, vol. 40, no. 5, article 021, pp. 1447–1459, 2007.
- [18] P. P. Pronko, S. K. Dutta, D. Du, and R. K. Singh, "Thermophysical effects in laser processing of materials with picosecond and femtosecond pulses," *Journal of Applied Physics*, vol. 78, no. 10, pp. 6233–6240, 1995.
- [19] K. H. Leitz and B. Redlingshöfer, "Metal ablation with short and ultrashort laser pulses," *Physics Procedia*, vol. 12, pp. 230–238, 2011.
- [20] K. C. Mills, S. U. Yuchu, L. I. Zushu, and R. F. Brooks, "Equations for the calculation of the thermo-physical properties of stainless steel," *ISIJ International*, vol. 44, no. 10, pp. 1661–1668, 2004.
- [21] J. Stašić and B. Gakovic, "Superficial changes on the Inconel 600 superalloy by picosecond Nd:YAG laser operating at 1064, 532, and 266 nm: Comparative Study," *Laser and Particle Beams*, vol. 30, p. 249, 2012.
- [22] E. G. Gamaly, A. V. Rode, B. Luther-Davies, and V. T. Tikhonchuk, "Ablation of solids by femtosecond lasers: ablation mechanism and ablation thresholds for metals and dielectrics," *Physics of Plasmas*, vol. 9, no. 3, p. 949, 2002.
- [23] C. H. Fan, J. Sun, and J. P. Longtin, "Plasma absorption of femtosecond laser pulses in dielectrics," *Journal of Heat Transfer*, vol. 124, no. 2, pp. 275–283, 2002.
- [24] R. Fedosejevs and R. Ottmann, "Absorption of femtosecond laser pulses in high-density plasma," *Physical Review Letters*, vol. 64, no. 11, pp. 1250–1253, 1990.
- [25] J. König and T. Bauer, *Fundamentals and Industrial Applications of Ultrashort Pulsed Lasers at Bosch*, Photonics West, San Francisco, Calif, USA, 2011.
- [26] A. Miotello and R. Kelly, "Laser-induced phase explosion: new physical problems when a condensed phase approaches the thermodynamic critical temperature," *Applied Physics A*, vol. 69, no. 7, pp. S67–S73, 1999.
- [27] L. M. Cabalin and J. J. Laserna, "Experimental determination of laser induced breakdown thresholds of metals under nanosecond Q-switched laser operation," *Spectrochimica Acta B*, vol. 53, no. 5, pp. 723–730, 1998.
- [28] M. Momcilovica and J. Limpouch, "Surface modification of copper using high intensity, 10¹⁵W/cm², femtosecond laser in vacuum," *Applied Surface Science*, vol. 258, p. 8908, 2012.
- [29] S. Amoruso, R. Bruzzese, M. Vitiello, N. N. Nedialkov, and P. A. Atanasov, "Experimental and theoretical investigations of femtosecond laser ablation of aluminum in vacuum," *Journal of Applied Physics*, vol. 98, no. 4, Article ID 044907, 2005.

Research Article

Fabrication of TiO₂@Yeast-Carbon Hybrid Composites with the Raspberry-Like Structure and Their Synergistic Adsorption-Photocatalysis Performance

Dang Yu, Bai Bo, and He Yunhua

Environmental Science & Engineering College, Chang'an University, Xi'an 710054, China

Correspondence should be addressed to Bai Bo; baibochina@163.com

Received 17 July 2013; Revised 27 August 2013; Accepted 28 August 2013

Academic Editor: Mengnan Qu

Copyright © 2013 Dang Yu et al. This is an open access article distributed under the Creative Commons Attribution License, which permits unrestricted use, distribution, and reproduction in any medium, provided the original work is properly cited.

In the present work, we report the preparation and photocatalytic properties of TiO₂@yeast-carbon with raspberry-like structure using a pyrolysis method. The products are characterized by field emission scanning electron microscopy (FE-SEM), energy dispersive spectrometry (EDS), X-ray diffraction (XRD), thermal gravimetric and differential thermal analysis (TGA-DTA), Fourier transformed infrared spectroscopy (FT-IR), and ultraviolet visible spectroscopy (UV-VIS), respectively. The results show that the hybrid TiO₂@yeast-carbon microspheres have ordered elliptic shapes of uniform size (length = $3.5 \pm 0.3 \mu\text{m}$; width = $2.5 \pm 0.5 \mu\text{m}$). UV-VIS ascertains that the as-prepared microspheres possess an obvious light response in a wide range of 250–400 nm. In the decomposition of typical model pollutants including methylene blue and congo red, the hybrid composites exhibited excellent photocatalytic activity for the methylene blue due to the enhanced adsorption ability. Further investigation reveals that the combined effect of adsorption from the yeast-carbon core and photocatalytic degradation from the attached TiO₂ nanoparticles were responsible for the improvement of the photocatalytic activities. Hereby, the raspberry-like TiO₂@yeast-carbon has promising applications in water purification.

1. Introduction

In the past few years, raspberry-like composite particles with well-defined structures have become the subject of rapidly growing interest due to their high surface roughness and potential applications [1, 2]. The unique raspberry-like composites have combined excellent characteristics of host particles and guest particles, such as higher surface area, increased chemical and biological stability, rich surface chemical component, and different magnetic or optical properties [3].

The high surface area, large pores (macroporosity), and the presence of surface hydroxyl groups make carbon substance an ideal catalyst support [4–6]. Like the titania photocatalysts supported on the carbon matrix by means of several strategies [7–9] appear to have various benefits and advantages for providing a cheap and effective wastewater treatment and remediation options [10, 11]. For example, Hu et al. [12] obtained TiO₂ nanoparticles/carbon nanotubes

particles with raspberry-like structure by combining sol-gel and electrospinning methods. Liu et al. [13] demonstrated the formation of TiO₂/carbon fibers (ACFs) composite photocatalyst via sol-gel method and the TiO₂/ACFs is especially helpful for the removal of low molecular weight organic pollutants in the contaminated water. Areerachakul et al. [14] prepared well-structured TiO₂/granular-activated carbon (GAC) hybrid particles. The TiO₂/GAC showed excellent capabilities in decomposing the herbicide of metsulfuron-methyl (MM) from waste water. In brief, using carbon materials above-mentioned as catalyst supports has increased the photodegradation rate by progressively allowing an increased quantity of substrate to come in contact with the TiO₂ by means of adsorption. In this respect, carbon matrix has been proven to be an invaluable support in promoting the photocatalytic process [15–17] through providing a synergistic effect by creating a common interface between both the carbon phase and the TiO₂ nanoparticle phase. Such synergistic effect can be explained as an enhanced adsorption

of the target pollutant onto the carbon phase followed closely by a transfer through an interphase to the TiO_2 phase, giving a complete photodegradation process [18].

The yeast-carbon is a porous and amorphous solid carbon material, which is derived mainly from baker's yeast. For instance, Nacoo and Aquarone [19] reported the fabrication of yeast-carbon by carbonizing in a gas-heated muffle. The obtained yeast-carbon possessed higher surface area. Similarly, Guan et al. [20] synthesized amphiphilic porous hollow carbonaceous materials via mild hydrothermal treatment of yeast cells. The resultant carbon material displayed effective adsorption of organic chemicals in wastewater treatment. Thus, in the present study, a novel TiO_2 @yeast-carbon microsphere with raspberry-like morphology was fabricated firstly by a single-step strategy based on the pyrolysis method. The obtained hybrid microspheres were characterized by FE-SEM, EDS, XRD, TGA-DTA, FT-IR, and UV-VIS, respectively. A possible mechanism for the formation of the composite microspheres was proposed. In addition, the synergistic effect of adsorption-photocatalysis performance in the TiO_2 @yeast-carbon microspheres was evaluated by examining the decolonization of methylene blue and congo red.

2. Materials and Methods

2.1. Materials. The powdered yeast was purchased from Angel Yeast Company. Photocatalyst was TiO_2 from Degussa and was used without further purification. In all preparations, absolute ethanol and double-distilled water were used. Methylene blue (MB) and congo red (CR) were analytic grades and were used as the model pollutants in present work.

2.2. Preparation of Raspberry-Like TiO_2 @Yeast-Carbon Hybrid Microspheres. In a typical synthesis procedure, 125.0 mg yeast powder was washed with distilled water and absolute ethanol for three times, respectively. The yeast was dissolved in 20.0 mL of distilled water and stirred vigorously for 30 minutes. The pH was adjusted to approximately 3 by adding drop wise sulfuric acid. Further, 10.0 mg TiO_2 was dispersed in 20.0 mL of distilled water, using ultrasonic vibration for 1.0 minute. The pH was adjusted to approximately 9-10 with sodium hydroxide and stirred for 30.0 min. Then the suspended TiO_2 and yeast were gathered by centrifugation from their own suspensions and redistributed in 20.0 mL of distilled water. Afterwards, TiO_2 and yeast suspensions were mixed and magnetically stirred for 1.5 h at room temperature and left for 3.0 h without further stirring or shaking to ensure the formation of TiO_2 @yeast particles. Thus, the mixture was centrifuged in three or more cycles to remove the undesired components and finally desiccated at 353 K for 1.0 h. Subsequently the TiO_2 @yeast particles were calcined at 573 K for 1.0 h in a nitrogen pipe furnace and cooled to room temperature. After that, the TiO_2 @yeast-carbon composite microspheres were obtained.

2.3. Sample Analysis. Philips XL-30 field emission scanning electron microscope (FE-SEM) was used to observe the morphology of samples. X-ray diffraction (XRD) patterns were collected on X. Pert Pro diffractometer using $\text{Cu K}\alpha$ radiation ($\lambda = 0.15418 \text{ nm}$) at a scanning rate of $10^\circ/\text{min}$. Thermal gravimetric analysis and differential thermal analysis (TGA-DTA) were carried out on an EXSTAR apparatus at a heating rate of $40^\circ/\text{min}$ in flowing high purity N_2 . Fourier-transform infrared spectroscopy measurements (FT-IR) were recorded with a Bio-Rad FTS135 spectrometer in the range of $370\text{--}4000 \text{ cm}^{-1}$. UV-VIS diffuse reflectance spectra (UV-VIS) were measured on a HITACHI 340 UV-VIS spectrophotometer.

2.4. Photocatalytic Activity. The methylene blue (MB) dye and congo red (CR) are widely used in dye industry. Therefore, the elimination of these compounds is becoming an increasingly important environmental problem. Photocatalytic degradation of MB and CR was evaluated under UV irradiation in an aqueous media. The initial concentration of MB and CR was set as 2~3 mg/L, respectively. The amount of photocatalysts including yeast-carbon and TiO_2 @yeast-carbon were kept at 0.25 g/L. Before UV irradiation, the suspension containing photocatalyst, MB, and CR was deposited within 50.0 min to establish adsorption-desorption equilibrium. Then the suspension was irradiated under a UV lamp (the intensity of irradiation is 60 W). The concentration of MB and CR was traced by UV-VIS spectroscopy. The absorbance characteristic at bands 666.4 nm and 499.0 nm was taken to determine MB and CR concentration by using a calibration curve, respectively.

3. Results and Discussion

3.1. Materials Characterization. The shape and structure of the samples are shown in Figure 1. The SEM image in Figure 1(a) shows that the prime yeast cells have a regular ellipsoidal shape with a diameter varying between 2.6 and $3.7 \mu\text{m}$. Figure 1(b) shows an image of the precursor of TiO_2 @yeast-carbon. Compared with the bared yeast, the size of the TiO_2 @yeast (length = $3.7 \pm 0.4 \mu\text{m}$; width = $2.6 \pm 0.5 \mu\text{m}$) was gently increased due to the attachment of TiO_2 nanoparticles. The picture in Figure 1(d) shows an overall image of the TiO_2 @yeast-carbon microspheres. The particles maintained the shape of the original precursor and had the average diameter (length = $3.7 \pm 0.3 \mu\text{m}$; width = $2.5 \pm 0.5 \mu\text{m}$). Further, higher resolution image in Figure 1(f) shows that the nano-sized TiO_2 particles randomly decorated the surface of yeast spheres, which have the morphology of raspberry-like composites. Similar morphology has been reported for the synthesis of the raspberry-like PMMA/ SiO_2 hybrid microspheres [21]. Moreover, the nanoparticles TiO_2 were relatively dispersed on the yeast-carbon in comparison with the agglomerated TiO_2 in the TiO_2 /spherical activated carbons composed by Oh et al. [22]. In addition, the raspberry-like morphology of the TiO_2 @yeast-carbon microspheres can be confirmed through the EDS analysis. In the insert image in Figure 1(f), the sample contained Ti, C, O,

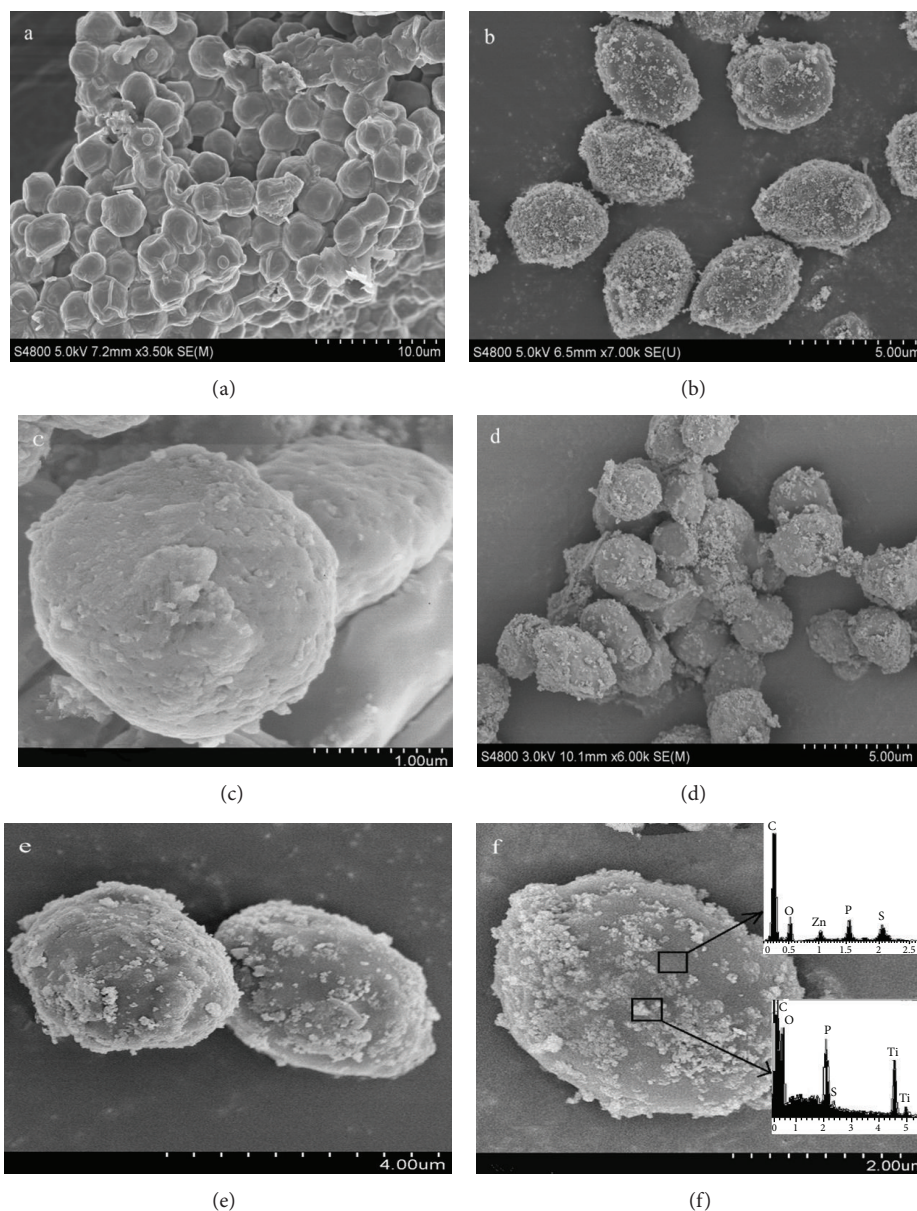


FIGURE 1: SEM images of (a) the naked yeast, (b) general observation of the raspberry-like TiO_2 @yeast precursor, (c) the yeast-carbon, (d) the overall view of the raspberry-like TiO_2 @yeast-carbon microspheres, (e) the selected raspberry-like TiO_2 @yeast-carbon microspheres, and (f) typical raspberry-like TiO_2 @yeast-carbon microspheres observed under high magnification.

S, and P; no other impurity element is detected, confirming that the TiO_2 particles were coated on the surface of the yeast-carbon. By comparing the TiO_2 @yeast precursor with the TiO_2 @yeast-carbon product, it can be seen that the color of particles changed from pure white to ash black. Thus, it can be inferred that the carbonization of the yeast occurred in the pyrolysis process. In this respect, the control experiments of the yeast-carbon without the attachment of nanoparticles TiO_2 have been conducted under the same conditions. The image of yeast-carbon in Figure 1(c) indicates that the yeast-carbon with an average diameter (length = $3.5 \pm 0.4 \mu\text{m}$; width = $2.3 \pm 0.50 \mu\text{m}$) has smooth surface morphology

and rich pore structure, which contrasts with the morphology of yeast-carbon synthesized by Shen et al. [23] in which a relatively high distribution of broken shells was observed.

XRD patterns of yeast, yeast-carbon, TiO_2 @yeast-carbon, and TiO_2 are displayed in Figure 2. The broad peak around $2\theta = 20^\circ$ indicates that the yeast carbon (in Figure 2(a)) and the yeast (in Figure 2(b)) can be assigned to amorphous species. In Figures 2(c) and 2(d) display the XRD patterns of the hybrid TiO_2 @yeast-carbon. The broad peaks centering at $2\theta = 25^\circ, 37^\circ, 48^\circ, 55^\circ,$ and 63° are assigned to anatase-type TiO_2 (JCPDS. No: 21-1272) [24]. Other diffraction peaks are in good agreement with diffraction peaks of rutile-type

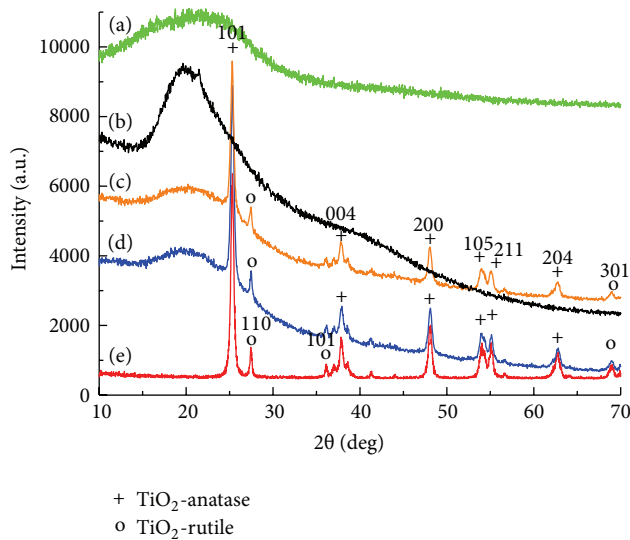


FIGURE 2: XRD patterns of (a) the prepared yeast-carbon, (b) the premier yeast, (c) the 80% of TiO_2 @yeast-carbon, (d) the 40% of TiO_2 @yeast-carbon, and (e) the pure TiO_2 .

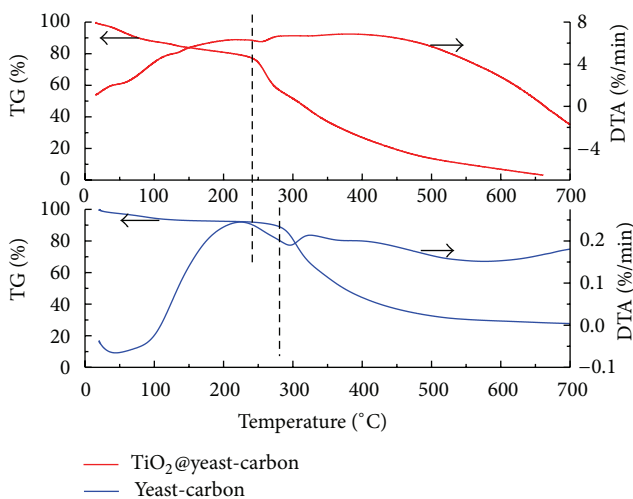


FIGURE 3: TGA-DTA curves of the yeast and the TiO_2 @yeast-carbon.

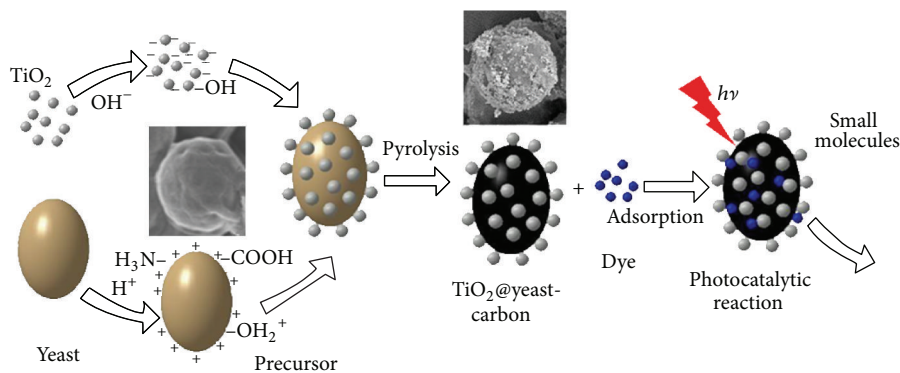
TiO_2 (JCPDS. No: 21-1276) [25]. The relative intensity of diffraction peaks of TiO_2 @yeast carbon is approximately identical with the original components of the TiO_2 as guest particles ($\text{P}_{25}\text{TiO}_2$: 78% anatase-type TiO_2 and 22% rutile-type TiO_2). The broad peaks at $2\theta = 20^\circ$ in the Figures 2(c) and 2(d) are mainly caused by the amorphous structure of yeast-carbon.

In Figure 3, the distinct decrease in weight of the bare yeast is shown during a wide temperature range of 280–600°C. The rapid weight loss of approximately 50.0% at the temperature range of 280–370°C may be associated with the split of the polysaccharide chains in the yeast [26, 27], which is accompanied by a broad exothermic peak at about 370°C in the DTA curve. The ultimate weight loss from 400 to 600°C can be resulted from the cross-linking of oligosaccharides

[28] in the yeast, which is accompanied by the endothermic peak at 500°C in the DTA curve. The total weight loss reaches to about 30.0% and the last weight of the residual ashes is approximately 70.0% of the original yeast biomass. In comparison with the naked yeast, the carbonization reaction of the TiO_2 @yeast precursor was started at temperatures about 250°C. The broad exothermic peak at around 200–300°C may be related to the carbonized decomposition of organic substrate in the yeast along with the rapid weight loss of 50.0%. It is worth noting that the broader exothermic peak appeared at around 300–450°C. This may be caused by the release of constitution water and further crystallization of TiO_2 [29]. The wider exothermic peak at 450–600°C can be ascribed to the crystal shift from anatase to rutile phase.

After pyrolysis entirely, the raspberry-like TiO_2 @yeast-carbon microspheres can be attained, which has been proved by SEM analysis. The connection between the guest particles TiO_2 and the host particles of the yeast-carbon can be elaborated further by FT-IR analysis. FT-IR spectra of the yeast, yeast-carbon, TiO_2 @yeast precursor, TiO_2 and TiO_2 @yeast-carbon composites are presented in Figure 4, respectively. For the yeast-carbon, the band around 1570 cm^{-1} can be ascribed to $-\text{C}=\text{C}-$ stretching bond originated from the inherent structure of yeast, and the bands at 1704 and 1210 cm^{-1} correspond to $\text{C}=\text{O}$, $\text{C}-\text{O}$ stretching of carboxyl groups, respectively [30]. As for TiO_2 @yeast-carbon composites, the broad and intense peak at $3500\text{--}3200\text{ cm}^{-1}$ can be assigned to the stretching of $-\text{OH}$ group due to the bound water in the TiO_2 @yeast-carbon composites [31, 32]. The stretching bond corresponding to skeletal $\text{Ti}-\text{O}-\text{Ti}$ is clearly represented in the region of 509 cm^{-1} . The band at 1171 cm^{-1} suggests the presence of $\text{C}-\text{O}$ bond [33]. The band at around 620 cm^{-1} can be attributed to the $\text{Ti}-\text{O}-\text{C}$ vibration, which indicates that TiO_2 nanoparticles were chemically bonded with yeast-carbon in hybrid particles [34]. Moreover, the band at 3350 cm^{-1} is more prominent in TiO_2 @yeast-carbon composites than that of TiO_2 , indicating that there were more hydroxyl groups in the TiO_2 @yeast-carbon hybrid particles. Generally, more hydroxyl groups lead to generation of more $\cdot\text{OH}$ radicals in photocatalysis, which can enhance the photocatalytic activity of TiO_2 [35].

Based on the characterization discussed above, the following mechanism that appeared in Scheme 1 is proposed to account for the formation procedure of the raspberry-like TiO_2 @yeast-carbon hybrid microspheres. In Scheme 1, the opposite zeta potentials of yeast cells with a positive charge (H^+) and the nanoparticles TiO_2 with a negative charge (OH^-) were adjusted previously by tuning the pH of their own aqueous suspensions. Then the TiO_2 @yeast hybrid precursor with raspberry-like morphology was obtained once the aforementioned aqueous suspensions were mixed [36]. In the obtained raspberry-like TiO_2 @yeast precursor, the yeast acted as the host cores and TiO_2 as the guest particles. Afterwards, the carbonization of yeast core in the precursors of raspberry-like TiO_2 @yeast can be fulfilled by a gradual temperature-rise procedure, which can obtain the hybrid TiO_2 @yeast-carbon composites. TGA-DTA results showed that the final weight loss is approximately 50.0% in the process



SCHEME 1: Schematic illustration for the formation of the raspberry-like TiO_2 @yeast-carbon and their synergistic effect in the removal of dyes aqueous solutions.

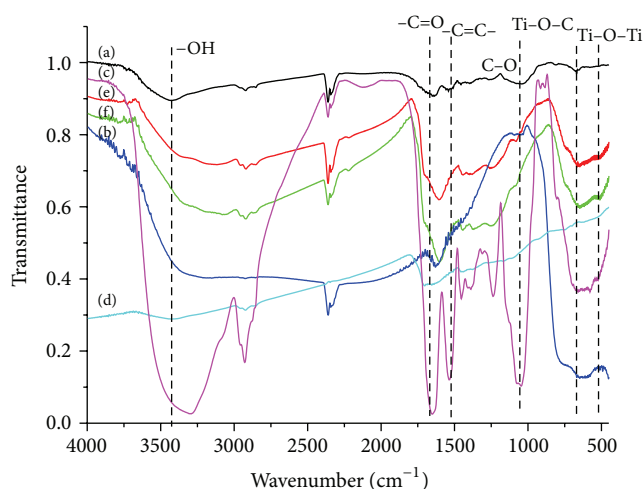


FIGURE 4: FT-IR spectrum of (a) the original yeast, (b) the TiO_2 nanoparticle, (c) the TiO_2 @yeast precursor, (d) the yeast-carbon, (e) the 80% TiO_2 @yeast-carbon, and (f) the 40% TiO_2 @yeast-carbon.

of carbonization. In the obtained raspberry-like TiO_2 @yeast-carbon, TiO_2 nanoparticles were chemically bonded with yeast-carbon through FT-IR analysis.

Figure 5 shows the UV-VIS diffuse reflectance spectra of the yeast-carbon, TiO_2 nanoparticles, and the TiO_2 @yeast-carbon hybrid particles. In Figure 5(a), the yeast-carbon showed a strong absorption in the range from the UV to the visible light, which was similar to the commercial activated carbon [37]. In Figure 5(b), the band gap energy (E_g) of nanoparticles TiO_2 is estimated about 3.2 eV [38], corresponding to a threshold wavelength of 376 nm. In comparison with the nanoparticles TiO_2 , in Figure 5(c), TiO_2 @yeast-carbon composites remain optical response in a wide range of 250–400 nm. Besides, in the insert images of Figure 5, the color of the TiO_2 @yeast-carbon sample was ash black in comparison with the pure white TiO_2 @yeast precursor, which was consistent with its adsorption spectrum.

3.2. Combined Adsorption and Photocatalytic Degradation of Methylene Blue and Congo Red. The raspberry-like TiO_2 @yeast-carbon microspheres containing an incom-

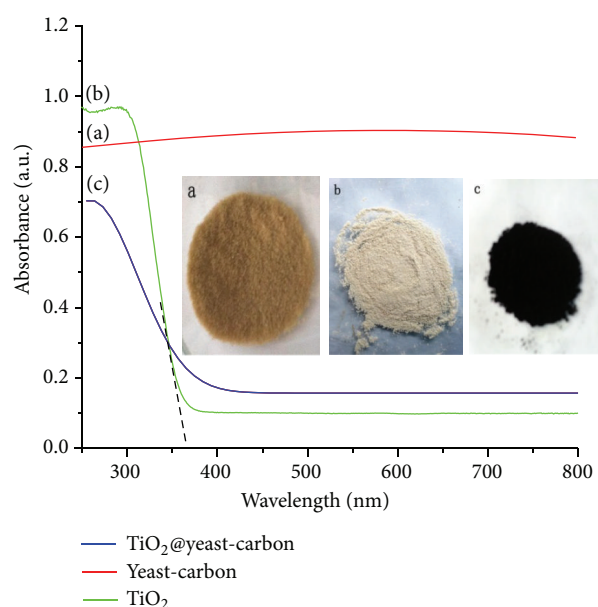
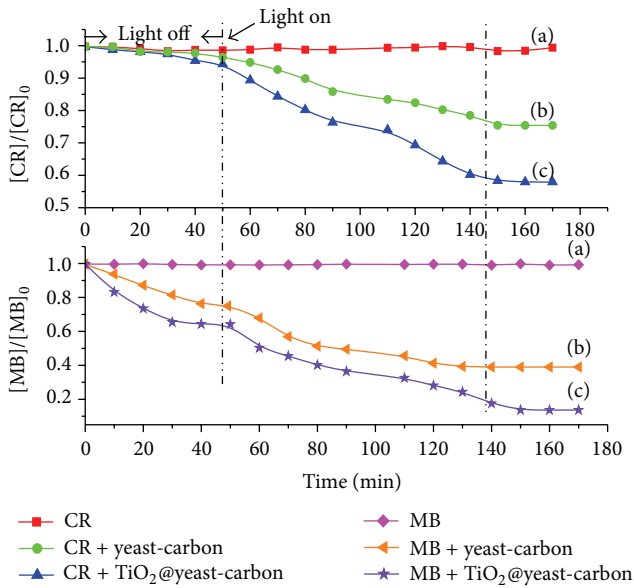


FIGURE 5: UV-VIS diffuse reflectance spectra of the yeast-carbon, TiO_2 nanoparticles, and the obtained raspberry-like TiO_2 @yeast-carbon samples ((a) the yeast-carbon, (b) the TiO_2 nanoparticles, and (c) the hybrid TiO_2 @yeast-carbon).

pletely covered surface of yeast-carbon may possess unique properties for getting rid of water pollutants. The rich pore structure of yeast-carbon might promote adsorption of organic dyes, while the outer TiO_2 nanoparticles can be in charge of the photocatalytic degradation of the dyes [39]. That is to say that immobilizing TiO_2 nanoparticles on adsorbent-like yeast-carbon can result in a synergistic effect on the efficient degradation of dye in the photocatalytic process. Specially, yeast-carbon core has the capability to extend the separation lifetime of photogenerated e^-/h^+ from outer TiO_2 nanoparticles [40] and thus increasing the quantum efficiency of TiO_2 . In turn, TiO_2 nanoparticles can destroy dyes by photocatalytic oxidation, thus regenerating the yeast-carbon in situ. In order to test the activity of the composite TiO_2 @yeast-carbon catalysts, the photocatalytic experiments

TABLE 1: Comparison of the adsorption constant for MB and CR.

Dyes	C_0 (mg/L)	q_e (mg/g)	Langmuir isotherm			Freundlich isotherm		
			Q_0 (mg/g)	b (1/mg)	R^2	K_F [(mg/g)((1/mg) ^{1/n})]	$1/n$	R^2
MB	1.00	0.23						
	2.00	0.56						
	3.00	0.87	1.53	1.25	0.99	0.78	0.94	0.83
	4.00	1.17						
	5.00	1.18						
CR	3.00	0.12						
	5.00	0.34						
	7.00	0.59	1.15	0.33	0.98	0.39	0.13	0.82
	9.00	0.74						
	11.00	0.75						

FIGURE 6: Photocatalytic activities of yeast-carbon and TiO_2 @yeast-carbon under UV irradiation.

were carried out for the degradation of MB and CR aqueous solution widely used as model compound for photocatalytic nanomaterial standardization.

From the results shown in Figure 6, the MB and CR aqueous solution is barely photolyzed by UV light irradiation in Figure 6(a). In Figure 6(b) the adsorption-desorption equilibrium was set up within 50.0 min dark environment. The adsorption capacity of the TiO_2 @yeast-carbon microspheres for MB was higher than that for CR, which can be assigned to the negatively charged surface of the catalyst. Hereafter, the experiments of the removal of dyes in aqueous solution were preceded for about 120.0 min under UV light irradiation. During 50.0~140.0 minutes, only the adsorption procedures of MB and CR dyes onto the yeast-carbon continuously occurred in the yeast-carbon suspension in Figure 6(b). In the presence of the TiO_2 @yeast-carbon catalysts, the adsorption and photocatalysis occurred

simultaneously in Figure 6(c). Thus, the degradation rate of the dye in the TiO_2 @yeast-carbon catalyst suspension was significantly higher than that in the yeast-carbon suspension. After 140.0 minutes, the adsorption of dyes onto the yeast-carbon tended to reach the adsorption equilibrium. However, the photocatalytic reactions under UV irradiation still proceeded constantly by TiO_2 @yeast-carbon catalysts. Finally, approximately 87.0% degradation rate of MB was achieved, whereas only around 30.0% CR was removed from the suspension. The distinct disparity of degradation rate between MB and CR dye aqueous solution can be attributed to their own adsorption performance onto the TiO_2 @yeast-carbon catalyst.

The adsorption constant for MB and CR was listed in Table 1. From the results in Table 1, the maximum adsorption amount of the hybrid TiO_2 @yeast-carbon catalysts for cationic MB was significantly higher than that for anionic CR. In addition, the Langmuir model for MB and CR yields a somewhat better fit than the Freundlich model. The value of $1/n$ is equal to 0.94 (MB) and (0.13), respectively, which indicates that the adsorption may belong to the favorable adsorption [41]. This prior adsorption of MB than CR dyes on the surface of the TiO_2 @yeast-carbon microspheres may be assigned to the negatively charged properties of composite catalyst. The discriminatory adsorption for the MB and CR dyes by the TiO_2 @yeast-carbon composite catalyst inevitably leads to the disparity of above-mentioned photocatalytic degradation rate. Therefore, the adsorption behavior on the surface of the TiO_2 @yeast-carbon microspheres has a direct impact on the photocatalytic degradation of the MB and CR dyes.

4. Conclusions

In summary, we prepared hybrid raspberry-like TiO_2 @yeast-carbon utilizing pyrolysis method. The as-synthesized hybrid TiO_2 @yeast-carbon had ordered elliptic shapes of uniform size (length = $3.7 \pm 0.3 \mu\text{m}$; width = $2.5 \pm 0.5 \mu\text{m}$). The potential applications of these novel composites for the removal of contaminants were ascertained for the removal of MB and CR. The results showed that the hybrid composites

exhibited excellent photocatalytic activity for the MB due to its enhanced adsorption ability. The novel TiO₂@yeast-carbon hybrid microspheres have potential applications not only in polluted water treatment but also in other areas such as sensors devices and dye sensitized solar cells.

Acknowledgments

This work was financially supported by China Postdoctoral Science Special Foundation, Scientific Research Foundation for the Returned Overseas Chinese Scholars, the National Natural Science Foundation of China (no. 21176031), Shaanxi Provincial Natural Science Foundation of China (no. 2011JM2011), and Fundamental Research Funds for the Central Universities (no. 2013G2291015).

References

- [1] C. L. Wang, J. T. Yan, X. J. Cui, and H. Y. Wang, "Synthesis of raspberry-like monodisperse magnetic hollow hybrid nanospheres by coating polystyrene template with Fe₃O₄@SiO₂ particles," *Journal of Colloid and Interface Science*, vol. 354, no. 1, pp. 94–99, 2011.
- [2] M. D'Acunzi, L. Mammen, M. Singh et al., "Superhydrophobic surfaces by hybrid raspberry-like particles," *Faraday Discussions*, vol. 146, pp. 35–48, 2010.
- [3] M. Agrawal, A. Pich, N. E. Zafeiropoulos et al., "Polystyrene-ZnO composite particles with controlled morphology," *Chemistry of Materials*, vol. 19, no. 7, pp. 1845–1852, 2007.
- [4] X. W. Zhang, M. H. Zhou, and L. C. Lei, "Enhancing the concentration of TiO₂ photocatalyst on the external surface of activated carbon by MOCVD," *Materials Research Bulletin*, vol. 40, no. 11, pp. 1899–1904, 2005.
- [5] A. H. El-Sheikh, A. P. Newman, H. Al-Daffaee, S. Phull, N. Cresswell, and S. York, "Deposition of anatase on the surface of activated carbon," *Surface and Coatings Technology*, vol. 187, no. 2-3, pp. 284–292, 2004.
- [6] Y. J. Li, X. D. Li, J. W. Li, and J. Yin, "Photocatalytic degradation of methyl orange by TiO₂-coated activated carbon and kinetic study," *Water Research*, vol. 40, no. 6, pp. 1119–1126, 2006.
- [7] J. Pouilleau, D. Devilliers, F. Garrido, S. Durand-Vidal, and E. Mahé, "Structure and composition of passive titanium oxide films," *Materials Science and Engineering B*, vol. 47, no. 3, pp. 235–243, 1997.
- [8] S. Karuppuchamy, K. Nonomura, T. Yoshida, T. Sugiura, and H. Minoura, "Cathodic electrodeposition of oxide semiconductor thin films and their application to dye-sensitized solar cells," *Solid State Ionics*, vol. 151, no. 1–4, pp. 19–27, 2002.
- [9] F.-D. Duminica, F. Maury, and F. Senocq, "Atmospheric pressure MOCVD of TiO₂ thin films using various reactive gas mixtures," *Surface and Coatings Technology*, vol. 188–189, no. 1–3, pp. 255–259, 2004.
- [10] C.-S. Kuo, Y.-H. Tseng, C.-H. Huang, and Y.-Y. Li, "Carbon-containing nano-titania prepared by chemical vapor deposition and its visible-light-responsive photocatalytic activity," *Journal of Molecular Catalysis A*, vol. 270, no. 1-2, pp. 93–100, 2007.
- [11] B.-Y. Jia, L.-Y. Duan, C.-L. Ma, and C.-M. Wang, "Characterization of TiO₂ loaded on activated carbon fibers and its photocatalytic reactivity," *Chinese Journal of Chemistry*, vol. 25, no. 4, pp. 553–557, 2007.
- [12] G. J. Hu, X. F. Meng, X. Y. Feng, Y. F. Ding, S. M. Zhang, and M. S. Yang, "Anatase TiO₂ nanoparticles/carbon nanotubes nanofibers: preparation, characterization and photocatalytic properties," *Journal of Materials Science*, vol. 42, no. 17, pp. 7162–7170, 2007.
- [13] J.-H. Liu, R. Yang, and S.-M. Li, "Preparation and application of efficient TiO₂/ACFs photocatalyst," *Journal of Environmental Sciences*, vol. 18, no. 5, pp. 979–982, 2006.
- [14] N. Areerachakul, S. Vigneswaran, H. H. Ngo, and J. Kandasamy, "Granular activated carbon (GAC) adsorption-photocatalysis hybrid system in the removal of herbicide from water," *Separation and Purification Technology*, vol. 55, no. 2, pp. 206–211, 2007.
- [15] M.-L. Chen, C.-S. Lim, and W.-C. Oh, "Preparation with different mixing ratios of anatase to activated carbon and their photocatalytic performance," *Journal of Ceramic Processing Research*, vol. 8, no. 2, pp. 119–124, 2007.
- [16] A. K. Subramani, K. Byrappa, S. Ananda, K. M. Lokanatha Rai, C. Ranganathaiah, and M. Yoshimura, "Photocatalytic degradation of indigo carmine dye using TiO₂ impregnated activated carbon," *Bulletin of Materials Science*, vol. 30, no. 1, pp. 37–41, 2007.
- [17] J. M. Dona, C. Garriga, J. Arana et al., "The effect of dosage on the photo-catalytic degradation of organic pollutants," *Research on Chemical Intermediates*, vol. 33, pp. 351–358, 2007.
- [18] G. Li Puma, A. Bono, and J. G. Collin, "Preparation of titanium dioxide photocatalyst loaded onto activated carbon support using chemical vapor deposition: a review paper," *Journal of Hazardous Materials*, vol. 157, no. 2-3, pp. 209–219, 2008.
- [19] R. Nacco and E. Aquarone, "Preparation of active carbon from yeast," *Carbon*, vol. 16, no. 1, pp. 31–34, 1978.
- [20] Z. G. Guan, L. Liu, L. L. He, and S. Yang, "Amphiphilic hollow carbonaceous microspheres for the sorption of phenol from water," *Journal of Hazardous Materials*, vol. 196, pp. 270–277, 2011.
- [21] M. Chen, S. X. Zhou, B. You, and L. M. Wu, "A novel preparation method of raspberry-like PMMA/SiO₂ hybrid microspheres," *Macromolecules*, vol. 38, no. 15, pp. 6411–6417, 2005.
- [22] W.-C. Oh, J.-G. Kim, H. Kim et al., "Synthesis of spherical carbons containing titania and their physicochemical and photochemical properties," *Journal of the Korean Ceramic Society*, vol. 48, no. 1, pp. 6–13, 2011.
- [23] W. Z. Shen, Y. He, S. C. Zhang, J. F. Li, and W. B. Fan, "Yeast-based micro-porous carbon materials for carbon dioxide capture," *ChemSusChem*, vol. 5, pp. 1274–1279, 2012.
- [24] A. Pottier, S. Cassaignon, C. Chanéac, F. Villain, E. Tronc, and J.-P. Jolivet, "Size tailoring of TiO₂ anatase nanoparticles in aqueous medium and synthesis of nanocomposites. Characterization by Raman spectroscopy," *Journal of Materials Chemistry*, vol. 13, no. 4, pp. 877–882, 2003.
- [25] H. Zhang and J. F. Banfield, "Understanding polymorphic phase transformation behavior during growth of nanocrystalline aggregates: insights from TiO₂," *Journal of Physical Chemistry B*, vol. 104, no. 15, pp. 3481–3487, 2000.
- [26] M. Sevilla and A. B. Fuertes, "Chemical and structural properties of carbonaceous products obtained by hydrothermal carbonization of saccharides," *Chemistry*, vol. 15, no. 16, pp. 4195–4203, 2009.
- [27] M. B. Wu, "Advance of research in making activated carbon by chemical activation," *Carbon Techniques*, vol. 4, no. 102, pp. 19–23.

- [28] N. Baccile, G. Laurent, F. Babonneau, F. Fayon, M.-M. Titirici, and M. Antonietti, "Structural characterization of hydrothermal carbon spheres by advanced solid-state MAS ^{13}C NMR investigations," *Journal of Physical Chemistry C*, vol. 113, no. 22, pp. 9644–9654, 2009.
- [29] X.-Y. Deng, Z.-L. Cui, F.-L. Du, and C. Peng, "Thermal analysis characterization of nanosized TiO_2 ," *Journal of Inorganic Materials*, vol. 16, no. 6, pp. 1089–1093, 2001.
- [30] R. Gnanasambandam and A. Proctor, "Determination of pectin degree of esterification by diffuse reflectance Fourier transform infrared spectroscopy," *Food Chemistry*, vol. 68, no. 3, pp. 327–332, 2000.
- [31] S. D. Jacobsen, S. Demouchy, D. J. Frost, T. B. Ballaran, and J. Kung, "A systematic study of OH in hydrous wadsleyite from polarized FTIR spectroscopy and single-crystal X-ray diffraction: oxygen sites for hydrogen storage in Earth's interior," *American Mineralogist*, vol. 90, no. 1, pp. 61–70, 2005.
- [32] P. C. Painter, R. W. Snyder, M. Starsinic, M. M. Coleman, D. W. Kuehn, and A. Davis, "Concerning the application of FT-IR to the study of coal: a critical assessment and band assignments and the application of spectral analysis programs," *Applied Spectroscopy*, vol. 35, no. 5, pp. 475–485, 1981.
- [33] W. Jiang, J. Joens, D. D. Dionysiou, and K. E. O'Shea, "Optimization of photocatalytic performance of TiO_2 coated glass microspheres using response surface methodology and the application for degradation of dimethyl phthalate," *Journal of Photochemistry and Photobiology A*, vol. 262, pp. 7–13, 2013.
- [34] Y. F. Zhu, L. I. Zhang, C. Gao, and L. L. Cao, "The synthesis of nanosized TiO_2 powder using a sol-gel method with TiCl_4 as a precursor," *Journal of Materials Science*, vol. 35, no. 16, pp. 4049–4054, 2000.
- [35] Y.-J. Li, Z.-J. Song, Z.-P. Li, Y.-Z. Ouyang, and W.-B. Yan, "Preparation and photocatalytic properties of activated carbon supported TiO_2 nanoparticles with Cu ions doping," *Chemical Journal of Chinese Universities*, vol. 28, no. 9, pp. 1710–1715, 2007.
- [36] B. Bai, N. Quici, Z. Y. Li, and G. L. Puma, "Novel one step fabrication of raspberry-like TiO_2 @yeast hybrid microspheres via electrostatic-interaction-driven self-assembled heterocoagulation for environmental applications," *Chemical Engineering Journal*, vol. 170, no. 2-3, pp. 451–456, 2011.
- [37] Y. Q. Gai, J. B. Li, S.-S. Li, J.-B. Xia, and S.-H. Wei, "Design of narrow-gap TiO_2 : a passivated codoping approach for enhanced photoelectrochemical activity," *Physical Review Letters*, vol. 102, no. 3, Article ID 036402, 4 pages, 2009.
- [38] M. Takeuchi, K. Sakamoto, G. Martra, S. Coluccia, and M. Anpo, "Mechanism of photoinduced superhydrophilicity on the TiO_2 photocatalyst surface," *Journal of Physical Chemistry B*, vol. 109, no. 32, pp. 15422–15428, 2005.
- [39] J. Matos, A. Garcia, T. Cordero, J.-M. Chovelon, and C. Ferronato, "Eco-friendly TiO_2 -AC photocatalyst for the selective photooxidation of 4-chlorophenol," *Catalysis Letters*, vol. 130, no. 3-4, pp. 568–574, 2009.
- [40] Z. B. Zhang, C. C. Wang, R. Zakaria, and J. Y. Ying, "Role of particle size in nano-crystalline TiO_2 -based photo-catalysts," *The Journal of Physical Chemistry B*, vol. 52, pp. 10871–10878, 1998.
- [41] R. J. Umpleby II, S. C. Baxter, Y. Z. Chen, R. N. Shah, and K. D. Shimizu, "Characterization of molecularly imprinted polymers with the Langmuir–Freundlich isotherm," *Analytical Chemistry*, vol. 73, no. 19, pp. 4584–4591, 2001.

Research Article

TiO₂-SiO₂/Ph-POSS Functional Hybrids: Preparation and Characterisation

Magdalena Nowacka, Damian Ambroźewicz, and Teofil Jesionowski

Institute of Chemical Technology and Engineering, Faculty of Chemical Technology, Poznan University of Technology, M. Skłodowskiej-Curie 2, 60965 Poznan, Poland

Correspondence should be addressed to Teofil Jesionowski; teofil.jesionowski@put.poznan.pl

Received 10 July 2013; Revised 20 August 2013; Accepted 20 August 2013

Academic Editor: Mengnan Qu

Copyright © 2013 Magdalena Nowacka et al. This is an open access article distributed under the Creative Commons Attribution License, which permits unrestricted use, distribution, and reproduction in any medium, provided the original work is properly cited.

The results of studies involving the innovative TiO₂-SiO₂/Ph-POSS hybrid were presented. An inorganic TiO₂-SiO₂ oxide composite was precipitated from an emulsion media. The functionalisation of surface for the obtained composite was carried out with the use of TriSilanolPhenyl POSS (Ph-POSS) and a silane coupling agent—phenyltrimethoxysilane (PTMS). Electrokinetic and physicochemical as well as structural characteristics of obtained hybrids were evaluated. The zeta potential value has been determined, which provides relevant information regarding the interactions between colloid particles. Measurement of the zeta potential values allowed for an indirect assessment of stability for the studied hybrid fillers. In the next step, the degree of dispersion and surface morphology were evaluated based on the obtained particle size distribution curves and TEM images. The hydrophilic-hydrophobic character of the surface was assessed by analysing the wettability profiles. The modification degree of the TiO₂-SiO₂ oxide composite was evaluated based on the infrared spectroscopy studies (FT-IR). Determination of the parameters of the porous structure was conducted by determining the specific surface area and the total volume and mean size of pores. Thermogravimetric measurements (TGA) were also carried out in order to measure the changes in sample mass as a function of temperature.

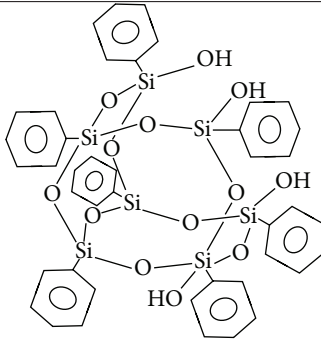
1. Introduction

Since the last decade, scientists work on the new organic-inorganic hybrid materials called silsesquioxanes. Polyhedral oligosilsesquioxanes (POSS) are considered a novel class of compounds with a general formula of (RSiO_{1.5})_n or R_nT_n, where R may stand for hydrogen, alkyl, aryl or other functional organic group. The inorganic skeleton may exhibit a completely condensed, closed, or open structure [1]. POSS is an intermediate product between silica (SiO₂) and silicone (R₂SiO) with a particle size ranging from several to dozens of nanometers, and its properties are determined by its composition and the type of organic substituents [2–4]. The specific structure of this type of compounds contributed to a broad range of applications [5–8].

Polyhedral oligosilsesquioxanes make for a significant base for the synthesis of novel functional materials and nanomaterials. Numerous researchers proved that POSS may

be successfully used for obtaining novel hybrid materials [9]. Since POSS compounds are costly fillers, several attempts have been made to combine them with inorganic oxide composites, such as: TiO₂-SiO₂, MgO-SiO₂, ZnO-SiO₂, or individual oxides for example, SiO₂ and TiO₂ [10–12]. Recently, the number of studies focused on obtaining such novel hybrid materials has considerably increased. Godnjavec et al. has confirmed that Trisilanolphenyl-POSS may be integrated into a poly(methyl methacrylate) chain, which allows for obtaining a composite with excellent properties [1]. In our previously published researches, Ambroźewicz et al. obtained hybrid materials based on magnesium silicate and POSS compounds. The inorganic matrix (MgO-SiO₂) was obtained according to the previously proposed method, described in [13]. The presented method in article [14] results confirmed that such products are thermally stable at the temperature of 600°C, which enables their use as fillers in the plastics industry.

TABLE 1: The POSS used for the surface modification of TiO_2 - SiO_2 oxide composite.

Chemical formula	Name of the POSS	Solvent solubility	Solvent insolubility
	TriSilanolPhenyl POSS (Ph-POSS)	THF, acetone, ethylacetate, toluene	Methanol, ethanol, water, acetonitrile, chloroform

In this study, the TiO_2 - SiO_2 oxide composite was selected as an inorganic carrier to be used in the process of obtaining hybrid filler due to its unique physicochemical properties. Such composites are often employed as efficient catalysts and photocatalyst which participate in various chemical reactions, such as the polycondensation of ethyl polyterephthalene, hydration of carbon oxide as well as selective oxidation in the liquid phase by organic peroxides. Additionally, these compounds serve as photocatalysts during the neutralisation of textile wastewater and production of nitriles, nylon, plastics and synthetic rubber [15–17].

In order to increase the possibility to use this type of oxide materials, the synthetic silicates are frequently subjected to surface modification with silane proadhesive compounds. Such surface functionalisation allows for the introduction of functional groups, which facilitate the bonding with polymers. The mechanism and modification method have been described in numerous scientific reports [18, 19].

When trying to evaluate the application potential of inorganic carrier/POSS hybrid materials (i.e., for the plastics industry), it is also important to determine their zeta potential values. The surface properties are a crucial factor which characterises nanoparticles, since, according to the DLVO theory, the parameters such as surface charge density, spherical interactions, or the Hamaker constant determine the dispersive properties in colloids [20].

The main aim of the presented studies was to obtain novel inorganic/organic hybrid fillers (TiO_2 - SiO_2 /Ph-POSS), which may be successfully used in the constantly developing plastics industry. In the second stage of studies, a detailed characterisation of electrokinetic and physicochemical properties was carried out for the obtained hybrid materials.

2. Experimental Section

2.1. Preparation of the Functionalised TiO_2 - SiO_2 /Ph-POSS Hybrids

2.1.1. Method of Obtaining the TiO_2 - SiO_2 Oxide Composite from an Emulsion Media. The TiO_2 - SiO_2 oxide composites were precipitated in the emulsion system; this type of production was described detailed by Siwinska-Stefanska et al. [21].

2.1.2. The Silane Proadhesive Agent. Phenyltrimethoxysilane (PTMS) produced by Fluka was used in order to introduce functional groups which facilitate the bonding with other active substances on the surface of the TiO_2 - SiO_2 oxide composite. An adequate amount of the substance was first hydrolysed in a methanol : water (4 : 1, v/v) system and then applied on the surface of the silica according to the “dry method”, which is described in detail in [18, 22]. The surface of the oxide composite was modified with 3, 5, and 10 weight parts by mass of the applied silane.

2.1.3. Surface Modification of the Precipitated TiO_2 - SiO_2 Oxide Composite with the Selected Silsesquioxane (Ph-POSS). In the next experimental stage, the precipitated TiO_2 - SiO_2 oxide composite was subjected to the modification with the use of Ph-POSS (purchased in Hybrid Plastics) in order to change its surface properties (see Table 1). TiO_2 - SiO_2 oxide composite was introduced into the reactor, and afterwards the Ph-POSS (in an amount of 3, 5, and 10 parts by mass) was dissolved in 10 cm^3 of toluene was introduced into the reactor. Simultaneously, the dispersion with modifying agent was intensively stirred for 1 h. Upon introducing the Ph-POSS, the solution was transferred into a Büchi Labortechnik AG R—210 rotary evaporator in order to evaporate the organic solvent.

2.2. Electrokinetic, Physicochemical, and Structural Analysis.

The zeta potential values have been determined with the use of the Zetasizer Nano ZS apparatus equipped with an autotitrator, which incorporates a combination of electrophoresis and laser determination of particle mobility based on the Doppler phenomena. The apparatus measures the speed of particle translocation in a liquid upon switching the electric field, which is referred to as electrophoretic mobility. Knowing this value, the zeta potential can be calculated from Henry's equation. The apparatus allows for determining the electrophoretic mobility of particles in the range of 5 nm to 100 μm . The zeta potential was determined in a pH range of 1.5–11, in a 0.001 M NaCl electrolyte. Simultaneously, the changes in the conductivity and pH values of the studied suspension were also studied during the measurement. Prior

to the measurement, the apparatus was calibrated by determining the zeta potential of a latex suspension and measuring the pH of buffer solutions with a pH value of 4 and 9. The analysed dispersions were stabilised in the ultrasonic bath for 15 minutes. In order to avoid potential measurement errors each analysed sample was measured ten times and the general standard deviation was ± 0.01 mV (zeta potential) and ± 0.01 (pH).

The particle size distribution curves of the analysed hybrid fillers were obtained by using a Zetasizer Nano ZS apparatus (Malvern Instruments Ltd.). The equipment allows for a dispersive evaluation of particles with a diameter ranging from 0.6 to 6000 nm. The apparatus employs the NIBS (*non-invasive back scattering*) technique.

Studies focused on assessing the microstructure and morphology of the obtained powder substances were carried out in order to obtain data regarding the morphology of seeds, the structure of a given particle as well as the agglomeration and dispersion characteristics. The JEOL 1200 EX II transmission electron microscope was used during these studies.

Analysis of composition and the degree of modification was based on FT-IR spectra obtained with the use of the EQUINOX 55 spectrophotometer (Bruker). The analysed materials were studied as KBr tablets.

The wettability profiles in aqueous systems were determined with the use of the K100 tensiometer with a specialised software from Krüss in order to evaluate the hydrophilic-hydrophobic character of the powder surface. These measurements were carried at an equal time interval (10 minutes) for a constant sample mass (0.4 g).

The parameters of porous structure of the obtained hybrid fillers were carried out with the use of the ASAP 2020 apparatus (Micromeritics Instrument Co.). In order to do this, the parameters such as the specific surface area as well as the volume and mean the pore size were determined. Prior to the measurement, the samples were degassed at the temperature of approx. 120°C for 4 h. The specific surface area was determined with the use of a multipoint BET (Brunauer-Emmett-Teller) equation. In order to assess the pore volume and the mean pore diameter value, a BJH (Barrett-Joyner-Halenda) algorithm was employed. Measurement of the parameters of porous structure of the samples analysed was performed based on the low-temperature nitrogen adsorption.

The thermal analysis of the obtained fillers was carried out with the use of Jupiter 449 TG/DTA/DSC apparatus (Netzsch). The mass of the sample was approx. 10 mg. The sample was heated at 10°C/min (in the temperature range of 30–600°C). The analyses were carried out in the atmosphere of nitrogen, with a flow rate of 10 cm³/min.

3. Results and Discussion

3.1. Zeta Potential of TiO₂-SiO₂/Ph-POSS, TiO₂-SiO₂/PTMS, and TiO₂-SiO₂/PTMS/Ph-POSS Hybrids. Nanoparticles in dispersive systems exhibit a notable tendency to agglomerate, however this process may be successfully controlled by measuring the zeta potential (which allows for determining the value of electrostatic interactions between colloid particles

dispersed in aqueous solutions) and analysing the particle size distribution curves [23–25].

In the first experimental stage, the values of the zeta potential for the unmodified TiO₂-SiO₂ oxide filler and the silsesquioxane (Ph-POSS) selected for subsequent surface modification were carried out (see Figure 1(a)). Next, the zeta potential values for the functionalised TiO₂-SiO₂/Ph-POSS hybrid fillers were measured, and the obtained results were presented in Figure 1(b). The measurement of the zeta potential values allows for determining the isoelectric point (i.e.p.), which is a crucial parameter for characterising solids dispersed in liquids. By knowing the i.e.p. value, the surface charge type can be recognised, that is, metal oxides exhibit a positive surface charge value in a pH range < p*H*_{i.e.p.} and a negative value in a pH range > p*H*_{i.e.p.}. This knowledge helps to understand the occurring coagulation and adhesion phenomena. Overall, the charge on the surface of metal oxides is influenced mainly by the pH and the ionic force of the solution. However, the charge and the overall course of the electrokinetic curve should not change as a result of changes in the electrolytes concentration [26]. The differences in acid-base properties of TiO₂-SiO₂ oxide composites and their modified forms have a profound impact on the obtained zeta potential values [27]. Upon analysing the course of the electrokinetic curve for the unmodified TiO₂-SiO₂ oxide composite it can be established that its zeta potential is decreasing with increasing the pH values, which confirms that the zeta potential value strongly depends on the pH value. The influence of the zeta potential on the distribution of the surface charge on oxide composites was presented detailed in previously published paper [13].

In our previously published studies [27], we reported that the zeta potential of unmodified TiO₂-SiO₂ oxide composites reaches the value of the isoelectric point at a pH value of approx. 4.9 and exhibits zeta potential values from 30 to –30 mV in the whole studied pH range (1.7–11). The TiO₂-SiO₂ oxide composite presented in the framework of this study is characterised by an isoelectric point at the pH value of 4.9 and reaches zeta potential values from 8 to –48 mV in the studied pH range. Marginal differences in the electrokinetic properties of the studied inorganic filler are a result of the proposed synthesis method and the percent composition of a given oxide. Lower i.e.p. value of the studied synthetic oxide composite is most likely caused by a higher percent composition of silica, which is characterised by an isoelectric point at a pH value of 2. The value of the point zero charge (PZC) and the isoelectric point for TiO₂ and SiO₂ has been an object of numerous studies and described in detail in several literature reports [28, 29].

The course of the electrokinetic curve for the analysed POSS compounds is similar to that obtained for SiO₂ [20]. Ph-POSS does not exhibit an i.e.p. value, however, the course of the curve suggests a tendency to reach i.e.p. at a pH value of approximately 1.0.

Upon analysing the results shown in Figure 1(b) it can be established, that the functionalisation of the TiO₂-SiO₂ oxide composites surface with the selected silsesquioxane does not decrease the electrokinetic stability of the studied

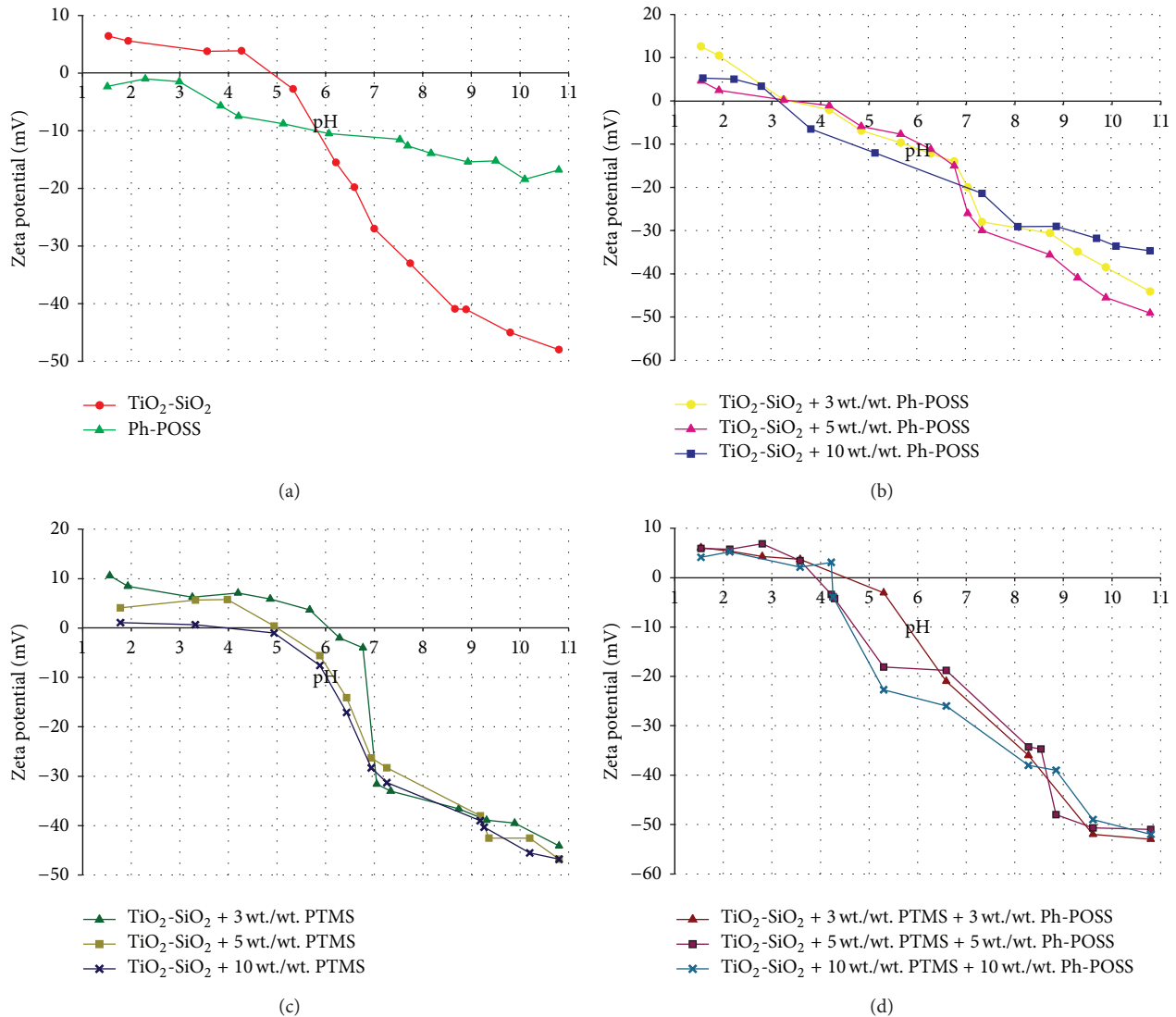


FIGURE 1: Zeta potential values as a function of pH for the (a) unmodified $\text{TiO}_2\text{-SiO}_2$ oxide composite and the analysed silsesquioxane (Ph-POSS). Then, (b) for the inorganic composite modified with Ph-POSS, (c) PTMS, and (d) additionally functionalised with Ph-POSS.

oxide systems in the whole range of the studied pH and that the course of electrokinetic curves as well as the change of the obtained isoelectric point values confirms the effectiveness of the employed surface functionalisation method.

The electrokinetic curves obtained for the oxide composite modified with various amounts of the selected silane (PTMS) were shown in Figure 1(c). The obtained results were compared with the electrokinetic potential of the unmodified carrier. The surface functionalisation of the $\text{TiO}_2\text{-SiO}_2$ oxide composite with the use of PTMS silane (see Figure 1(c)) did not contribute to any notable changes in the electrokinetic stability compared to the base oxide composite. The modified hybrid fillers are characterised by a zeta potential value ranging from 5 to -50 mV, and their stability is high in the pH values from 6 to 11.

In the next experimental stage, the zeta potential values for the oxide composite modified with the use of the

selected silanes and further functionalised with the use of the silsesquioxane (Ph-POSS) were measured. The obtained results were presented in Figure 1(d). The proposed method of bifunctionalisation of the composite surface did not notably change the obtained zeta potential values.

3.2. Particle Size Distributions and Surface Morphology and Microstructure Analysis. In the next experimental stage the dispersive and morphological characteristics of the studied hybrid fillers were analysed. The particle size distribution curve in relation to the volume percent for the base inorganic filler (see Figure 2(a)) shows a single band in the range of 164–531 nm. The maximum volume percent (26.4%) was observed for particles with a diameter of 295 nm. The results obtained for the composite upon surface modification with 10 weight parts by mass of Ph-POSS led to a single broad band in

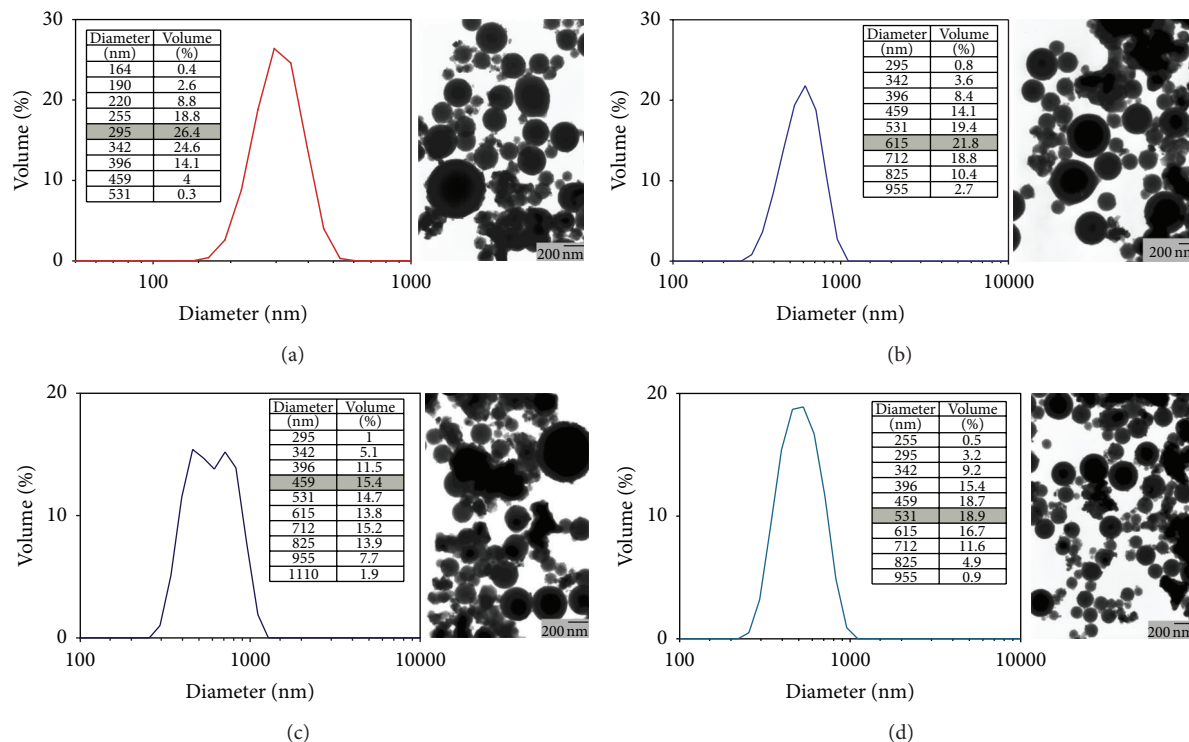


FIGURE 2: Particle size distribution curves and TEM images for (a) the unmodified $\text{TiO}_2\text{-SiO}_2$ oxide composite, (b) the composite modified with 10 weight parts by mass of Ph-POSS, (c) PTMS, and (d) the $\text{TiO}_2\text{-SiO}_2$ oxide composite bifunctionalised with 10 weight parts by mass of PTMS and Ph-POSS.

the range of 295–955 nm, with a maximum volume percent (21.8%) for particles with a diameter of 615 nm (Figure 2(b)).

Studies focused on assessing the microstructure and morphology of the obtained powder substances were carried out in order to obtain data regarding the morphology of seeds, the structure of a given particle as well as the agglomeration and dispersion characteristics. The presented TEM images of the analysed oxide systems (both for the unmodified composite and after modification with the POSS compound) show that the particles are characterised by a regular, spherical shape with a marginal tendency to form agglomerated structures. Upon analysing the TEM pictures, the Ph-POSS bonded to the surface of the inorganic carrier can also be observed. The particle size distribution curves and TEM images for the $\text{TiO}_2\text{-SiO}_2$ synthetic composite modified with 10 weight parts by mass of PTMS were shown in Figure 2(c).

In the case of the particle size distribution curve in relation to the volume percent obtained for the oxide composite upon modification with 10 weight parts by mass of PTMS, a band in the range of 295–1110 nm can be observed. The maximum volume percent (15.4%) can be attributed to particles with a diameter of 459 nm. The obtained TEM images confirm that the particles had a spherical shape. A detailed procedure for the modification of the $\text{TiO}_2\text{-SiO}_2$ oxide composite with silane proadhesive agents has been described in a previous publication [30].

In the next step, the morphological characteristics of the oxide composite modified with the PTMS silane and

additionally functionalised with the selected silsesquioxanes (Ph-POSS) have been carried out, and the obtained results were shown in Figure 2(d).

In the case of sample modified with 10 weight parts by mass of the PTMS and the POSS compound, a single band ranging from 255 to 955 nm could be observed. The maximum volume percent (18.9%) could be attributed to particles with a diameter of 531 nm. The TEM image showed that these particles were of regular spherical shape and a marginal tendency to form agglomeration structures.

3.3. Water Wettability Profiles. Analysis of the water wettability profiles for the synthetic $\text{TiO}_2\text{-SiO}_2$ composite modified with a POSS compound showed that the studied samples exhibit a lower mass increase in time compared to unmodified samples (see Figure 3(a)).

The lowest mass increase was observed for samples modified with 10 weight parts by mass of Ph-POSS, which confirms that, with the increase of the surface functionalised with Ph-POSS, the hydrophobicity of the analysed oxide system is increased.

Analysing the water wettability profiles of samples modified with silane proadhesive agents and subsequently functionalised with the POSS compound (see Figure 3(c)), it can be observed that the lowest mass increase in time occurred for samples modified with 10 weight parts by mass of PTMS and Ph-POSS. This suggests that the increase of hydrophobic

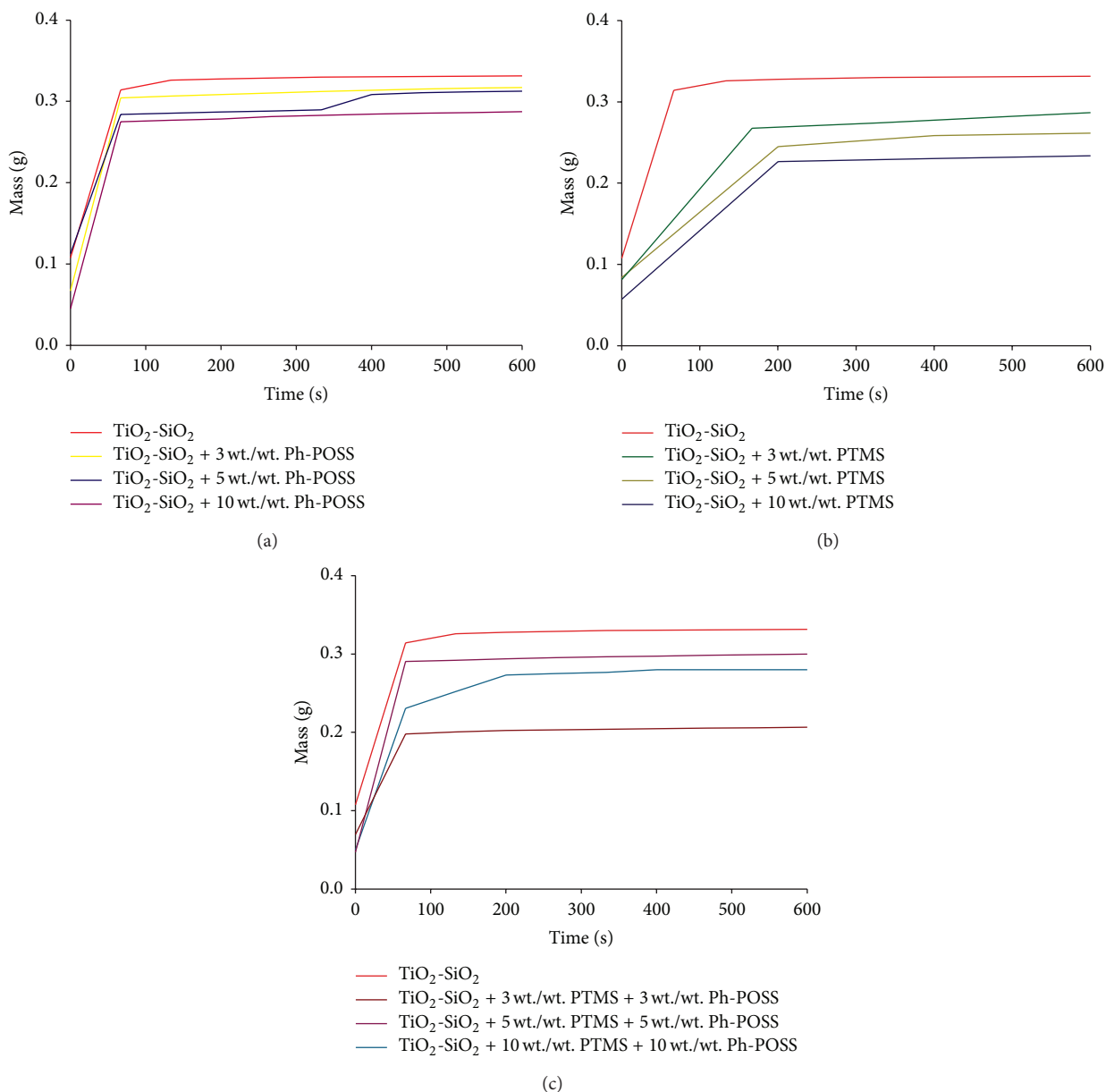


FIGURE 3: Water wettability profiles (a) for the unmodified TiO₂-SiO₂ oxide composite and (b) composite modified with PTMS and (c) for the composite bifunctionalised with PTMS and Ph-POSS.

properties in comparison to the unmodified composite was greatest in this case.

3.4. FT-IR Evaluations. The spectroscopic studies were carried out in order to evaluate the efficiency of the modification process (appearance of characteristic functional groups) for the selected samples of unmodified and modified TiO₂-SiO₂ composite. The obtained spectra were shown in Figure 4.

The carried out FT-IR analysis proved that the modification of the base sample with the use of Ph-POSS leads to a decrease of intensity for the -OH band with a wavenumber of approx. 3620 cm⁻¹ which is proportional to the amount of the POSS compound used for the modification of the

carriers surface. The broad band between 500 and 800 cm⁻¹ is associated with the Ti-O-Ti group. The bands corresponding to the silsesquioxane “cages” can be observed at approx. 1118 cm⁻¹. Other visible bands include CH₂ (2927 cm⁻¹) and CH₃ (2954 and 2871 cm⁻¹) groups [31].

The FT-IR spectra for the unmodified TiO₂-SiO₂ oxide composite and the modified 10 parts by mass were shown in Figure 4(a); sample unmodified and bifunctionalised were shown in Figure 4(b). The presented spectra confirm the efficiency of the surface functionalisation process for the analysed oxide composite.

The Si-OH absorption bands of silicate matrix are shown at 3750 cm⁻¹ as well as width bands related in the range of

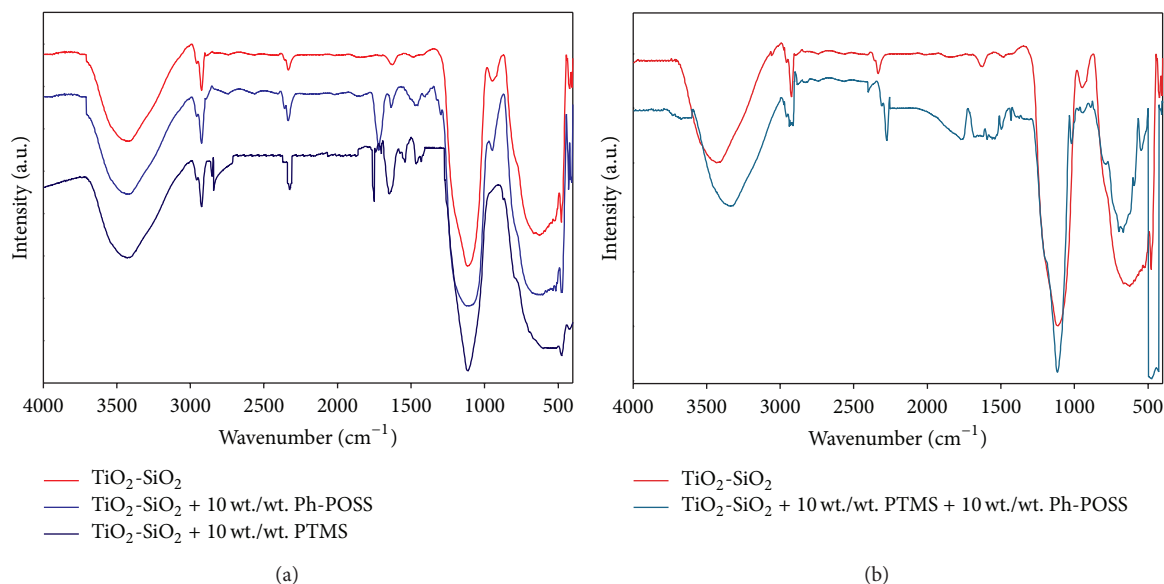


FIGURE 4: FT-IR spectra obtained (a) for the unmodified $\text{TiO}_2\text{-SiO}_2$ oxide composite and composite modified with Ph-POSS and PTMS, (b) for the composite bifunctionalised with PTMS and Ph-POSS.

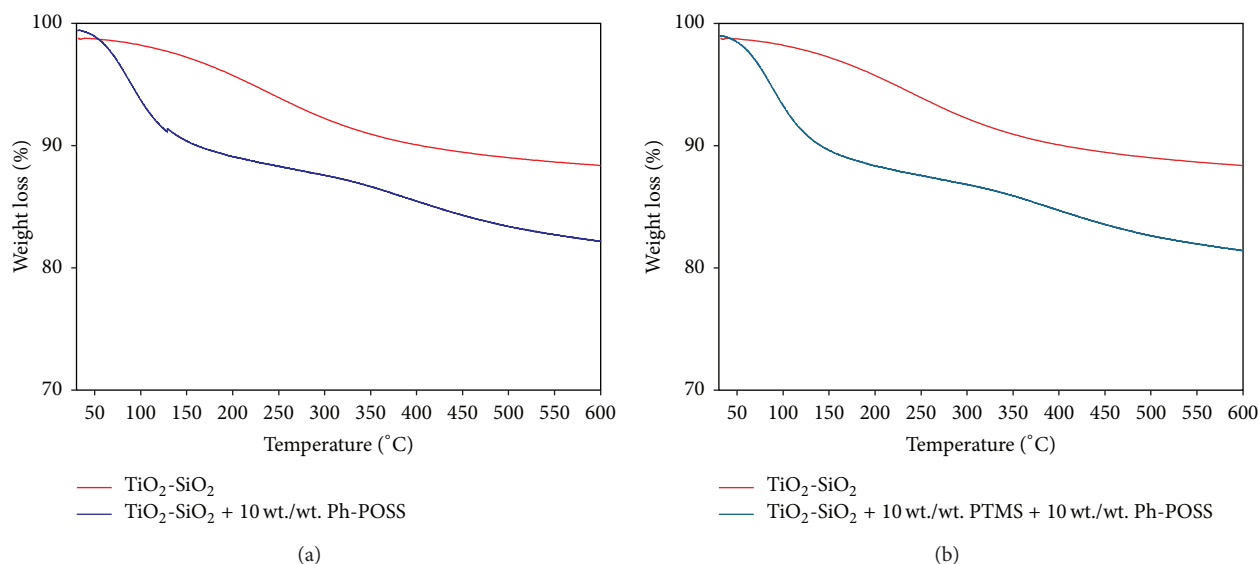
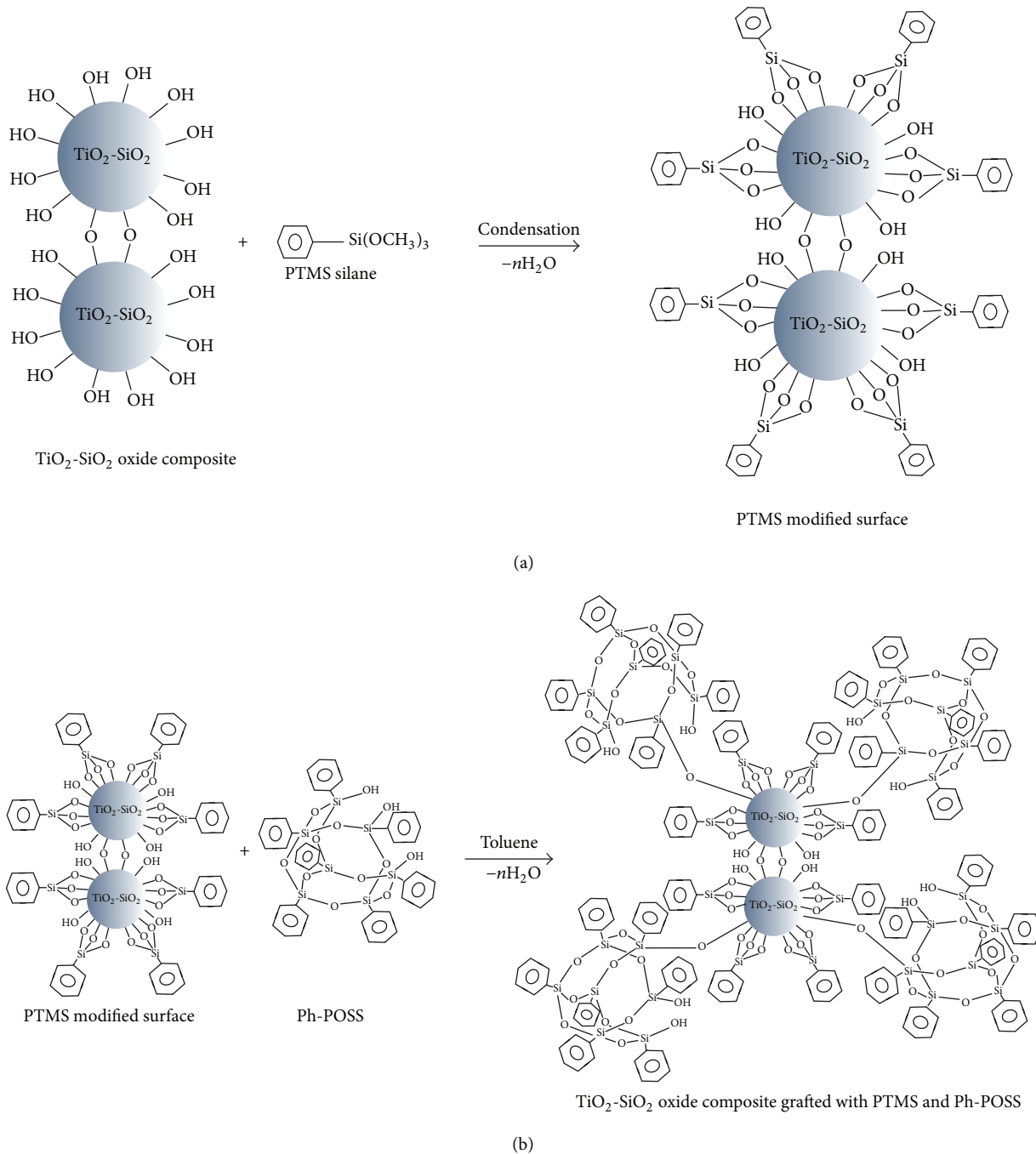


FIGURE 5: TGA curves obtained (a) for the unmodified $\text{TiO}_2\text{-SiO}_2$ oxide composite and composite modified with Ph-POSS and (b) composite bifunctionalised with 10 weight parts by mass of PTMS and Ph-POSS.

$3500\text{--}3000\text{ cm}^{-1}$ with physically adsorbed water has been noted. The band at 1106 cm^{-1} can be associated with the stretching vibration of Si-O-Si groups. A visible band corresponding to Ti-O-Si groups is also visible at 970 and 1400 cm^{-1} . The band at 1106 cm^{-1} can be associated with the stretching vibration of Si-O-Si groups. For the sample modified with PTMS, we can observe the peaks at 3044 cm^{-1} (CH stretching vibrations) and 1580 , 1554 , and 1542 cm^{-1} (C=C vibrational stretching of phenyl groups). Two distinct changes can be observed in the FT-IR spectra of POSS silanol (TriSilanolPhenyl POSS). The absorption peaks of the Si-OH

groups at $3750\text{--}3000\text{ cm}^{-1}$ as well as the wide band at $3500\text{--}3000\text{ cm}^{-1}$ decrease in intensity obviously. This suggests that the condensation reaction of the Si-OH group between POSS silanols and hydroxyl-terminated on silicate surface has taken place. Another distinct change is the peak intensity between 1000 and 1300 cm^{-1} . The intensity of the Si-O-Si absorption band increases with the incorporation of POSS silanol. A visible band corresponding to Ti-O-Si groups is also visible at 970 and 1400 cm^{-1} . A band of the trisilanol-silsesquioxane cage appeared at 1118 cm^{-1} and was accompanied by CH_2 (2927 cm^{-1}) and CH_3 (2954 and 2871 cm^{-1}) stretching and



SCHEME 1: Mechanism of PTMS silane modification (a) and Ph-POSS grafting of $\text{TiO}_2\text{-SiO}_2$ oxide composite (b).

corresponding deformational modes (1461 , 1350 , 1230 , and 839 cm^{-1}). Band corresponding to CH_3 at 2950 and 1230 cm^{-1} indicates the occupation of the free sites on the surface.

In Scheme 1, proposed mechanism of PTMS modification and grafting with Ph-POSS of $\text{TiO}_2\text{-SiO}_2$ oxide composite is presented.

3.5. Structural Properties. In the next experimental stage, the parameters of the porous structure of the unmodified and

modified $\text{TiO}_2\text{-SiO}_2$ oxide composite have been determined, and the obtained results were shown in Table 2.

The value of specific surface area of the unmodified $\text{TiO}_2\text{-SiO}_2$ composite sample was at $24.8\text{ m}^2/\text{g}$, while the pore volume was at $0.040\text{ cm}^3/\text{g}$. The average pore diameter value was 5.9 nm . Subjecting the $\text{TiO}_2\text{-SiO}_2$ oxide composite to modification with the selected silsesquioxane contributed to a notable decrease of the basic adsorptive parameters. Upon modification with 10 weight parts by mass of Ph-POSS, the studied oxide composite reached a specific surface area value

TABLE 2: Parameters of porous structure of both unmodified and modified TiO₂-SiO₂ oxide composite.

Sample	A_{BET} (m ² /g)	V_p (cm ³ /g)	S_p (nm)
TiO ₂ -SiO ₂	24.8	0.040	5.9
TiO ₂ -SiO ₂ + 10 weight parts by mass of Ph-POSS	7.0	0.030	17.1
TiO ₂ -SiO ₂ + 10 weight parts by mass of PTMS	6.6	0.020	12.6
TiO ₂ -SiO ₂ + 10 weight parts by mass of PTMS + 10 weight parts by mass of Ph-POSS	3.3	0.008	10.4

of 7.0 m²/g and a pore volume of 0.030 cm³/g. The average pore diameter value for the oxide composite modified with 10 weight parts by mass of Ph-POSS was 17.1 nm.

Measuring the specific surface area showed that the changes occurring on the surface of the TiO₂-SiO₂ oxide composite subjected to the functionalisation process with POSS type compounds are very notable. Due to this process the active centers on the surface of the composite are blocked.

In the next experimental stage, the obtained functionalised TiO₂-SiO₂/PTMS/POSS hybrid fillers were subjected to an analysis of their structural properties. The obtained results suggest that the use of silanes (PTMS) for functionalisation of the oxide composite surface contributes to a decrease of the BET specific surface area. This effect is a result of blocking active centres present on the surface of the composite. Due to subsequent modification of the functionalised composite with POSS compounds, a further decrease of the specific surface area was observed. The obtained results may also be used for an indirect confirmation of the proposed modification methods efficiency.

3.5.1. Thermogravimetric Analysis. Thermal analysis is an important method which enables the determination of the thermal durability or lifetime for the studied materials and allows for evaluating the thermodynamic and kinetic parameters of the reaction. Due to this fact, the thermal analyses are frequently employed in several branches of science and industry. In the framework of the presented studies the TGA technique was used, which allows for registering the changes in sample mass as a function of temperature.

The thermogravimetric curves obtained for the unmodified TiO₂-SiO₂ oxide composite and the composite modified with 10 weight parts by mass of Ph-POSS were shown in Figure 5(a). The total decrease of mass for the analysed samples changes with the increase in temperature. The highest decrease of mass for the TiO₂-SiO₂/Ph-POSS hybrid filler was observed at 150°C. On the other hand, the highest decrease of mass for the unmodified oxide composite was observed at approx. 300°C [32].

The thermogravimetric curves obtained for the unmodified TiO₂-SiO₂ oxide composite and the composite modified with 10 weight parts by mass of PTMS and Ph-POSS were shown in Figures 5(a) and 5(b). It was observed that up to the temperature of 150°C, the physically and chemically bound

water is removed from the sample, while for samples modified at 300°C, the degradation of groups from the open cage occurs. Since the cages consist of 8 silica atoms, they are more thermally stable compared to POSS with open cages, which tend to bond more easily but are less thermally resistant.

4. Conclusions

In the framework of the presented studies, the efficiency of the proposed surface modification method for TiO₂-SiO₂ oxide composites with POSS compounds and bifunctionalisation of surface with POSS and selected silane proadhesive agents has been presented and confirmed by the results of FT-IR and TGA analyses.

Based on the obtained results, it was established that bifunctionalisation leads to the deterioration of dispersive-morphological properties compared to samples modified with the use of silsesquioxanes only. The samples obtained upon modification with silanes and subsequent modification with POSS exhibit a higher tendency to form agglomeration structures, which is why the disappearance of nanometric particles can be observed. This fact becomes especially visible with increasing amounts of the silane used for modification. The electrokinetic studies have shown that the samples modified with POSS only exhibit better stability. Modification of the TiO₂-SiO₂ oxide composite with the mentioned silsesquioxane improves its hydrophobic properties, as confirmed by the water wettability studies. It was established that the bifunctionalisation with PTMS and POSS leads to a marginal increase of the hydrophobic properties for the analysed hybrid fillers.

To summarize, from the point of future applications of this type of functionalised hybrids, better electrokinetic and physicochemical properties were exhibited by oxide composites modified only with POSS-type compounds. Based on the obtained results, it can be established that the proposed TiO₂-SiO₂/Ph-POSS hybrids may be successfully applied in the constantly developing plastics industry and others applications.

Conflict of Interests

The authors declare no conflict of interests in respect of their submitted paper.

Authors' Contribution

The authors equally contributed in this paper.

Acknowledgments

This work was supported by the Polish National Centre of Science (Research Grant no. 2011/01/B/ST/03961).

References

- [1] J. Godnjavec, B. Znoj, N. Veronovski, and P. Venturini, "Polyhedral oligomeric silsesquioxanes as titanium dioxide surface

- modifiers for transparent acrylic UV blocking hybrid coating,” *Progress in Organic Coatings*, vol. 74, no. 4, pp. 654–659, 2011.
- [2] I. Blanco, L. Abate, F. A. Bottino, and P. Bottino, “Thermal degradation of hepta cyclopentyl, mono phenyl-polyhedral oligomeric silsesquioxane (hcp-POSS)/polystyrene (PS) nanocomposites,” *Polymer Degradation and Stability*, vol. 97, no. 6, pp. 849–855, 2012.
- [3] M. Hoyos, A. Fina, F. Carniato, M. Prato, and O. Monticelli, “Novel hybrid systems based on poly(propylene-g-maleic anhydride) and Ti-POSS by direct reactive blending,” *Polymer Degradation and Stability*, vol. 96, no. 10, pp. 1793–1798, 2011.
- [4] W. Du, J. Shan, Y. Wu, R. Xu, and D. Yu, “Preparation and characterization of polybenzoxazine/trisilanol polyhedral oligomeric silsesquioxanes composites,” *Materials and Design*, vol. 31, no. 4, pp. 1720–1725, 2010.
- [5] A. Fina, D. Tabuani, and G. Camino, “Polypropylene-polysilsesquioxane blends,” *European Polymer Journal*, vol. 46, no. 1, pp. 14–23, 2010.
- [6] X. Z. Zhang, Y. J. Song, and Y. D. Huang, “Properties of silsesquioxane coating modified carbon fibre/polyarylacetylene composites,” *Composites Science and Technology*, vol. 67, no. 14, pp. 3014–3022, 2007.
- [7] C. Jin, S. List, S. Yamanaka et al., “Deposition and characterization of porous silica xerogel films,” in *Proceedings of the MRS Fall Meeting*, vol. 443, pp. 99–104, December 1996.
- [8] H. Fong, S. H. Dickens, and G. M. Flaim, “Evaluation of dental restorative composites containing polyhedral oligomeric silsesquioxane methacrylate,” *Dental Materials*, vol. 21, no. 6, pp. 520–529, 2005.
- [9] L. Barral, F. J. Díez, S. García-Garabal et al., “Thermodegradation kinetics of a hybrid inorganic-organic epoxy system,” *European Polymer Journal*, vol. 41, no. 7, pp. 1662–1666, 2005.
- [10] F. Carniato, C. Bisio, L. Sordelli, E. Gavrilova, and M. Guidotti, “Ti-POSS covalently immobilized onto mesoporous silica: a model for active sites in heterogeneous catalytic epoxidation,” *Inorganica Chimica Acta*, vol. 380, no. 1, pp. 244–251, 2012.
- [11] X. Chen, D. Wang, X. Li, Y. Liu, and L. Hu, “POSS/TiO₂ nanohybrids as sun protection factors for skin changes caused by ultraviolet a radiation,” *Materials Science Forum*, vol. 610, pp. 1039–1043, 2009.
- [12] P. A. Wheeler, R. Misra, R. D. Cook, and S. E. Morgan, “Polyhedral oligomeric silsesquioxane trisilanols as dispersants for titanium oxide nanopowder,” *Journal of Applied Polymer Science*, vol. 108, no. 4, pp. 2503–2508, 2008.
- [13] F. Ciesielczyk, M. Nowacka, A. Przybylska, and T. Jesionowski, “Dispersive and electrokinetic evaluations of alkoxy silane-modified MgO-SiO₂ oxide composite and pigment hybrids supported on it,” *Colloids and Surfaces A*, vol. 376, no. 1–3, pp. 21–30, 2011.
- [14] D. Ambrozewicz, B. Marciniak, and T. Jesionowski, “New POSS/magnesium silicate nano-hybrids obtained by chemical or mechanical methods,” *Chemical Engineering Journal*, vol. 210, no. 1, pp. 229–236, 2012.
- [15] A. N. Murashkevich, A. S. Lavitskaya, O. A. Alisienok, and I. M. Zharskii, “Fabrication and properties of SiO₂/TiO₂ composites,” *Inorganic Materials*, vol. 45, no. 10, pp. 1146–1152, 2009.
- [16] M. Bellardita, M. Addamo, A. Di Paola et al., “Photocatalytic activity of TiO₂/SiO₂ systems,” *Journal of Hazardous Materials*, vol. 174, no. 1–3, pp. 707–713, 2010.
- [17] A. Nilchi, S. Janitabar-Darzi, A. R. Mahjoub, and S. Rasouli-Garmarodi, “New TiO₂/SiO₂ nanocomposites-phase transformations and photocatalytic studies,” *Colloids and Surfaces A*, vol. 361, no. 1–3, pp. 25–30, 2010.
- [18] T. Jesionowski, F. Ciesielczyk, and A. Krysztafkiwicz, “Influence of selected alkoxy silanes on dispersive properties and surface chemistry of spherical silica precipitated in emulsion media,” *Materials Chemistry and Physics*, vol. 119, no. 1–2, pp. 65–74, 2010.
- [19] M. E. McGovern, K. M. R. Kallury, and M. Thompson, “Role of solvent on the silanization of glass with octadecyltrichlorosilane,” *Langmuir*, vol. 10, no. 10, pp. 3607–3614, 1994.
- [20] C. H. Lee, S. H. Park, W. Chung, J. Y. Kim, and S. H. Kim, “Preparation and characterization of surface modified silica nanoparticles with organo-silane compounds,” *Colloids and Surfaces A*, vol. 384, no. 1–3, pp. 318–322, 2011.
- [21] K. Siwinska-Stefanska, F. Ciesielczyk, A. Kolodziejczak-Radzimska, D. Paukszta, J. Sójka-Ledakowicz, and T. Jesionowski, “TiO₂-SiO₂ inorganic barrier composites: from synthesis to application,” *Pigment and Resin Technology*, vol. 41, no. 3, pp. 139–148, 2012.
- [22] T. Jesionowski and A. Krysztafkiwicz, “Comparison of the techniques used to modify amorphous hydrated silicas,” *Journal of Non-Crystalline Solids*, vol. 277, no. 1, pp. 45–57, 2000.
- [23] E. P. Plueddemann, *Silane Coupling Agents*, Plenum Press, New York, NY, USA, 1982.
- [24] M. Doğan, Y. Turhan, M. Alkan, H. Namli, P. Turan, and Ö. Demirbaş, “Functionalized sepiolite for heavy metal ions adsorption,” *Desalination*, vol. 230, no. 1–3, pp. 248–268, 2008.
- [25] D. J. Shaw, *Introduction to Colloid and Surface Chemistry*, Butterworths, London, UK, 1970.
- [26] D. Thiemig and A. Bund, “Characterization of electrodeposited Ni-TiO₂ nanocomposite coatings,” *Surface and Coatings Technology*, vol. 202, no. 13, pp. 2976–2984, 2008.
- [27] K. Siwińska-Stefańska, M. Nowacka, A. Kołodziejczak-Radzimska, and T. Jesionowski, “Preparation of hybrid pigments via adsorption of selected food dyes onto inorganic oxides based on anatase titanium dioxide,” *Dyes and Pigments*, vol. 94, no. 2, pp. 338–348, 2012.
- [28] M. Kosmulski, “pH-dependent surface charging and points of zero charge. IV. Update and new approach,” *Journal of Colloid and Interface Science*, vol. 337, no. 2, pp. 439–448, 2009.
- [29] M. Kosmulski, “The pH-dependent surface charging and points of zero charge. V. Update,” *Journal of Colloid and Interface Science*, vol. 353, no. 1, pp. 1–15, 2011.
- [30] K. Siwinska-Stefanska, F. Ciesielczyk, M. Nowacka, and T. Jesionowski, “Influence of selected alkoxy silanes on dispersive properties and surface chemistry of titanium dioxide and TiO₂-SiO₂ composite material,” *Journal of Nanomaterials*, vol. 2012, Article ID 316173, 19 pages, 2012.
- [31] I. Jerman, M. Mihelčič, D. Verhovek, J. Kovač, and B. Orel, “Polyhedral oligomeric silsesquioxane trisilanols as pigment surface modifiers for fluoropolymer based Thickness Sensitive Spectrally Selective (TSSS) paint coatings,” *Solar Energy Materials and Solar Cells*, vol. 95, no. 2, pp. 423–431, 2011.
- [32] T. Ozawa, “Thermal analysis: review and prospect,” *Thermochimica Acta*, vol. 355, no. 1–2, pp. 35–42, 2000.

Research Article

Preparation and Characterization of Multifunctional Chitin/Lignin Materials

**Łukasz Klapiszewski,¹ Marcin Wysokowski,¹
Izabela Majchrzak,¹ Tomasz Szatkowski,¹ Magdalena Nowacka,¹
Katarzyna Siwińska-Stefańska,¹ Karolina Swarc-Rzepka,¹ Przemysław Bartczak,¹
Hermann Ehrlich,² and Teofil Jesionowski¹**

¹ *Institute of Chemical Technology and Engineering, Faculty of Chemical Technology, Poznan University of Technology, M. Skłodowskiej-Curie 2, 60965 Poznan, Poland*

² *Institute of Experimental Physics, Faculty of Chemistry and Physics, TU Bergakademie Freiberg, 09599 Freiberg, Germany*

Correspondence should be addressed to Teofil Jesionowski; teofil.jesionowski@put.poznan.pl

Received 16 July 2013; Revised 16 August 2013; Accepted 17 August 2013

Academic Editor: Yuan Zhang

Copyright © 2013 Łukasz Klapiszewski et al. This is an open access article distributed under the Creative Commons Attribution License, which permits unrestricted use, distribution, and reproduction in any medium, provided the original work is properly cited.

Multifunctional chitin/lignin materials were synthesized. In order to combine mechanical milling of the biopolymers with simultaneous mixing, a centrifugal ball mill was utilized. The resulting materials, differing in terms of the proportions of precursors used, underwent detailed physicochemical and dispersive-morphological analysis. On the basis of FT-IR spectra and results of elemental analysis, the efficiency of the preparation of the materials was determined. The influence of the precursors on the thermal stability of the resulting systems was also evaluated. Zeta potential was determined as a function of pH to describe the electrokinetic stability of aqueous dispersions. This is important for evaluating the utility of the materials and indirectly confirms the effectiveness of the proposed method of synthesis of chitin/lignin products. Measurements were performed to determine basic colorimetric parameters, crucial in the production technology of multiple colored materials. It is expected that chitin/lignin materials will find a wide range of applications (biosorbents, polymer fillers, and electrochemical sensors), as they combine the unique properties of chitin with the specific structural features of lignin to provide a multifunctional material.

1. Introduction

Lignin is an organic substance found in wood and the lignified elements of plants, such as straw. From a chemical point of view, the parent lignin is an amorphous, polyphenolic material arising from enzyme-mediated dehydrogenative polymerization of three phenylpropanoid monomers: p-coumaryl, coniferyl, and sinapyl alcohols [1–4]. The copolymer thus formed consists of substituted C9 units (6 aromatic and 3 propene carbons) interconnected by C–O (mostly etheric) or C–C bonds [5].

Lignin from various pulping processes has been shown to be applicable in electrochemical sensors owing to its residual quinone moieties, which are redox and thus electroactive [6, 7]. In order to intensify the chemical properties of lignin that make it suitable for electrochemical applications,

various methods of combining these materials with electrical conductors (carbon nanotubes or conducting polymers) have been proposed [8, 9]. Lignin has been also studied as a potential low-cost “green” biosorbent of heavy metals [10–12]. The usefulness of lignin in the adsorption of harmful organic compounds (including heavy metals) results from the presence of multiple functional groups in its structure, including phenolic, hydroxyl, carboxyl, and methoxy groups. In addition to the sorption of metals, lignin is also used for the removal of other compounds, such as dyes, pesticides, and phenols [13]. Lignin can also serve as an additive to synthetic polymers, giving them distinctive and unique properties [14, 15].

Numbers of scientific reports prove that chitin is one of the key polymers of the 21st century [16, 17]. Chitin is a building block of the skeletons of crustaceans [18, 19], insects

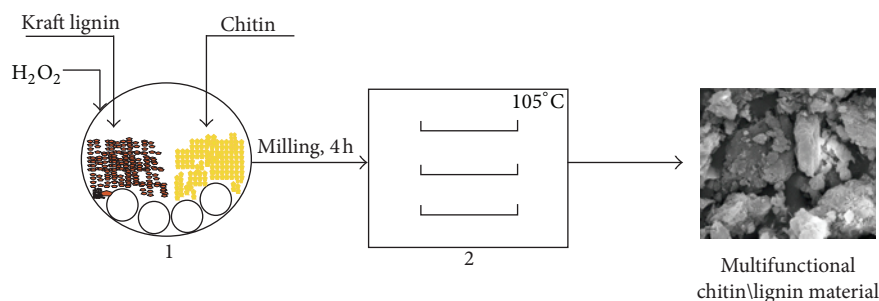


FIGURE 1: Scheme of chitin/lignin material preparation: (1) ball mill and (2) stationary drier.

[20], and diatoms [21]. Recently the biopolymer has been discovered in the skeletons of several species of marine sponges [22–24]. From a chemical point of view chitin is a linear aminopolysaccharide, composed of *N*-acetylglucosamine units linked by β -1,4-glycosidic bonds [25]. The unique properties of chitin are due to the presence of (acetyl)amino groups in the polysaccharide backbone [26]. For instance, biodegradability, nontoxicity, and bioactivity contribute to applications of chitin in various areas of biomedicine [27–30]. On the other hand, its high affinity to peptides and metal complexation is interesting from the point of view of catalysis [31] and of waste water treatment [32, 33]. The presence of reactive –OH and –NH groups in chitin's structure also provides opportunities for its functionalization [34]. This property enables the obtaining of novel, advanced chitin-based materials with a wide spectrum of application, including polymer fillers, adsorbents, biosensors [35], a drug delivery systems.

Consequently, in this study, chitin powder was modified with Kraft lignin solution to obtain multifunctional chitin/lignin materials. Combination of these two polymers has been poorly studied in the literature. However, Wang and Xing [36] proved that modification of chitin with lignin leads to improvement in the adsorption of hydrophobic organic compounds. In this study a synthesis of advanced materials was performed by a mechanochemical method. This method was chosen because it can promote reactions between solids quickly and quantitatively, with either no added solvent or only nominal amounts. Additionally, it is highly efficient with regard to the use of energy, time, and materials [37]. In comparison with the method described by Wang and Xing [36], the main advantage of the proposed mechanochemical method is the elimination of the need to use organic solvent (acetone), which makes the process environmentally friendly.

2. Experimental Section

2.1. Materials. Chitin powder from crab shells was mechanically combined with Kraft lignin (both biopolymers were purchased from Sigma-Aldrich). The final chitin/lignin products were obtained using various proportions of the reagents, which were additionally treated with 15% hydrogen peroxide (Chempur).

2.2. Preparation of Multifunctional Chitin/Lignin Materials. Chitin and lignin were combined using a process of

mechanical milling of the materials with simultaneous homogenization, using a centrifugal ball mill (Fritsch). The substrates were soaked in a small amount of 15% hydrogen peroxide and were closed in a milling container together with the milling balls. The container with the precursors was then fitted to the mill's metal base. Milling took place with simultaneous movement of the metal base and container. The rotational speed of the rotating milling container was 300 rpm. In order to achieve the required homogeneity of the final material, milling was carried out for 4 hours. The product was then placed in a stationary drier at a high temperature of 105°C for 12 hours. A simplified process scheme of the preparation of chitin/lignin products is shown in Figure 1.

Immediately after the drying process, the chitin/lignin materials were passed through a sieve with size equal 100 μm , thus increasing their uniformity. Products with varying content of chitin in proportion to lignin were obtained. In the further part of the research, the products were subjected to physicochemical analysis.

2.3. Evaluation of Physicochemical Properties

2.3.1. Scanning Electron Microscopy. The morphology and microstructure of the chitin/lignin products were analyzed to obtain detailed information concerning such properties as dispersion, morphology of the grains, structure of individual particles, and agglomeration characteristics. The observations were based on SEM images recorded from a EVO40 scanning electron microscope (Zeiss). Prior to testing, the samples were coated with Au for a time of 15 seconds, using a Balzers PV205P coater.

2.3.2. FT-IR Analysis. The chitin/lignin materials and precursors (chitin and Kraft lignin) were also subjected to FT-IR spectral analysis, using an IFS 66 v/S instrument (Bruker). Here the materials were analyzed in tablet form made by pressing a mixture of anhydrous KBr (ca. 0.1 g) and 1 mg of the tested substance in a special steel ring, under a pressure of approximately 10 MPa. The transparent tablet was placed in a cuvette, which was then fitted in the clamp of the apparatus, at the focal point of the light beam. Analysis was performed over a wave number range of 4000 to 400 cm^{-1} (at a resolution of 0.5 cm^{-1}).

2.3.3. Elemental Analysis. The elemental contents of the products were established using a Vario EL Cube instrument (Elementar Analysensysteme GmbH), which is capable of registering the percentage content of carbon, hydrogen, nitrogen, and sulfur within samples, after high-temperature combustion. A properly weighed sample was placed on an 80-position autosampler and combusted. The decomposed sample was carried in a stream of helium gas into a chromatography column, where the percentage of each element was analyzed.

2.3.4. Electrokinetic Characteristics. The zeta potential was measured with a Zetasizer Nano ZS equipped with an autotitrator. The measurements were performed in a 0.001 M solution of NaCl. This instrument employs a combination of electrophoresis and laser measurement of particle mobility, based on the Doppler phenomenon. The speed of particles moving in the liquid in an electric field, known as the electrophoretic mobility, is measured. Then from the Henry equation (1), the value of the zeta potential is obtained:

$$\mu_E = \frac{2\varepsilon\zeta f(\kappa a)}{3\eta}, \quad (1)$$

where μ_E denotes electrophoretic mobility, ε denotes the dielectric constant, ζ denotes the electrokinetic (zeta) potential, η denotes the viscosity, and $f(\kappa a)$ denotes the Henry function.

The Henry function $f(\kappa a)$ is monotonic, increasing from 1.0 at $\kappa a = 0$ to 1.5 at $\kappa a = \infty$. At the lower limit, it reduces to the Hückel equation ($\mu_E = 2\varepsilon\zeta/3\eta$), and at the upper limit, it reduces to the Smoluchowski equation ($\mu_E = \varepsilon\zeta/\eta$).

2.3.5. Thermal Stability. A thermogravimetric analyzer (TG/DTA/DSC, model Jupiter STA 449F3, Netzsch) was used to investigate the thermal decomposition behavior of the samples. Measurements were carried out under flowing nitrogen (10 cm³/min) at a heating rate of 10°C/min over a temperature range of 25–1000°C, with an initial sample weight of approximately 5 mg.

2.3.6. Porous Structure Analysis. In order to characterize the parameters of the porous structure of the examined substances, nitrogen adsorption/desorption isotherms at 77 K, surface area, pore volume, and average pore size were determined using an ASAP 2020 (Accelerated Surface Area and Porosimetry) instrument (Micromeritics Instrument Co.). All samples were degassed at 120°C for 4 hours in a vacuum chamber prior to measurement. The specific surface area was determined by the multipoint BET method using adsorption data under relative pressure (p/p_0). The BJH (Barrett-Joyner-Halenda) method was applied to determine the total pore volume and the average pore size.

2.3.7. Adsorption Experiments. Adsorption tests were performed with the use of tetrahydrate cadmium nitrate as a precursor of cadmium(II) ions (POCh SA). In order to determine the optimum time of heavy metal removal from aqueous solutions, the adsorption process was carried out

over 30, 60, 90, 120, and 180 minutes, with the cadmium(II) ion concentration equal to 30 mg/dm³. Time optimization was performed for three sorbent types independently: pure lignin, chitin, and the final chitin/lignin material in a weight ratio of 1:1. The prepared cadmium(II) solutions were placed in a conical flask, into which 5.0 g of sorbent was added. The system was stirred using a magnetic stirrer (Ika Werke Labortechnik GmbH) for the set length of time. After stirring, the mixture was filtered under reduced pressure, with the use of special apparatus and filters (Sartorius). The resulting precipitate was dried for 2 hours at 105°C. The filtrate was then analyzed to determine the efficiency of adsorption.

2.3.8. Evaluation of Adsorption Efficiency. An important goal was to determine the effectiveness of removal of cadmium(II) ions from aqueous solution. For this purpose, atomic absorption spectrometry was used, which enables the detection of ions in the filtrate after the adsorption process. The analysis was performed on a Z-8200 spectrometer (Hitachi). Before the analysis, it was necessary to prepare a calibration curve. The results of the AAS analysis were used in calculations to determine the efficiency of cadmium(II) ion removal. For this purpose, the following equation was used:

$$\% \text{ removal} = \left(\frac{c_0 - c_e}{c_0} \right) \times 100\%, \quad (2)$$

where c_0 and c_e are, respectively, the initial and equilibrium concentrations of cadmium(II) ions (expressed in mg/dm³).

2.3.9. Colorimetric Analysis. Colorimetric analysis was performed using a colorimeter (Specbos 4000, JETI Technische Instrumente GmbH). Daylight (D65) was used as a standard light source. The instrument evaluated the color in terms of the CIE $L^*a^*b^*$ color space system. This describes all the colors visible to human eye and was created to serve as a device-independent model, extremely useful for the preparation of a reference sample. In this color space, L^* represents the brightness, and a^* and b^* are appropriate color coordinates. The parameter dE describes the total color change.

3. Results and Discussion

3.1. Dispersive-Morphological Properties. In order to evaluate the morphology and microstructures of the biopolymers, SEM photographs were taken (Figure 2). In the pictures shown it is easily observable how the precursors differ from each other. Chitin (Figure 2(a)) is characterized by nonhomogeneity and the presence of irregular fragments in its structure. Lignin possesses irregularly shaped particles as well, but its structure is slightly more homogeneous (Figure 2(b)).

SEM photographs were taken for selected products (Figure 3). It is easily noticeable that the ratio of the biopolymers used to make the samples significantly influences their morphological and microstructural properties. The character of a given sample clearly depends on the quantities of precursors used.

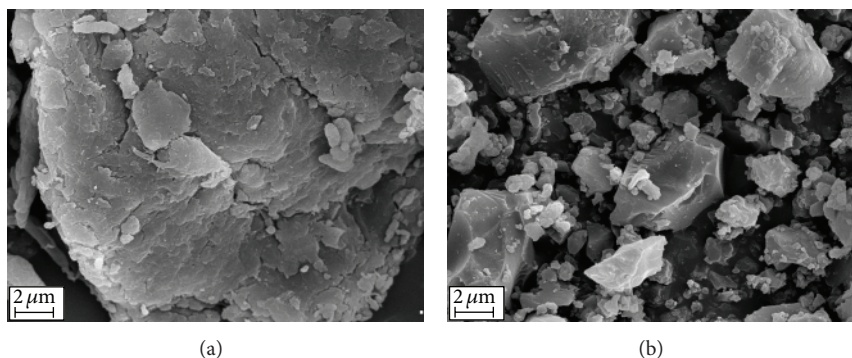


FIGURE 2: SEM images of chitin powder from crab shells (a) and Kraft lignin (b).

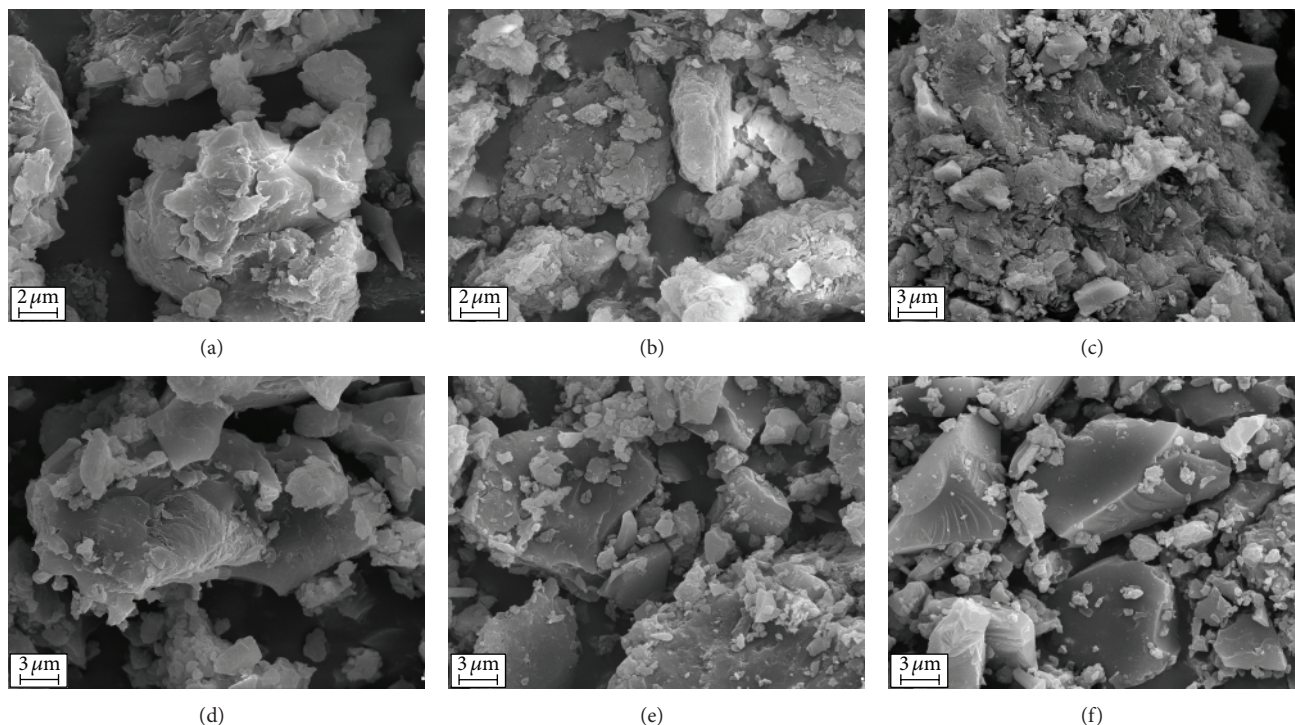


FIGURE 3: SEM images of chitin/lignin material samples: 1 (a), 4 (b), 7 (c), 8 (d), 10 (e), and 13 (f).

3.2. FT-IR Analysis. Analysis of the FT-IR spectra were carried out to confirm the presence of characteristic functional groups in the tested compounds, through measurement of the absorption intensity of specific infrared radiation. Additionally, based on the adsorption band, conclusions can be drawn regarding the appropriateness and effectiveness of the proposed methodology of multifunctional chitin/lignin material synthesis. Figure 4 shows the FT-IR spectra of the precursors, lignin and chitin, and final chitin/lignin materials obtained by the proposed method.

In analysis of the lignin spectrum, the following bands were detected: stretching vibrations of O-H groups (phenolic -OH and aliphatic -OH) in the range $3600\text{--}3200\text{ cm}^{-1}$ and C-H stretching vibrations in the range $2960\text{--}2920\text{ cm}^{-1}$ (CH_3 and CH_2) and $2850\text{--}2840\text{ cm}^{-1}$ (OCH_3). A wider band in the range $1710\text{--}1550\text{ cm}^{-1}$ results from stretching vibrations

of C=O bonds. Also of significance in the analysis of the lignin FT-IR spectrum are bands with absorption maxima at the wave numbers 1375 cm^{-1} , 1265 cm^{-1} , and 1220 cm^{-1} , associated with stretching vibrations of C-O, C-O(H), and C-O(Ar) bonds of phenolic groups, as well as etheric bonds, which play an important role in the connection of elements in the analyzed biopolymer. The presence of C-O-C etheric bonds is additionally confirmed by a stretching vibration band at wave number 1045 cm^{-1} . The last noteworthy group of bands in the case of lignin consists of in-plane deformation bands $\delta_{\text{ip}}\text{Ar C-H}$ (1140 cm^{-1}) and out-of-plane $\delta_{\text{op}}\text{Ar C-H}$ (bands at wave numbers below 1000 cm^{-1} , including 854 cm^{-1} , 816 cm^{-1} , and 790 cm^{-1}). The analysis of Kraft lignin performed for the purpose of this work is in agreement with the data presented in previously published papers [38, 39].

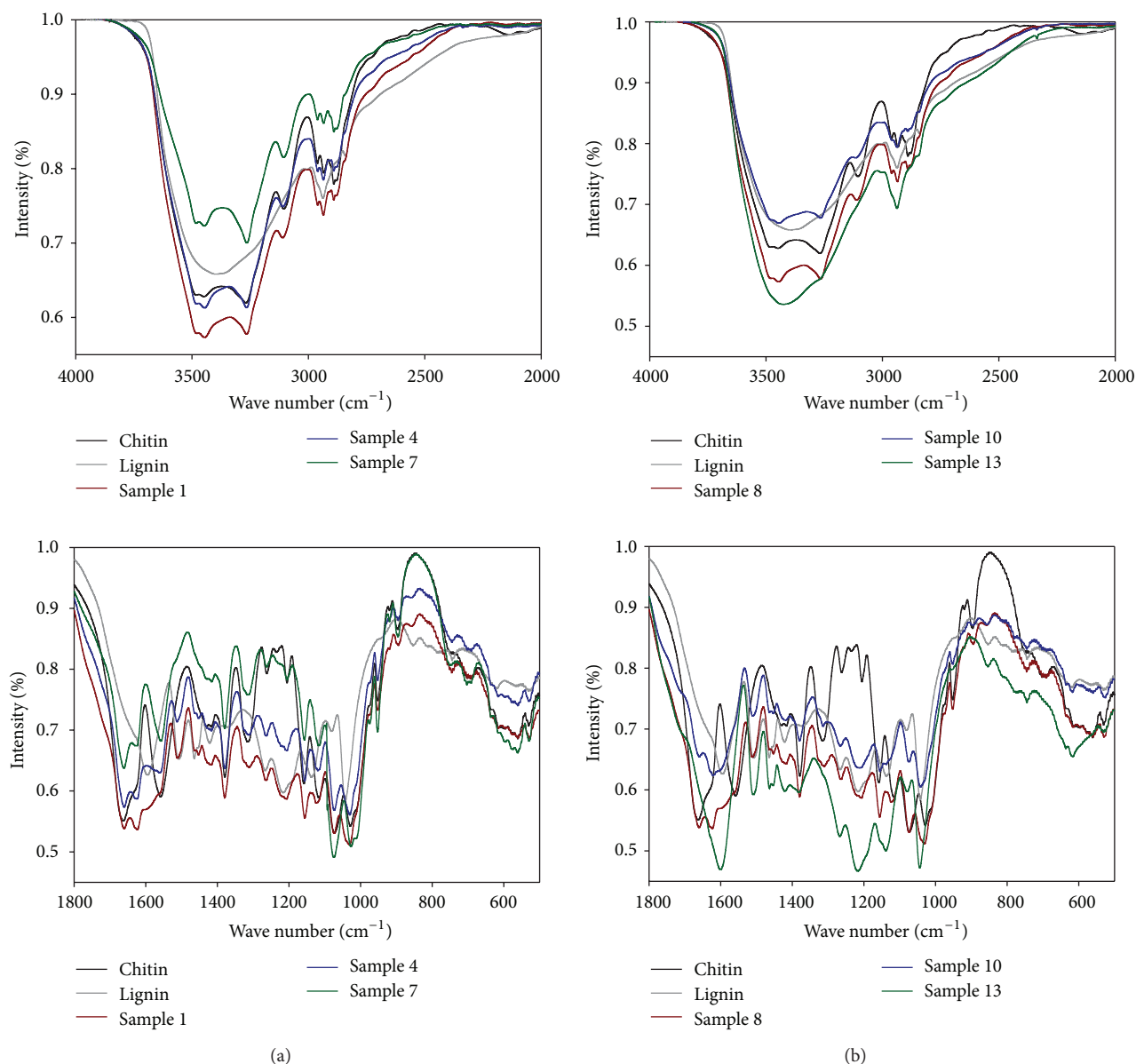


FIGURE 4: FT-IR spectra of the precursors and of selected chitin/lignin materials: samples 1, 4, and 7 (a) and 8, 10, and 12 (b).

In turn, the analysis of chitin revealed the presence of bands corresponding to stretching vibrations of O-H groups in the range $3600\text{--}3400\text{ cm}^{-1}$, asymmetric stretching vibrations at wave number 3268 cm^{-1} , and symmetric vibrations at 3106 cm^{-1} originating from N-H groups. A stretching vibration band in the range $3000\text{--}2800\text{ cm}^{-1}$ is associated with the presence of $(\text{CH}_3 + \text{CH}_2)$ groups. A wider band corresponding to stretching vibrations in the range $1660\text{--}1620\text{ cm}^{-1}$ is the so-called first amide band characteristic of chitin, which results from the overlapping of stretching vibration bands of C=O groups. The second amide band is visible in the chitin spectrum at a wave number of 1558 cm^{-1} . This band is undoubtedly associated with stretching vibrations of C-N groups and bending vibrations of N-H. The region in range $1420\text{--}1375\text{ cm}^{-1}$ is attributed to bending vibrations

associated with $-\text{CH}_2$ and $\text{C}-\text{CH}_3$ groups. A weak absorption band of stretching and bending vibrations at wave number 1312 cm^{-1} (the third amide band) is associated with C-N and N-H groups, respectively. A wide band in the range $1250\text{--}950\text{ cm}^{-1}$ is attributed to asymmetric stretching vibrations of C-O-C groups and stretching vibrations of C-O groups. Of importance in the chitin spectrum is a weak band in the range $896\text{--}890\text{ cm}^{-1}$, which confirms the presence of the β -1,4-glycoside bond in the biopolymer structure. The analysis carried out for chitin is in agreement with available literature data concerning α -chitin [40–42].

In Figures 4(a) and 4(b), FT-IR spectra for selected chitin/lignin materials are presented. Analysis of the spectra indicates that the process of chitin/lignin product synthesis was fully controlled and completed with satisfactory results.

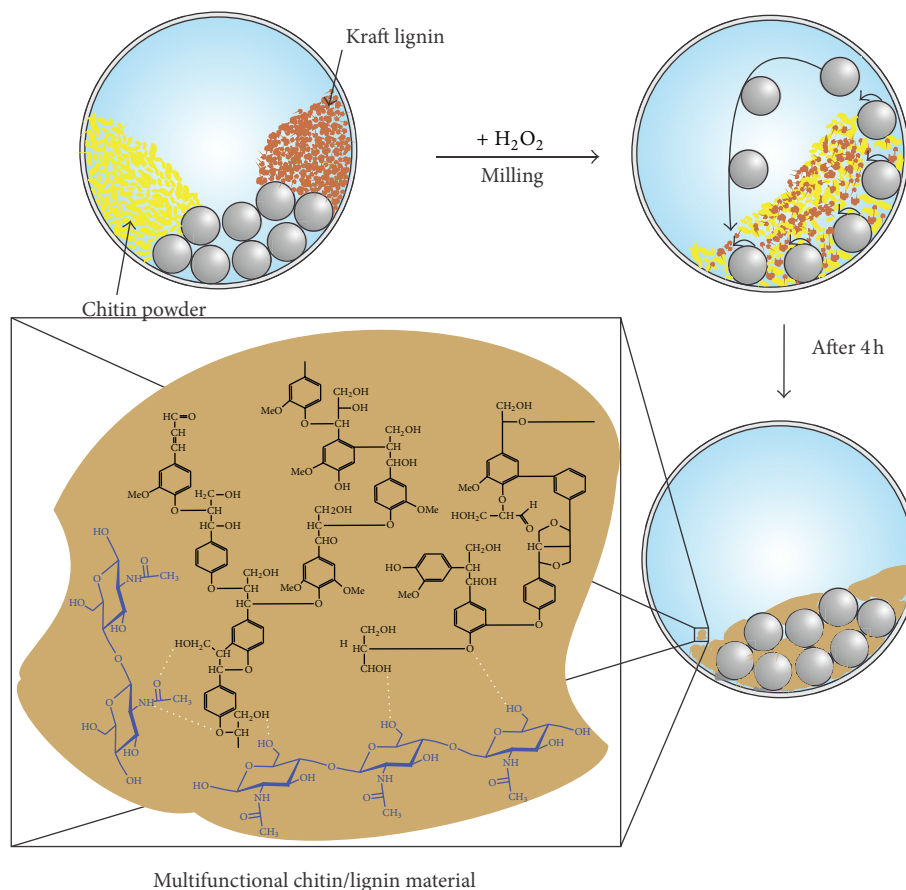


FIGURE 5: Schematic representation of possible interactions in the obtained chitin/lignin materials.

Individual bands characteristic of the discussed precursors overlap with bands obtained for the final products. Additionally, modification of the mass fraction of any of the precursors causes changes in the peaks' intensity. For instance, when the mass fraction of lignin decreases in products 1 to 7, the intensity of the bands in the spectrum also decreases. The results obtained at this stage of the investigation confirmed the effectiveness of chitin/lignin preparation. An interesting relationship was observed for product 13 (with a chitin : lignin weight ratio of 0.05:1). The spectrum of this product is similar to the spectrum of pure lignin. This observation is obviously justified and additionally confirms the correctness of the suggested research methodology. The spectra reveal shifts and deformations of the first and second amide bands, which are probably the results of hydrogen bond formation between chitin and lignin. At this stage of the research a simplified mechanism of chitin and lignin combination was constructed (Figure 5). The proposed mechanism is based on the formation of hydrogen bonds between $-OH$ groups of lignin and functional $C=O$, $-OH$, and NH groups of chitin.

3.3. Elemental Analysis. Elemental analysis, determining the percentage content of nitrogen, carbon, hydrogen, and sulfur, was performed for selected final products and for their synthesis precursors. The results are given in Table 1.

TABLE 1: Elemental content of nitrogen, carbon, hydrogen, and sulfur in the precursors and in chitin/lignin materials.

Sample number	Elemental content (%)			
	N	C	H	S
Pure chitin	6.21	40.54	7.36	—
Pure lignin	—	42.21	5.02	3.14
1	6.06	45.25	8.26	3.13
2	6.04	44.60	8.18	2.23
3	5.99	44.44	8.14	1.11
4	6.06	44.32	8.11	0.85
5	6.17	43.01	8.04	0.51
6	6.04	42.80	8.04	0.30
7	6.12	42.82	8.03	0.05
8	4.32	43.54	7.34	3.11
9	2.34	44.51	6.61	3.10
10	1.67	44.45	6.54	3.10
11	1.19	44.19	6.11	3.06
12	0.87	44.14	6.05	3.11
13	0.38	43.93	5.85	3.14

In analysis of the results obtained for the elemental composition of selected chitin/lignin materials, the quantities

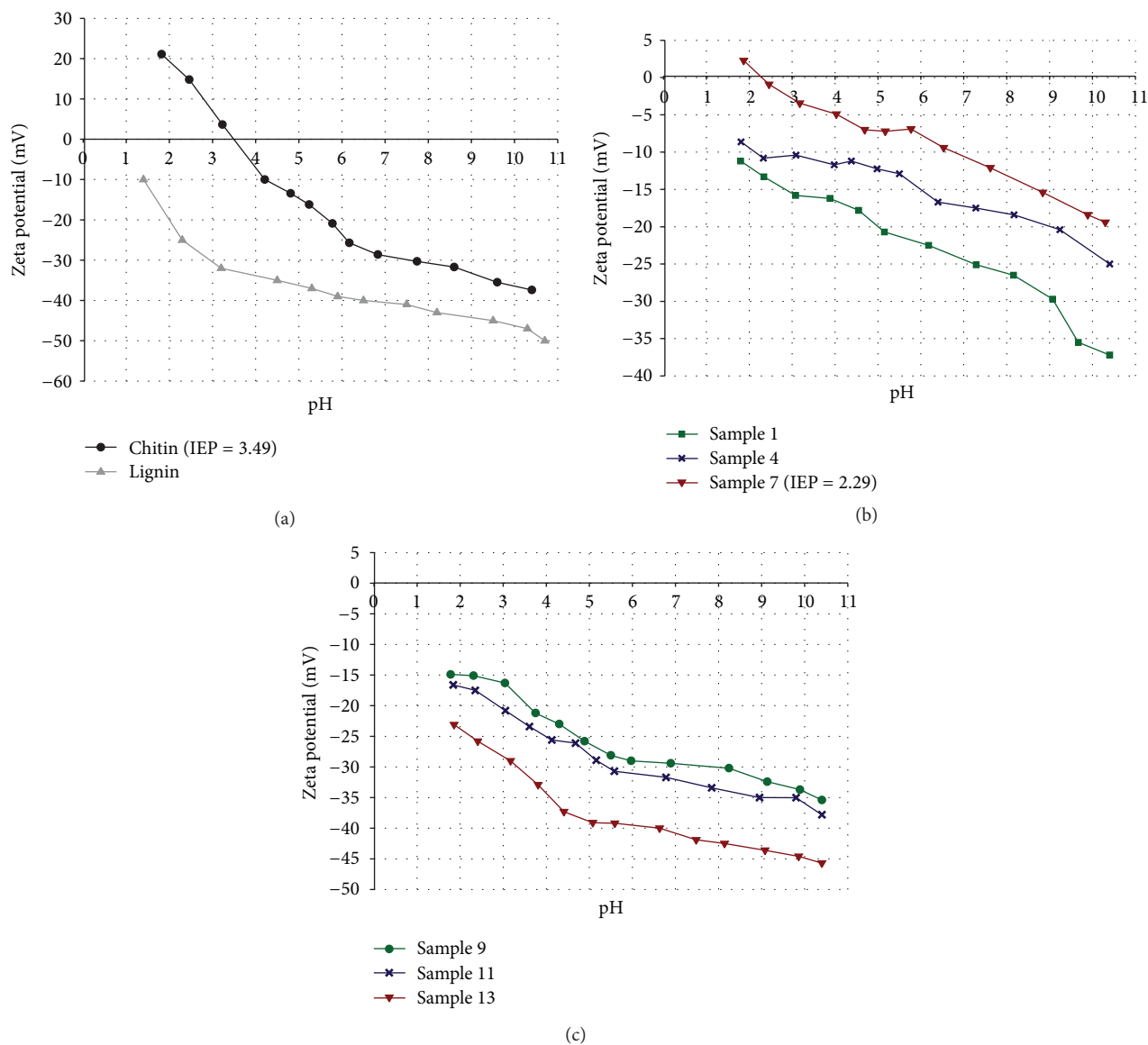


FIGURE 6: Zeta potential versus pH of precursors (a) and chitin/lignin materials ((b) and (c)).

of precursors used in the preparation of the final products are found to have a noticeable influence. The largest differences were observed for the percentage content of nitrogen and sulfur. Similar nitrogen content was found in samples with constant chitin content and variable lignin content (samples 1–7), which is to be expected since chitin has acetamide groups in its structure. In samples 9, 11, and 13 a decrease in nitrogen content is observed, which is a result of the diminishing fraction of chitin. A similar situation is found for sulfur content. In samples 1 to 7 the lignin content gradually decreases as is clearly confirmed by the decreasing percentage of sulfur in the products. In the other materials (samples 8–13) lignin content remains unchanged, while chitin content varies; thus the sulfur percentage content is similar. The changes in the percentage contents of carbon and hydrogen were comparably small. The highest carbon content was recorded for sample 1 (chitin : lignin ratio 1 : 1),

and the smallest was recorded for sample 7 (chitin : lignin ratio 1 : 0.05).

Elemental analysis enables estimation of the percentage elemental contribution in the precursors and in the final multifunctional chitin/lignin materials. The analysis provides proof of the different elemental compositions of the various samples and indirectly confirms the effectiveness of the preparation of chitin/lignin materials.

3.4. Electrokinetic Properties. Electrokinetic properties undoubtedly depend on the surface character of the examined materials. Thus in the next part of the research, the value of the zeta potential was determined as a function of pH (Figure 6), providing information about the electrokinetic properties of particles dispersed in aqueous systems.

Zeta potential was determined for the precursors (chitin and Kraft lignin) and for the obtained chitin/lignin materials

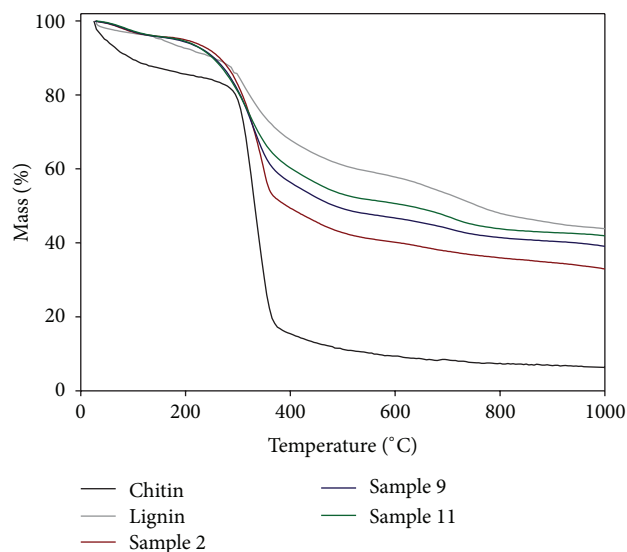


FIGURE 7: Thermogravimetric curves of precursors and resulting chitin/lignin materials.

with various weight fractions of the precursors. Measurements were carried out over a wide pH range (1–11) in 0.001 M NaCl solution. The stability of water dispersions was indirectly determined through the value of zeta potential. In addition, the effectiveness of the proposed multifunctional material synthesis was confirmed.

Chitin is obtained industrially via chemical isolation in three stages: demineralization, deproteinization, and depigmentation. The deproteinization stage is usually carried out using aqueous solution of NaOH or KOH, which hydrolyses some of the acetamide bonds present in poly-1,4-*N*-acetylglucosamine. Thus the process needs to be strictly controlled. Chitin is always a copolymer of *N*-acetylglucosamine and glucosamine mers, with a degree of deacetylation in the range 50–95% [43]. Various functional groups present on the surface of chitin undergo protonation at solution pH values lower than pH_{IEP} . Amine groups ($R-NH_2$) undergo proteinization to $(RNH_3)^+$. Consequently, in this solution, pH range, a formation of a positive surface charge, has been observed on the surface of chitin [44, 45]. The formation of the surface charge on chitin dispersed in an aqueous system can be expressed by the following reaction:



Surface $-NH_3^+$ groups cause repulsive electrostatic forces between particles dispersed in aqueous systems. The $R-NH_3^+$ group is weakly acidic, and its degree of proteinization is described by the value pK_a . According to calculations based on the value of pK_a , published in [45], surface amine groups are completely proteinized at a pH of 3.5 or lower and undergo complete dissociation at a pH of 7. Between these two pH values, amine groups are only partly protonated [46]. From the results obtained for chitin's zeta potential, it was concluded that the isoelectric point (IEP) is equal to 3.49. At this point the colloidal system is the least stable. Over

the analyzed pH range, chitin has zeta potential values ranging from 21 to -38 mV. Chitin dispersed in aqueous systems exhibits good electrokinetic stability, particularly at alkaline pH. Thus in these measurement conditions, repulsive forces prevail between dispersed chitin particles.

The electrokinetic curve of Kraft lignin, obtained as a result of zeta potential measurement, does not reach the isoelectric point; however, its shape suggests that it approaches IEP at a pH of around 1. Functional groups present on the surface of lignin have a significant influence on the obtained values of isoelectric point. Kraft lignin has a negative zeta potential over the entire pH range. The surface charge formed strongly depends on the degree of dissociation of such functional groups as $-OH$, $-COOH$, and $-SH$ present on the surface of the particles dispersed in the aqueous system [47]. From the work carried out under the present study and from available literature data, it can be concluded that a significant quantity of carboxyl and phenolic groups (and others) is present on the surface of Kraft lignin. The mechanism of surface charge formation has been discussed in detail in [48, 49]. The significant changes in zeta potential (and therefore in surface charge density) as a function of solution pH confirm unequivocally that in the analyzed dispersive system the potential-forming ions are H^+ and OH^- . The electrokinetic analysis of Kraft lignin is in agreement with literature data available for the compound [48, 50].

Figures 6(b) and 6(c) show the electrokinetic curves of the obtained chitin/lignin materials with various weight fractions of the components. The suggested methodology of chitin/lignin system preparation makes it possible to obtain a final product with specified electrokinetic properties. The results of zeta potential measurements indirectly confirm the effectiveness of the proposed method of synthesis. Increasing the content of lignin in proportion to chitin causes a proportional decrease in the electrokinetic (zeta) potential values obtained. This is particularly noticeable for samples 9, 11, and 13 (Figure 6(c)), with chitin : lignin weight ratios of 0.5 : 1, 0.2 : 1, and 0.05 : 1, respectively. In turn, increasing the weight contribution of chitin in proportion to lignin caused a shift of the electrokinetic curve toward higher values of zeta potential. The most visible change in the surface charge was recorded for sample 7 (chitin : lignin ratio 1 : 0.05). The analyzed systems offer relatively good electrokinetic stability over a wide pH range. In these conditions particles will tend not to form agglomerates, due to the presence of repulsive forces between them, which is of great importance from the point of view of potential applications. The stability improves when the weight fraction of lignin relative to chitin increases.

3.5. Thermal Stability. Thermal stability measurements were performed for selected chitin/lignin materials. For comparison purposes, measurements were also made for the biopolymers. The obtained thermogravimetric curves show mass loss caused by the transformations that occur as the temperature increases. Figure 7 shows the TG curves obtained for the precursors and the results of the thermal analysis of selected final products.

The curves obtained for the initial biopolymers (Figure 7) show that chitin has a lower resistance to high temperature.

The TG curve for chitin shows relatively significant mass loss of over 90%. This occurs in two important stages. The first, at a temperature below 200°C, involves desorption of water. The second, starting from ~300°C, involves considerable mass loss (~75%) associated with a one-step thermal degradation of the biopolymer [18]. Data published in the literature [51] confirm the results obtained in the present research.

In the case of lignin the thermogravimetric curve does not demonstrate such significant mass loss as with chitin (mass loss ~60% of initial sample mass). The TG curve for lignin indicates three clear stages. The first, as in the case of chitin, is associated with loss of water. The second, the most important stage of high mass loss (about 35%) in the temperature range 200–600°C, is related to a complicated thermal decomposition of the compound, which includes bonds newly formed in cross-linking reactions. The third and last stage starts at a temperature of about 600°C and is associated with fragmentarization of the lignin compound and gradual thermal degradation. The data obtained are in agreement with the literature [52, 53].

Figure 7 shows the thermogravimetric curves of selected chitin/lignin products. Sample 2, containing the largest amount of chitin in proportion to lignin among the three analyzed products, displayed the lowest thermal stability (mass loss as high as 70% of the initial sample mass). Slightly better thermal properties were displayed by the other two materials, samples 9 and 11, which had similar mass loss values of 58% (sample 11) and 60% (sample 9). The results at this stage of the experiment are in agreement with expectations. It is clear that the addition of lignin slightly improves the thermal stability of the resulting multifunctional chitin/lignin materials.

3.6. Porous Structure Analysis. In order to determine the porous structure parameters of the final products, analysis was carried out to determine the BET specific surface area, total volume, and mean size of pores. The results are shown in Figure 8. For comparison purposes, analysis of the precursors (chitin and lignin) was also carried out.

Values recorded for the BET specific surface area are relatively low, equal to 2.7 m²/g and 0.1 m²/g for chitin and lignin, respectively. Pore volume in chitin is significantly higher than in lignin. The mean size of chitin pores is 25.9 nm, while that of lignin pores is smaller, at 12.1 nm.

The lowest value of BET specific surface area among the analyzed samples was recorded for sample 13 (1.2 m²/g), and the highest one was recorded for sample 7 (3.0 m²/g). In the case of BET specific surface area, there are clear differences in the values obtained depending on the ratio of precursors used to prepare the final products. The values of total pore volume and pore size also clearly depend on the quantities of the precursors. With an increase in the chitin-to-lignin ratio (samples 1–7; Figure 8(c)), total pore volume increases up to 0.019 cm³/g. Pore size also rises gradually, reaching a value of 25.1 nm for sample 7. Samples 8–13 (Figure 8(d)) show the reverse behavior. The values obtained for these samples show a gradual decrease in total pore volume and in pore size. Although the BET specific surface area is relatively low, the biomaterials should nonetheless be considered efficient

and selective biosorbents, especially for harmful chemical substances, most importantly heavy metal ions. Very often, with the aim of improving lignin's adsorptive properties, surface activation is carried out in order to increase its surface area. One such process was suggested in [54]. The authors described a method of physical activation of lignin, consisting of carbonization of lignin in a nitrogen atmosphere in the first step and its activation using CO₂ in the second. In this way a product was prepared with a surprisingly high BET surface area of 1613 m²/g. It was reported that depending on the type of lignin used, activated carbon with various specific surface area parameters can be obtained [54].

Another method which may enable an increase in the specific surface area of biopolymers of this type is combination with an inorganic support offering excellent porous structure parameters, for instance, silica or magnesium silicate. The procedure significantly extends lignin's application as a selective biosorbent and results in an increase in capacity for heavy metal ion adsorption [55, 56].

Chitin, like lignin, has a great number of various functional groups in its structure; this means that in spite of the small BET surface area, these compounds cannot be excluded as biosorbents with good long-term promise.

The chitin/lignin material obtained can be identified with unique properties which enable it to be used as an effective sorbent of heavy metals. As part of the study, a test of the removal of cadmium(II) ions from aqueous solution was carried out using the chitin/lignin biosorbent, as well as native chitin and lignin. The influence of process duration (30–180 min) on the effectiveness of adsorption of cadmium(II) ions (30 mg/dm³) was determined, as shown in Figure 9. It can be concluded that adsorption equilibrium was established after 60 minutes for both the chitin/lignin sorbent and the pure precursors. This can therefore be considered to be the most effective length of time for which the adsorption process should be maintained. Most importantly, the chitin/lignin sorbent proved to be the most effective. The efficiency of cadmium(II) ion removal reached values in the range 95.7–98.4%, while for the lignin and chitin precursors, the values were only 65.9–71.8% and 78.0–84.8%, respectively.

The results of the analyses indicate that chitin/lignin hybrids are excellent sorbents of heavy metal ions. It is expected that the investigated materials will be equally effective in the sorption of other heavy metals such as lead, mercury, chromium, and uranium. The results obtained provide a basis for realization of the adsorption process in real industrial waste systems.

3.7. Colorimetric Analysis. For the synthesized chitin/lignin products as well as for the initial precursors, colorimetric analysis was carried out using the CIE $L^*a^*b^*$ color system. The results are given in Table 2.

Chitin has a light beige color, while lignin is a dark brown solid. The parameter L^* , determining brightness, is 85.47 for pure chitin and 41.26 for lignin. The parameters a^* and b^* , reflecting the contribution of red and yellow in a sample's color, were as follows: for chitin $a^* = 1.42$ and $b^* = 14.43$; for pure lignin $a^* = 10.16$ and $b^* = 25.92$. Another important parameter in colorimetric analysis is the dE variable, which

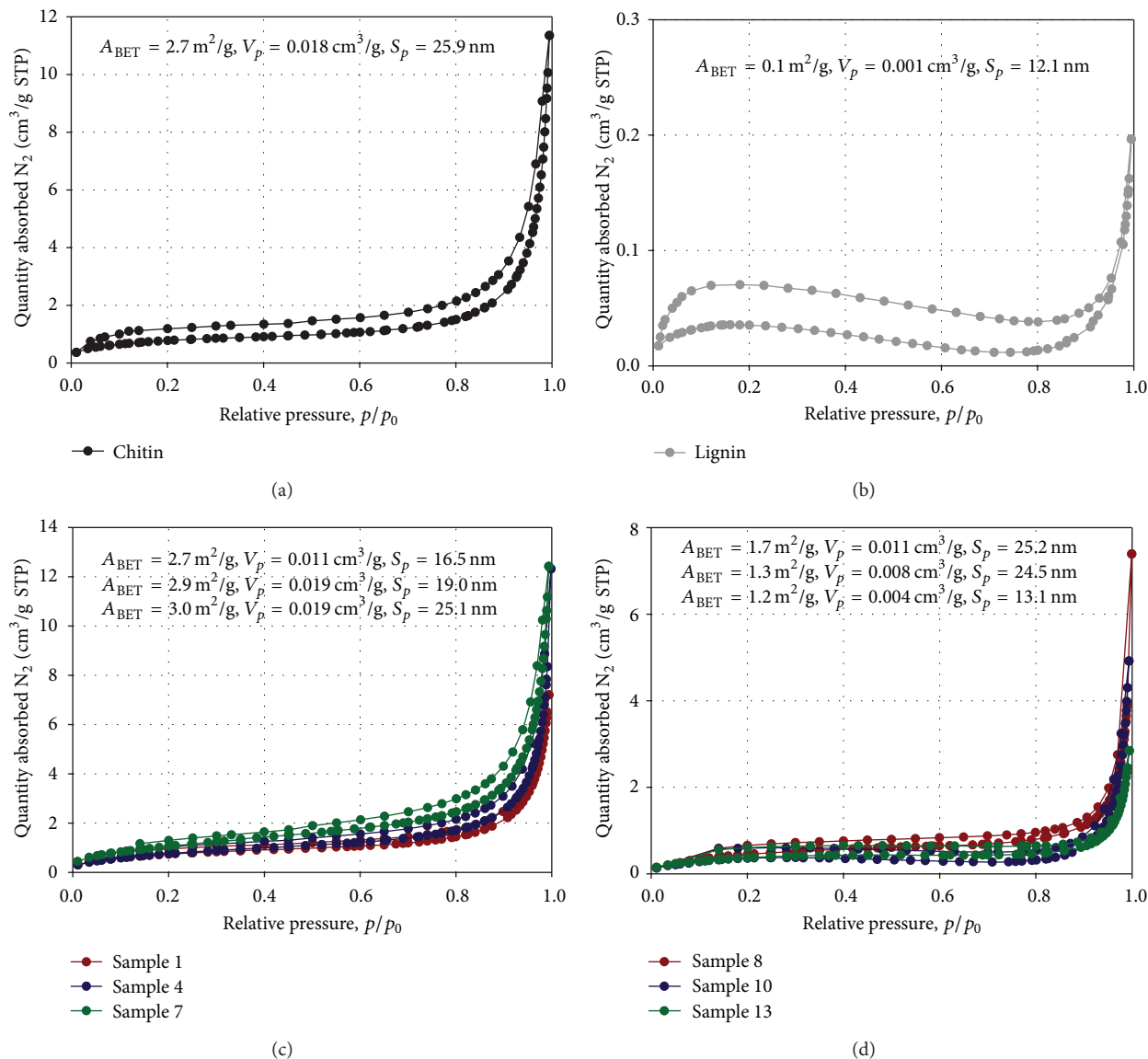


FIGURE 8: Nitrogen adsorption/desorption isotherms and adsorptive properties for chitin (a), lignin (b), and chitin/lignin materials ((c) and (d)).

determines total color change. For lignin its value is 58.24, and for chitin it is 14.41.

On analyzing the values of L^* , it is noticeable that for samples 1–7, containing a constant amount of chitin and gradually diminishing amount of lignin, the value of the parameter systematically increases, reaching a value of 83.95 for sample 7. This is similar to the value obtained for pure chitin. For chitin/lignin samples from 8 to 13, where the chitin fraction decreases, the brightness parameter L^* was found to decrease, down to a value of 50.98 for sample 13 (chitin : lignin ratio 0.25 : 1).

Comparing the values of parameters a^* and b^* for the final products 1–7, a progressive decrease in red (parameter a^*) and yellow (b^*) color is observed. For samples 8–13, the values of these parameters systematically increase, reflecting the increasing color intensity of the obtained materials in

which the content of chitin varies against a constant amount of lignin. The values of dE confirm the correctness of the measurements. Initially its value decreases (samples 1–7), but in the later stage it increases (samples 8–13). The results obtained in this phase of the study are in agreement with expectations and confirm the appropriateness of the proposed method of synthesis. This means that the products may be utilized in various fields of industry in which color is a significant factor in production.

4. Conclusions

Advanced multifunctional materials have been obtained as a combination of natural polymers: chitin powder from crab shells and Kraft lignin. These precursors underwent a mechanical milling process with simultaneous mixing in

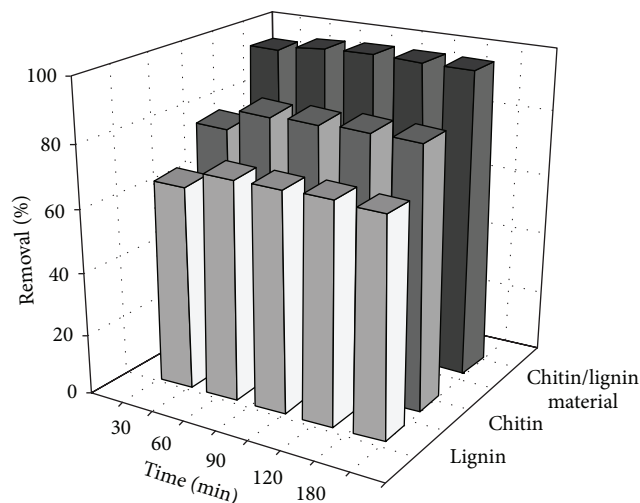


FIGURE 9: Effect of contact time on cadmium(II) removal efficiency by lignin, chitin, and chitin/lignin material.

TABLE 2: Colorimetric data of precursors (pure chitin and lignin) and chitin/lignin materials.

Sample number	Colorimetric data			
	L^*	a^*	b^*	dE
Pure chitin	85.47	1.42	14.43	14.41
Pure lignin	41.26	10.16	25.92	58.24
1	67.31	12.56	39.51	46.93
2	67.37	11.74	38.69	45.26
3	68.82	10.11	35.42	43.21
4	71.08	8.46	32.92	38.64
5	78.77	4.87	26.08	29.79
6	81.29	3.63	22.32	24.92
7	83.95	1.03	19.96	18.80
8	60.66	12.13	38.21	50.08
9	58.48	12.54	30.51	50.24
10	58.02	13.17	34.73	50.86
11	57.30	13.62	34.98	51.50
12	57.09	14.04	36.80	52.42
13	50.98	14.13	38.21	53.50

a centrifugal ball mill. The final chitin/lignin products and the precursors were subjected to detailed physicochemical, dispersive-morphological, electrokinetic, thermal, and colorimetric analyses. The effectiveness of the preparation of chitin/lignin materials was confirmed by FT-IR spectra and elemental analysis. We suggest that the formation of chitin/lignin materials occurs by hydrogen bonding of the -OH and =NH groups of chitin with -OH groups from lignin. Increasing the quantity of lignin relative to chitin results in an improvement in the thermal properties of the analyzed systems, thus creating an opportunity to utilize the materials in biodegradable polymer fillers. The results of electrokinetic (zeta) potential measurements confirm the effectiveness of the preparation of the chitin/lignin materials. Moreover, their good electrokinetic stability gives reason to

believe that they will find a wide spectrum of applications, including in medicine and pharmacy. Additionally, color measurements determined the most important colorimetric parameters, which may play a vital role in the production technology of new materials. The results of the analyses performed indicate that chitin/lignin hybrids act as excellent sorbents of heavy metal ions.

Acknowledgments

This work was supported by Poznan University of Technology research Grant no. 32-375/2013-DS, Mobilność Plus Program 920/MOB/2012/0, and DAAD Scholarship no. A/12/84687.

References

- [1] H. L. Chum, *Biomass (Organic Electrochemistry). An Introduction and Guide*, H. Lund and H. M. Baizer, Eds., Marcel Dekker, New York, NY, USA, 1991.
- [2] J. Ralph, K. Lundquist, G. Brunow et al., "Lignins: natural polymers from oxidative coupling of 4-hydroxyphenyl-propanoids," *Phytochemistry Reviews*, vol. 3, no. 1-2, pp. 29-60, 2004.
- [3] S. R. Collinson and W. Thielemans, "The catalytic oxidation of biomass to new materials focusing on starch, cellulose and lignin," *Coordination Chemistry Reviews*, vol. 254, no. 15-16, pp. 1854-1870, 2010.
- [4] M. Micic, K. Radotic, M. Jeremic, D. Djikanovic, and S. B. Kämmer, "Study of the lignin model compound supramolecular structure by combination of near-field scanning optical microscopy and atomic force microscopy," *Colloids and Surfaces B*, vol. 34, no. 1, pp. 33-40, 2004.
- [5] L. A. Donaldson, "Lignification and lignin topochemistry—an ultrastructural view," *Phytochemistry*, vol. 57, no. 6, pp. 859-873, 2001.
- [6] G. Milczarek, "Preparation and characterization of a lignin modified electrode," *Electroanalysis*, vol. 19, no. 13, pp. 1411-1414, 2007.
- [7] G. Milczarek, "Lignosulfonate-modified electrodes: electrochemical properties and electrocatalysis of NADH oxidation," *Langmuir*, vol. 25, no. 17, pp. 10345-10353, 2009.
- [8] G. Milczarek, "Kraft lignin as dispersing agent for carbon nanotubes," *Journal of Electroanalytical Chemistry*, vol. 638, no. 1, pp. 178-181, 2010.
- [9] G. Milczarek and T. Rebis, "Synthesis and electroanalytical performance of a composite material based on poly(3,4-ethylenedioxythiophene) doped with lignosulfonate," *International Journal of Electrochemistry*, vol. 2012, Article ID 130980, 7 pages, 2012.
- [10] S. K. Srivastava, A. K. Singh, and A. Sharma, "Studies on the uptake of lead and zinc by lignin obtained from black liquor—a paper industry waste material," *Environmental Technology*, vol. 15, no. 4, pp. 353-361, 1994.
- [11] D. Mohan, C. U. Pittman Jr., and P. H. Steele, "Single, binary and multi-component adsorption of copper and cadmium from aqueous solutions on Kraft lignin—a biosorbent," *Journal of Colloid and Interface Science*, vol. 297, no. 2, pp. 489-504, 2006.
- [12] S. Babel and T. A. Kurniawan, "Low-cost adsorbents for heavy metals uptake from contaminated water: a review," *Journal of Hazardous Materials*, vol. 97, no. 1-3, pp. 219-243, 2003.

- [13] T. Dizhbite, G. Zakis, A. Kizima et al., "Lignin—a useful bioresource for the production of sorption-active materials," *Bioresource Technology*, vol. 67, no. 3, pp. 221–228, 1999.
- [14] T. Kunanopparat, P. Menut, M.-H. Morel, and S. Guilbert, "Improving wheat gluten materials properties by Kraft lignin addition," *Journal of Applied Polymer Science*, vol. 125, no. 2, pp. 1391–1399, 2012.
- [15] A. A. Morandim-Giannetti, J. A. M. Agnelli, B. Z. Lanças, R. Magnabosco, S. A. Casarin, and S. H. P. Bettini, "Lignin as additive in polypropylene/coir composites: thermal, mechanical and morphological properties," *Carbohydrate Polymers*, vol. 87, no. 4, pp. 2563–2568, 2012.
- [16] J. N. Sheikh and K. H. Prabhu, "Chitin and chitosan biopolymers of the 21 st century," *International Dyer*, vol. 195, no. 7, pp. 20–25, 2010.
- [17] F. Khoussab and M. Yamabhai, "Chitin research revisited," *Marine Drugs*, vol. 8, no. 7, pp. 1988–2012, 2010.
- [18] Y. Wang, Y. Chang, L. Yu et al., "Crystalline structure and thermal property characterization of chitin from Antarctic krill (*Euphausia superba*)," *Carbohydrate Polymers*, vol. 92, no. 1, pp. 90–97, 2013.
- [19] S. Ifuku, M. Nogi, K. Abe et al., "Simple preparation method of chitin nanofibers with a uniform width of 10–20 nm from prawn shell under neutral conditions," *Carbohydrate Polymers*, vol. 84, no. 2, pp. 762–764, 2011.
- [20] W. Sajomsang and P. Gonil, "Preparation and characterization of α -chitin from cicada sloughs," *Materials Science and Engineering C*, vol. 30, no. 3, pp. 357–363, 2010.
- [21] E. Brunner, P. Richthammer, H. Ehrlich et al., "Chitin-based organic networks: an integral part of cell wall biosilica in the diatom thalassiosira pseudonana," *Angewandte Chemie International Edition*, vol. 48, no. 51, pp. 9724–9727, 2009.
- [22] H. Ehrlich, M. Maldonado, K.-D. Spindler et al., "First evidence of chitin as a component of the skeletal fibers of marine sponges. Part I. Verongidae (Demospongia: Porifera)," *Journal of Experimental Zoology B*, vol. 308, no. 4, pp. 347–356, 2007.
- [23] H. Ehrlich, M. Krautter, T. Hanke et al., "First evidence of the presence of chitin in skeletons of marine sponges. Part II. Glass sponges (Hexactinellida: Porifera)," *Journal of Experimental Zoology B*, vol. 308, no. 4, pp. 473–483, 2007.
- [24] E. Brunner, H. Ehrlich, P. Schupp et al., "Chitin-based scaffolds are an integral part of the skeleton of the marine demosponge *Ianthella basta*," *Journal of Structural Biology*, vol. 168, no. 3, pp. 539–547, 2009.
- [25] M. Rinaudo, "Chitin and chitosan: properties and applications," *Progress in Polymer Science*, vol. 31, no. 7, pp. 603–632, 2006.
- [26] K. Kurita, "Chitin and chitosan: functional biopolymers from marine crustaceans," *Marine Biotechnology*, vol. 8, no. 3, pp. 203–226, 2006.
- [27] R. Jayakumar, M. Prabakaran, P. T. Sudheesh Kumar, S. V. Nair, and H. Tamura, "Biomaterials based on chitin and chitosan in wound dressing applications," *Biotechnology Advances*, vol. 29, no. 3, pp. 322–337, 2011.
- [28] R. Jayakumar, K. P. Chennazhi, S. Srinivasan, S. V. Nair, T. Furuike, and H. Tamura, "Chitin scaffolds in tissue engineering," *International Journal of Molecular Sciences*, vol. 12, no. 3, pp. 1876–1887, 2011.
- [29] R. Jayakumar, A. Nair, N. S. Rejinold, S. Maya, and S. V. Nair, "Doxorubicin-loaded pH-responsive chitin nanogels for drug delivery to cancer cells," *Carbohydrate Polymers*, vol. 87, no. 3, pp. 2352–2356, 2012.
- [30] K. T. Smitha, A. Anitha, T. Furuike, H. Tamura, S. V. Nair, and R. Jayakumar, "In vitro evaluation of paclitaxel loaded amorphous chitin nanoparticles for colon cancer drug delivery," *Colloids and Surfaces B*, vol. 104, pp. 245–253, 2013.
- [31] H. Ehrlich, E. Steck, M. Ilan et al., "Three-dimensional chitin-based scaffolds from Verongida sponges (Demospongiae: Porifera). Part II: biomimetic potential and applications," *International Journal of Biological Macromolecules*, vol. 47, no. 2, pp. 141–145, 2010.
- [32] P. X. Pinto, S. R. Al-Abed, and D. J. Reisman, "Biosorption of heavy metals from mining influenced water onto chitin products," *Chemical Engineering Journal*, vol. 166, no. 3, pp. 1002–1009, 2011.
- [33] H. Tang, W. Zhou, and L. Zhang, "Adsorption isotherms and kinetics studies of malachite green on chitin hydrogels," *Journal of Hazardous Materials*, vol. 209–210, pp. 218–225, 2012.
- [34] K. Kurita, "Controlled functionalization of the polysaccharide chitin," *Progress in Polymer Science*, vol. 26, no. 9, pp. 1921–1971, 2001.
- [35] J. D. Kittle, C. Wang, C. Qian et al., "Ultrathin chitin films for nanocomposites and biosensors," *Biomacromolecules*, vol. 13, no. 3, pp. 714–718, 2012.
- [36] X. Wang and B. Xing, "Importance of structural makeup of biopolymers for organic contaminant sorption," *Environmental Science and Technology*, vol. 41, no. 10, pp. 3559–3565, 2007.
- [37] S. L. James, C. J. Adams, C. Bolm et al., "Mechanochemistry: opportunities for new and cleaner synthesis," *Chemical Society Reviews*, vol. 41, no. 1, pp. 413–447, 2012.
- [38] A. Tejado, C. Peña, J. Labidi, J. M. Echeverria, and I. Mondragon, "Physico-chemical characterization of lignins from different sources for use in phenol-formaldehyde resin synthesis," *Bioresource Technology*, vol. 98, no. 8, pp. 1655–1663, 2007.
- [39] M. G. Alriols, A. García, R. Llano-ponte, and J. Labidi, "Combined organosolv and ultrafiltration lignocellulosic biorefinery process," *Chemical Engineering Journal*, vol. 157, no. 1, pp. 113–120, 2010.
- [40] G. Cárdenas, G. Cabrera, E. Taboada, and S. P. Miranda, "Chitin characterization by SEM, FTIR, XRD, and ^{13}C cross polarization/mass angle spinning NMR," *Journal of Applied Polymer Science*, vol. 93, no. 4, pp. 1876–1885, 2004.
- [41] R. L. Lavall, O. B. G. Assis, and S. P. Campana-Filho, " β -Chitin from the pens of *Loligo* sp.: extraction and characterization," *Bioresource Technology*, vol. 98, no. 13, pp. 2465–2472, 2007.
- [42] M.-K. Jang, B.-G. Kong, Y.-I. Jeong, C. H. Lee, and J.-W. Nah, "Physicochemical characterization of α -chitin, β -chitin, and γ -chitin separated from natural resources," *Journal of Polymer Science A*, vol. 42, no. 14, pp. 3423–3432, 2004.
- [43] R. J. Krupadam, P. Sridevi, and S. Sakunthala, "Removal of endocrine disrupting chemicals from contaminated industrial groundwater using chitin as a biosorbent," *Journal of Chemical Technology and Biotechnology*, vol. 86, no. 3, pp. 367–374, 2011.
- [44] G. Annadurai, M. Chellapandian, and M. R. V. Krishnan, "Adsorption of reactive dye on chitin," *Environmental Monitoring and Assessment*, vol. 59, no. 1, pp. 111–119, 1999.
- [45] L. Raymond, F. G. Morin, and R. H. Marchessault, "Degree of deacetylation of chitosan using conductometric titration and solid-state NMR," *Carbohydrate Research*, vol. 246, pp. 331–336, 1993.
- [46] J. Li, J.-F. Revol, E. Naranjo, and R. H. Marchessault, "Effect of electrostatic interaction on phase separation behaviour of chitin crystallite suspensions," *International Journal of Biological Macromolecules*, vol. 18, no. 3, pp. 177–187, 1996.

- [47] W. Janusz and M. Matysek, "Coadsorption of Cd(II) and oxalate ions at the TiO₂/electrolyte solution interface," *Journal of Colloid and Interface Science*, vol. 296, no. 1, pp. 22–29, 2006.
- [48] D. Dong, A. L. Fricke, B. M. Moudgil, and H. Johnson, "Electrokinetic study of kraft lignin," *Tappi Journal*, vol. 79, no. 7, pp. 191–197, 1996.
- [49] Ł. Klapiszewski, M. Nowacka, G. Milczarek, and T. Jesionowski, "Physicochemical and electrokinetic properties of silica/lignin biocomposites," *Carbohydrate Polymers*, vol. 94, no. 1, pp. 345–355, 2013.
- [50] H. Harmita, K. G. Karthikeyan, and X. Pan, "Copper and cadmium sorption onto kraft and organosolv lignins," *Bioresource Technology*, vol. 100, no. 24, pp. 6183–6191, 2009.
- [51] D. Stawski, S. Rabiej, L. Herczyńska, and Z. Draczyński, "Thermogravimetric analysis of chitins of different origin," *Journal of Thermal Analysis and Calorimetry*, vol. 93, no. 2, pp. 489–494, 2008.
- [52] J. Rodríguez-Mirasol, T. Cordero, and J. J. Rodríguez, "CO₂-reactivity of eucalyptus kraft lignin chars," *Carbon*, vol. 31, no. 1, pp. 53–61, 1993.
- [53] M. Kijima, T. Hirukawa, F. Hanawa, and T. Hata, "Thermal conversion of alkaline lignin and its structured derivatives to porous carbonized materials," *Bioresource Technology*, vol. 102, no. 10, pp. 6279–6285, 2011.
- [54] S. Suhas, P. J. M. Carrott, and M. M. L. Ribeiro Carrott, "Lignin—from natural adsorbent to activated carbon: a review," *Bioresource Technology*, vol. 98, no. 12, pp. 2301–2312, 2007.
- [55] G. Telysheva, T. Dizhbite, L. Jashina et al., "Synthesis of lignin-based inorganic/organic hybrid materials favorable for detoxification of ecosystem components," *BioResources*, vol. 4, no. 4, pp. 1276–1284, 2009.
- [56] R. Saad and J. Hawari, "Grafting of lignin onto nanostructured silica SBA-15: preparation and characterization," *Journal of Porous Materials*, vol. 20, pp. 227–233, 2013.

Research Article

Magnetic Properties and Microstructure of $\text{FeO}_x/\text{Fe}/\text{FePt}$ and FeO_x/FePt Films

Jai-Lin Tsai, Po-Ran Chen, Yi-Hsiu Chen, and Qi-Shao Luo

Department of Materials Science and Engineering, National Chung Hsing University, 250 Kuo Kuang Road, Taichung 402, Taiwan

Correspondence should be addressed to Jai-Lin Tsai; tsajl@dragon.nchu.edu.tw

Received 9 July 2013; Revised 13 August 2013; Accepted 15 August 2013

Academic Editor: Guangyu Zhao

Copyright © 2013 Jai-Lin Tsai et al. This is an open access article distributed under the Creative Commons Attribution License, which permits unrestricted use, distribution, and reproduction in any medium, provided the original work is properly cited.

The $\text{Fe}(6\text{ nm})/\text{FePt}$ film with perpendicular magnetization was deposited on the glass substrate. To study the oxygen diffusion effect on the coupling of Fe/FePt bilayer, the plasma oxidation with 0.5~7% oxygen flow ratio was performed during sputtered part of Fe layer and formed the $\text{FeO}_x(3\text{ nm})/\text{Fe}(3\text{ nm})/\text{FePt}$ trilayer. Two-step magnetic hysteresis loops were found in trilayer with oxygen flow ratio above 1%. The magnetization in FeO_x and Fe/FePt layers was decoupled. The moments in FeO_x layer were first reversed and followed by coupled Fe/FePt bilayer. The trilayer was annealed again at 500°C and 800°C for 3 minutes. When the $\text{FeO}_x(3\text{ nm})/\text{Fe}(3\text{ nm})/\text{FePt}$ trilayer was annealed at 500°C, the layers structure was changed to $\text{FeO}_x(6\text{ nm})/\text{FePt}$ bilayer due to oxygen diffusion. The hard-magnetic $\text{FeO}_x(6\text{ nm})/\text{FePt}$ film was coupled with single switching field. The $\text{FeO}_x/(\text{disordered FePt})$ layer structure was observed with further annealing at 800°C and presented soft-magnetic loop. In summary, the coupling between soft-magnetic Fe , FeO_x layer, and hard-magnetic Ll_0 FePt layer can be controlled by the oxygen diffusion behavior, and the oxidation of Fe layer was tuned by the annealing temperature. The ordered Ll_0 FePt layer was deteriorated by oxygen and became disordered FePt when the annealed temperature was up to 800°C.

1. Introduction

Equiatomic FePt film with anisotropic face-centered tetragonal (fct) Ll_0 ordered structure has high magnetocrystalline anisotropy which is the promised material in energy assisted perpendicular magnetic recording. The Ll_0 FePt phase was ordered from disordered FePt phase with face-centered cubic (fcc) structure after high temperature annealing [1–6]. The disordered and Ll_0 FePt phases show soft- and hard-magnetic properties, respectively. The ordering degree can be changed from 0 (disordered) to 1 (ordered) that depends on the process temperature or condition. The granular structure with columnar grains [7, 8] and well c -axis alignment normal to the film surface with low switching field distribution are required for FePt perpendicular recording media. For c -axis alignment, [001] textured FePt films have been prepared on amorphous glass substrate or MgO underlayer with lower ordering temperatures [9–11]. To write in perpendicular recording media, measure can be taken from energy assisted writing process called heat assisted magnetic recording (HAMR) [12]. To down the writing temperature

under fixed writing field, minor adjusting of the intrinsic magnetic anisotropy of FePt film was required. The magnetic anisotropy and the coercivity of FePt film can be tuned by composition and the third element addition [13]. The [001] textured FePt film was not easily formed when target composition far deviated from equal atomic ration. In addition, the magnetic anisotropy was usually diluted by nonmagnetic doping. As a result, it is necessary to have high [001] textured FePt granular film with lower coercivity that was accepted by writing temperature and field. Traditionally, exchange spring media and exchange coupled composite (ECC) media with higher and lower magnetic anisotropic layer were introduced to reduce the writing field requirement and maintain the same thermal stability and grater insensitivity to easy axis [14–20]. The motivations of this work are try (1) to know the oxygen diffusion effects on magnetic properties of FePt film and prove the change of magnetic properties by the second annealing process, (2) to modify the morphology of dewetted FePt film by FeO_x , and (3) to study the coupling effect via $\text{FeO}_x/\text{Fe}/\text{FePt}$ trilayer structure. The structure of FeO_x may be cubic FeO , tetragonal $\gamma\text{-Fe}_2\text{O}_3$ (maghemite)

or spinel Fe_3O_4 (magnetite), with ferrimagnetism. Plasma oxidation and further annealing were proposed and proven to change the magnetic properties and microstructure of $\text{FeO}_x/\text{Fe}/\text{FePt}$ films. The [001] textured FeO_x/FePt dewetted film with perpendicular magnetization was also observed.

2. Experimental

The FePt film was deposited on a glass substrate at room temperature (RT) by magnetron sputtering. The sputtering system was designed for ultrahigh vacuum with base pressure of 5×10^{-8} Torr, and the load-lock system was used to transfer the substrate via prechamber with base pressure of 5×10^{-7} Torr. The FePt and Fe targets were used, and a working pressure was fixed at 1.5×10^{-3} Torr under high purity argon gas. The total thickness of FePt film is 10 nm, and the chemical composition of the FePt layer was $\text{Fe}_{48}\text{Pt}_{52}$ measured by an energy dispersive spectrometer (EDS) on a single thicker FePt layer. After deposition, the films were annealed under argon atmosphere by using a rapid thermal annealing process (RTP) at 800°C for 3 minutes with heating rate of $10^\circ\text{C}/\text{s}$ and formed the L1_0 FePt thin film. The Fe layer with thickness of 6 nm was deposited at RT on FePt film and formed the Fe/FePt bilayer. To study the oxygen diffusion effect on the coupling of Fe(6 nm)/FePt bilayer, the plasma oxidation with varied oxygen flow ratio [$P = P_{\text{O}_2}/(P_{\text{O}_2} + P_{\text{Ar}}) = 0.3, 0.5, 1, 3, 7\%$] was performed during sputtered part of Fe layer and formed the $\text{FeO}_x(3\text{ nm})/\text{Fe}(3\text{ nm})/\text{FePt}$ trilayer. More precisely, the oxygen was introduced during sputtering in half of the Fe layer thickness which is 3 nm. The trilayer was further annealed at 500°C , 800°C and finally formed the FeO_x/FePt , $\text{FeO}_x/(\text{disordered FePt})$, respectively. The thickness of each layer or sputtering rate of each material was measured by atomic force microscopy. The crystal structure of the samples was identified using a standard X-ray diffraction (XRD) technique (BRUKER, D8 Discover). The film microstructure was observed by scanning electron microscopy (JEOL JSM-6700F) and atomic force microscopy (DI 3100). The surface chemical property was measured by X-ray photoelectron spectroscopy ((XPS) PHI5000Versa-Probe). Magnetic hysteresis loops were measured at room temperature using a vibration sample magnetometer ((VSM) Lakeshore 7400) with a maximum magnetic field of 2T. The magnetic field was applied to be parallel and perpendicular to film surface to obtain in-plane and out-of-plane hysteresis loops, respectively.

3. Results and Discussion

Figures 1(a)–1(f) show standard XRD patterns of FePt single layer, Fe(6 nm)/FePt bilayer, and $\text{FeO}_x/\text{Fe}/\text{FePt}$ films. In Figure 1(a), the FePt single layer was ordered in L1_0 phase, and the (001) superlattice diffraction peak and the (002) fundamental reflection are clearly observed. The XRD profiles suggest that the L1_0 FePt crystal has a [001] texture. Figures 1(b)–1(f) show the XRD patterns of Fe(6 nm)/FePt bilayer and $\text{FeO}_x(P)/\text{Fe}/\text{FePt}$ trilayer ($P = 0.5, 1, 3, \text{ and } 7\%$). In Figures 1(b)–1(f), the L1_0 FePt films also show strong (001) and (002)

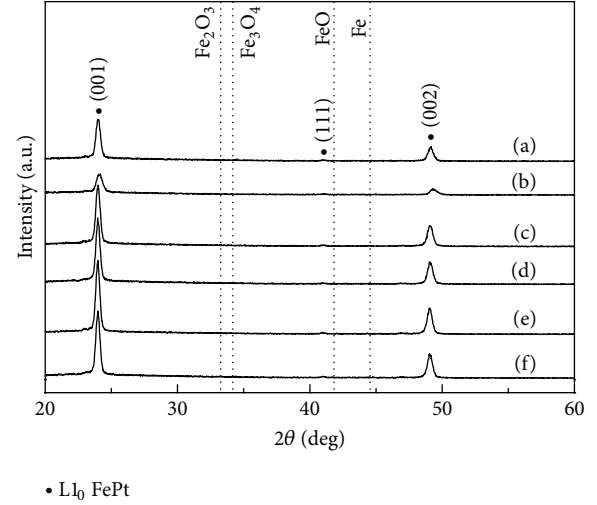


FIGURE 1: XRD patterns of (a) FePt single layer, (b) Fe(6 nm)/FePt bilayer, and $\text{FeO}_x(P)/\text{Fe}/\text{FePt}$ films with different oxygen flow ratios, $P =$ (c) 0.5%, (d) 1%, (e) 3%, and (f) 7%.

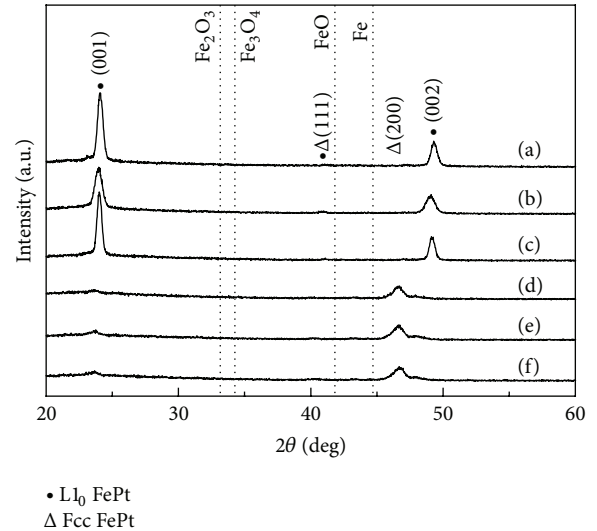


FIGURE 2: XRD patterns of $\text{FeO}_x(P)/\text{Fe}/\text{FePt}$ trilayer further annealed at 500°C with $P =$ (a) 1%, (b) 3%, and (c) 7% and 800°C with $P =$ (d) 1%, (e) 3%, (f) 7%.

peaks that were not smeared out by Fe and FeO_x deposited at RT. The peaks of Fe and FeO_x were not found in standard X-ray diffraction (XRD) due to strong FePt (001) texturing. The standard X-ray peaks of Fe (JCPDS 89-7194), FeO (JCPDS 89-7100), Fe_2O_3 (JCPDS 89-8104), and Fe_3O_4 (JCPDS 89-6466) were marked in Figures 1 and 2. The ordering parameter, S , was calculated from $(I_{(002)}^*/I_{(001)}^*)^{1/2} (I_{(001)}/I_{(002)})^{1/2}$ or proportional to $I_{(001)}/I_{(002)}$ ratio [21]. The $(I_{(002)}^*/I_{(001)}^*)^{1/2}$ value, for example, 0.4915 in L1_0 FePt film, was obtained after considering all the corrected factors in the XRD data. Fully-ordered L1_0 FePt X-ray diffraction peak intensity is given by $(I_{002}^*/I_{001}^*) = (|F|^2 \times \text{LPDA})_{002} / (|F|^2 \times \text{LPDA})_{001}$ [21]. For L1_0 FePt, the structure factor F is $F_{hkl} = f_{\text{Fe}}(1 + e^{\pi i(h+k)}) + f_{\text{Pt}}(e^{\pi i(k+l)} + e^{\pi i(h+l)})$, and f is atomic scattering factor [21]. The

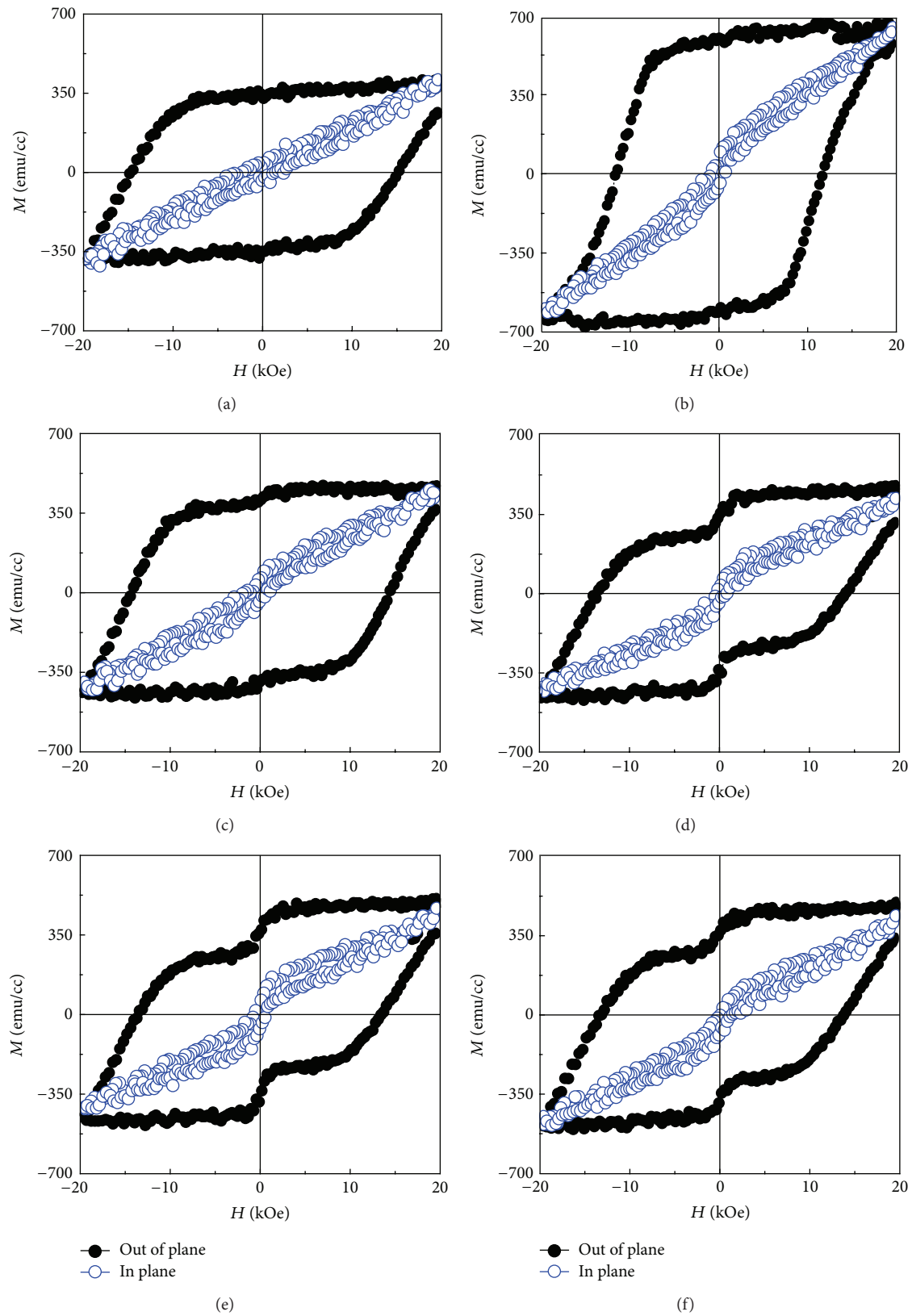


FIGURE 3: In-plane and out-of-plane magnetic hysteresis loops of (a) FePt single layer, (b) Fe(6 nm)/FePt bilayer, and $\text{FeO}_x(\text{P})/\text{Fe}/\text{FePt}$ films with different oxygen flow ratios; $P =$ (c) 0.5%, (d) 1%, (e) 3%, and (f) 7%.

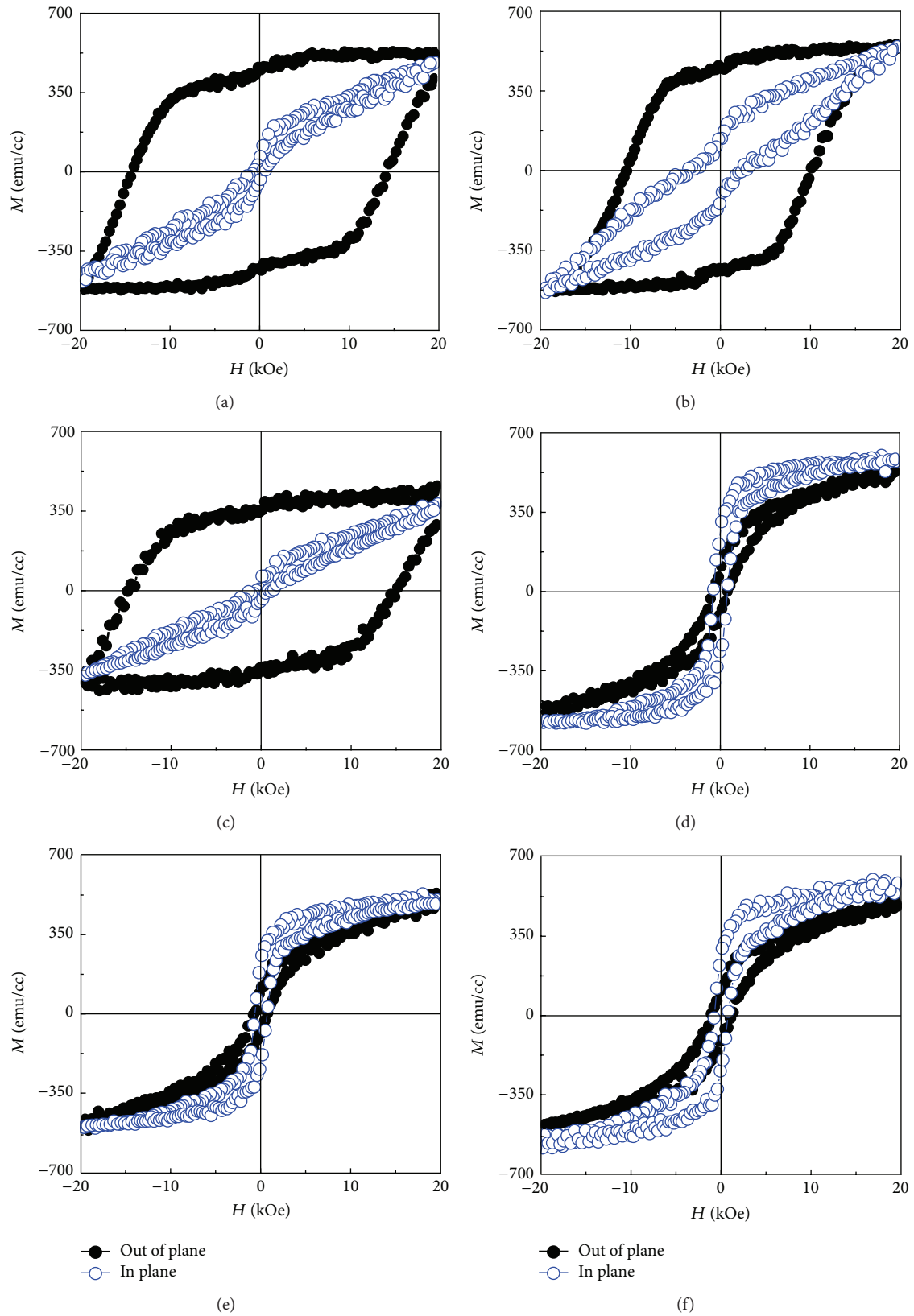


FIGURE 4: In-plane and out-of-plane magnetic hysteresis loops of $\text{FeO}_x(\text{P})/\text{Fe}/\text{FePt}$ trilayer further annealed at 500°C with $P =$ (a) 1%, (b) 3%, and (c) 7% and 800°C with $P =$ (d) 1%, (e) 3%, and (f) 7%.

Lorentz factor (L) is $[1/\sin^2(\theta)\cos(\theta)]$, and the polarization factor (P) is $(1 + \cos^2(2\theta))$. The temperature factor (D) is e^{-2M} and $M = (\sin(\theta)/\lambda)^2$, and absorption factor (A) is $1 - \exp(-2\mu t/(\sin\theta))$. The average mass absorption coefficient was estimated as $\mu = [\mu_{\text{Fe}} \times \text{wt}\% \text{Fe} + \mu_{\text{Pt}} \times \text{wt}\% \text{Pt}] \times [X_{\text{Fe}}\rho_{\text{Fe}} + X_{\text{Pt}}\rho_{\text{Pt}}]$ [21], and the value is 3323.8 in this study. Here, X_{Fe} , X_{Pt} and ρ_{Fe} , ρ_{Pt} are the atomic fraction and density of Fe and Pt, respectively. The values for μ_{Fe} and μ_{Pt} are tabulated [21]. $I_{(001)}^*$ and $I_{(002)}^*$ mean the theoretical integrated intensity of X-ray diffraction peaks, and the $I_{(001)}$ and $I_{(002)}$ are the integrated peak intensity from the experimental results for a partially ordered film. In Figure 1(a), the ordering parameter S estimated from $(I_{(002)}^*/I_{(001)}^*)^{1/2}(I_{(001)}/I_{(002)})^{1/2}$ is 0.75, and the S value in Figures 1(c)–1(f) is 0.71~0.72.

Figures 2(a)–2(f) show standard XRD patterns of $\text{FeO}_x/\text{Fe}/\text{FePt}$ trilayer further annealed at 500°C and 800°C, respectively. In Figures 2(a)–2(c), the $\text{FeO}_x/\text{Fe}/\text{FePt}$ trilayer was further annealed at 500°C and became FeO_x/FePt bilayer. In addition to the wideness (full width of half maximum (FWHM)) of (001) and (002) peaks in Figure 2(b), the $L1_0$ FePt still shows strong (001) texture. It means that the $L1_0$ FePt layer was not influenced almost by further being annealed at 500°C. In Figures 2(d)–2(f), the $\text{FeO}_x/\text{Fe}/\text{FePt}$ trilayer was further annealed at 800°C, and the (001) texture was almost diminished, and (200) disordered FePt peak was observed. It is suggested that the oxygen was diffused into the $L1_0$ FePt layer and the layer, structure was changed to $\text{FeO}_x/(\text{disordered FePt})$. The FePt (111) peak was not found in standard XRD patterns in Figures 1 and 2 due to strong FePt (001) texture. The ordered or disordered FePt (111) peak was indexed in grazing incident X-ray diffraction (GID). The nonsymmetric GID was used to measure the grains in nonoriented area in textured film.

Figure 3 shows in-plane and out-of-plane magnetic hysteresis loops of FePt single layer, Fe(6 nm)/FePt bilayer, and $\text{FeO}_x(3 \text{ nm})/\text{Fe}(3 \text{ nm})/\text{FePt}$ trilayer. In Figure 3(a), the FePt single layer shows high perpendicular magnetization, and the out-of-plane coercivity (H_c) is 15.3 kOe. The component in in-plane magnetization is nearly zero and shows the linear loop. In Figure 3(b), the magnetization was increased, and the H_c was reduced to 11.8 kOe in soft/hard exchange coupled Fe/FePt bilayer. Figures 3(c)–3(f) show the loops of $\text{FeO}_x/\text{Fe}/\text{FePt}$ trilayer with different oxygen flow ratios [$P = P_{\text{O}_2}/(P_{\text{O}_2} + P_{\text{Ar}}) = 0.5, 1, 3, 7\%$]. In Figure 3(c), there is just a minor shoulder in the loop of $\text{FeO}_x/\text{Fe}/\text{FePt}$ film with low oxygen flow ratios ($P = 0.5\%$). When the oxygen flow ratio was increased to 1, 3, and 7%, the step or shoulder was found in magnetization curve in Figures 3(d)–3(f). The FeO_x layer was decoupled to the Fe/FePt bilayer and reversed the magnetization previously. The magnetization in FeO_x layer was decreased as the negative applied field increased, and, up to the critical value, the magnetization was not changed with increased field. The critical value was defined as the H_c of FeO_x layer. In Figures 3(d)–3(f), the H_c of the FeO_x layer is 1.37, 1.66, and 1.09 kOe, and the H_c values of Fe(3 nm)/FePt bilayer are 13.7, 13.7, and 13.4 kOe, respectively. The H_c value of Fe(3 nm)/FePt is between FePt single layer in Figure 3(a) and Fe(6 nm)/FePt in Figure 3(b).

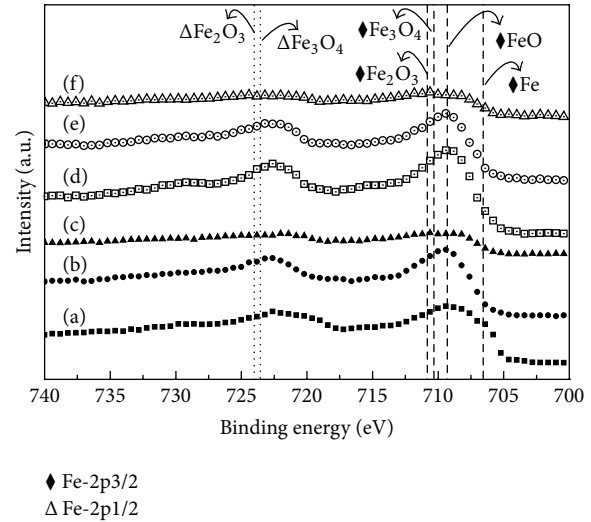


FIGURE 5: The Fe-2p X-ray photoelectron spectra of $\text{FeO}_x(3 \text{ nm})/\text{Fe}(3 \text{ nm})/\text{FePt}$ films at the depth position below 3 nm from film surface: (a) RT, (b) 500°C, and (c) 800°C, and at the depth position within 3 nm from film surface: (d) RT, (e) 500°C, and (f) 800°C.

The samples in Figures 3(d)–3(f) are the same to Figures 4(a)–4(c). The trilayers (samples in Figures 3(d)–3(f)) were further annealed at 500°C and 800°C, respectively. Figure 4 shows in-plane and out-of-plane magnetic hysteresis loops of annealed $\text{FeO}_x(3 \text{ nm})/\text{Fe}(3 \text{ nm})/\text{FePt}$ trilayer. Figures 4(a)–4(c) show the loops of $\text{FeO}_x(3 \text{ nm})/\text{Fe}(3 \text{ nm})/\text{FePt}$ films annealed at 500°C with oxygen flow ratios of 1%, 3%, and 7%, respectively. The shoulders appearing in the loops in Figures 3(d)–3(f) disappeared after further annealing, and the loops present single magnetization reversal process. It suggested that the Fe layer was further oxidative, and the layer structure was changed to exchange coupled FeO_x/FePt film. In Figures 4(a)–4(c), the out-of-plane H_c were 14.4, 10.4, and 14.8 kOe which are similar to the measured H_c in Figures 3(d)–3(f). Figures 4(d)–4(f) show the loops of $\text{FeO}_x(3 \text{ nm})/\text{Fe}(3 \text{ nm})/\text{FePt}$ films annealed at 800°C with oxygen flow ratios of 1%, 3%, and 7%, respectively, and the soft-magnetic loops were obtained. The oxygen was diffused into FePt layer and disordered the $L1_0$ phase, and the layer structure was changed to $\text{FeO}_x/(\text{disordered FePt})$. In summary, the interlayer coupling and magnetic anisotropy were tuned by the kinetic diffusion behavior of oxygen driven by temperature.

To understand the oxidation state of Fe and FeO_x (oxygen flow ratio of 3%) layer in $\text{FeO}_x(3 \text{ nm})/\text{Fe}(3 \text{ nm})/\text{FePt}$ film, XPS were performed on samples with different depth profiles. Figures 5(a)–5(c) show the Fe-2p X-ray photoelectron spectra of $\text{FeO}_x(3 \text{ nm})/\text{Fe}(3 \text{ nm})/\text{FePt}$ films at the depth position below 3 nm from film surface. The curve in Figure 5(a) shows the Fe^0 spectrum that is obtained in $\text{FeO}_x(3 \text{ nm})/\text{Fe}(3 \text{ nm})/\text{FePt}$ film without further annealing. The metallic $\text{Fe-2p}_{3/2}$ shows the peak at the binding energy of 706.5 eV [22]. In Figure 5(b), the $\text{FeO}_x(3 \text{ nm})/\text{Fe}(3 \text{ nm})/\text{FePt}$ films were further annealed at 500°C, and the binding energy shifts the $\text{Fe-2p}_{3/2}$ core level to 709~711 eV. This shift may

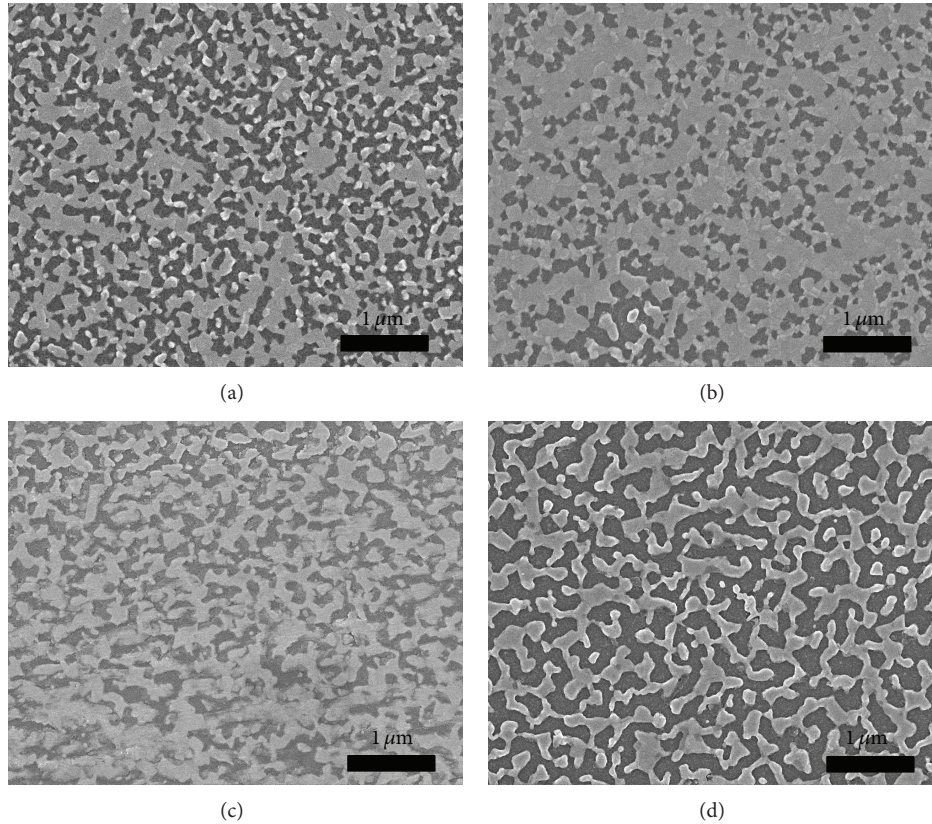


FIGURE 6: SEM images of (a) Fe/FePt film, (b) $\text{FeO}_x(7\%)/\text{Fe}/\text{FePt}$ trilayer, (c) $\text{FeO}_x(7\%)/\text{Fe}/\text{FePt}$ film annealed at 500°C , and (d) $\text{FeO}_x(7\%)/\text{Fe}/\text{FePt}$ film annealed at 800°C .

prove the formation of iron in the Fe^{2+} oxidation state that was FeO, and the binding energy of the Fe- $2p_{3/2}$ core level was shifted around to 709.6 eV [23]. In Figure 5(c), the $\text{FeO}_x(3\text{ nm})/\text{Fe}(3\text{ nm})/\text{FePt}$ films were further annealed at 800°C , and the peak was smeared out in the iron-oxide area. Figures 5(d)–5(f) show the Fe-2p X-ray photoelectron spectra of $\text{FeO}_x(3\text{ nm})/\text{Fe}(3\text{ nm})/\text{FePt}$ films at the depth within 3 nm from film surface. In Figures 5(d)–5(e), the FeO_x layer before and after further annealing at 500°C was in the Fe^{2+} oxidation state that was FeO, and the binding energy of the Fe- $2p_{3/2}$ core level was shifted around to 709.3 eV. In Figure 5(f), the peak was also smeared out in the iron-oxide area when annealed at 800°C . In summary, first, further annealed at 500°C , the Fe (3 nm) may oxidize or mix with FePt film and form FeO_x/FePt layer structure. Second, further annealed at 800°C , the oxygen was diffused into the FePt lattice, deteriorated the ordering degree, and formed the $\text{FeO}_x/(\text{disorder FePt})$ film.

Figure 6 shows the scanning electron microscopy (SEM) image of Fe(6 nm)/FePt and $\text{FeO}_x(3\text{ nm})/\text{Fe}(3\text{ nm})/\text{FePt}$ films with oxygen flow ration of 7%. In Figure 6(a), the annealed Fe(6 nm)/FePt film was dewetted in the network structure, and the dewetted area was 44%. When the Fe layer was partially plasma oxidized and formed the $\text{FeO}_x(3\text{ nm})/\text{Fe}(3\text{ nm})/\text{FePt}$ layer structure, the dewetted area was reduced to 30% as shown in Figure 6(b). The FeO_x has lower surface energy than FePt and was easy to wet on the glass substrate. As a result, the dewetted area

was reduced around 14%. In Figures 6(c) and 6(d), the $\text{FeO}_x(3\text{ nm})/\text{Fe}(3\text{ nm})/\text{FePt}$ film was further annealed at 500°C , 800°C , and the dewetted area was 42%, 55%, respectively. Due to large difference of surface energy between FePt and glass substrate, the dewetted area was increased again with annealing temperature.

Figure 7 shows the surface roughness of Fe/FePt and $\text{FeO}_x/\text{Fe}/\text{FePt}$ film with oxygen flow ration of 7% measured by atomic force microscopy (AFM). In Figure 7(a), the average surface roughness of Fe/FePt film was 7.1 nm. In Figures 7(b) and 7(c), when the FeO_x layer was capped on Fe/FePt film at RT without annealing or with further annealing at 500°C , the average surface roughness became 4.9 nm and 3.2 nm, respectively. In Figure 7(d), the surface roughness was up to 13 nm when the annealed temperature was high to 800°C . In summary, the dewetted area in Fe/FePt film was partially covered by FeO_x layer deposited at RT but aggregated into small area again with further annealing at high temperature. The surface roughness shows the same tendency to the dewetted area. The FePt film with thickness of 10 nm was dewetted due to strain release when the ordering (rapid phase transformation) was complete at 800°C . The dewetted area and surface roughness were increased with annealing temperature, and the critical dewetted temperature is 650°C in this study. After annealing, the sample was cooled down naturally in the argon atmosphere in RTP system. Cooling rate was not changed in this experiment and will be check in the future.

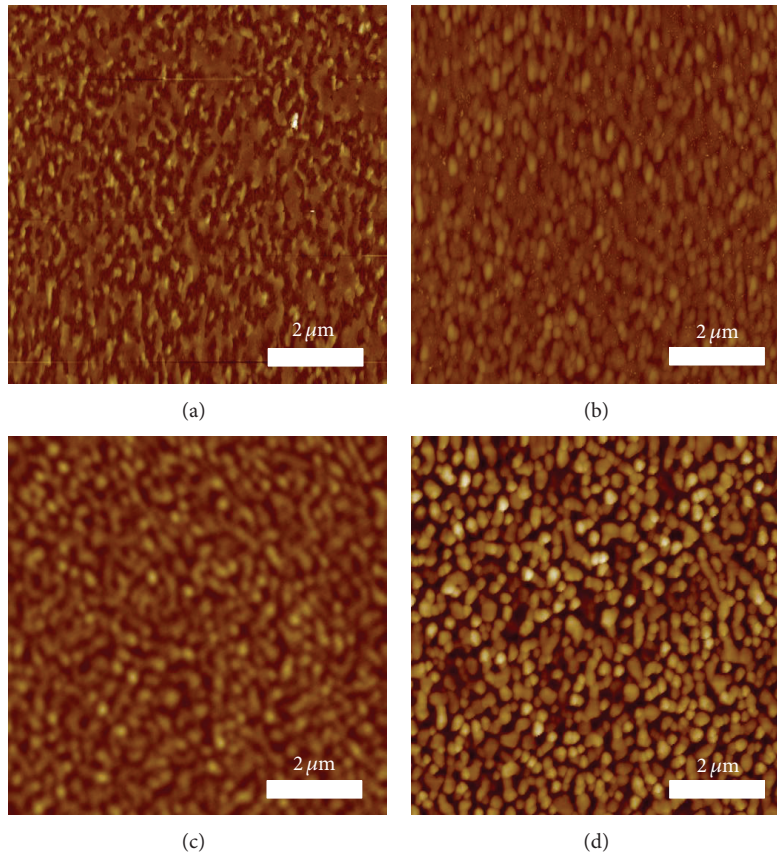


FIGURE 7: AFM images of (a) Fe/FePt film, (b) $\text{FeO}_x(7\%)/\text{Fe}/\text{FePt}$ trilayer, (c) $\text{FeO}_x(7\%)/\text{Fe}/\text{FePt}$ film annealed at 500°C , and (d) $\text{FeO}_x(7\%)/\text{Fe}/\text{FePt}$ film annealed at 800°C .

4. Conclusions

The plasma oxidation was performed during sputtered part of Fe layer in Fe/FePt film and formed the $\text{FeO}_x(3\text{ nm})/\text{Fe}(3\text{ nm})/\text{FePt}$ trilayer. The magnetization in FeO_x and Fe/FePt layers was decoupled and shown the shoulders in hysteresis loops. When the $\text{FeO}_x(3\text{ nm})/\text{Fe}(3\text{ nm})/\text{FePt}$ trilayer was further annealed at 500°C , the layers structure was changed to $\text{FeO}_x(6\text{ nm})/\text{FePt}$ bilayer due to oxygen diffusion. The hard-magnetic $\text{FeO}_x(6\text{ nm})/\text{FePt}$ film was coupled with single switching field. The coupling between soft-magnetic Fe, FeO_x layer, and hard-magnetic L_{10} FePt layer was tuned by two-stage annealing process.

Acknowledgments

The authors would like to thank the National Science Council, Taiwan, for financial support under the Grant no. NSC 102-2221-E-005-025. They also thank the Center of Nanoscience and Nanotechnology in NCHU for TEM investigations.

References

- [1] D. Weller, A. Moser, L. Folks et al., "High ku materials approach to 100 gbits/in²," *IEEE Transactions on Magnetics*, vol. 36, no. 1, pp. 10–15, 2000.
- [2] M. H. Hong, K. Hono, and M. Watanabe, "Microstructure of FePt/Pt magnetic thin films with high perpendicular coercivity," *Journal of Applied Physics*, vol. 84, pp. 4403–4409, 1998.
- [3] S. N. Piramanayagam, "Perpendicular recording media for hard disk drives," *Journal of Applied Physics*, vol. 102, no. 1, Article ID 011301, 22 pages, 2007.
- [4] H. J. Richter, "The transition from longitudinal to perpendicular recording," *Journal of Physics D*, vol. 40, no. 9, article R149, 2007.
- [5] J. P. Liu, C. P. Luo, Y. Liu, and D. J. Sellmyer, "High energy products in rapidly annealed nanoscale Fe/Pt multilayers," *Applied Physics Letters*, vol. 72, no. 4, article 483, 3 pages, 1998.
- [6] T. Shima, K. Takashi, Y. K. Takahashi, and K. Hono, "Formation of octahedral FePt nanoparticles by alternate deposition of FePt and MgO," *Applied Physics Letters*, vol. 88, no. 6, Article ID 063117, 3 pages, 2006.
- [7] H. H. Li, J. F. Hu, G. Ju, G. M. Chow, and J. S. Chen, "Effects of CrRu-SiO_x underlayer with MgO intermediate layer on the microstructure and magnetic properties of FePt-C film," *Journal of Applied Physics*, vol. 109, Article ID 07A736, 2009.
- [8] E. Yang, H. Ho, D. E. Laughlin, and J. G. Zhu, "Columnar grain growth of FePt(L10) thin films," *Journal of Applied Physics*, vol. 111, Article ID 07B720, 2012.
- [9] Y. Xu, J. S. Chen, and J. P. Wang, "In situ ordering of FePt thin films with face-centered-tetragonal (001) texture on Cr_{100-x}Ru_x underlayer at low substrate temperature," *Applied Physics Letters*, vol. 80, no. 18, article 3325, 3 pages, 2002.

- [10] Y. C. Wu, L. W. Wang, and C. H. Lai, "Low-temperature ordering of (001) granular FePt films by inserting ultrathin SiO₂ layers," *Applied Physics Letters*, vol. 91, no. 7, Article ID 072502, 3 pages, 2007.
- [11] M. L. Yan, N. Powers, and D. J. Sellmyer, "Highly oriented nonepitaxially grown L1₀ FePt films," *Journal of Applied Physics*, vol. 93, no. 10, article 8292, 3 pages, 2003.
- [12] M. H. Kryder, E. C. Gage, T. W. Mcdaniel et al., "Heat assisted magnetic recording," *Proceedings of the IEEE*, vol. 96, no. 11, pp. 1810–1835, 2008.
- [13] D. A. Gilbert, L. W. Wang, T. J. Klemmer, J. U. Thiele, C. H. Lai, and K. Liu, "Tuning magnetic anisotropy in (001) oriented L10 (Fe_{1-x}Cu_x)₅₅Pt₄₅ films," *Applied Physics Letters*, vol. 102, no. 13, Article ID 132406, 4 pages, 2013.
- [14] J. L. Tsai, H. T. Tzeng, and G. B. Lin, "Magnetization reversal process in Fe/FePt films," *Applied Physics Letters*, vol. 96, no. 3, Article ID 032505, 3 pages, 2010.
- [15] R. H. Victora and X. Shen, "Composite media for perpendicular magnetic recording," *IEEE Transactions on Magnetics*, vol. 41, no. 2, pp. 537–542, 2005.
- [16] A. Yu. Dobin and H. J. Richter, "Domain wall assisted magnetic recording," *Applied Physics Letters*, vol. 89, no. 6, Article ID 062512, 3 pages, 2006.
- [17] D. Goll and A. Breitling, "Coercivity of ledge-type L1₀-FePt/Fe nanocomposites with perpendicular magnetization," *Applied Physics Letters*, vol. 94, no. 5, Article ID 052502, 3 pages, 2009.
- [18] D. Suess, "Multilayer exchange spring media for magnetic recording," *Applied Physics Letters*, vol. 89, no. 11, Article ID 113105, 3 pages, 2006.
- [19] J. L. Tsai, H. T. Tzeng, and B. F. Liu, "Magnetic properties and microstructure of graded Fe/FePt films," *Journal of Applied Physics*, vol. 107, no. 11, Article ID 113923, 5 pages, 2010.
- [20] A. Goncharov, T. Schrefl, G. Hrkac et al., "Recording simulations on graded media for area densities of up to 1 Tbit in 2," *Applied Physics Letters*, vol. 91, no. 22, Article ID 222502, 2007.
- [21] S. D. Granz and M. H. Kryder, "Granular L1₀ FePt (0 0 1) thin films for heat assisted magnetic recording," *Journal of Magnetism and Magnetic Materials*, vol. 324, no. 3, pp. 287–294, 2012.
- [22] D. D. Hawn and B. M. Dekoven, "Deconvolution as a correction for photoelectron inelastic energy losses in the core level XPS spectra of iron oxides," *Surface and Interface Analysis*, vol. 10, no. 2-3, pp. 63–74, 1987.
- [23] D. Brion, "Etude par spectroscopie de photoelectrons de la degradation superficielle de FeS₂, CuFeS₂, ZnS et PbS a l'air et dans l'eau," *Results Applied Surface Science*, vol. 5, no. 2, pp. 133–152, 1980.

Research Article

Cytocompatibility of Plasma and Thermally Treated Biopolymers

**Petr Slepíčka,¹ Iva Michaljaničová,¹ Nikola Slepíčková Kasálková,¹
Petr Sajdl,² Zdeňka Kolská,³ and Václav Švorčík¹**

¹ Department of Solid State Engineering, Institute of Chemical Technology, 166 28 Prague, Czech Republic

² Department of Power Engineering, Institute of Chemical Technology, 166 28 Prague, Czech Republic

³ Faculty of Science, J. E. Purkyně University, 400 96 Ústí nad Labem, Czech Republic

Correspondence should be addressed to Petr Slepíčka; petr.slepicka@vscht.cz

Received 3 June 2013; Revised 21 June 2013; Accepted 21 June 2013

Academic Editor: Jiamin Wu

Copyright © 2013 Petr Slepíčka et al. This is an open access article distributed under the Creative Commons Attribution License, which permits unrestricted use, distribution, and reproduction in any medium, provided the original work is properly cited.

This paper is focused on the surface characterization of plasma and consequently thermally treated biocompatible polymers. PLLA (poly(L-lactide acid) and PMP (poly-4-methyl-1-pentene) are studied. The influence of Ar plasma treatment on the surface polarity of substrate measured immediately after treatment and during the polymer surface aging is studied. Surface roughness, morphology, wettability, and surface chemistry were determined. Plasma treatment leads to significant changes in PLLA surface morphology and chemistry, with the PMP being slightly affected. The higher resistance to plasma fluence results in smaller ablation of PMP than that of PLLA. The plasma treatment improves cell adhesion and proliferation on the PMP. Plasma treatment of PLLA influences mostly the homogeneity of adhered and proliferated VSMC.

1. Introduction

The aim of the material engineering is to observe and modify the properties of materials with the purpose of consecutive application in different branches of science and engineering. The interdisciplinary studies are arising from the fields of applied physics and chemistry, which are focusing on the relationships between materials' structure on the molecular and atomic levels and their macroscopic behavior. The nanotechnology allows for manipulating and studying the materials on an atomic level (or the properties less than 100 nm in one dimension), so that both the manipulation and sensitive analysis can be performed [1]. The nanotechnology involves the study of metals, semiconductors, special glasses, and also polymers in different forms, which can be also applied as biomaterials.

The observations in this field are crucial for the applications in medicine, pharmacology, biology, tissue engineering [2], or material science. The usage of biomaterials (polymers, ceramics, and others) can be found in dental replacements

[3], orthopedic or spinal implants [4], or the materials for the application of targeted drug release [5]. The biomaterials can be either separate types, for example, metals, ceramics or polymers, or their combinations of specific type, composites, which are combined from one or more substances with different properties. The biocompatibility of polymeric materials can be also increased by excimer lamp irradiation [6] ion beam modification [7] or consequent carbon layer deposition [8]. Such materials can be successfully applied in tissue engineering [9, 10].

Polymers exhibit interesting mechanical and physicochemical properties as a scaffold in tissue engineering [11]. The surface physicochemical properties of polymer cell carriers can be also improved by surface grafting processes [12–14], which can mainly enhance the cell adhesion and proliferation. The methods of modification allow significant changes of surface properties, while the bulk properties (mostly mechanical) remain almost unchanged. Application of biomaterials for the cell cultivation is determined by the cell adhesion and their consecutive cell growth. Cell adhesion

or their tenacity is closely connected with material surface properties, for example, its wettability, polarity, surface energy, electrical properties, morphology, roughness, and chemical structure. These properties can be also naturally altered by various types of surface modification [15–17]. Wettability (water contact angle) is one of the most important parameters influencing the cell's adhesion. The contact angle measurement is mostly used for its quantitative analysis. There is no "optimal" contact angle for the cell adhesion and proliferation in common; different cell types "need," for example, different surface polarity and surface roughness. Neither too hydrophilic nor hydrophobic materials are demanded [18]. For example, the observation of adhesion and growth of Chinese hamster ovary (CHO) cells revealed that the best results were obtained for the surface with contact angle of 50° [19]. The amount of "well" adhered cells can be also influenced by the chemical structure, that is, types of functional group present on the polymer surface and their concentration.

This work studies surface properties of two materials: (i) poly(L-lactide acid) (PLLA) and (ii) poly-4-methyl-1-pentene (PMP). The PLLA substrate was chosen since it is biodegradable polymer; the biodegradation after successful growth of different types of cell lines is its great benefit. PMP is widely used polymer in tissue engineering with excellent mechanical properties. Therefore the improvement of its biocompatibility and the altering of its surface properties are of great importance. The initial part is devoted to the influence of modification of Ar plasma on polarity immediately after modification and during aging process. The thickness of ablated layer and surface morphology induced by plasma was determined. In the next section, attention is paid to thermal stress in combination with plasma adjustment, during which the study was focused on the surface morphology. The results from adhesion and proliferation of cells on selected substrates are also presented.

2. Materials and Methods

2.1. Materials, Plasma, and Heat Treatment. Biopolymer (i) poly(L-lactide acid) (PLLA, density 1.25 g cm^{-3} , $T_g = 60^\circ\text{C}$, crystallinity 60–70%, $50 \mu\text{m}$ thick foils, supplied by Goodfellow, Ltd.) and (ii) linear isotactic poly-4-methyl-1-pentene (PMP, density 0.835 g cm^{-3} , $T_g = 25^\circ\text{C}$, $T_m = 228^\circ\text{C}$, crystallinity 52%, $50 \mu\text{m}$ thick foils, supplied by Goodfellow, Ltd.) were used for the experiments.

The samples were modified in diode plasma discharge on Balzers SCD 050 device for 0–480 s, using DC Ar plasma (gas purity was 99.997%, power 5 and 10 W). Chamber parameters were Ar flow 0.3 l s^{-1} , Ar pressure 10 Pa, electrode area 48 cm^2 , the interelectrode electrode distance of 50 mm, and chamber volume 1000 cm^3 .

Thermal treatment of the polymers was accomplished in thermostat BINDER. The samples were heated at 60°C (PLLA) and 160°C (PMP, Vicat softening point). The pristine and modified samples (immediately after plasma treatment) were heated for 30 minutes and then they were cooled down to room temperature.

2.2. Measurement Techniques

2.2.1. Contact Angle and Surface Free Energy. Contact angle was determined by goniometry with static water drop method. The measurements of water contact angles (error $\pm 5\%$) were performed using distilled water (9 different positions) using the Surface Energy Evaluation System (SEE System, Advex Instruments, Czech Republic). By Automatic pipette the water drop of volume (8.0 ± 0.2) mL was deposited on the polymer's surface and the consequent photo was evaluated. Estimation of surface energy was also based on a measurement with SEE System, and two liquids (water and glycerol) were used. On the basis of Owens-Wendt method the values of surface free energy for the two liquids were evaluated. The measurement was carried out at room temperature.

2.2.2. X-Ray Photoelectron Spectroscopy. The presence of oxygen and carbon in the modified PMP and PLLA surface layer was proved by X-ray photoelectron spectroscopy (XPS). An Omicron Nanotechnology ESCAProbeP spectrometer was used. The exposed and analyzed area had a dimension of $2 \times 3 \text{ mm}^2$. The X-ray source was monochromated at 1486.7 eV and the measurement was performed with a step size of 0.05 eV. Characteristic O(1s) and C(1s) S(2s) peaks were searched for. Atomic concentrations of elements were determined by CASA XPS program using integrated area of spectrum lines and relative sensitivity factors which are quoted in the database of CASA XPS. The intensity calibration was carried out by the measurement of copper and the calculation of calibration constant for each used pass energy.

2.2.3. Surface Morphology. Surface morphology and roughness of the pristine and modified polymer samples were examined by the AFM technique using a VEECO CP II device in tapping mode. A Si probe RTESPA-CP with the spring constant $20\text{--}80 \text{ N m}^{-1}$ was used. The mean roughness value (R_a) represents the arithmetic average of the deviations from the central plane of the sample.

2.2.4. Gravimetry. Thickness of the ablated surface layer after plasma treatment was measured using a Mettler Toledo UMX2. In order to enhance the sensitivity of the measurement the samples (diameter 2.5 cm) were exposed to plasma from both sides. The thickness of the ablated layer was calculated from the change in weight of 10 samples before and after the treatment using tabulated polymer density. The depolarization high-frequency gate was used to eliminate surface discharge in order to minimize the influence of surface electrostatic charge on the measurement.

2.2.5. Electrokinetic Analysis. Zeta potential determination of all samples was accomplished on SurPASS Instrument (Anton Paar GmbH, Austria) by two methods (streaming current and streaming potential) and calculated by two equations (Helmholtz-Smoluchowski, HS, and Fairbrother-Mastins, FM). Samples were studied inside the adjustable gap cell with an electrolyte of $0.001 \text{ mol dm}^{-3}$ KCl at constant

pH = 6.1 and at room temperature. Two samples of each surface were measured four times with the relative error of 5%.

2.3. Cell Culture, Adhesion, Proliferation, and Cell Number Determination. For cell culture experiments, four pristine and the same number of plasma modified samples (power 5 and 10 W, exposure times 40 and 240 s) were used. The samples were sterilized for 1 hour in ethanol (75%), air-dried, inserted into polystyrene 12-well plates (TPP, Switzerland), and seeded with vascular smooth muscle cells (VSMCs) derived from the rat aorta by an explantation method. VSMCs were seeded on the samples with the density of 50,000 cells/well (i.e., about 17,000 cells cm⁻²) into 3 mL of Dulbecco's modified Eagle's Minimum Essential Medium (DMEM; Sigma, USA, Cat. no. D5648), containing 10% fetal bovine serum (FBS; Sebak GmbH, Aidenbach, Germany). Cells were cultivated at 37°C in a humidified air atmosphere containing 5% of CO₂. The number and the morphology of initially adhered cells were evaluated 24 hours after seeding. The cell adhesion and proliferation activity was estimated from the increase in the cell numbers achieved 1, 2, 5, and 7 days after seeding. Phosphate buffer (PBS) was used for cell rinsing, and trypsin with ethylenediaminetetraacetic acid (EDTA) was used for cell releasing from the substrate surface.

For the cell number determination the method of visual field was chosen. The results obtained on pristine and plasma treated PLLA and PMP were confronted with those obtained on TCPS (tissue polystyrene). The method was used for the cell number determination of adhered cells (24 and 48 hours from seeding) and the number of proliferated cells (120 and 168 hours from seeding). The samples were rinsed with PBS and fixed by 70% ethanol solution (-20°C). The fluorescence dyes were consequently used for the coloring of plasmatic membranes (Texas Red C2 maleimide) and chromosomes in cell nuclei (Hoechst # 33342). The coloring was performed for 1 hour at room temperature. When colored the samples were rinsed with PBS again and placed between microscopic glasses. The Olympus IX51 was used for taking 20 photos from different positions on each of the samples. The number of cells was consequently processed with Lucia software and Origin 8.0. The Vi-CELL utilizes the widely accepted trypan blue dye exclusion method to determine cellular viability. When cells die their membranes become permeable, thus allowing for the uptake of the trypan blue dye. As a result, the dead or nonviable cells become darker than the viable cells. It is this contrast that is measured to determine viability.

The standard deviations for the data introduced in the graphs in the paper were calculated with the standard Excel function STDEV (corrected sample standard deviation):

$$s = \sqrt{\frac{1}{N-1} \sum_{i=1}^N (x_i - \bar{x})^2}, \quad (1)$$

where (x_1, \dots, x_n) are the observed sample values and \bar{x} is the mean value of these observations, while the denominator N stands for the number of the values.

The R_a determination (average roughness, AFM) is constructed from the matrix 512 × 512 points; the equation is

$$R_a = \frac{\sum_{i=1}^N |Z_i - Z_{cp}|}{N}, \quad (2)$$

where Z_{cp} is the value of the central plane, Z_i is the actual Z value, and N is the number of points, where the Z_i is evaluated.

3. Results and Discussion

3.1. Contact Angle and Surface Energy Measurement. The influence of plasma treatment (exposure time 5–240 s, power 5 and 10 W) on PLLA and PMP surface polarity was studied with goniometry which can be determined by contact angle measurement [20–23]. From contact angles of distilled water and glycerol the surface energy was observed. As the results indicate, the pristine samples exhibit low values of surface energy and the plasma treatment causes its significant increase (Figures 1(a) and 1(b)). The value of surface energy 31.9 mJ m⁻² was determined for pristine PLLA. Even the short time of plasma treatment results in sharp increase in polymer surface energy. The PMP samples exhibit “more regular” behavior. The value of pristine PMP sample was determined to have surface energy 18.8 mJ m⁻². By the plasma treatment the value of the PMP's surface energy significantly grows. For higher exposure times (>15 s) the energy remains almost constant with the value of 74 mJ m⁻².

3.2. Aging of Treated Polymers. The good stability of substrate properties in tissue engineering is important for their application as biomaterials. Due to this we study also the behavior of properties during aging of samples. For potential application of biomaterial in tissue engineering it is very important to determine whether the material exhibits “constant” behavior in time. It is clear from Figure 2 that the time from the plasma treatment significantly influences the values of contact angle. The aging measurements were performed for power 5 and 10 W and exposure time 240 s. This combination resulted previously in the highest decrease in contact angle both for PLLA and PMP; therefore the combination of parameters was chosen for the aging studies. Both the tested polymers exhibit the same trend of contact angle during aging process in general. The PLLA sample exhibits the value of pristine foil 71.1°, as was mentioned before. The sharp decrease immediately after the treatment is changed to increase with increasing aging time. This increase reaches the saturated value of 83° for PLLA treated with 5 W (Figure 2(a)), with the aging time being 50 hours. Also the treatment of PLLA with 10 W leads after 50 hours of aging process to estimation of a saturated value of ca 87° (Figure 2(a)). Both saturated values are higher than pristine PLLA sample, which is the result of a lower polarity of PLLA after the aging process. A significant difference is that the PMP samples also exhibits almost similar values for both applied plasma powers (Figure 2(b)), with the value being lower than that for pristine PMP (ca 104°). The orientation of the oxygen containing groups, the rearrangement of degraded macromolecules and molecular

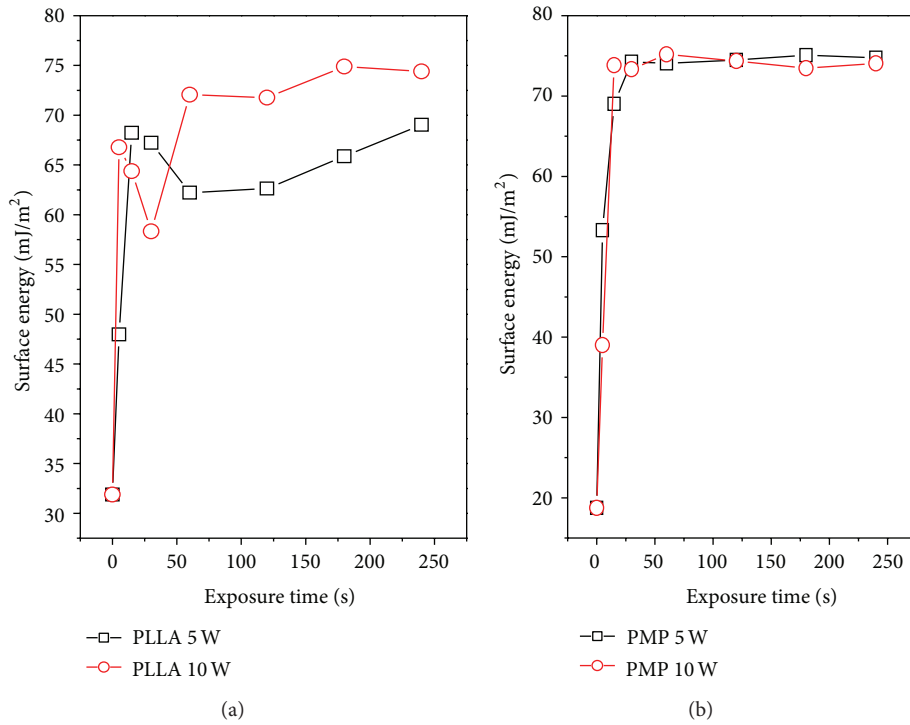


FIGURE 1: Dependence of the surface energy of plasma treated (with 5 and 10 W) PLLA (a) and PMP (b) on Ar plasma exposure time.

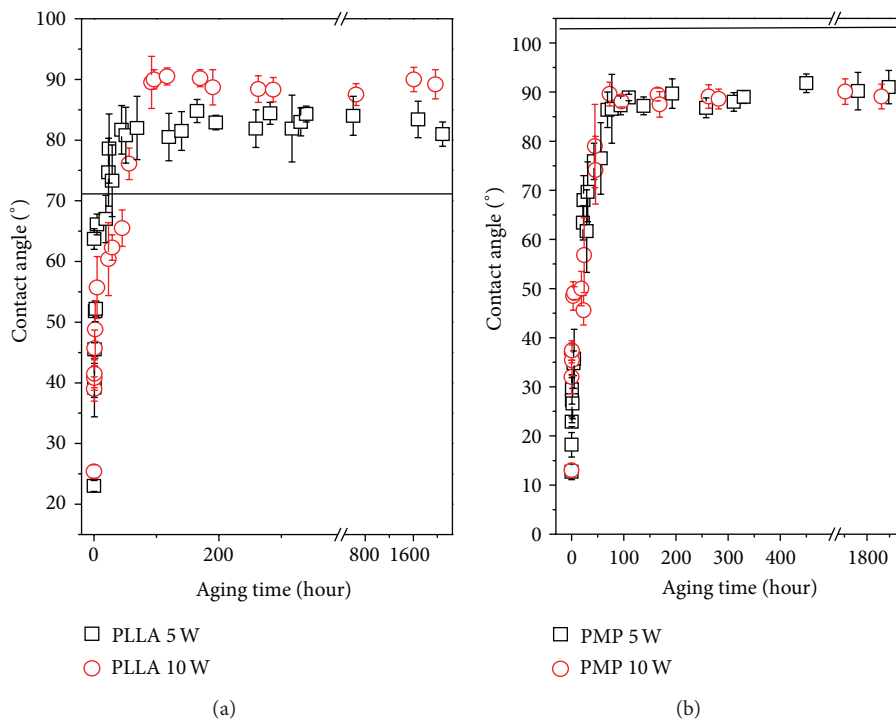


FIGURE 2: Dependence of contact angle of plasma treated (with 5 and 10 W) PLLA (a) and PMP (b) on aging time. Values for pristine polymers are shown by solid line.

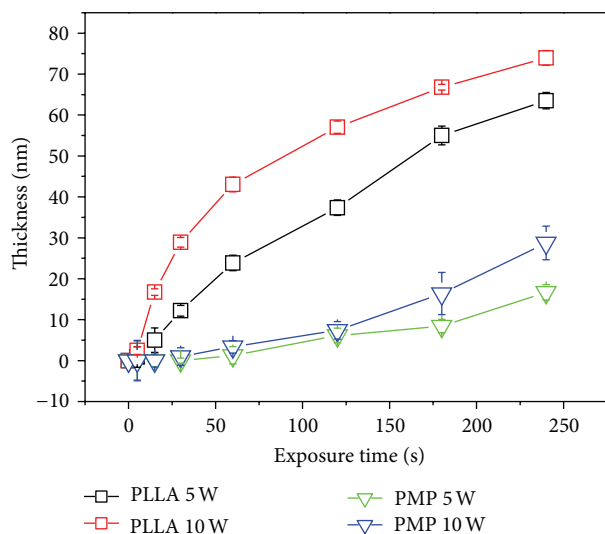


FIGURE 3: Dependence of the thickness of the ablated layer of PLLA and PMP on the Ar plasma exposure time (power 5 and 10 W).

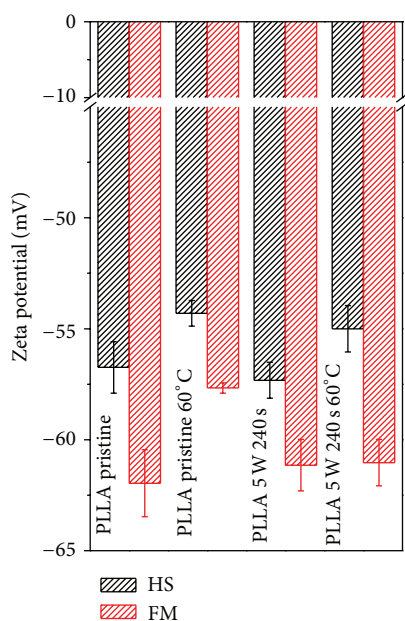


FIGURE 4: Zeta potential results for PLLA pristine (PLLA), plasma treated (PLLA/5 W/240 s), and annealed ones at 60°C (PLLA/60°C and PLLA/5 W/240 s/60°C). HS means the streaming current method and Helmholtz-Smoluchowski equation; FM means the streaming potential method and Fairbrother-Mastins equation.

fragments into the polymer bulk, which may occur on the polymer surface in the process of aging, is the main reason for the increase in contact angle during the aging process.

3.3. Ablation, Zeta Potential, and Surface Morphology. During plasma treatment process the ablation of polymer takes place. The ablation has been studied gravimetrically. The ablation loss of polymer was consecutively recalculated to

polymer thickness. From Figure 3 it is apparent that the exposure time and power significantly influence the ablation of both polymers. The samples were modified using plasma by 5 and 10 W and exposure times from 5 to 240 s. As expected, with increasing the exposure power and time the higher ablation loss is apparent. This phenomenon is more progressed in case of PLLA. This implicates that surface of PMP is more resistant to plasma treatment than PLLA surface. The highest ablation loss was observed for PLLA foil modified with 10 W and 240 s. The thickness of ablated material was ca 73 nm (see Figure 3). The mass loss for treatment parameters (10 W and 240 s) was $18.5 \mu\text{g cm}^{-2}$ for PLLA and $4.8 \mu\text{g cm}^{-2}$ for PMP. From Figure 3 it can be concluded that the ablation is more pronounced on the PLLA.

Results of electrokinetic analysis are presented in Figure 4. Because PMP was the slightly affected in comparison with PLLA, we present results for only PLLA. The trend of zeta potential changes obtained by both of the applied methods, streaming current (HS) and streaming potential (FM), is the same. As it is clear, the plasma treatment (after the aging process and surface relaxation) does not exhibit significant changes in surface charge represented by zeta potential. It can be explained by the high ablation of surface during treatment discussed above. On the other hand, zeta potential of pristine PLLA and also plasma treated one increases after annealing at 60°C due to increasing surface polarity. Therefore it can be concluded that the annealing process has a significant effect on the ability to influence the surface-ion interaction.

Surface morphology of pristine and treated samples was studied with AFM. The pristine PLLA exhibits the surface morphology with no obvious surface irregularities and surface roughness $R_a = 6.9 \text{ nm}$ (Figure 5). The plasma treatment has significant effect on the surface morphology. As a result of the plasma irradiation, the surface roughness dramatically increases and sharp fragments appear on the modified surface. The ablation takes place (as discussed in Section 3.3, 1st paragraph), preferentially with the amorphous phase being ablated and the crystalline amount of PLLA surface being revealed. Rather different situation arises in case of PMP. A mild decrease in surface roughness after treatment of PMP surface has been observed. The surface morphology is almost unaltered by the plasma treatment. From the surface morphology study it can be concluded that PMP is more plasma resistant than PLLA and no significant changes are made as a result of plasma treatment. The surface morphology can be also significantly influenced by the surface etching, which will be discussed later.

3.4. Thermal Treatment. The thermal treatment of pristine PLLA caused mild increase in surface roughness (see Figures 5 and 6). The change of surface morphology of pristine PLLA induced by thermal treatment is minor. The situation is dramatically changed after plasma treatment. It is obvious from Figure 5 that the combination of plasma and consecutive thermal treatment leads to significant changes in surface morphology and roughness. This change is strongly influenced by the plasma power. It is evident that lower plasma power

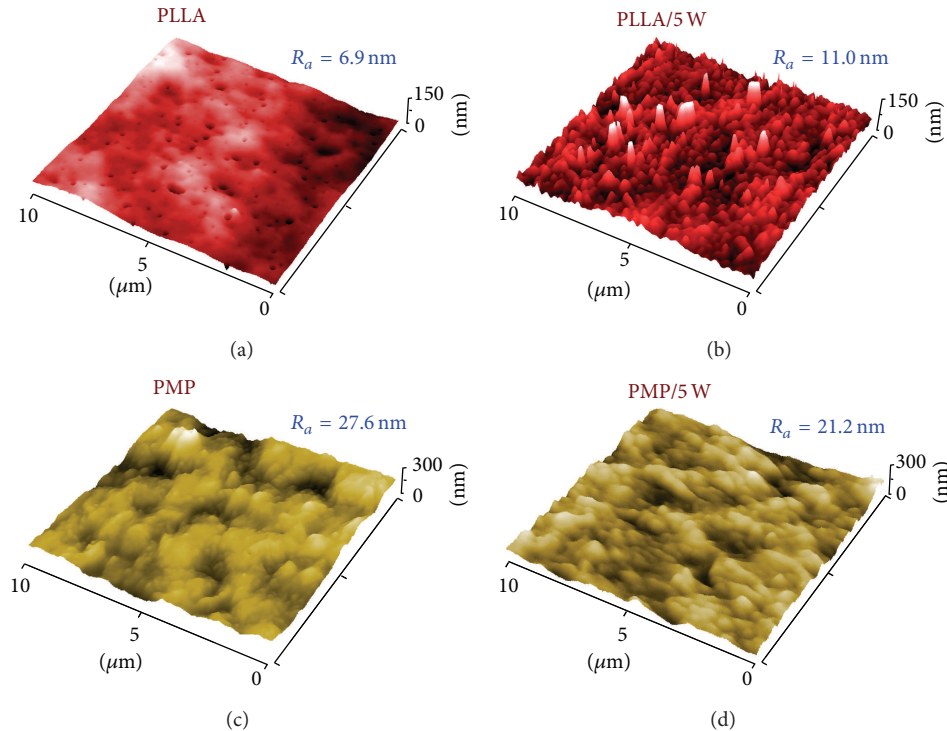


FIGURE 5: AFM images of pristine polymers (PLLA and PMP) and polymers treated with Ar plasma (power 5 W and time 240 s) (PLLA/5 W and PMP/5 W). R_a is average surface roughness in nm.

(5 W) in combination with thermal treatment leads to change of surface roughness from 7.0 to 13.0 nm and the surface structure gets a “worm-like character.” The most pronounced changes were observed for the samples modified for 10 W (240 s) and then thermally treated. The dramatic increase in surface roughness up to 23 nm combined with significant change of surface morphology (worm-like structure) was observed. The changes in surface morphology and roughness are probably induced by different amount of crystalline and amorphous phase on the very surface of modified PLLA layer, affecting the melting process and process of solidification.

The PMP foils were heated to 160°C (Vicat softening point) and their morphological stability was determined. For the sake of clarity only the surface morphology of PLLA heated samples was introduced in Figure 6. The thermal treatment has no significant effect neither on surface morphology nor roughness in case of plasma modified PMP samples. After thermal treatment, both the surface morphology of 5 and that of 10 W exposed PMP samples remained only mildly altered. This effect is in good correspondence with previously obtained results from gravimetry (see Figure 3). The higher resistance to plasma influence results in smaller ablation of PMP material and thus supports the morphological stability during thermal treatment of plasma exposed samples.

3.5. Chemistry of Modified Polymers. The surface chemical structure of polymers was studied with XPS. The selected results for PMP and PLLA treated with 5 and 10 W are introduced in Table 1. The oxygen concentration dramatically

increases on the PMP surface after plasma treatment (from 0.3 to 20.5%). The oxygen concentration is further increased by the surface aging. This surprising fact can be probably caused by additional surface oxidation and polymer segments reorientation (increase of 4%). The difference may be due to combination of applied plasma power, which together with surface morphology changes, and air oxygen could induce this slight increase in surface oxygen concentration. The observation of increasing oxygen concentration during aging process was also observed for PMMA [24].

3.6. Cells Adhesion and Proliferation. For the cell proliferation and differentiation studying their adhesion on the substrate is essential. After successful adhesion the lag phase occurs, usually between the first and the second day from seeding, but it can be up to 72 hours. The cells adapt on their new environment. After this phase the proliferation phase develops. For the cell compatibility studies the PLLA was selected. The vascular smooth muscle cells (VSMC) were seeded also on tissue polystyrene (TCPS) as a material standard (Figure 7).

The cell adhesion represents the first stage of the cell-substrate interaction and the quality of this phase influences the cell ability to proliferate and differentiate in the contact with the substrate. The initial number of cells (17000 cm⁻²) was seeded on studied substrates and the decrease to 4500 cells cm⁻² after 24 hours was observed. This decrease was caused by the processes of adhesion of cell to substrate, where approximately one fourth of the cells survived. If we

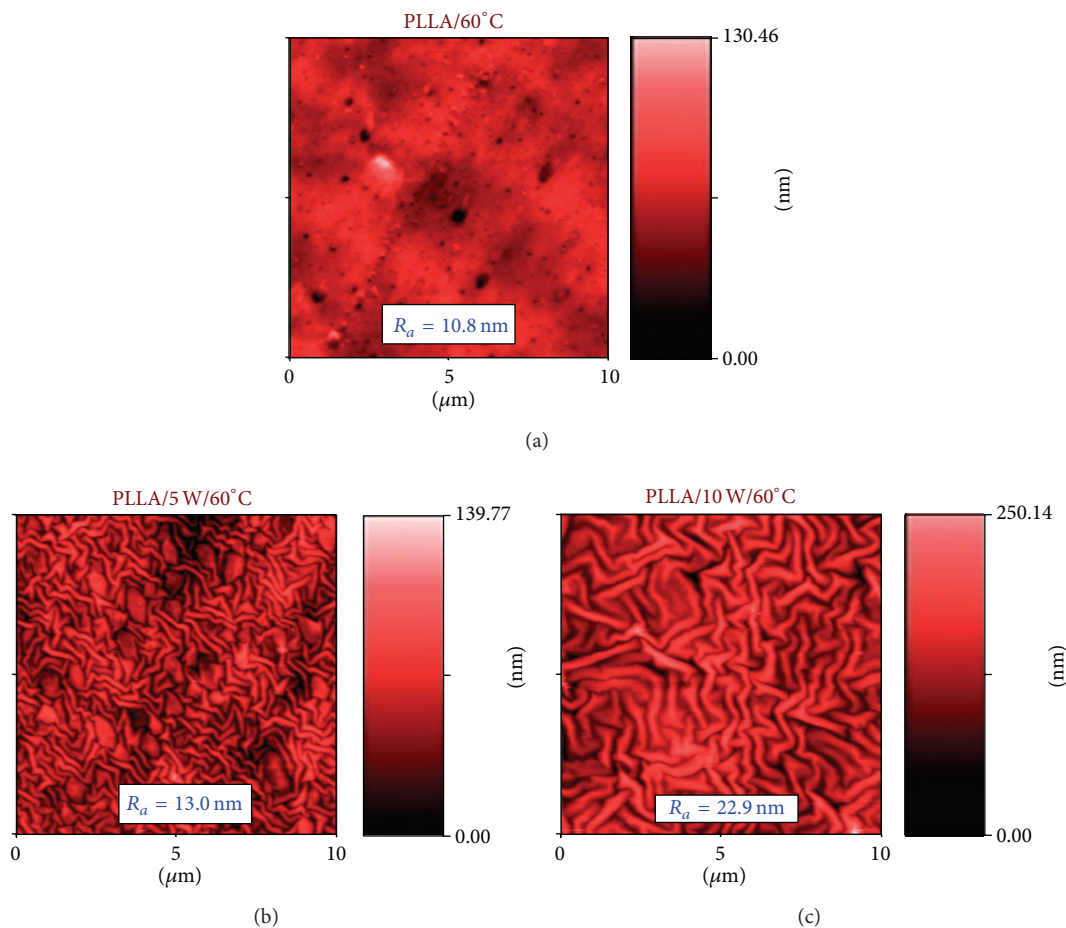


FIGURE 6: 2D AFM images of PLLA thermally treated by 60°C: pristine (PLLA/60°C), PLLA treated with plasma (5 W and 240 s) (PLLA/5 W/60°C), and PLLA treated with plasma (10 W and 240 s) (PLLA/10 W/60°C). R_a is the surface roughness in nm.

compare the shape and distribution of cells during the initial adhesion stage we can conclude that the cells of pristine polymers are small, round shaped, and not well spread. The TCPS exhibits slightly better distribution of cells on the surface. The modified surfaces (both PLLA and PMP) exhibit during the initial adhesion stage (first day) the best results according to the shape and distribution over the surface. The Live/Dead assay by the Vi-CELL instrument (Table 2) revealed that the results except for pristine PMP (first day) were better than 70% and for TCPS were better than 80%.

48 hours after seeding the evident increase in cell number was detected (about $2000 \text{ cells cm}^{-2}$) for the samples modified with plasma (5 W, 40 and 240 s) and (10 W, 240 s) as well as on standard TCPS. The pristine PLLA and PLLA modified (10 W, 40 s) exhibited almost no progress in cell number. After 5 days from seeding, when the lag phase is over, the cell differentiation starts to increase. The most successful was evaluated PLLA sample modified with 10 W and 240 s after 5 days from seeding (Figure 7). The lowest cell number was detected, on the contrary, on the PLLA modified with 5 W and 240 s. The PLLA polymer itself also exhibited “very good” results, that is, high cell numbers. The best result for PMP substrate was determined for modification with

5 W and 40 s (Figure 7). The reason for the enhancing of VSMC proliferation on PLLA with 10 W and 240 s and PMP with 5 W and 40 s, compared to pristine samples, lies in the change of its roughness in combination with their surface wettability. Compared to the surface wettability, roughness, and chemistry the PLLA modified with 10 W and 240 s has the pronounced globular structures on its surface with high roughness, while the PMP modified with 5 W and 40 s exhibits significant increase in oxygen concentration compared to pristine PMP, which may be the main reason for the enhancing of VSMC proliferation.

The selected pictures of PLLA polymer modified with 10 W for 40 and 240 s are introduced in Figure 8. The photos from comparative material TCPS after the first and seventh days are introduced in Figures 8(a) and 8(b) too. The results on TCPS revealed the highest number of proliferated cells from all studied samples. The inhomogeneous cell distribution in the first stage of the cell growth is apparent (Figures 8(c), and 8(d)). The dimensions of cells after successful adhesion process may be in relatively wide interval. Also the shape of the cells implicates that the “width” dimension could be approx. $40\text{--}50 \mu\text{m}$ and the “length” dimension about $150\text{--}200 \mu\text{m}$. The diameter of cell core is approx. $15 \mu\text{m}$. The

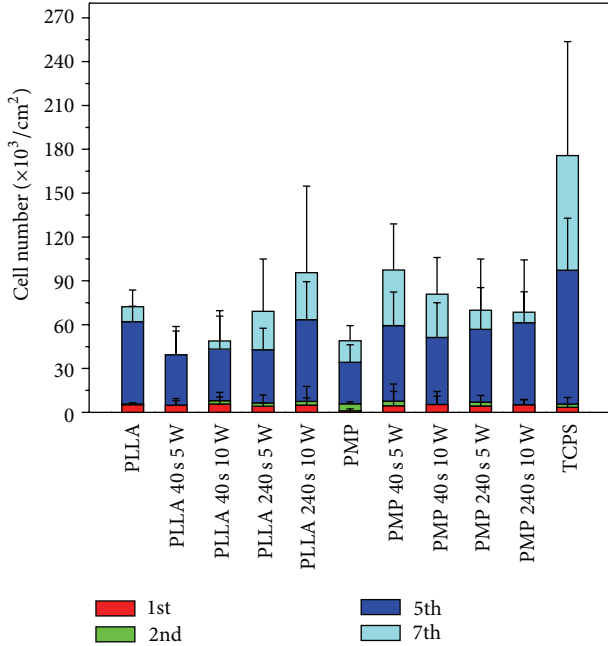


FIGURE 7: Dependence of the number of adhered and proliferated cells after 1, 2, 5, and 7 days from seeding on pristine PLLA and PMP and PLLA and PMP treated in plasma (power 5 and 10 W, time 40 and 240 s). The values for tissue polystyrene as standard material (TCPS) were also introduced for comparison.

dimensions of the cell significantly depend on the density of cells on particular surface area. Seven days from seeding the cells are joined into conglomerates and form continuous layer (Figure 8(f)). From those figures it is obvious that the higher number of cells was determined on the sample treated with power 10 W and 240 s, but the cell's dimensions are significantly higher in comparison to those on TCPS (see Figure 8).

4. Conclusions

The influence of Ar plasma and thermal treatment on the surface properties of PLLA and PMP was determined by different techniques. The process of aging of the modified polymers was studied too. The pristine and treated polymers were used as substrates for cultivation of VSMC. The plasma treatment significantly alters the contact angle between surface and water (wettability) of polymer. Due to plasma treatment the contact angle decreases and the surface energy increases. With the increasing aging time the surface polarity is spontaneously reduced. The ablation caused by Ar plasma was more pronounced on the PLLA in comparison to PMP. The surface morphology of PLLA was significantly altered with both plasma modification and consecutive thermal treatment. The higher resistance to plasma treatment resulted in smaller ablation of PMP and thus supported the morphological stability during thermal treatment of plasma treated samples. The increase in oxygen concentration on PMP surface induced by plasma treatment was proved. The

TABLE 1: The element concentration on the PMP and PLLA samples. The values were determined by XPS method for pristine, plasma treated (5 W or 10 W, 240 s), plasma treated, and aged samples.

Sample	Element concentration (at. %)	
	Carbon	Oxygen
PMP		
Pristine	99.7	0.3
Plasma 5 W	79.5	20.5
Plasma 5 W/aged	75.5	24.5
Plasma 10 W	80.3	19.7
Plasma 10 W/aged	75.6	24.4
PLLA		
Pristine	66.1	33.9
Plasma 5 W	66.3	33.7
Plasma 5 W/aged	61.5	38.5
Plasma 10 W	66.6	33.4
Plasma 10 W/aged	64.8	35.2

TABLE 2: Live/Dead assay by the Vi-CELL instrument for the studied samples (in %).

	1st day	2nd day	5th day	7th day
PLLA 5 W 40 s	87	83	81	79
PLLA 10 W 40 s	88	100	76	85
PLLA 5 W 240 s	73	76	76	83
PLLA 10 W 240 s	88	85	70	80
PLLA pristine	100	95	82	86
PMP 5 W 40 s	88	87	83	82
PMP 10 W 40 s	88	88	84	82
PMP 5 W 240 s	100	92	78	82
PMP 10 W 240 s	92	93	81	79
PMP pristine	65	86	84	72
TCPS	94	87	89	86

plasma treatment improves cell adhesion and proliferation on the PMP. The higher number of cells was determined on the sample treated with power 10 W and 240 s, but the cell's dimensions are significantly larger in comparison to those on TCPS. The potential application of plasma treated PLLA and PMP is connected with construction of biodegradable and biocompatible scaffolds for the growth of different types of cell lines.

Conflict of Interests

Petr Slepíčka, as the first author of the paper, hereby declares that he does not have any direct financial relation with the commercial identity mentioned in the paper that might lead to a conflict of interests for any of the authors. He hereby declares on behalf of all the coauthors of the paper that the same statement is valid for all of them.

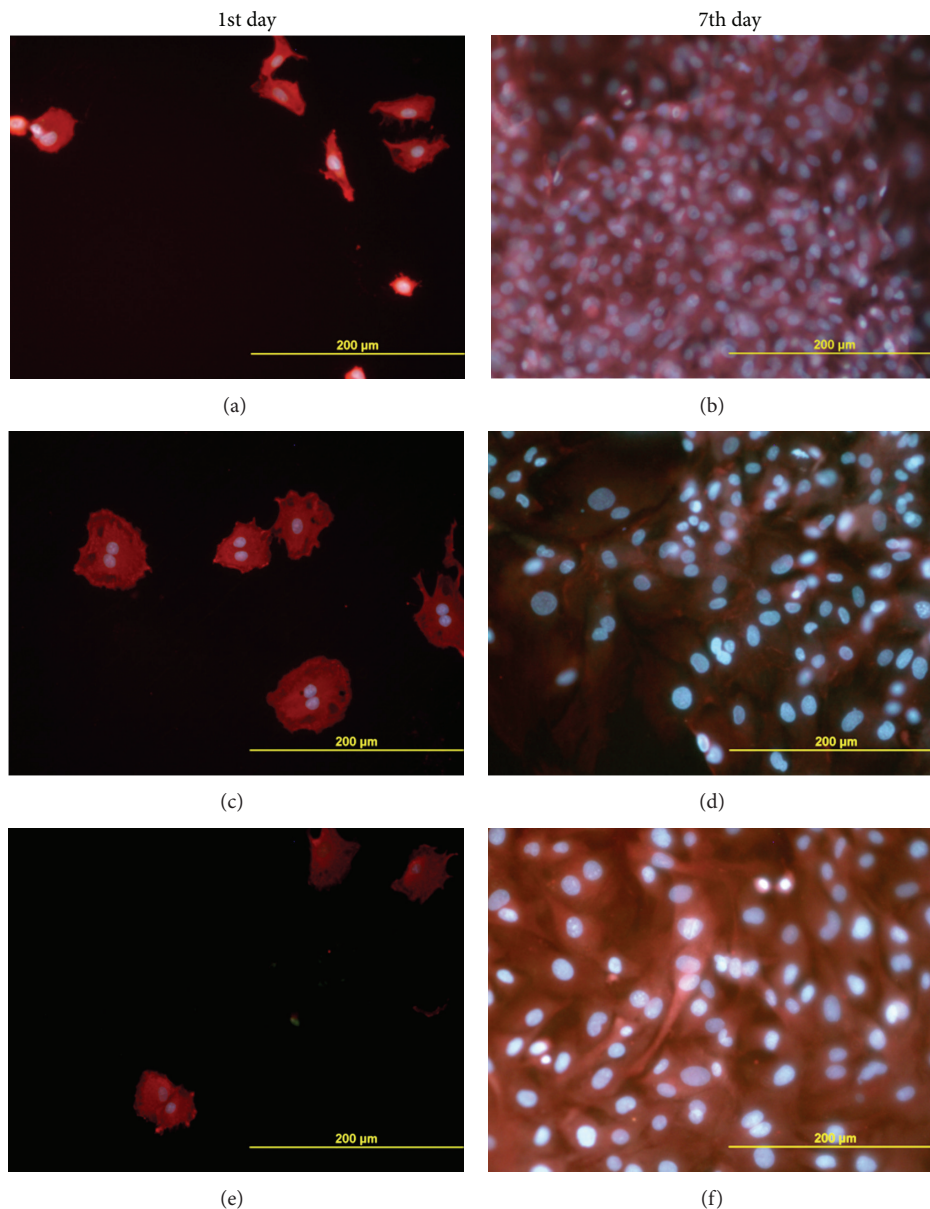


FIGURE 8: Photographs of adhered (first day, first column) and proliferated (seventh day, second column) VSMCs from seeding on tissue polystyrene (TCPS) ((a) and (b)), treated PLLA (10 W and 40 s) ((c) and (d)), and PLLA treated by 10 W and 240 s ((e) and (f)).

Acknowledgment

This work was supported by the GACR under Project P108/12/G108.

References

- [1] J. C. Miller, R. M. Serrato, J. M. Represas-Cardenas, and G. A. Kundahl, *The Handbook of Nanotechnology*, John Wiley & Sons, Hoboken, NJ, USA, 2005.
- [2] B. D. Ratner, *Biomaterials Science: An Introduction to Materials in Medicine*, Elsevier Academic Press, San Diego, Calif, USA, 2nd edition, 2004.
- [3] N. Nakabayashi, "Dental biomaterials and the healing of dental tissue," *Biomaterials*, vol. 24, no. 13, pp. 2437–2439, 2003.
- [4] S. M. Kurtz and J. N. Devine, "PEEK biomaterials in trauma, orthopedic, and spinal implants," *Biomaterials*, vol. 28, no. 32, pp. 4845–4869, 2007.
- [5] M. L. Hans and A. M. Lowman, "Biodegradable nanoparticles for drug delivery and targeting," *Current Opinion in Solid State and Materials Science*, vol. 6, no. 4, pp. 319–327, 2002.
- [6] J. Heitz, V. Švorčík, L. Bačáková et al., "Fibroblast and smooth muscle cell adhesion on UV-modified PTFE in ammonium atmosphaera," *Journal of Biomedical Materials Research A*, vol. 67, no. 1, pp. 130–137, 2003.
- [7] K. Walachová, V. Švorčík, L. Bačáková, and V. Hnatowicz, "Colonization of ion-modified polyethylene with vascular smooth muscle cells in vitro," *Biomaterials*, vol. 23, no. 14, pp. 2989–2996, 2002.

- [8] V. Švorčík, T. Hubáček, P. Slepíčka et al., “Characterization of carbon nanolayers flash evaporated on PET and PTFE,” *Carbon*, vol. 47, no. 7, pp. 1770–1778, 2009.
- [9] F. Groeber, M. Holeiter, M. Hampel, S. Hinderer, and K. Schenke-Layland, “Skin tissue engineering—in vivo and in vitro applications,” *Advanced Drug Delivery Reviews*, vol. 63, no. 4-5, pp. 352–366, 2011.
- [10] J. M. Kelm, V. Lorber, J. G. Snedeker et al., “A novel concept for scaffold-free vessel tissue engineering: self-assembly of microtissue building blocks,” *Journal of Biotechnology*, vol. 148, no. 1, pp. 46–55, 2010.
- [11] S. J. Hollister, “Porous scaffold design for tissue engineering,” *Nature Materials*, vol. 4, no. 7, pp. 518–524, 2005.
- [12] V. Švorčík, N. Kasálková, P. Slepíčka et al., “Cytocompatibility of Ar plasma-treated and Au nanoparticle-grafted PE,” *Nuclear Instruments and Methods in Physics Research B*, vol. 267, no. 11, pp. 1904–1910, 2009.
- [13] K. Ročková, V. Švorčík, L. Bačáková, B. Dvořánková, and J. Heitz, “Biocompatibility of ion beam modified and RGD-grafted polyethylene,” *Nuclear Instruments and Methods in Physics Research B*, vol. 225, no. 3, pp. 275–282, 2004.
- [14] H. Chen, L. Yuan, W. Song, Z. Wu, and D. Li, “Biocompatible polymer materials: role of protein-surface interactions,” *Progress in Polymer Science*, vol. 33, no. 11, pp. 1059–1087, 2008.
- [15] C. H. Wanke, J. L. Feijó, L. G. Barbosa, L. F. Campo, R. V. B. de Oliveira, and F. Horowitz, “Tuning of polypropylene wettability by plasma and polyhedral oligomeric silsesquioxane modifications,” *Polymer*, vol. 52, no. 8, pp. 1797–1802, 2011.
- [16] J. M. Goddard and J. H. Hotchkiss, “Polymer surface modification for the attachment of bioactive compounds,” *Progress in Polymer Science*, vol. 32, no. 7, pp. 698–725, 2007.
- [17] N. Kasálková, Z. Makajová, M. Pařízek et al., “Cell adhesion and proliferation on plasma-treated and poly(ethylene glycol)-grafted polyethylene,” *Journal of Adhesion Science and Technology*, vol. 24, no. 4, pp. 743–754, 2010.
- [18] I. Pashkuleva, P. M. López-Pérez, H. S. Azevedo, and R. L. Reis, “Highly porous and interconnected starch-based scaffolds: production, characterization and surface modification,” *Materials Science and Engineering C*, vol. 30, no. 7, pp. 981–989, 2010.
- [19] J. H. Lee, J. W. Lee, G. Khang, and H. B. Lee, “Interaction of cells on chargeable functional group gradient surfaces,” *Biomaterials*, vol. 18, no. 4, pp. 351–358, 1997.
- [20] K. S. Kim, C. M. Ryu, C. S. Park, G. S. Sur, and C. E. Park, “Investigation of crystallinity effects on the surface of oxygen plasma treated low density polyethylene using X-ray photoelectron spectroscopy,” *Polymer*, vol. 44, no. 20, pp. 6287–6295, 2003.
- [21] P. Slepíčka, S. Trostová, N. Slepíčková Kasálková et al., “Nanostructuring of polymethylpentene by plasma and heat treatment for improved biocompatibility,” *Polymer Degradation and Stability*, vol. 97, no. 7, pp. 1075–1082, 2012.
- [22] V. Švorčík, A. Chaloupka, P. Řezanka et al., “Au-nanoparticles grafted on plasma treated PE,” *Radiation Physics and Chemistry*, vol. 79, no. 3, pp. 315–317, 2010.
- [23] V. Švorčík, A. Řezníčková, Z. Kolská, P. Slepíčka, and V. Hnatowicz, “Variable surface properties of PTFE foils,” *e-Polymers*, vol. 133, no. 1–6, 2010.
- [24] A. Vesel and M. Mozetic, “Surface modification and ageing of PMMA polymer by oxygen plasma treatment,” *Vacuum*, vol. 86, no. 6, pp. 634–637, 2012.

Research Article

Heterogeneous Deposition of Cu₂O Nanoparticles on TiO₂ Nanotube Array Films in Organic Solvent

Xinwen Huang^{1,2} and Zongjian Liu¹

¹ Resource & Environment Catalysis Institute, College of Chemical Engineering and Materials Science, Zhejiang University of Technology, Hangzhou 300014, China

² College of Biological and Environmental Engineering, Zhejiang University of Technology, Hangzhou 300014, China

Correspondence should be addressed to Zongjian Liu; zjliu@zjut.edu.cn

Received 27 June 2013; Accepted 26 July 2013

Academic Editor: Guangyu Zhao

Copyright © 2013 X. Huang and Z. Liu. This is an open access article distributed under the Creative Commons Attribution License, which permits unrestricted use, distribution, and reproduction in any medium, provided the original work is properly cited.

A novel method for decoration of anodic TiO₂ nanotube array films (NAFs) with Cu₂O nanoparticles has been reported. The method is based on the reduction of Cu(II) in a mixture of ethylene glycol and N,N-dimethylformamide at 120°C for 16 h, where the resulting Cu₂O can heterogeneously nucleate and grow on TiO₂ NAFs. The nanosized Cu₂O is found to be well dispersed on the wall of TiO₂ nanotubes without blocking the nanotube, a commonly observed phenomenon in the case of deposition of Cu₂O via electrochemical method. The amount of Cu₂O deposited on the TiO₂ NAFs can be varied by adjusting the concentration of Cu(II) in the organic solution. UV-vis spectra measurement indicates that the decoration of TiO₂ NAFs with Cu₂O nanoparticles greatly improves their ability to respond to visible light. By examining the photocurrent and photodegradation of methyl orange under simulated sunlight, it is found that these Cu₂O-decorated TiO₂ NAFs show much more photoactive in comparison with the as-prepared TiO₂ NAFs.

1. Introduction

Because of their large aspect ratio and high specific surface area, materials with one-dimensional (1D) structures, for example, nanotubes and nanowires, often exhibit different performances compared to the bulk counterparts. The unique properties of these 1D nanostructures have shown potential applications in many fields, such as electronics, catalysis, data storage, optics, and sensors [1–3]. 1D TiO₂ nanostructures are of great scientific and technical interest because they exhibit excellent photocatalytic activities [4–7]. Over the past decade, great attention has been paid into the synthesis and application of TiO₂ nanotube arrays prepared by anodic oxidation of Ti metal in F⁻-containing solutions [7–11]. The highly ordered nanotube arrays not only possess high surface area, but also provide an efficient transport channel for photogenerated electrons [12]. Furthermore, unlike the powder-typed TiO₂ photocatalysts which often need be immobilized onto solid substrates for practical application [13, 14], the TiO₂ nanotube arrays are grown on Ti substrates

and thus the formed TiO₂ nanotube array films (NAFs) can be directly used as photoanodes for photoinduced redox reactions such as water splitting [15] and decomposition of harmful compounds [7].

However, TiO₂ nanotube arrays possess a wide band gap (~3.2 eV) and thus only respond well to ultraviolet light, which is a great hindrance to their use under sunlight. To extend their light-response scope from ultraviolet to visible light region, a common approach is postdecoration of TiO₂ NAFs with narrow band gap semiconductors, for example, Cu₂O [16–20], Fe₂O₃ [21] and CdS [22]. When TiO₂ NAFs are decorated with Cu₂O, a p-type semiconductor with a direct band gap of ~2.2 eV, electrons excited under visible light may transfer from the conduction band of Cu₂O to that of TiO₂ since the conduction band (CB) edge for Cu₂O is much higher than that of TiO₂ [23]. As a result, the recombination probability of the photoexcited electrons and holes will be reduced, leading to a great improvement in photocatalytic activity. So far, the methods for the decoration

of TiO₂ nanotube arrays with Cu₂O mainly include electrodeposition [16–18], sonoelectrochemical deposition [19], and photocatalytic reduction [20]. In the present work, we report a new method for loading of Cu₂O nanoparticles onto TiO₂ NAFs. The method is based on the reduction of Cu (II) in a mixture of ethylene glycol (EG) and N,N-dimethylformamide (DMF), where the resulting Cu₂O can heterogeneously nucleate and grow on TiO₂ NAFs. In comparison with commonly used electrodeposition (including sonoelectrochemical deposition), the size of Cu₂O is small, and the nanosized Cu₂O is well dispersed on the wall of TiO₂ nanotubes without blocking the nanotube.

2. Experimental Details

2.1. Synthesis of the Films. Ti foils were cut into pieces (7.2 cm × 1.7 cm × 0.4 mm), polished with abrasive paper, and then washed with deionized water. The polished Ti pieces were degreased in a mixed solution of NaOH and Na₂CO₃ (the ratio of NaOH : Na₂CO₃ : H₂O by weight is 5 : 2 : 100, resp.) at 85°C for 1.5 h, and then washed with deionized water. Before anodic oxidization, one side of the pretreated Ti piece was sealed with epoxy resin, and then etched in a 10 wt% HF aqueous solution at room temperature for about 20 s, followed by washing with deionized water. The anodic oxidization of the Ti piece was conducted in an EG solution containing KF (0.7 wt%) and H₂O (1.8 wt%) at ~25°C, where a Cu plate was used as cathode and a constant voltage of 50 V was applied between two electrodes. The anodic oxide layer was formed by a three-step method. Firstly, the Ti piece was anodized for 2 h, and then the grown oxide layer was removed by an adhesive tape. Secondly, the above procedure was repeated. Finally, the Ti piece was reanodized under the same conditions for 1 h. After anodization, the sample was washed thoroughly with deionized water and then dried in the oven at 40°C for about 12 h.

Deposition of Cu₂O on TiO₂ NAFs was conducted in a 50 mL Teflon-lined autoclave. The autoclave was filled with a solution containing 30 mL of EG and 10 mL of DMF, where a certain amount of CuSO₄ (ranging from 0.005 to 0.05 g) was previously dissolved. The as-prepared TiO₂ NAFs were immersed in the organic solution, and then the sealed autoclave was kept in an oven at 120°C for 16 h. After the autoclave was cooled down to room temperature naturally, the resulting samples were removed from the organic solution, washed several times with deionized water, and subsequently dried in an oven at 40°C for about 12 h.

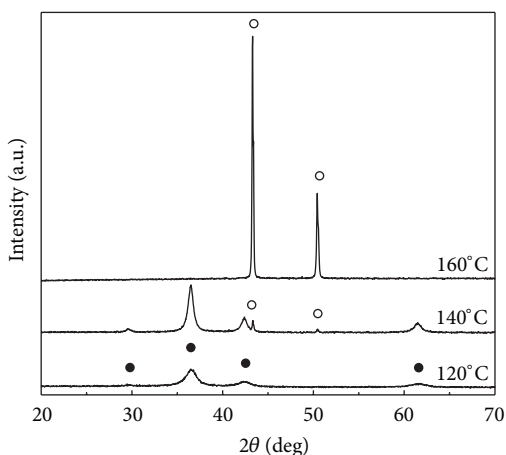
2.2. Characterization and Photocatalytic Activity Evaluation of the Films. The surface morphology of the films was examined using a scanning electron microscope (SEM, Hitachi S-4700) operating at 15 kV. X-ray diffraction (XRD) analysis was performed on a Thermo ARL XTRA X-ray diffractometer using Cu K α X-ray source. The chemical composition of the as-prepared film was characterized by an energy-dispersive X-ray spectrometer (EDS) attached to SEM operating at 15 kV. The ultraviolet-visible (UV-vis) diffuse reflectance spectra

were recorded on a UV-2550 (SHIMADSU) spectrophotometer with BaSO₄ as the reference. The photoelectrochemical property of the film electrodes was evaluated in a three-electrode cell using a Pt wire as counter electrode and a saturated calomel electrode (SCE) as reference electrodes. If needed, the working electrode could be irradiated from the front side by a sunlight-simulation lamp (Osram Ultra Vitalux 300W). The current with or without irradiation was measured in a 0.25 M Na₂SO₄ aqueous solution using a potentiostat (CHI 620B, CHI Co.). Photocatalytic activities of the samples were evaluated by the photodegradation of methyl orange (MO) solution with an initial concentration of 5.0 mg/L under simulated sunlight. The photodegradation experiments were conducted in a quartz reactor. In each test, one piece of the sample was hung in the liquid. Prior to irradiation, the suspension was kept in the dark for 60 min to achieve the adsorption-desorption equilibrium between the photocatalyst and methyl orange. Then, the solution was exposed to the light irradiation, and samples were taken at given time interval to analyze the concentration of MO by measuring the absorbance with the spectrophotometer.

3. Results and Discussion

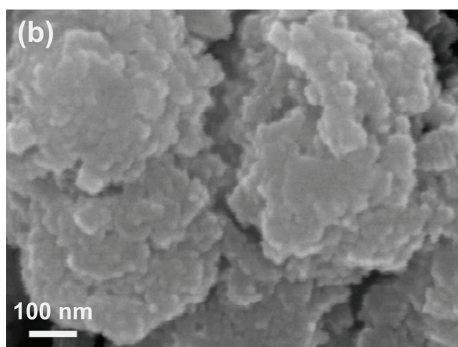
To decorate TiO₂ NAFs with nanosized Cu₂O, a suitable condition for reduction of Cu²⁺ in organic solvent should be chosen. Figure 1(a) shows the XRD patterns of the products obtained by reduction of Cu²⁺ (2 mmol) in a mixture of EG and DMF at different temperatures. At a temperature of 120°C, all the diffraction peaks appearing in the XRD pattern of the product (indicated by the solid circles) can be indexed to cubic Cu₂O phase (JCPDS number 65-3288), at which the peaks at 2θ values of 29.6°, 36.5°, 42.4°, and 61.5° correspond to 110, 111, 200, and 220 lattice planes of Cu₂O, respectively. The broaden peaks indicate that the size of Cu₂O is very small. The average crystal size calculated by Scherrer's equation for (111) reflections of Cu₂O is about 10 nm. The SEM image shown in Figure 1(b) reveals that these small-sized Cu₂O nanocrystals are severely aggregated as a result of reduction in surface energy. When the reduction is conducted at 140°C, we can observe two new peaks at 2θ of 43.2° and 50.4° (indicated by open circles), which can be, respectively, assigned to the diffraction of (111) and (200) planes of cubic Cu (JCPDS number 04-0836). The result indicates the formation of Cu at 140°C. As the temperature is raised to 160°C, all the diffraction peaks of Cu₂O disappear. Moreover, the peaks assigned to Cu become very sharp, suggesting that the growth of Cu crystals of large size occurs. This is confirmed by the SEM image of this sample (see Figure 1(c)), where Cu microcrystals can be observed. Therefore, we chose a temperature of 120°C to deposit Cu₂O on TiO₂ nanotube arrays, where the concentration of Cu²⁺ in the mixture of EG and DMF is changed to control the amount of Cu₂O deposited on the films.

Figure 2(a) presents the digital photos of TiO₂ NAFs before and after being treated in the mixture of EG and DMF containing different amounts of CuSO₄ at 120°C for 16 h. Compared with the untreated TiO₂ film, the treatment in

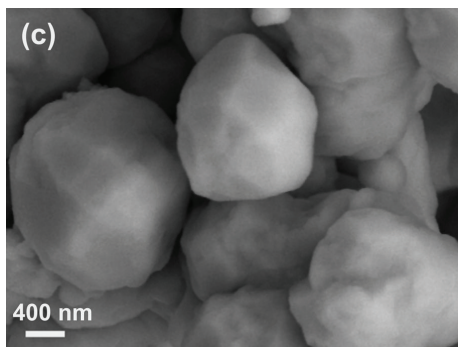


○ Cu
● Cu₂O

(a)



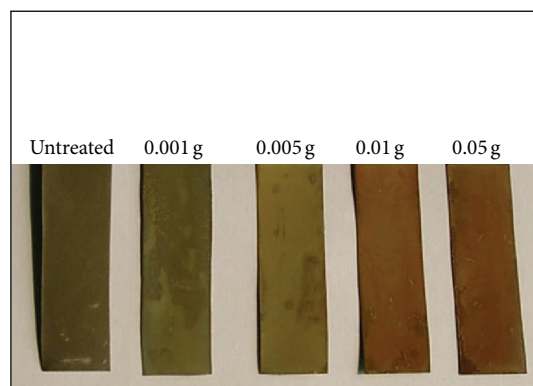
(b)



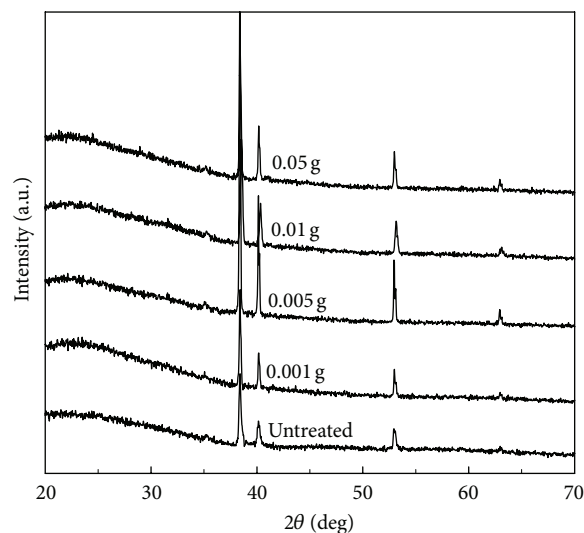
(c)

FIGURE 1: (a) XRD patterns of the products obtained by reduction of CuSO₄ (2 mmol) in a mixture of EG and DMF at different temperatures. (b) and (c) are the corresponding SEM images of the products obtained at 120°C and 160°C, respectively.

CuSO₄-containing organic solution can result in an obvious color change, and the color of the treated TiO₂ NAFs changes from light yellow to dull red as the amount of CuSO₄ in the organic solution increases. These results hint that the deposition of Cu₂O on the TiO₂ NAFs occurs after treatment in CuSO₄-containing organic solutions, especially when the amount of CuSO₄ is high. The XRD patterns of



(a)



(b)

FIGURE 2: (a) Digital photos and (b) XRD patterns of TiO₂ NAFs before and after treatment in the mixture of EG and DMF containing different amounts of CuSO₄ at 120°C for 16 h.

these untreated and treated TiO₂ NAFs films are shown in Figure 2(b). In the XRD pattern of the untreated TiO₂ film, the peaks at 35.1°, 38.4°, 40.2°, 53.0°, and 63.0° can be attributed to the background of Ti (JCPDS 44-1294). These peaks correspond to the diffraction of (100), (002), (101), (102), and (110) lattice planes of Ti, respectively. No diffraction peak attributed to TiO₂ phase can be observed, indicating that the TiO₂ nanotube arrays are amorphous. After being treated in CuSO₄-containing organic solutions at 120°C for 16 h, the TiO₂ nanotube arrays are still in the amorphous state. In addition, in the XRD patterns of all treated NAFs we cannot observe any diffraction peak which can be assigned to the Cu₂O phase, indicating that Cu₂O might be well-dispersed on TiO₂ NAFs.

The chemical composition of TiO₂ NAFs before and after being treated in CuSO₄-containing organic solution was characterized by EDS. Figure 3(a) shows the EDS spectra of these films, and the amount of Cu calculated from the spectra is presented in Figure 3(b) (see open circles). It is obvious that a small amount of fluorine is incorporated into

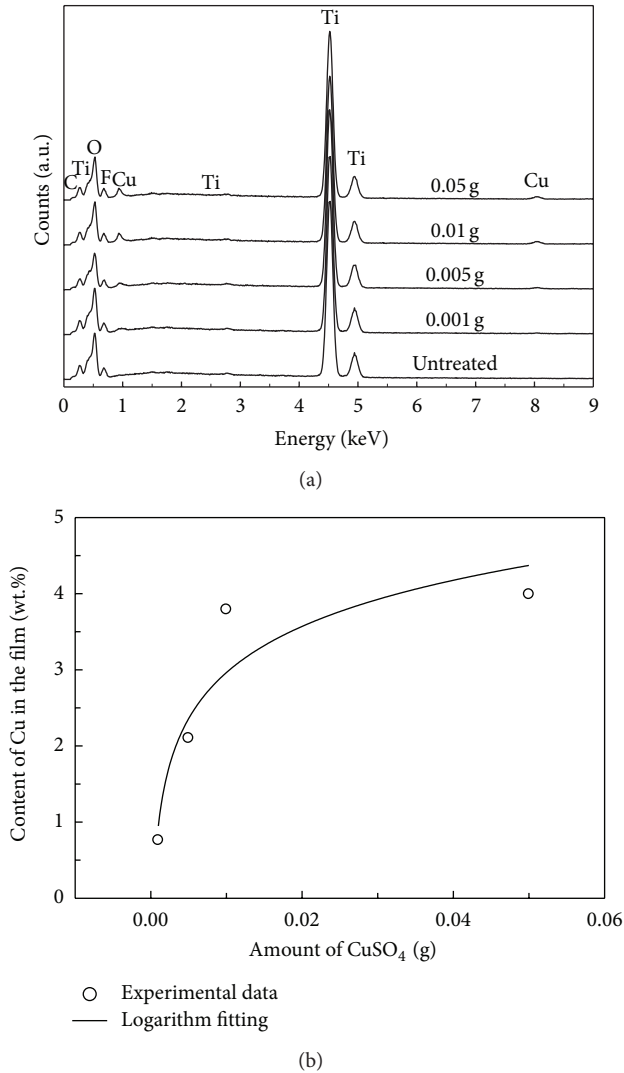


FIGURE 3: (a) EDS spectra of TiO_2 NAFs before and after treatment in the mixture of EG and DMF containing different amounts of CuSO_4 at 120°C for 16 h; (b) plot of content of Cu in the film against the amount of CuSO_4 in the solution (see open circles). The curve is the fitting result using a logarithm equation of $y = a + b\ln x$.

TiO_2 nanotubes, and treatment in CuSO_4 -containing organic solution cannot remove fluorine from the TiO_2 nanotube layer. The observation of fluorine in the nanotube layer should result from the fact that F^- will migrate towards the Ti anode during the anodizing process [24]. From Figure 3(b), we can also find that the amount of Cu in the film shows an increasing trend as the concentration of CuSO_4 in the organic solution increases. The increasing trend can be roughly fitted by a logarithm equation of $y = 6.991 + 0.8747\ln x$. The surface morphology of treated TiO_2 NAFs can be found in Figure 4. As can be seen from Figures 4(a) and 4(b), after being treated in organic solution containing a small amount of CuSO_4 (viz. 0.001 g and 0.005 g), the amount of Cu_2O decorated on the film (indicated by white arrows) is very small. When the amount of CuSO_4 is raised to 0.01 g or 0.05 g (see Figures 4(c) or 4(d)), we can observe many nanoparticles

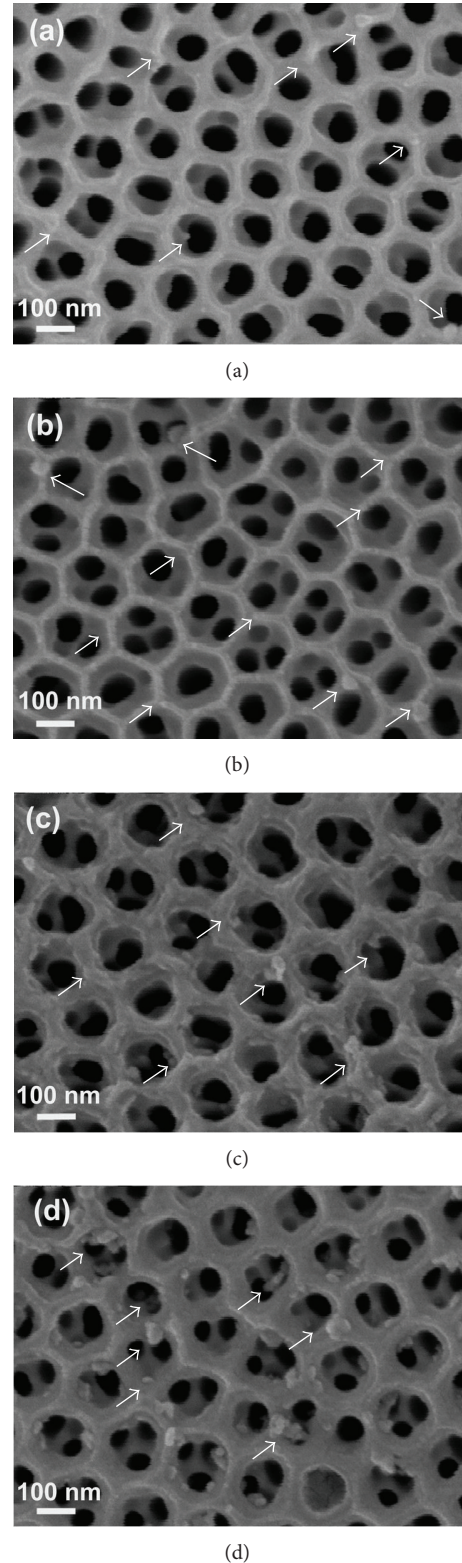
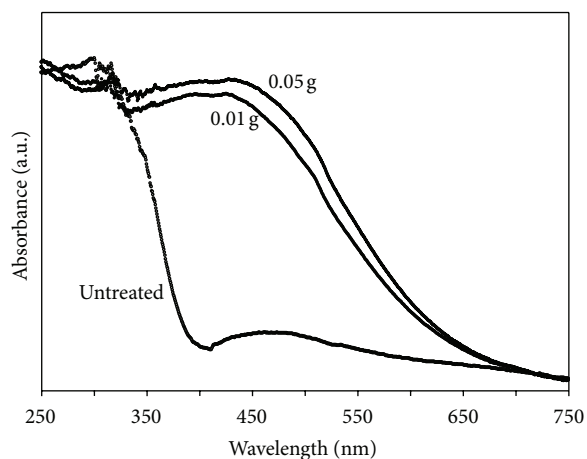
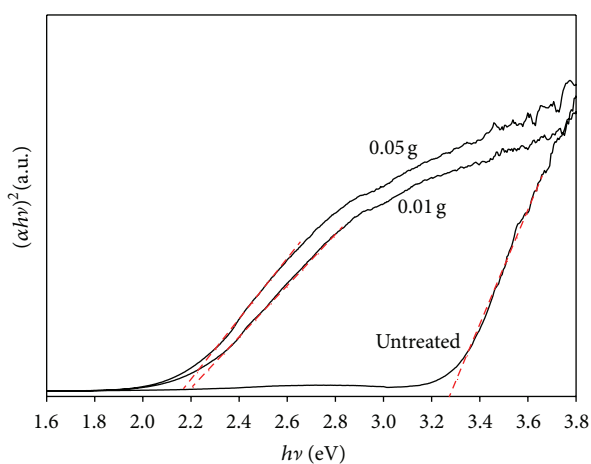


FIGURE 4: SEM images of TiO_2 NAFs after treatment in the mixture of EG and DMF containing different amounts of CuSO_4 at 120°C for 16 h: (a) 0.001 g, (b) 0.005 g, (c) 0.01 g, and (d) 0.05 g.

deposited on the films (indicated by white arrows). These nanosized Cu_2O particles are well dispersed on the wall of



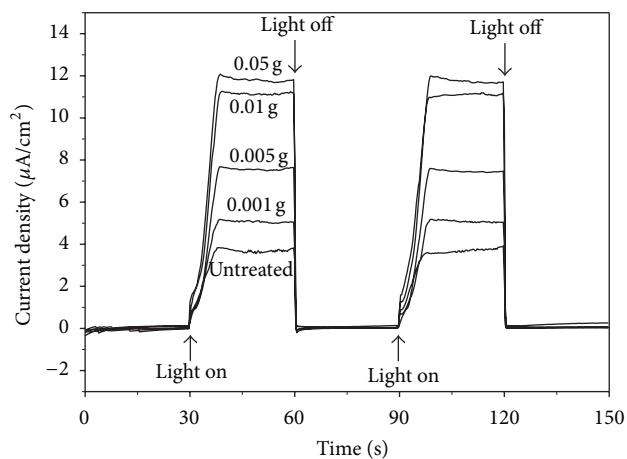
(a)



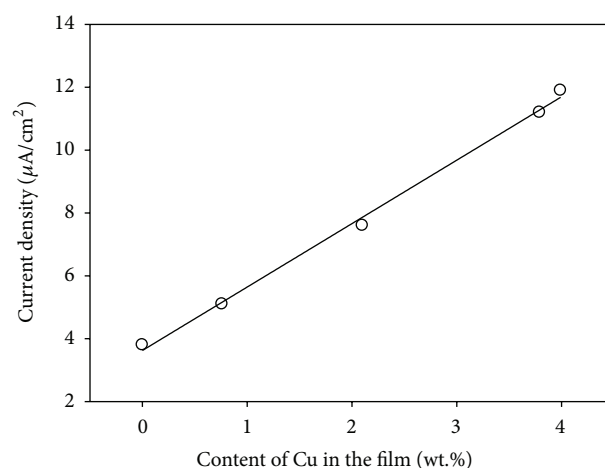
(b)

FIGURE 5: (a) UV-vis diffuse reflectance spectrum of TiO₂ NAFs before and after treatment in the mixture of EG and DMF containing 0.01 or 0.05 g CuSO₄ at 120°C for 16 h; (b) plot of $(\alpha h\nu)^2$ against photon energy ($h\nu$) for these three TiO₂ NAFs.

TiO₂ nanotubes without blocking the nanotube, a commonly observed phenomenon in the case of deposition of Cu₂O via electrochemical method [16–19]. The observed result might be related to the fact that in the case of electrodeposition the applied voltage favors the formation of Cu₂O crystals of large size [16–19], which may easily block the nanotube, while in our case the growth of Cu₂O resulting from the reduction of Cu(II) in organic solvent tends to form Cu₂O nanocrystals (see Figure 1(a)). In addition, when Cu₂O heterogeneously deposits on TiO₂ NAFs, the interaction between Cu₂O and TiO₂ can reduce the surface energy of Cu₂O nanocrystals and thus reduces their aggregation degree (namely, very large particles as observed in Figure 1(b) are not formed by aggregation of Cu₂O nanocrystals). As a result, the nanotubes are not easily blocked by these small-sized Cu₂O particles. Despite the observation of Cu₂O nanoparticles on the film surface, however, these Cu₂O nanoparticles cannot be detected by XRD (see Figure 2(b)). The possible reason for this is that these Cu₂O nanoparticles are distributed on



(a)



○ Experimental data
— Linear fitting

(b)

FIGURE 6: (a) Measured photocurrent density of TiO₂ NAFs before and after treatment in the mixture of EG and DMF containing different amounts of CuSO₄ at 120°C for 16 h; (b) plot of photocurrent density against the amount of Cu in the film.

the film surface. Compared with the corresponding powder materials, nanosized materials dispersed on the film surface is often more difficult to be detected by conventional XRD technique when their crystal size or amount is not large enough. In addition, since the small-sized Cu₂O particles tend to aggregate due to high surface energy (see Figure 1(b)), the particles of large size observed in Figure 4 might also be composed of several small-sized particles, which further make it difficult to detect Cu₂O phase by XRD.

To determine whether the treatment of TiO₂ NAFs in CuSO₄-containing organic solution can extend their light-response scope from ultraviolet to visible light region, we have measured the UV-vis diffuse reflectance spectrum of the TiO₂ NAFs treated in organic solution containing relatively high amount of CuSO₄ (viz. 0.01 g and 0.05 g). Figure 5(a) shows the UV-vis diffuse reflectance spectrum of these two

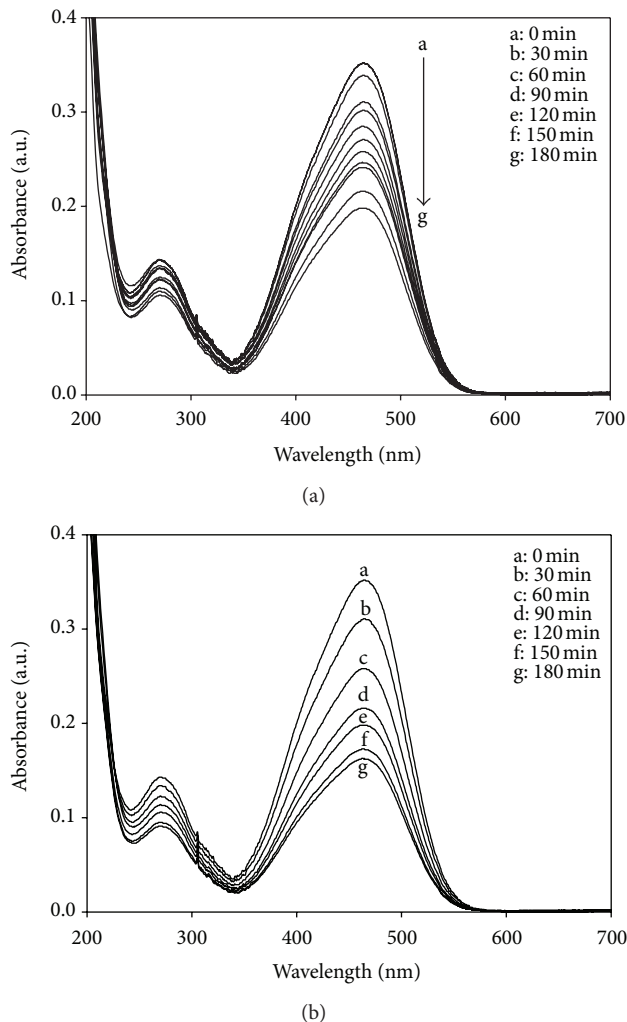


FIGURE 7: Comparison of the temporal evolution of the adsorption spectra of MO solution degraded by two TiO_2 NAFs: (a) untreated and (b) after treatment in the mixture of EG and DMF containing 0.05 g CuSO_4 at 120°C for 16 h.

treated TiO_2 NAFs. For comparison, the UV-vis diffuse reflectance spectrum of the untreated film is also shown. Compared with the untreated film, both two treated TiO_2 NAFs exhibit significant increases in photoadsorption at the wavelength larger than 400 nm, suggesting that they can respond well to visible light. The absorption coefficient α follows the equation $\alpha h\nu = A(h\nu - E_g)^\gamma$, where h , ν , A , E_g , and γ are, respectively, plank constant, light frequency, proportionality coefficient that depends on the properties of the material, band gap, and a constant that can take different values depending on the type of electronic transition [25]. For a permitted direct transition, $\gamma = 0.5$. Figure 5(b) shows the plot of $(\alpha h\nu)^2$ against $h\nu$ for three films, where the value of E_g is obtained by extrapolating the linear part of the graphics to the axis of the abscissa (see dashed red lines). The band gaps estimated from the plots of $(\alpha h\nu)^2$ verses photon energy ($h\nu$) are about 3.27, 2.20, and 2.16 eV for untreated TiO_2 NAF and two treated TiO_2 NAFs, respectively, (see Figure 5(b)).

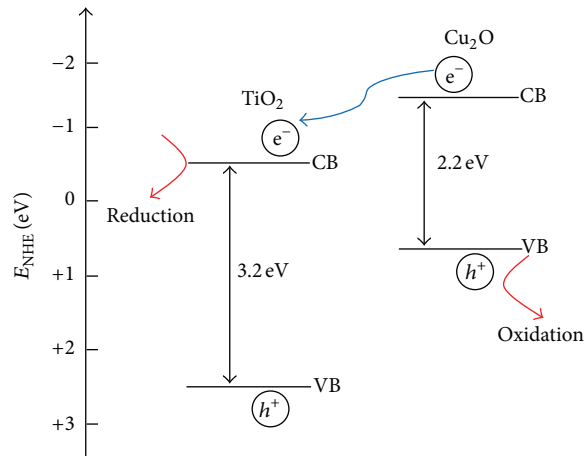


FIGURE 8: Schematic diagram for describing the band gap and electron transfer for the $\text{Cu}_2\text{O}/\text{TiO}_2$ system. CB, VB, and NHE are the abbreviations of conduction band, valence band, and normal hydrogen electrode, respectively.

The observed decrease in the band gap after treatment in CuSO_4 -containing organic solutions is in line with the UV-vis adsorption spectra with a red shift. Since the band gap of Cu_2O is about 2.2 eV, the value of 2.20 and 2.16 eV obtained for two treated NAFs confirms that Cu_2O is deposited on TiO_2 NAF.

The photoelectrochemical property of the as-prepared or Cu_2O -decorated TiO_2 film electrodes is investigated by measuring the anodic photocurrent in a 0.25 M Na_2SO_4 aqueous solution. As can be seen from Figure 6(a), without light irradiation (from 0–30 s), the dark currents for all films are almost equal to zero. When the light is on (from 30 to 60 s), the photocurrent increases sharply till reaching a certain value. If the light is off (from 60 to 90 s), the photocurrent declines rapidly to about zero. A similar phenomenon can also be observed in the range of 90–150 s. The observed photocurrent represents the anodic oxidation of water to oxygen by the photogenerated holes at the film electrode under light irradiation. For the untreated TiO_2 film, under light irradiation the electrons are excited from the valence band to conduction band of TiO_2 to form photogenerated electron-hole pairs. The photogenerated electrons and holes are separated under the external potential bias, and most electrons are transferred to titanium substrate to produce photocurrent with the hole oxidizing water to oxygen on the surface of the anode. It is clear from Figure 6(a) that the decoration of Cu_2O can lead to a great rise in photocurrent density, where the photocurrent density for the treated TiO_2 NAF in organic solution containing 0.05 g CuSO_4 is about 3 times higher than that for the untreated TiO_2 NAF. It is also interesting to note that the photocurrent density almost increases linearly with the amount of Cu in the film (see Figure 6(b)). These results suggest that the decoration of Cu_2O can greatly improve the water splitting performance of the TiO_2 NAFs under sunlight. The comparison of photocatalytic activity between untreated and treated TiO_2 NAFs in organic solution containing 0.05 g CuSO_4 is also evaluated

by the photodegradation of MO. The MO aqueous solution shows an intense absorption band centered at ~ 464 nm and the peak intensity is proportional to its concentration. Figure 7 shows a comparison of the temporal evolution of the adsorption spectra of MO solution degraded by two films. It is obvious that the Cu_2O -decorated TiO_2 NAF exhibits better photocatalytic activity than the undecorated one. The degradation efficiency of MO for the Cu_2O -decorated film reaches $\sim 54.7\%$ in 3 h, while that for the undecorated film is $\sim 31.2\%$.

The enhanced activity of the Cu_2O -decorated NAFs observed in our experiments can be attributed to the combined effect of several factors. Firstly, under simulated sunlight, TiO_2 can be excited by UV light, and Cu_2O can be excited by visible light, which will generate more electrons and holes for photocatalytic reactions as compared to undecorated TiO_2 NAF. Secondly, the combination of TiO_2 with Cu_2O will lead to a reduced recombination of the photoexcited electrons and holes due to the difference between the band edges of Cu_2O and TiO_2 semiconductors. As shown in Figure 8, the electron excited under visible light may transfer from the conduction band of Cu_2O to that of TiO_2 since the conduction band edge for Cu_2O is higher than that of TiO_2 [23]. As a result, the recombination probability of the photoexcited electrons and holes will be reduced, leading to an improvement in photocatalytic activity.

4. Conclusions

In summary, we have presented a novel method for modification of anodic TiO_2 nanotube array films with Cu_2O nanoparticles. The method is based on the theory of heterogeneous nucleation and growth in an organic solvent (ethylene glycol and *N,N*-dimethylformamide) containing CuSO_4 . The Cu_2O nanoparticles are found to be well dispersed on the wall of TiO_2 nanotubes without blocking the nanotube, and the amount of Cu_2O deposited on the TiO_2 nanotube array films shows an increasing trend as the concentration of CuSO_4 increases. The decorated nanotube array films can respond well to both ultraviolet and visible light and show much better photocatalytic activity than the undecorated film.

Acknowledgment

This work was supported by the Natural Science Foundation of Zhejiang Province (no. LY12B07011).

References

- [1] Y. Xia, P. Yang, Y. Sun et al., "One-dimensional nanostructures: synthesis, characterization, and applications," *Advanced Materials*, vol. 15, no. 5, pp. 353–389, 2003.
- [2] W. Zhou, H. Liu, R. I. Boughton et al., "One-dimensional single-crystalline Ti-O based nanostructures: properties, synthesis, modifications and applications," *Journal of Materials Chemistry*, vol. 20, no. 29, pp. 5993–6008, 2010.
- [3] J. Pan, H. Shen, and S. Mathur, "One-dimensional SnO_2 nanostructures: synthesis and applications," *Journal of Nanotechnology*, vol. 2012, Article ID 917320, 12 pages, 2012.
- [4] J. Qu and C. Lai, "One-dimensional TiO_2 nanostructures as photoanodes for dye-sensitized solar cells," *Journal of Nanomaterials*, vol. 2013, Article ID 762730, 11 pages, 2013.
- [5] S. Wang, T. Wang, Y. W. Ding et al., "Gas-supported high-photoactivity TiO_2 nanotubes," *Journal of Nanomaterials*, vol. 2012, Article ID 909473, 6 pages, 2012.
- [6] J. Jitputti, Y. Suzuki, and S. Yoshikawa, "Synthesis of TiO_2 nanowires and their photocatalytic activity for hydrogen evolution," *Catalysis Communications*, vol. 9, no. 6, pp. 1265–1271, 2008.
- [7] Q. Zhang, H. Xu, and W. Yan, "Highly ordered TiO_2 nanotube arrays: recent advances in fabrication and environmental applications—a review," *Nanoscience and Nanotechnology Letters*, vol. 4, no. 5, pp. 505–519, 2012.
- [8] K. M. Kummer, E. Taylor, and T. J. Webster, "Biological applications of anodized TiO_2 nanostructures: a review from orthopedic to stent applications," *Nanoscience and Nanotechnology Letters*, vol. 4, no. 5, pp. 83–493, 2012.
- [9] Y. Ku, Y.-S. Chen, W.-M. Hou, and Y.-C. Chou, "Effect of NH_4F concentration in electrolyte on the fabrication of TiO_2 nanotube arrays prepared by anodisation," *Micro & Nano Letters*, vol. 7, no. 9, pp. 939–942, 2012.
- [10] Z. C. Xu, Q. Li, S. A. Gao, and J. K. Shang, "Synthesis and characterization of niobium-doped TiO_2 nanotube arrays by anodization of Ti-20Nb alloys," *Journal of Materials Science & Technology*, vol. 28, no. 10, pp. 865–870, 2012.
- [11] C. A. Grimes, "Synthesis and application of highly ordered arrays of TiO_2 nanotubes," *Journal of Materials Chemistry*, vol. 17, no. 15, pp. 1451–1457, 2007.
- [12] M. Paulose, K. Shankar, O. K. Varghese, G. K. Mor, and C. A. Grimes, "Application of highly-ordered TiO_2 nanotube-arrays in heterojunction dye-sensitized solar cells," *Journal of Physics D*, vol. 39, no. 12, pp. 2498–2503, 2006.
- [13] S. Mozia, P. Brozek, J. Przepiorski, B. Tryba, and A. W. Morawski, "Immobilized TiO_2 for phenol degradation in a pilot-scale photocatalytic reactor," *Journal of Nanomaterials*, vol. 2012, Article ID 949764, 10 pages, 2012.
- [14] W. Y. Zhao, W. Y. Fu, H. B. Yang et al., "Synthesis and photocatalytic activity of Fe-doped TiO_2 supported on hollow glass microbeads," *Nano-Micro Letters*, vol. 3, no. 1, pp. 20–24, 2011.
- [15] C. W. Lai and S. Sreekanth, " TiO_2 nanotubes arrays: improved photoelectrochemical water splitting by adding optimum amount of ethylene glycol in KOH Electrolyte," *Nanoscience and Nanotechnology Letters*, vol. 5, no. 1, pp. 57–62, 2013.
- [16] S. Zhang, S. Zhang, F. Peng, H. Zhang, H. Liu, and H. Zhao, "Electrodeposition of polyhedral Cu_2O on TiO_2 nanotube arrays for enhancing visible light photocatalytic performance," *Electrochemistry Communications*, vol. 13, no. 8, pp. 861–864, 2011.
- [17] S. S. Zhang, C. Liu, X. L. Liu et al., "Nanocrystal Cu_2O -loaded TiO_2 nanotube array films as high-performance visible-light bactericidal photocatalyst," *Applied Microbiology and Biotechnology*, vol. 96, no. 5, pp. 1201–1207, 2012.
- [18] L. Huang, S. Zhang, F. Peng et al., "Electrodeposition preparation of octahedral- Cu_2O -loaded TiO_2 nanotube arrays for visible light-driven photocatalysis," *Scripta Materialia*, vol. 63, no. 2, pp. 159–161, 2010.
- [19] Y. B. Liu, H. B. Zhou, J. H. Li et al., "Enhanced photoelectrochemical properties of Cu_2O -Loaded Short TiO_2 nanotube array electrode prepared by sonoelectrochemical deposition," *Nano-Micro Letters*, vol. 2, no. 4, pp. 277–284, 2010.

- [20] Y. Hou, X. Y. Li, Q. D. Zhao, X. Quan, and G. H. Chen, "Fabrication of $\text{Cu}_2\text{O}/\text{TiO}_2$ nanotube heterojunction arrays and investigation of its photoelectrochemical behavior," *Applied Physics Letters*, vol. 95, no. 9, Article ID 093108, 2009.
- [21] Y. Q. Cong, Z. Li, Q. Wang, Y. Zhang, Q. Xu, and F. X. Fu, "Enhanced photoelectrocatalytic activity of TiO_2 nanotube arrays modified with simple transition metal oxides (Fe_2O_3 , CuO , NiO)," *Acta Physico-Chimica Sinica*, vol. 28, no. 6, pp. 1489–1496, 2012.
- [22] G. S. Li, L. Wu, F. Li, P. P. Xu, D. Q. Zhang, and H. X. Li, "Photoelectrocatalytic degradation of organic pollutants via a CdS quantum dots enhanced TiO_2 nanotube array electrode under visible light irradiation," *Nanoscale*, vol. 5, no. 5, pp. 2118–2125, 2013.
- [23] M. Ni, M. K. H. Leung, D. Y. C. Leung, and K. Sumathy, "A review and recent developments in photocatalytic water-splitting using TiO_2 for hydrogen production," *Renewable and Sustainable Energy Reviews*, vol. 11, no. 3, pp. 401–425, 2007.
- [24] G. D. Sulka, J. Kapusta-Kołodziej, A. Brzózka, and M. Jaskuła, "Fabrication of nanoporous TiO_2 by electrochemical anodization," *Electrochimica Acta*, vol. 55, no. 14, pp. 4359–4367, 2010.
- [25] A. Duret and M. Grätzel, "Visible light-induced water oxidation on mesoscopic $\alpha\text{-Fe}_2\text{O}_3$ films made by ultrasonic spray pyrolysis," *Journal of Physical Chemistry B*, vol. 109, no. 36, pp. 17184–17191, 2005.

Review Article

Molecular Design and Applications of Self-Assembling Surfactant-Like Peptides

Chengkang Tang,^{1,2} Feng Qiu,^{1,2} and Xiaojun Zhao¹

¹ Nanomedicine Laboratory, West China Hospital, Sichuan University, Chengdu 610041, China

² Regenerative Medicine Research Center, West China Hospital, Sichuan University, Chengdu 610041, China

Correspondence should be addressed to Xiaojun Zhao; xiaojunz@mit.edu

Received 17 July 2013; Accepted 12 August 2013

Academic Editor: Yuan Zhang

Copyright © 2013 Chengkang Tang et al. This is an open access article distributed under the Creative Commons Attribution License, which permits unrestricted use, distribution, and reproduction in any medium, provided the original work is properly cited.

Self-assembling surfactant-like peptides have been explored as emerging nanobiomaterials in recent years. These peptides are usually amphiphilic, typically possessing a hydrophobic moiety and a hydrophilic moiety. The structural characteristics can promote many peptide molecules to self-assemble into various nanostructures. Furthermore, properties of peptide molecules such as charge distribution and geometrical shape could also alter the formation of the self-assembling nanostructures. Based on their diverse self-assembling behaviours and nanostructures, self-assembling surfactant-like peptides exhibit great potentials in many fields, including membrane protein stabilization, drug delivery, and tissue engineering. This review mainly focuses on recent advances in studying self-assembling surfactant-like peptides, introducing their designs and the potential applications in nanobiotechnology.

1. Introduction

Molecular self-assembly is a universal phenomenon in nature: phospholipid molecules can self-assemble into millimeter-size lipid tubules, silk fibroins can be fabricated into silk materials over 2 km in length [1], and so on. Molecular self-assembly is usually driven by noncovalent bonds such as ionic bond, hydrophobic interaction, van der Waals interaction, and hydrogen bonding, which could promote self-assembling molecules to spontaneously aggregate into well-ordered structures. As a bottom-up strategy to fabricate nanomaterials, molecular self-assembly has received considerable attentions.

Recently, nature-inspired investigators have designed novel nanobiomaterials based on self-assembling peptides, which are usually composed of natural L-amino acids and have excellent biocompatibility. As a novel category of self-assembling nanomaterials, self-assembling peptides have become especially attractive, for their successful applications in many fields, including three-dimensional cell culture and reparative or regenerative medicine [2–8], tissue engineering [9–11], and drug release [12–14]. In this review, we will focus on a family of surfactant-like peptides designed by mimicking

the structure of traditional surfactants and introduce their applications in biological surface engineering.

2. Design of Typical Surfactant-Like Peptides

Surfactants are defined as materials that can greatly decrease the surface tension of solvents when used at very low concentrations [15]. Surfactants are usually a category of amphiphiles composed of hydrophobic tail and hydrophilic head. Recently, a family of surfactant-like peptides has been designed by mimicking the structure of traditional surfactants [16–18]. A typical surfactant-like peptide molecule consists of two parts: a hydrophobic tail composed of several consecutive hydrophobic amino acids and a hydrophilic head composed of one or two hydrophilic amino acids.

Based on this rule, researchers have selected different hydrophobic or hydrophilic amino acids to design various surfactant-like peptides freely. For example, the hydrophilic head could be designed as positively charged Arg, Lys, and His, or negatively charged Asp and Glu, producing cationic or anionic surfactant-like peptides. On the other hand, the hydrophobic tail could be designed by choosing different

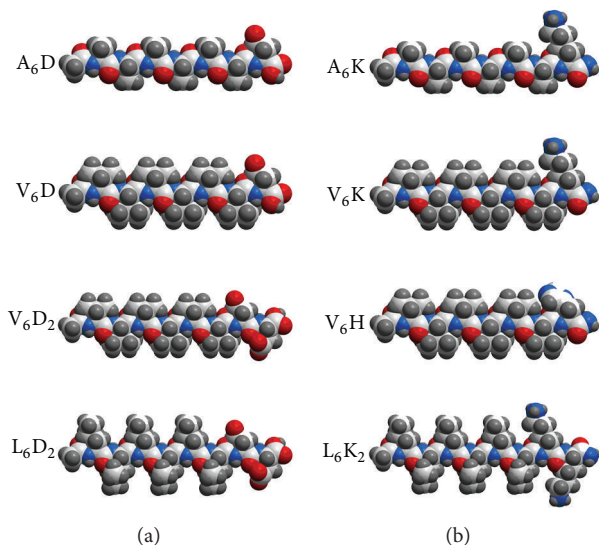


FIGURE 1: The molecular models of several classic surfactant-like peptides. (a) Negatively charged surfactant-like peptides; (b) positively charged surfactant-like peptides, grey = hydrogen atom, white = carbon atom, red = oxygen atom, blue = nitrogen atom.

hydrophobic amino acids such as Gly, Ala, Val, Leu, and Ile with different levels of hydrophobicity, so that the overall hydrophobicity of a surfactant-like peptide could be controlled. Recently, a number of typical surfactant-like peptides have been designed (Figure 1).

The flexible design of typical surfactant-like peptide is not based on the selection of amino acids only. The position of the hydrophilic head could be changed to generate new surfactant-like peptides. An example is that the hydrophilic heads of those peptides in Figure 1 are set at the C-terminal, while the heads of KVVVVVV (KV₆) and HHVVVVVV (H₂V₆) are set at the N-terminal [18]. The length of a surfactant-like peptide could also be a design strategy by usually controlling the number of hydrophobic amino acids in the tail. Although the tail of a surfactant-like peptide molecule is generally composed of six hydrophobic amino acids, making the whole peptide molecule about 2.5 nm in length, which is similar to the length of natural phospholipids, novel surfactant-like peptide molecules, with a longer hydrophobic tail, have the same self-assembling behavior, except that the self-assembling nanostructures become more polydisperse [17].

3. Self-Assembling Mechanism of Typical Surfactant-Like Peptides

Like the classic formation of lipid bilayer, one self-assembling model of surfactant-like peptides is proposed that molecules could undergo a tail-to-tail alignment to form bilayer structures, which further form nanotubes and nanovesicles (Figure 2(a)). In this model, surfactant-like peptides, such as A₆D, V₆D, V₆D₂, L₆D₂, are composed of 1~2 charged amino acids and 4~8 hydrophobic amino acids and undergo self-assembly in aqueous solution to form nanotubes or

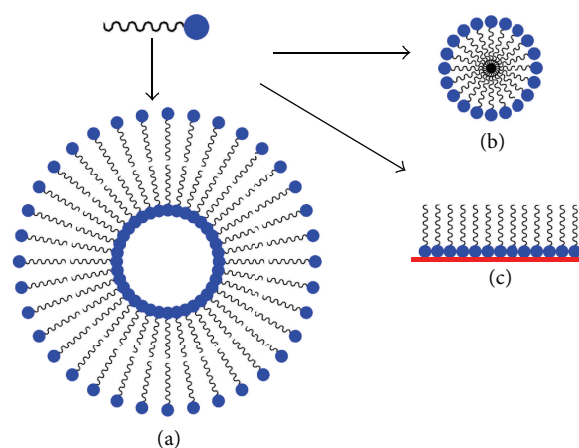


FIGURE 2: The self-assembling models of typical surfactant-like peptides. (a) Bilayer tube or vesicle. (b) The formation of micelle. (c) Monolayer on mica surface.

nanovesicles with diameter of 30~50 nm, which could further form network with three-way junctions [16–20]. These nanostructures were highly unstable and dynamic so that a special quick-freeze/deep-etch technique was required to fix and visualize them. These peptide molecules take an irregular secondary structure as revealed by circular dichroism (CD), which seems less important for the self-assembling process, and the hydrophobic interaction between tails is regarded as the major driving force. Generally, surfactant-like peptides with tail of Ala or Val could form more stable nanostructures than those with tail of Gly, Leu, and Ile [15, 16].

In addition to forming tail-to-tail bilayer structure, traditional surfactants could also form micelles by packing the tails in a hydrophobic core and exposing the hydrophilic heads outside. This kind of self-assembling model has also been observed for surfactant-like peptides, which could form nanofibers instead of nanotubes or nanovesicles [21]. As observed by atomic force microscopy (AFM) and transmission electron microscopy (TEM), A₆K, a cationic surfactant-like peptide, could form nanofibers, nanorods, and nanospheres with various length [21]. These nanostructures are quite different with the nanotubes and nanovesicles described in an earlier report. For example, the diameter of these nanostructures is about 10 nm, much smaller than 30~50 nm; the nanofibers are separated from each other, rather than forming a network by three-way connection. All these differences indicated that these nanostructures are generated by different self-assembling model. The molecular model has also been proposed to explain this alternative self-assembling behavior. As shown in Figure 2(b), peptide molecules pack their hydrophobic tail in a core and expose their hydrophilic head outside, undergoing the formation of cylindrical or spherical micelles to form nanofibers or nanospheres.

The nanostructures formed of surfactant-like peptides could be closely associated with environments. When the A₆K solution was spread on mica surface for AFM observation, a kind of membrane-like structure was observed in addition to nanofibers [21]. It is likely that the A₆K

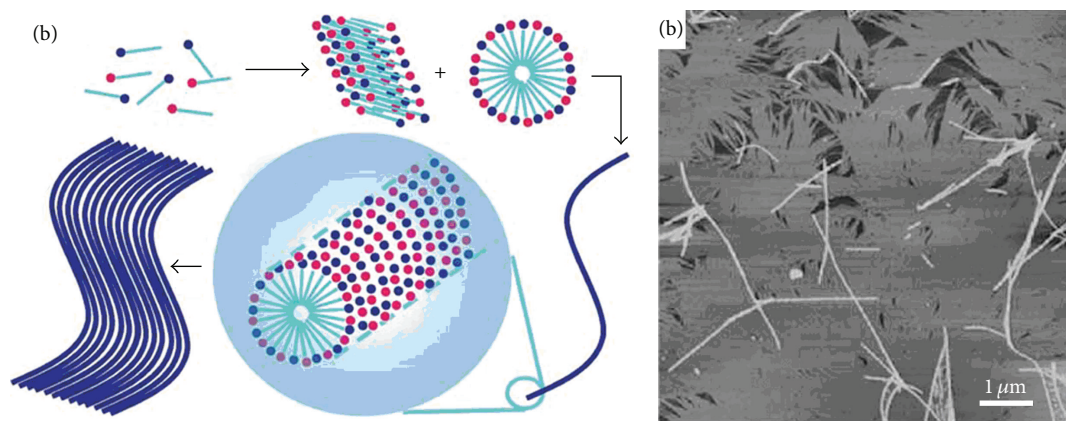


FIGURE 3: Self-assembly of catanionic surfactant-like peptides (reprinted from [25]). (a) Proposed self-assembling model. (b) Well aligned nanoropes observed by AFM.

monomers could attach their positively charged heads to the negatively charged mica surface, while stretching their hydrophobic tails up to air, forming a layer of peptide monomers aligned shoulder by shoulder (Figure 2(c)). In this manner, the peptide monolayer could cover the hydrophilic mica surface and transform it to a hydrophobic one. This interesting self-assembling behavior of A_6K on mica surface could act as a very simple technique for surface modification. It is not clear why all kinds of structures fabricated by the same surfactant-like peptide could coexist if no preferential condition is applied, but it is no doubt that the new pathway to form various nanostructures is very helpful to understand the behavior of these self-assembling surfactant-like peptides and to further exploit their potential applications.

4. Other Surfactant-Like Peptides

4.1. Catanionic and Zwitterionic Surfactant-Like Peptides.

Typical surfactant-like peptides, despite anionic or cationic surfactant-like peptides, often form a mixture of various nanostructures such as nanotubes/nanovesicles and nanofibers/nanospheres. These nanostructures are dynamic and unstable, which becomes an obstacle for their application. For this reason, chemical complementarity should be considered to exploit new surfactant-like peptides with stable self-assembling behavior, which means the preferred formation of a certain type of nanostructure or forming nanostructures with better mechanical/thermal stability at lower critical micelle concentration (CMC). In fact, ionic bond has been proved to be a very important noncovalent force to drive the self-assembling process and determine the properties of self-assembled structures. In order to exploit self-assembling surfactant-like peptides with better stabilities, researchers have made several attempts to introduce ionic bonds into the system of typical surfactant-like peptides.

Catanionic and zwitterionic surfactants are different from typical anionic and cationic surfactants. Catanionic surfactants are the mixed systems of traditional anionic and cationic surfactants [22], and zwitterionic surfactants are the surfactants bearing both positive and negative charges in a single

hydrophilic head [23, 24]. Possibly because of the ionic bonds between oppositely charged heads, these two special groups of surfactants could form structures with better stability compared with typical surfactants [25–28]. Recently, Khoe and colleagues have studied the self-assembling behaviors of several catanionic surfactant-like peptides systems, which were the mixtures of cationic surfactant-like peptide A_6K and anionic surfactant-like peptide A_6D at various ratios [25]. They found that, when A_6D and A_6K were mixed at the ratio of 2:1, the catanionic system could form well-ordered nanofibers (Figure 3), indicating that in a catanionic system, the interaction between positively and negatively charged heads has significant effects on the self-assembling behavior, pointing out a promising approach to design novel nanomaterials based on mixed surfactant-like peptides.

Recently, we have designed a zwitterionic surfactant-like peptide by simply removing the C-terminal protective amide of A_6K and exposing the dissociable carboxyl group [21]. This new peptide, named A_6K^\pm , could simultaneously bear a positive and a negative charge at its C-terminal. This study showed that A_6K^\pm could form much longer nanofibers compared with typical anionic or cationic surfactant-like peptides (Figure 4), synergistically driven by the ionic bonds among hydrophilic heads and the hydrophobic interaction among tails. Moreover, the self-assembling structures formed by A_6K^\pm were also more mechanically and thermally stable than A_6K . A_6K^\pm could also more sensitively respond to the change of environmental pH and undergo complicated transformation. These results indicated that novel stable and smart nanomaterials could be obtained by designing zwitterionic surfactant-like peptides.

4.2. Bolaamphiphilic Peptides. Different from typical surfactants with only one hydrophilic head, bolaamphiphile, named after a special weapon “bola,” has two hydrophilic heads connected by a hydrophobic section [29, 30]. Bolaamphiphiles have been proven to be a category of emerging nanomaterials for their ability to self-assemble into various valuable nanostructures, including membrane-mimetic films for bioactive functions [31, 32], nanotubes for metallic nanowire [33–35],

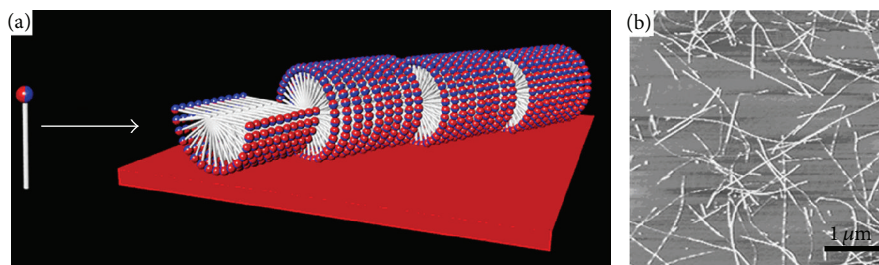


FIGURE 4: Self-assembly of zwitterionic surfactant-like peptides. (a) Proposed self-assembling model. (b) Long nanofibers observed by AFM.

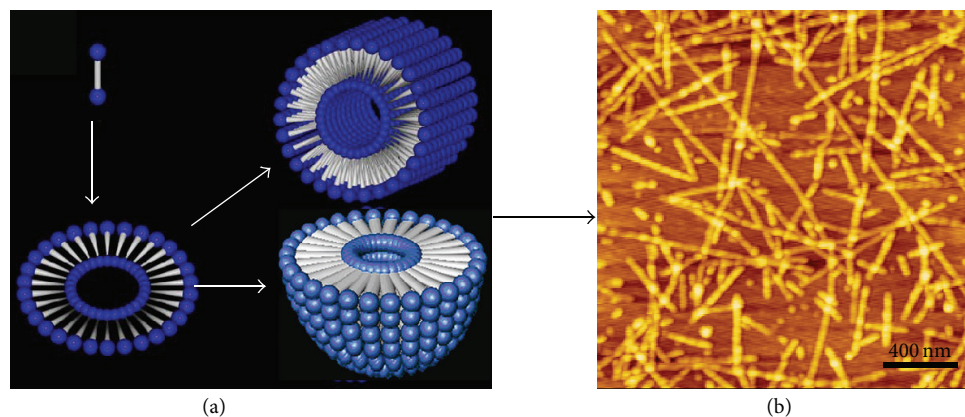


FIGURE 5: (a) Self-assembling model of bolaamphiphilic peptides. (b) AFM image of bolaamphiphilic peptide KA_6K .

nanofibers [35], helical ribbons [36], and nanovesicles for drug and gene delivery [37].

By mimicking the structure of these bolaamphiphiles, our laboratory has designed a series of bolaamphiphilic peptides, which are composed of Gly, Ala, and Val as their hydrophobic sections and charged Lys or Asp as their hydrophilic heads [38]. By adjusting hydrophobic or hydrophilic amino acids, the length and hydrophobicity of the bolaamphiphilic peptide molecule could be controlled to generate different self-assembling nanostructures, such as nanofibers or nanospheres with hydrophilic core and surface (Figure 5). Different from the nanotubes and nanovesicles with diameter about 30~50 nm formed by typical surfactant-like peptides, these nanostructures formed by bolaamphiphilic peptides have a diameter less than 10 nm. The smaller size and the hydrophilic core might be important features for their application as cell-targeting carriers for hydrophilic molecules such as DNA, RNA, and some hydrophilic drugs. Furthermore, it has been found that after destroyed by sonication, the nanostructures formed by bolaamphiphilic peptides could undergo a slow process of reassembly to recovery, which is also an important feature for the potential of encapsulating small molecular components. Recently, bolaamphiphilic peptides with alkyl group as their hydrophobic sections have also been designed, which could self-assemble into nanofibers with hydrophilic core and surface [39].

4.3. Surfactant-Like Peptides with Ameliorated Geometrical Shape. It is well known that chemical complementarity

and geometrical compatibility are two basic elements for molecular self-assembly [40, 41]. For this reason, when ameliorating the structure of self-assembling molecules for better properties, geometrical compatibility should be considered. Our laboratory has designed several surfactant-like peptides with different geometrical shapes in order to study the effect of geometrical shape on the self-assembling behavior of surfactant-like peptides [42]. Briefly, by changing the amino acids, which have different spatial structures, AVK^{\pm} (Ac-AAAVVVK) has a wedge-like shape, and AGK^{\pm} (Ac-AAAGGGK) has a shape of inverted wedge. Compared with A_6K^{\pm} (Ac-AAAAAAK), which has a straight shape, the wedge-shaped AVK^{\pm} undergoes a more homogeneous self-assembling behavior to form much longer nanofibers, and these nanofibers are relatively more stable and less prone to be transformed to nanospheres, while the self-assembling behavior of A_6K^{\pm} is very dynamic and it tends to form mixture of nanofibers with various lengths and nanospheres. On the contrary, AGK^{\pm} , with inverted-wedge-like shape, couldn't undergo self-assembly in aqueous solution but could self-assemble into nanofibers with various lengths in nonpolar solvent.

As shown in Figure 6, 3D molecular models have been proposed to illuminate the effects of geometrical shape on self-assembling behaviors. For AVK^{\pm} , the wedge-like shape could efficiently reduce the spatial encumbrance when AVK^{\pm} molecules self-assemble into micelles, so that they can form stable cylindrical micelle nanofibers. For AGK^{\pm} , the inverted-wedge-like shape promotes them to embed the small

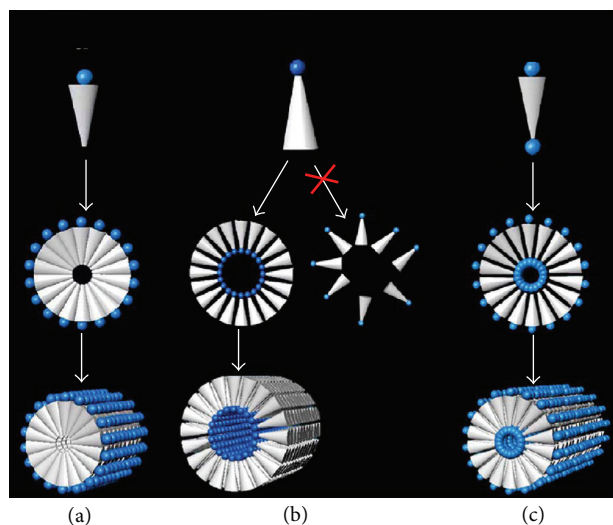


FIGURE 6: Self-assembly of surfactant-like peptides with different geometrical shape. (a) Wedge-shaped surfactant-like peptides form cylindrical micelle nanofibers in water solution. (b) Reversed-wedge-shaped surfactant-like peptide forms reverse micelle nanofibers in nonpolar environment. (c) Wedge-shaped bolaamphiphilic peptides form cylindrical micelle nanofibers in water solution.

hydrophilic head inside and expose the large hydrophobic tail to the nonpolar solution, finally forming reversed micelle nanofibers.

When the geometrical shape of the hydrophobic tail of a peptide was concerned, the property of the hydrophilic head seems to be less important. Similar to the self-assembling behavior of AVK^{\pm} , it has also been found that a negatively charged surfactant-like peptide A_3V_3D with wedge-like shape could also form smooth long nanofibers [43]. On the other hand, more hydrophobic amino acids could also be used to design surfactant-like peptide with geometrical shape effect. For example, a cone-shaped amphiphilic peptide $Ac-GAVILRR-NH_2$ could self-assemble into nanodonut structure through the fusion or elongation of spherical micelles [44]. These studies suggested that geometrical shape plays a crucial role in controlling the self-assembling behavior of surfactant-like peptides to form certain nanostructure.

As for the typical surfactant-like peptide system described above, geometrical shape could also greatly affect the self-assembling structure of bolaamphiphilic peptide. Our group has designed a novel bolaamphiphilic $KGGAAVVK$, which exhibited a wedge-like shape for the increasing size from Gly to Val. Unlike KA_6K with straight shape which self-assemble into mixture of nanofibers and nanospheres, $KGGAAVVK$ could selectively form long and smooth nanofibers [43]. Similar to the model proposed for typical surfactant-like peptide, the wedge-like shape of the peptide was also regarded as an important factor for the formation of such long nanofibers.

Besides those surfactant-like peptides totally composed of natural amino acids introduced above, some other similar self-assembling peptides containing special groups have also been studied in recent years. One of the most extensively

studied categories is peptide amphiphiles developed by Weber et al. [45, 46]. In these peptide amphiphiles, a typical molecule contains an alkyl chain as its hydrophobic tail and a functional peptide group as its hydrophilic head. By forming micellar nanofibers and exposing functional peptide groups outside, peptide amphiphiles have been proved to be potential nanomaterials which have been widely used in many fields including 3D cell culture and tissue engineering. Moreover, surfactant-like peptide has also been combined with traditional surfactant and shown novel self-assembling behavior which could be used as template for Au nanoparticles [47].

5. Applications of Surfactant-Like Peptides

5.1. Surfactant-Like Peptides Stabilizing Membrane Protein. According to the computational analyses of completely sequenced genomes, about one-third of all cellular proteins are membrane proteins, which contain at least one trans-membrane domain and have critical roles in many important life activities such as cell signaling, cell migration and movement, energy transformation, and substance transport [48]. However, most molecular structures of membrane proteins remain elusive, which is in sharp contrast to their great important functions in cells. The reason for this paradox is that natural membrane proteins are usually embedded in lipid bilayer, traditional purification, and crystallization methods for water-soluble proteins will remove lipids from membrane proteins, and affect the solubility and conformation stability of membrane proteins. In the past decades, many traditional surfactants such as detergents and lipids have been used for the stabilization, purification, and crystallization of membrane proteins; however, due to the complexity of membrane protein-detergent-lipid interactions, the efficacy is still far from satisfaction. Thus, the discovery and design of novel surfactants are acutely necessary to facilitate membrane protein purification and crystallization for structural studies.

Recently, surfactant-like peptides have shown promising potential in the study of membrane proteins. These surfactant-like peptides have structural properties similar to lipid: peptide molecule has a hydrophobic tail composed of several consecutive hydrophobic amino acids and a hydrophilic head composed of one or two hydrophilic amino acids. Based on the molecular structure, surfactant-like peptides could bind to the hydrophobic section of a membrane protein by using their hydrophobic tails and sequester it from water, preventing membrane protein from denaturation.

G protein-coupled receptors (GPCRs) are a large class of membrane proteins, which play a crucial role in cell signaling pathways and become a worldwide hotspot in the pharmaceutical industries. Unfortunately, the structures of most GPCRs remain elusive. To study the structure and function of diverse GPCRs, researchers have stabilized these membrane proteins with surfactant-like peptides. For example, Zhao has chosen bovine rhodopsin, one of GPCRs, and investigated the stabilization of bovine rhodopsin in solution by using a new class of surfactant-like peptides [49]. As shown in Figure 7, these surfactant-like peptides not only enhance the stability of bovine rhodopsin in the presence of lipids and the

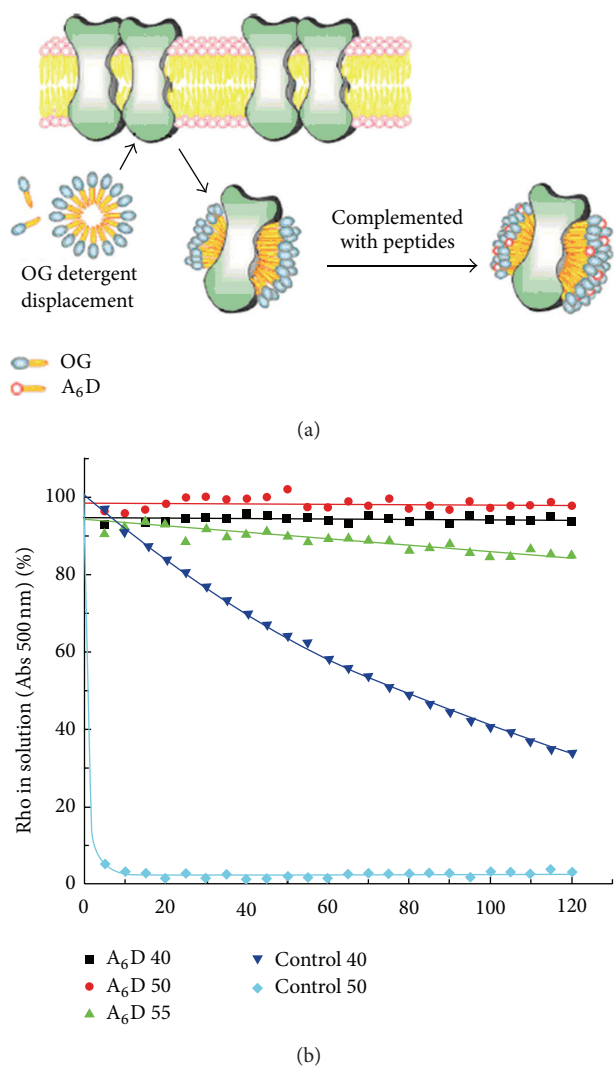


FIGURE 7: Surfactant-like peptides stabilize membrane proteins. (a) The proposed mechanism of surfactant-like peptide A_6D stabilizing membrane proteins (reprinted from [49]). (b) Stability of rhodopsin (Rho) in the absence of OG at different temperatures. Half-life of rhodopsin was as follows: not available in 2.5 mM A_6D at 40°C, 50°C, and 55°C; 101 min in control solution (1.25 mM A_6D /1% OG) at 40°C; <5 min in control solution at 50°C (reprinted from [49]).

common surfactants n-dodecyl- β -D-maltoside and octyl-D-glucoside but also effectively stabilize rhodopsin under thermal denaturation conditions even after the lipids were removed.

Additionally, researchers have investigated whether photosynthetic complexes could be effectively stabilized by surfactant-like peptides. Photosynthetic complexes are crucial proteins located in the membrane of chloroplast and are capable of transforming solar energy with amazing high efficacy, which promotes photosynthetic complexes to be made into nanodevices of solar biobattery as a safe and sustainable energy resource. To develop such solar biobattery, the stabilizing of photosynthetic complexes with bioactivity is

the first step. Researchers have certified the feasibility of stabilizing photosynthetic complexes with designed surfactant-like peptides. The fluorescence spectrum of photosystem I (PSI) stabilized by surfactant-like peptides had no significant difference compared with PSI directly extracted from leaves of spinach. Surprisingly, PSI could even maintain its bioactivity on a dry surface in a considerably long period by the protection of an anionic surfactant-like peptide V_6D [48].

5.2. Surfactant-Like Peptides as Drug and Gene Carriers. Since the surfactant-like peptide molecules can be easily designed and modified to form various nanostructures, they can be easily tailored for drug or gene delivery. These peptides have a unique amphiphilic structure, and the hydrophobic tail could promote surfactant-like peptides to self-assemble into the nanostructure with a hydrophobic core, which has potential to encapsulate water-insoluble molecules and deliver drugs and other biological molecules. On the other hand, the hydrophilic head could be modified as functional group for cell-targeting. Recently, a surfactant-like peptide with fatty tail was investigated as a hydrophobic drug carrier [50].

So far, gene therapy endeavors have still lacked optimal DNA delivery systems that are highly efficient, nontoxic, and simple to produce in large scales. Recently, it was found that a number of cationic surfactant-like peptides have great potential for gene delivery [51]. Compared with hydrophobic drug delivery, negatively charged DNA is expected to bind to the positively charged head of surfactant-like peptides. For example, cholesterol-conjugated HR15 and HR20 oligopeptides were synthesized, which were able to self-assemble into cationic micelles. The formation of the micelles increased local density of cationic charge, leading to greater DNA binding efficiency and thus higher gene transfection efficiency in both HepG2 and HEK293 cell lines [51]. Furthermore, surfactant-like peptide FA32 could form small micelles with particle size of about 100 nm, which could deliver hydrophobic drug DOX inside the cells efficiently. Meanwhile, these micelles could deliver DNA into HepG2 cells with high efficiency. These findings suggest that surfactant-like peptides could have the great potential to deliver hydrophobic drug and gene simultaneously into the same cells to achieve synergistic therapeutic effect [52].

5.3. Surfactant-Like Peptides for Tissue Engineering. Recently, tissue engineering, aimed at resolving the problems in organ repairing and tissue regeneration, has become an important strategy in modern biomedical technology. Generally, tissue engineering requires two complementary ingredients: suitable cells and compatible scaffolds [53]. It would be necessary to apply compatible biological scaffolds, which could stimulate and promote cell differentiation, as well as regenerating tissues without harm. For this purpose, many scaffold-forming self-assembling peptides have been reported [54–60]. However, the use of scaffold materials is inevitably accompanied by some side effects such as fibrosis and inflammatory response. Alternatively, another kind of scaffold-free tissue engineering strategy, cell sheet technology, has been

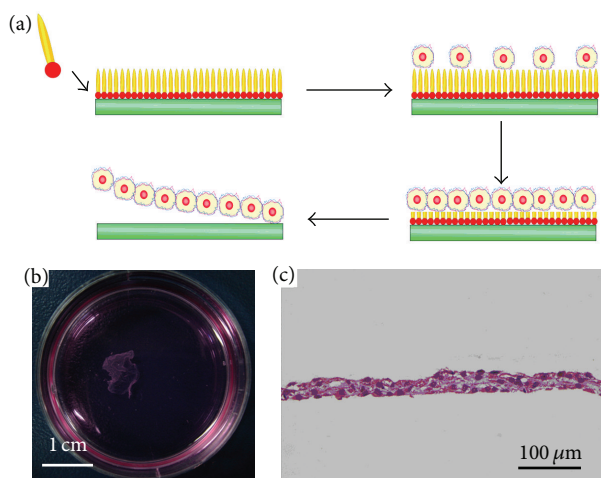


FIGURE 8: Cell sheet technology based on surfactant-like peptides. (a) Mechanism of harvesting cell sheet on mica surface modified by surfactant-like peptides. (b) Harvested cell sheet. (c) HE staining of cell sheet (reprinted from [65]).

widely investigated in recent years. This is a novel technique in which a sheet-like integration of cells is cultured and harvested by certain methods. Cell sheet could maintain cell-to-cell connections and the cellular matrix, and the bionic structures could promote cell sheet to regenerate organs as a small piece of artificial tissue [61–64].

In recent years, this scaffold-free tissue engineering strategy has received rapid development and become an important complementary to traditional scaffold-involved strategy. In this field, surfactant-like peptides as a novel type of surface modifying molecules have shown its potential. It was found that A_6K , a cationic surfactant-like peptide, could self-assemble on mica surface to form a monolayer. In this way, a hydrophilic mica surface could be modified into a hydrophobic one, which is suitable for cell adhesion and growth. Along with the growth of cultured cells, A_6K peptide composed of natural L-amino acids could be gradually biodegraded, and the hydrophilic mica surface could be reexposed, which is adverse for cell adhesion, and thus an integrate of cell sheet could be easily released from the mica surface (Figure 8) [65]. This novel cell sheet technique based on surfactant-like peptide is very simple, effective, and safe and may become a very important technique for the development of cell sheet technique.

5.4. Surfactant-Like Peptides as Template for Nanofabrication. For the development of nanoscience and nanotechnology, fabricating nanostructures and nanodevices is the first important task. In this field, many self-assembling structures have been successfully used as template for nanofabrication. Recently, a surfactant-like peptide AGD, which could undergo self-assembly in nonpolar solvent system, has shown its potential for such application. This peptide was designed to have a shape like an inverted wedge which prevented it to self-assemble in aqueous solution. But in nonpolar mixture of water and tetrahydrofuran, and with the existence of

copper ion, the peptide could self-assemble into nanorings by forming reversed micelle [66]. It was proved that copper ions were bound with the negatively charged head of the peptide and embedded in the core of the nanoring. In this manner, the peptide could be applied as a template for fabricating novel metallic nanostructures.

6. Conclusion and Outlook

The field of the design and application of surfactant-like peptides has been developed very rapidly in recent years. These peptides are easy to be designed and synthesized, which could guarantee their quality and purity; moreover, the biocompatibility of surfactant-like peptides makes them perfect materials for biological and biomedical applications. Their applications in the fields of membrane protein stabilizing and tissue engineering have proved their great potential. On the other hand, the chemical structure and self-assembling mechanism of surfactant-like peptides are very simple and clear; thus, surfactant-like peptides also provide a simple self-assembling model to study the folding and assembling of natural proteins, which might be very helpful to understand the mechanism of protein conformational diseases.

However, challenge remains when considering the practical application of the family of surfactant-like peptide. One reason might be due to the complicated self-assembling behavior of surfactant-like peptides which were highly sensitive to environmental parameters such as pH, ion strength, and peptide concentration. Although several attempts have been tried to obtain controllable self-assembling nanostructures, further investigations are still needed to be carried out to clarify the molecular mechanism for the self-assembling of surfactant like peptides, as well as their interaction with other biological molecules. This may be of great importance to exploit the application of surfactant-like peptides, especially as potential drug delivery nanomaterials.

Acknowledgments

This work was supported in part by the National 985 Key Project of Sichuan University of the Education Ministry of China. The authors thank Professor Shuguang Zhang (Massachusetts Institute of Technology) for his permission to use his figures in this paper.

References

- [1] S. Winkler, S. Szela, P. Avtges, R. Valluzzi, D. A. Kirschner, and D. Kaplan, "Designing recombinant spider silk proteins to control assembly," *International Journal of Biological Macromolecules*, vol. 24, no. 2-3, pp. 265–270, 1999.
- [2] S. Zhang, T. C. Holmes, C. M. DiPersio, R. O. Hynes, X. Su, and A. Rich, "Self-complementary oligopeptide matrices support mammalian cell attachment," *Biomaterials*, vol. 16, no. 18, pp. 1385–1393, 1995.
- [3] T. C. Holmes, S. de Lacalle, X. Su, G. Liu, A. Rich, and S. Zhang, "Extensive neurite outgrowth and active synapse formation on self-assembling peptide scaffolds," *Proceedings of the National*

- Academy of Sciences of the United States of America*, vol. 97, no. 12, pp. 6728–6733, 2000.
- [4] J. Kisiday, M. Jin, B. Kurz et al., “Self-assembling peptide hydrogel fosters chondrocyte extracellular matrix production and cell division: implications for cartilage tissue repair,” *Proceedings of the National Academy of Sciences of the United States of America*, vol. 99, no. 15, pp. 9996–10001, 2002.
 - [5] M. A. Bokhari, G. Akay, S. Zhang, and M. A. Birch, “The enhancement of osteoblast growth and differentiation in vitro on a peptide hydrogel—PolyHIPE polymer hybrid material,” *Biomaterials*, vol. 26, no. 25, pp. 5198–5208, 2005.
 - [6] R. G. Ellis-Behnke, Y.-X. Liang, S.-W. You et al., “Nano neuro knitting: peptide nanofiber scaffold for brain repair and axon regeneration with functional return of vision,” *Proceedings of the National Academy of Sciences of the United States of America*, vol. 103, no. 13, pp. 5054–5059, 2006.
 - [7] S. Zhang, F. Gelain, and X. Zhao, “Designer self-assembling peptide nanofiber scaffolds for 3D tissue cell cultures,” *Seminars in Cancer Biology*, vol. 15, no. 5, pp. 413–420, 2005.
 - [8] S. Koutsopoulos and S. Zhang, “Long-term three-dimensional neural tissue cultures in functionalized self-assembling peptide hydrogels, Matrigel and Collagen I,” *Acta Biomaterialia*, vol. 9, no. 2, pp. 5162–5169, 2013.
 - [9] C. E. Semino, J. Kasahara, Y. Hayashi, and S. Zhang, “Entrapment of migrating hippocampal neural cells in three-dimensional peptide nanofiber scaffold,” *Tissue Engineering*, vol. 10, no. 3–4, pp. 643–655, 2004.
 - [10] M. Nune, P. Kumaraswamy, U. M. Krishnan, and S. Sethuraman, “Self-assembling peptide nanofibrous scaffolds for tissue engineering: novel approaches and strategies for effective functional regeneration,” *Current Protein & Peptide Science*, vol. 14, no. 1, pp. 70–84, 2013.
 - [11] T. Y. Cheng, M. H. Chen, W. H. Chang, M. Y. Huang, and T. W. Wang, “Neural stem cells encapsulated in a functionalized self-assembling peptide hydrogel for brain tissue engineering,” *Biomaterials*, vol. 34, no. 8, pp. 2005–2016, 2013.
 - [12] R. Bawa, S.-Y. Fung, A. Shiozaki et al., “Self-assembling peptide-based nanoparticles enhance cellular delivery of the hydrophobic anticancer drug ellipticine through caveolae-dependent endocytosis,” *Nanomedicine*, vol. 8, no. 5, pp. 647–654, 2012.
 - [13] S. Koutsopoulos and S. Zhang, “Two-layered injectable self-assembling peptide scaffold hydrogels for long-term sustained release of human antibodies,” *Journal of Controlled Release*, vol. 160, no. 3, pp. 451–458, 2012.
 - [14] S. Deshayes, K. Konate, A. Rydstrom et al., “Self-assembling peptide-based nanoparticles for siRNA delivery in primary cell lines,” *Small*, vol. 8, no. 14, pp. 2184–2188, 2012.
 - [15] X. Zhao, “Design of self-assembling surfactant-like peptides and their applications,” *Current Opinion in Colloid and Interface Science*, vol. 14, no. 5, pp. 340–348, 2009.
 - [16] S. Vauthey, S. Santoso, H. Gong, N. Watson, and S. Zhang, “Molecular self-assembly of surfactant-like peptides to form nanotubes and nanovesicles,” *Proceedings of the National Academy of Sciences of the United States of America*, vol. 99, no. 8, pp. 5355–5360, 2002.
 - [17] S. Santoso, W. Hwang, H. Hartman, and S. Zhang, “Self-assembly of surfactant-like peptides with variable glycine tails to form nanotubes and nanovesicles,” *Nano Letters*, vol. 2, no. 7, pp. 687–691, 2002.
 - [18] G. Maltzahn, S. Vauthey, S. Santoso, and S. Zhang, “Positively charged surfactant-like peptides self-assemble into nanostructures,” *Langmuir*, vol. 19, no. 10, pp. 4332–4337, 2003.
 - [19] S. J. Yang and S. Zhang, “Self-assembling behavior of designer lipid-like peptides,” *Supramolecular Chemistry*, vol. 18, no. 5, pp. 389–396, 2006.
 - [20] A. Nagai, Y. Nagai, H. Qu, and S. Zhang, “Dynamic behaviors of lipid-like self-assembling peptide A₆D and A₆K nanotubes,” *Journal of Nanoscience and Nanotechnology*, vol. 7, no. 7, pp. 2246–2252, 2007.
 - [21] F. Qiu, Y. Chen, and X. Zhao, “Comparative studies on the self-assembling behaviors of cationic and catanionic surfactant-like peptides,” *Journal of Colloid and Interface Science*, vol. 336, no. 2, pp. 477–484, 2009.
 - [22] P. Jokela, B. Jönsson, and A. Khan, “Phase equilibria of catanionic surfactant-water systems,” *Journal of Physical Chemistry*, vol. 91, no. 12, pp. 3291–3298, 1987.
 - [23] K. Tsubone and N. Uchida, “Syntheses of 2-(N-alkyl-N,N-dimethylammonio)ethyl hydrogen phosphates and their physicochemical properties,” *Journal of the American Oil Chemists’ Society*, vol. 67, no. 3, pp. 149–153, 1990.
 - [24] L. M. Camillo, B. Sesta, M. G. Bonicelli, and G. F. Ceccaroni, “Phase diagram of the binary system water-(dodecyldimethylammonio)propanesulfonate,” *Langmuir*, vol. 6, no. 4, pp. 728–731, 1990.
 - [25] U. Khoe, Y. Yang, and S. Zhang, “Synergistic effect and hierarchical nanostructure formation in mixing two designer lipid-like peptide surfactants Ac-A₆D-OH and Ac-A₆K-NH₂,” *Macromolecular Bioscience*, vol. 8, no. 11, pp. 1060–1067, 2008.
 - [26] B. F. B. Silva and E. F. Marques, “Thermotropic behavior of asymmetric chain length catanionic surfactants: the influence of the polar head group,” *Journal of Colloid and Interface Science*, vol. 290, no. 1, pp. 267–274, 2005.
 - [27] J. Wang, A. Song, X. Jia, J. Hao, W. Liu, and H. Hoffmann, “Two routes to vesicle formation: metal-ligand complexation and ionic interactions,” *Journal of Physical Chemistry B*, vol. 109, no. 22, pp. 11126–11134, 2005.
 - [28] B. Yue, C.-Y. Huang, M.-P. Nieh, C. J. Glinka, and J. Katsaras, “Highly stable phospholipid unilamellar vesicles from spontaneous vesiculation: a DLS and SANS study,” *Journal of Physical Chemistry B*, vol. 109, no. 1, pp. 609–616, 2005.
 - [29] J.-H. Fuhrhop and J. Mathieu, “Routes to functional vesicle membranes without proteins,” *Angewandte Chemie*, vol. 23, no. 2, pp. 100–113, 1984.
 - [30] J.-H. Fuhrhop, H.-H. David, J. Mathieu, U. Liman, H.-J. Winter, and E. Boekema, “Bolaamphiphiles and monolayer lipid membranes made from 1,6,19,24-tetraoxa-3,21-cyclohexatriacontadiene-2,5,20,23-tetrone,” *Journal of the American Chemical Society*, vol. 108, no. 8, pp. 1785–1791, 1986.
 - [31] X.-L. Sun, N. Biswas, T. Kai, Z. Dai, R. A. Dluhy, and E. L. Chaikof, “Membrane-mimetic films of asymmetric phosphatidylcholine lipid bolaamphiphiles,” *Langmuir*, vol. 22, no. 3, pp. 1201–1208, 2006.
 - [32] L. M. Cameron, T. M. Fyles, and C.-W. Hu, “Synthesis and membrane activity of a bis(metacyclophane)bolaamphiphile,” *Journal of Organic Chemistry*, vol. 67, no. 5, pp. 1548–1553, 2002.
 - [33] C. Zhan, P. Gao, and M. Liu, “Self-assembled helical spherical-nanotubes from an L-glutamic acid based bolaamphiphilic low molecular mass organogelator,” *Chemical Communications*, no. 4, pp. 462–464, 2005.
 - [34] P. Gao and M. Liu, “Compression induced helical nanotubes in a spreading film of a bolaamphiphile at the air/water interface,” *Langmuir*, vol. 22, no. 16, pp. 6727–6729, 2006.

- [35] P. Gao, C. Zhan, and M. Liu, "Controlled synthesis of double- and multiwall silver nanotubes with template organogel from a bolaamphiphile," *Langmuir*, vol. 22, no. 2, pp. 775–779, 2006.
- [36] J. Song, Q. Cheng, and R. C. Stevens, "Morphological manipulation of bolaamphiphilic polydiacetylene assemblies by controlled lipid doping," *Chemistry and Physics of Lipids*, vol. 114, no. 2, pp. 203–214, 2002.
- [37] V. Weissig and V. P. Torchilin, "Mitochondriotropic cationic vesicles: a strategy towards mitochondrial gene therapy," *Current Pharmaceutical Biotechnology*, vol. 1, no. 4, pp. 325–346, 2000.
- [38] F. Qiu, Y. Chen, C. Tang et al., "De novo design of a bolaamphiphilic peptide with only natural amino acids," *Macromolecular Bioscience*, vol. 8, no. 11, pp. 1053–1059, 2008.
- [39] R. C. Claussen, B. M. Rabatic, and S. I. Stupp, "Aqueous self-assembly of unsymmetric peptide bolaamphiphiles into nanofibers with hydrophilic cores and surfaces," *Journal of the American Chemical Society*, vol. 125, no. 42, pp. 12680–12681, 2003.
- [40] S. Zhang, "Emerging biological materials through molecular self-assembly," *Biotechnology Advances*, vol. 20, no. 5–6, pp. 321–339, 2002.
- [41] X. Zhao and S. Zhang, "Designer self-assembling peptide materials," *Macromolecular Bioscience*, vol. 7, no. 1, pp. 13–22, 2007.
- [42] Y. Chen, F. Qiu, Y. Lu, Y.-K. Shi, and X. Zhao, "Geometrical shape of hydrophobic section determines the self-assembling structure of peptide detergents and bolaamphiphilic peptides," *Current Nanoscience*, vol. 5, no. 1, pp. 69–74, 2009.
- [43] Y.-Z. Chen, F. Qiu, and X.-J. Zhao, "Self-assembling structure and mechanism of a wedge-shaped peptide detergent A_3V_3D ," *Gaodeng Xuexiao Huaxue Xuebao/Chemical Journal of Chinese Universities*, vol. 30, no. 7, pp. 1337–1341, 2009.
- [44] U. Khoe, Y. Yang, and S. Zhang, "Self-assembly of nanodonor structure from a cone-shaped designer lipid-like peptide surfactant," *Langmuir*, vol. 25, no. 7, pp. 4111–4114, 2009.
- [45] M. J. Webber, J. Tongers, M.-A. Renault, J. G. Roncalli, D. W. Losordo, and S. I. Stupp, "Development of bioactive peptide amphiphiles for therapeutic cell delivery," *Acta Biomaterialia*, vol. 6, no. 1, pp. 3–11, 2010.
- [46] M. J. Webber, J. A. Kessler, and S. I. Stupp, "Emerging peptide nanomedicine to regenerate tissues and organs," *Journal of Internal Medicine*, vol. 267, no. 1, pp. 71–88, 2010.
- [47] Y. Dou, H. Xu, and J. Hao, "Self-assembly and accurate preparation of Au nanoparticles in the aqueous solution of a peptide A_6D and a zwitterionic Cl_4DMAO ," *Soft Matter*, vol. 9, no. 23, pp. 5572–5580, 2013.
- [48] P. Kiley, X. Zhao, M. Vaughn, M. A. Baldo, B. D. Bruce, and S. Zhang, "Self-assembling peptide detergents stabilize isolated photosystem I on a dry surface for an extended time," *PLoS Biology*, vol. 3, no. 7, article e230, 2005.
- [49] X. Zhao, Y. Nagai, P. J. Reeves, P. Kiley, H. G. Khorana, and S. Zhang, "Designer short peptide surfactants stabilize G protein-coupled receptor bovine rhodopsin," *Proceedings of the National Academy of Sciences of the United States of America*, vol. 103, no. 47, pp. 17707–17712, 2006.
- [50] J.-X. Chen, H.-Y. Wang, C. Li, K. Han, X.-Z. Zhang, and R.-X. Zhuo, "Construction of surfactant-like tetra-tail amphiphilic peptide with RGD ligand for encapsulation of porphyrin for photodynamic therapy," *Biomaterials*, vol. 32, no. 6, pp. 1678–1684, 2011.
- [51] X. D. Guo, F. Tandiono, N. Wiradharma et al., "Cationic micelles self-assembled from cholesterol-conjugated oligopeptides as an efficient gene delivery vector," *Biomaterials*, vol. 29, no. 36, pp. 4838–4846, 2008.
- [52] N. Wiradharma, Y. W. Tong, and Y.-Y. Yang, "Self-assembled oligopeptide nanostructures for co-delivery of drug and gene with synergistic therapeutic effect," *Biomaterials*, vol. 30, no. 17, pp. 3100–3109, 2009.
- [53] R. Langer and J. P. Vacanti, "Tissue engineering," *Science*, vol. 260, no. 5110, pp. 920–926, 1993.
- [54] M. J. Webber, J. Tongers, M.-A. Renault, J. G. Roncalli, D. W. Losordo, and S. I. Stupp, "Development of bioactive peptide amphiphiles for therapeutic cell delivery," *Acta Biomaterialia*, vol. 6, no. 1, pp. 3–11, 2010.
- [55] M. J. Webber, J. A. Kessler, and S. I. Stupp, "Emerging peptide nanomedicine to regenerate tissues and organs," *Journal of Internal Medicine*, vol. 267, no. 1, pp. 71–88, 2010.
- [56] S. M. Standley, D. J. Toft, H. Cheng et al., "Induction of cancer cell death by self-assembling nanostructures incorporating a cytotoxic peptide," *Cancer Research*, vol. 70, no. 8, pp. 3020–3026, 2010.
- [57] K. Rajangam, M. S. Arnold, M. A. Rocco, and S. I. Stupp, "Peptide amphiphile nanostructure-heparin interactions and their relationship to bioactivity," *Biomaterials*, vol. 29, no. 23, pp. 3298–3305, 2008.
- [58] J. D. Tovar, B. M. Rabatic, and S. I. Stupp, "Conducting polymers confined within bioactive peptide amphiphile nanostructures," *Small*, vol. 3, no. 12, pp. 2024–2028, 2007.
- [59] E. Beniash, J. D. Hartgerink, H. Storrie, J. C. Stendahl, and S. I. Stupp, "Self-assembling peptide amphiphile nanofiber matrices for cell entrapment," *Acta Biomaterialia*, vol. 1, no. 4, pp. 387–397, 2005.
- [60] G. A. Silva, C. Czeisler, K. L. Niece et al., "Selective differentiation of neural progenitor cells by high-epitope density nanofibers," *Science*, vol. 303, no. 5662, pp. 1352–1355, 2004.
- [61] A. Ito, H. Jitsunobu, Y. Kawabe, and M. Kamihira, "Construction of heterotypic cell sheets by magnetic force-based 3-D coculture of HepG2 and NIH3T3 cells," *Journal of Bioscience and Bioengineering*, vol. 104, no. 5, pp. 371–378, 2007.
- [62] K. Ohashi, T. Yokoyama, M. Yamato et al., "Engineering functional two- and three-dimensional liver systems in vivo using hepatic tissue sheets," *Nature Medicine*, vol. 13, no. 7, pp. 880–885, 2007.
- [63] Y. Miyahara, N. Nagaya, M. Kataoka et al., "Monolayered mesenchymal stem cells repair scarred myocardium after myocardial infarction," *Nature Medicine*, vol. 12, no. 4, pp. 459–465, 2006.
- [64] H. Kobayashi, T. Shimizu, M. Yamato et al., "Fibroblast sheets co-cultured with endothelial progenitor cells improve cardiac function of infarcted hearts," *Journal of Artificial Organs*, vol. 11, no. 3, pp. 141–147, 2008.
- [65] F. Qiu, Y. Chen, J. Cheng, C. Wang, H. Xu, and X. Zhao, "A simple method for cell sheet fabrication using mica surfaces grafted with peptide detergent A_6K ," *Macromolecular Bioscience*, vol. 10, no. 8, pp. 881–886, 2010.
- [66] F. Qiu, Y. Chen, C. Tang, J. Cheng, and X. Zhao, "Formation of reversed micelle nanoring by a designed surfactant-like peptide," *Nano*, vol. 7, no. 4, 2012.

Research Article

Upconversion Luminescence and Photodegradation Performances of Pr Doped Y_2SiO_5 Nanomaterials

Yi Yang,^{1,2} Cheng Liu,¹ Ping Mao,^{1,2} and Lian-Jun Wang^{1,2}

¹ School of Environmental and Biological Engineering, Nanjing University of Science and Technology, Nanjing 210094, China

² Lianyungang Institute, Nanjing University of Science and Technology, Lianyungang 222006, China

Correspondence should be addressed to Yi Yang; yyi301@163.com

Received 12 July 2013; Accepted 2 August 2013

Academic Editor: Guangyu Zhao

Copyright © 2013 Yi Yang et al. This is an open access article distributed under the Creative Commons Attribution License, which permits unrestricted use, distribution, and reproduction in any medium, provided the original work is properly cited.

Yttrium silicates Y_2SiO_5 upconversion nanomaterials with different doping concentrations of praseodymium ion Pr are prepared by using a sol-gel method. X-ray diffractometer, SEM, Fourier transform infrared spectrometer, and fluorescence spectrometer have been employed to test the crystal structure and upconversion luminescence performances. The results indicate that samples calcined higher than 950°C present fine crystal structures, of which Si-O-Si band at 757–1048 cm^{-1} splits into three fine peaks. The crystal size of the samples calcined at 950°C and 1000°C is 29.1 nm and 66.7 nm, respectively. The luminescence intensities of the samples are increasing at first and then decreasing, with the increasing of the doping concentrations of 0.47%, 0.77%, 0.96%, 2.95%, and 4.93%. Nanomaterial sample doped 0.96% Pr emits the highest upconversion luminescence intensity of 6.43×10^6 cps and shows the best photodegradation performance for nitrobenzene wastewater. It demonstrates that too much of Pr doping concentration would result in quenching of the fluorescence. Nevertheless, as the degradation time expands, sample doped 0.96% Pr shows much faster increasing of photodegradation rate than samples of other doping concentrations and reaches to a high photodegradation rate of 97.14% in 6 hours for 10 mg/L nitrobenzene wastewater.

1. Introduction

Upconversion nanomaterials are known for its efficient emission of ultraviolet fluorescence under the exciting visible light [1]. It has been extensively studied since mid-1960s and widely applied in many areas [2–4]. The emission of short wavelength light excited by long wavelength light is called anti-stokes luminescence, namely, upconversion luminescence. Upconversion nanomaterials and upconversion luminescence can be widely used in the degradation of organic pollutants in environmental governance [5] and the killing of harmful bacteria in medical treatment or biological areas [6–8], because of the ultraviolet light emitted in the upconversion processes. The upconversion nanomaterials, which is differ from ultraviolet lamp, can be excited by visible light, such as sun light, instead of electricity.

In the past decades, high-quality rare earth-doped upconversion nanomaterials have been successfully synthesized with the rapid development of nanotechnology and are becoming more prominent in biological and environmental

sciences [9–11]. However, till now, the low luminescence efficiency is still one of the main limiting factors for upconversion materials. A suitable host material with lower phonon energy is one of the most important factors to obtain high upconversion luminescence efficiency. Up to now, host materials, including fluoride, chloride, and bromide, have been shown to enhance upconversion luminescence intensity. As a substrate for upconversion materials, yttrium silicates Y_2SiO_5 show high thermal stability, good optical performance, simple manufacture process, and has been widely used in fluorescent technique, optical information storage, and anticounterfeit technology [12].

To get the highest upconversion luminescence efficiency, another critical factor is doping with other ions to occupy or replace the ions in the host material [13–15]. In the molecular geometry of yttrium silicates Y_2SiO_5 , yttrium ion Y is located on two different positions and its corresponding coordinate numbers are 7 and 9 in X1 molecular configuration, while 6 and 7 in X2 molecular configuration [16]. The particular geometry leads to a possible replace of Y by other element

ions. Praseodymium ion has a similar ionic radius with Y ion, but more suitable energy levels and longer excited state lifetimes than Y. This leads to the transition of Pr to a lower energy band after absorbing two photons continuously. As a result, higher energy photons could be emitted. Therefore, Praseodymium ion is a potential doping element ion for the Y_2SiO_5 system to obtain high energy photons and excellent upconversion performances.

Besides the host materials and doping ions, the synthetic methods are also critical for the high quality upconversion nanomaterials to obtain high luminescence efficiency. The synthesis methods are usually phase-based processes. So far, three kinds of methods are commonly used to synthesize upconversion nanomaterials, including thermal decomposition [17–19], hydrothermal synthesis [20, 21], and ionic liquids-based synthesis [22]. In addition, sol-gel method has potential for synthesizing high quality upconversion nanomaterials of high luminescence efficiency and usually used as the first choice to doping ions since it provides a way of mixing in molecular level of the reactants [23, 24], which has also been used in this study.

Many researches focused on the optical properties, luminescence properties, and fluorescence quenching mechanisms of Pr doped Y_2SiO_5 crystals [25–27]. Also, a number of studies report the application of Pr doped Y_2SiO_5 nanomaterials in biological, medical, sensing, optical areas, and so on [2, 3, 5–8]. In particular, the upconversion nanomaterials unique property of emitting visible light under NIR irradiation makes them a suitable candidate both for in vivo and in vitro bioimaging [28, 29]. However, the research and application of Pr doped Y_2SiO_5 nanomaterials on environment or pollutants degradation are seldom reported. In this study, nitrobenzene wastewater, which is from a TNT factory, has been used as the target pollutant to test the photodegradation performances of the prepared Pr(III) doped Y_2SiO_5 upconversion nanomaterials.

2. Materials and Methods

Praseodymium ion Pr(III), doped Y_2SiO_5 upconversion nanomaterials were prepared by using a sol-gel method. First, 0.1 mol/L praseodymium nitrate solution was added into the mixture (1:1, vol) of HNO_3 and H_2O dissolved 0.663 g Y_2O_3 . Heating was followed until the solution becomes a viscous mixture. A number of crystals were seed out after cooling down. The crystal was collected and dissolved in ethanol. Tetraethyl orthosilicate (TEOS) was added and mixed with the ethanol solution of the crystals. The obtained mixture was put into a water bath of $70^\circ C$ until a gel was formed. The gel was dried in an oven of $104^\circ C$ and then grinded into powder. At last, the powder was calcined at a temperature of $900^\circ C$, $950^\circ C$, and $1000^\circ C$ for 3 h in a muffle furnace to get the final product of Pr(III) doped Y_2SiO_5 upconversion nanomaterials. The Pr(III) doping concentrations, 0.47%, 0.77%, 0.96%, 2.95%, and 4.93%, which were confirmed by using inductively coupled plasma (ICP) spectrometer, were adjusted by changing the adding volume of the 0.1 mol/L praseodymium nitrate solution at the first stage.

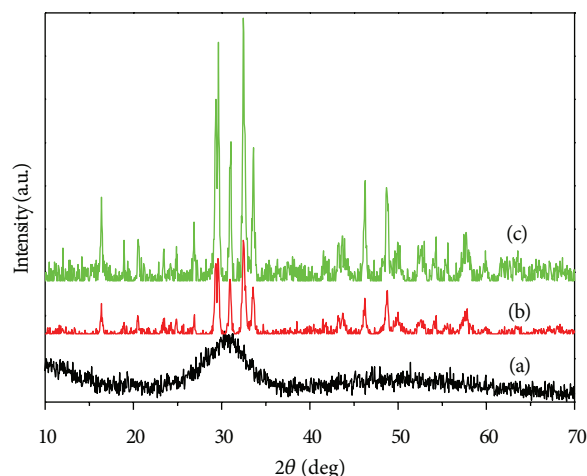


FIGURE 1: XRD patterns of Pr(III) doped samples calcined at different temperatures: (a) $900^\circ C$, (b) $950^\circ C$, (c) $1000^\circ C$.

X-ray diffractometer (D8 Advance, Bruker Corporation, German) was used to characterize the crystal form of the samples. A scanning electron microscopy (Hitachi S4800, SEM, Japan) was employed to characterize the particle size of the samples. Fourier transform infrared spectrometer (FTIR, MB154S, ABB BOMEN Corporation, Canada) was employed to check the crystal and groups of samples. The upconversion luminescence of the nanomaterials was tested by using a fluorescence spectrometer (FL3-TCSPC, Horiba Jobin Yvon Corporation, France). The exciting parameters were selected as 425 nm of the excitation wavelength, 370 nm of the optical filters, and 2 nm of the slit.

Nitrobenzene wastewater, 10 mg/L, which was from a TNT factory, was used as a target pollutant to test the photodegradation performances of the prepared Pr(III) doped Y_2SiO_5 upconversion nanomaterials. Filament lamp, 52 W, was used as the exciting light source for the upconversion nanomaterials. The treatment time was lasting for 1 h to 6.5 h. The degradation rate of nitrobenzene was tested by comparing the ultraviolet absorption values to the original value of the wastewater. The ultraviolet absorption values were tested by using an ultraviolet-visible spectrophotometer. The relationship of the nitrobenzene concentrations (x), in the range of 0–15 mg/L, with the ultraviolet absorption values (y), was determined by a linear equation: $y = 0.072x + 0.012$, with a correlation R^2 of 0.9987.

3. Results and Discussion

3.1. Heat Treatment on the Crystal of Upconversion Nanomaterials. The heat treatment temperature is an important parameter for the crystal structure and crystal size of many kinds of nanomaterials, as well as upconversion nanomaterials. Figure 1 shows the XRD patterns of Pr(III) doped samples at the heat treatment temperature of $900^\circ C$, $950^\circ C$, and $1000^\circ C$.

Without obvious diffraction peak appears on the XRD pattern of sample calcined at $900^\circ C$, except for a broad curve at the 2θ angle about 30° . It means that Y_2SiO_5 under

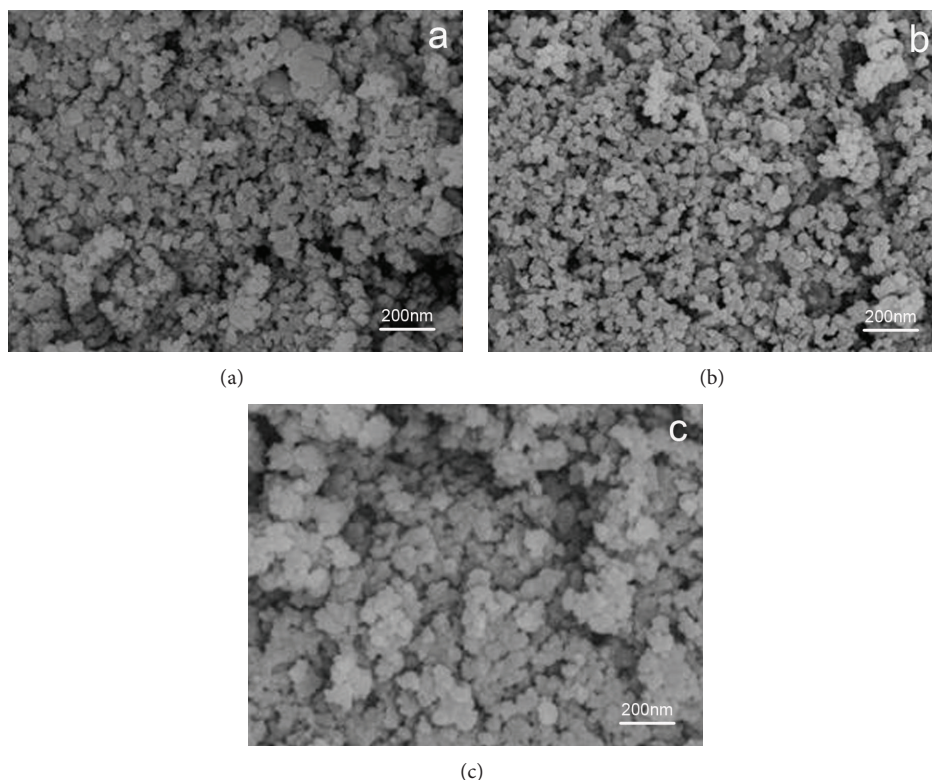


FIGURE 2: SEM images of Pr(III) doped samples calcined at different temperature (a) 900°C; (b) 950°C; (c) 1000°C.

the heat treatment temperature of 900°C is amorphous. Meanwhile, a higher heat treatment temperature of 950°C or 1000°C leads to good crystal forms of the Pr(III) doped Y_2SiO_5 upconversion nanomaterials, of which diffraction peak positions show high consistency with that of $X1-Y_2SiO_5$ phase [30]. The temperature is further lower than the report postanneal temperature 1373 K for $X1-Y_2SiO_5$ phase [30]. However, sample calcined at 1000°C shows much higher diffraction peaks than that of sample calcined at 950°C. This phenomenon states a conclusion that the crystal size of the later is smaller than that of the former, 29.1 nm and 66.7 nm at 2θ angle 32.67° , respectively, which are calculated by the Scherrer equation: $D = K\lambda/(\beta \cos \theta)$, where D is the crystal size (nm); K is 0.89, the Scherrer constant; β is the full width at half maximum (FWHM) of the main diffraction peaks (rad); θ is the diffraction angle which the diffraction peaks located ($^\circ$); λ is 0.154056 nm, the X-ray wavelength.

It indicates that the crystal structure transition temperature of Pr (III) doped $X1$ pattern Y_2SiO_5 is about 950°C, heat treatment temperature higher than 950°C is not good for the forming of small crystal size for the materials.

The particle size of the samples characterized by a scanning electron microscopy also shows high dependence on the heat treatment temperature, as shown in Figure 2. With the increasing of heat treatment temperature, the particle sizes of the samples are increasing gradually, 42 nm, 55 nm, and 96 nm for the treatment temperature of 900°C, 950°C, and 1000°C, respectively. It shows a good consistent tendency to the crystal size of samples. Particle sizes in SEM bigger than its

crystal size of the corresponding sample are reasonable, since a particle in SEM is always composed by several crystals, not to mention the congregating of particles themselves.

It has been proved that the crystal structures and bond groups of phosphor materials show high dependence on the heat treatment or thermal annealing temperature [31]. An FTIR spectrometer is employed to test the effect of heat treatment temperature on the crystal structure of the Pr(III) doped Y_2SiO_5 upconversion nanomaterials, as shown in Figure 3. Sample calcined at 900°C shows two big absorption bands on the FTIR spectrum curve, in the range of $757\text{--}1048\text{ cm}^{-1}$ and $1260\text{--}1620\text{ cm}^{-1}$, which can be roughly identified to the vibration absorption of Si-O-Si bond and the bending vibration of O-H bond, respectively. When heat treatment temperature is increased to 950°C or 1000°C, both of the two absorption bands show a great change: the lower wavenumber absorption band splits into three absorption peaks, and the higher wavenumber absorption band disappears thoroughly.

High heat treatment temperature is believed to be beneficial to the forming of fine crystal structures of the nanomaterials. Therefore, as a result, when the upconversion nanomaterials are calcined at the temperature of 950°C and 1000°C, the absorption band at $757\text{--}1048\text{ cm}^{-1}$ splits into three fine peaks at 849.7 cm^{-1} , 933.8 cm^{-1} , and 1008.3 cm^{-1} , which result from the bending vibration absorption of Si-O bond, the symmetric vibration absorption of Si-O-Si bond, and the asymmetric vibration absorption of Si-O-Si bond, respectively, as curves (b) and (c) shown in Figure 3. It further demonstrates that samples calcined at 950°C have been converted

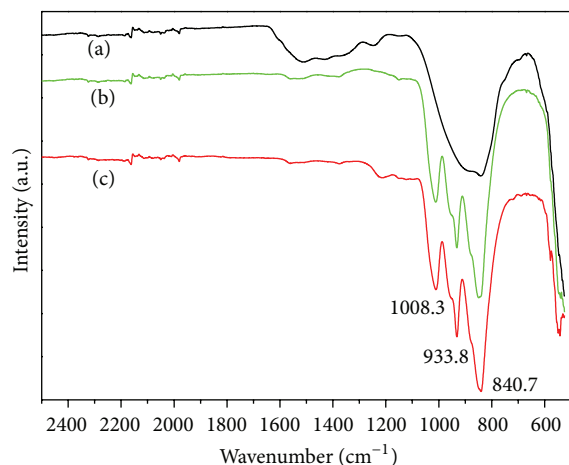


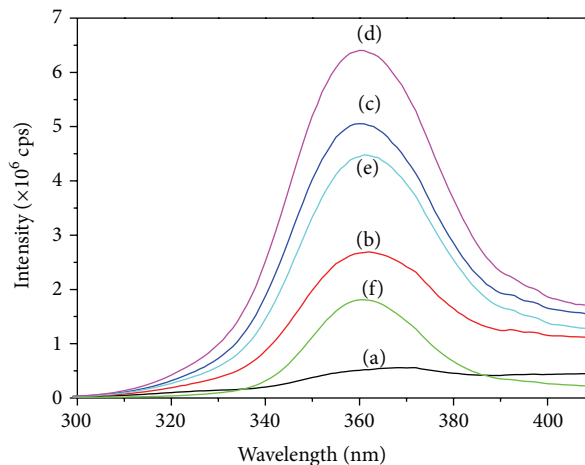
FIGURE 3: FTIR spectra of Pr(III) doped samples calcined at different temperatures: (a) 900°C, (b) 950°C, (c) 1000°C.

from amorphous state to crystal structure, which shows high consistency with the results of Figure 1.

The absorption bands at 1260–1620 cm^{-1} are attributed to the bending vibration of O-H bond or H_2O , which is adsorbed on the internal holes surface of the nanomaterials or bonded with the nanomaterials in other forms. The bonded H_2O in the materials is difficult to desorb at 900°C. A higher heat treatment temperature is usually beneficial to the desorption of the bonded or adsorbed H_2O in the materials, and lead to the disappearing of the absorption bands at 1260–1620 cm^{-1} at the temperature of 950°C or 1000°C, as curves (b) and (c) shown in Figure 3.

3.2. The Upconversion Luminescence of Y_2SiO_5 Nanomaterials. Since the ionic radius of Pr(III) and Y(III), 113 pm and 104 pm, respectively, is very close [32], the lattice parameter of Y_2SiO_5 nanomaterials would not change a lot when Pr(III) dopes in and replaces the position of Y(III) in the lattice. Therefore, X-ray diffraction patterns of Y_2SiO_5 upconversion nanomaterials show little dependence on the dope concentrations of Pr(III). However, the segregation of doped ions strongly modifies the luminescence properties of nanocrystals [33]. It means that the doping concentrations of Pr(III) play an important role on the upconversion luminescence of Y_2SiO_5 nanomaterials, as shown in Figure 4.

The blank sample, the sample without doped Pr(III), shows relative low luminescence intensity. On the other hand, those samples doped Pr(III) emit obvious luminescence spectra at the wavelength of 360 nm. With the increasing of the dope concentration of Pr(III), the emission luminescence intensities are also enhanced obviously to a maximum of 6.43×10^6 cps (count per second) with the Pr(III) doping concentration of 0.96%. It shows an excellent enhancement of Pr(III) doping for the emission luminescence of Y_2SiO_5 nanomaterials. However, further increasing of Pr(III) doping concentration leads to a sharp decrease of the emission luminescence intensity. It is believed that too high of doping



Peak values:

(a) 0.57×10^6 cps	(d) 6.43×10^6 cps
(b) 2.67×10^6 cps	(e) 4.49×10^6 cps
(c) 5.06×10^6 cps	(f) 1.83×10^6 cps

FIGURE 4: Emission spectra of Y_2SiO_5 doped different concentrations: of Pr(III), (a) 0.0%, (b) 0.47%, (c) 0.77%, (d) 0.96%, (e) 2.95% and (f) 4.93%.

concentration of Pr(III) would result in luminescent quenching [34]. As a result, the highest doping concentration of 4.93% Pr(III) results in the lowest luminescence intensity, 1.83×10^6 cps, of all the samples except for the blank sample, as shown in Figure 4.

3.3. Photodegradation of Nitrobenzene Wastewater. As a typical environmental priority control pollutant, nitrobenzene wastewater usually comes from the factories manufacturing medicines, pesticides, plastics, explosives. It is difficult to degrade by normal methods because of its particular molecular structures [35]. In this study, 10 mg/L nitrobenzene wastewater is used to test the photodegradation performances of Pr(III) doped Y_2SiO_5 upconversion nanomaterials. The doping concentrations of Pr(III), 0.47%, 0.96%, 4.93%, and the degradation time, 1 h to 6.5 h, have been taken into account to learn the degradation rate of nitrobenzene in the water, as shown in Figure 5.

Sample doped 0.96% Pr(III) shows much higher photodegradation rate at all the time than the samples of the other two doping concentrations, 0.47% and 4.93%. It can be concluded that higher luminescence emission sample, such as Y_2SiO_5 nanomaterials doped 0.96% Pr(III) as shown in Figure 4, would show a higher photodegradation rate on the pollutant. Too much of doping concentration is not a benefit to the increasing of photodegradation rate. On the other hand, as the time expands, the degradation rates of all the upconversion nanometer samples are increasing obviously at different rate. It is interesting that the slopes of the fitting lines show the same tendency with the degradation rates of the doping concentrations. That is to say, higher degradation rate of the sample is also corresponding to higher slope of fitting line and showing faster photodegradation on the nitrobenzene.

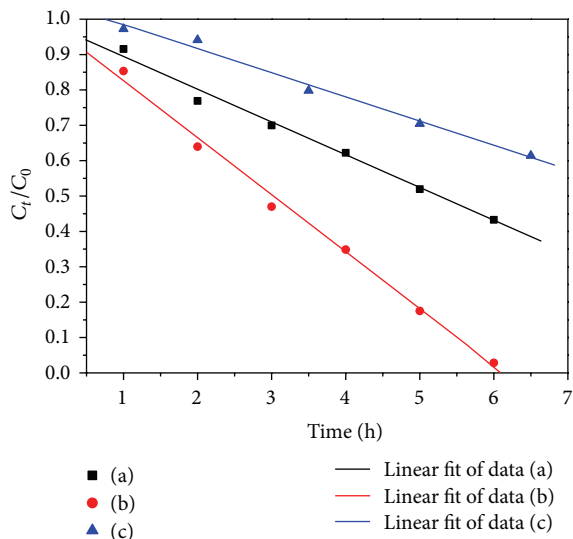


FIGURE 5: The photodegradation performances of Pr(III) doped Y_2SiO_5 nanomaterials (a) 0.47%, (b) 0.96% and (c) 4.93%.

First-order fitting of the $\ln(C_0/C)$ versus time for the photodegradation of pollutants, such as methyl orange and methylene blue, is usually used to study the reaction kinetics [36]. Based on the photodegradation rates of nitrobenzene with time, the photodegradation reaction kinetics lines are drawn out, as shown in Figure 6.

The best photodegradation belongs to the upconversion nanomaterials doped 0.96% of Pr(III), and too much of doping concentrations of Pr(III) would not show high photodegradation of upconversion nanomaterials, which confirms high consistency with the test results indicated in Figure 5. On the other hand, linear relationships appear between the degradation time and the value of $\ln(C_t/C_0)$, where C_t is the concentration of nitrobenzene in the water at a time (t) and C_0 is the original concentration of nitrobenzene 10 mg/L, as shown in Figure 6. Each of the doping concentration of Pr(III), 0.47%, 0.96%, and 4.93%, is according to a reaction kinetics linear equation and correlation indexes: $\ln C_t/C_0 = -0.14399t + 0.05826$, $R = -0.99414$, $\ln C_t/C_0 = -0.29939t + 0.14481$ ($t = 1$ to 4 h), $R = -0.99992$, and $\ln C_t/C_0 = -0.08688t + 0.08227$, $R = -0.99486$, respectively. It can be concluded that the degradation reaction of nitrobenzene under the visible light follows the first-order kinetic law by the photodegradation of Pr(III) doped Y_2SiO_5 upconversion nanomaterials. However, as shown in Figure 6, the fit line for the sample doped 0.96% Pr is linearly only at the first 4 hours. After that, the degradation reaction of nitrobenzene would not follow the first-order kinetics law.

4. Conclusions

Praseodymium ion, Pr(III), doped Y_2SiO_5 upconversion nanomaterials are prepared by using a sol-gel method. The doping concentrations of Pr(III) play important roles on the upconversion of the nanomaterials. The emission luminescence intensity of the nanomaterial reaches a maximum of

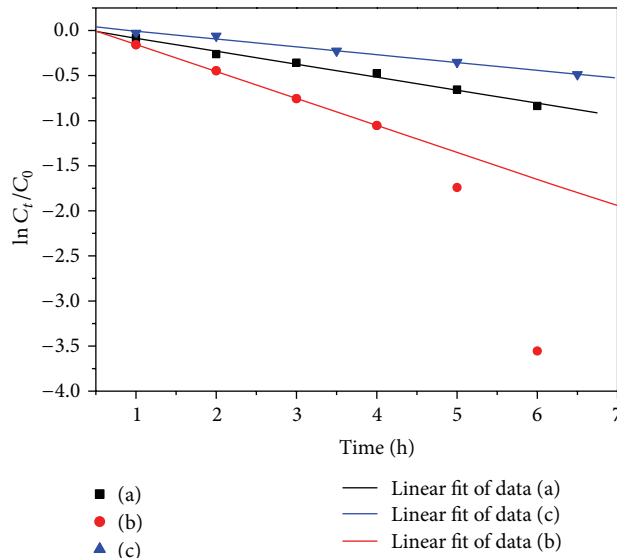


FIGURE 6: The photodegradation reaction kinetics data of nanomaterials (a) 0.47%, (b) 0.96% and (c) 4.93%.

6.43×10^6 cps (count per second) with the Pr(III) doping concentration of 0.96%. In addition, the optimized doping sample shows the best photodegradation performance in all the samples. For 10 mg/L of nitrobenzene wastewater, the photodegradation rate is up to 97.14% in 6 hours. The photodegradation reaction kinetics data indicated that the degradation reaction of nitrobenzene under the visible light follows the first-order kinetic law at the first 4 hours.

Acknowledgment

The work was supported by the Foundation of Jiangsu Environmental Protection Department, China (no. 2012015).

References

- [1] Y. Sun, Y. Chen, L. Tian et al., "Controlled synthesis and morphology dependent upconversion luminescence of $NaYF_4:Yb, Er$ nanocrystals," *Nanotechnology*, vol. 18, no. 27, Article ID 275609, 2007.
- [2] J. Chen and J. X. Zhao, "Upconversion nanomaterials: synthesis, mechanism, and applications in sensing," *Sensors*, vol. 12, no. 3, pp. 2414–2435, 2012.
- [3] C. Feldmann, T. Jüstel, C. R. Ronda, and P. J. Schmidt, "Inorganic luminescent materials: 100 Years of research and application," *Advanced Functional Materials*, vol. 13, no. 7, pp. 511–516, 2003.
- [4] M. Kottaisamy, D. Jeyakumar, R. Jagannathan, and M. M. Rao, "Yttrium oxide: Eu^{3+} red phosphor by self-propagating high temperature synthesis," *Materials Research Bulletin*, vol. 31, no. 8, pp. 1013–1020, 1996.
- [5] E. L. Cates, M. Cho, and J.-H. Kim, "Converting visible light into UVC: microbial inactivation by Pr^{3+} -activated upconversion materials," *Environmental Science and Technology*, vol. 45, no. 8, pp. 3680–3686, 2011.

- [6] Q. Liu, Y. Sun, T. Yang, W. Feng, C. Li, and F. Li, "Sub-10 nm hexagonal lanthanide-doped NaLuF₄ upconversion nanocrystals for sensitive bioimaging *in vivo*," *Journal of the American Chemical Society*, vol. 133, no. 43, pp. 17122–17125, 2011.
- [7] C. Bouzigues, T. Gacoin, and A. Alexandrou, "Biological applications of rare-earth based nanoparticles," *ACS Nano*, vol. 5, no. 11, pp. 8488–8505, 2011.
- [8] M. Wang, G. Abbineni, A. Clevenger, C. Mao, and S. Xu, "Upconversion nanoparticles: synthesis, surface modification and biological applications," *Nanomedicine*, vol. 7, no. 6, pp. 710–729, 2011.
- [9] Z. Li, L. Zheng, L. Zhang, and L. Xiong, "Synthesis, characterization and upconversion emission properties of the nanocrystals of Yb³⁺/Er³⁺-codoped YF₃-YOF-Y₂O₃ system," *Journal of Luminescence*, vol. 126, no. 2, pp. 481–486, 2007.
- [10] D. Yin, K. Song, Y. Ou, C. Wang, B. Liu, and M. Wu, "Synthesis of NaYF₄, NaLuF₄ and NaGdF₄-based upconversion nanocrystals with hydro (solvo) thermal methods," *Journal of Nanoscience and Nanotechnology*, vol. 13, no. 6, pp. 4162–4167, 2013.
- [11] H. Mi Noh, H. Kyoung Yang, B. Kee Moon, B. Chun Choi, J. Hyun Jeong, and H. Choi, "Concentration enhanced upconversion luminescence in ZrO₂:Ho³⁺, Yb³⁺ nanophosphors," *Journal of Nanoscience and Nanotechnology*, vol. 13, pp. 4006–4009, 2013.
- [12] G. Yi, Y. Peng, and Z. Gao, "Strong red-emitting near-infrared-to-visible upconversion fluorescent nanoparticles," *Chemistry of Materials*, vol. 23, no. 11, pp. 2729–2734, 2011.
- [13] J. Lin, Q. Su, H. Zhang, and S. Wang, "Crystal structure dependence of the luminescence of rare earth ions (Ce³⁺, Tb³⁺, Sm³⁺) in Y₂SiO₅," *Materials Research Bulletin*, vol. 31, no. 2, pp. 189–196, 1996.
- [14] T. Anh, P. Benalloul, C. Barthou, L. T. Giang, N. Vu, and L. Minh, "Luminescence, energy transfer, and upconversion mechanisms of Y₂O₃ nanomaterials doped with Eu³⁺, Tb³⁺, Tm³⁺, Er³⁺, and Yb³⁺ ions," *Journal of Nanomaterials*, vol. 2007, Article ID 48247, 10 pages, 2007.
- [15] N. Nguyen, M. H. Nam, T. K. Anh, L. Q. Minh, and E. Tanguy, "Optical properties of Eu³⁺ doped Y₂O₃ nanophosphors," *Advances in Natural Sciences*, vol. 6, pp. 119–123, 2006.
- [16] J. Lin, Q. Su, S. Wang, and H. Zhang, "Influence of crystal structure on the luminescence properties of bismuth (III), europium(III) and dysprosium(III) in Y₂SiO₅," *Journal of Materials Chemistry*, vol. 6, no. 2, pp. 265–269, 1996.
- [17] H.-X. Mai, Y.-W. Zhang, L.-D. Sun, and C.-H. Yan, "Size- and phase-controlled synthesis of monodisperse NaYF₄: Yb,Er nanocrystals from a unique delayed nucleation pathway monitored with upconversion spectroscopy," *Journal of Physical Chemistry C*, vol. 111, no. 37, pp. 13730–13739, 2007.
- [18] H.-X. Mai, Y.-W. Zhang, R. Si et al., "High-quality sodium rare-earth fluoride nanocrystals: controlled synthesis and optical properties," *Journal of the American Chemical Society*, vol. 128, no. 19, pp. 6426–6436, 2006.
- [19] J.-C. Boyer, L. A. Cuccia, and J. A. Capobianco, "Synthesis of colloidal upconverting NaYF₄: Er³⁺/Yb³⁺ and Tm³⁺/Yb³⁺ monodisperse nanocrystals," *Nano Letters*, vol. 7, no. 3, pp. 847–852, 2007.
- [20] G. Yi, B. Sun, F. Yang, D. Chen, Y. Zhou, and J. Cheng, "Synthesis and characterization of high-efficiency nanocrystal up-conversion phosphors: Ytterbium and erbium codoped lanthanum molybdate," *Chemistry of Materials*, vol. 14, no. 7, pp. 2910–2914, 2002.
- [21] J.-H. Zeng, J. Su, Z.-H. Li, R.-X. Yan, and Y.-D. Li, "Synthesis and upconversion luminescence of hexagonal-phase NaYF₄: Yb, Er³⁺ phosphors of controlled size and morphology," *Advanced Materials*, vol. 17, no. 17, pp. 2119–2123, 2005.
- [22] Y. Wei, F. Lu, X. Zhang, and D. Chen, "Synthesis of oil-dispersible hexagonal-phase and hexagonal-shaped NaYF₄: Yb,Er nanoplates," *Chemistry of Materials*, vol. 18, no. 24, pp. 5733–5737, 2006.
- [23] G. H. Mhlongo, O. M. Ntwaeaborwa, M. S. Dhlamini, H. C. Swart, and K. T. Hillie, "Effects of Ce³⁺ concentration, beam voltage and current on the cathodoluminescence intensity of SiO₂:Pr³⁺-Ce³⁺ nanophosphor," *Journal of Alloys and Compounds*, vol. 509, no. 6, pp. 2986–2992, 2011.
- [24] K. Tan, H. Zhang, C. Xie, H. Zheng, Y. Gu, and W. F. Zhang, "Visible-light absorption and photocatalytic activity in molybdenum- and nitrogen-codoped TiO₂," *Catalysis Communications*, vol. 11, no. 5, pp. 331–335, 2010.
- [25] Y. V. Malyukin, A. A. Masalov, P. N. Zhmurin, N. V. Znamenskii, E. A. Petrenko, and T. G. Yukina, "Two mechanisms of ¹D₂ fluorescence quenching of Pr³⁺-doped Y₂SiO₅ crystal," *Physica Status Solidi (B) Basic Research*, vol. 240, no. 3, pp. 655–662, 2003.
- [26] A. Novoselov, H. Ogino, A. Yoshikawa et al., "Crystal growth, optical and luminescence properties of Pr-doped Y₂SiO₅ single crystals," *Optical Materials*, vol. 29, no. 11, pp. 1381–1384, 2007.
- [27] C. L. Sun, J. F. Li, C. H. Hu, H. M. Jiang, and Z. K. Jiang, "Ultraviolet upconversion in Pr³⁺: Y₂SiO₅ crystal by Ar⁺ laser (488 nm) excitation," *European Physical Journal D*, vol. 39, no. 2, pp. 303–306, 2006.
- [28] S. F. Lim, R. Riehn, W. S. Ryu et al., "In vivo and scanning electron microscopy imaging of upconverting nanophosphors in *Caenorhabditis elegans*," *Nano Letters*, vol. 6, no. 2, pp. 169–174, 2006.
- [29] L. Xiong, Z. Chen, Q. Tian, T. Cao, C. Xu, and F. Li, "High contrast upconversion luminescence targeted imaging *in vivo* using peptide-labeled nanophosphors," *Analytical Chemistry*, vol. 81, no. 21, pp. 8687–8694, 2009.
- [30] D. Cervantes-Vásquez, O.E. Contreras, and G.A. Hirata, "Quantum efficiency of silica-coated rare-earth doped yttrium silicate," *Journal of Luminescence*, vol. 143, pp. 226–232, 2013.
- [31] M. K. Chong, K. Pita, and C. H. Kam, "Thermal annealing effect on Y₂O₃: Eu³⁺ phosphor films prepared by yttrium 2-methoxyethoxide sol-gel precursor," *Materials Chemistry and Physics*, vol. 100, no. 2-3, pp. 329–332, 2006.
- [32] T. H. Meen, H. D. Yang, W. J. Huang et al., "Ionic-size effect on the structure and T_c of T'^l-(R_{1-x}R'_x)_{1.85}Ce_{0.15}CuO₄ (R = Pr, Nd, Sm and Eu; R' = Gd and Y)," *Physica C*, vol. 260, no. 1-2, pp. 117–124, 1996.
- [33] V. V. Seminko, A. A. Masalov, Y. I. Boyko, and Y. V. Malyukin, "Strong segregation of doped ions in Y₂SiO₅:Pr³⁺ nanocrystals," *Journal of Luminescence*, vol. 132, no. 9, pp. 2443–2446, 2012.
- [34] L. Jia, Z. Shao, Q. Lü, Y. Tian, and J. Han, "Optimum europium doped aluminoborates phosphors and their photoluminescence properties under VUV and UV excitation," *Optics & Laser Technology*, vol. 54, pp. 79–83, 2013.
- [35] X. Fu, J. Ji, W. Tang, W. Liu, and S. Chen, "Mo-W based copper oxides: preparation, characterizations, and photocatalytic reduction of nitrobenzene," *Materials Chemistry and Physics*, vol. 141, no. 2-3, pp. 719–726, 2013.
- [36] Y. Li, W. Wang, X. Qiu et al., "Comparing Cr, and N only doping with (Cr, N)-codoping for enhancing visible light reactivity of TiO₂," *Applied Catalysis B*, vol. 110, pp. 148–153, 2011.

Research Article

Interaction of Silver Nanoparticles and Chitin Powder with Different Sizes and Surface Structures: The Correlation with Antimicrobial Activities

Vinh Quang Nguyen,^{1,2} Masayuki Ishihara,² Shingo Nakamura,³ Hidemi Hattori,² Takeshi Ono,⁴ Yasushi Miyahira,⁴ and Takemi Matsui¹

¹ Faculty of System Design, Tokyo Metropolitan University, 6-6 Asahigaoka, Hino, Tokyo 191-0065, Japan

² Research Institute, National Defense Medical College, 3-2 Namiki, Tokorozawa, Saitama 359-1324, Japan

³ Department of Surgery, National Defense Medical College, 3-2 Namiki, Tokorozawa, Saitama 359-8513, Japan

⁴ Department of Global Infectious Diseases and Tropical Medicine, National Defense Medical College, 3-2 Namiki, Tokorozawa, Saitama 359-8513, Japan

Correspondence should be addressed to Masayuki Ishihara; ishihara@ndmc.ac.jp

Received 10 July 2013; Revised 2 August 2013; Accepted 3 August 2013

Academic Editor: Jiamin Wu

Copyright © 2013 Vinh Quang Nguyen et al. This is an open access article distributed under the Creative Commons Attribution License, which permits unrestricted use, distribution, and reproduction in any medium, provided the original work is properly cited.

Silver nanoparticles (Ag NPs) were 5.17 ± 1.9 nm in diameter, and four <5% deacetylated chitins (A, B, C, and D) differing in size of powder and surface structure properties were used in the study. Chitin/Ag NP composites were synthesized by mixing Ag NP suspensions with each chitin powder at room temperature for 30 min. The Ag NPs were homogeneously dispersed and stably adsorbed onto the chitins A and B powders. The resulting chitin/Ag NP composites were brown; darker composites were obtained when larger amounts of Ag NPs were reacted with chitin. Approximately, 26 and 22 μg of Ag NPs maximally adsorbed to 1 mg of chitins A and B, respectively, whereas only 2.5 and 1.5 μg of Ag NPs maximally adsorbed to chitins C and D, respectively. As the bactericidal and antifungal activities of the chitin/Ag NP composites increased with increasing amounts of Ag NPs adsorbed to the chitin, the antimicrobial activity of chitins A and B/Ag NP composites was much higher than that of chitins C and D/Ag NP composites. These results suggest that the particle size and surface structure of the chitin powder critically influence both the adsorption and antimicrobial activity of Ag NPs.

1. Introduction

With the rise in microbial resistance to multiple antibiotics, considerable research has been carried out to develop effective antimicrobial agents free of resistance. This has led to resurgence in the use of silver- (Ag-) based antiseptics that have broad-spectrum antimicrobial activity and a much lower propensity to induce microbial resistance compared with antibiotics [1]. In fact, it is well known that Ag ions and Ag-based compounds are highly toxic to a broad range of microorganisms [2].

The chemical properties of Ag nanoparticles (Ag NPs) are significantly different from those of silver ingot or Ag ion, and thus Ag NPs have been studied by many researchers due to their wide variety of potential applications [3, 4]. The

special and unique properties of Ag NPs can be attributed to their smaller size and the larger specific surface area relative to bulk materials, and many preparation processes have been proposed for controlling the physical and/or chemical characteristics of Ag NPs [5–9].

Processes utilizing safe materials which do not require complicated purification steps can be employed to prepare Ag NPs for biomedical and environmental applications. It was reported that Ag NPs of less than 10 nm diameter can be produced through a process that employs D-glucose as the reducing agent and soluble starch as the stabilizing agent [10]. The size of Ag NPs can be controlled by modifying reaction system parameters such as pH, temperature, and reactant concentrations. The choice of stabilizing agent is an important factor for controlling the size of Ag NPs because once

they are generated, Ag NPs tend to fuse together and form aggregates that can grow to the size of microparticles [11].

The antimicrobial activity of zero-valent Ag is strictly depending on the surface development of the solid phase. When the solid phase is in a nanoparticle form, the antimicrobial activity of the resulting particles can be remarkably enhanced; as such, the antimicrobial activity of the smaller Ag NPs may be several orders of magnitude greater than that of the corresponding bulk solid. Therefore, adsorption of Ag NPs to the surface of various biomaterials could be a means of fabricating novel antimicrobial materials [12, 13].

Size is one of the most fundamental parameters affecting the optical [14], antimicrobial [15–17], and antiviral properties of Ag NPs [18, 19]. Sondi et al. reported that the antimicrobial activity of Ag NPs against Gram-negative bacteria such as *Escherichia coli* is dependent on particle concentration and that Ag NPs form “pits” in the bacterial cell wall, thus compromising its structural integrity [15]. Ag NPs also exhibit potent antifungal activity, probably through a similar mechanism involving compromise of membrane integrity [20].

On the other hand, there are some concerns about the biological and environmental risks associated with Ag NPs. It was reported that Ag NPs might adversely affect some aquatic organisms. For example, there are reports that Ag NPs may be cytotoxic and genotoxic to fish [21] and that Ag NPs may inhibit photosynthesis in algae [22]. Other evidence indicates that Ag NPs may also adversely affect mammals, as a significant decline in mouse spermatogonial stem cells was linked with exposure to Ag NPs [23]. Therefore, methods to prevent the diffusion of Ag NPs into the environment and inhibit their uptake by living organisms are needed before Ag NP-containing antimicrobial materials can be used [21–23].

In a previous study, we developed a safe and easy process for controlling the size distribution of Ag NPs [24]. The process uses three materials: AgNO₃-containing glass powder, glucose, and water. Synthesis of Ag NPs using this process was performed by autoclaving the particles in aqueous medium. Particle size can be regulated by varying the glucose concentration; that is, 0.25, 1.0, and 4.0 wt% of glucose produce small (3.48 ± 1.83 nm in diameter), medium (6.63 ± 1.78 nm in diameter), and large (12.9 ± 2.5 nm in diameter) particles, respectively [24]. Furthermore, chitin powder with low degrees of deacetylation (DDAc < 5%) and with an average particle size of 250 ± 70 μm was added as a stabilizer to the Ag NP suspension to both remove the caramel generated during autoclaving and prevent aggregation and precipitation of the Ag NPs [25]. The much stronger bactericidal (against *E. coli* strain DH5α) and antifungal (against *Aspergillus niger*) activities of chitin/Ag NP composites have been demonstrated [25].

Chitin/chitosan is the collective name for a family of de-*N*-acetylated chitin with different degrees of deacetylation (DDAc) [26]. In general, when the number of *N*-acetylglucosamine units exceeds 50% (DDAc > 50%), the biopolymer is termed chitosan, whereas the term “chitin” is used to describe the polymer when the DDAc is less than 50%. In this study, we observed that the antimicrobial activities and adsorption properties of Ag NPs are correlated with chitin particle size and surface structures of chitin powder.

2. Materials and Methods

2.1. Materials. Silver-containing glass powder (BSP21, Ag content: 1 wt%; average grain size: 10 μm) was purchased from Kankyo Science (Kyoto, Japan). All chitins (A, B, C, and D) used in this study were <5% DAc and were commercially available. D-Glucose was purchased from Wako Pure Chemical Industries, Ltd. (Osaka, Japan). All chemicals were used as received.

2.2. Preparation of Ag NPs. A suspension of size-controlled Ag NPs was prepared as previously described [24]. Briefly, 0.5 g of Ag-containing glass powder was dispersed in 50 mL of an aqueous solution of 0.8 wt% glucose in a 100 mL glass vial. The mixture was autoclaved at 121°C and 200 kPa for 20 min and then gradually cooled to room temperature, after which it was centrifuged at 1,000 g for 10 min. The resulting brown supernatant containing the Ag NP suspension was stored in the dark at 4°C. The average diameter of Ag NPs prepared with 0.8 wt% glucose was 5.17 ± 1.92 nm, and the suspension contained about 60 μg/mL of Ag NPs.

2.3. Preparation of Chitin/Ag NP Composites. First, 20, 10, 5, 2.5, 1.25, or 0.6 mg of chitin A (average particle size: 31 ± 11 μm), chitin B (104 ± 42 μm), chitin C (894 ± 121 μm), or chitin D (1,510 ± 460 μm) (all chitins: >5% DDAc) was added to 1 mL of Ag NP suspension (about 60 μg/mL) and mixed well (at pH 7.2) for 30 min using a shaker (MildMixer PR-36; TAITEC, Tokyo, Japan). The chitin/Ag NP composites were washed twice with distilled water by centrifugation. The Ag NPs were homogeneously dispersed and immobilized on the chitin powder. The composites were brown; darker composites were obtained when larger amounts of Ag NPs were reacted with each chitin. In addition, chitins C and D were suspended in 0.2 M acetate and mixed on the shaker for 18 h. The resulting powders were washed twice with distilled water by centrifugation and allowed to air dry. The air-dried chitin C and D powders were ground thoroughly using a mortar and pestle to make the particles smaller, and then the ground chitin/Ag NP composites were produced as described above.

UV-vis spectra were obtained at room temperature using a Jasco V-630 spectrophotometer (Jasco Corporation, Tokyo, Japan). Scanning electron microscopy (SEM) specimens of the chitins were coated with gold plasma to enhance conductivity using a plasma multicoater PMC-5000 (Meiwafosis Co., Ltd., Tokyo, Japan). SEM was performed using a JSM-6340F microscope (JEOL, Tokyo, Japan) operated at 5 kV.

Transmission electron microscopy (TEM) specimens were prepared by casting a small drop of a suspension of chitin/Ag NPs onto a carbon-coated copper grid; excess solution was then removed using filter paper, and the specimens were dried at room temperature. TEM images were obtained using a JEOL JEM-1010 microscope (Nihon Electronics Inc., Tokyo, Japan) operated at 80 kV.

2.4. Bactericidal Activity of Chitin/Ag NP Composites. A culture of *E. coli* strain DH5α (Takara Co., Kyoto, Japan) was stored at –80°C in Luria-Bertani (LB) broth containing 50%

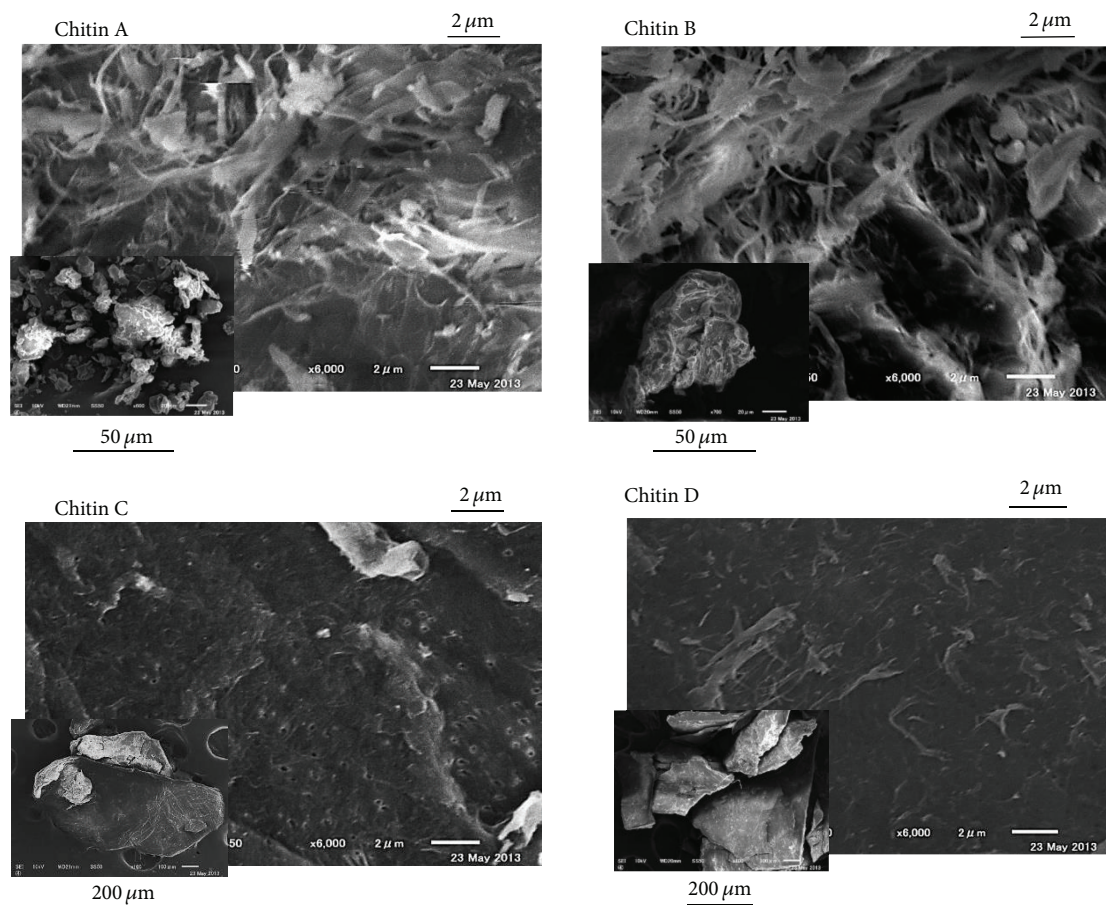


FIGURE 1: SEM micrographs of chitins A, B, C, and D.

sterile glycerol. Overnight cultures were prepared by growing a single *E. coli* colony overnight at 37°C in 5 mL of LB medium. On the next day, 200 μL of the overnight culture was inoculated into 2 mL of LB medium and incubated at 37°C for 6 h or until the optical density at 600 nm (OD_{600}) reached 0.260. The *E. coli* culture was then diluted 4-fold with LB broth, after which 50 μL of the diluted suspension was added to separate sterile 1.5-mL ClickFit polypropylene microcentrifuge tubes (TreffLab AG, Degersheim, Switzerland) containing dried chitin/Ag NP composites with 2, 1, 0.5, or 0 μg of Ag NPs adsorbed to 10 mg of each chitin type. The samples were then incubated at 37°C for 18 h, after which 1 mL of LB medium was added to each suspension and mixed well. The suspensions were allowed to stand for 3 min to precipitate the chitin/Ag NP composites. Viable cells were enumerated by plating 50 μL of 10-fold serial dilutions of the suspensions onto LB agar (ForMedium Ltd., Hunstanton, UK) in a 90 \times 15 mm Petri dish, followed by incubation at 37°C for 24 h.

2.5. Antifungal Activity of the Ag NP/Chitin Composites. *Aspergillus niger* NBRC105649 (Japan Collection of Microorganisms; Wako, Saitama, Japan) was maintained in molten potato dextrose agar (PDA) medium (Difco, Becton Dickinson & Co., Sparks, MD, USA). Aliquots (20 μL) of a suspension of *A. niger* spores (6.35×10^4 spores/mL) were inoculated into each well of a 24-well plate (well diameter:

17 mm; Sumitomo Bakelite Co., Ltd., Tokyo, Japan) containing 1 mL of PDA prepared with 60, 30, 15, or 7.5 $\mu\text{g}/\text{mL}$ of Ag NPs adsorbed onto 5 mg of each chitin. The plates were incubated in the dark at 25°C for 3 days, after which the *A. niger* spores were recovered into 500 μL of 0.3% sterile Tween 80 solution using a platinum loop. After vortexing, the absorbance of each spore suspension was measured at 550 nm using a Jasco V-630 spectrophotometer [25].

3. Results and Discussion

3.1. Characterization of the Chitin/Ag NP Composites. In this work, <5% DAC chitins A, B, C, ground C (G-C), D and ground D (G-D) with various particle sizes and with various surface structures were added to the Ag NP suspensions to remove the caramel produced during autoclaving and to prevent aggregation and precipitation of the Ag NPs. The Ag NPs were adsorbed tightly to chitins A and B by just mixing at pH 7.0 for 30 min. The chitins A and B/Ag NP composites were substantially more stable than Ag NPs alone. Caramel was removed from the chitin/Ag NP composites by washing them twice with distilled water. The caramel had to be removed because of its inadequate growth effect of microbial growth.

Typical SEM micrographs of chitins A, B, C, and D are shown in Figure 1. Chitins A and B exhibited smaller powder

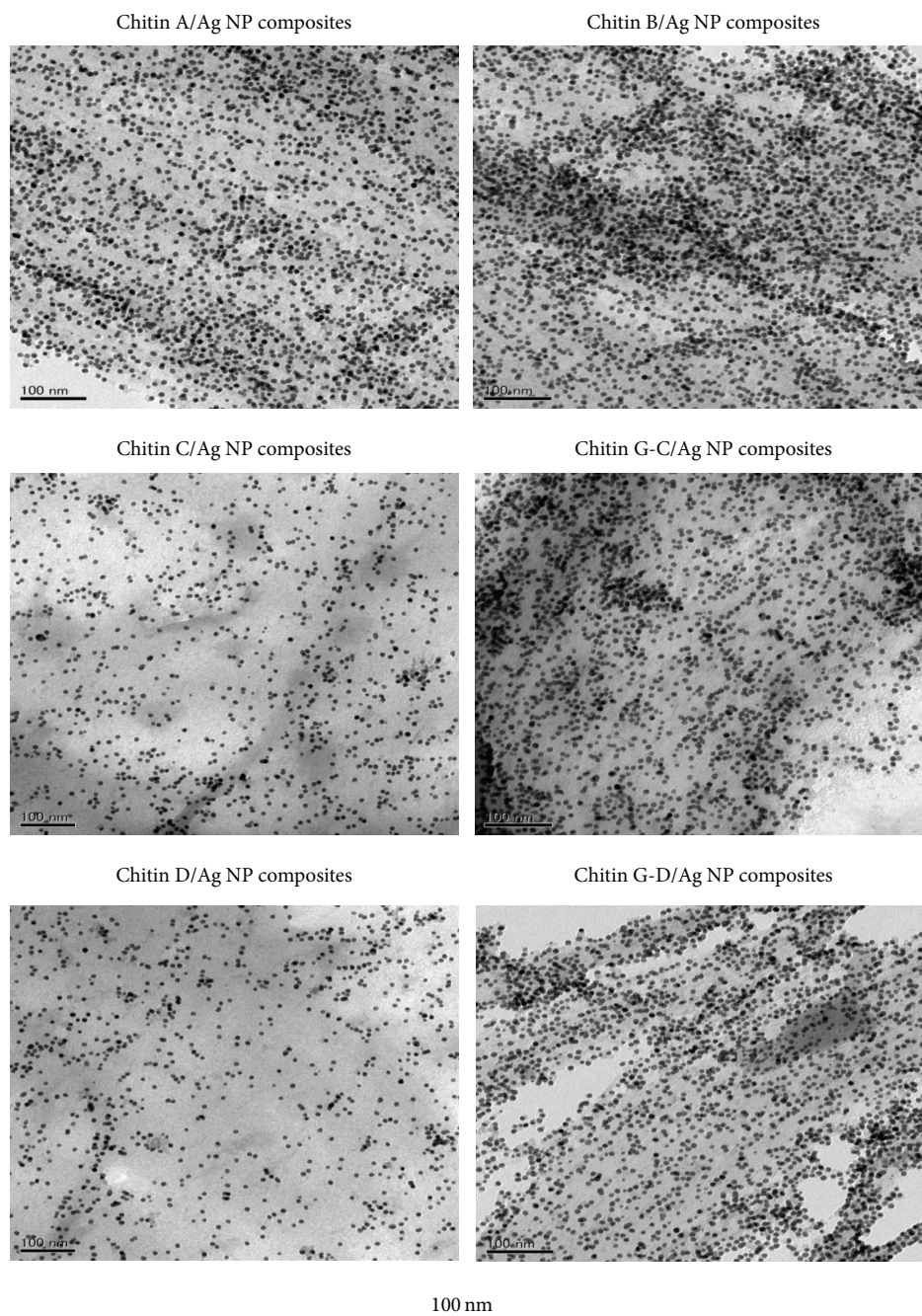


FIGURE 2: TEM micrographs of chitins A, B, C, G-C, D, and G-D/Ag NP composites ($\times 250,000$). A total of 1 mg of each chitin were added to a $10 \mu\text{g}/\text{mL}$ suspension of Ag NPs and mixed for 30 min prior to analysis.

particle size and a nanoscale fiber-like surface structure, whereas chitins C and D showed a larger powder particle size and a flat/smooth film-like surface structure. Chitins G-C and G-D exhibited a smaller powder particle size and a nanoscale fiber-like surface structure similar to that of chitins A and B (data not shown). The powder sizes and shapes of the Ag NPs adsorbed to all of the chitins examined were identical to those of the original Ag NPs used for synthesizing the composites (Figure 2). The average particle size of chitin G-C and chitin G-D was 146 ± 62 and $181 \pm 52 \mu\text{m}$, respectively

(Table 1), indicating that larger chitin powder particles with a flat/smooth film-like surface structure can be changed into smaller particles with a nanoscale fiber-like surface structure by grinding. The color of the composites was brown; a darker composite was obtained when larger amounts of Ag NPs were adsorbed to the chitin.

As shown in Table 1, approximately 26, 22, 2.5, 20, 1.5 and $18 \mu\text{g}$ of Ag NPs maximally adsorbed to 1 mg of chitins A, B, C, G-C, D, and G-D, respectively. Figures 3 and 4 show UV-vis spectra of Ag NPs in suspension and spectra of the

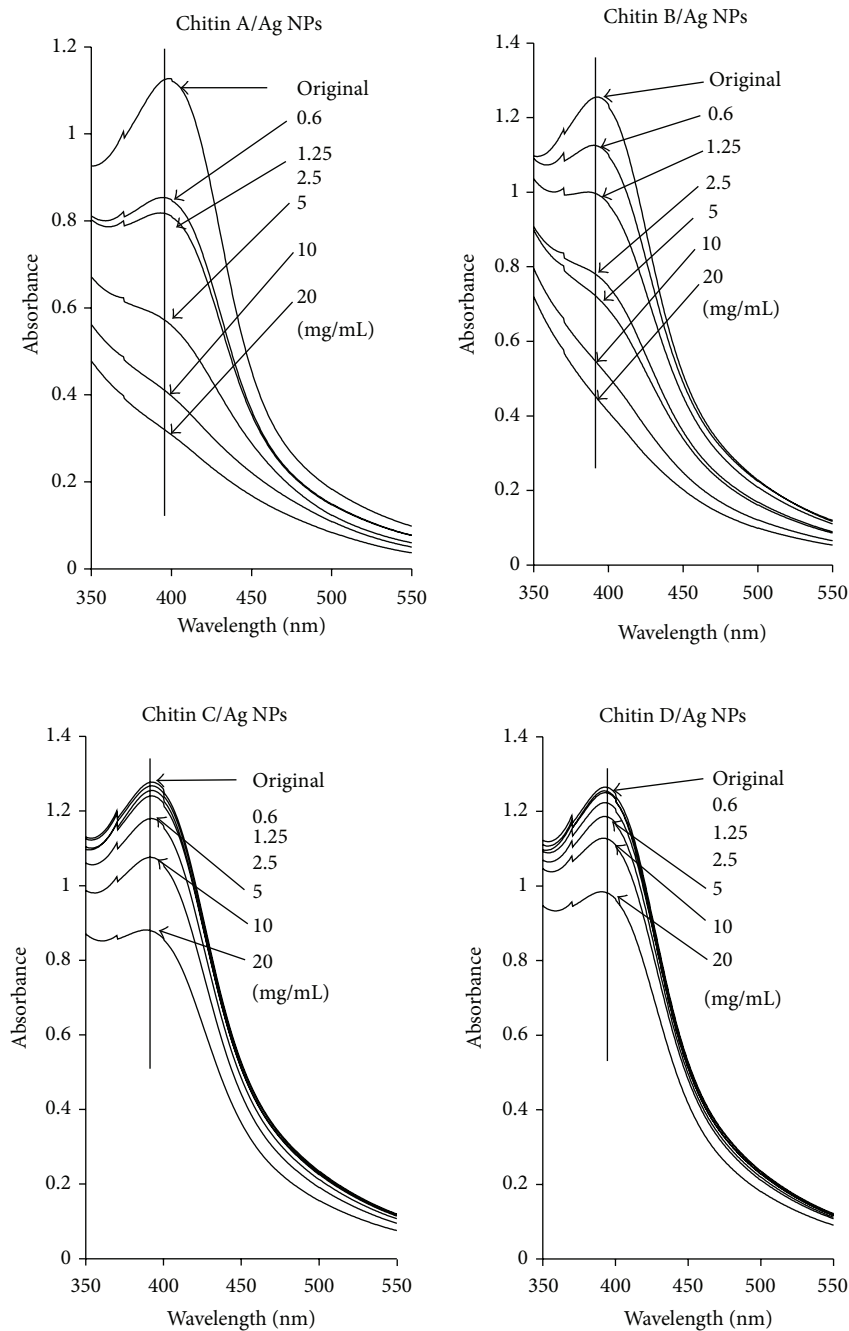


FIGURE 3: UV-vis spectra of original Ag NPs in suspension (original) and supernatants from the postreaction mixtures in which various amounts of chitins A, B, C, and D reacted with Ag NPs. Excess Ag NPs in the supernatants of the postreaction mixtures decreased as the amount of chitin added increased.

supernatants of the postreaction mixtures in which various amounts of chitin reacted with the Ag NPs. The peak at 390.5 nm is representative of the spherical Ag NPs used in this work [12, 24]. There was a proportional relationship between the absorbance at 390.5 nm and the concentration of Ag NPs in the suspension [25]. The amount of Ag NPs remaining in the supernatants of the postreaction mixtures decreased as the concentration of chitin in the reaction mixture increased (Figures 3 and 4). Thus, Ag NPs selectively reacted with chitins G-C and G-D in addition to chitins A and B.

3.2. Antimicrobial Activity of the Chitin/Ag NP Composites.

The antimicrobial activity of Ag NPs has been demonstrated in a number of studies [13–15, 18, 20]. Investigation of this phenomenon has gained importance due to the rise in resistance to antibiotics caused by their overuse. The bactericidal activity of each chitin type alone and each chitin/Ag NP composite was evaluated against *E. coli*. The individual chitins alone exhibited only weak bactericidal activity. Composites with various amounts of Ag NPs in 10 mg/mL of chitins A, B, G-C, or G-D showed strong, concentration-dependent

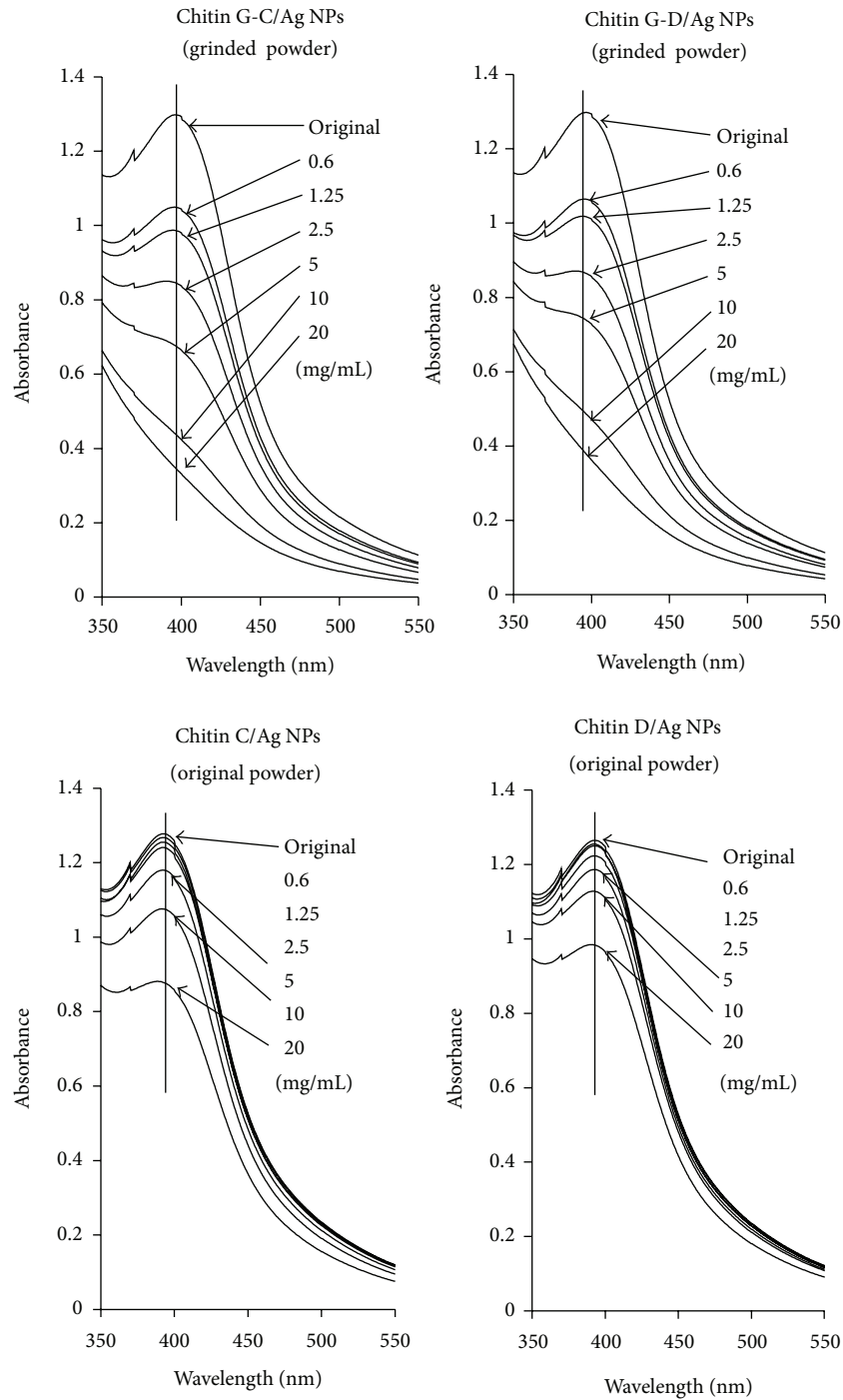


FIGURE 4: UV-vis spectra of original Ag NPs in suspension (original) and supernatants from the postreaction mixtures in which various amounts of chitins G-C, G-D, C, and D reacted with Ag NPs. Excess Ag NPs in the supernatants of the postreaction mixtures decreased as the amount of chitin added increased.

bactericidal activity, whereas the chitins C and D/Ag NP composites demonstrated only weak bactericidal activity because of lower interactions between the chitin and Ag NPs (Table 1 and Figure 5).

The antifungal activity of each chitin type alone and each chitin/Ag NP composite was evaluated against *A. niger*. Fungi were incubated in molten PDA containing the test

materials. Chitin alone (5 mg/mL) exhibited weak antifungal activity (Figure 6). When composites with various amounts of Ag NPs in 5 mg/mL of chitin were added to the fungal cultures in PDA, composites containing chitins A, B, G-C, and G-D showed strong, concentration-dependent antifungal activity, with half-growth inhibition occurring at Ag NP concentrations of 10, 12, 14, and 15 $\mu\text{g/mL}$, respectively

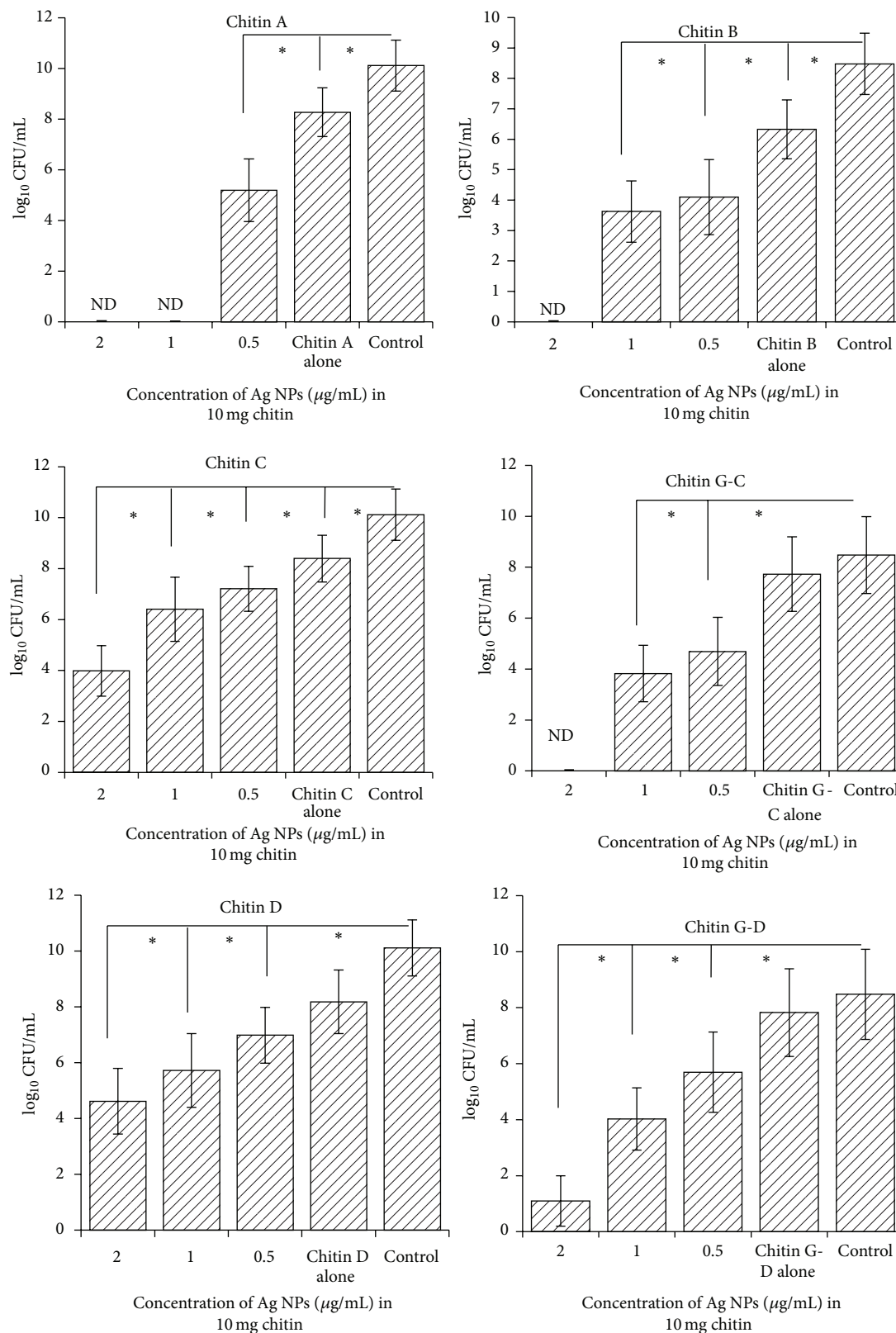


FIGURE 5: Chitins A, B, C, G-C, D, and G-D/Ag NP composites were evaluated for their bactericidal (against *E. coli*) activity in LB medium. The composites contained various amounts of Ag NPs in 10 mg of chitin and exhibited a strong, concentration-dependent bactericidal activity. Data are the mean \pm standard deviation; $n = 6$. ND = not detected. Asterisks (*) denote statistically significant differences ($P < 0.01$) as determined using a two-sample *t*-test.

TABLE 1: Evaluation of each chitin/Ag NP composites.

	Maximal amount of Ag NPs (μg) absorbed in 1 mg chitin ($\mu\text{g}/\text{mg}$)	Half-bactericidal activity with $\log_{10}\text{CFU}/\text{mL}$ for Ag NPs (μg) in 10 mg chitin ($\mu\text{g}/10\text{ mL}$)	Half-antifungal activity for Ag NPs (μg) in 5 mg chitin ($\mu\text{g}/5\text{ mL}$)
Chitin A	26	0.5	10
Chitin B	22	0.5	12
Chitin C	2.5	2.0	>60
Chitin G-C	20	0.5	14
Chitin D	1.5	>2.0	>60
Chitin G-D	18	0.5	15

Chitin A, powder size: average $31\ \mu\text{m}$, nanofiber-like structures.
 Chitin B, powder size: average $104\ \mu\text{m}$, nanofiber-like structures.
 Chitin C, powder size: average $894\ \mu\text{m}$, smooth film-like structures.
 Chitin G-C, powder size: average $146\ \mu\text{m}$, nanofiber-like structures.
 Chitin D, powder size: average $>1500\ \mu\text{m}$, smooth film-like structures.
 Chitin G-D powder size: average $181\ \mu\text{m}$, nanofiber-like structures.
 Ag NPs: average diameter $5.17 \pm 1.9\ \text{nm}$, G-: ground.

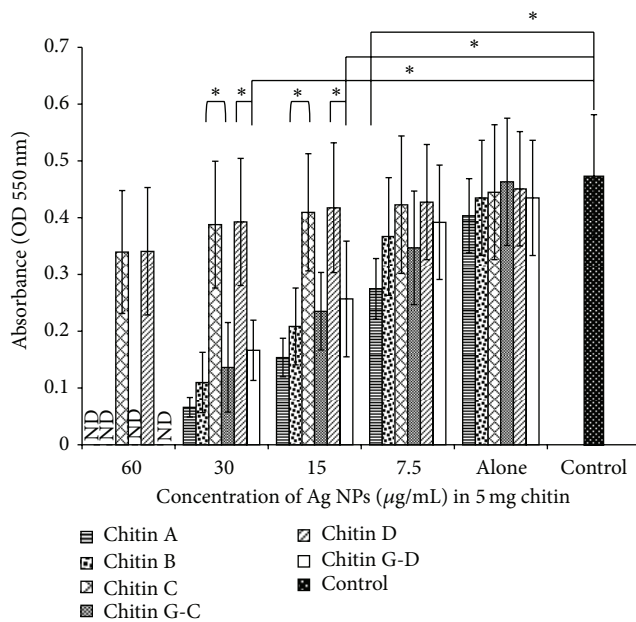


FIGURE 6: Chitins A, B, C, G-C, D, and G-D/Ag NP composites were evaluated for their antifungal activity against *A. niger* by incubating fungal spores on PDA with composites consisting of various amounts of Ag NPs in 5 mg/mL suspensions of each chitin. The composites exhibited a strong Ag NP concentration-dependent antifungal activity. Data are the mean \pm standard deviation; $n = 6$. Asterisks (*) denote statistically significant differences ($P < 0.01$) as determined using a two-sample *t*-test.

(Figure 6). Composites containing chitins C and D exhibited only weak antifungal activity. These results demonstrated that the antifungal activity of chitin/Ag NP composites increases as the amount of Ag NPs adsorbed to the chitin particles increases. The antimicrobial activity of Ag NPs adsorbed onto the smaller chitin powder particles with a nanoscale fiber-like surface structure was enhanced for two main reasons: (i) the available binding area for Ag NPs increases with decreasing chitin powder particle size together with the

presence of the nanoscale fiber-like surface structure; (ii) chitin/Ag NP composites with higher amounts of Ag NPs are able to interact with microorganisms more efficiently. The sizes and morphologies of bound Ag NPs onto each chitin were maintained for at least 3 months.

The mechanism of the bactericidal action of Ag ions is closely related to their interaction with proteins, particularly with thiol groups (sulfhydryl, -SH), which is believed to be bridged by Ag ions, thus binding protein molecules together and disrupting their function. Because many proteins function as enzymes, disruption of function leads to a breakdown in cellular metabolism, followed by death [13, 14]. However, the bactericidal and antifungal mechanisms of Ag NPs have not been investigated extensively. It has been reported that the activity of Ag NPs against gram-negative bacteria such as *E. coli* is dependent on the Ag NP concentration and involves the formation of “pits” in the bacterial cell wall [13]. The bactericidal activity of Ag NPs (against *E. coli*) is likely due to direct binding of the microbial envelope glycoproteins by the Ag NPs adsorbed to the nanoscale fiber-like surface structures of the small chitin powder particles, facilitating an interaction with the membrane that compromises its integrity. The potent antifungal activity (against *A. niger*) of the chitin/Ag NP composites is also probably related to compromise of membrane integrity [20]. In large chitin/Ag NP composites containing lower amounts of Ag NPs, spatial restriction due to the larger size of the chitin powder particles may prevent or weaken the interaction between microorganisms and the Ag NPs. In contrast, composites prepared with small chitin powder particles and with higher amounts of Ag NPs appear to interact more efficiently with the microbial cell surface [25].

4. Conclusion

In this work, various chitins with small powder particle sizes and nanoscale fiber-like surface structures were used to stabilize Ag NPs in suspensions and remove the caramel generated during autoclaving, thus preventing aggregation and precipitation of the Ag NPs. The Ag NPs were homogeneously

dispersed and stably adsorbed onto nanoscale fiber-like surface of the smaller chitin powder particles. The bactericidal and antifungal activities of the chitin/Ag NP composites we examined increased as the amount of Ag NPs adsorbed to the chitin particles increased. These results demonstrate the potential applications of small chitin powders with nanoscale fiber-like surface structures as a novel stabilizer and carrier for Ag NPs. Furthermore, chitin/Ag NP composites could be used directly as antimicrobial materials.

Conflict of Interests

The authors state that they have no conflict of interests.

Acknowledgment

This study was carried out using commercially available materials and equipment. The authors would like thank Ms. Y. Ichiki from the Laboratory Center of the National Defense Medical College (Tokorozawa, Japan) for help with electron microscopy experiments.

References

- [1] D. J. Anderson and M. Moskovits, "A SERS-active system based on silver nanoparticles tethered to a deposited silver film," *Journal of Physical Chemistry B*, vol. 110, no. 28, pp. 13722–13727, 2006.
- [2] A. Kumar, P. K. Vemula, P. M. Ajayan, and G. John, "Silver-nanoparticle-embedded antimicrobial paints based on vegetable oil," *Nature Materials*, vol. 7, no. 3, pp. 236–241, 2008.
- [3] S. Sharma, N. Ahmad, A. Prakash, V. N. Singh, A. K. Ghosh, and B. R. Mehta, "Synthesis of crystalline Ag nanoparticles, (Ag NPs) from microorganisms," *Materials Sciences and Applications*, vol. 1, pp. 1–7, 2010.
- [4] W. Ngeontae, W. Janrungroatsakul, P. Maneewattanapinyo, S. Ekgasit, W. Aeungmaitrepirom, and T. Tuntulani, "Novel potentiometric approach in glucose biosensor using silver nanoparticles as redox marker," *Sensors and Actuators B*, vol. 137, no. 1, pp. 320–326, 2009.
- [5] S. Komarneni, D. Li, B. Newalkar, H. Katsuki, and A. S. Bhalla, "Microwave-polyol process for Pt and Ag nanoparticles," *Langmuir*, vol. 18, no. 15, pp. 5959–5962, 2002.
- [6] S. Navaladian, B. Viswanathan, R. P. Viswanath, and T. K. Varadarajan, "Thermal decomposition as route for silver nanoparticles," *Nanoscale Research Letters*, vol. 2, no. 1, pp. 44–48, 2007.
- [7] N. Vigneshwaran, N. M. Ashtaputre, P. V. Varadarajan, R. P. Nachane, K. M. Paralikar, and R. H. Balasubramanya, "Biological synthesis of silver nanoparticles using the fungus *Aspergillus flavus*," *Materials Letters*, vol. 61, no. 6, pp. 1413–1418, 2007.
- [8] M. Z. Kassae, A. Akhavan, N. Sheikh, and R. Beteshobabrud, "γ-Ray synthesis of starch-stabilized silver nanoparticles with antibacterial activities," *Radiation Physics and Chemistry*, vol. 77, no. 9, pp. 1074–1078, 2008.
- [9] G. N. Xu, X. L. Qiao, X. L. Qiu, and J. G. Chen, "Preparation and characterization of stable monodisperse silver nanoparticles via photoreduction," *Colloids and Surfaces A*, vol. 320, no. 1–3, pp. 222–226, 2008.
- [10] P. Raveendran, J. Fu, and S. L. Wallen, "Completely "Green" Synthesis and Stabilization of Metal Nanoparticles," *Journal of the American Chemical Society*, vol. 125, no. 46, pp. 13940–13941, 2003.
- [11] N. Vigneshwaran, R. P. Nachane, R. H. Balasubramanya, and P. V. Varadarajan, "A novel one-pot "Green" synthesis of stable silver nanoparticles using soluble starch," *Carbohydrate Research*, vol. 341, no. 12, pp. 2012–2018, 2006.
- [12] I. O. Sosa, C. Noguez, and R. G. Barrera, "Optical properties of metal nanoparticles with arbitrary shapes," *Journal of Physical Chemistry B*, vol. 107, no. 26, pp. 6269–6275, 2003.
- [13] I. Sondi and B. Salopek-Sondi, "Silver nanoparticles as antimicrobial agent: a case study on *E. coli* as a model for Gram-negative bacteria," *Journal of Colloid and Interface Science*, vol. 275, no. 1, pp. 177–182, 2004.
- [14] J. R. Morones, J. L. Elechiguerra, A. Camacho et al., "The bactericidal effect of silver nanoparticles," *Nanotechnology*, vol. 16, no. 10, pp. 2346–2353, 2005.
- [15] X. L. Cao, C. Cheng, Y. L. Ma, and C. S. Zhao, "Preparation of silver nanoparticles with antimicrobial activities and the researches of their biocompatibilities," *Journal of Materials Science*, vol. 21, no. 10, pp. 2861–2868, 2010.
- [16] P. Pallavicini, A. Taglietti, G. Dacarro et al., "Self-assembled monolayers of silver nanoparticles firmly grafted on glass surfaces: low Ag⁺ release for an efficient antibacterial activity," *Journal of Colloid and Interface Science*, vol. 350, no. 1, pp. 110–116, 2010.
- [17] P. Dallas, V. K. Sharma, and R. Zboril, "Silver polymeric nanocomposites as advanced antimicrobial agents: classification, synthetic paths, applications, and perspectives," *Advances in Colloid and Interface Science*, vol. 166, no. 1–2, pp. 119–135, 2011.
- [18] J. L. Elechiguerra, J. L. Burt, J. R. Morones et al., "Interaction of silver nanoparticles with HIV-1," *Journal of Nanobiotechnology*, vol. 3, p. 6, 2005.
- [19] H. H. Lara, N. V. Ayala-Nuñez, L. Ixtepan-Turrent, and C. Rodriguez-Padilla, "Mode of antiviral action of silver nanoparticles against HIV-1," *Journal of Nanobiotechnology*, vol. 8, p. 1, 2010.
- [20] K. J. Kim, W. S. Sung, B. K. Suh et al., "Antifungal activity and mode of action of silver nanoparticles on *Candida albicans*," *BioMetals*, vol. 22, no. 2, pp. 235–242, 2009.
- [21] J. P. Wise, B. C. Goodale, S. S. Wise et al., "Silver nanospheres are cytotoxic and genotoxic to fish cells," *Aquatic Toxicology*, vol. 97, no. 1, pp. 34–41, 2010.
- [22] E. Navarro, F. Piccapietra, B. Wagner et al., "Toxicity of silver nanoparticles to *Chlamydomonas reinhardtii*," *Environmental Science and Technology*, vol. 42, no. 23, pp. 8959–8964, 2008.
- [23] L. K. Braydich-Stolle, B. Lucas, A. Schrand et al., "Silver nanoparticles disrupt GDNF/Fyn kinase signaling in spermatogonial stem cells," *Toxicological Sciences*, vol. 116, no. 2, pp. 577–589, 2010.
- [24] Y. Mori, T. Tagawa, M. Fujita et al., "Simple and environmentally friendly preparation and size control of silver nanoparticles using an inhomogeneous system with silver-containing glass powder," *Journal of Nanoparticle Research*, vol. 13, no. 7, pp. 2799–2806, 2011.
- [25] V. Q. Nguyen, M. Ishihara, Y. Mori et al., "Preparation of size-controlled silver nanoparticles and Chitin-based composites and their antimicrobial activities," *Journal of Nanomaterials*, vol. 2013, Article ID 693486, 7 pages, 2013.
- [26] C. Shi, Y. Zhu, X. Ran, M. Wang, Y. Su, and T. Cheng, "Therapeutic potential of chitosan and its derivatives in regenerative medicine," *Journal of Surgical Research*, vol. 133, no. 2, pp. 185–192, 2006.

Research Article

Fabrication of Polystyrene/Detonation Nanographite Composite Microspheres with the Core/Shell Structure via Pickering Emulsion Polymerization

Hou Xuemei¹ and Ying Hao²

¹ College of Automation, Xi'an Institute of Post and Telecommunication, Xi'an 710121, China

² College of Environmental Science and Engineering, Chang'an University, Xi'an 710054, China

Correspondence should be addressed to Hou Xuemei; hxmqz@sina.com.cn

Received 20 June 2013; Revised 23 July 2013; Accepted 27 July 2013

Academic Editor: Mengnan Qu

Copyright © 2013 H. Xuemei and Y. Hao. This is an open access article distributed under the Creative Commons Attribution License, which permits unrestricted use, distribution, and reproduction in any medium, provided the original work is properly cited.

Polystyrene microspheres coated with detonation nanographite particles have been prepared by Pickering emulsion polymerization using azobisisobutyronitrile (AIBN) as initiator in aqueous solutions. In the present techniques, the pristine detonation nanographite particles were employed as stabilizer of Pickering emulsion and then were armored on the as-prepared polystyrene cores by the thermal polymerization. The composite microspheres of polystyrene/detonation nano-graphite (PS/DNG) were characterized by field emission scanning electron microscopy (FE-SEM), X-ray diffraction (XRD), thermogravimetric and differential thermal analysis (TGA-DTA), and Fourier transformation infrared spectrum (FT-IR). FE-SEM indicates that the resulting samples retain spherical shape, with the uniform size ranging from 100 to 150 μm and good dispersity. FT-IR presents the possible formation mechanisms of PS/DNG composites. The functional groups on the surface of polystyrene and modified detonation nano-graphite particles have played an important role for the formation of PS/DNG composites. Moreover, the wettability of different nanographite was also tested.

1. Introduction

In the past years, constructions of inorganic-organic composites have opened up a novel route to get new materials with predefined structure and performance [1, 2]. In such hybrid inorganic-organic materials, the armored nanoparticles can endow the composites with some special properties [3], such as excellent photovoltage properties [4], photocatalytic performance [5, 6], special optical property [7], and magnetic property [8]. In such hybrid inorganic-organic materials, the inorganic particles contribute to increasing the complexity and functionality of the composites through incorporation as one component in a multilevel-structured material where there is a synergistic interaction between the organic and inorganic components [9, 10].

Graphite, which is naturally abundant, has been widely used as electronically conducting filler for preparing and conducting polymer composites in the last decades [11–13].

To achieve a high performance graphite-based inorganic-organic composite, disperses of the expanded graphite nanosheets, layered graphite oxide, or nature flake graphite in the various polymer matrixes have attracted active research interest. Typically, graphite/PMMA [14], graphite/PS [15], graphite/PVC [16], graphite/nylon 6 [17], and other hybrid composites have been obtained in the presence of graphite particles. Meanwhile, the introduction of inorganic expanded graphite particles into polymer matrix has led to a remarkable improvement in thermal, mechanical, and electrical properties in comparison with the pure polymer materials and hence can offer a wide range of potential applications, such as electromagnetic interference (EMI) shielding of computers and electronic equipments, electrode materials, conductive adhesive for electronics packaging, flip-chips, cold solders, static charge dissipating materials, cathode ray tubes and fuel cells, corrosion resistant and radar absorbent coating, and switching devices [18–21]. Up to now,

a variety of methods have been established to fabricate the above-mentioned graphite-based inorganic-organic composites including the mechanical mixing [22], melt mixing [23], and in situ controlled radical polymerization [24]. Among those techniques, the emulsion polymerization has been paid much attention because of its versatile and robust traits to prepare well-defined hybrid composites. The graphite-based inorganic-organic composites were facilely attained by the free radical emulsion polymerization of styrene in the presence of the graphite particles. However, in comparison with the great achievement in the expended graphite/polymer composites, few studies have been reported on the fabrication of composites of polystyrene/detonation nanographite with the core/shell structure.

Detonation nanographite materials synthesized by detonation of oxygen-deficient explosives, with their advantages of good thermal and electrical conductivity, microwave absorption, and lubricating ability, have been widely used in industry, for example, as coating materials for electrical conductors, as graphite emulsions for kinescopes, as electromagnetic shields, as gaskets, and as absorbents for removing spilled oil from water system [25–27]. In order to further develop and widen the applications of detonation nanographite (DNG), we attempt to fabricate the polystyrene/detonation nanographite (PS/DNG) composites via Pickering emulsion of styrene in the presence of the detonation nanographite particles. In this route, nanographite solid particles are absorbed irreversibly on the monomer-water interface and act as effective stabilizers to construct the Pickering emulsion firstly. Then, the particles are captured on the surface of polymer microspheres during the processes of thermal polymerization. Compared with conventional preparation techniques, the polystyrene/detonation nanographite (PS/DNG) composites could be obtained in a one-pot synthesis with the absence of common stabilizers via Pickering emulsion [28–30]. Moreover, the structures of resultant PS/DNG composites have been characterized by FESEM, XRD, TGA-DTA, and FT-IR, respectively. A possible formation mechanism was proposed to explain the structure of products accordingly.

2. Experimental Section

2.1. Materials. Detonation nanographite particle samples (primary particle size, 16 nm; specific surface area $583.6 \text{ m}^2 \cdot \text{g}^{-1}$ by BET, density $1.58 \text{ g} \cdot \text{cm}^{-3}$) used for this investigation were provided by Shaanxi Yilin Company, a professional detonation diamond producer. Ethyl alcohol, sulphuric acid, and oleic acid were purchased from Xi'an Reagent Company (analytical grade). Styrene of analytical grade (Tianjin Reagents Company) was distilled under reduced pressure before use. Azobisisobutyronitrile (AIBN, Tianjin Reagents Company) was of chemical grade and was utilized without further purification. Deionized water was used throughout the experimental work.

2.2. Synthesis of PS/DNG Composites. Acid treatment of primitive detonation nanographite was used to improve their

wettability behaviors in water by the soak methods with the sulphuric acid and oleic acid, respectively. In a typical procedure, 0.5 g DNG was mixed with 40 mL concentrated sulphuric acid (98%). The mixture was then heated to 60°C for 20 min and cooled naturally to room temperature (25°C). Afterwards, the suspensions were centrifuged. The obtained solid particles were named as sulphuric acid-modified nanographite. Similarly, mixture of 0.5 g DNG and 40 mL oleic acid was used to prepare the oleic-modified nano-graphite.

Polystyrene/detonation nanographite (PS/DNG) composites were synthesized through Pickering emulsion polymerization. A typical preparation procedure is detailed as follows: a quantity of 0.0020 g of detonation nanographites was dispersed in 30 mL of deionized water to form the detonation nanographite/water dispersions. A quantity of 0.3000 g of azobisisobutyronitrile was dissolved in 2 mL of styrene and subsequently was mixed with the aqueous detonation nanographite dispersions. The stable styrene-in-water Pickering emulsion stabilized by detonation nanographite was generated via ultrasonic processor for 20 min. The system was degassed by purging with nitrogen gas for 10 min and was subsequently polymerized at 75°C for 8 h. After reaction, the mixture systems were centrifuged. The obtained polystyrene/detonation nanographite (PS/DNG) composites were washed with water and ethyl alcohol, respectively, and followed by being dried in vacuum at 40°C for 4 h.

2.3. Characterizations of PS/DNG Composites. The type of Pickering emulsion was inferred by observing what happened when a drop of emulsion was added into water or styrene. Oil-in-water emulsions were dispersed in water and remained as drops in oil, while water-in-oil emulsions were dispersed in oil and remained as drops in water [31, 32]. X-ray diffraction (XRD) patterns were obtained by a Rigaku D/MAX-3C X-ray diffraction meter, using $\text{Cu K}\alpha$ radiation ($\lambda = 1.54178 \text{ \AA}$) in the 2θ range from 20° to 70° with $0.02^\circ/\text{min}$. FT-IR traces of products were collected by a Nicolet 360 Fourier transmitting infrared spectrometer. The differential thermal analysis (DTA) and thermogravimetry analysis (TGA) were performed using a TA-50H thermal analyzer (Shimadzu) at a heating rate of $20^\circ\text{C}/\text{min}$ under the stream of nitrogen.

3. Results and Discussion

The scheme, as illustrated in Figure 1, was the formation processes of polystyrene (PS) microspheres encapsulated with the detonation nanographite by Pickering emulsion method. In this route, the detonation nanographite was employed as Pickering stabilizer and encapsulated in the Pickering droplet by sonication emulsification. After thermal polymerization, polystyrene (PS) microspheres armored with detonation nanographite were formed.

3.1. Character of Pickering Emulsion. According to the fundamentals of Pickering emulsions, the wettability behaviors of inorganic nanosized particles in oil-water (styrene-water) system should play critical roles for the fabrication of stable Pickering emulsions [33, 34]. Hereby, it is essential to

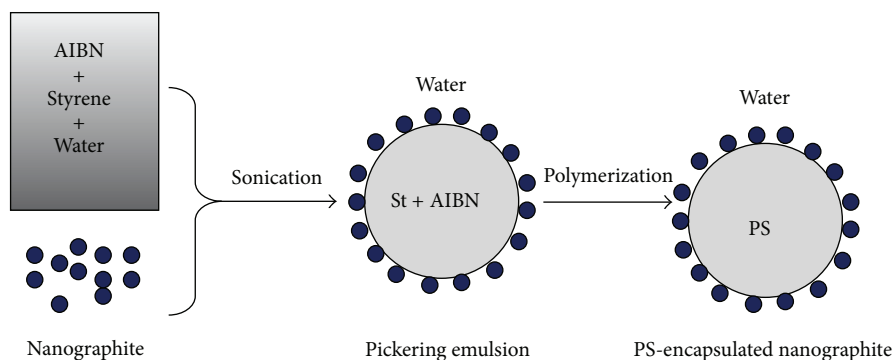


FIGURE 1: Formation of PS microspheres with encapsulated nanographite by Pickering emulsion.

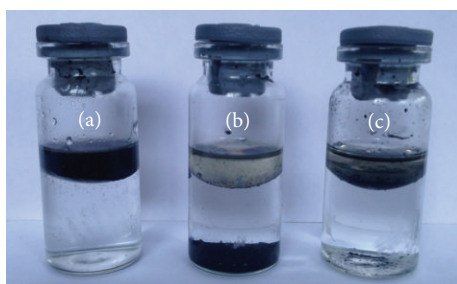


FIGURE 2: Distribution of pristine detonation nano-graphite, sulphuric acid-modified nanographite, and oleic-modified nanographite in styrene-water system.

check the location of detonation nanographite particles in oil-water system during the formation processes of stable nanographite-styrene (AIBN)-water Pickering emulsion. In the experiment of hydrophilicity or hydrophobicity testing of detonation nanographite particles, a droplet of nanographite suspension was diluted into a styrene-water mixture, followed by violent shaking and undisturbed settling. The optical micrograph of distribution of pristine detonation nano-graphite, sulphuric acid modified-nanographite, and oleic-modified nanographite in styrene-water system are shown in Figure 2, respectively. From Figure 2(a), it can be seen that the oleic-modified nanographite particles disperse preferentially in the upper layer of styrene due to their hydrophobicity, while sulphuric acid-modified nanographite particles disperse mainly in the under layer of water due to their hydrophilicity in Figure 2(b). Only pristine detonation nanographite particles can assemble spontaneously at water-styrene interface and congregate into an elastic particle-formed film at interface as shown in Figure 2(c). Therefore, the pristine detonation nanographite particles should be the optimal nanosized inorganic particles to form a stable nanographite-styrene (AIBN)-water Pickering emulsion in comparison with the oleic-modified or sulphuric acid-modified nanographite particles.

Based on the above-mentioned test, the nanographite-styrene (AIBN)-water Pickering emulsion can be formed via adding pristine detonation nanographite particles into styrene (AIBN)-water system by succeeding sonication

emulsification technique. In our experiments, the optical images were taken firstly to analyze the status of nano-graphite-styrene (AIBN)-water Pickering emulsion. Figure 3 shows the typical optical micrographs of Pickering emulsion for the fabrication of polystyrene/detonation nanographite (PS/DNG) microspheres. It can be seen that the emulsions are oil-in-water type, as referred from the fact that the emulsions were dispersed rapidly in water and remained as drops of styrene. The droplets were polydisperse in size due to employing sonication emulsification technique, in which the droplets size is governed by the sonication time and ultrasonic intensity on the emulsion droplets [35]. Compared to the pure styrene droplets, the decline in transparency is ascribed to the cases that large amount of nanographite particles were densely anchored onto the surface of styrene droplets as seen in Figure 3(b), while a few nanographite particles were encapsulated within the droplets. Moreover, it has been ascertained that the Pickering emulsion stabilized by the detonation nanographite particles depended largely on the nanographite concentrations [36]. When nanographite concentration was low, the droplets were sparsely covered by particles and were more liable to coalesce into big droplets.

3.2. Morphology of PS/DNG Composite Microspheres.

The formation of polystyrene/detonation nanographite (PS/DNG) composite microspheres can be classified as polymerization initiated by AIBN. During the emulsification process of styrene and nanographite dispersion, styrene is a hydrophobic monomer, and the droplets of styrene dispersing in the aqueous phase can be well-protected by nanographite particles to form a stable suspension in water. That is to say, the detonation nanographite particles as surfactants have anchored at the interface of styrene monomer and water. The styrene monomer and AIBN initiator were well-protected by detonation nanographite particles. From above-mentioned mechanisms, it can be inferred that polymerization reaction should occur mainly in styrene droplets since AIBN is also a hydrophobic initiator. As a result, the core-shell structure polystyrene/detonation nanographite microspheres should be fabricated by subsequently thermal polymerization in the Pickering emulsion system of nanographite-styrene (AIBN)-water.

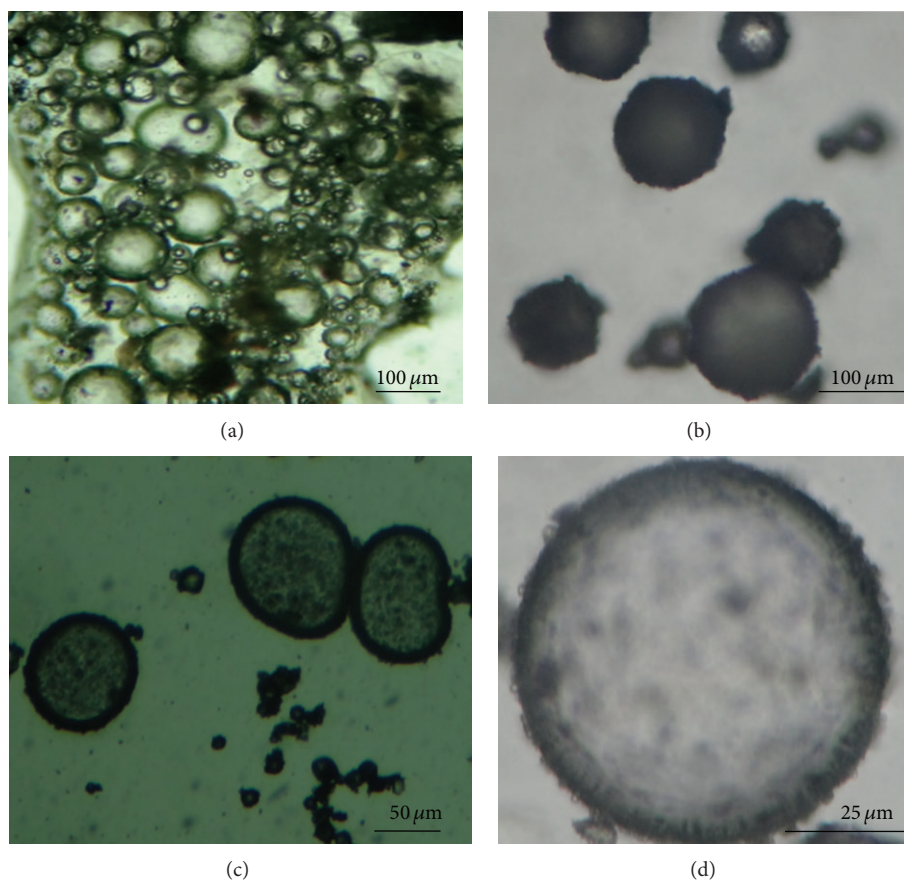


FIGURE 3: Optical picture of a droplet of the styrene-in-water Pickering emulsion stabilized by detonation nanographite particles.

SEM micrographs of PS/DNG samples are shown in Figure 4. Figure 4(a) displays general images of PS/DNG composite microspheres; it can be clearly seen that the polystyrene/detonation nanographite (PS/DNG) composite microspheres have ordered spherical shape and possess a good dispersion. SEM image in Figure 4(b) reveals the morphology of PS/DNG microspheres under high magnifications observation. In Figure 4(c), the spherical structure of polystyrene/detonation nanographite microspheres can be further verified, and the diameter of PS/DNG microspheres ranges from $100\ \mu\text{m}$ to $150\ \mu\text{m}$. Careful observation of a typical PS/DNG microsphere in Figure 4(d) shows that the surfaces of the PS cores are attached by many detonation nanographite particles, and the shells have roughly textural properties, exhibiting a distinct core-shell morphology. Moreover, the diameter of nanographite attached onto the PS cores is about 10–20 nm estimated from Figure 4(d).

3.3. FT-IR of PS/DNG Composite Microspheres. The formation textures of polystyrene (PS) microspheres encapsulated with the detonation nano-graphites by Pickering emulsion method can be demonstrated by the changes of Fourier transformation infrared spectrum. The transformations of surface functional groups of pristine detonation nano-graphite, sulphuric acid-modified nano-graphite,

oleic-modified nanographite particle, pure polystyrene, and polystyrene/detonation composite samples are observed in Figure 5, respectively. In Figures 5(a) and 5(b), the typical adsorption bands of polystyrene at $3030\text{--}2800\ \text{cm}^{-1}$, $1400\text{--}1300\ \text{cm}^{-1}$, and $756\text{--}698\ \text{cm}^{-1}$ are clearly seen [37, 38], confirming that PS indeed has been synthesized in the emulsion polymerization using azobisisobutyronitrile (AIBN) as initiator in aqueous solutions. For the spectrum of pristine and surface modified detonation nanographite samples, the broadband from $3500\text{--}3300\ \text{cm}^{-1}$ is the absorption peak corresponding to the stretching of --OH . The band at $1329\ \text{cm}^{-1}$ is attributed to the stretching vibration of --OH . The characteristic absorption peaks of graphite at 1212 and $1096\ \text{cm}^{-1}$ are due to the stretching of the --C--O bonds. The absorptions at 1475 , 812 , and $505\ \text{cm}^{-1}$ are overlapped and related to the C--H outer bending vibrations [39–41]. In the FT-IR spectrum of sulphuric acid-modified nanographite (Figure 5(e)), the bands at $2750\text{--}3000\ \text{cm}^{-1}$ are the C--H out-of-plane bending vibrations. The peaks at $1700\ \text{cm}^{-1}$ and $1200\ \text{cm}^{-1}$ are corresponded to the --C=O and --C=C stretching vibration [42]. In the FT-IR spectrum of oleic-modified nanographite particle (Figure 5(d)), one strengthening --OH vibration absorption bands at $3500\text{--}3300\ \text{cm}^{-1}$ appears when the nanographite is treated by oleic acid [43]. In comparison, the characteristic peaks in

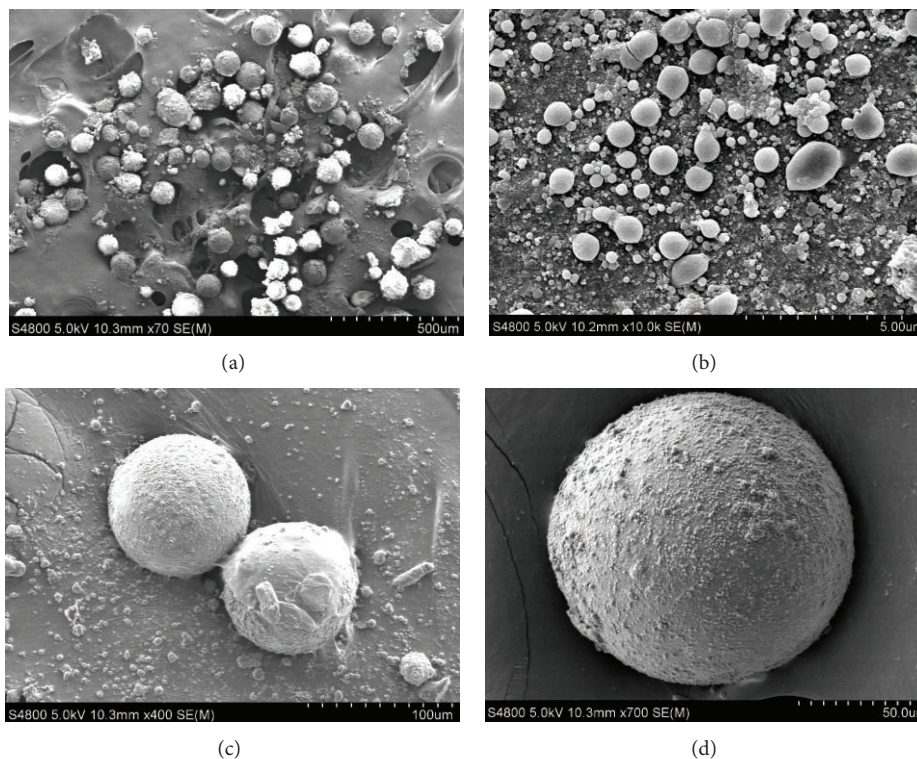


FIGURE 4: SEM micrographs of polystyrene/detonation nanographite (PS/DNG) composite microspheres.

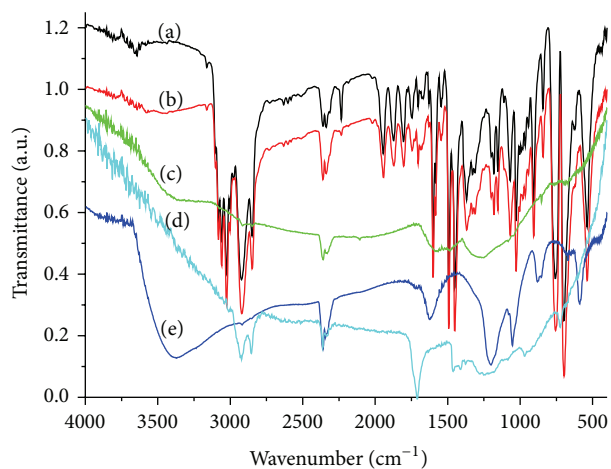


FIGURE 5: FT-IR of samples of (a) pure polystyrene, (b) polystyrene/detonation nanographite (PS/DNG), (c) pristine detonation nanographite, (d) oleic-modified nanographite particle, and (e) sulphuric acid-modified nanographite samples.

the polystyrene/detonation nanographite (PS/DNG) composite microspheres expected at 3425 cm^{-1} , 1700 cm^{-1} and 1200 cm^{-1} have shifted, respectively, to 3432 , 1708 , and 1206 cm^{-1} . All of these shifts imply that the $-\text{OH}$, $-\text{C}=\text{O}$, $-\text{C}=\text{C}$ functional groups of PS have interacted with the nanographite particles [44, 45]. Hence, it is further illustrated that PS cores were not simply encapsulated by detonation nanographite particles, but a molecular interaction may

exist at the interface of PS copolymer and nanographite particles.

3.4. XRD of PS/DNG Composite Microspheres. XRD patterns of nanographite particles, polystyrene/detonation nanographite (PS/DNG) composites, and pure polystyrene are shown in Figure 6, respectively. In Figure 6(a), detonation nanographite particles are belonged to graphite-2 h structure (JCPDS file no. 41-1487) [46]. The three main peaks at $2\theta = 26.6^\circ$, 44.6° , and 76.4° can be attributed to (002), (101), and (110) planes [46]. Thereinto, the (002) peak represents the perpendicular direction (c -axis) of graphite hexagonal planes [47]. The spectrum in Figure 6(a) is a broadened band, which shows that the nanographite grains are very small. The crystallite size can be estimated from broadening peaks by Scherrer equation [48]:

$$D = \frac{k \cdot \lambda}{\beta \cdot \cos \theta}, \quad (1)$$

where D is the crystallite size, λ is the wavelength of X-ray radiation (Cu $K\alpha$ radiation $\lambda = 1.5418\text{ \AA}$), k is a constant and usually taken as 0.89, β is the full width at half maximum (FWHM), after subtraction of equipment broadening, and θ is the Bragg angle of peak. From XRD results, the average sizes of the building blocks are estimated to be for about 15.0 nm. XRD patterns of pure polystyrene are shown in Figure 6(b). The largest specific diffraction peak at 2θ between 15° – 22° indicates that the polystyrene is amorphous. In comparison with the pristine detonation nanographite samples and

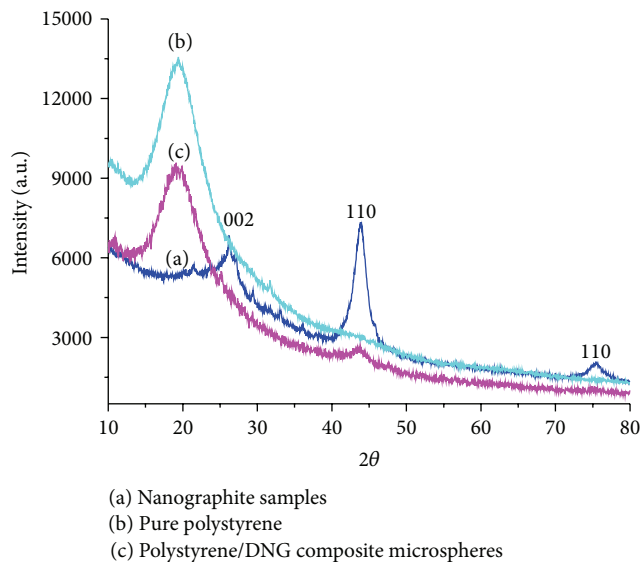


FIGURE 6: XRD patterns of detonation nanographite particles, polystyrene/detonation nanographite (PS/DNG) composites, and pure polystyrene samples.

pure polystyrene, XRD patterns of polystyrene/detonation nanographite (PS/DNG) composite microspheres are almost the same as that of pure polystyrene. Nevertheless, the main peaks corresponding to (110) planes of nanographite particles can be distinguished. From the XRD patterns, it can be further ascertained that the crystal structures of detonation nanographite particles are not altered by the polystyrene. In the polymerization process of nano-graphite-styrene (AIBN)-water Pickering emulsion, detonation nanographite particles play an important role as surfactants, which are adsorbed on the surfaces of styrene (AIBN) droplets to form stable latex. The final composite products have distinct core-shell morphology (detonation nanographite particles acting as shell particles and polystyrene as cores). As a result, XRD pattern of polystyrene/detonation nanographite (PS/DNG) composite microspheres combines the characteristics of both detonation nanographite particles and polystyrene.

3.5. TGA-DTA of PS/DNG Composite Microspheres. In order to provide more details information about the covalent nature of the grafting, thermogravimetric measurements and differential thermal analysis (TGA-DTA) were carried out. TGA-DTA curves of polystyrene/detonation nanographite (PS/DNG) composites and polystyrene are shown in Figure 7. The gradual and slight weight loss is the release of water molecular and residual organic solute in pure PS samples between 50°C and 200°C. Correspondingly, a small exothermic peak appeared. Then, an abrupt decrease in weight of composite samples is observed in a narrow temperature range of 350–450°C, accompanied with single shoulder peaks at about 410°C. Pure PS polymer matrix has completed decomposition at approximately 450°C, and it is pyrolyzed directly to gaseous species without forming any molten states during the thermal decomposition [49, 50]. Compared

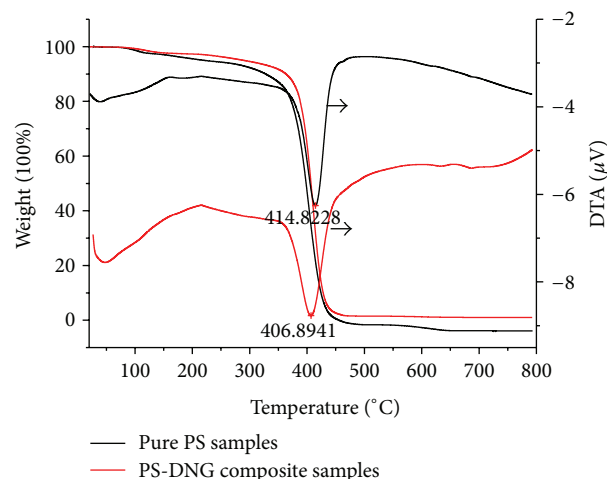


FIGURE 7: TGA-DTA curves of polystyrene/detonation nanographite (PS/DNG) composites and pure polystyrene samples.

to the thermogram of pure PS polymer, decomposition of polystyrene/detonation nanographite (PS/DNG) composites begins at about 370°C, which is 5°C lower than that of pure polystyrene. Correspondingly, the glass transition temperature of the composites is also lower than that of pure polystyrene in DTA curves. The excellent thermal conductivity functions of the detonation nanographite particles should contribute to the heat transferring from the shell of the nanographite particles to the core of polystyrene. After 450°C, the PS/DNG composite samples are no longer loss of weight with the increasing of temperature. The total weight loss of composite samples attains to approximately 100% at 450°C. Specifically, the shell of inorganic nanosized detonation graphite particles and the core of organic polystyrene are burned to gaseous CO₂ and H₂O entirely.

4. Conclusion

In summary, the polystyrene/detonation nanographite (PS/DNG) with core-shell structure was successfully obtained via Pickering emulsion polymerization using detonation nanographite particles as emulsifier for the stabilization of styrene (AIBN)-water Pickering emulsions. The as-prepared products have a well-defined spherical morphology and uniform diameters of 100~150 μm. The possible formation mechanisms of PS/DNG composites based on the interaction between the functional groups of the PS and detonation nano-graphite particles have been proposed. Using styrene as monomer, azobisisobutyronitrile (AIBN) as initiator, and detonation nanographite particles as stabilizer, the method has combined the advantages of suspension polymerization and Pickering emulsion polymerization. Moreover, the present strategy also can be extended for the simple and robust synthesis of other hybrid microspheres with similar structure.

Acknowledgment

This work was financially supported by the Foundation Project for Young Talents of Xi'an University of Posts and Telecommunications (ZL2012-15).

References

- [1] P. J. Hagrman, D. Hagrman, and J. Zubieta, "Organic-inorganic hybrid materials: from simple coordination polymers to organodiamine-templated molybdenum oxides," *Angewandte Chemie*, vol. 38, no. 18, pp. 2638–2684, 1999.
- [2] M. F. Ashby and Y. J. M. Bréchet, "Designing hybrid materials," *Acta Materialia*, vol. 51, no. 19, pp. 5801–5821, 2003.
- [3] H. P. Cong and S. H. Yu, "Self-assembly of functionalized inorganic-organic hybrids," *Current Opinion in Colloid and Interface Science*, vol. 14, no. 2, pp. 71–80, 2009.
- [4] M. Zhang, G. Gao, D. C. Zhao et al., "Crystallization and surface photovoltage properties of polystyrene coated by TiO₂ nanoparticles," *Chemical Journal of Chinese Universities*, vol. 25, no. 11, p. 2122, 2004.
- [5] Y. H. Chen, Y. Y. Liu, R. H. Lin, and F. S. Yen, "Photocatalytic degradation of p-phenylenediamine with TiO₂-coated magnetic PMMA microspheres in an aqueous solution," *Journal of Hazardous Materials*, vol. 163, no. 2-3, pp. 973–981, 2009.
- [6] M. E. Fabiyi and R. L. Skelton, "Photocatalytic mineralisation of methylene blue using buoyant TiO₂-coated polystyrene beads," *Journal of Photochemistry and Photobiology A*, vol. 132, no. 1-2, pp. 121–128, 2000.
- [7] K. J. Huang, P. Rajendran, and C. M. Liddell, "Chemical bath deposition synthesis of sub-micron ZnS-coated polystyrene," *Journal of Colloid and Interface Science*, vol. 308, no. 1, pp. 112–120, 2007.
- [8] D. Z. Yin, X. Du, H. Liu, Q. Y. Zhang, and L. Ma, "Facile one-step fabrication of polymer microspheres with high magnetism and armored inorganic particles by Pickering emulsion polymerization," *Colloids and Surfaces A*, vol. 414, pp. 289–295, 2012.
- [9] J. Pyun and K. Matyjaszewski, "Synthesis of nanocomposite organic/inorganic hybrid materials using controlled/"living" radical polymerization," *Chemistry of Materials*, vol. 13, no. 10, pp. 3436–3448, 2001.
- [10] P. D. Cozzoli, T. Pellegrino, and L. Manna, "Synthesis, properties and perspectives of hybrid nanocrystal structures," *Chemical Society Reviews*, vol. 35, no. 11, pp. 1195–1208, 2006.
- [11] G. Chen, C. Wu, W. Weng, D. Wu, and W. Yan, "Preparation of polystyrene/graphite nanosheet composite," *Polymer*, vol. 44, no. 6, pp. 1781–1784, 2003.
- [12] D. S. Saunders, S. C. Galea, and G. K. Deirmendjian, "The development of fatigue damage around fastener holes in thick graphite/epoxy composite laminates," *Composites*, vol. 24, no. 4, pp. 309–321, 1993.
- [13] T. A. Ezquerro, M. Kuleszcza, and F. J. Baltá-Calleja, "Electrical transport in polyethylene-graphite composite materials," *Synthetic Metals*, vol. 41, no. 3, pp. 915–920, 1991.
- [14] G. H. Chen, D. J. Wu, W. G. Weng, and W. L. Yan, "Preparation of polymer/graphite conducting nanocomposite by intercalation polymerization," *Journal of Applied Polymer Science*, vol. 82, no. 10, pp. 2506–2513, 2001.
- [15] J. Roussel and B. Boutevin, "Preparation of polystyrene-graphite conducting nanocomposites via intercalation polymerization," *Polymer International*, vol. 50, no. 9, pp. 980–985, 2001.
- [16] G. H. Chen, D. J. Wu, W. G. Weng, and W. L. Yan, "Dispersion of graphite nanosheets in a polymer matrix and the conducting property of the nanocomposites," *Polymer Engineering and Science*, vol. 41, no. 12, pp. 2148–2154, 2001.
- [17] Y. X. Pan, Z. Z. Yu, Y. C. Ou, and G. H. Hu, "A new process of fabricating electrically conducting nylon 6/graphite nanocomposites via intercalation polymerization," *Journal of Polymer Science B*, vol. 38, no. 12, pp. 1626–1633, 2000.
- [18] W. Zheng, X. Lu, and S. C. Wong, "Electrical and mechanical properties of expanded graphite-reinforced high-density polyethylene," *Journal of Applied Polymer Science*, vol. 91, no. 5, pp. 2781–2788, 2004.
- [19] G. Chen, C. Wu, W. Weng, D. Wu, and W. Yan, "Preparation of polystyrene/graphite nanosheet composite," *Polymer*, vol. 44, no. 6, pp. 1781–1784, 2003.
- [20] R. K. Goyal, P. A. Jagadale, and U. P. Mulik, "Thermal, mechanical, and dielectric properties of polystyrene/expanded graphite nanocomposites," *Journal of Applied Polymer Science*, vol. 111, no. 4, pp. 2071–2077, 2009.
- [21] A. Yasmin and I. M. Daniel, "Mechanical and thermal properties of graphite platelet/epoxy composites," *Polymer*, vol. 45, no. 24, pp. 8211–8219, 2004.
- [22] H. Wu, W. Zhao, H. Hu, and G. Chen, "One-step in situ ball milling synthesis of polymer-functionalized graphene nanocomposites," *Journal of Materials Chemistry*, vol. 21, no. 24, pp. 8626–8632, 2011.
- [23] F. M. Uhl and C. A. Wilkie, "Preparation of nanocomposites from styrene and modified graphite oxides," *Polymer Degradation and Stability*, vol. 84, no. 2, pp. 215–226, 2004.
- [24] R. Ding, Y. Hu, Z. Gui, R. Zong, Z. Chen, and W. Fan, "Preparation and characterization of polystyrene/graphite oxide nanocomposite by emulsion polymerization," *Polymer Degradation and Stability*, vol. 81, no. 3, pp. 473–476, 2003.
- [25] X. Li, Y. Qu, H. Yan, and X. Wang, "Research progress on nanosized materials synthesized by detonation method," *Rare Metal Materials and Engineering*, vol. 36, no. 12, pp. 2069–2074, 2007.
- [26] C. Wen, Z. Jin, J. Guan, X. Li, G. Zhou, and G. Zhou, "Nanographite synthesized by explosive detonation," *Rare Metal Materials and Engineering*, vol. 33, no. 6, pp. 628–631, 2004.
- [27] Q. Chen and S. R. Yun, "Exploration of the mechanism of synthesis ultradispersed diamond by detonation," *Explosion and Shock Waves*, vol. 16, no. 4, pp. 326–332, 1996.
- [28] J. H. Chen, C. Y. Cheng, W. Y. Chiu, C. F. Lee, and N. Y. Liang, "Synthesis of ZnO/polystyrene composites particles by Pickering emulsion polymerization," *European Polymer Journal*, vol. 44, no. 10, pp. 3271–3279, 2008.
- [29] Z. Cao, A. Schrade, K. Landfester, and U. Ziener, "Synthesis of raspberry-like organic-inorganic hybrid nanocapsules via pickering miniemulsion polymerization: colloidal stability and morphology," *Journal of Polymer Science A*, vol. 49, no. 11, pp. 2382–2394, 2011.
- [30] X. Li, Y. Qu, H. Yan, and X. Wang, "Research progress on nanosized materials synthesized by detonation method," *Rare Metal Materials and Engineering*, vol. 36, no. 12, pp. 2069–2074, 2007.
- [31] D. Yin, Q. Zhang, H. Zhang, and C. Yin, "Fabrication of covalently-bonded polystyrene/SiO₂ composites by Pickering emulsion polymerization," *Journal of Polymer Research*, vol. 17, no. 5, pp. 689–696, 2010.

- [32] K. Zhang, W. Wu, H. Meng, K. Guo, and J. F. Chen, "Pickering emulsion polymerization: preparation of polystyrene/nano-SiO₂ composite microspheres with core-shell structure," *Powder Technology*, vol. 190, no. 3, pp. 393–400, 2009.
- [33] S. Sacanna, W. K. Kegel, and A. P. Philipse, "Thermodynamically stable pickering emulsions," *Physical Review Letters*, vol. 98, no. 15, Article ID 158301, 2007.
- [34] B. P. Binks and J. H. Clint, "Solid wettability from surface energy components: relevance to pickering emulsions," *Langmuir*, vol. 18, no. 4, pp. 1270–1273, 2002.
- [35] G. Chen, C. Wu, W. Weng, D. Wu, and W. Yan, "Preparation of polystyrene/graphite nanosheet composite," *Polymer*, vol. 44, no. 6, pp. 1781–1784, 2003.
- [36] H. O. Zhou, T. J. Shi, and X. Zhou, "Preparation of polystyrene/SiO₂ microsphere via Pickering emulsion polymerization: synergistic effect of SiO₂ concentrations and initiator sorts," *Applied Surface Science*, vol. 266, pp. 33–38, 2013.
- [37] N. Liu, S. Qi, S. Li, X. Wu, and L. Wu, "Preparation and characterization of phenol formaldehyde/Ag/graphite nanosheet composites," *Polymer Testing*, vol. 30, no. 4, pp. 390–396, 2011.
- [38] G. M. Chen, S. H. Liu, S. J. Chen, and Z. N. Qi, "FTIR spectra, thermal properties, and dispersibility of a polystyrene/montmorillonite nanocomposite," *Macromolecular Chemistry and Physics*, vol. 202, no. 7, pp. 1189–1193, 2001.
- [39] Y. Rong, H. Z. Chen, G. Wu, and M. Wang, "Preparation and characterization of titanium dioxide nanoparticle/ polystyrene composites via radical polymerization," *Materials Chemistry and Physics*, vol. 91, no. 2-3, pp. 370–374, 2005.
- [40] A. Imhof, "Preparation and characterization of titania-coated polystyrene spheres and hollow titania shells," *Langmuir*, vol. 17, no. 12, pp. 3579–3585, 2002.
- [41] W. Lin, X. Xi, and C. Yu, "Research of silver plating nano-graphite filled conductive adhesive," *Synthetic Metals*, vol. 159, no. 7-8, pp. 619–624, 2009.
- [42] D. Ni, L. Wang, Y. Sun, Z. Guan, S. Yang, and K. Zhou, "Amphiphilic hollow carbonaceous microspheres with permeable shells," *Angewandte Chemie*, vol. 49, no. 25, pp. 4223–4227, 2010.
- [43] R. Gnanasambandam and A. Proctor, "Determination of pectin degree of esterification by diffuse reflectance Fourier transform infrared spectroscopy," *Food Chemistry*, vol. 68, no. 3, pp. 327–332, 2000.
- [44] C. Wen, Z. H. Jin, J. Q. Guan et al., "Infrared spectroscopy studies of nano-graphite synthesized by explosive detonation," *Chemical Research in Chinese Universities*, vol. 25, no. 6, pp. 1043–1045, 2004.
- [45] N. Liu, S. Qi, S. Li, X. Wu, and L. Wu, "Preparation and characterization of phenol formaldehyde/Ag/graphite nanosheet composites," *Polymer Testing*, vol. 30, no. 4, pp. 390–396, 2011.
- [46] P. S. Gaal, *Thermal Conductivity 24: and Thermal Expansion 12*, CRC Press, Pennsylvania, Pa, USA, 1999.
- [47] G. Sun, X. Li, Y. Qu, X. Wang, H. Yan, and Y. Zhang, "Preparation and characterization of graphite nanosheets from detonation technique," *Materials Letters*, vol. 62, no. 4-5, pp. 703–706, 2008.
- [48] A. Hagfeldt and M. Gratzel, "Light-induced redox reactions in nanocrystalline systems," *Chemical Reviews*, vol. 95, no. 1, pp. 49–68, 1995.
- [49] B. N. Jang and C. A. Wilkie, "The thermal degradation of polystyrene nanocomposite," *Polymer*, vol. 46, no. 9, pp. 2933–2942, 2005.
- [50] F. Vilaplana, A. Ribes-Greus, and S. Karlsson, "Degradation of recycled high-impact polystyrene. Simulation by reprocessing and thermo-oxidation," *Polymer Degradation and Stability*, vol. 91, no. 9, pp. 2163–2170, 2006.

Research Article

I-V Characteristics of $\text{Pt}_x\text{Co}_{1-x}$ ($x = 0.2, 0.5, \text{ and } 0.7$) Thin Films

M. Erkovan,^{1,2} E. Şentürk,³ Y. Şahin,⁴ and M. Okutan⁵

¹ Department of Physics, Gebze Institute of Technology, 41400 Gebze, Kocaeli, Turkey

² Metallurgical and Materials Engineering, Sakarya University, 54187 Esentepe, Sakarya, Turkey

³ Department of Physics, Sakarya University, 54187 Esentepe, Sakarya, Turkey

⁴ Council of Forensic Medicine, 34196 Istanbul, Turkey

⁵ Department of Physics, Yildiz Technical University, Davutpasa, 34210 Istanbul, Turkey

Correspondence should be addressed to M. Okutan; okutan@yildiz.edu.tr

Received 27 April 2013; Revised 2 July 2013; Accepted 4 July 2013

Academic Editor: Mengnan Qu

Copyright © 2013 M. Erkovan et al. This is an open access article distributed under the Creative Commons Attribution License, which permits unrestricted use, distribution, and reproduction in any medium, provided the original work is properly cited.

Three different chemical ratios of $\text{Pt}_x\text{Co}_{1-x}$ thin films were grown on p-type native oxide Si (100) by Magneto Sputtering System with cosputtering technique at 350°C temperature to investigate electrical prosperities. X-ray photoelectron spectroscopy analysis technique was used to specify chemical ratios of these films. The current-voltage (*I-V*) measurements of metal-semiconductor (MS) Schottky diodes were carried out at room temperature. From the *I-V* analysis of the samples, ideality factor (*n*), barrier height (ϕ), and contact resistance values were determined by using thermionic emission (TE) theory. Some important parameters such as barrier height, ideality factor, and serial resistance were calculated from the *I-V* characteristics based on thermionic emission mechanism. The ideality factors of the samples were not much greater than unity, and the serial resistances of the samples were also very low.

1. Introduction

Thin films have nowadays very wide usage area in technological applications [1–6]. They show very distinct difference from bulk films such as Curie temperature and the electrical properties. They get more and more important with the preparation systems progress. In particular after Ultra High Vacuum (UHV) systems became popular, they have been prepared with good quality and cleanness [1]. There are several preparation techniques to meet user's need. Some of them for UHV systems are magnetron sputtering deposition, molecular beam epitaxial and e-beam evaporation, and pulse laser deposition [7]. Due to the advantages of the preparation techniques, thin films started being used widely in technological applications such as optics [2], optoelectronics [3], electronics [4], magnetic applications [5], and sensors [6]. Firstly, thin films were prepared as a single layer with monoelement structure. After a little while due to some technological requirements, they started being prepared as multilayer structures and alloy forms with two or more elements. Multilayer forms started to be popular after Giant

Magneto Resistance (GMR) [8, 9] effect and Tunneling Magneto Resistance (TMR) [10] effect were observed in the 1980s. The other thin film form is alloy film which started solving some of technological problems, and they gained more importance when compared to single layer films. When two or more elements compose themselves to be alloys, generally every one of them loses some of its own properties and gains new properties. PtCo alloys are very good examples to clarify this situation due to magnetic properties [11]. Platinum is naturally nonmagnetic material so it has not got any magnetic moment [12]. When it composes its with ferromagnetic cobalt, it gains some net magnetic moment and starts behaving as a magnetic material as a paramagnetic and also changes the magnetic properties of cobalt [13]. For example, the magnetocrystalline anisotropy is a key parameter for data storage media. Pt affects the magnetocrystalline anisotropy of cobalt. The magnetocrystalline anisotropy constant of Cobalt (410 $\text{KJ}\cdot\text{m}^{-3}$) [14] is ten times smaller than the magnetocrystalline anisotropy constant of PtCo (4,9 $\text{MJ}\cdot\text{m}^{-3}$) [14]. SmCo_5 are used now for data storage media, and the magnetocrystalline anisotropy

constant PtCo is very close to SmCo_5 's ($17.2 \text{ MJ}\cdot\text{m}^{-3}$) [14], so PtCo alloy still is an active research area and the one of good candidates is for next generation data storage media [15]. Besides their magnetic properties, PtCo alloys also have catalytic properties [16–20]. Another most important point is that they can be prepared easily in different chemical ratios, and their phase is very stable [21]. We believe that if these structures come into use in next generation magnetic data storage media, their electrical properties may be gained significantly.

The other hand semiconductor base materials exhibit an interesting combination of magnetic and electrical properties, which are essential for future generation spintronics device applications [22]. Two of these electrical properties are Schottky barriers (SB) and tunneling diode.

They can be used in microwave detector diodes [23]. Schottky diodes with low barrier height have some applications in devices operating as infrared detectors and imaging sensors at high frequencies [24, 25]. Schottky Metal (SM) contacts have an important role in electronic technology [26, 27]. Metal-semiconductor (MS) contact is one of the most widely used rectifying contacts in electronic industry [28, 29]. Electronic properties of a Schottky diode are characterized by its series resistance, barrier height, and ideality factor parameters [30, 31]. Schottky barrier height, and other characteristic parameters can affect device performance, stability and reliability [32–35]. Electrical properties of PtCo alloys have not been investigated so far. So in this study, we focused on surface and volume resistivity of different stoichiometry of PtCo alloys films. In order to realize this goal, we prepared three different chemical ratios of $\text{Pt}_x\text{Co}_{1-x}$ ($x = 0.2, 0.5, 0.7$) alloy films with magnetron sputtering technique at UHV conditions. X-ray photoelectron spectroscopy was used to determine the chemical ratio of the films and the deposition rate of Pt and Co.

In the scope of this work, the $\text{Pt}_x\text{Co}_{1-x}$ ($x = 0.2, 0.5, 0.7$) alloy films were prepared for the new generation data storage and catalytic material by Magneto Sputtering System. They were examined with current-voltage (I - V) measurement techniques. This method is a reliable tool for investigating the behaviors of electrical properties and for optimizing metal-semiconductor and magnetic-semiconductor materials.

2. Experiments

All the experiments were performed in a cluster Ultra High Vacuum (UHV) chamber. The chamber is combined with magnetron sputtering deposition chamber and analytical chamber. There is a load-lock chamber between them. PtCo alloy films were grown on native p-type Si (100) substrate by magnetron sputtering deposition technique with base pressure $<1 \times 10^{-8}$ mbar. All the substrates were cleaned with ethanol and methanol baths before being transferred into UHV conditions. Then they were subjected to annealing process at 600°C for 30 minutes by a pyrolytic boron nitride (PBN) heater which is located under the substrate at the sample holder. It has the capability of annealing up to 1200°C . The sample holder is cooled by chilled water to

hold the sample temperature for different processes. For deposition, Ar process gas (6N purity) was exposed to the magnetron sputtering chamber so the base pressure level increased to 1.3×10^{-3} – 1.4×10^{-4} mbar. In order to prepare $\text{Pt}_x\text{Co}_{1-x}$ ($x: 0.2, 0.5, 0.7$) alloy films, the Pt (99,99% purity) and Cobalt (99,98% purity) elemental targets were used. Their sizes are three inches to provide uniform deposition surface. The distance between the substrate and target was 100 mm and always kept for all growth process. Thickness calibration of the films was conducted with Quartz Crystal Monitoring (QCM) during deposition in situ. X-ray photoelectron spectroscopy (XPS) was used for QCM calibration. Before synthesizing PtCo alloy films, both Pt and Co deposition ratios were calculated. $\text{Pt}_x\text{Co}_{1-x}$ ($x: 0.2, 0.5, 0.7$) alloy films were grown using cosputtering technique. The number of sequences was kept 100 for all samples; on the other hand, the Pt and Co deposition time was calculated depending on the chemical ratio of $\text{Pt}_x\text{Co}_{1-x}$ ($x: 0.2, 0.5, 0.7$) alloy films. The power applied to Co target was 30 Watt and the corresponding deposition rate was $0.3 \text{ \AA}/\text{sec}$. The Pt deposition rate was $0.1 \text{ \AA}/\text{sec}$ with 2 Watt. The Pt and Co targets were operated at the same time, and the temperature was held at 350°C . The films thicknesses were 300 \AA .

The current-voltage (I - V) and resistivity of the thin films were studied using a four-point probe measurement with the Lucas Signatone system. I - V and surface resistance were measured using a Keithley 2400 Source-Meter in a four-point probe technique and converted to the surface resistivity. The I - V and surface resistance measurements were carried out at room temperature.

3. Result and Discussion

XPS was used to determine the selected chemical ratios of alloy films in situ. Figure 1 shows survey XPS spectra for $\text{Pt}_{0.5}\text{Co}_{0.5}$ and $\text{Pt}_{0.7}\text{Co}_{0.3}$. High resolution XPS spectra for the major photoemission Co 2p and Pt 4f regions were also taken (Figure 2) for analysis in commercial software CasaXPS 2.3.14. We used the Shirley background function to fit and analyze the peaks. The Voigt function identifying the photoemission nature was used to calculate the peak area of Co and Pt. The calculated peak areas of Co and Pt were divided by the atomic sensitivity factors (ASFs) which depend on both elemental properties and XPS setup (3.59 for Pt 4f, and 5.75 for Co 2p). The calculated Pt to Co ratios within alloy films are 20 : 80, 50 : 50, and 70 : 30.

Beside these analyses, the XPS spectra were given both Pt peaks and Co peaks from both their pure and the $\text{Pt}_{0.6}\text{Co}_{0.4}$ films (Figure 3). Because of their alloy form, both Pt and Co peaks came from $\text{Pt}_{0.6}\text{Co}_{0.4}$ films; they are shifted from the low binding energy value to the high binding energy value. Their peak shape also expanded due to their chemical bonding.

The typical forwarded bias voltage (V) and current (I) characteristics obtained from the samples are shown in Figure 4. I - V curves of the samples are linear at low bias voltage and nonlinear at high bias voltage. All the curves

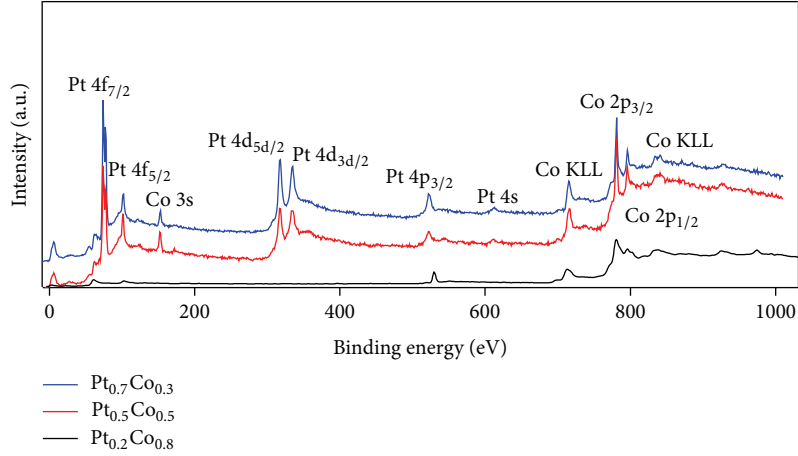


FIGURE 1: XPS survey spectra from the alloy surface of the $\text{Pt}_{0.2}\text{Co}_{0.8}$, $\text{Pt}_{0.5}\text{Co}_{0.5}$, and $\text{Pt}_{0.7}\text{Co}_{0.3}$ films.

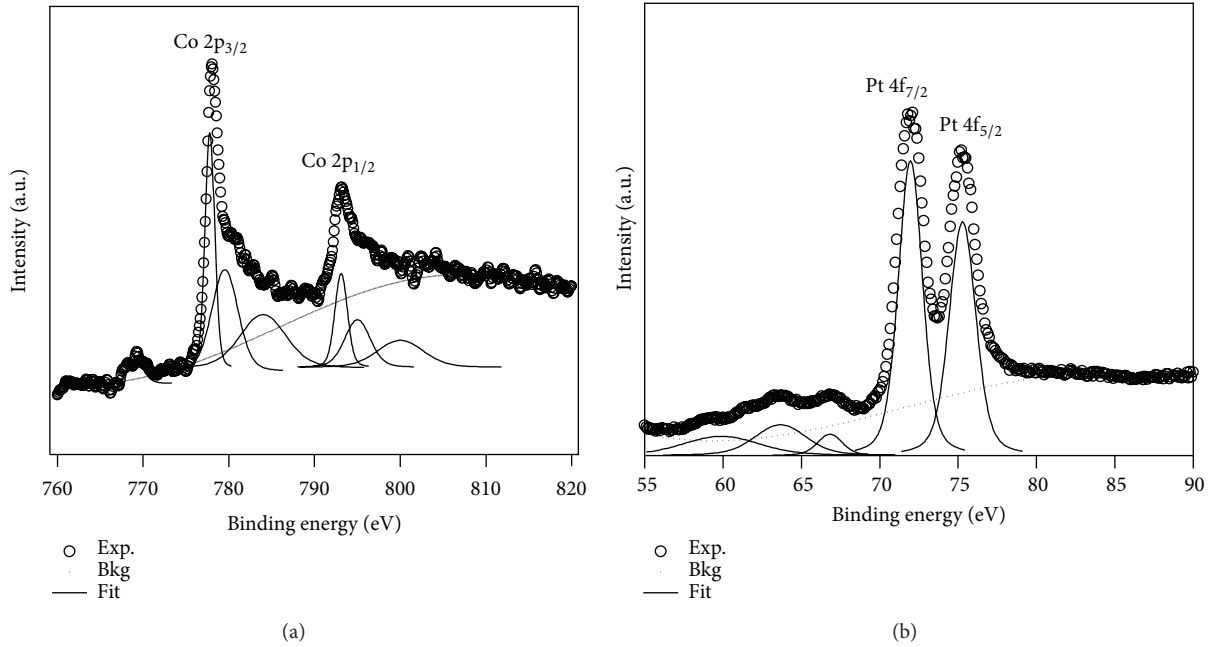


FIGURE 2: XPS spectrum from $\text{Pt}_{0.5}\text{Co}_{0.5}$ for both Pt and Co major peaks. The ratios of peak areas under the Pt 4f and Co 2p regions provide the ratio of Pt and Co atoms.

show an intersection at low forward biases (about 0.1–0.2 V). The I - V curvature quickly (at low forward bias) becomes dominant with a resistance from contact wires or bulk resistance of the samples. If the current passes through MS Schottky diode at a forward bias voltage ($3kT/q \leq V$), a high resistive potential barrier created by grains is considered in these systems [36]. The observed results require a serial resistance [37]. Serial or parasitic resistance, R_s , includes bulk and contact resistances. The I - V results deviated from ideality can be explained by thermionic emission theory with a serial resistance. The TE model considers that I - V characteristic of an MS type Schottky diode is given as follows [38]:

$$I = I_o \exp\left(\frac{q(V - IR_s)}{nkT}\right) \left[1 - \exp\left(-\frac{q(V - IR_s)}{kT}\right)\right], \quad (1)$$

where q is electron charge, k is Boltzmann constant, T is absolute temperature, n is ideality factor (close to 1), and finally I_o is saturation current. $V - IR_s$ is voltage drop across the diode. The saturation current can be written as

$$I_o = AA^* T^2 \exp\left(-\frac{q\phi_b}{kT}\right), \quad (2)$$

where ϕ_b , A , and A^* are apparent barrier height, effective contact area, and Richardson constant, respectively. All these physical parameters have an importance for technological application. Richardson constant is equal to $32 \text{ Acm}^{-2} \text{ K}^{-2}$ for p-type Si [39]. The saturation current can be obtained from an extrapolation to current axis in I - V plot at zero bias voltage. At relatively high forward bias voltages, the parasitic or serial resistance goes to a constant value. In general, low serial resistance is required for a device application [40, 41].

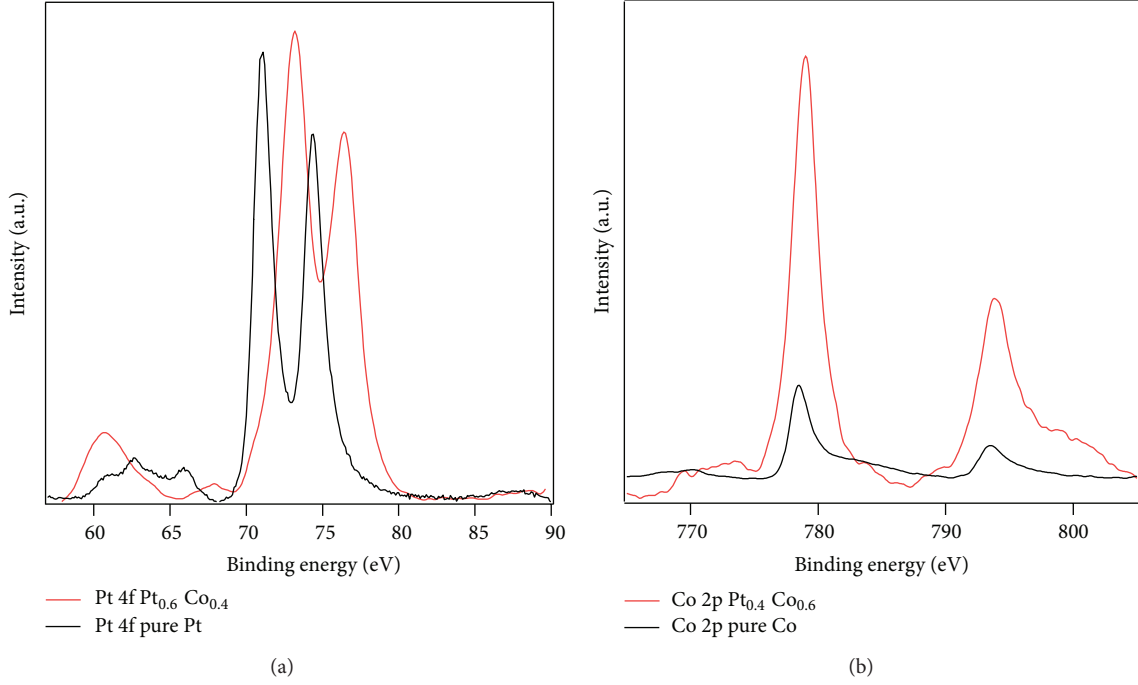


FIGURE 3: The comparison of both Pt 4f and Co 2p peaks that came from both their pure films and Pt_{0.6}Co_{0.4} films.

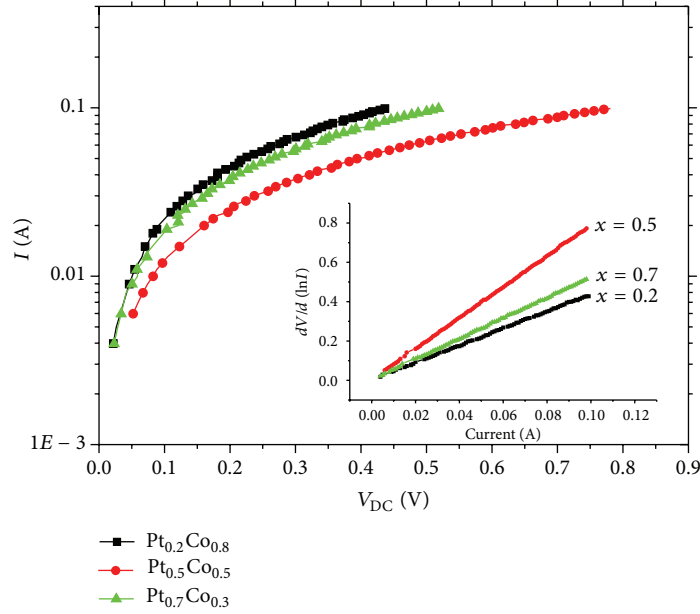


FIGURE 4: Current-voltage graph and inset: $dV/d(\ln I) - I$ plot.

The series resistance, ideality factor, and barrier height are determined by using Cheung's functions as follows [42]:

$$\frac{dV}{d(\ln I)} = IR_s + \frac{nkT}{q}, \quad (3)$$

$$H(I) = V(I) - \frac{nkT}{q} \ln\left(\frac{I}{AA^*T^2}\right), \quad (4)$$

and another form of $H(I)$ function is given as follows:

$$H(I) = n\phi_b + IR_s. \quad (5)$$

The $dV/d(\ln I) - I$ plot is shown in inset of Figure 4. All curves are straight lines with low and different slopes. The ideality factor can be obtained by using (3) from the slope of the linear curves. The obtained values of the ideality factor are given in Table 1. It is clear from the table that the values

TABLE 1: I - V characteristics parameters of the samples.

	R_s (Ω)	n	ϕ_b (eV)
$x = 0.2$	3.89	1.32	0.26
$x = 0.5$	6.64	1.83	0.27
$x = 0.7$	4.60	1.03	0.25

of the ideality factor for the samples are really low. The low values (~ 1) of the ideality factor may result from homogeneity of film thickness [43], series resistance effect, low interface state, and the interface charges.

The simple analysis of (5) yields n and ϕ_b parameters. The change in R_s , n , and ϕ_b with composition at room temperature is shown in Table 1. It is clear from the data obtained from Figure 4 that the parameters have strong composition dependence.

4. Conclusion

This work indicates that coating of p-type Si (100) with $\text{Pt}_x\text{Co}_{1-x}$ alloys thin films can be prepared by Magnetron Sputtering Deposition at UHV condition. XPS was used for three different goals. One was to determine the deposition rate of cobalt and platinum. The other one was determination of the chemical ratio of PtCo alloy films. The last one was that the PtCo alloy forms were proved by XPS results. The performance and reliability of metal-semiconductor or metal-insulator-semiconductor diodes depend on barrier height, properties of interface layer, and R_s . I - V characteristics of the samples were investigated at room temperature. The nonideal type I - V behavior observed was attributed to a serial resistance in the MS type Schottky diode. The serial resistances were found to be 3.89 Ω , 6.64 Ω and 4.60 Ω for $x = 0.2$, 0.5, and 0.7, respectively.

Acknowledgments

This work was partially supported by TÜBİTAK (The Scientific and Technological Research Council of Turkey) through the project no. 212T217 and Yildiz Technical University through the project no. 2011-01-01-KAP01. The authors gratefully acknowledge that all samples used in this study were grown at the Nanotechnology Center of Gebze Institute of Technology.

References

- [1] R. F. Soohoo, *Magnetic Thin Films*, Harper and Row, New York, NY, USA, 1965.
- [2] D. E. Aspnes, "Optical properties of thin films," *Thin Solid Films*, vol. 89, no. 3, pp. 249–262, 1982.
- [3] G. Eda and M. Chhowala, "Chemically derived graphene oxide: towards large-area thin-film electronics and optoelectronics," *Advanced Materials*, vol. 22, no. 22, pp. 2392–2415, 2010.
- [4] M. S. Boon, W. P. S. Saw, and M. Mariatti, "Magnetic, dielectric and thermal stability of NiZn ferrite-epoxy composite thin films for electronic applications," *Journal of Magnetism and Magnetic Materials*, vol. 324, no. 5, pp. 755–760, 2012.
- [5] M. Erkovan, R. Topkaya, S. T. Öztürk, M. Özdemir, B. Aktaş, and O. Öztürk, "Ferromagnetic resonance investigation of Py/Cr multilayer system," *Journal of Applied Physics*, vol. 110, no. 2, Article ID 023908, 6 pages, 2011.
- [6] G. Sberveglieri, "Recent developments in semiconducting thin-film gas sensors," *Sensors and Actuators B*, vol. 23, no. 2-3, pp. 103–109, 1995.
- [7] T. Shima and K. Takahashi, "Hard magnetic thin films," in *Handbook of Magnetism and Advanced Magnetic Materials*, vol. 4, Wiley & Sons, Chichester, UK, 2007.
- [8] M. N. Baibich, J. M. Broto, A. Fert et al., "Giant magnetoresistance of (001)Fe/(001)Cr magnetic superlattices," *Physical Review Letters*, vol. 61, no. 21, pp. 2472–2475, 1988.
- [9] G. Binasch, P. Grünberg, F. Saurenbach, and W. Zinn, "Giant magnetoresistance in antiferromagnetic Co/Cu multilayers," *Physical Review B*, vol. 39, p. 7, 1991.
- [10] J. S. Moodera, L. R. Kinder, T. M. Wong, and R. Meservey, "Large magnetoresistance at room temperature in ferromagnetic thin film tunnel junctions," *Physical Review Letters*, vol. 74, no. 16, pp. 3273–3276, 1995.
- [11] M. Öztürk, E. Sınır, E. Demirci, M. Erkovan, O. Öztürk, and N. Akdoğan, "Exchange bias properties of $[\text{Co}/\text{CoO}]_n$ multilayers," *Journal of Applied Physics*, vol. 112, Article ID 093911, 2012.
- [12] E. E. Shalgyina and K. Shin, "Influence of nonmagnetic layer (Ti, Zr, Pt) on magnetic and magneto-optical properties of Fe/NML bilayers and Fe/NML/Fe trilayers," *Journal of Magnetism and Magnetic Materials*, vol. 220, no. 2-3, pp. 167–174, 2000.
- [13] J. Wang, T. Sannomiya, J. Shi, and Y. Nakamura, "Influence of interface roughness on the exchange bias of Co/CoO multilayers," *Journal of Applied Physics*, vol. 113, no. 17, Article ID 17D707, 3 pages, 2013.
- [14] J. M. D. Coey, *Magnetism and Magnetic Materials*, Cambridge University, Cambridge, UK, 2010.
- [15] N. Sharma, G. A. Jones, S. M. Casey, and P. J. Grundy, "The microstructure and magnetic properties of cobalt-rich Co-Pt alloy thin films grown using ion-beam-assisted deposition," *Journal of Physics D*, vol. 31, no. 21, pp. 3020–3027, 1998.
- [16] V. R. Stamenkovic, B. S. Mun, M. Arenz et al., "Trends in electrocatalysis on extended and nanoscale Pt-bimetallic alloy surfaces," *Nature Materials*, vol. 6, no. 3, pp. 241–247, 2007.
- [17] U. Bardi, A. Atrei, E. Zanazzi, G. Roviada, and P. N. Ross, "Study of the reconstructed (001) surface of the $\text{Pt}_{80}\text{Co}_{20}$ alloy," *Vacuum*, vol. 41, no. 1–3, pp. 437–440, 1990.
- [18] U. Bardi, B. C. Beard, and P. N. Ross, "CO chemisorption on the [111] and [100] oriented single crystal surfaces of the alloy CoPt_3 ," *Journal of Catalysis*, vol. 124, no. 1, pp. 22–29, 1990.
- [19] Y. Kiros, "Electrocatalytic properties of Co, Pt, and Pt-Co on carbon for the reduction of oxygen in alkaline fuel cells," *Journal of the Electrochemical Society*, vol. 143, no. 7, pp. 2152–2157, 1996.
- [20] L. Xiong, A. M. Kannan, and A. Manthiram, "Pt-M (M1/4Fe, Co, Ni and Cu) electrocatalysts synthesized by an aqueous route for proton exchange membrane fuel cells," *Electrochemistry Communications*, vol. 4, no. 11, pp. 898–903, 2002.
- [21] J. H. Cho, B. Y. Kim, H. D. Kim et al., "Enhanced ferromagnetism in Co-doped TiO_2 powders," *Physica Status Solidi B*, vol. 241, no. 7, pp. 1537–1540, 2004.
- [22] N. W. Ashcroft and N. D. Mermin, *Solid State Physics*, Saunders College, London, UK, 1976.
- [23] J. N. Schulman, V. Kolinko, M. Morgan et al., "W-band direct detection circuit performance with Sb-heterostructure diodes,"

- IEEE Microwave and Wireless Components Letters*, vol. 14, no. 7, pp. 316–318, 2004.
- [24] M. Kimata, “Metal silicide Schottky infrared detector arrays,” in *Infrared Detectors and Emitters: Materials and Devices*, P. Capper and C. T. Elliott, Eds., pp. 77–98, Kluwer Academic, Boston, Mass, USA, 2000.
- [25] W. F. Kosonocky, “State of the art in Schottky-barrier IR image sensors,” in *Infrared Detectors and Focal Plane Arrays II*, Proceedings of SPIE, pp. 2–19, April 1992.
- [26] X. Lu, X. Xu, N. Wang, Q. Zhang, and M. C. Lin, “Chemisorption and decomposition of thiophene and furan on the Si(100)- 2×1 surface: a quantum chemical study,” *Journal of Physical Chemistry B*, vol. 105, no. 41, pp. 10069–10075, 2001.
- [27] M. Biber, M. Çakar, and A. Türüt, “The effect of anodic oxide treatment on n-GaAs Schottky barrier diodes,” *Journal of Materials Science*, vol. 12, no. 10, pp. 575–579, 2001.
- [28] G. Liang, T. Cui, and K. Varahramyan, “Electrical characteristics of diodes fabricated with organic semiconductors,” *Microelectronic Engineering*, vol. 65, no. 3, pp. 279–284, 2003.
- [29] G. Liang, T. Cui, and K. Varahramyan, “Fabrication and electrical characteristics of polymer-based Schottky diode,” *Solid-State Electronics*, vol. 47, no. 4, pp. 691–694, 2003.
- [30] M. Okutan, E. Basaran, and F. Yakuphanoglu, “Electronic and interface state density distribution properties of Ag/p-Si Schottky diode,” *Applied Surface Science*, vol. 252, no. 5, pp. 1966–1973, 2005.
- [31] M. Okutan and F. Yakuphanoglu, “Analysis of interface states and series resistance of Ag/SiO₂/n-Si MIS Schottky diode using current-voltage and impedance spectroscopy methods,” *Microelectronic Engineering*, vol. 85, no. 3, pp. 646–653, 2008.
- [32] P. L. Hanselaer, W. H. Laflère, R. L. van Meirhaeghe, and F. Cardon, “Current-voltage characteristic of Ti-pSi metal-oxide-semiconductor diodes,” *Journal of Applied Physics*, vol. 56, no. 8, pp. 2309–2314, 1984.
- [33] G. Liang, T. Cui, and K. Varahramyan, “Fabrication and electrical characteristics of polymer-based Schottky diode,” *Solid-State Electronics*, vol. 47, no. 4, pp. 691–694, 2003.
- [34] S. M. Sze, *Physics of Semiconductor Devices*, Wiley, New York, NY, USA, 2nd edition, 1981.
- [35] E. H. Rhoderick, *Metal-Semiconductor Contacts*, vol. 121 of p. 136, Oxford University Press, Oxford, UK, 1978.
- [36] R. Gross, L. Alff, B. Büchner et al., “Physics of grain boundaries in the colossal magnetoresistance manganites,” *Journal of Magnetism and Magnetic Materials*, vol. 211, no. 1–3, pp. 150–159, 2000.
- [37] B. Kinaci, S. Şebnem Çetin, A. Bengi, and S. Özçelik, “The temperature dependent analysis of Au/TiO₂ (rutile)/n-Si (MIS) SBDs using current-voltage-temperature (*I-V-T*) characteristics,” *Materials Science in Semiconductor Processing*, vol. 15, no. 5, pp. 531–535, 2012.
- [38] H. Uslu, Ş. Altindal, U. Aydemir, I. Dökme, and I. M. Afandiyeva, “The interface states and series resistance effects on the forward and reverse bias *I-V*, *C-V* and *G/ω-V* characteristics of Al-TiW-Pd 2Si/n-Si Schottky barrier diodes,” *Journal of Alloys and Compounds*, vol. 503, no. 1, pp. 96–102, 2010.
- [39] A. Tataroğlu and S. Altindal, “Analysis of interface states and series resistance of MIS Schottky diodes using the current-voltage (*I-V*) characteristics,” *Microelectronic Engineering*, vol. 85, no. 1, pp. 233–237, 2008.
- [40] N. Tuğluoğlu and S. Karadeniz, “Analysis of current-voltage and capacitance-voltage characteristics of perylene-monoimide/n-Si Schottky contact,” *Current Applied Physics*, vol. 12, no. 6, pp. 1529–1535, 2012.
- [41] S. Demirezen, Z. Sönmez, U. Aydemir, and S. Altindal, “Effect of series resistance and interface states on the *I-V*, *C-V* and *G/ω-V* characteristics in Au/Bi-doped polyvinyl alcohol (PVA)/n-Si Schottky barrier diodes at room temperature,” *Current Applied Physics*, vol. 12, no. 1, pp. 266–272, 2012.
- [42] R. Şahingöz, H. Kanbur, M. Voigt, and C. Soykan, “The determination of interface states and series resistance profile of Al/polymer/PEDOT-PSS/ITO heterojunction diode by *I-V* and *C-V* methods,” *Synthetic Metals*, vol. 158, no. 17–18, pp. 727–731, 2008.
- [43] M. B. Reddy, A. A. Kumar, V. Janardhanam, V. R. Reddy, and P. N. Reddy, “Rapid thermal annealing effects on electrical and structural properties of Pd/Au Schottky contacts to n-type InP(111),” *Current Applied Physics*, vol. 9, pp. 972–977, 2009.

Research Article

Effect of RGD Peptide-Coated TiO₂ Nanotubes on the Attachment, Proliferation, and Functionality of Bone-Related Cells

Seunghan Oh,¹ Kyung Suk Moon,¹ and Seung Hoon Lee²

¹ Department of Dental Biomaterials and Institute of Biomaterials-Implant, College of Dentistry, Wonkwang University, Jeonbuk, Iksan 570-749, Republic of Korea

² Department of Oral Microbiology and Immunology, College of Dentistry, Wonkwang University, Jeonbuk, Iksan 570-749, Republic of Korea

Correspondence should be addressed to Seunghan Oh; shoh@wku.ac.kr and Seung Hoon Lee; leesh2@wku.ac.kr

Received 4 June 2013; Revised 12 July 2013; Accepted 12 July 2013

Academic Editor: Jiamin Wu

Copyright © 2013 Seunghan Oh et al. This is an open access article distributed under the Creative Commons Attribution License, which permits unrestricted use, distribution, and reproduction in any medium, provided the original work is properly cited.

The purpose of this research was to characterize an Arg-Gly-Asp (RGD) peptide immobilized on TiO₂ nanotubes. In addition, we investigated the effects of the RGD peptide-coated TiO₂ nanotubes on the cellular response, proliferation, and functionality of osteogenic-induced human mesenchymal stem cells (hMSCs), which are osteoclasts that have been induced by bone marrow macrophages. The RGD peptide was grafted covalently onto the surface of TiO₂ nanotubes based on the results of SEM, FT-IR, and XPS. Furthermore, the RGD peptide promoted the initial attachment and proliferation of the hMSCs, regardless of the size of the TiO₂ nanotubes. However, the RGD peptide did not prominently affect the osteogenic functionality of the hMSCs because the peptide suppressed hMSC motility associated with osteogenic differentiation. The result of an *in vitro* osteoclast test showed that the RGD peptide accelerated the initial attachment of preosteoclasts and the formation of mature osteoclasts, which could resorb the bone matrix. Therefore, we believe that an RGD coating on TiO₂ nanotubes synthesized on Ti implants might not offer significant acceleration of bone formation *in vivo* because osteoblasts and osteoclasts reside in the same compartment.

1. Introduction

The clinical success and long-term stability of implants are determined by osseointegration between implantation materials and bone tissue [1]. Several studies exploring various surface treatments of the Ti implants have been conducted because of the excellent amenability to surface coating, which can promote successful bonding between bone tissue and implants and reduce the implantation healing period [1, 2]. To overcome the limitation of current osseointegration of implants and to enhance the tissue response *in vivo*, recent developments in implant surface treatments have focused on optimizing the interfacial reaction between the implant and the surrounding bone tissue on the basis of the chemical properties, charge, microstructure, and porosity of the implant surfaces [1–4].

Various chemical and physical methods such as chemical oxidation, plasma oxidation, and electrochemical anodization techniques have been adopted to prepare a biologically feasible oxide layer on a Ti surface [5]. Among them, anodization of the Ti surface has the potential to increase the porosity of the Ti surface and improve the surface area to promote cell attachment [6–8].

Nanostructures, including TiO₂ nanotubes, have recently been the focus of great interest for biological and biomedical applications owing to their high surface-to-volume ratio and higher structural plasticity compared to that of microscale structures. In terms of biomaterial development and implant technology, cellular responses can be affected by topographical circumstances. It is well known that variability in cell responses due to nanostructural topography *in vitro* alters cell morphology, cytoskeletal structure, gene expression, and

so forth [9–15]. Nanosized topographical factors have been shown to affect cells and tissues *in vivo* as well [8, 16–19]. In addition, a nanotopographical factor plays a critical role in improving the rate of cell proliferation and tissue acceptance, thereby ultimately determining the usefulness of the implanted biomaterial.

Recently, many studies using biochemical materials such as the extracellular matrix (ECM), growth factors, and bioactive materials as surface coating have been conducted to achieve osteoinduction and osteoconduction together. Osteoconduction is the growth of bones on the surface of the implant, and it relates to the biocompatibility of the implant materials. Osteoinduction is the phenomenon whereby osteogenesis is induced, and it is supposed to be a bone-healing process as it recruits immature cells and stimulates the cells into becoming osteoblasts [20]. Therefore, to achieve excellent osseointegration, osteoconduction and osteoinduction can be determined from the characteristics of the biochemical materials used, and materials that promote osteogenesis among immature cells in the body can be selected [21].

The Arg-Gly-Asp (RGD) peptide is a prospective bioactive factor and an amino acid present in integrin. The RGD peptide also regulates the attachment of cell proteins and the ECM. This peptide mediates the bonds between cellular, plasma, and ECM proteins, such as fibronectin, vitronectin, collagen type I, osteopontin, and bone sialoprotein [22–24].

Methods of grafting of the RGD peptide onto the surface of implants are generally based on physical adhesion and chemical immobilization [25]. Physical adhesion is mainly related to the spontaneous adhesion of coating materials to the surface of an implant material. This method is effective for coating bioactive materials to the surface of implants but is limited in its application to a number of materials. On the contrary, chemical fixation has the advantage of forming firm and stable coating layers, although these methods comprise several complicated processes [4].

Most studies have focused on the attachment, proliferation, and osteogenic functionality of bone-forming cells. However, a few studies have been carried out to investigate the relationship between the RGD peptide and bone-resorbing cells such as osteoclasts [26, 27].

The purpose of this work was to (1) characterize RGD peptide immobilized on the surface of 30- and 100-nm TiO₂ nanotubes and (2) to examine the effects of RGD peptide-coated TiO₂ nanotubes on the cellular response and functionality of osteogenic-induced human mesenchymal stem cells (hMSCs), which are osteoclasts that have been induced by bone marrow macrophages.

2. Experimental Section

2.1. TiO₂ Nanotubes Fabrication. TiO₂ nanotube surfaces were prepared by previous reports [14], and the anodization process was carried out as follows. The bare Ti sheet (Hyundai Titanium Co., 0.2 mm thick, 99.5%, Republic of Korea) was cleaned with acetone and deionized water. TiO₂ nanotubes were prepared in 0.5 w/v% hydrofluoric acid (Merck, 48 w/v%, NJ, USA) in water with acetic acid (JT Baker, 98 w/v%,

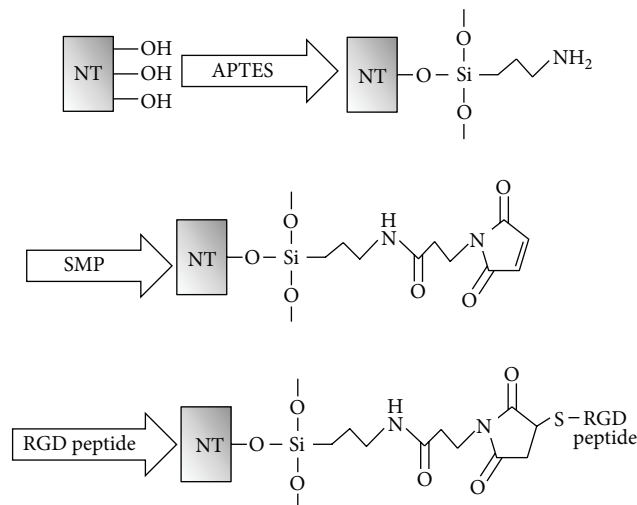


FIGURE 1: Reaction schematic diagram of TiO₂ nanotube surface modification procedure: (I) silane (APTES) treatment; (II) bifunctional cross-linker (SMP) connection; and (III) Arg-Gly-Asp (RGD) peptide grafting.

NJ, USA; volumetric ratio = 7 : 1) at 5, 10, 15, and 20 V for 1 h. A platinum electrode (DSM Co., 99.99%, South Korea) served as the counterpart. The samples were then rinsed with deionized water, dried at 60°C, and heat-treated at 500°C for 2 hrs to crystallize amorphous TiO₂ nanotubes into anatase structures. The morphology of TiO₂ nanotube arrays was observed by field emission scanning electron microscope (FE-SEM; S4800, Hitachi/Horiba Co., Japan).

2.2. RGD Peptide-Coating Process. RGD peptide was obtained from Sigma (A8052, MO, USA) in this research. The procedure of RGD peptide immobilization (see Figure 1) contains the grafting of a 3-aminopropyltriethoxysilane (APTES) onto the surface of TiO₂ nanotubes, and the substitution of the terminal amine to maleimide group reacted with thiol group of RGD peptide via a heterobifunctional cross-linker (3-succinimidyl-3-maleimido propionate: SMP, Sigma, MO, USA). The whole processes of silanization, substitution, and RGD peptide immobilization were listed in previous reports [23, 28]. Briefly, UV-sterilized TiO₂ nanotube samples (1.27 × 1.27 cm²) were silanized by immersing experimental samples in 10 mM APTES dissolved in hexane for 2 h. The silanized TiO₂ nanotubes were substituted for maleimide groups by using 2 mM bifunctional cross-linker SMP dissolved in DMF for 2 h. And then, thiolized RGD peptide dissolved in anhydrous DMF was immobilized on TiO₂ nanotubes by stirring for 2 h. Thiolized RGD peptides were prepared by previous research [29]. All experimental procedures were performed under Ar atmosphere.

2.3. Surface Analysis. To analyze the chemical composition change of TiO₂ nanotubes before and after RGD peptide immobilization, X-ray diffractometer (X'Pert PRO MRD,

PANalytical B.V., the Netherlands) with Ni-filtered Cu-K α ray, Fourier transform infrared spectroscopy (FT-IR; Nicolet, Thermo Co., WI, USA) and X-ray photoelectron spectroscopy (XPS, K-Alpha ESKA system; Thermo, USA) were carried out. In terms of XRD measurement, the glancing angle of the specimen was fixed at 5° against the incident beam enabling the detection of XRD patterns to be at the depth of less than 5 μ m from the top surface of the substrate.

2.4. hMSCs Cell Culture. We obtained human mesenchymal stem cells (hMSCs) from Lonza Corporation (Poietics hMSCs, Switzerland). Also, we used cell growth media composed of α -MEM (Invitrogen, CA, USA), 10% fetal bovine serum (FBS) (Invitrogen), and 1% penicillin-streptomycin (Invitrogen). The CO₂ incubator conditions of hMSCs were 37°C and 5% CO₂ atmosphere. The experiments of hMSCs were conducted with cultures at passage 4-5. After the confluence of hMSCs, they were seeded onto TiO₂ nanotube experimental substrate placed on a 12-well plate (cell density of 25,000 cells in each well) and were stored in a CO₂ incubator for a range of incubation times. Osteogenic induction media were prepared by adding 10 mM β -glycerol phosphate (Sigma Co., MO, USA), 150 μ g/mL ascorbic acid (Sigma), and 10 nM dexamethasone (Sigma) to cell growth media and was added to promote the osteogenic differentiation of hMSCs after 3 days of incubation. Osteogenic induction media were changed every 2-3 days.

2.5. Cell Adhesion and Proliferation Test. To estimate the degree of cell adhesion at the beginning of incubation time, fluorescein diacetate (FDA; Sigma, MO, USA) techniques was conducted to count viable hMSCs adhered to the experimental specimen. At 2, 24, and 48 hrs after plating, hMSCs on the substrates were rinsed with phosphate buffered saline solution (PBS) solution (Invitrogen, CA, USA) and were incubated with an FDA working solution (50 μ g FDA dissolved in 10 mL PBS solution) for 30 seconds and were then washed three times by PBS solution. The washed specimens were viewed under an inverted fluorescence microscope (CKX41, Olympus Co., Japan). We counted FDA-stained hMSCs adhered at all four corners of a specimen and at the center of the specimen.

MTT (3-(4,5-dimethylthiazol-2-yl)-2,5-diphenyltetrazolium bromide) assay was conducted to investigate the proliferation of hMSCs cultured on various experimental specimens. The samples were washed by PBS solution and were transferred to a new 12-well plate after the selected incubation periods. 1 mL of MTT dye agent (Sigma) was added to each well. After 3 hrs of incubation in 5% CO₂ incubator, 1 mL of isopropanol was added to each well, and the 12-well plate was then shaken for 30 minutes. The absorbance of each solution was measured at 570 nm by a microplate ELISA reader (Spectra Max 250, Thermo Electron Co., USA). The MTT value of each experimental group was relatively evaluated by that of uncoated 30 nm TiO₂ nanotubes.

2.6. Alkaline Phosphatase (ALP) Activity Test. To confirm the osteogenic differentiation and functionality of hMSCs,

alkaline phosphatase (ALP) activity test was used. After 2 weeks of incubation, the experimental samples were rinsed with PBS solution and lysed by using lysis buffer solution (25 mM Tris, pH 7.6, 150 mM NaCl, and 1% NP-40) and were stored in ice for 30 minutes. 50 μ L of cell lysate was used for ALP activity assay, and the rest of the cell lysate was used to measure the total protein content (Bradford Protein Assay Kit, Bio-Rad Laboratories, USA). 50 μ L of cell lysate was mixed with 200 μ L of para-nitrophenylphosphate (p-NPP, Sigma, MO, USA), and the mixed solution was stored at 37°C for 30 min to activate the reaction. After 30 minutes, 50 μ L of 3N NaOH (Sigma, MO, USA) was added to the mixed solution to stop the reaction. The absorbance of each solution was measured at 405 nm by a microplate ELISA reader (Spectra Max 250, Molecular Device, CA, USA). The level of activity was normalized with the amounts of total protein in the cell lysates (units/mg protein).

2.7. Motility Test of hMSCs. The motility of hMSCs cultured on 30 and 100 nm TiO₂ nanotubes was examined by modified FDA staining technique. Half of TiO₂ nanotubes samples was covered by cellophane tape. And then, hMSCs were seeded onto TiO₂ nanotube experimental substrate placed on a 12-well plate (cell density of 25,000 cells in each well) and were stored in a CO₂ incubator for 24 hrs. After 24 h of incubation, cellophane tape was removed, and hMSCs cultured on experimental samples were cultured for additional 24 h. After 48 hrs of incubations, live hMSCs were stained by FDA solution, and the motility images of live hMSCs cultured on TiO₂ nanotubes were obtained by inverted fluorescence microscope.

2.8. Mice and Reagents for Osteoclast Experiment. C57BL/6 mice were purchased from Orient Bio Inc. (SungNam, Republic of Korea), and were used to produce bone marrow-derived-macrophages (BMMs). All mice used in these experiments were 6–8 weeks old, and all experiments were approved by the Animal Studies Committee of Wonkwang University. All cell culture media and supplements were obtained from Thermo Scientific Corporation (IL, USA). Soluble recombinant mouse RANKL was purified from insect cells as described previously [30], and recombinant human M-CSF was a gift from Daved H. Fremont (Washington University, St. Louis, MO, USA).

2.9. Osteoclast Formation and Staining on Peptide-Coated TiO₂ Nanotube. Murine osteoclasts were prepared from bone marrow cells using the standard methods as previously described with minor modification [30]. In brief, bone marrow (BM) cells were obtained by flushing femur and tibia from C57BL/6 mice. For stromal cell-free bone marrow-derived macrophage (BMM) culture, bone marrow cells were cultured with M-CSF (50 ng/mL) for 3 day in α -MEM containing 10% FBS, and attached cells were used as osteoclast precursors, BMMs. BMMs (6×10^4 cell/wells in 24-well plates) were loaded onto control or peptide-coated TiO₂ nanotube pieces (1.27 cm \times 1.27 cm), having 30 nm and 100 nm diameters, and were subsequently differentiated into

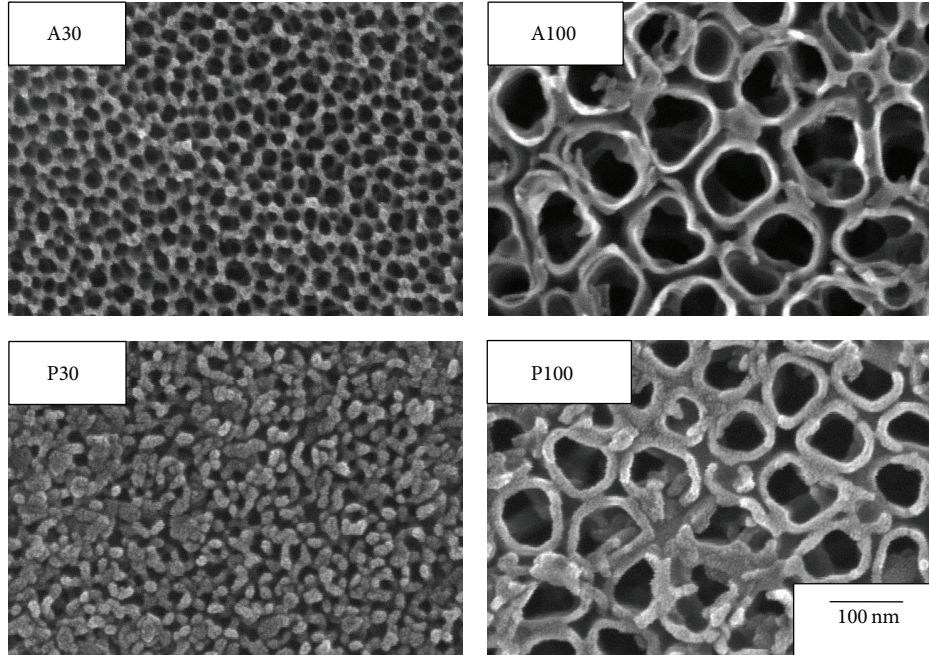


FIGURE 2: SEM micrographs of self-aligned 30 (A30), 100 (A100) nm TiO_2 nanotubes and RGD peptide-coated 30 (P30), 100 (P100) nm TiO_2 nanotubes. (The scale bar of all figures is 100 nm).

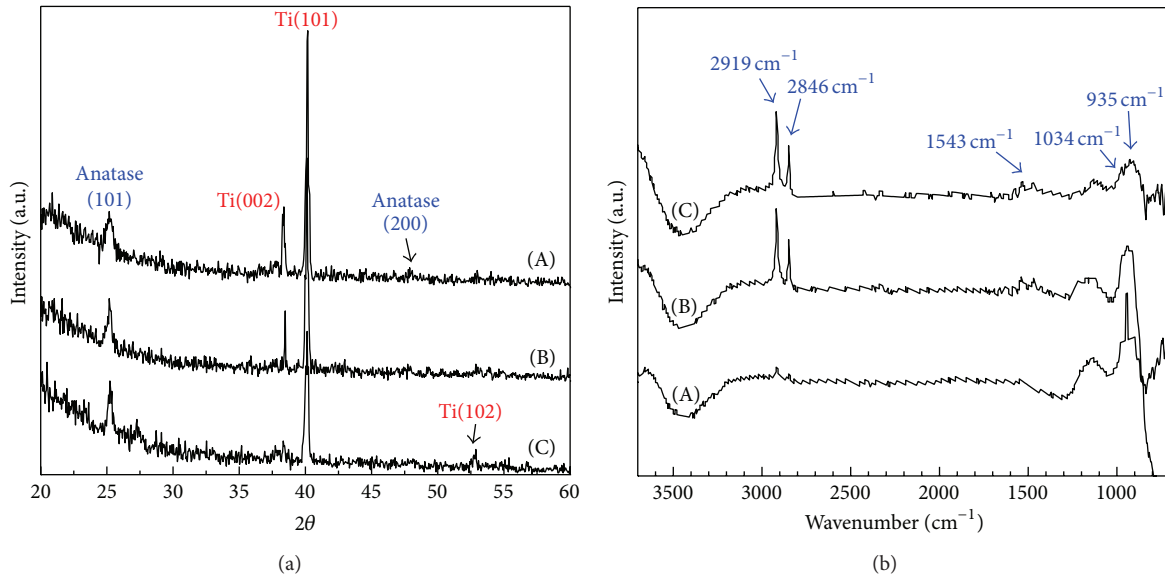
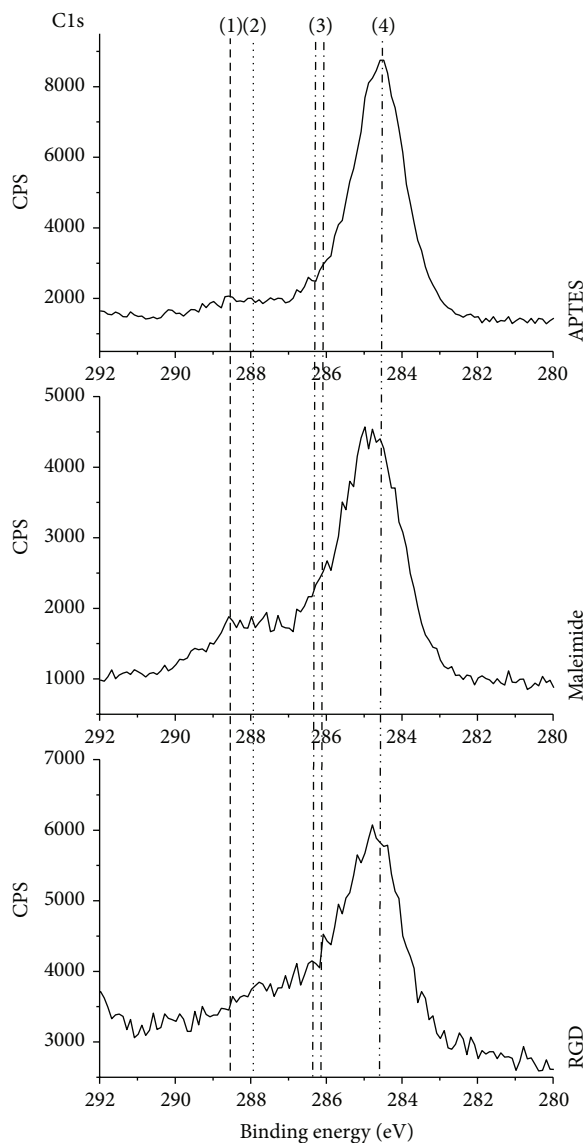


FIGURE 3: (a) XRD patterns and (b) FT-IR spectra of (A) uncoated, (B) silanized, and (C) RGD peptide-coated 100 nm TiO_2 nanotubes.

osteoclasts with M-CSF (50 ng/mL) and RANKL (100 ng/mL) for 4 day. Fresh media containing M-CSF and RANKL were resupplied at day 3. For coculture, bone marrow cells (6×10^5 cells/well) were cultured with calvaria-derived osteoblast (6×10^4 cells/well) on TiO_2 nanotubes. BM cells were differentiated into osteoclasts in α -MEM containing 10% FBS and were supplemented with $1\alpha,25(\text{OH})_2\text{D}_3$ (2×10^{-8} M) for 7 day. Cells were then stained with fluorescein diacetate (FDA; Sigma, MO, USA) as reported previously [31] and were pictured by an inverted fluorescence microscope (DM

IL LED, Leica Microsystems GmbH, Wetzlar, Germany). We tested osteoclast formation on TiO_2 nanotubes by three times and counted the number of mature osteoclast having characteristic actin ring. The representative data were shown.

2.10. Data Analysis. All data were expressed as mean \pm standard deviation and were statistically analyzed by one-way ANOVA (SPSS 12.0, SPSS GmbH, Germany) and the Student-Newman-Keuls method as a post hoc test. Significant differences were determined at P values at least less than 0.05.



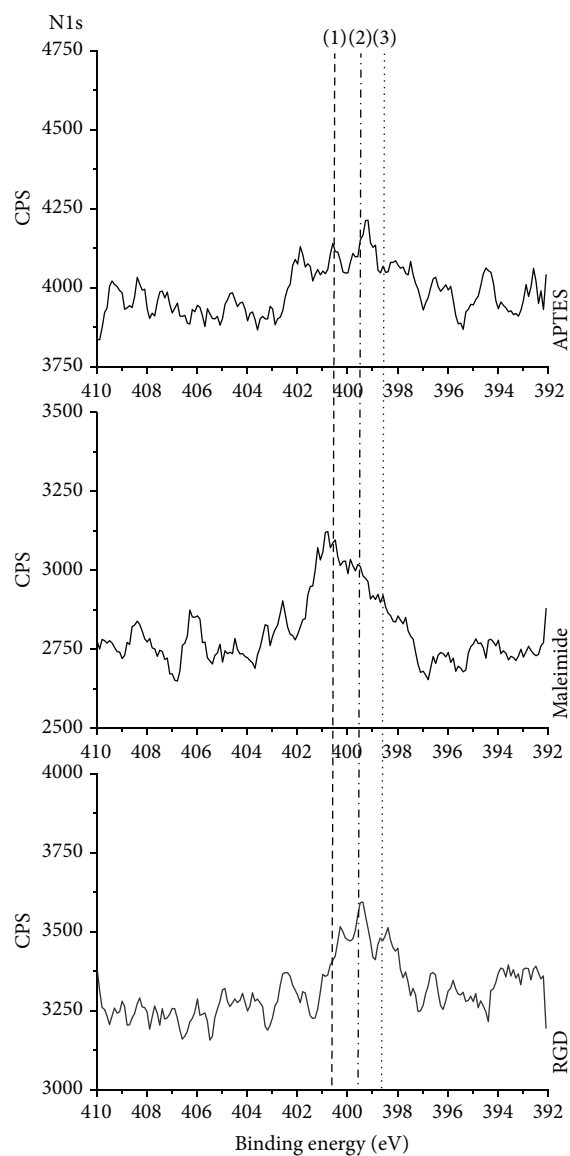
The list of related peak position

- (1) O=C-O (289 eV)
- (2) C=O, (288.3 eV)
- (3) N-C=O (286.4 eV), and C-NH₂, C-O (285.9–286.1 eV)
- (4) CH_x or C-C (284.8 eV)

FIGURE 4: XPS C1s spectra of silanized (APTES), bifunctional cross-linked (maleimide), and (c) RGD peptide-coated 100 nm TiO₂ nanotubes.

3. Results and Discussion

3.1. Analysis of RGD Peptide Grafted onto TiO₂ Nanotubes. Figure 2 shows SEM micrographs of uncoated and RGD peptide-coated 30 and 100 nm TiO₂ nanotubes. As shown in the P30 and P100 images of Figure 2, 10–20 nm nanoparticles were deposited on the top surfaces of the TiO₂ nanotubes. We also tried to coat the RGD peptide onto TiO₂ nanotubes using 20 mM APTES and found that APTES coated the TiO₂ nanotubes completely, thereby blocking the pores (data not



The list of related peak position

- (1) Maleimide (399.7–400.7 eV)
- (2) N-C=O (399.7–400.8 eV)
- (3) C-NH₂, C-O (398.9 eV)

FIGURE 5: XPS N1s spectra of silanized (APTES), bifunctional cross-linked (maleimide), and (c) RGD peptide-coated 100 nm TiO₂ nanotubes.

shown). Therefore, we expect that 10 mM APTES is suitable for coating the RGD peptide onto the top surfaces of TiO₂ nanotubes effectively.

Figure 3 indicates the XRD patterns of FT-IR spectra of uncoated, silanized, and RGD peptide-coated 100-nm TiO₂ nanotubes, respectively. As shown by the XRD patterns, the crystal structures of the TiO₂ nanotubes prepared in this study were anatase. In the FT-IR spectra, some new peaks corresponding to the covalent grafting of APTES were detected at 935 (Si-OH), 1034 (Si-O-Si), 1543, 2846,

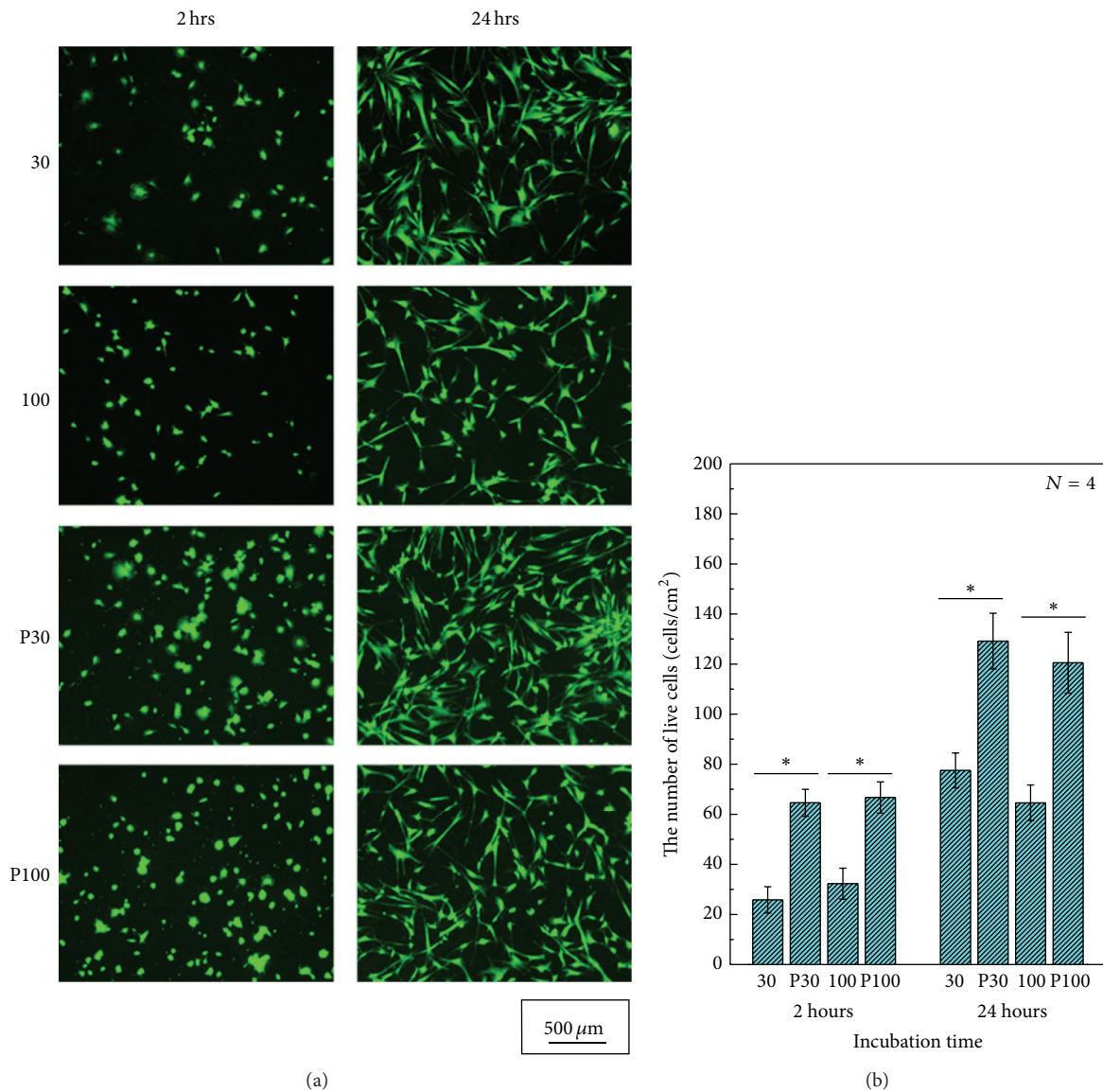


FIGURE 6: (a) Fluorescein diacetate (FDA) images and (b) the number of live hMSCs cultured on uncoated and RGD peptide-coated 30 and 100 nm TiO₂ nanotubes.

and 2919 cm⁻¹ for the FT-IR spectra of the silanized and RGD peptide-coated TiO₂ nanotubes [32, 33]. As previously reported, these peaks originated from the formation of SiO_{3/2} (silsesquioxane) nanoparticles [34]. From the results of FT-IR analysis of the RGD peptide, it was difficult to identify the existence of RGD peptides immobilized on TiO₂ nanotubes because of the overlap of the FT-IR spectral peaks between APTES and the RGD peptide. Therefore, XPS analysis was used to confirm the covalent grafting of the RGD peptide onto the TiO₂ nanotube surface.

Figures 4 and 5 show the XPS spectra of Cls and NIs for silanized (APTES), bifunctional cross-linked (maleimide), and the RGD peptide-coated TiO₂ nanotube substrates, respectively. Four kinds of Cls peaks were detected on the surfaces of the APTES, maleimide, and RGD peptide-coated

TiO₂ nanotubes as shown in Figure 4. From the 4 kinds of Cls peaks, lines 1 and 2 (binding energies of 289 and 288.3) indicate the portions of O=C-O and C=O derived from maleimide and RGD peptide, respectively. Line 3 (binding energy of 285.9–286.4 eV) indicates the existence of the RGD peptide. Line 4 (binding energy of 284.8 eV) represents the silanization by APTES [35]. As seen in Figure 5, the 3 kinds of NIs peaks were detected on the surface of APTES, maleimide, and the RGD peptide-coated TiO₂ nanotubes. Line 1 and 2 show the overlap of maleimide and the RGD peptide. However, line 3 indicates the portions of C-NH₃ and C-O bonds that originated from the RGD peptide [36, 37].

From the SEM observations and the results of FT-IR analysis, it was confirmed that 10–20 nm SiO_{3/2} nanoparticles were deposited on the surfaces of the TiO₂ nanotubes. In

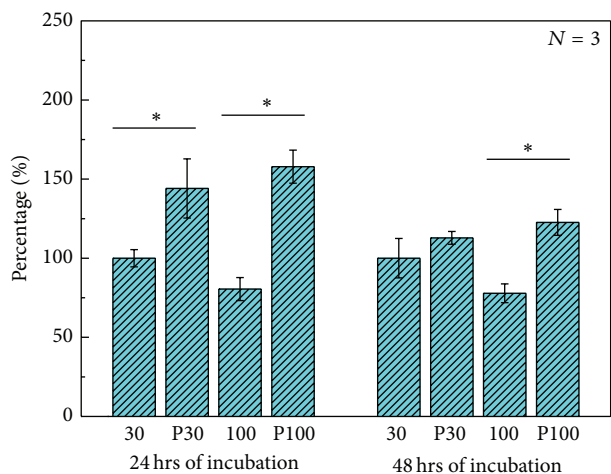


FIGURE 7: The result of the MTT with hMSCs cultured on uncoated and RGD peptide-coated 30 and 100 nm TiO_2 nanotubes after 24 h and 48 hrs of incubation. * denotes significance between uncoated and RGD peptide-coated TiO_2 nanotubes.

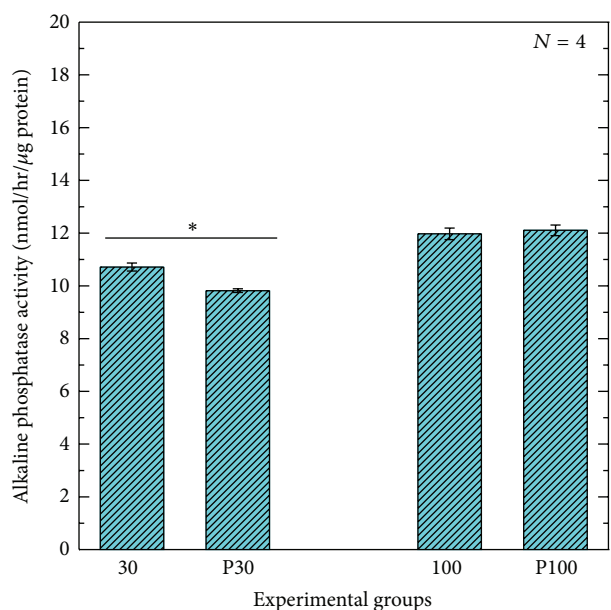


FIGURE 8: Alkaline phosphatase (ALP) activity of hMSCs cultured on uncoated and RGD peptide-coated 30 and 100 nm TiO_2 nanotubes after 2 weeks of incubation. * denotes significance between uncoated 30 nm TiO_2 nanotubes versus RGD peptide-coated 30 nm TiO_2 nanotubes.

addition, the XPS analysis indicated that the RGD peptide was coated onto the surface of TiO_2 nanotubes through silanization and bifunctional cross-linking.

3.2. Initial Attachment and Proliferation of hMSCs. Figure 6 shows images of FDA stained, live hMSCs cultured on uncoated and RGD peptide-coated 30 and 100 nm TiO_2 nanotubes after 2 and 24 hours of incubation. As shown

in Figure 6(b), after 2 and 24 hours of incubation, the number of hMSCs that were cultured on the RGD peptide-coated TiO_2 nanotubes was significantly higher than that on uncoated TiO_2 nanotubes, regardless of the diameter of the TiO_2 nanotubes ($P < 0.05$). Thus, it was confirmed that the RGD peptide-coating enhanced the initial attachment of hMSCs to the surface of TiO_2 nanotubes within 24 h of incubation.

Figure 7 shows the MTT assay results for uncoated and RGD peptide-coated 30 and 100 nm TiO_2 nanotubes after 24 and 48 h of incubation. The values for the RGD peptide-coated TiO_2 nanotubes were significantly higher than those for the uncoated TiO_2 nanotubes ($P < 0.05$). However, no significant difference was observed between the uncoated and RGD peptide-coated 30 nm TiO_2 nanotubes after 48 h of incubation ($P > 0.05$). Previous reports have shown that the initial attachment and proliferation of cells cultured on 30 nm TiO_2 nanotubes are higher than those on 100 nm TiO_2 nanotubes at the beginning of incubation time [15, 38]. Therefore, 48 h of incubation may have been long enough to overcome RGD peptide feature promoting the initial cell attachment when it was coated onto the surface of 30 nm TiO_2 nanotubes. Thus, the MTT assay results for the uncoated and RGD peptide-coated 30 nm TiO_2 nanotubes after 48 h of incubation can be considered similar.

From the results of FDA staining and the MTT assay, we confirmed that the RGD peptide promoted the attachment and proliferation of hMSCs cultured on TiO_2 nanotubes at the beginning of incubation.

3.3. ALP Activity of hMSCs. Figure 8 shows the results of the ALP activity assay of hMSCs cultured on uncoated and RGD peptide-coated 30 and 100 nm TiO_2 nanotubes after 2 weeks of incubation. The ALP activity of the hMSCs cultured on RGD peptide-coated 30 nm TiO_2 nanotubes was significantly lower than that of hMSCs cultured on uncoated 30 nm TiO_2 nanotubes ($P < 0.05$). In addition, no significant difference was observed in the ALP activity between uncoated and the RGD peptide-coated 100 nm TiO_2 nanotubes ($P > 0.05$).

Although the results of FDA staining and the MTT assay were similar to those obtained in previous studies [39], the results of the ALP activity assay were not as consistent. The bond status of the RGD peptide, nature of the biomaterials, and cell culture periods play important roles during initial attachment, in osteogenic differentiation and in the functionality of mesenchymal stem cells [40–43]. In this study, we prepared thiolized RGD peptide instead of purchasing cysteine-conjugated RGD peptide, which was used in previous studies [23, 28, 39]. Therefore, the bond status of the functional groups between the thiolized RGD peptide and the cysteine-conjugated RGD peptide can be safely assumed to be different, which makes the results, in terms of cellular response, obtained using these 2 peptides different. Furthermore, many published studies on the effects of the RGD peptide on cellular responses have focused on ceramic surfaces instead of metal surfaces, which would result in discrepancies in the results in terms of cellular proliferation and differentiation [44–47].

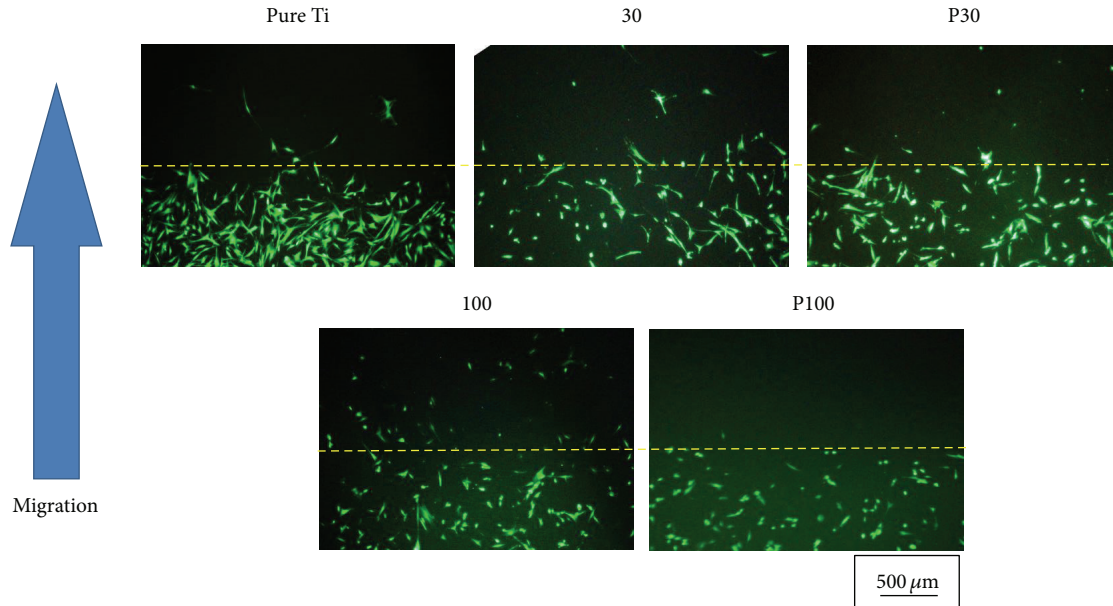


FIGURE 9: Fluorescein diacetate (FDA) images of live hMSCs cultured on pure Ti, uncoated, and RGD peptide-coated 30 and 100 nm TiO_2 nanotube after 48 hours of incubation. (Motility test of hMSCs). # Upper half area is covered by cellophane tape when hMSCs are seeded onto substrate. After 24 h of incubation, cellophane tape was removed, and then hMSCs was cultured for addition 24 h.

In addition, the motility and mechanical strain of hMSCs cultured on biomaterials promote the osteogenic differentiation of hMSCs [48, 49]. To prove the correlation between cell motility and osteogenic differentiation, the motility of the hMSCs during 24 hours of incubation was examined using through FDA staining. As shown in Figure 9, the motility of the hMSCs cultured on uncoated TiO_2 nanotubes seemed to be higher than that of hMSCs cultured on RGD peptide-coated TiO_2 nanotubes. Therefore, we believe that the RGD peptide that coated the surfaces of the TiO_2 nanotubes suppressed hMSC motility. We also think that the results of the ALP activity assay were affected by the properties of the RGD peptide, nature of the biomaterial surface, and motility of cells that are cultured on variously sized TiO_2 nanotubes. Further investigation is performed to resolve the inconsistency between MTT and ALP activity results more clearly.

3.4. Attachment and Proliferation of BMM and Maturation of Osteoclasts. *In vivo*, osteoblasts, which are bone-forming cells, reside with osteoclasts, which are bone-resorbing cells, within the same compartment. Therefore, examining the effect of RGD peptide-coated TiO_2 nanotubes on osteoclast formation, together with their effect on osteoblasts, is important. We cultured osteoclasts on RGD peptide-coated TiO_2 nanotubes and assessed the effect of the RGD peptide-coating on the formation of mature osteoclast. Previously, we reported that the adhesion ability of osteoclast precursors attached to TiO_2 nanotubes of various pore diameters (30–100 nm) was not different. However, osteoclast formation decreased with increasing nanotube diameter [50]. Consistent with our previous data, Figure 10 shows that the formation of mature osteoclasts on uncoated 100 nm TiO_2

nanotubes was significantly less than that on uncoated 30 nm TiO_2 nanotubes in both culture systems (BMM culture and coculture). Although mature osteoclast formation on the RGD peptide-coated 30-nm TiO_2 nanotubes was diminished slightly than uncoated 30 nm TiO_2 nanotubes, however, mature osteoclast formation was highly maintained on RGD peptide-coated 30 nm TiO_2 in the BMM culture (Figure 10(a)). Moreover, mature osteoclast formation was dramatically increased on the RGD peptide-coated 100 nm TiO_2 nanotubes compared to that of uncoated 100 nm TiO_2 nanotubes which inhibited mature osteoclast formation (Figure 10(a)). In addition, mature osteoclast formation on the RGD peptide-coated 100 nm TiO_2 nanotubes also increased significantly to the same level as that of the RGD peptide-coated or uncoated 30 nm TiO_2 nanotubes in the coculture system (Figure 10(b)). These data suggest that the RGD peptide-coated onto the TiO_2 nanotubes promoted the initial attachment of osteoclasts [51, 52] and that it helped overcome the inhibitory effect of nanotubes with large pores on osteoclast formation. As mentioned above, cell attachment and functionality depend on many factors such as cell phenotype, shape, culture media, and the surface used for cell culture. However, in this study, the RGD peptide seemed to enhance the initial attachment and proliferation of hMSCs and BMMs, and the maturation of preosteoclasts into bone-resorbing mature osteoclasts.

4. Conclusions

In this study, the RGD peptide was grafted covalently onto the surface of TiO_2 nanotubes based on the results of SEM analysis, FT-IR, and XPS. Furthermore, the RGD peptide promoted the initial attachment and proliferation of hMSCs,

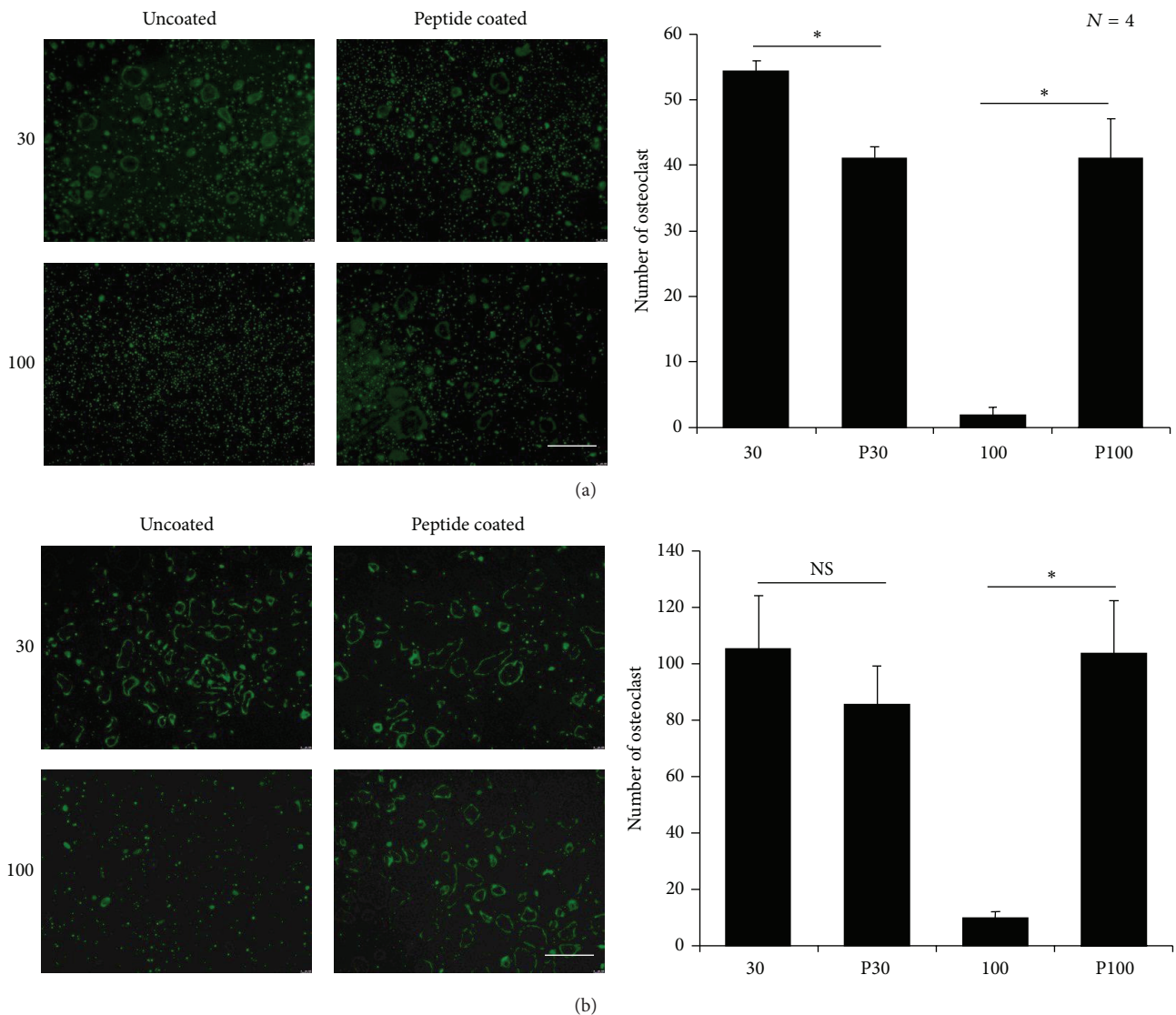


FIGURE 10: Bone marrow derived-macrophages under M-CSF and RANKL treatment were cultured, (a) and bone marrow cells under $1\alpha,25(\text{OH})_2\text{D}_3$ treatment were cocultured with osteoblast (b) on uncoated (30 and 100) and RGD peptide- (P30 and P100) coated TiO_2 nanotubes. Cells were then stained with fluorescein diacetate (FDA). Cells having actin ring were counted as mature osteoclast. Bar = 500 μm .

regardless of the size of the TiO_2 nanotube. However, the RGD peptide did not prominently affect the osteogenic functionality of the hMSCs because the peptide suppressed the motility of the hMSCs during osteogenic differentiation. The result of the osteoclast *in vitro* test showed that the RGD peptide accelerated the initial attachment of preosteoclasts and the formation of mature osteoclasts, which can resorb the bone matrix. Therefore, we believe that applying an RGD coating onto TiO_2 nanotubes synthesized on Ti implants that are used in medicine might not accelerate bone formation *in vivo* significantly because osteoblasts and osteoclasts reside in the same compartment.

Acknowledgment

This paper was supported by Wonkwang University in 2011.

References

- [1] L. Le Guéhenec, A. Soueidan, P. Layrolle, and Y. Amouriq, "Surface treatments of titanium dental implants for rapid osseointegration," *Dental Materials*, vol. 23, no. 7, pp. 844–854, 2007.
- [2] R. Junker, A. Dimakis, M. Thoneick, and J. A. Jansen, "Effects of implant surface coatings and composition on bone integration: a systematic review," *Clinical Oral Implants Research*, vol. 20, no. 4, pp. 185–206, 2009.
- [3] D. A. Puleo and A. Nanci, "Understanding and controlling the bone-implant interface," *Biomaterials*, vol. 20, no. 23-24, pp. 2311–2321, 1999.
- [4] M. Dettin, M. T. Conconi, R. Gambaretto et al., "Effect of synthetic peptides on osteoblast adhesion," *Biomaterials*, vol. 26, no. 22, pp. 4507–4515, 2005.
- [5] Y. Kataoka, Y. Tamaki, and T. Miyazaki, "Synergistic responses of superficial chemistry and micro topography of titanium

- created by wire-type electric discharge machining,” *Bio-medical Materials and Engineering*, vol. 21, no. 2, pp. 113–121, 2011.
- [6] K. Kim, T. Kwon, S. Kim et al., “Preparation and characterization of anodized titanium surfaces and their effect on osteoblast responses,” *The Journal of Oral Implantology*, vol. 32, no. 1, pp. 8–13, 2006.
 - [7] G. Balasundaram, C. Yao, and T. J. Webster, “TiO₂ nanotubes functionalized with regions of bone morphogenetic protein-2 increases osteoblast adhesion,” *Journal of Biomedical Materials Research A*, vol. 84, no. 2, pp. 447–453, 2008.
 - [8] M. Sato and T. J. Webster, “Nanobiotechnology: implications for the future of nanotechnology in orthopedic applications,” *Expert Review of Medical Devices*, vol. 1, no. 1, pp. 105–114, 2004.
 - [9] K. S. Brammer, S. Oh, J. O. Gallagher, and S. Jin, “Enhanced cellular mobility guided by TiO₂ nanotube surfaces,” *Nano Letters*, vol. 8, no. 3, pp. 786–793, 2008.
 - [10] M. J. Dalby, L. Di Silvio, E. J. Harper, and W. Bonfield, “Initial interaction of osteoblasts with the surface of a hydroxyapatite-poly(methylmethacrylate) cement,” *Biomaterials*, vol. 22, no. 13, pp. 1739–1747, 2001.
 - [11] M. J. Dalby, N. Gadegaard, P. Herzyk et al., “Nanomechanotransduction and interphase nuclear organization influence on genomic control,” *Journal of Cellular Biochemistry*, vol. 102, no. 5, pp. 1234–1244, 2007.
 - [12] M. J. Dalby, “Nanostructured surfaces: cell engineering and cell biology,” *Nanomedicine*, vol. 4, no. 3, pp. 247–248, 2009.
 - [13] J. O. Gallagher, K. F. McGhee, C. D. W. Wilkinson, and M. O. Riehle, “Interaction of animal cells with ordered nanotopography,” *IEEE Transactions on Nanobioscience*, vol. 1, no. 1, pp. 24–28, 2002.
 - [14] S. Oh, C. Daraio, L. Chen, T. R. Pisanic, R. R. Fiñones, and S. Jin, “Significantly accelerated osteoblast cell growth on aligned TiO₂ nanotubes,” *Journal of Biomedical Materials Research A*, vol. 78, no. 1, pp. 97–103, 2006.
 - [15] J. Park, S. Bauer, K. Von Der Mark, and P. Schmuki, “Nanosize and vitality: TiO₂ nanotube diameter directs cell fate,” *Nano Letters*, vol. 7, no. 6, pp. 1686–1691, 2007.
 - [16] L. M. Bjursten, L. Rasmusson, S. Oh, G. C. Smith, K. S. Brammer, and S. Jin, “Titanium dioxide nanotubes enhance bone bonding in vivo,” *Journal of Biomedical Materials Research A*, vol. 92, no. 3, pp. 1218–1224, 2010.
 - [17] L. Meirelles, L. Melin, T. Peltola et al., “Effect of hydroxyapatite and titania nanostructures on early in vivo bone response,” *Clinical Implant Dentistry and Related Research*, vol. 10, no. 4, pp. 245–254, 2008.
 - [18] G. Giavaresi, M. Tschon, J. H. Daly et al., “In vitro and in vivo response to nanotopographically-modified surfaces of poly(3-hydroxybutyrate-co-3-hydroxyvalerate) and polycaprolactone,” *Journal of Biomaterials Science*, vol. 17, no. 12, pp. 1405–1423, 2006.
 - [19] K. Huo, X. Zhang, H. Wang, L. Zhao, X. Liu, and P. K. Chu, “Osteogenic activity and antibacterial effects on titanium surfaces modified with Zn-incorporated nanotube arrays,” *Biomaterials*, vol. 34, no. 13, pp. 3467–3478, 2013.
 - [20] T. Albrektsson and C. Johansson, “Osteoinduction, osteoconduction and osseointegration,” *European Spine Journal*, vol. 10, no. 2, pp. S96–S101, 2001.
 - [21] M. Dard, A. Sewing, J. Meyer, S. Verrier, S. Roessler, and D. Scharnweber, “Tools for tissue engineering of mineralized oral structures,” *Clinical oral investigations*, vol. 4, no. 2, pp. 126–129, 2000.
 - [22] E. Ruoslahti and M. D. Pierschbacher, “Arg-Gly-Asp: a versatile cell recognition signal,” *Cell*, vol. 44, no. 4, pp. 517–518, 1986.
 - [23] S. Xiao, M. Textor, N. D. Spencer, and H. Sigrist, “Covalent attachment of cell-adhesive, (Arg-Gly-Asp)-containing peptides to titanium surfaces,” *Langmuir*, vol. 14, no. 19, pp. 5507–5516, 1998.
 - [24] S. P. Massia and J. A. Hubbell, “Covalently attached GRGD on polymer surfaces promotes biospecific adhesion of mammalian cells,” *Annals of the New York Academy of Sciences*, vol. 589, pp. 261–270, 1990.
 - [25] A. Reznia, R. Johnson, A. R. Lefkow, and K. E. Healy, “Bioactivation of metal oxide surfaces. I. Surface characterization and cell response,” *Langmuir*, vol. 15, no. 20, pp. 6931–6939, 1999.
 - [26] K. Yip and D. J. Marsh, “An Arg-Gly-Asp peptide stimulates constriction in rat afferent arteriole,” *American Journal of Physiology*, vol. 273, no. 5, pp. F768–F776, 1997.
 - [27] J. Reed, W. E. Hull, C.-W. Von Der Lieth, D. Kubler, S. Suhai, and V. Kinzel, “Secondary structure of the Arg-Gly-Asp recognition site in proteins involved in cell-surface adhesion. Evidence for the occurrence of nested β -bends in the model hexapeptide GRGDSF,” *European Journal of Biochemistry*, vol. 178, no. 1, pp. 141–154, 1988.
 - [28] M. C. Durrieu, S. Pallu, F. Guillemot et al., “Grafting RGD containing peptides onto hydroxyapatite to promote osteoblastic cells adhesion,” *Journal of Materials Science*, vol. 15, no. 7, pp. 779–786, 2004.
 - [29] J. Carter, “Conjugation of peptide to carrier proteins via m-Maleimidobenzoyl-N-Hydroxysuccinimide ester (MBS),” in *The Protein Protocols Handbook*, pp. 689–692, 1996.
 - [30] S. H. Lee, T. Kim, D. Jeong, N. Kim, and Y. Choi, “The Tec family tyrosine kinase Btk regulates RANKL-induced osteoclast maturation,” *The Journal of Biological Chemistry*, vol. 283, no. 17, pp. 11526–11534, 2008.
 - [31] K. Moon, S. Yu, J. Bae, and S. Oh, “Biphasic osteogenic characteristics of human mesenchymal stem cells cultured on TiO₂ nanotubes of different diameters,” *Journal of Nanomaterials*, vol. 2012, Article ID 252481, 8 pages, 2012.
 - [32] Y. Zhang, Y. Yuan, and C. Liu, “Fluorescent labeling of nanometer hydroxyapatite,” *Journal of Materials Science and Technology*, vol. 24, no. 2, pp. 187–191, 2008.
 - [33] E. T. Vandenberg, L. Bertilsson, B. Liedberg et al., “Structure of 3-aminopropyl triethoxy silane on silicon oxide,” *Journal of Colloid And Interface Science*, vol. 147, no. 1, pp. 103–118, 1991.
 - [34] G. Lu, Y. Huang, Y. Yan, T. Zhao, and Y. Yu, “Synthesis and properties of bismaleimide-modified novolak resin/silsesquioxane nanocomposites,” *Journal of Polymer Science A*, vol. 41, no. 16, pp. 2599–2606, 2003.
 - [35] M. C. Durrieu, S. Pallu, F. Guillemot et al., “Grafting RGD containing peptides onto hydroxyapatite to promote osteoblastic cells adhesion,” *Journal of Materials Science*, vol. 15, no. 7, pp. 779–786, 2004.
 - [36] J. Charlier, V. Detalle, F. Valin, C. Bureau, and G. Lécayon, “Study of ultrathin polyamide-6,6 films on clean copper and platinum,” *Journal of Vacuum Science and Technology A*, vol. 15, no. 2, pp. 353–364, 1997.
 - [37] L. N. Bui, M. Thompson, N. B. McKeown, A. D. Romaschin, and P. G. Kalman, “Surface modification of the biomedical polymer poly(ethylene terephthalate),” *The Analyst*, vol. 118, no. 5, pp. 463–474, 1993.
 - [38] S. Oh, K. S. Brammer, Y. S. J. Li et al., “Stem cell fate dictated solely by altered nanotube dimension,” *Proceedings of*

- the National Academy of Sciences of the United States of America*, vol. 106, no. 7, pp. 2130–2135, 2009.
- [39] X. Cao, W. Yu, J. Qiu, Y. Zhao, Y. Zhang, and F. Zhang, “RGD peptide immobilized on TiO₂ nanotubes for increased bone marrow stromal cells adhesion and osteogenic gene expression,” *Journal of Materials Science*, vol. 23, pp. 527–536, 2012.
- [40] E. Ruoslahti, “RGD and other recognition sequences for integrins,” *Annual Review of Cell and Developmental Biology*, vol. 12, pp. 697–715, 1996.
- [41] Z. Qu, J. Yan, B. Li, J. Zhuang, and Y. Huang, “Improving bone marrow stromal cell attachment on chitosan/hydroxyapatite scaffolds by an immobilized RGD peptide,” *Biomedical Materials*, vol. 5, no. 6, Article ID 065001, 2010.
- [42] Y. Huang, J. Ren, T. Ren et al., “Bone marrow stromal cells cultured on poly (lactide-co-glycolide)/nano- hydroxyapatite composites with chemical immobilization of Arg-Gly-Asp peptide and preliminary bone regeneration of mandibular defect thereof,” *Journal of Biomedical Materials Research A*, vol. 95, no. 4, pp. 993–1003, 2010.
- [43] C. Yang, K. Cheng, W. Weng, and C. Yang, “Immobilization of RGD peptide on HA coating through a chemical bonding approach,” *Journal of Materials Science*, vol. 20, no. 11, pp. 2349–2352, 2009.
- [44] M. Jager, C. Boge, R. Janissen et al., “Osteoblastic potency of bone marrow cells cultivated on functionalized biomaterials with cyclic RGD-peptide,” *Journal of Biomedical Materials Research A*, 2013.
- [45] D. Le Guillou-Buffello, R. Bareille, M. Gindre, A. Sewing, P. Laugier, and J. Amédée, “Additive effect of RGD coating to functionalized titanium surfaces on human osteoprogenitor cell adhesion and spreading,” *Tissue Engineering A*, vol. 14, no. 8, pp. 1445–1455, 2008.
- [46] S. Tosatti, Z. Schwartz, C. Campbell et al., “RGD-containing peptide GCRGYGRGDSPG reduces enhancement of osteoblast differentiation by poly(L-lysine)-graft-poly(ethylene glycol)-coated titanium surfaces,” *Journal of Biomedical Materials Research - Part A*, vol. 68, no. 3, pp. 458–472, 2004.
- [47] S. Pallu, C. Bourget, R. Bareille et al., “The effect of cyclo-DfKRG peptide immobilization on titanium on the adhesion and differentiation of human osteoprogenitor cells,” *Biomaterials*, vol. 26, no. 34, pp. 6932–6940, 2005.
- [48] T. Briggs, M. D. Treiser, P. F. Holmes, J. Kohn, P. V. Moghe, and T. L. Arinzeh, “Osteogenic differentiation of human mesenchymal stem cells on poly(ethylene glycol)-variant biomaterials,” *Journal of Biomedical Materials Research A*, vol. 91, no. 4, pp. 975–984, 2009.
- [49] R. D. Sumanasinghe, S. H. Bernacki, and E. G. Lobo, “Osteogenic differentiation of human mesenchymal stem cells in collagen matrices: effect of uniaxial cyclic tensile strain on bone morphogenetic protein (BMP-2) mRNA expression,” *Tissue Engineering*, vol. 12, no. 12, pp. 3459–3465, 2006.
- [50] S. Oh and S. H. Lee, “Ability of osteoclasts adhesion and differentiation on various pore scale of TiO₂ nanotube surface,” *The Journal of the Korea Society For Dental Research Materials*, vol. 36, no. 4, pp. 315–320, 2009.
- [51] P. T. Lakkakorpi, G. Wesolowski, Z. Zimolo, G. A. Rodan, and S. B. Rodan, “Phosphatidylinositol 3-kinase association with the osteoclast cytoskeleton, and its involvement in osteoclast attachment and spreading,” *Experimental Cell Research*, vol. 237, no. 2, pp. 296–306, 1997.
- [52] B. Christensen, C. C. Kazanecki, T. E. Petersen, S. R. Rittling, D. T. Denhardt, and E. S. Sørensen, “Cell type-specific post-translational modifications of mouse osteopontin are associated with different adhesive properties,” *The Journal of Biological Chemistry*, vol. 282, no. 27, pp. 19463–19472, 2007.

Research Article

Formation of Various Pyramidal Structures on Monocrystalline Silicon Surface and Their Influence on the Solar Cells

Yangang Han,^{1,2} Xuegong Yu,¹ Dong Wang,¹ and Deren Yang¹

¹ State Key Lab of Silicon Materials, Zhejiang University, Hangzhou 310027, China

² Zhejiang Institute of Quality Inspection Science, Hangzhou 310013, China

Correspondence should be addressed to Xuegong Yu; yuxuegong@zju.edu.cn

Received 22 June 2013; Accepted 13 July 2013

Academic Editor: Jiamin Wu

Copyright © 2013 Yangang Han et al. This is an open access article distributed under the Creative Commons Attribution License, which permits unrestricted use, distribution, and reproduction in any medium, provided the original work is properly cited.

Texturization is a useful method to enhance the optical absorption of monocrystalline silicon wafers by light-trapping effect in solar cell processing. In present study, a series of textured wafers with various pyramid sizes ranging from 200 nm to 10 μm were fabricated by modified wet-chemical method and characterized. The results show that there is little difference in the reflectance with the pyramid sizes from 1 to 10 μm , which is consistent with the ray-tracing simulation results. However, the light-trapping function of the 200 nm sample below the geometrical optics limit is much weaker. The solar cells fabricated from the 1 μm samples own the highest power conversion efficiency of 18.17% due to a better coverage of metal finger lines than the larger ones, and the 200 nm samples have the lowest efficiency of 10.53%.

1. Introduction

The demand for utilizing solar energy has significantly increased in the past few years. Despite relevant photovoltaic technologies being available for more than half a century, the power conversion efficiencies remain relatively low, which lie in the 10–18% range for most of the manufactured output [1, 2]. Up to now, anisotropic etching on (100)-oriented monocrystalline silicon wafers to form square-based pyramid units randomly distributed over the surface using alkaline solution has been proved to be an important and effective way to reduce the reflectivity from the front surface of silicon solar cells and improve the efficiency [3, 4]. As a result, the reflectivity of the textured silicon wafers is about 20% lower than that of the flat ones. The alkaline solution containing sodium hydroxide (NaOH) and isopropyl alcohol (IPA) is widely used in industrial batch process [5]. Normally the average pyramid size is varying from 2 μm to 8 μm , and the corresponding reflectivity is in the range of 14–15% [6–9]. To maintain stability during the texturing process, IPA must be added to the solution frequently to keep it in the same concentration because of the evaporation of IPA. Recent researches have been concentrated on investigating new texturing methods and alternative solutions. Nishimoto and Vallejo textured

silicon wafers by using sodium carbonate solution without adding IPA [10, 11], and the resultant pyramid size was in the range of 4–7 μm . Chu textured silicon wafers using a metal grid with suitable openings on them to confine the hydrogen bubbles, and the structure with the pyramid size of 6 to 9 μm was obtained [12, 13]. However, it was very difficult to fabricate large-area metal grids and control the distance between the grid and silicon wafers. Chen fabricated more uniform pyramids in the size of 1 μm using reactive ion etching (RIE) [14] and achieved a lower reflectivity. Mavrokefalos synthesized inverted nanopyramid applicable for thin silicon films using standard scalable microfabrication techniques based on interference lithography and wet silicon etching [15]. A broadband enhancement in absorption was achieved using that two-step method with prepatterned holes. Ordered pyramidal structures can also be fabricated by colloidal lithography with packed polystyrene spheres [16] or silica colloidal crystals as masks [17]. However, the process was complicated and needed expensive instruments.

As we mentioned above, textured silicon wafers with different pyramid size can only be synthesized using separate method. And the influence of texture feature size on the optical performance and conversion efficiency of silicon solar cells is still unknown. In present study, textured

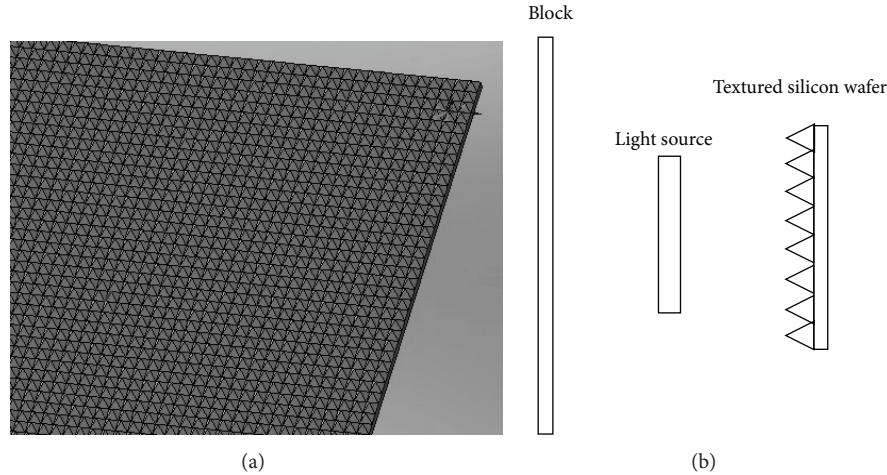


FIGURE 1: (a) Model of textured silicon wafer used in our simulations and (b) schematic diagram of the simulation system. The block behind the light source is used to collect the reflective rays.

monocrystalline silicon wafers with various pyramid sizes (from 200 nm to 10 μm) were fabricated in the same way using different additives. The light-trapping function was evaluated by measuring the reflectivity of different textured wafers. Also the ray-tracing simulations of light-trapping in textured wafers based on geometrical optics were conducted. Finally, solar cells made from different textured wafers were fabricated, and a power conversion efficiency of 18.17% was achieved under optimized conditions.

2. Experimental Section

2.1. Texturing Process. The p-type, (100)-oriented monocrystalline silicon wafers with a resistivity of 0.5–3 $\Omega\cdot\text{cm}$ and a thickness of 200 μm were used in our experiments. Before any etching process, the wafers were cleaned by Radio Corporation America (RCA) method to remove the metal ions and rinsed in deionized water (18 M Ω). Then, the saw damage removal (SDR) was carried out by dipping the wafers into an aqueous solution containing 20 wt% NaOH at 80°C for 10 min and then rinsed thoroughly. The thickness of the wafers decreased to about 170 μm after that procedure. After the pretreatments mentioned above, the wafers were dipped in modified texturing solutions containing NaOH (1.5 wt%), IPA (4 vol%), and one kind of additives (0.1 wt% of Na_2SiO_3 , 0.06 vol% of PEG, and 0.01 vol% of NPE) for 25 min. The reaction vessel was sealed during the whole process in order to prevent the chemicals from evaporation, and no agitation was needed. The inside temperature was kept at 80°C. After etching, the wafers were rinsed again in the flowing deionized water and dried with blowing N_2 . The surface morphology of textured wafers was investigated by a HITACHI S-4800 Scanning Electron Microscope (SEM), and the optical property was measured with a HITACHI U-4100 Spectrophotometer.

2.2. Software Simulations. The process of simulations obeys the law of geometrical optics. When an incident ray arrives at

the surface of the silicon wafer, it is divided into the refraction ray which is absorbed by the silicon and the reflection ray which is reflected back to the air. The intensities of those two kinds of rays depend on the refractive index of silicon [18]. The simulations were performed on TracePro 6.0 developed by Lambda Research Corporation based on geometrical optics. An area of 480 $\mu\text{m} \times 480 \mu\text{m}$ and a thickness of 170 μm were used in our simulations. The light source area was 240 $\mu\text{m} \times 240 \mu\text{m}$ and the wavelength of the light source was between 300 and 1100 nm. A ray of 90000 numbers was randomly generated with a total power of 1 W. The optical property of the reference model could be obtained by testing the reflectivity of a polished monocrystalline silicon wafer. The front surface of the wafer was textured to pyramidal structure with the top angle of 70.6°, while the back surface was polished as shown in Figure 1. The intensity of final reflection ray is much lower than that of initial incident ray because of the repetitious reflection and absorption by the silicon.

2.3. Fabrication of Solar Cell Devices. The solar cells were made from different types of textured wafers and fabricated via a conventional solar cell process, which includes phosphorous doping on the textured front side, thermal diffusion of phosphorus, formation of a silicon nitride antireflection coating on the textured front side, metallization, and firing. The size of the solar cells was 125 mm \times 125 mm. After the device fabrication process, the I-V characteristics under illumination were measured using an Oriel I-V Test Station under Air Mass 1.5 Global (AM 1.5G) illumination conditions at room temperature. All measurements were carried out using 16 samples, and the mean values were used as the results.

3. Results and Discussion

3.1. Morphology of Textured Wafers. Figure 2 shows typical SEM images of the wafers etched in NaOH/IPA solutions

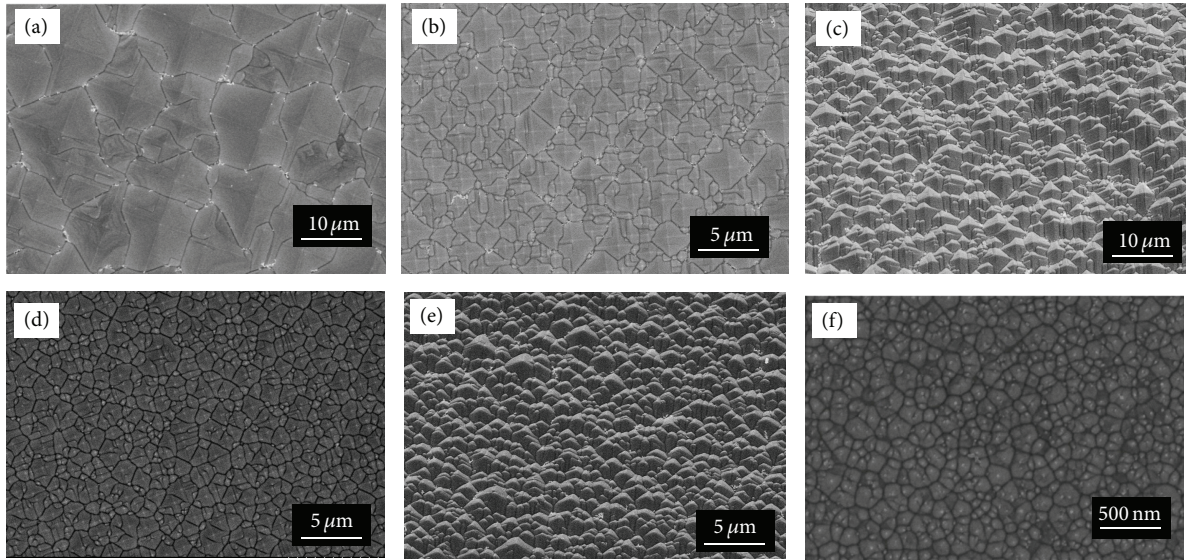


FIGURE 2: Typical SEM images of the wafers textured at 80°C for 25 min with different additives: (a) no additive, (b) and (c) Na_2SiO_3 , (d) and (e) PEG, and (f) NPE.

at 80°C for 25 min. Different additives (Na_2SiO_3 , PEG, and NPE) were used to moderate the reaction speed and reduce the silicon/electrolyte interfacial energy to obtain special pyramid units [5]. Etching without additives was also conducted for comparison. As shown in Figure 2, various sizes of upright pyramids ranging from 10 μm to 200 nm and distributed on the surface of the wafers have been prepared. For the traditional sample etched without additive, typical structure with the pyramid size of about 10 μm can be obtained. However, there are many smaller pyramids around larger ones. For the sample etched with Na_2SiO_3 , the typical pyramid size decreases to about 5 μm , and the uniformity has been improved. Na_2SiO_3 aqueous solution contains large numbers of nonpolar and polar functional parts, which reduces the surface tension of the etching solution and provides sufficient pyramid nucleation points to make the surface arrangement closer. PEG and NPE, which have many hydroxyl groups on the polymer chains, might play the same role as IPA during etching. The etching solutions containing PEG or NPE could be employed to fabricate the pyramid units of about 1 μm or 200 nm, respectively.

3.2. Optical Property of Textured Wafers. The reflectivity of textured wafers with different pyramid sizes was plotted in Figure 3. The 1 μm sample owns the lowest reflectivity of 11.2%, and there is little difference in the reflectivity especially in the visible region, with the exception of the 200 nm sample. The degradation of the reflectance with respect to the geometrical optics limit when the pyramid size is below 300 nm is then related to diffraction effects becoming noticeable, approaching that of a flat surface for smaller sizes [19].

Nearly no dependence of reflectance on the pyramid size could be explained by ray-tracing in the geometrical optics regime when the surface features are much larger than the wavelength. When the pyramid size decreases to

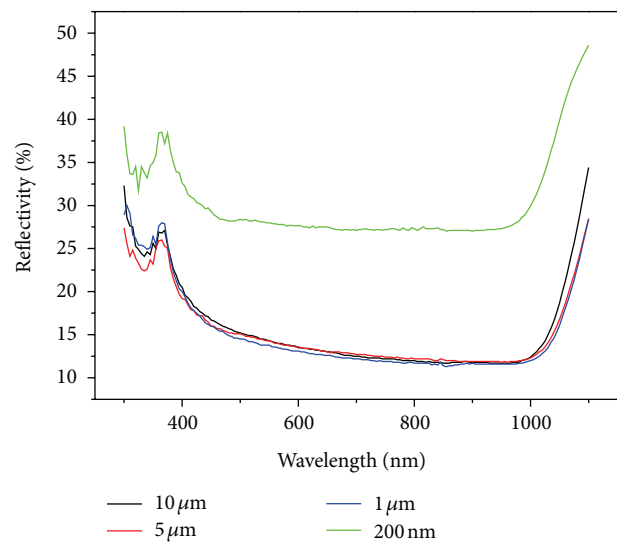


FIGURE 3: The reflectivity of textured wafers with different pyramid sizes.

a value which is lower than the wavelength of the incident light, the law of geometrical optics does not fit for that structure because the light should be seen as a wave. Figure 4 compares the reflectivity of simulation values and chemical-etching wafers with different pyramid sizes (1–10 μm). The wavelength of the incident light was 400, 500, 600, and 700 nm, respectively. The top angle was set to 70.6°, which is similar to the chemical-etching structure. As we can see from the picture, the simulated reflectivity is almost the same for different wafers under every incident light and the value is close to the experimental result. The experimental value is slightly higher than the simulated one because the structure used in our simulations is much more uniform and regular [18].

TABLE 1: Device parameters of the solar cells based on textured wafers with different pyramid sizes.

Wafer type	I_{sc} (A)	V_{oc} (V)	FF	Eff. (%)
10 μm	5.74 (0.0108 ^a)	0.62 (0.0170)	0.77 (0.0117)	17.81 (0.1126)
5 μm	5.72 (0.0108)	0.62 (0.0169)	0.76 (0.0115)	17.62 (0.1114)
1 μm	5.76 (0.0109)	0.63 (0.0166)	0.78 (0.0118)	18.17 (0.1148)
200 nm	4.61 (0.0087)	0.62 (0.0129)	0.56 (0.0085)	10.53 (0.0665)

^aStandard deviation.

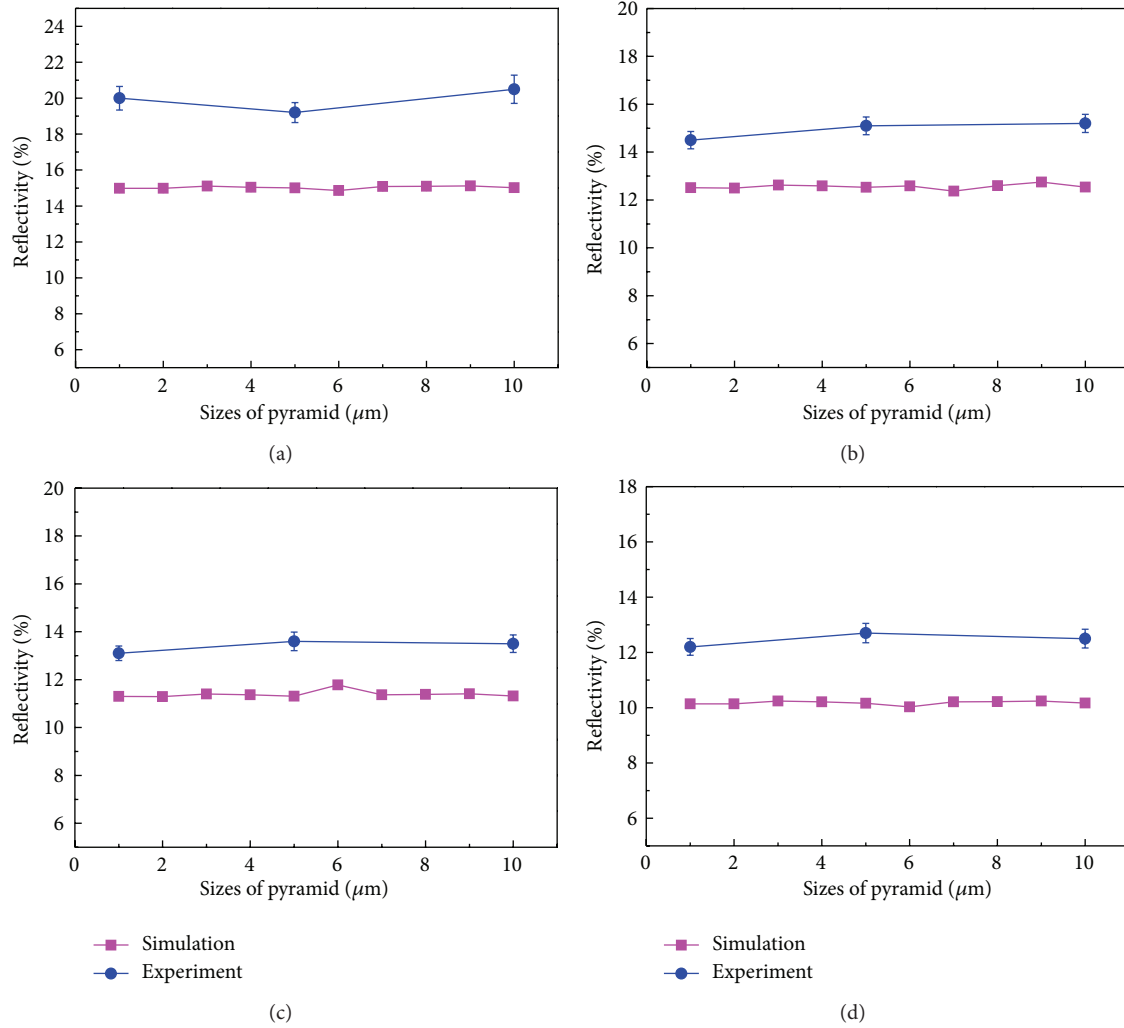


FIGURE 4: Influence of the pyramid size on the reflectivity of textured wafers. The wavelength of the incident light is (a) 400 nm, (b) 500 nm, (c) 600 nm, and (d) 700 nm. Each point and error bar (in blue) represents the mean value and standard deviation of five replicate experiments, respectively.

3.3. Performance of Solar Cell Devices. The solar cells made from different types of textured wafers were fabricated via a conventional solar cell process, and the device parameters are summarized in Table 1. The textured morphology does not affect the open circuit voltage (V_{oc}) for all the devices. However, the cell made from the 200 nm wafer has a short circuit current (I_{sc}) of 4.61 A and an overall conversion efficiency (Eff.) of 10.53%, which are both much lower than those of the other three devices because of high reflection loss and less formed electron-hole pairs [20]. The 10 μm and 5 μm devices have the similar cell performance. Although

different textured samples except the 200 nm one show similar reflectance values, the device fabricated from the 1 μm wafer exhibits a highest conversion efficiency of 18.17% for the possible reason that the printing metal finger lines could have a better coverage on smaller pyramidal structure than larger one [21].

4. Conclusions

Different pyramidal surface structures were realized on etched monocrystalline silicon wafers with modified alkaline

solutions, and the typical pyramid sizes were ranging from 200 nm to 10 μm . Little dependence of reflectance on the size of the textured pyramids is observed except the 200 nm wafer, which is approved by the effective and reliable ray-tracing simulation technology. The solar cells fabricated using the 1 μm wafers own the highest conversion efficiency of 18.17% among all the four kinds of devices due to the better coverage of metal finger lines on smaller pyramidal structures.

References

- [1] A. Polman and H. A. Atwater, "Photonic design principles for ultrahigh-efficiency photovoltaics," *Nature Materials*, vol. 11, no. 3, pp. 174–177, 2012.
- [2] X. Y. Huang, S. Y. Han, W. Huang, and X. G. Liu, "Enhancing solar cell efficiency: the search for luminescent materials as spectral converters," *Chemical Society Reviews*, vol. 42, no. 1, pp. 173–201, 2013.
- [3] M. A. Green, "Crystalline and thin-film silicon solar cells: state of the art and future potential," *Solar Energy*, vol. 74, no. 3, pp. 181–192, 2003.
- [4] L. Forbes, "Texturing, reflectivity, diffuse scattering and light trapping in silicon solar cells," *Solar Energy*, vol. 86, no. 1, pp. 319–325, 2012.
- [5] E. Vazsonyi, K. De Clercq, R. Einhaus et al., "Improved anisotropic etching process for industrial texturing of silicon solar cells," *Solar Energy Materials and Solar Cells*, vol. 57, no. 2, pp. 179–188, 1999.
- [6] R. Barrio, N. González, J. Cárabe, and J. J. Gandía, "Optimisation of NaOH texturisation process of silicon wafers for heterojunction solar-cells applications," *Solar Energy*, vol. 86, no. 3, pp. 845–854, 2012.
- [7] E. Manea, E. Budianu, M. Purica et al., "Optimization of front surface texturing processes for high-efficiency silicon solar cells," *Solar Energy Materials and Solar Cells*, vol. 87, no. 1–4, pp. 423–431, 2005.
- [8] Z. Q. Xi, D. R. Yang, W. Dan, C. Jun, X. H. Li, and D. L. Que, "Investigation of texturization for monocrystalline silicon solar cells with different kinds of alkaline," *Renewable Energy*, vol. 29, no. 13, pp. 2101–2107, 2004.
- [9] Z. Q. Xi, D. R. Yang, and D. L. Que, "Texturization of monocrystalline silicon with tribasic sodium phosphate," *Solar Energy Materials and Solar Cells*, vol. 77, no. 3, pp. 255–263, 2003.
- [10] B. Vallejo, M. González-Mañas, J. Martínez-López, and M. A. Caballero, "On the texturization of monocrystalline silicon with sodium carbonate solutions," *Solar Energy*, vol. 81, no. 5, pp. 565–569, 2007.
- [11] Y. Nishimoto and K. Namba, "Investigation of texturization for crystalline silicon solar cells with sodium carbonate solutions," *Solar Energy Materials and Solar Cells*, vol. 61, no. 4, pp. 393–402, 2000.
- [12] A. K. Chu, J. S. Wang, Z. Y. Tsai, and C. K. Lee, "A simple and cost-effective approach for fabricating pyramids on crystalline silicon wafers," *Solar Energy Materials and Solar Cells*, vol. 93, no. 8, pp. 1276–1280, 2009.
- [13] H. H. Li, W. F. Liu, A. Liu, F. Qiao, Z. Hu, and Y. Liu, "Metal grids-based texturization of monocrystalline silicon wafers for solar cells," *Solar Energy Materials and Solar Cells*, vol. 94, no. 6, pp. 942–945, 2010.
- [14] H. L. Chen, W. Fan, C. C. Cheng, C. H. Lin, and K. T. Huang, "Fabrication of texturing antireflection structures in solar cells by using the defocusing exposure in optical lithography," *Journal of the Electrochemical Society*, vol. 153, no. 9, pp. G802–G806, 2006.
- [15] A. Mavrokefalos, S. E. Han, S. Yerci, M. S. Branham, and G. Chen, "Efficient light trapping in inverted nanopillar thin crystalline silicon membranes for solar cell applications," *Nano Letters*, vol. 12, no. 6, pp. 2792–2796, 2012.
- [16] H. L. Chen, S. Y. Chuang, C. H. Lin, and Y. H. Lin, "Using colloidal lithography to fabricate and optimize sub-wavelength pyramidal and honeycomb structures in solar cells," *Optics Express*, vol. 15, no. 22, pp. 14793–14803, 2007.
- [17] X. M. Zhang, J. H. Zhang, Z. Y. Ren et al., "Morphology and wettability control of silicon cone arrays using colloidal lithography," *Langmuir*, vol. 25, no. 13, pp. 7375–7382, 2009.
- [18] X.-S. Hua, Y.-J. Zhang, and H.-W. Wang, "The effect of texture unit shape on silicon surface on the absorption properties," *Solar Energy Materials and Solar Cells*, vol. 94, no. 2, pp. 258–262, 2010.
- [19] F. Llopis and I. Tobías, "Influence of texture feature size on the optical performance of silicon solar cells," *Progress in Photovoltaics*, vol. 13, no. 1, pp. 27–36, 2005.
- [20] H. Sai, Y. Kanamori, K. Arafune, Y. Ohshita, and M. Yamaguchi, "Light trapping effect of submicron surface textures in crystalline Si solar cells," *Progress in Photovoltaics*, vol. 15, no. 5, pp. 415–423, 2007.
- [21] U. Gangopadhyay, K. H. Kim, S. K. Dhungel et al., "A novel low cost texturization method for large area commercial monocrystalline silicon solar cells," *Solar Energy Materials and Solar Cells*, vol. 90, no. 20, pp. 3557–3567, 2006.

Research Article

Synthesis of Coral-Like, Straw-Tied-Like, and Flower-Like Antimony Sulfides by a Facile Wet-Chemical Method

Jutarat Kavinchan,¹ Titipun Thongtem,² Somchai Thongtem,^{3,4} and Eksuree Saksornchai¹

¹ Division of Chemistry, School of Science, University of Phayao, Phayao 56000, Thailand

² Department of Chemistry, Faculty of Science, Chiang Mai University, Chiang Mai 50200, Thailand

³ Department of Physics and Materials Science, Faculty of Science, Chiang Mai University, Chiang Mai 50200, Thailand

⁴ Materials Science Research Center, Faculty of Science, Chiang Mai University, Chiang Mai 50200, Thailand

Correspondence should be addressed to Titipun Thongtem; tpthongtem@yahoo.com and Somchai Thongtem; schthongtem@yahoo.com

Received 30 May 2013; Revised 26 June 2013; Accepted 27 June 2013

Academic Editor: Jiamin Wu

Copyright © 2013 Jutarat Kavinchan et al. This is an open access article distributed under the Creative Commons Attribution License, which permits unrestricted use, distribution, and reproduction in any medium, provided the original work is properly cited.

Antimony sulfide (Sb_2S_3) was successfully synthesized from antimony chloride (SbCl_3) and sodium thiosulfate pentahydrate ($\text{Na}_2\text{S}_2\text{O}_3 \cdot 5\text{H}_2\text{O}$) in ethylene glycol (EG) without using any template by a facile wet-chemical method. X-ray diffraction (XRD), scanning electron microscopy (SEM), and transmission electron microscopy (TEM) show that the products were orthorhombic Sb_2S_3 nanorods forming the coral-like, straw-tied-like, and flower-like architectures with the nanorods growing along the [001] direction. The energy gap (E_g) was determined by UV-visible absorption to be 1.52 eV.

1. Introduction

Sb_2S_3 is an orthorhombic V-VI semiconductor with 1.78–2.50 eV direct band gap, covering the visible and near IR range of solar spectrum [1]. It has a potential application for solar cells and thermoelectric and optoelectronic devices [1, 2]. A number of processes were used to synthesize antimony sulfide with different morphologies: single-crystal Sb_2S_3 nanotubes via EDTA-assisted hydrothermal route [1], nanocrystalline Sb_2S_3 by microwave-assisted synthesis [2], Sb_2S_3 peanut-shaped superstructures [3], rod-like Sb_2S_3 dendrites [4] and Sb_2S_3 nanorods [5] by hydrothermal reaction, double sheaf-like Sb_2S_3 by copolymer-assisted hydrothermal synthesis [6], Sb_2S_3 nanowires [7] and Sb_2S_3 nanoribbons [8] by solvothermal route, Sb_2S_3 nanowires by PEG-assisted solvothermal process [9], and orthorhombic Sb_2S_3 twin flowers in the solutions containing CTAB by a cyclic microwave radiation [10]. Crystal structures, crystalline degree, different phases, purities, defects, and others can play a role in the properties of materials, such as strength and corrosion resistance, including electrical and thermal conductivities. Previously, Sb_2S_3 with different morphologies was successfully synthesized by

different methods: straw-tied-like architectures by a one-pot hydrothermal method both with and without CTAB as an additive [11], hydrothermal synthesis [12], a novel precursor—solvothermal—pyrolysis route [13], and a refluxing polyol process of the solution containing PVP as a surfactant [14], including flower-like Sb_2S_3 by a refluxing polyol process of the solution containing PVP as a surfactant [14] and a refluxing method of the solution containing PEG400 as a surfactant [15]. The above methods require high temperature and pressure, different additives, and complicated equipment. Thus, the purpose of the present research is to synthesize Sb_2S_3 with different morphologies by a facile wet-chemical method without using a template. This method is novel, very simple, and inexpensive. The influences of the experimental parameters on the structures and morphologies were also investigated.

2. Experiment

A wet-chemical route was used in this research of which 0.002 mol SbCl_3 (assay: 99%, Sigma-Aldrich) and 0.003 mol

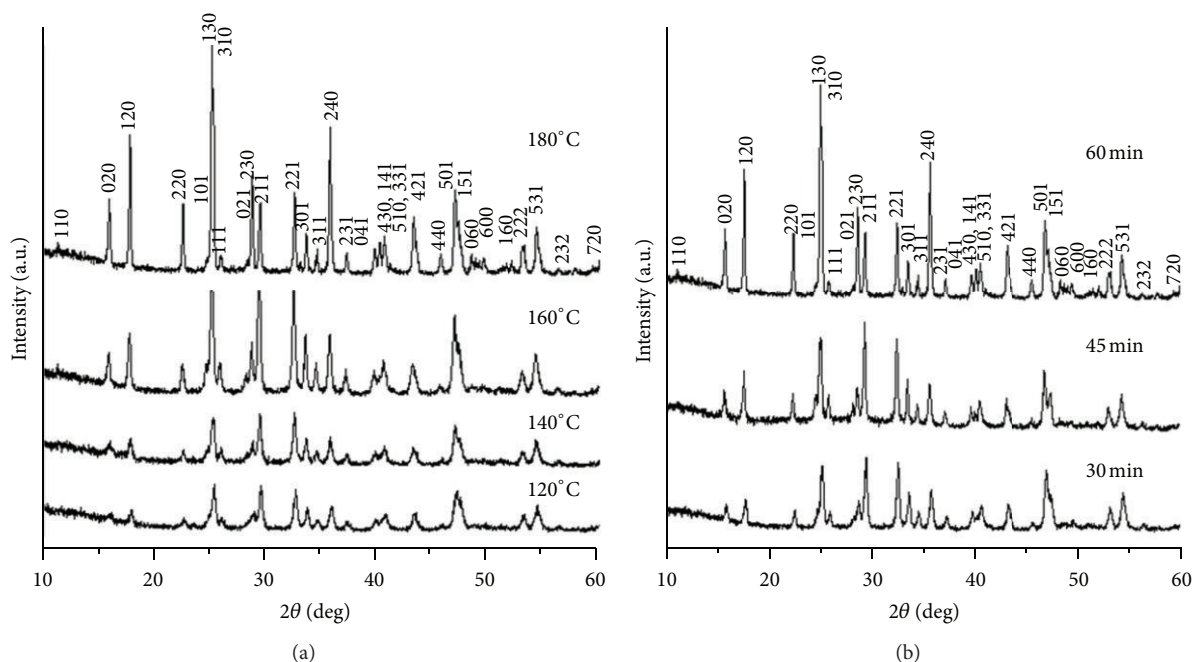


FIGURE 1: XRD spectra of the products synthesized at (a) 120, 140, 160, and 180 °C for 60 min and (b) 180 °C for 30, 45, and 60 min in EG.

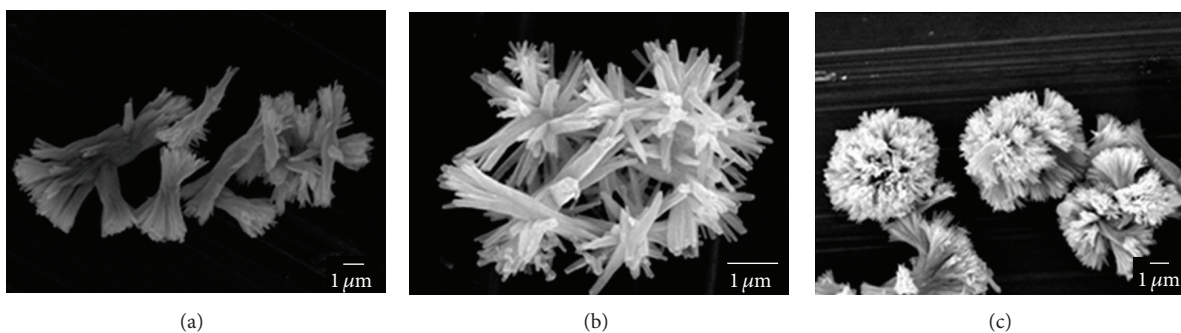


FIGURE 2: SEM images of Sb_2S_3 synthesized in EG at (a)–(c) 120 °C, 140 °C, and 160 °C for 60 min, respectively.

$\text{Na}_2\text{S}_2\text{O}_3 \cdot 5\text{H}_2\text{O}$ (assay: $\geq 99.5\%$, Sigma-Aldrich) were dissolved in 30 mL ethylene glycol (EG, assay: 99.5%, QREc) and mixed homogeneously by 15 min stirring in a beaker at room temperature. Subsequently, orange colloidal complexes immediately formed. To synthesize Sb_2S_3 with different morphologies, each of the solutions was directly heated in an electric oven at different constant temperatures of 180, 160, 140, and 120 °C for 60 min, including at a constant temperature of 180 °C for 30 and 45 min. Finally, black precipitates were synthesized, separated by filtration, washed with absolute ethanol, and dried at 70 °C for 24 h.

The products were characterized by an X-ray diffractometer (XRD, SIEMENS D500) operating at 20 kV, 15 mA, and using Cu-K_α line from a copper target; a scanning electron microscope (SEM, JEOL JSM-6335F) equipped with an energy dispersive X-ray (EDX) analyzer operating at 15 kV; a transmission electron microscope (TEM, JEOL JEM-2010) as well as a high-resolution transmission electron microscope

(HRTEM) and selected area electron diffractometer (SAED) operating at 200 kV; and a UV-visible spectrometer (Lambda 25 PerkinElmer) using a UV lamp with the resolution of 1 nm.

3. Results and Discussion

Figure 1 shows XRD spectra of the products synthesized under different temperatures and lengths of time. At different temperatures of 180, 160, 140, and 120 °C for 60 min, the products were specified as orthorhombic Sb_2S_3 (JCPDS number 06-0474) [16] with pure crystal. To save energy consumption, the temperature was reduced in series of steps from 180 to 120 °C. The results show that the intensity of XRD spectra became lowered and the crystalline degree was lessened. At 180 °C for different lengths of time in EG, XRD spectra became sharper and narrower by increasing the lengths of time from 30 to 60 min, and the crystalline degree was improved in sequence.

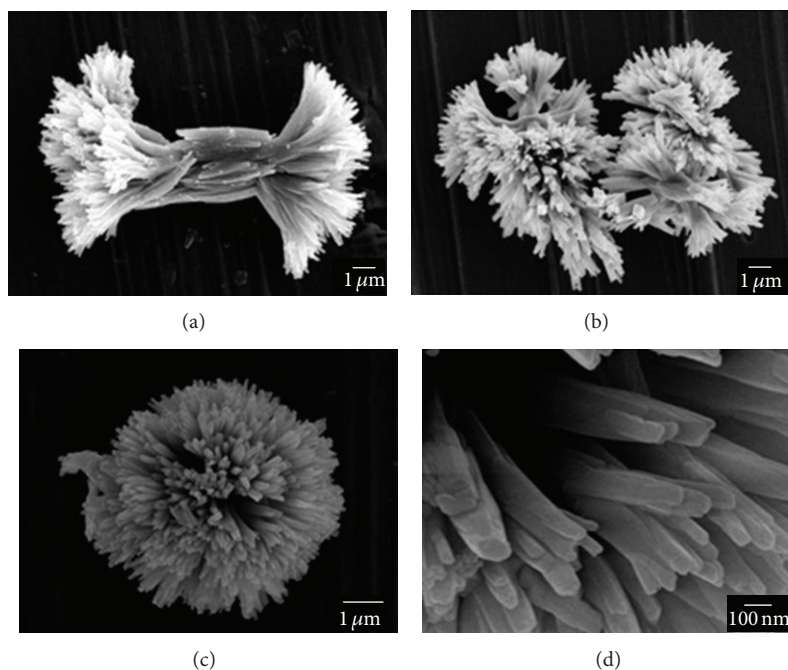


FIGURE 3: SEM images of Sb_2S_3 synthesized in EG at 180°C for (a) 30 min, (b) 45 min, and (c, d) 60 min.

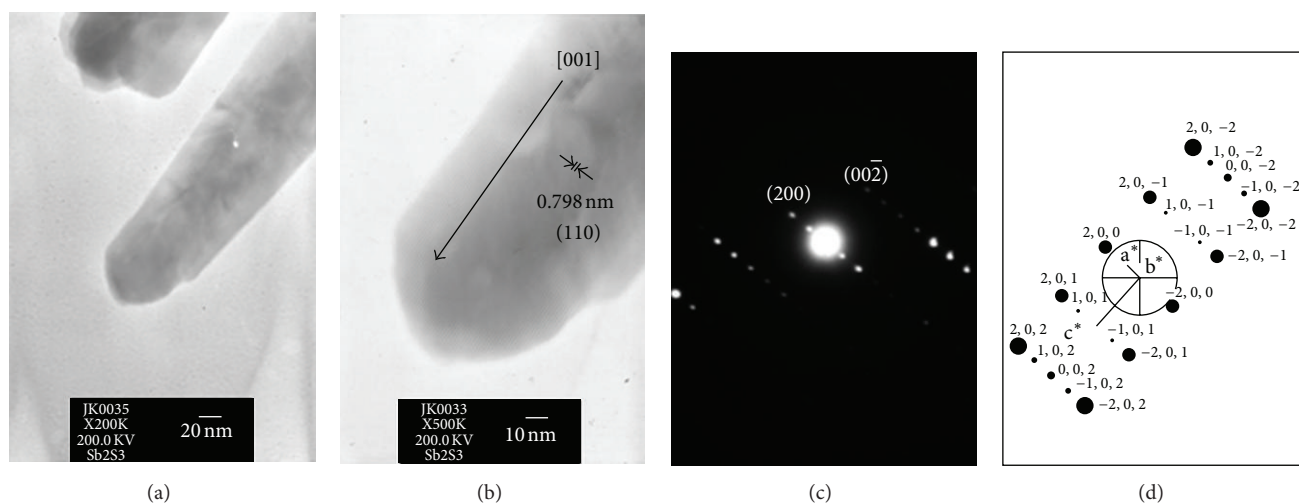
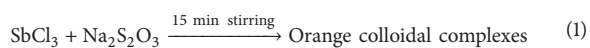
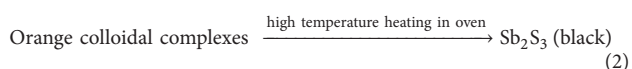


FIGURE 4: (a), (b) TEM and HRTEM images, (c) SAED, and (d) simulated patterns of Sb_2S_3 synthesized by wet-chemical method at 180°C for 60 min.

In the present research, SbCl_3 and $\text{Na}_2\text{S}_2\text{O}_3$ were mixed in EG by 15 min stirring, and orange colloidal complexes formed:



The orange colloidal complexes were the intermediate products, which were subsequently transformed into Sb_2S_3 black precipitates by heating at high temperatures:



SEM images (Figures 2 and 3) show Sb_2S_3 products synthesized at different temperatures and lengths of time. Their surfaces were smooth and clean. Increasing in the temperatures and lengths of time has the influence on the change in morphology of the products. For those synthesized at different temperatures, the as-produced Sb_2S_3 was straw-tied-like architecture at 120°C for 60 min. Then, the temperature was increased to 140°C with the length of time kept constant for 60 min; the product transformed into coral-like architecture. Finally, the products gradually transformed into nanostructured flowers at 160 and 180°C within 60 min. Moreover, the length of time also has the influence on

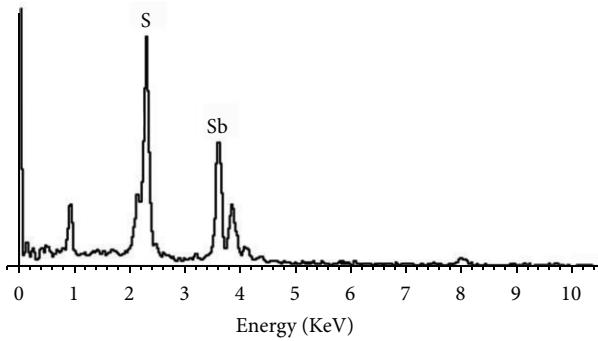


FIGURE 5: EDX spectrum of Sb_2S_3 synthesized by wet-chemical method at 180°C for 60 min.

the morphology formation of Sb_2S_3 . SEM images of the products at 180°C for different lengths of time were compared. The Sb_2S_3 product, synthesized at 180°C for 30 min, was straw-tied-like architecture with a number of rods split at their ends. The extent of opening or splitting was influenced by the temperatures and lengths of time. As time passed, nanorods formed, grew, and split at their ends [17, 18]. Hence, the flower-like architecture began to form at 180°C for 45 min and constantly formed at 180°C for 60 min. At this stage, the as-synthesized product became complete flowers. The present phenomenon is similar to the report of Zhu et al. [15] who stated that flower-like structured Sb_2S_3 could be transformed into nanorods by increasing in the length of time from 1 to 2 h during 85°C refluxing of the solutions containing PEG400. Previously, orthorhombic Sb_2S_3 twin flowers, composed of single crystalline square nanorod petals, were successfully synthesized in the solutions containing CTAB as a template and splitting agent by a cyclic microwave radiation [10], including the flower-like Sb_2S_3 by refluxing polyol process of the solution containing PVP as a surfactant [14] and by refluxing method of the solution containing PEG400 as a surfactant [15]. But for the present research, Sb_2S_3 coral-like and flower-like architectures were successfully synthesized by a facile wet-chemical method without the use of any template and splitting agent.

TEM and HRTEM images, SAED, and simulated patterns [19] of Sb_2S_3 synthesized in EG at 180°C for 60 min are shown in Figure 4. TEM and HRTEM images show the flower-like architecture which consisted of nanorods. SAED and simulated patterns of the synthesized Sb_2S_3 also show that each flower was composed of Sb_2S_3 nanorods, growing along the [001] direction (along the *c*-axis)—in accordance with the growth direction characterized by Yang et al. [2], Wang et al. [11], Ota et al. [17], and Hu et al. [20]. The (110) planes along the growth direction were also detected, showing that the nanorod was single crystal. In addition, the interpreted SAED pattern, composed of bright spots in lattice array, was specified that each nanorod was single crystal, corresponding to orthorhombic Sb_2S_3 [16]. To justify the presence of Sb_2S_3 single crystal, its pattern was simulated [19] and appears as systematic spots—in good accordance with the above interpretation.

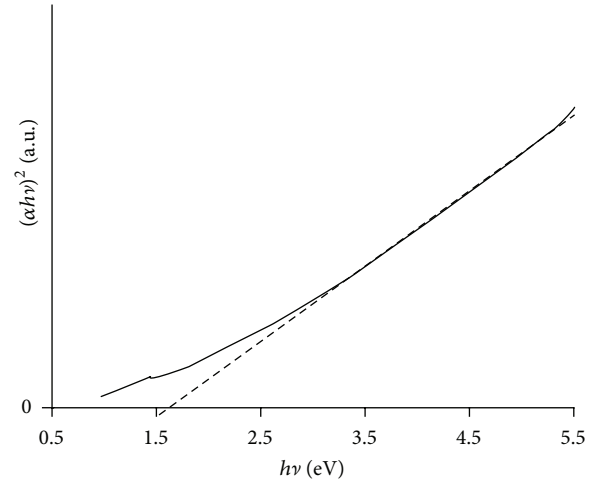


FIGURE 6: The $(\alpha h\nu)^2$ and $h\nu$ plot of Sb_2S_3 synthesized by wet-chemical method at 180°C for 60 min.

Figure 5 shows the EDX spectroscopy measurement of Sb_2S_3 synthesized at 180°C for 60 min. It shows the characteristic peaks of only S ($K_{\alpha 1,2}$ at 2.31 keV) and Sb (L_{α} at 3.61 keV and $L_{\beta 1}$ at 3.84 keV), suggesting that the product contains only antimony and sulfur elements. Quantitative EDX analysis shows that the atomic ratio of Sb:S was 40.85:59.15, close to 2:3, confirming that the product was really crystalline Sb_2S_3 . It should be noted that Cu of the stub was also detected at 0.93 keV (L_{α}) and 8.04 keV ($K_{\alpha 1,2}$).

An optical absorption experiment has been carried out using a UV-vis absorption spectrometer, which provides an effective method for explaining some features concerning the band structure of Sb_2S_3 nanorods. Figure 6 shows the $(\alpha h\nu)^2$ and $(h\nu)$ plot for the direct allowed transition, where α , h , and ν are the total absorption coefficient, Planck constant, and photonic frequency, respectively [1, 15]. In this research, the photonic wave attenuated through the solid. The change of photonic absorption was controlled by two photonic energy ranges. When the photonic energy is higher than the energy gap, absorption was linearly increased with the increasing of photonic energy. But for the photonic energy with less than the energy gap, the absorption became different from linearity which was influenced by the absorption relating to defect levels between the valence and conduction bands of the product. Its band gap, determined by extrapolation of the linear curve to zero absorbance, corresponds to 1.52 eV—in accordance with 1.52 eV band gap of Sb_2S_3 nanorods determined by Zhu et al. [15]. It should be noted that this value is less than the 2.43 eV of the as-deposited thin film [21] and 1.95 eV thin film deposited on the 300 K substrate [22], which were lessened by high-temperature annealing [21, 22]. This value is blue shift relative to 1.28 eV energy gap of Bi_2S_3 [23]. Generally, different morphologies and crystalline degrees can play a role in the properties of products, such as energy gap and photoluminescence (PL) [6, 24–28]. The value of the band-gap energy for Sb_2S_3 nanorods is close to the optimum value for the photovoltaic conversion, solar energy converters, and optical nanodevices [15].

4. Conclusions

The coral-like, straw-tied-like, and flower-like Sb_2S_3 products were successfully synthesized by a facile wet-chemical method in EG. The phase was detected by XRD and SAED. SEM and TEM revealed the transformation of the as-synthesized straw-tied-like at 120°C into flower-like at 180°C . The flowers were good crystalline nanorods with 1.52 eV direct band gap.

Acknowledgments

The authors wish to thank the Thailand's Office of the Higher Education Commission for providing financial support through the National Research University (NRU) project for Chiang Mai University and the National Nanotechnology Center (NANOTEC), National Science and Technology Development Agency, for providing financial support through the Project P-10-11345.

References

- [1] G. Y. Chen, W. X. Zhang, and A. W. Xu, "Synthesis and characterization of single-crystal Sb_2S_3 nanotubes via an EDTA-assisted hydrothermal route," *Materials Chemistry and Physics*, vol. 123, no. 1, pp. 236–240, 2010.
- [2] H. Yang, X. Su, and A. Tang, "Microwave synthesis of nanocrystalline Sb_2S_3 and its electrochemical properties," *Materials Research Bulletin*, vol. 42, no. 7, pp. 1357–1363, 2007.
- [3] Q. Han, L. Chen, W. Zhu et al., "Synthesis of Sb_2S_3 peanut-shaped superstructures," *Materials Letters*, vol. 63, no. 12, pp. 1030–1032, 2009.
- [4] L. Chen, W. Zhu, Q. Han, X. Yang, L. Lu, and X. Wang, "Preparation of rod-like Sb_2S_3 dendrites processed in conventional hydrothermal," *Materials Letters*, vol. 63, no. 15, pp. 1258–1261, 2009.
- [5] C. Li, X. Yang, Y. Liu, Z. Zhao, and Y. Qian, "Growth of crystalline Sb_2S_3 nanorods by hydrothermal method," *Journal of Crystal Growth*, vol. 255, no. 3–4, pp. 342–347, 2003.
- [6] C. Pilapong, T. Thongtem, and S. Thongtem, "Hydrothermal synthesis of double sheaf-like Sb_2S_3 using copolymer as a crystal splitting agent," *Journal of Alloys and Compounds*, vol. 507, no. 2, pp. L38–L42, 2010.
- [7] Z. R. Geng, M. X. Wang, G. H. Yue, and P. X. Yan, "Growth of single-crystal Sb_2S_3 nanowires via solvothermal route," *Journal of Crystal Growth*, vol. 310, no. 2, pp. 341–344, 2008.
- [8] Y. Xinyu, Z. Jiasong, L. Lijun, L. Xiaojuan, L. Haitao, and X. Weidong, "L-cystine-assisted growth of Sb_2S_3 nanoribbons via solvothermal route," *Materials Chemistry and Physics*, vol. 118, no. 2–3, pp. 432–437, 2009.
- [9] G. Wang and C. L. Cheung, "Building crystalline Sb_2S_3 nanowire dandelions with multiple crystal splitting motif," *Materials Letters*, vol. 67, no. 1, pp. 222–225, 2012.
- [10] J. Kavinchan, T. Thongtem, and S. Thongtem, "Cyclic microwave assisted synthesis of Sb_2S_3 twin flowers in solutions containing a template and splitting agent," *Chalcogenide Letters*, vol. 9, no. 9, pp. 365–370, 2012.
- [11] D. Wang, C. Song, X. Fu, and X. Li, "Growth of one-dimensional Sb_2S_3 and Sb_2Se_3 crystals with straw-tied-like architectures," *Journal of Crystal Growth*, vol. 281, no. 2–4, pp. 611–615, 2005.
- [12] P. G. Sheikhiabadi, M. Salavati-Niasari, and F. Davar, "Hydrothermal synthesis and optical properties of antimony sulfide micro and nano-size with different morphologies," *Materials Letters*, vol. 71, pp. 168–171, 2012.
- [13] M. Mo, Z. Zhu, X. Yang et al., "Growth of single-crystal Sb_2S_3 nanorods, dendrites and straw-tied-like architectures via a precursor-solvothermal-pyrolysis route," *Journal of Crystal Growth*, vol. 256, no. 3–4, pp. 377–382, 2003.
- [14] R. Zhang, X. Chen, M. Mo et al., "Morphology-controlled growth of crystalline antimony sulfide via a refluxing polyol process," *Journal of Crystal Growth*, vol. 262, no. 1–4, pp. 449–455, 2004.
- [15] Q. Zhu, M. Gong, C. Zhang, G. Yong, and S. Xiang, "Preparation of Sb_2S_3 nanomaterials with different morphologies via a refluxing approach," *Journal of Crystal Growth*, vol. 311, no. 14, pp. 3651–3655, 2009.
- [16] Powder Diffraction File, JCPDS-ICDD, 12 Campus Boulevard, Newtown Square, PA 19073-3273, USA, 2001.
- [17] J. Ota, P. Roy, S. K. Srivastava, B. B. Nayak, and A. K. Saxena, "Morphology evolution of Sb_2S_3 under hydrothermal conditions: flowerlike structure to nanorods," *Crystal Growth and Design*, vol. 8, no. 6, pp. 2019–2023, 2008.
- [18] J. Tang and A. P. Alivisatos, "Crystal splitting in the growth of Bi_2S_3 ," *Nano Letters*, vol. 6, no. 12, pp. 2701–2706, 2006.
- [19] C. Boudias and D. Monceau, *CaRIne Crystallography 3.1*, DIVERGENT S.A., Compiègne, France, 1989–1998.
- [20] H. Hu, M. Mo, B. Yang et al., "Solvothermal synthesis of Sb_2S_3 nanowires on a large scale," *Journal of Crystal Growth*, vol. 258, pp. 106–112, 2003.
- [21] N. J. Mathew, R. Oommen, and U. P. Rajalakshmi, "Optical and electrical studies on thermally evaporated Sb_2S_3 thin films," *Chalcogenide Letters*, vol. 7, pp. 701–706, 2010.
- [22] N. Tigau, V. Ciupina, G. I. Rusu, G. Prodan, and E. Vasile, "Influence of substrate temperature on the structural and optical properties of Sb_2S_3 thin films," *Romanian Journal of Physics*, vol. 50, pp. 859–868, 2005.
- [23] J. Lu, Z. Wang, Y. Zhang, and X. Zhou, "Hydrothermal synthesis of Bi_2S_3 nanorods from a single-source precursor and their promotional effect on the photocatalysis of TiO_2 ," *Journal of Nanomaterials*, vol. 2013, Article ID 125409, 6 pages, 2013.
- [24] T. Thongtem, S. Jattukul, C. Pilapong, and S. Thongtem, "Hydroxyethyl cellulose-assisted hydrothermal synthesis of Bi_2S_3 urchin-like colonies," *Current Applied Physics*, vol. 12, no. 1, pp. 23–30, 2012.
- [25] S. Thongtem, C. Wichasilp, and T. Thongtem, "Transient solid-state production of nanostructured CuS flowers," *Materials Letters*, vol. 63, no. 28, pp. 2409–2412, 2009.
- [26] S. Kaowphong, T. Thongtem, O. Yayapao, and S. Thongtem, "The effect of solvents on ZnS nanostructures synthesized by biomolecule-assisted solvothermal method," *Materials Letters*, vol. 65, no. 23–24, pp. 3405–3407, 2011.
- [27] T. Thongtem, A. Phuruangrat, and S. Thongtem, "Free surfactant synthesis of microcrystalline CdS by solvothermal reaction," *Materials Letters*, vol. 61, no. 14–15, pp. 3235–3238, 2007.
- [28] T. Thongtem, C. Pilapong, and S. Thongtem, "Solvothermal synthesis of CdS nanorods using hydroxyethyl cellulose as a template," *Current Applied Physics*, vol. 9, no. 6, pp. 1272–1277, 2009.

Research Article

Structure and Properties of Nanostructured (Ti-Hf-Zr-V-Nb)N Coatings

Alexander D. Pogrebnjak

Department of Nanoelectronic, Sumy State University, 2, Rymsky Korsakov Street, Sumy 40007, Ukraine

Correspondence should be addressed to Alexander D. Pogrebnjak; alexp@i.ua

Received 22 February 2013; Revised 29 April 2013; Accepted 14 May 2013

Academic Editor: Jiamin Wu

Copyright © 2013 Alexander D. Pogrebnjak. This is an open access article distributed under the Creative Commons Attribution License, which permits unrestricted use, distribution, and reproduction in any medium, provided the original work is properly cited.

Nanostructured coatings of (Ti-Zr-Hf-V-Nb)N were obtained by the Cathodic Arc Vapor Deposition (CAVD) method. To investigate these coatings, a number of complementary methods of elemental and structural analysis were used, namely, slow positron beam (SPB), proton microbeam (μ -PIXE), micro- and nanoelectron beam (EDS and SEM analyses), and X-ray diffraction method (XRD), including method of " α - $\sin^2\varphi$ " measurement of a stress-strain state (X-ray strain measurement). Additionally, the texture of coatings before and after annealing up to 873 K (for time of annealing $\tau = 30$ min) was also investigated. It was shown that increasing of stress-strain state in the coating during deposition increases the resistance to oxidation at high temperatures of annealing. It was also found that the redistribution of elements and defects, as well as their alignment (segregation), appeared due to thermally stimulated diffusion. It is also connected with the process of spinodal segregation near grain boundaries and interfaces around the grains and subgrains.

1. Introduction

Due to the low grain size (≤ 10 nm) and the great importance of the boundary zones (a surface boundary in particular) surrounding individual grains and nanograin joints, behavior and properties of nanocomposites crucially differ from conventional materials with the grain sizes of more than 100 nm [1–7]. Therefore, fabrication of new combinations of nanocomposite materials (nanostructured coatings) based on (Ti-Zr-Hf-V-Nb)N using cathodic vacuum-arc deposition and studies of their physical and mechanical properties turns to be a very promising trend of modern material science [7–24]. On the other hand, the theory of multicomponent high entropy alloys, which demonstrated improved thermal stability, was already proposed and demonstrated experimentally [5–7, 14, 20–23]. According to this theory, the high mixing entropy can stabilize the formation of a single-phase state in the form of a nonordered solid solution phase and prevent the formation of intermetallic phases in the process of crystallization. Thus, the fabricated highentropy alloys may

feature an increased strength combined with good resistance to oxidation and corrosion. Therefore, the alloy must consist of five or more basic elements with the atomic concentration between 5 and 40%.

Thus, such elements as V and Nb, which stabilize the bcc lattice, and refractory composites of Hf, Zr, and Ti (due to their high affinity for nitrogen) [24–32] have crucial effect on formation of a nitride phase in high entropy one-component alloy.

The goal of this research is the investigation of structure and tribological properties of nanostructured (Ti-Hf-Zr-V-Nb)N coatings before and after annealing up to 873°K and also the analysis of the redistribution of defects and impurities in these coatings.

In this work, cathodes of high entropy alloys Ti-Zr-Hf-V-Nb were fabricated using vacuum arc melting in atmosphere of high purity argon. Melting was carried out by a nonexpensive tungsten electrode into a copper water-cooled tank (hearth). The obtained ingots were homogenized by 6-7 time melting with a cooling rate of 50 K/s [14].

2. Experimental Details

Deposition of coatings was performed by the cathode vacuum-arc deposition method on the apparatus Bulat-6 [1] under constant negative potential $U_s = (-40-200)$ V, which was applied to a substrate. The arc current did not exceed 85 A, and the pressure of residual gas was 0.0066 Pa. Deposition conditions, which were employed for all of samples, are presented in Table 1.

Thermal annealing of coatings was performed in the furnace VacuTherm-Ceram VT 1200 at temperature 873 K for 30 minutes. Residual pressure P was 100 Pa.

The elemental composition was studied with scanning electron microscope (SEM) with EDX microanalysis JEOL-7000 F (Japan). To perform the element analysis over a sample depth, we employed the Rutherford backscattering (RBS) method with He^+ ions of 1.7 MeV (the scattering angle was $\theta = 170^\circ$) with a normal fall of probing ions to the surface of coated samples. The energy resolution of detector was 16 keV. A dose of helium ions was $5 \mu\text{Ci}$. To interpret the RBS spectra and to obtain the element profiles over the coatings depth, we employed standard software [24].

A positron annihilation spectroscopy (PAS) (Halle, Germany) was used for analysis of vacancy type defects in the coating. Using slow positron microbeam was obtained by positron annihilation energy spectra, which let us calculate an important characteristic of material, the S -parameter of Doppler broadening of an annihilation peak. It depends on energy of the incident positron beam (30 keV), that is, on the depth of the analysis [33].

Proton microbeam ($\mu\text{-PIXE}$) was employed for elemental analysis of coatings. The initial energy of an electrostatic accelerator IAP (Sumy) was 1.4 MeV with the beam size of $0.4 \mu\text{m}$ (the charge was 3×10^{-10} C/pixel, the raster was 50×50 , and the step size was $0.5 \mu\text{m}$) [34]. We obtained maps of the elements Ti, Zr, Hf, V, Nb distribution before (as deposited) and after annealing up to 873 K.

The phase composition and structural studies were performed on the X-ray diffractometer DRON-3M and Rigaku RINT-2500, MDG Japan, in the filtered radiation of Cu-K α using in the secondary beam graphite monochromator. The diffraction spectra were surveyed in the point-by-point scanning mode with a step $2\theta = 0.05-0.1^\circ$. We also employed the diffraction of X-rays using a grazing incidence beam, in Cr emission, at angle 3° . In order to study the stress-strain state of the coatings, we employed the method of X-ray strain measurements (" $\alpha\text{-sin}^2\varphi$ " method) and its modifications, which are commonly applied to the coatings with strong axial texture [10-14].

Tribological tests were performed on automated friction machine "Tribometer," CSM Instruments in air by "ball-disk" scheme at 293 K. The ball with diameter of 6 mm was made of sintered certificated material- Al_2O_3 . The coatings were deposited on steel (45 HRC = 55) discs with a diameter of 50 mm and a thickness of 5 mm. The load was 3.0 N, sliding velocity 10 cm/s.

3. Results and Discussion

The (Ti, Hf, Zr, V, Nb)N coating had a face-centered cubic (FCC) crystal structure rather than coexisting separated nitrides. TiN, HfN, ZrN, VN, and NbN had an FCC structure. Thus, the (Ti, Hf, Zr, V, Nb)N coating also exhibited an FCC solid solution structure, in which the Ti, Hf, Zr, V, and Nb atoms were randomly distributed over the metal sublattice. The same phenomena were also reported for as-deposited mixtures of FCC forming multiprincipal element nitrides such as AlCrTsTiZr [35], AlCrNbSiTiV [36], and TiVCrZrY [37]. This result not only implied the formation of a solid solution from all constituted nitrides, but also confirmed the effect of high mixing entropy on the simplification of the crystal structure.

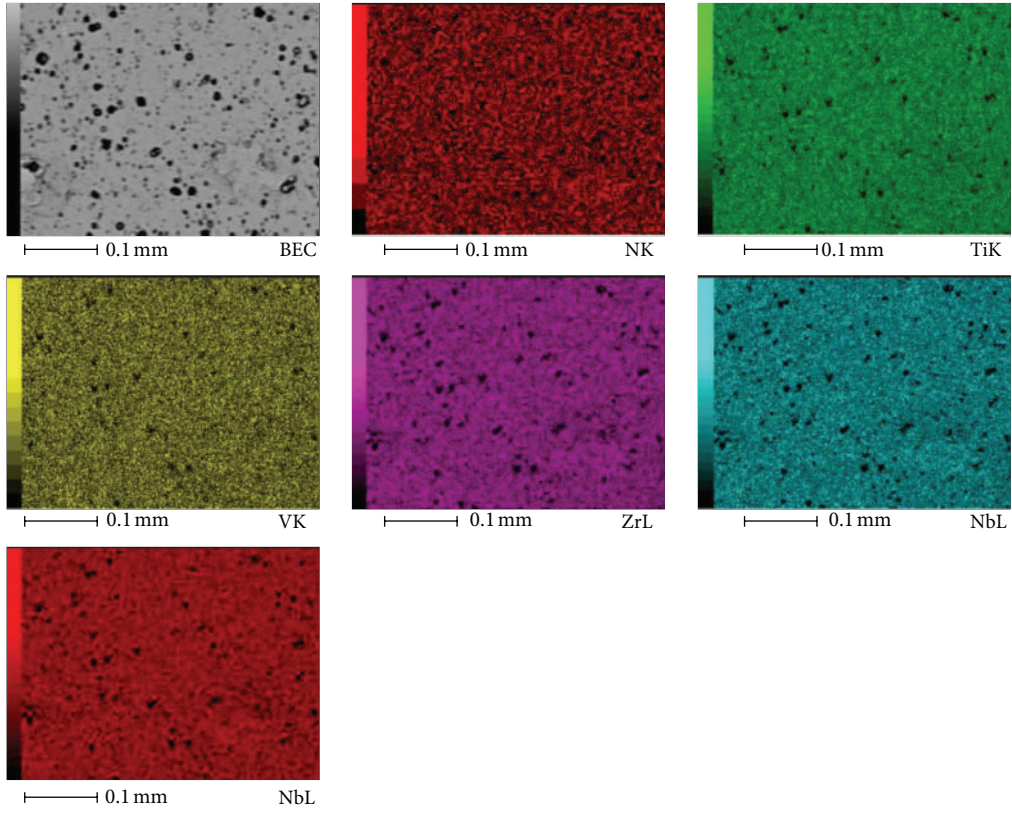
The solid solution phase with an FCC structure was also thermodynamically stable because it did not decompose or form other compounds even during annealing up to 873 K for 30 min. The stability of the FCC solid solution phase was also due to the high entropy effect. In addition, as shown in the paper, the crystal size and lattice constant are shown.

Based on RBS, EDX, and XRD information, the composition variation and phase separation can be excluded since the composition and structures of coating hardly had any change. The stress relaxation of as-deposited coatings after annealing has been noted from a shift in the XRD peak position. This finding is attributed to the diffusion of implanted atoms to the surface, hence the annihilation of the stress-inducing defects, as will be shown using results of measurement of Doppler broadening of the annihilated peak (DBAP) of slow positron beam. Accordingly, the lattice decline was believed to result from a release of intrinsic microstress.

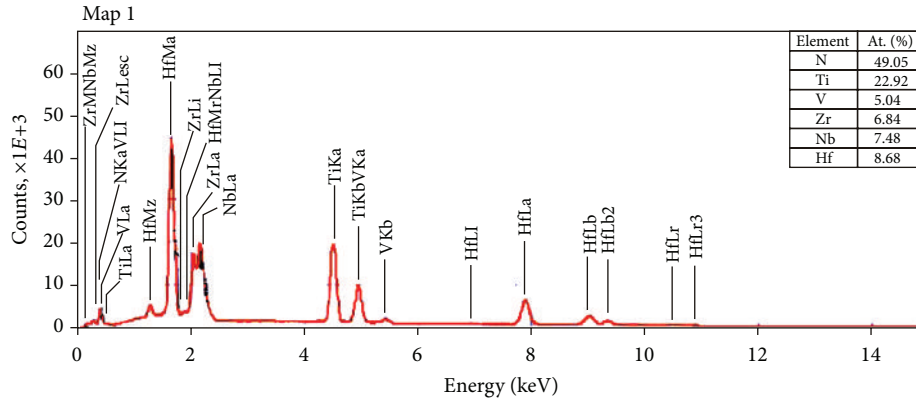
The morphology of coating surfaces and the element distribution were studied using the scanning electron microscope with EDS analysis JEOL-7000 F.

Figure 1(a) shows the distribution of elements on the surface of samples in elemental contrast. Integrated analysis was obtained from the area of $0.1 \text{ mm} \times 10 \text{ mm}$. The intensity of the color indicates the concentration of elements. The dark spots on the surface of coating are the drop fraction, which appeared during the deposition of coating. Figures 1(b) and 1(c) show results of microanalysis (EDX) of coatings obtained under different deposition conditions, and Figure 1(d) shows results of microanalysis after annealing 873°K (for 30 min, at pressure in chamber 100 Pa).

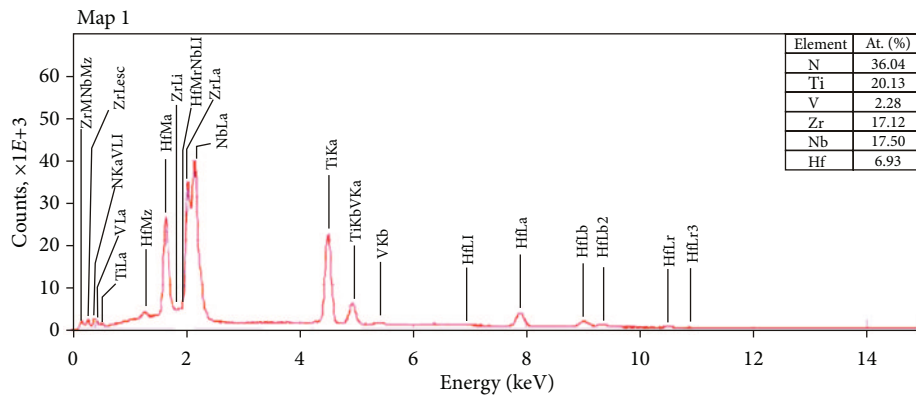
As you can see from these results the element concentration in the coating is N = 49.05 at.%, Ti = 22.92 at.%, V = 5.04 at.%, Zr = 6.84 at.%, Nb = 7.47 at.%, and Hf = 8.68 at.% at pressure 2×10^{-2} Pa. When the pressure decreases to 3×10^{-2} Pa, the spectra indicate a reduction of the specific content of the nitrogen atoms in the coating composition to N = 36.04 at.%, Ti = 20.13 at.%, V = 2.28 at.%, Zr = 17.12 at.%, Nb = 17.50 at.%, and Hf = 6.93 at.%. It means a significant deficiency of nitrogen atoms in nitrides of the multicomponent systems in comparison with stoichiometric ones at high pressure 3×10^{-2} Pa. The results of RBS (Figures 2(a) and 2(b)) and EDX analyses indicate a crucial effect of the radiation factor (achieved by increasing of negative bias potential applied to the substrate) on segregation processes



(a)



(b)



(c)

FIGURE 1: Continued.

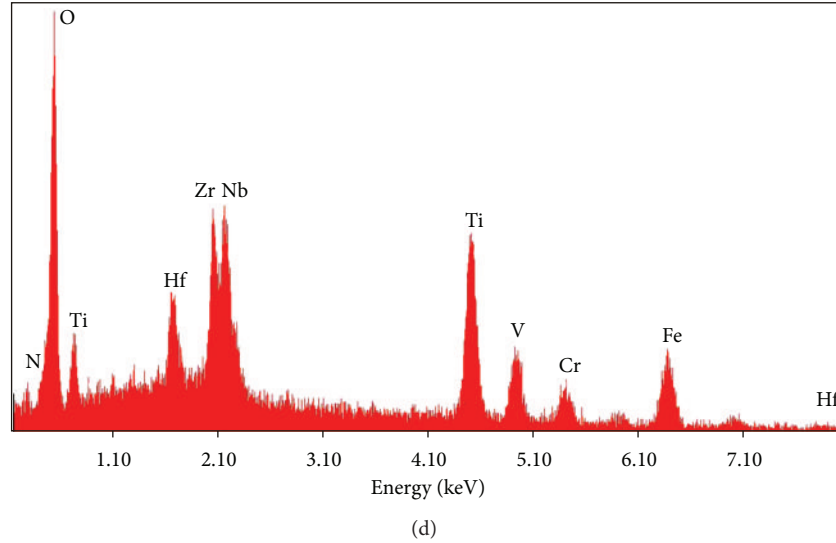


FIGURE 1: Images obtained by the scanning microscope JEOL-7000 F: (a) is the coating surface in reflected electrons; (b) shows microanalysis of coatings, N, Ti, V, Zr, Nb, obtained under $U_{\text{bias}} = -100$ V, pressure $P = 2 \times 10^{-2}$; (c) shows microanalysis of coatings, N, Ti, V, Zr, Nb, obtained under $U_{\text{bias}} = -200$ V, pressure $P = 3 \times 10^{-2}$; (d) shows microanalysis of coatings, N, Ti, V, Zr, Nb after annealing 873 K (for 30 min, at pressure in chamber 100 Pa).

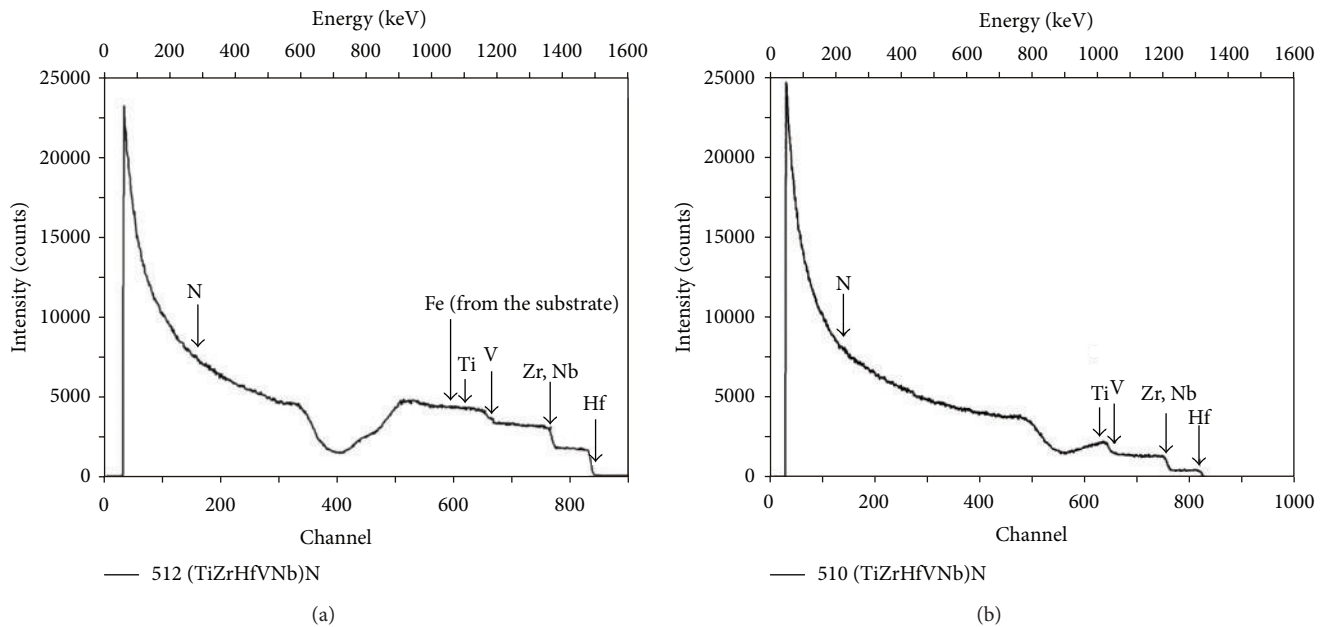


FIGURE 2: Results of the analysis of RBS spectra from samples 512 (a) and 510 (b).

arising during coating deposition. In other words, the energy of ion plasma flux increases due to the rising bias potential, which enhances the contribution of the radiation factor. It is known that the formation of a two-phase nanostructured film requires two terms: (1) the increased rate of atomic diffusion along the grain interfaces and (2) the high temperature of 873°K in the process of deposition to complete the process of spinodal segregation [18, 19, 26].

From results of EDX analysis (see Figure 1(d)) after annealing of coatings, an oxide film is forming on the surface.

It is also confirmed by XRD analysis of this sample presented in Figure 5(b). The appearance of elements Fe and Cr on EDX spectra can be explained by diffusion of these elements from substrate (which is made of steel). The deviation of the values of N concentration in coatings was not more than 0.26 at.% for coating with concentration of N = 49,05 at.% and not more than 0.18 at.% for coatings with concentration of N = 36.05 at.%.

PAS experiments demonstrated that positrons are well localized in the areas of low electron density (i.e.,

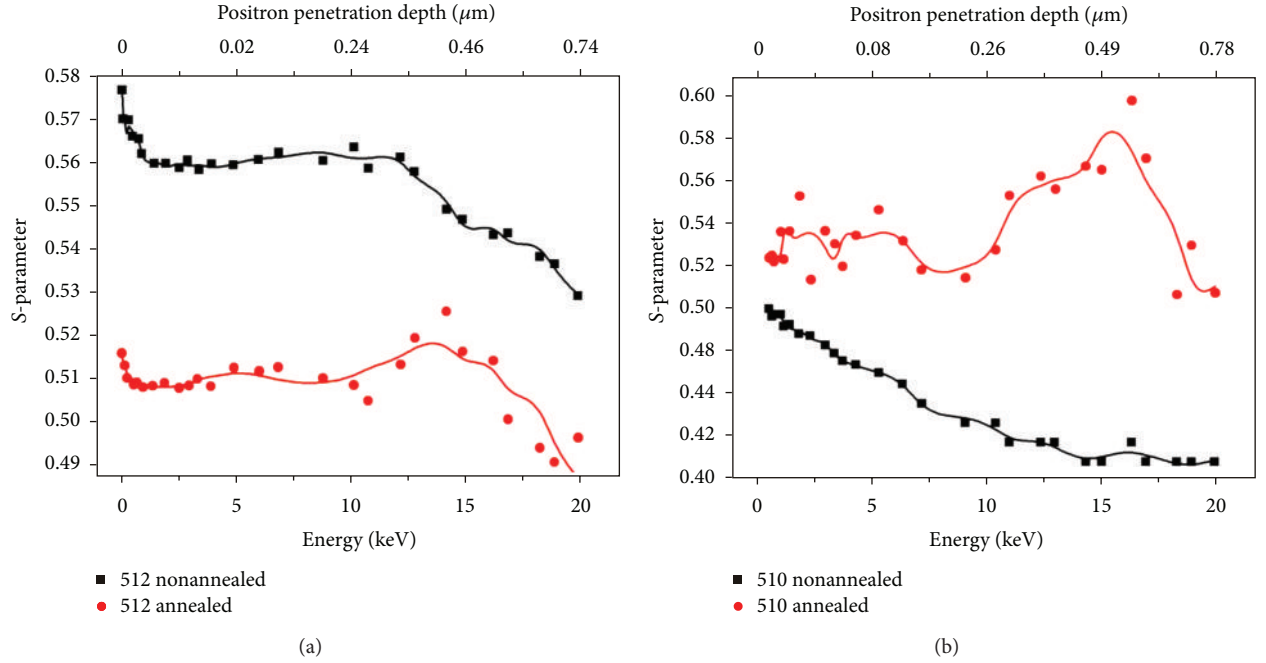


FIGURE 3: Dependencies of the S-parameter of the annihilation peak Doppler broadening measured over (Ti-Zr-Hf-V-Nb)N coating depth, for the samples 512 (a) and 510 (b), after deposition and annealing at 873 K, (100 Pa).

TABLE 1: Parameters of deposition and concentration of obtained coatings using C-PVD (concentration was measured using EDX-JEOL-7007F).

No.	Material	U_{bias}, V	P, Pa	Concentration, %					
				N	Ti	V	Zr	Nb	Hf
505	TiZrHfVNbN	110	0.5×10^{-1}	49.15	16.63	5.91	8.17	8.88	11.26
506	TiZrHfVNbN	100	0.2×10^{-1}	49.05	22.92	5.04	6.84	7.47	8.68
507	TiZrHfVNbN	50	5×10^{-2}	51.13	25.31	4.72	5.70	6.31	6.84
509	TiZrHfVNbN	100	3×10^{-1}	44.7	25.31	4.57	7.60	7.99	9.83
510	TiZrHfVNbN	50	2×10^{-1}	49.11	19.67	5.65	7.68	8.24	9.64
512	TiZrHfVNbN	200	8×10^{-2}	46.65	17.03	2.79	12.01	12.54	8.98
513	TiZrHfVNb	40	8×10^{-2}	—	34.66	8.88	19.53	23.16	13.76
514	TiZrHfVNbN	200	2×10^{-1}	47.69	16.41	1.93	13.34	13.90	6.72
515	TiZrHfVNbN	200	3×10^{-2}	36.05	20.13	2.28	17.12	17.50	6.93
523	TiZrHfVNbN	200	2×10^{-1}	43.44	17.80	1.45	16.39	16.99	3.92

vacancy-type defects divacancies, conglomerates of various vacancies, vacancy complexes, and plus two or three interstitial atoms [26–29]). As it follows from [27–32], the nanostructured materials, fabricated using the compaction, are good traps for positrons, which then annihilate with two or three components of the positron lifetime τ_2 , τ_3 . It is associated with positron annihilation at the grain interfaces, that is, the quasi-amorphous phase, in our case. The presented results (Figures 3(a) and 3(b)) clearly indicate that the defect profiles (S-parameter) significantly differ for various deposition conditions; see, for example, samples 510 and 512. At the same time, thermal annealing in a chamber with at high enough residual pressure (100 Pa) leads to even greater changes of the S-parameter over the coating depth. The value of S-parameter for the sample 512

decreases from 0.58-0.56 to 0.52-0.51 after annealing, and only when the analyzing energy of positrons approaches (12.5–15) keV, it increases to 0.53. Analysis of S-parameter curve of the nonannealed sample 510 (3b) allows to conclude that positron-sensitive defects are almost absent throughout the whole coating depth. This means that annihilation occurred mainly with the electrons of the defect-free areas. Therefore, the value of S-parameter was minimal and equal to 0.49. As a result of annealing at 873 K, the value of S-parameter increased significantly to 0.53 in the surface layer of the coating. The value of S-parameter further increased at positron energy of 14 to 17 keV and approached the maximum possible value 0.59.

It should be mentioned that the S-parameter depends on both the concentration and the type of vacancy defects,

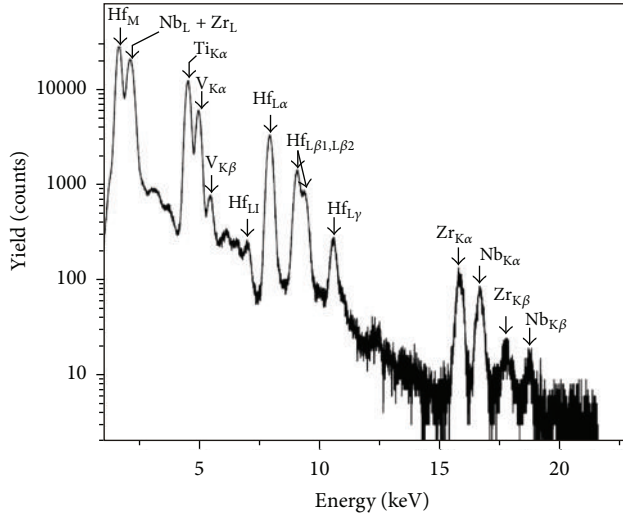


FIGURE 4: A common PIXE spectrum (in a logarithmic scale) obtained from a sample of the 512, when it was irradiated by a proton beam of 1.4 MeV energy.

at which positrons are captured and subsequently annihilate there in the areas of low electron density [27–29].

Since a grain size of the nanostructured coatings is smaller than a length of positron diffusion track in defect-free nanograin, all positrons can reach the grain surface and consequently the interfaces. In this case, most of the volume of available information concerns the defects in the interfaces and triple or more joints. Since the grain size in our experiments varies from 40 to 60 nm, the volume fraction of the interfaces may reach 30 to 35 vol.%, and the interfaces of triple joints may be about 5 to 10 vol.%, and then almost all positrons have to be captured along the interfaces [27].

According to results presented in [32], the total fraction of interfaces can be evaluated as

$$V_{Si} = 1 - \frac{[3S \cdot (L/S)]}{L^3} \approx \frac{3S}{L}, \quad (1)$$

where L is the grain size and S is the interface width (the near-interface zone). A fraction of the inherent grain interfaces is

$$V_{Ii} = \frac{[3S \cdot (L/S)]}{L^3}, \quad (2)$$

And a fraction of triple joints is

$$V_{Ti} = V_{Si} - V_{Ii}. \quad (3)$$

If the distance between the defects is essentially shorter than the positron diffusion length, all positrons have to be captured by defects; that is, we observe the capture saturation. In this case, the positron lifetime spectrum contains only one component [27, 28], and the S -parameter of Doppler broadening seems to have a maximum value.

Figure 4 shows the integral spectrum obtained by PIXE of the element concentrations for (Ti-Zr-Hf-V-Nb)N coatings number 512 after annealing at 873 K (30 min). We can evidently see the redistribution of elements over depth after

thermal annealing. Studying these spectra, we found all the elements constituting the nanostructured coating. As it will be shown later in the text, the μ -PIXE element distribution maps taken from the (Ti-Zr-Hf-V-Nb)N coating before and after annealing up to 873 K in Figures 7(a) and 7(b) can be seen.

The X-ray diffraction data for the sample 512 shows formation of a strong texture with the (111) axis, which is perpendicular to the plane of growth (Figure 5). The data of X-ray strain measurements indicate that the samples 512 are characterized by the highest value of a lattice period in a stress-free cross-section ($a = 0.442$ nm). It correlates with the results of elemental analysis, according to which the highest concentration of nitrogen is observed when the working pressures of coating deposition are high.

An appearance of biaxial texture with (111) and (110) axes at $U_{bias} = -200$ V resulted in formation of coatings with the highest hardness reaching 58 to 60 GPa and very uniform and smooth surfaces [29–32].

In this case, thermal annealing does not significantly change a structure-phase state of the coatings (Figure 5(a)). However, it reduces a little the deformed state of compression from the strain ratio of 2.76% in initial state (as-deposited state) to 2.59% after annealing.

It was found that there was only a slight increase from 56 nm to 68 nm of crystal size and a decrease from 0.4424 Å to 0.4386 Å of lattice constant, with an increase of annealing temperature from RT to 873 K. The barely changed structure and grain size during high temperature annealing are believed to be attributed to the small driving force because of the low grain boundary energy and low kinetics from the sluggish diffusion. The grain boundary energy comes from the energy difference between the state of grain boundaries and that inside the grains. The large lattice distortion effect because of large atomic size difference (the atomic size Ti, 1.462 Å; V, 1.316 Å; Zr, 1.603 Å; Hf, 1.578 Å, Nb, 3.301 Å, Zr, 1.603 Å; Hf, 1.578 Å) can markedly raise the overall free energy of crystalline structure.

Therefore, the actual grain boundary energy was largely lowered, leading to very small driving force for coarsening. A detailed mechanism has been proposed by Huang and Yeh [36] in case of (AlCrNbSiTiV)N coating. The sluggish diffusion originating from the higher packing density because of the packing of atoms with different sizes made the effective diffusion distances very short, which led to the enhanced difficulty of grain growth. Regarding the lattice decline, the following three possible factors must be considered: composition variation, phase separation, and residual stress.

At lower pressures of deposition $P_N = 0.1$, the decrease of the lattice period in a stress-free sections was observed at 0.438 nm, which seemed to be associated with a lower content of nitrogen atoms in the coating. Annealing of the samples 510 not only led to a significant change of the stress-strain state but also of the phase composition (see Figure 5(b), curve 2).

These figures show that samples number 510 demonstrate a decrease of the intensity of textured reflexes of an FCC metallic crystal lattice (compare spectra 1 and 2 in Figure 5(b)). In this case, nitrogen atoms are in the form of

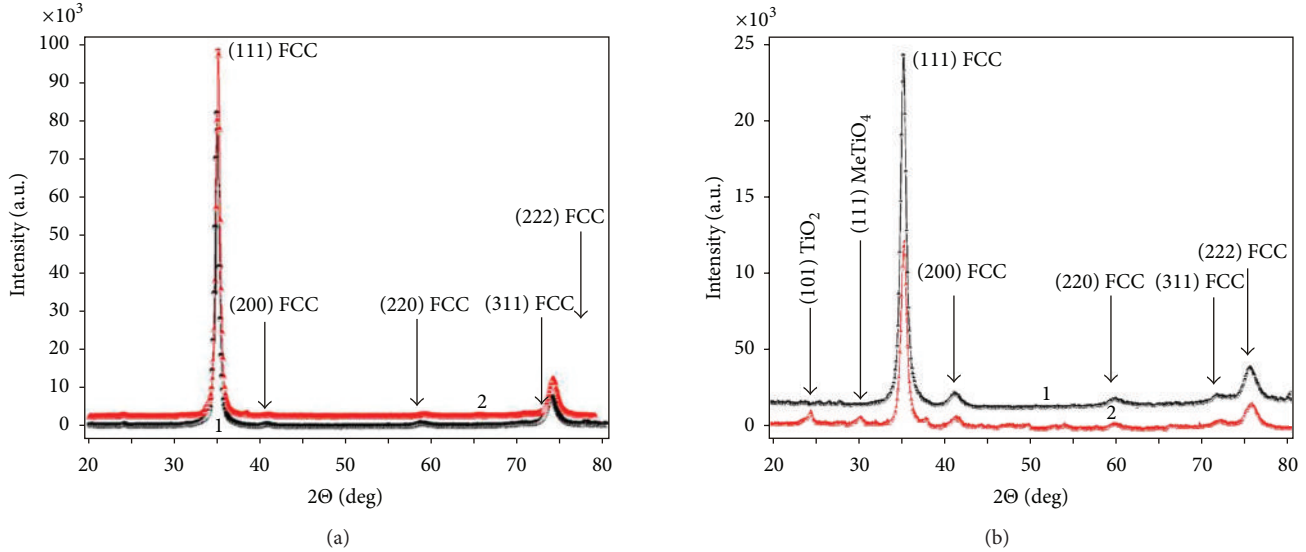


FIGURE 5: (a) The XRD spectra for a coating fabricated at $P_N = 0.7$ Pa and $U_b = -200$ V (sample 512): (1) before annealing; (2) after thermal annealing. (b) The XRD spectra of a coating fabricated at $P_N = 0.2$ Pa and $U_b = -50$ V (sample 510) before annealing (1) and after thermal annealing at 873 K (2).

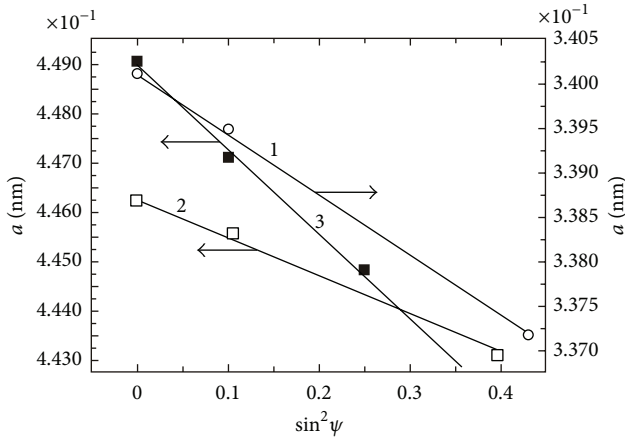


FIGURE 6: Dependences of $\alpha\text{-sin}^2\psi$ obtained for the texture axis (110) of a highentropy alloy Ti-V-Zr-Nb-Hf deposited in a nitrogen-free atmosphere (1), for the texture axis (111) (a straight line 2) and (110) (a straight line 3), which was the coating of the highest hardness (58–60) GPa deposited in the nitrogen atmosphere at $P_N = 0.27$ Pa and $U_b = -200$ V, using a method of crystalline groups.

the FCC sublattice shifted by $1/2$ space diagonal forming the so-called NaCl structural lattice type. The appearance of reflections at small angles was also observed, corresponding to the formation of oxides of TiO_2 (JCPDS 01-0562) and oxide-type MeTiO_4 , where Me corresponds to the content of Zr and Hf. The structural type of this oxide is similar to an oxide of an isostructural (allomeric) ZrTiO_4 (JCPDS 07-0290) and HfTiO_4 (JCPDS 14-0103). Upon annealing of the sample, the strain state of compression decreased from -1.9% (before annealing) to -0.7% (after annealing).

A characteristic form of $\alpha\text{-sin}^2\psi$ plots for highentropy metallic coating with a bcc lattice and a nitride one with an FCC metallic lattice of NaCl type is demonstrated in Figure 6. We can see that a compressing deformation exceeding 2% was developing in the CAVD coatings. Inclination angles of the plots are different for all investigated nitride coatings and crystalline groups of definite textures in this work (Figure 6, plots 2 and 3). According to Roy's model of stress uniformity [25, 33], such difference indicates an essential contribution of oriented microstresses of the deformation mode, surveyed by the $\alpha\text{-sin}^2\psi$ method. In this case, if a region of the uniform microdeformation is comparable to the crystallite size, the latter demonstrates anisotropy of an elastic modulus. In the case of complexes of textured crystallites, such deformation can be considered as a factor of nonuniformity of stresses and deformations due to intercrystalline interactions [31, 34]. Measurements of the material elastic characteristics, which were performed using the macro- and microbeams and calculated according to the Vergard's rule, along with the element analysis indicated that a period of crystalline lattice was about 0.3371 nm for the highentropy coating $\text{Ti}_{0.23}\text{-V}_{0.05}\text{-Zr}_{0.07}\text{-Hf}_{0.078}\text{-N}_{0.49}$. This value corresponds to that of the stress-free cross-section $2\nu/(1 + \nu) = 0.45$ in terms of the plotted for this coating $\alpha\text{-sin}^2\psi$ (plot 1, Figure 6), where ν is the Poisson coefficient. From here $\nu = 0.29$, and the elastic strain of compression developing in such coating has the value 2.2 GPa. The previously mentioned approach can be applied for calculations of stresses in the nitride single-axis oriented coatings. In the case of double-axis-orientation (plots 2 and 3, Figure 6), application of averaged meaning allows us only to perform a correct evaluation of the deformed state of the crystal lattice.

The results of RBS (Figures 2(a) and 2(b)) and EDX analyses for the samples 510 (for which the value of the

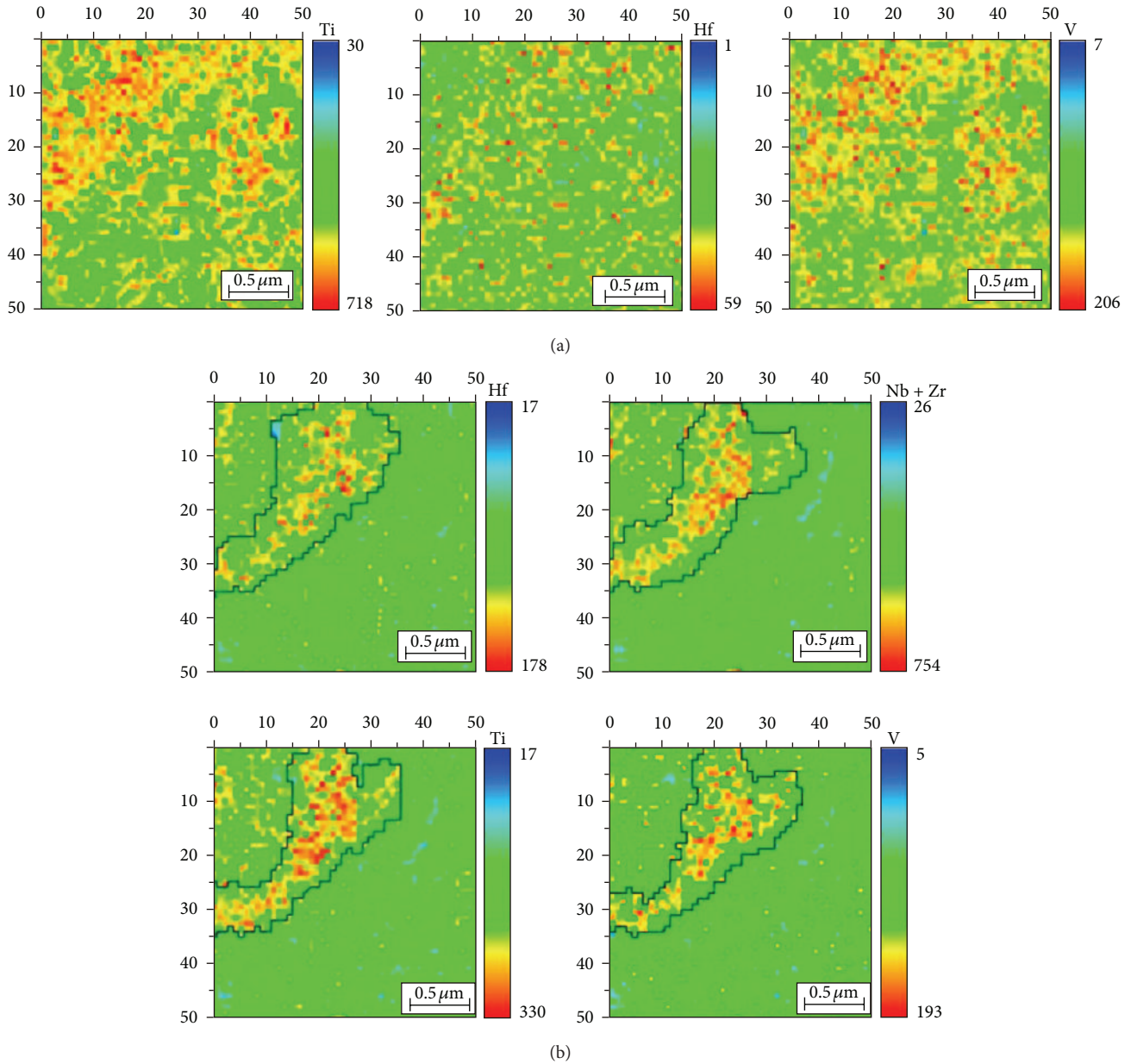


FIGURE 7: Maps of the element distribution in the area of $2.5 \times 2.5 \mu\text{m}$ (the raster of 50×50 , the step size of $0.5 \mu\text{m}$) for the sample 512 before (a) and after (b) annealing.

elastic stress in the initial state is much lower than for sample 512) indicated that two peaks are formed on the curve of S-parameter when the energy of the positron beam is $(3 \div 5) \text{ keV}$ and $(14 \div 17) \text{ keV}$. This can be explained by the increased diffusion process of both nitrogen and oxygen atoms near the surfaces of the samples 510. This indicates the appearance of new channels for the annihilation of positrons, which are more efficiently attracted by defects, which appeared at the interface as a result of annealing and formed the new quasi-amorphous and nanostructured phases of nitrides. This conclusion is supported by the results of PIXE- μ analysis, which indicated that an oxide film was formed on the surface, and therefore the value of

S-parameter increased. In the coating depth, the elements are redistributed, which confirmed the assumption about the end of the process of spinodal segregation and the formation of new phases along nanograin interfaces [30–34]. It must be noted that the grain growth during annealing is the most obvious mechanism of structural relaxation. The segregation of nitrogen at the grain interfaces hampers the growth of nanocrystals.

Evaluation of the nanograins size by XRD, according to the Debye-Scherrer, gave the nanograins size of 55–58 nm for samples 512, which did not change after thermal annealing. Evaluation of the diffusion length of positrons was $L + \approx 100 \text{ nm}$, which was essentially longer than the size of

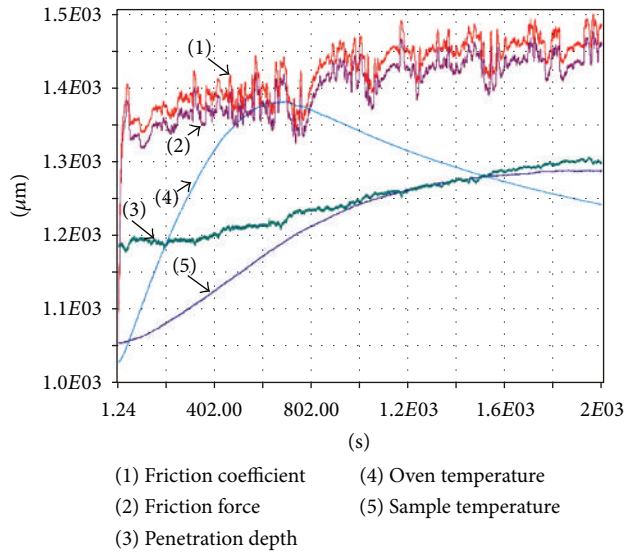


FIGURE 8: Results of tribological tests of steel substrate (steel 45).

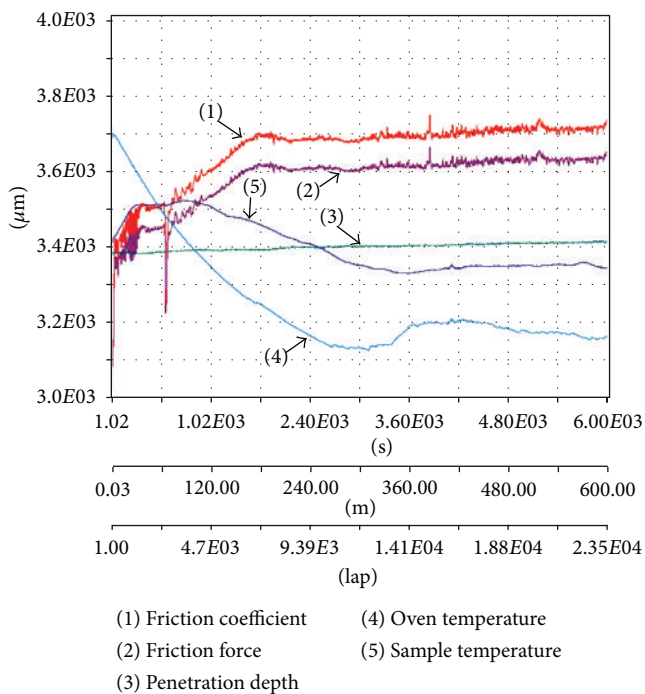


FIGURE 9: The results of tribological tests of the "steel 45 + coating (Ti-Hf-Nb-Zr-V)N-Al₂O₃ counterface."

nanograins. According to the conventional interpretation, the nanopores are primarily placed at the lines of intersection of three or more interfaces. Thus, the ratio of intensities of the positron lifetime components should decrease with the increase of crystallite size. It was confirmed by the theoretical and experimental studies [27–29, 33]. Therefore, reduction of the S-parameter (sample 512) may be connected to the annealing of interface vacancies, resulting in a decrease of the S-parameter intensity [38–40].

Moreover, additional nanopores may appear due to the vacancy agglomeration taking place in the process of crystallite growing, even if the latter is not very significant. This may result in the increase of the S-parameter. This was reported in the work of [32], where the intensity of the second component of positron lifetime increased.

As it follows from the RBS (Figures 2(a) and 2(b)) and EDX analyses, the strongly structured coatings number 512 with a high level of compressive strain in the as-deposited states (−2.76%) demonstrate the high oxidation resistance after annealing. This occurred due to low oxygen diffusion to the coating depth and a high degree of filling of the octahedral interstitials by nitrogen atoms during the deposition of coating under conditions of high nitrogen pressure in the chamber. Thus, this system does not form a nitride interlayer between nanograins, due to the low diffusion resulting from high compressive stresses. It seems that the annealing temperature is insufficient or the energy of atoms is too low to form the interlayer. Therefore, the main channel allowing the nitrogen atoms to sink for the formation of the nitride interlayer is the interphase "coating substrate" boundary (see the S-parameter curve of the maximum value 0.53 at energy of analyzing positron beam of 13–14 keV).

Figure 7(a) shows the 3D map of the element distribution in the area of $2.5 \times 2.5 \mu\text{m}$ for the sample 512, with scanning step $0.5 \mu\text{m}$. As we can see in this figure, the elements are distributed almost evenly over the surface and in the bulk. At the same time, thermal annealing up to 873 K (for 30 min, at pressure in chamber 100 Pa) leads to the segregation of impurities at the grain interfaces, and the maps of these distributions clearly indicate these regions, see Figure 7(b). We pay attention to the fact that almost all the elements forming the coating are arranged, and since the method PIXE is insensitive to nitrogen, the spectrum does not indicate it. The width of these interfaces is about $0.12 \pm 0.25 \mu\text{m}$, and the size of large grains reaches up to $0.3\text{--}0.8 \mu\text{m}$. Thus, considering the results of XRD analysis and $\mu\text{-PIXE}$ with S-parameter before and after annealing, we can say that in the structure of (Ti-Zr-Hf-V-Nb)N the grains of $0.3\text{--}0.8 \mu\text{m}$ with nanograins of 45–60 nm fragmented into them are formed. Dimensions of these nanograins were determined by XRD. After annealing, the impurities are segregated at the interfaces of large grains due to thermostimulated diffusion, and an interphase interlayer is formed at small grains as an agglutinating phase.

The results of research obtained by electron diffraction microscope (TEM) demonstrated that the structural-phase state of coatings with different contents of alloying elements (Si, B, Al) in the system TiN even at high diffusion mobility of atoms (i.e., at deposition temperature 673–773 K) formed the two-phase textured grain structures. The grains of a submicron size $0.2\text{--}0.6 \mu\text{m}$ in such systems were fragmented by the low-angle interfaces with the disorientation angles of 5° and by nanograins of 20–30 nm [13].

According to [12, 13, 17], increasing of content of low-soluble alloying elements, upon reaching their critical concentration and/or diffusion mobility, leads to enrichment of interfaces of growing crystals with these elements (taking into account the values of mixing entropy of separate nitrides,

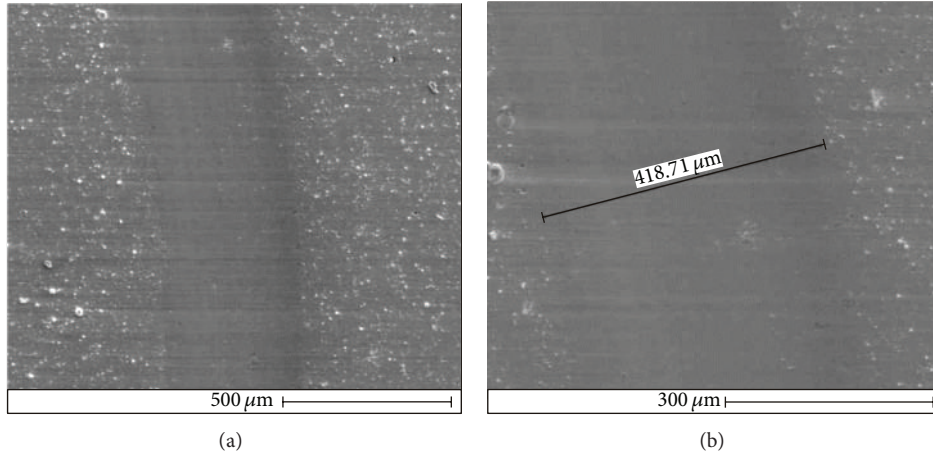


FIGURE 10: Photographs of the surface morphology of friction: (a) general view and (b) friction track.

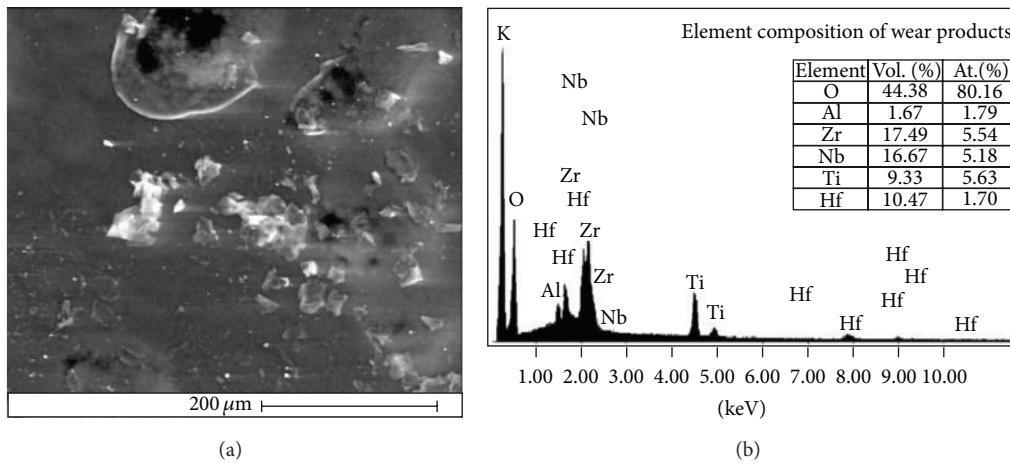


FIGURE 11: Micrograph of wear products (a) and its energy spectrum (b).

TABLE 2: The enthalpies of formation (ΔH) of the five binary nitrides.

	TiN	VN	ZrN	HfN	NbN
ΔH , KJ/mole	-337.7	-217.2	365.3	-373	-234.7

presented in Table 2, and also the total entropy of all metals and nitrides on its basis included to the coatings), and to corresponding decrease of the grain size [41]. This effect, along with the nonequilibrium deposition conditions, promoted the formation of randomly oriented nanocrystallites. It should be noted that the maximum nanohardness of $H = 58$ GPa was obtained also for the samples 512. Elastic modulus for these samples reached the value of $E = 618$ GPa. For samples 509 and 510, hardness values were of little lower rates -52 GPa and 46 GPa, respectively.

Analysis of the wear byproducts, wear track structure (on the sample), and wear spots (on counterface ball) was provided along with microscopic study of the wear tracks

structure on the coating surface and the change of wear spots on the ball. Measurement of the vertical section of wear tracks was performed by profilometer in four diametrically and orthogonally opposite fields and determined the average cross-sectional area and wear tracks. Figure 8 presents the results of tribological wear test of the steel substrate. The vacuum-arc coatings of Ti-Zr-Hf-Nb-V (4.0 mm thick) were deposited in the nitrogen reaction gas environment on the polished steel disc. The results of the friction tests showed the increase of the surface roughness due to the drop component of the plasma flow (see Figure 9 and Table 3).

Deposition of coatings on the substrate of steel 45 provides an increased durability, thus reducing the wear of steel. The study of friction tracks is of great interest, which can give the information about the mechanism of wear. Figure 10 shows photographs of friction tracks in vacuum-arc coating (Ti-Hf-Nb-Zr-V)N. Results of the study of wear products in the friction process for the coating (Ti-Hf-Nb-Zr-V)N- Al_2O_3 counterface are shown in Figure 11.

TABLE 3: Tribological characteristics of the different systems based on Ti, Zr, Hf, Nb, V, N.

Sample	Friction coefficient, μ		Wear factor $\text{mm}^3 \times \text{H}^{-1} \times \text{mm}^{-1}$	
	Initial	During experiment	Of counterface ($\times 10^{-5}$)	Of sample ($\times 10^{-5}$)
Coatings Ti-Hf-Nb-Zr-V-N	0.221	1.030	1.12	0.027
Steel 45	0.204	0.674	0.269	35.36

4. Conclusion

Present work reports original results revealing the mechanisms of formation of interfaces in multicomponent coatings and formation of the stress states of nanocrystals, as well as their effect on thermal diffusion of nitrogen and oxygen atoms. We found that by changing the deposition conditions, it is possible to influence on thermal stability and hardness of multicomponent nanostructured coatings.

We also considered an effect of defect migration, which occurs in the process of annealing, on hampering the nanocrystal growing, when the annealing temperature increased. It turned out that the highentropy nitride alloys and nanostructured coatings on their base contained only the single-phase solid solutions. Its structure was composed of the submicron grains of 0.3–0.8 μm , at the interfaces of which the interlayers of impurity atoms were formed. At the same time, the fragmented nanograin structures of 40–60 nm size with subgrains of the nitride phases were formed in the submicron grains. The sluggish diffusion originating from the higher packing density because of the packing of atoms with different sizes made the effective diffusion distances very short, which led to the enhanced difficulty of grain growth. Regarding the lattice decline, the following three possible factors must be considered: composition variation, phase separation, and residual stress.

Acknowledgments

This work was supported by the Ministry of Education and Science, Youth and Sports of Ukraine in the framework of the state program (order no. 411) and in collaboration with the National Institute of Material Science, Tsukuba, and Japan, Martin-Luther Universitat Halle-Wittenberg, and Ion Beam Center FWIZ, Dresden, and partially by the Project FRSF-041/20, Ukraine. The author is grateful to V. F. Gorban, S. A. Firstova, and A. A. Andreev, for the help in preparation of coatings, to S. S. Mel'nik, for the help in providing of experiments on proton microbeam, and to Professor R. Krause-Rehberg, M. Jungman, M. Muchow, and J. Haeberle and Martin-Luther-Universitat Halle-Wittenberg, Halle, Germany, and M. Kaverin for the help in research using slow positron beam, to Professor Sobol O. V., for the help in providing of XRD analysis and " $\alpha\text{-sin}^2\psi$ " analysis, to Professor Beresnev V. M., for the help in interpretation of nanoscratch tests, to Dr. Kolesnikov D. A. Belgorod State University, Nano-Center, Russia, and to Professor Y. Takeda from NIMS, Tsukuba, Japan, for the help in providing of SIMS with EDX measurements.

References

- [1] A. D. Pogrebnjak, A. P. Shpak, N. A. Azarenkov, and V. M. Beresnev, "Structures and properties of hard and superhard nanocomposite coatings," *Physics-Uspekhi*, vol. 52, no. 1, pp. 29–54, 2009.
- [2] A. D. Pogrebnjak, A. G. Ponomarev, A. P. Shpak, and Y. A. Kunitskii, "Application of micro- and nanoprobes to the analysis of small-sized 3D materials, nanosystems, and nanoobjects," *Physics-Uspekhi*, vol. 55, no. 3, pp. 270–300, 2012.
- [3] A. D. Pogrebnjak, V. M. Beresnev, A. A. Demianenko et al., "Adhesive strength, superhardness, and the phase and elemental compositions of nanostructured coatings based on Ti-Hf-Si-N," *Physics of the Solid State*, vol. 54, no. 9, pp. 1882–1890, 2012.
- [4] A. D. Pogrebnjak, O. V. Sobol', V. M. Beresnev et al., "Features of the structural state and mechanical properties of ZrN and Zr(Ti)-Si-N coatings obtained by ion-plasma deposition technique," *Technical Physics Letters*, vol. 35, no. 10, pp. 925–928, 2009.
- [5] V. Dolique, A.-L. Thomann, P. Brault, Y. Tessier, and P. Gillon, "Complex structure/composition relationship in thin films of AlCoCrCuFeNi high entropy alloy," *Materials Chemistry and Physics*, vol. 117, no. 1, pp. 142–147, 2009.
- [6] M.-H. Tsai, C.-W. Wang, C.-W. Tsai et al., "Thermal stability and performance of NbSiTaTiZr high-entropy alloy barrier for copper metallization," *Journal of the Electrochemical Society*, vol. 158, no. 11, pp. H1161–H1165, 2011.
- [7] A. Li and X. Zhang, "Thermodynamic analysis of the simple microstructure of AlCrFeNiCu high-entropy alloy with multi-principal elements," *Acta Metallurgica Sinica*, vol. 22, no. 3, pp. 219–224, 2009.
- [8] S. A. Firstov, V. F. Gorban, N. A. Krapivka, and E. P. Pechkovsky, "Hardening and mechanical properties of as-cast high-entropy alloys," *Composites and Nanostures*, vol. 2, pp. 5–20, 2011.
- [9] A. D. Pogrebnjak, V. V. Uglov, M. V. Il'yashenko et al., "Nanocomposite and combined coatings on Ti-Si-N/WC-Co-Cr/steel and Ti-Si-N/(Cr₃C₂)₇₅-(NiCr)₂₅ base: their structure and properties," in *Nanostructured Materials and Nanotechnology IV: Ceramic Engineering and Science Proceedings*, vol. 31, pp. 115–126, John Wiley & Sons, Hoboken, NJ, USA, 2010.
- [10] O. V. Sobol', A. D. Pogrebnjak, and V. M. Beresnev, "Effect of the preparation conditions on the phase composition, structure, and mechanical characteristics of vacuum-Arc Zr-Ti-Si-N coatings," *The Physics of Metals and Metallography*, vol. 112, no. 2, pp. 188–195, 2011.
- [11] J. Musil, J. Vlček, and P. Zeman, "Hard amorphous nanocomposite coatings with oxidation resistance above 1000°C," *Advances in Applied Ceramics*, vol. 107, no. 3, pp. 148–154, 2008.
- [12] A. D. Korotaev, D. P. Borisov, V. Y. Moshkov, S. V. Ovchinnikov, Y. P. Pinzhin, and A. N. Tyumentsev, "Elastic stress state in superhard multielement coatings," *Physical Mesomechanics*, vol. 12, no. 5-6, pp. 269–279, 2009.

- [13] A. D. Pogrebnjak, V. M. Beresnev, D. A. Kolesnikov et al., "The effect of segregation and thermodiffusion on the formation of interfaces in nanostructured (Ti-Hf-Zr-V-Nb)N multielement coatings," *Technical Physics Letters*, vol. 39, no. 3, pp. 280–283, 2013.
- [14] O. V. Sobol', A. A. Andreev, V. F. Gorban et al., "Reproducibility of the single-phase structural state of the multielement high-entropy Ti-V-Zr-Nb-Hf system and related superhard nitrides formed by the vacuum-arc method," *Technical Physics Letters*, vol. 38, no. 7, pp. 616–619, 2012.
- [15] I. V. Blinkov, A. O. Volkhonsky, V. N. Anikin, M. I. Petrzhik, and D. E. Derevtsova, "Phase composition and properties of wear-resistant Ti-Al-Cr-Zr-Nb-N PVD coatings," *Physics and Chemistry of Materials Processing*, vol. 4, pp. 37–43, 2010 (Russian).
- [16] S.-Y. Lin, S.-Y. Chang, Y.-C. Huang, F.-S. Shieu, and J.-W. Yeh, "Mechanical performance and nanoindenting deformation of (AlCrTaTiZr)NCy multi-component coatings co-sputtered with bias," *Surface and Coatings Technology*, vol. 206, no. 24, pp. 5096–5102, 2012.
- [17] J. Musil, "Hard nanocomposite coatings: thermal stability, oxidation resistance and toughness," *Surface and Coatings Technology*, vol. 207, pp. 50–65, 2012.
- [18] A. D. Pogrebnjak and V. M. Beresnev, *Nanocoatings Nanosystems Nanotechnologies*, Bentham Science, 2012.
- [19] A. D. Pogrebnjak, A. P. Shpak, V. M. Beresnev et al., "Effect of thermal annealing in vacuum and in air on nanograin sizes in hard and superhard coatings Zr-Ti-Si-N," *Journal of Nanoscience and Nanotechnology*, vol. 12, pp. 9213–9219, 2012.
- [20] H.-W. Chang, P.-K. Huang, J.-W. Yeh, A. Davison, C.-H. Tsau, and C.-C. Yang, "Influence of substrate bias, deposition temperature and post-deposition annealing on the structure and properties of multi-principal-component (AlCrMoSiTi)N coatings," *Surface and Coatings Technology*, vol. 202, no. 14, pp. 3360–3366, 2008.
- [21] C.-H. Lai, K.-H. Cheng, S.-J. Lin, and J.-W. Yeh, "Mechanical and tribological properties of multi-element (AlCrTaTiZr)N coatings," *Surface and Coatings Technology*, vol. 202, no. 15, pp. 3732–3738, 2008.
- [22] C.-H. Lai, M.-H. Tsai, S.-J. Lin, and J.-W. Yeh, "Influence of substrate temperature on structure and mechanical, properties of multi-element (AlCrTaTiZr)N coatings," *Surface and Coatings Technology*, vol. 201, no. 16–17, pp. 6993–6998, 2007.
- [23] J.-W. Yeh, Y.-L. Chen, S.-J. Lin, and S.-K. Chen, "High-entropy alloys—a new era of exploitation," *Materials Science Forum*, vol. 560, pp. 1–9, 2007.
- [24] <http://www.simnra.com>.
- [25] N. A. Azarenkov, O. V. Sobol', A. D. Pogrebnjak, and V. M. Beresnev, *Engineering Vacuum-Plasma Coatings*, Academy of Kyungpook National University, Kharkov, Ukraine, 2011.
- [26] H. E. Shaefer, "Investigation of thermal equilibrium vacancies in metals by positron annihilation," *Physica Status Solidi*, vol. 102, no. 1, pp. 47–65, 1987.
- [27] S. V. Rempel' and A. I. Gusev, "Surface segregation in decomposing carbide solid solutions," *JETP Letters*, vol. 88, no. 7, pp. 435–440, 2008.
- [28] R. Würschum, P. Farber, R. Dittmar, P. Scharwaechter, W. Frank, and H.-E. Schaefer, "Thermal vacancy formation and self-diffusion in intermetallic Fe₃Si nanocrystallites of nanocomposite alloys," *Physical Review Letters*, vol. 79, no. 24, pp. 4918–4921, 1997.
- [29] V. I. Lavrent'yev, A. D. Pogrebnjak, and R. Sandrik, "Evolution of vacancy defects in the surface layers of a metal irradiated with a pulsed electron beam," *JETP Letters*, vol. 65, no. 8, pp. 651–655, 1997.
- [30] S. Vepřek, "The search for novel, superhard materials," *Journal of Vacuum Science & Technology A*, vol. 17, no. 5, pp. 2401–2421, 1999.
- [31] J. Musil, "Hard and superhard nanocomposite coatings," *Surface and Coatings Technology*, vol. 125, no. 1–3, pp. 322–330, 2000.
- [32] A. I. Gusev, *Nanomaterials, Nanostructures and Nanotechnology*, Fizmatlit, Moscow, Russia, 2005.
- [33] R. Krause-Rehberg and H. S. Leipner, *Positron Annihilation in Semiconductors*, vol. 127 of *Solid-State Sciences*, Springer, Berlin, Germany, 1999.
- [34] A. D. Pogrebnjak, A. G. Ponomarev, D. A. Kolesnikov et al., "Effect of mass transfer and segregation on the formation of superhard nanostructured Ti-Hf-N(Fe) catings," *Technical Physics Letters*, vol. 38, no. 7, pp. 623–626, 2012.
- [35] S.-Y. Chang, S.-Y. Lin, Y.-C. Huang, and C.-L. Wu, "Mechanical properties, deformation behaviors and interface adhesion of (AlCrTaTiZr)Nx multi-component coatings," *Surface and Coatings Technology*, vol. 204, no. 20, pp. 3307–3314, 2010.
- [36] P.-K. Huang and J.-W. Yeh, "Effects of nitrogen content on structure and mechanical properties of multi-element (AlCrNbSi-TiV)N coating," *Surface and Coatings Technology*, vol. 203, no. 13, pp. 1891–1896, 2009.
- [37] D.-C. Tsai, Y.-L. Huang, S.-R. Lin, S.-C. Liang, and F.-S. Shieu, "Effect of nitrogen flow ratios on the structure and mechanical properties of (TiVCrZrY)N coatings prepared by reactive magnetron sputtering," *Applied Surface Science*, vol. 257, no. 4, pp. 1361–1367, 2010.
- [38] A. D. Pogrebnjak, O. V. Sobol', V. M. Beresnev et al., "Phase composition, thermal stability, physical and mechanical properties of superhard on base Zr-Ti-Si-N nanocomposite coatings," *Ceramic Engineering and Science Proceedings*, vol. 31, no. 7, pp. 127–138, 2010.
- [39] A. D. Pogrebnjak, S. M. Ruzimov, D. L. Alontseva et al., "Structure and properties of coatings on Ni base deposited using a plasma jet before and after electron a beam irradiation," *Vacuum*, vol. 81, no. 10, pp. 1243–1251, 2007.
- [40] A. D. Pogrebnjak, O. G. Bakharev, N. A. Pogrebnjak Jr. et al., "Certain features of high-dose and intensive implantation of Al ions in iron," *Physics Letters A*, vol. 265, no. 3, pp. 225–232, 2000.
- [41] P. Misaelides, A. Hatzidimitriou, F. Noli, E. Pavlidou, and A. D. Pogrebnjak, "Investigation of the characteristics and corrosion resistance of Al₂O₃/TiN coatings," *Applied Surface Science*, vol. 252, no. 23, pp. 8043–8049, 2006.

Research Article

Photocatalytic and Magnetic Behaviors Observed in BiFeO₃ Nanofibers by Electrospinning

Xuehui Zhang,¹ Haiyang Liu,¹ Bin Zheng,² Yuanhua Lin,¹ Deping Liu,³ and Ce-Wen Nan¹

¹ State Key Laboratory of New Ceramics and Fine Processing, Department of Materials Science and Engineering, Tsinghua University, Beijing 100084, China

² Department of Materials Science and Engineering, Beijing University of Chemical Technology, Beijing 100029, China

³ Department of Cardiology, Beijing Hospital, The Ministry of Health, Beijing 100730, China

Correspondence should be addressed to Yuanhua Lin; linyh@tsinghua.edu.cn

Received 4 May 2013; Accepted 31 May 2013

Academic Editor: Jiamin Wu

Copyright © 2013 Xuehui Zhang et al. This is an open access article distributed under the Creative Commons Attribution License, which permits unrestricted use, distribution, and reproduction in any medium, provided the original work is properly cited.

Perovskite-type BiFeO₃ nanofibers with wave nodes-like morphology were prepared by electrospinning. The nanofibers show a highly enhanced visible-light-active photocatalytic property. The results also showed that the diameter could affect the band gap and photocatalytic performances of nanofibers. Additionally, weak ferromagnetic behaviors can be observed at room temperature, which should be correlated to the size-confinement effect on the magnetic ordering of BiFeO₃ structure.

1. Introduction

BiFeO₃ (BFO), as a kind of multiferroic materials, which shows simultaneously spontaneous magnetic and electric ordering, has attracted much attention [1–3]. According to recent studies, BFO is also an important visible-light responsive semiconductor photocatalyst for water splitting and degradation of organic pollutants due to its suitable band gap (~2.2 eV) and excellent chemical stability [4, 5]. The synthesis method used to obtain the desired nanostructures plays a crucial role in affecting electric, magnetic, and optical properties of nanoscale BFO. Various procedures have been developed to synthesize BFO nanostructure materials such as nanoparticles [6–9], nanocubes [10, 11], nanotubes [12, 13], and nanowires [14, 15]. Gao and his coworkers reported the synthesis of BFO nanoparticles by a sol-gel technique and their photocatalytic and magnetic properties [6]. Joshi et al. investigated a microwave synthesis of single crystalline perovskite BFO nanocubes [10]. Templates methods were used to prepare BFO nanotubes [12] and nanowires [15], respectively, but there were some disadvantages including low-yield, polycrystalline structure and easy agglomeration.

Electrospinning as a simple and effective method for fabricating ultrathin nanofibers has been used widely [16–18].

Xie et al. prepared BFO nanofibers of the polycrystalline structure fired under a protective atmosphere [19]. In addition, there were some researchers investigated the ferroelectricity [20, 21] and photocatalytic activity under UV-light irradiation [22, 23] in electrospun BFO nanofibers. However, to our knowledge, there are no reports that focused on the BFO nanofibers as a visible-light-active photocatalytic decomposition material. In the present work, we reported the successful synthesis of BFO ultralong nanofibers by electrospinning and investigated the photocatalytic activity under visible light and their magnetic behaviors.

2. Materials and Methods

BFO ultrafine fibers were synthesized by electrospinning as follows. The BiFeO₃ precursor was prepared as previously reported [24]. The precursor was prepared from citrate acid-based solution, using iron (III) nitrate nonahydrate (99.99%, Alfa Aesar), bismuth (III) nitrate pentahydrate with a purity of 98% (Alfa Aesar), citrate acid (Sigma Aldrich) as the solutes, and N,N-dimethylformamide (DMF, China National Chemicals Corporation Ltd.) as the solution. The final concentration of the two precursor solutions were 0.2 M and 0.4 M, respectively. Excess Bi of about 5 mol% was used to

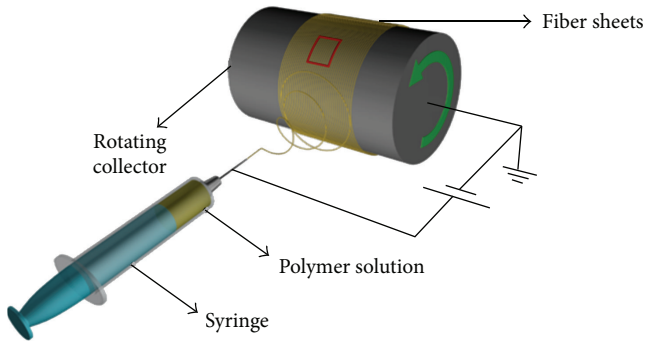


FIGURE 1: Schematic illustration for preparation of nanofibers by electrospinning.

compensate for the bismuth loss during the heating process. Polyvinylpyrrolidone (PVP, $M_w=1,300,000$ g/mol, Aldrich) was then added to the solution directly and stirred for 6 h at room temperature to obtain homogeneous solution for the electrospinning process.

This solution was fed into 20 mL syringe and electrospun through 0.5 mm diameter needle using an electrostatic spinning apparatus (Figure 1). The flow rate of spinning solution was maintained to 0.5 mL/h using a syringe pump, and an applied voltage was kept at 15 kV. The as-spun nanofibrous membranes were collected on an aluminium roller with a diameter of 100 mm at a rotating speed of 1000 rpm. The distance between the needle tip and the roller was 15 cm. And then the as-spun nanofibrous membranes were stabilized at 150°C for 10 min in air and heated at 600°C for 2 h in air to obtain the BFO nanofibers. The heating rate was kept at 10°C/min.

The crystallinity and morphology of the BFO nanofibers were examined by X-ray diffraction (XRD, Rigaku D/max 2500 V, Rigaku Corporation), scanning electron microscopy (SEM, JSM-7001F, JEOL Ltd.), and high-resolution TEM (HRTEM, JEOL2011). The average diameters of the nanofibers were calculated from 100 filaments based on the SEM images using image analysis software (Image J, National Institutes of Health, USA). The Raman spectrum measurements were performed in backscattering geometry with a radiation of Ar^+ laser at 633 nm by using a microscope-based Raman spectroscopy system (LabRAM HR, Horiba, NJ, USA). UV-visible diffuse reflectance absorption spectra were measured by a UV-vis spectrophotometer (Hitachi UV-3310). The magnetization of the samples was measured using superconducting quantum interference device (SQUID, MPMS-7, Quantum Design, San Diego, CA, USA) magnetometer. The photocatalytic activities were evaluated by the degradation of Congo red (CR) in aqueous solution under visible-light irradiation using a 500 W Xe lamp with a cutoff filter ($\lambda > 400$ nm) according to our previous study [25]. Briefly, aqueous suspensions of CR (50 mL, 20 mg/L) and BFO nanofibers (2 g/L) were placed in an open reactor, and the suspension was placed in darkness for one hour with magnetic stirring before irradiation to reach absorption/desorption equilibrium. The reaction temperature was kept at room temperature by cooling water to prevent any thermal catalytic effect.

The degradation of CR was evaluated by centrifuging the retrieved samples and recording the intensity of absorption peak of CR (495 nm) relative to its initial intensity (C/C_0) using a spectrophotometer.

3. Results and Discussion

Figure 2 shows SEM images of as-spun BFO-gel/PVP fibers and BFO nanofibers. The as-spun fibers (Figures 2(a) and 2(c)) are round in shape and have a rather uniform diameter over its length. The average diameter increased from 300 nm to 800 nm as the concentration of the solution increased from 0.2 M to 0.4 M. Figures 2(b) and 2(d) show that the BFO nanofibers have a reduced diameter of 100 nm and 300 nm after being heated. The reduction in diameter can be attributed to the thermal treatment, which has pyrolyzed the polymer at 600°C. In addition, the fibers surface became rougher after heating and annealing, which could be mainly assigned to a dramatic change in crystal structure [22].

The XRD patterns of the BFO nanofibers are shown in Figure 3(a). The reflection peaks of the different samples can be indexed as a single-phase perovskite structure belonging to the space group R3c (JCPDS card no. 86-1518), and no obvious peaks from other phase were detected, demonstrating that well-crystallized single phase BFO can be obtained under the current synthesis conditions. Fe_3O_4 and $\gamma\text{-Fe}_2\text{O}_3$ are not present as impurity phases according to the XRD pattern recorded at a very slow scan rate in the regions (33°–36° and 48°–50°) where the maximum intense peaks of $\gamma\text{-Fe}_2\text{O}_3$ and Fe_3O_4 are expected.

To get further insight on the structural variations of BFO nanofibers, typical Raman spectra of our BFO nanofibers were shown in Figure 3(b). The peaks at 140, 171, and 219 cm^{-1} can be assigned to A_1 (1TO), A_1 (2TO), and A_1 (3TO) modes for the rhombohedral BFO system, respectively, which is in good agreement with that of previously reported data [26]. Meanwhile, the E (TO) phonon modes were also quite consistent with our previous study [27].

The crystalline structure of BFO ultrafine nanofibers is further examined by HRTEM, as shown in Figure 4. It is observed from TEM images (Figures 4(a) and 4(b)) that BFO nanofibers are wave nodes-like, and the difference of diameter of nanofibers from 0.2 M and 0.4 M BFO solution was significant. The reason for this variation can rely on the increase of the concentration of the precursor solution, which results in increase of nanofibers under the same condition of electrospinning technique [28]. It indicated that the wave nodes-like morphology of nanofibers was produced by regulating the concentration of the precursor solution to a certain extent. The selected area electron diffraction (SAED) pattern from the pane area marked with dashed line in Figure 4(a) shows very sharp diffraction spots, proving the well-developed single-crystalline structure. Figure 4(c) is a HRTEM image of the grain boundary. The regular spacings of the observed lattice are 0.396 and 0.287 nm, which are corresponding to the (012) and (110) crystal planes of a rhombohedral BFO phase, respectively. This result was consistent with previous study [29].

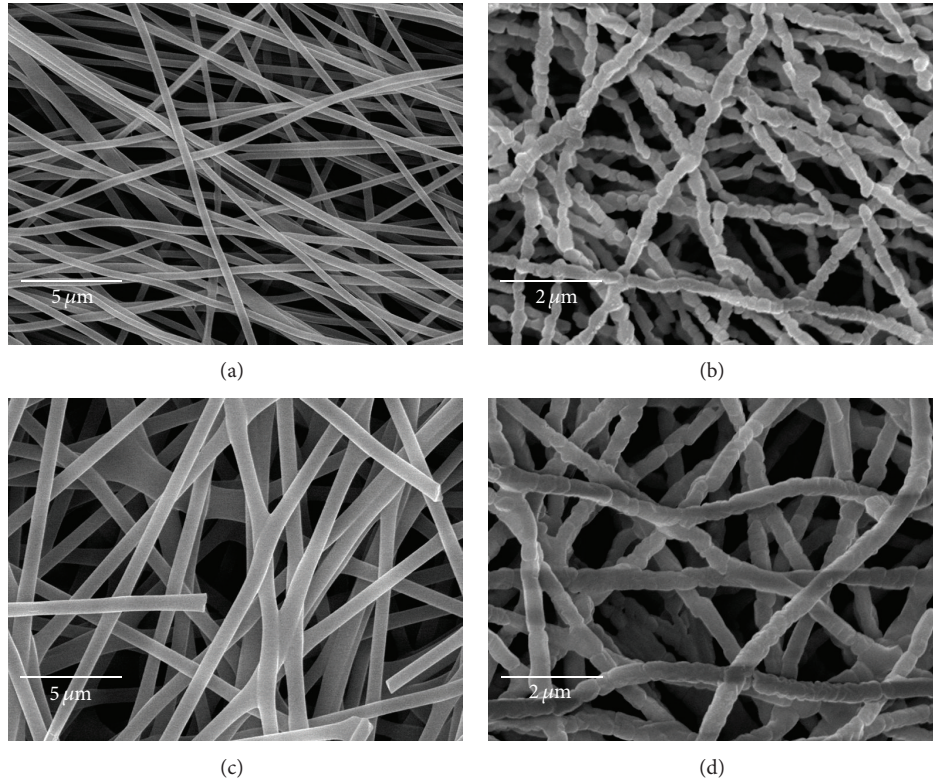


FIGURE 2: SEM images of (a) as-spun BFO-gel/PVP fibers without heat treatment and (b) BFO nanofibers after heat treatment synthesized with 0.2 M BFO solution; (c) as-spun BFO-gel/PVP fibers without heat treatment and (d) BFO nanofibers after heat treatment synthesized with 0.4 M BFO solution.

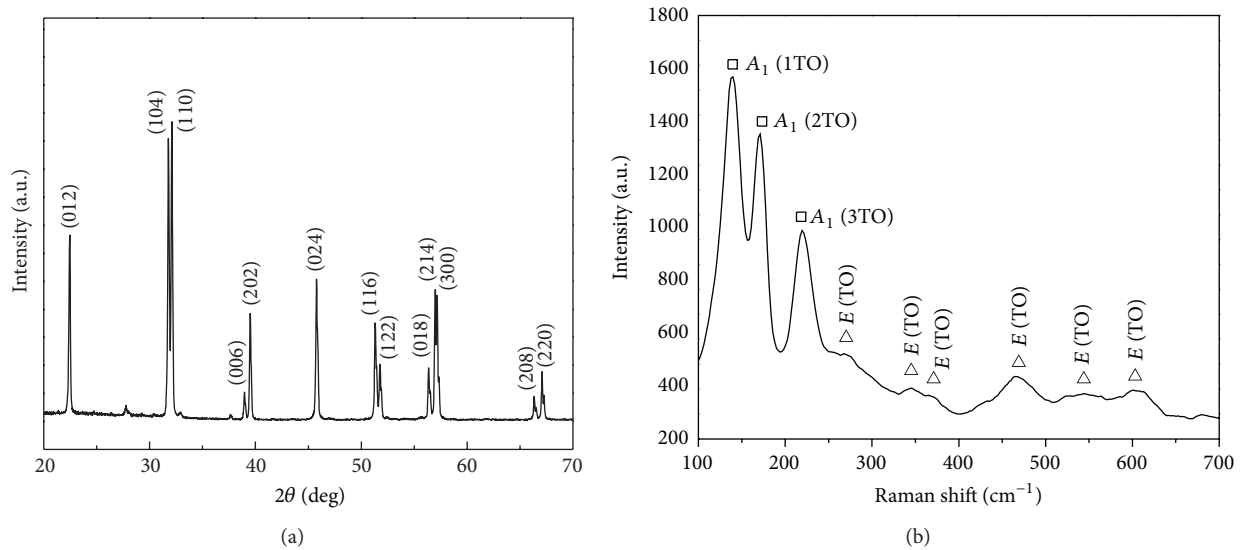


FIGURE 3: (a) XRD patterns of BFO nanofibers; (b) Raman spectra of BFO nanofibers.

Generally, the optical absorption performance of semiconductors is related to the electronic structure feature and their band gaps [30]. The optical properties of samples were studied by measuring their UV-vis diffuse reflectance absorption spectra. As shown in Figure 5(a), the absorption spectra of BFO nanofibers with different diameters were measured. The absorption spectra show that BFO nanofibers

can absorb considerable amounts of visible light, suggesting their potential applications as visible-light-driven photocatalysts. And compared with the BFO nanofibers with the diameter of 300 nm, the BFO nanofibers with the smaller diameter (100 nm) show higher visible-light absorption. This difference was mainly due to the nanoscale size effect including ultrafine diameter and large specific surface area [31].

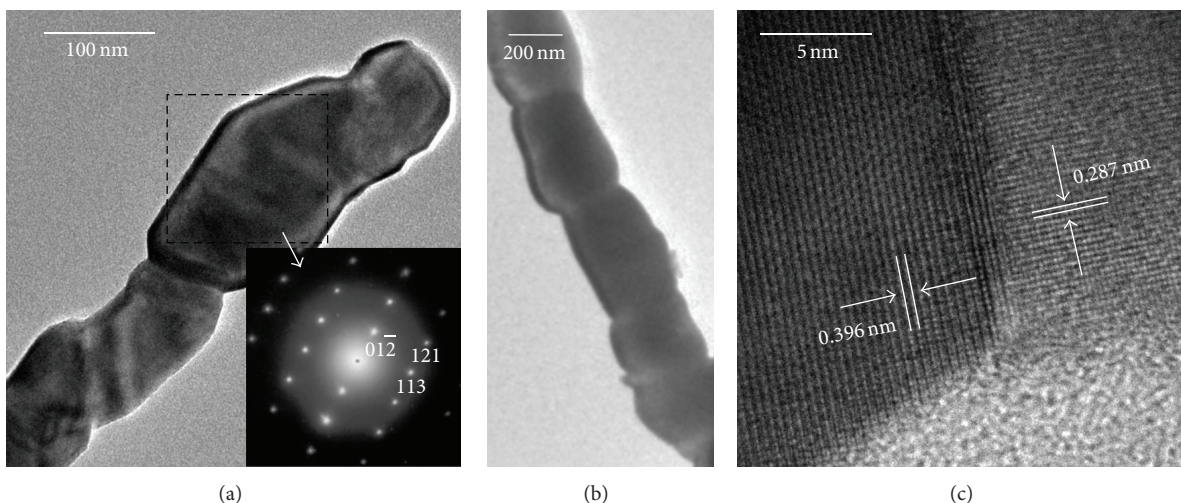


FIGURE 4: (a) TEM image of part of a single BFO nanofiber synthesized with 0.2 M BFO solution; inset is the selected area electron diffraction (SAED) pattern from the pane area marked with dashed line; (b) TEM image of part of a single BFO nanofiber synthesized with 0.4 M BFO solution; (c) HRTEM image of the grain boundary of BFO nanofibers.

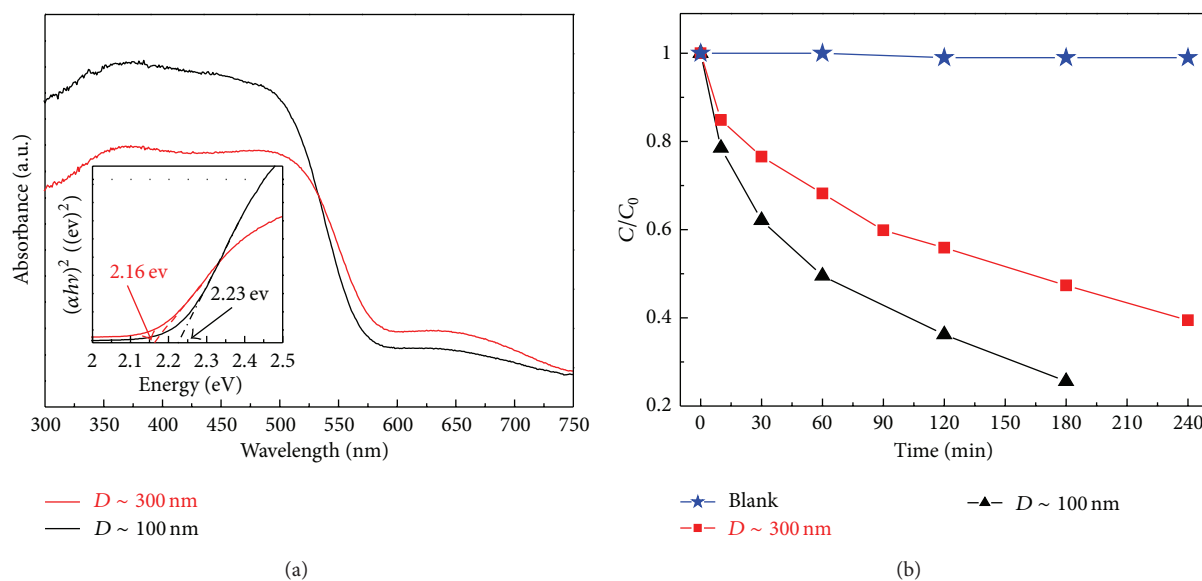


FIGURE 5: (a) UV-vis diffuse reflectance absorption spectra of BFO nanofibers with different diameters; inset is the calculation diagrams of the corresponding band gap; (b) photodegradation of CR in the presence of BFO nanofibers with different diameters under visible-light irradiation.

The optical absorption coefficient near the band edge follows [32]:

$$\alpha h\nu = A(h\nu - E_g)^{n/2}, \quad (1)$$

where α , h , ν , E_g , and A are absorption coefficient, Planck constant, light frequency, band gap, and a constant, respectively. Considering that BFO is a direct band gap material, the value of n for BiFeO_3 is 1 [33]. The corresponding values of direct band gap of BFO nanofibers can be evaluated by extrapolating the linear portion of $(\alpha h\nu)^2$ versus $(h\nu)$, as shown in the inset of Figure 5(a). After calculations, the values of the nanofibers with the diameters of 300 nm and 100 nm are 2.16 eV and 2.23 eV, respectively, which is quite

consistent with previous results [15, 34]. The obvious shift in absorption edge for the samples may be due to the change of fibers size [35]. In addition, a secondary edge that can also be assigned to crystal field transition was observed at higher wavelengths for the nanofibers.

To further evaluate the visible light photocatalytic activity of as-synthesized samples, Congo red (CR) with a major absorption peak at 495 nm was chosen as a model organic pollutant. Visible-light irradiation of aqueous CR/BFO led to an apparent decrease in absorption. Figure 5(b) gives the concentration changes of CR at 495 nm by BFO nanofibers as a function of irradiation time under visible light during the degradation process. A dark experiment (without irradiation)

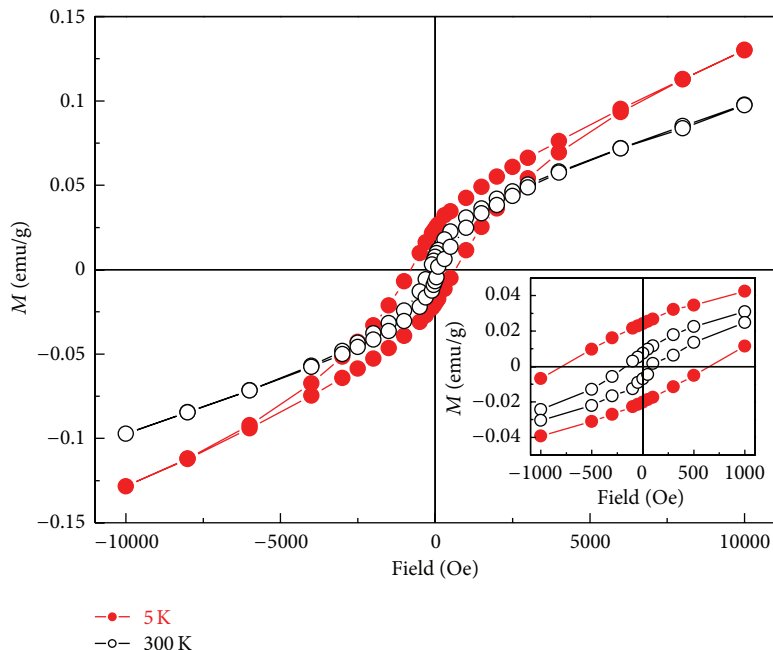


FIGURE 6: The magnetization hysteresis loops of BFO nanofibers at RT and 5 K, and inset is the partially enlarged curves, respectively.

was also performed, in which the CR decomposition was negligible. The BFO nanofibers show good photocatalytic efficiency. After being exposed to visible light for 3 hours, 75% of the CR was photodegraded with the BFO nanofibers of 100 nm diameter as photocatalysts, showing better photocatalytic activity than that of 300 nm diameter (50%). The reason may be that the smaller nanofibers have higher surface-area-to-volume ratios. In our earlier studies, the BFO nanoparticles with 100 nm size could only degrade almost 40% of the initial dye after 2 h under the same conditions [7], while the BFO nanofibers with the same size can degrade 65%. This can be attributed to the ultralong longitudinal dimension of nanofibers that provides a sufficiently spacious transport channel for charge separation [36]. It indicated that electrospinning technology for fabricating BFO nanofibers has more significant advantages in photocatalytic performance than other fabrication methods.

Considering the importance of the multiferroic property of BFO [37, 38], the magnetic ordering of the BFO nanofibers of 100 nm diameter was measured by SQUID (Figure 6). It is important to note that the saturated M is ~ 0.01 emu/g at RT, much smaller than that (~ 0.04 emu/g) of BFO nanowires [15] with 50 nm diameter prepared by AAO templates. It may be due to the size effect. The partially enlarged M-H curve is shown in the inset, which reveals that the RT coercive field of the BFO nanofibers is quite small (~ 150 Oe), similar to that of the nanoparticles [6, 8] and the nanowires [15]. The grain size of our nanofibers is larger than the 62 nm wavelength of the intrinsic spiral-modulated spin structure in bulk BiFeO_3 as previously reported [39]. It was reported that the cycloid structure becomes more anharmonic at lower T , and its detrimental effect on the magnetic ordering is devalued [39], leading to stronger ferromagnetics (FM), evidenced by the

M-H loop at $T = 5$ K, as shown in Figure 6. These results indicated that BFO nanofibers show weak ferromagnetic at RT and 5 K, similar to that of nanoparticles.

4. Conclusions

In summary, we have successfully prepared BFO nanofibers with 100 nm and 300 nm diameters by electrospinning. These nanofibers with bamboo-like morphology show a highly enhanced visible-light-active photocatalytic property, compared with the BFO nanoparticles. Our results also showed that the diameter could affect the band gap and photocatalytic performances of nanofibers. In addition, magnetic studies revealed their weak ferromagnetic behaviors at RT and 5 K. These BFO nanofibers can be useful for developing multifunctional devices combining magnetic, electronic, and optical properties.

Acknowledgments

This work was supported by the Ministry of Science and Technology of China through a 973-Project under Grant no. 2009CB623303, NSF of China (51025205, 51272181, and 51272121).

References

- [1] M. Fiebig, T. Lottermoser, D. Fröhlich, A. V. Goltsev, and R. V. Pisarev, "Observation of coupled magnetic and electric domains," *Nature*, vol. 419, no. 6909, pp. 818–820, 2002.
- [2] J. Wang, J. B. Neaton, H. Zheng et al., "Epitaxial BiFeO_3 multiferroic thin film heterostructures," *Science*, vol. 299, no. 5613, pp. 1719–1722, 2003.

- [3] S. Y. Yang, J. Seidel, S. J. Byrnes et al., "Above-bandgap voltages from ferroelectric photovoltaic devices," *Nature Nanotechnology*, vol. 5, no. 2, pp. 143–147, 2010.
- [4] A. Fujishima and K. Honda, "Electrochemical photolysis of water at a semiconductor electrode," *Nature*, vol. 238, no. 5358, pp. 37–38, 1972.
- [5] F. Gao, Y. Yuan, K. F. Wang et al., "Preparation and photoabsorption characterization BiFeO₃ nanowires," *Applied Physics Letters*, vol. 89, no. 10, Article ID 102506, pp. 2506–2508, 2006.
- [6] F. Gao, X. Chen, K. Yin et al., "Visible-light photocatalytic properties of weak magnetic BiFeO₃ nanoparticles," *Advanced Materials*, vol. 19, no. 19, pp. 2889–2892, 2007.
- [7] S. Li, Y. Lin, B. Zhang, C. Nan, and Y. Wang, "Photocatalytic and magnetic behaviors observed in nanostructured BiFeO₃ particles," *Journal of Applied Physics*, vol. 105, no. 5, Article ID 056105, 2009.
- [8] S. Li, Y. Lin, B. Zhang, Y. Wang, and C. Nan, "Controlled fabrication of BiFeO₃ uniform microcrystals and their magnetic and photocatalytic behaviors," *Journal of Physical Chemistry C*, vol. 114, no. 7, pp. 2903–2908, 2010.
- [9] Y. G. Wang, G. Xu, Z. H. Ren et al., "Mineralizer-assisted hydrothermal synthesis and characterization of BiFeO₃ nanoparticles," *Journal of the American Ceramic Society*, vol. 90, no. 8, pp. 2615–2617, 2007.
- [10] U. A. Joshi, J. S. Jang, P. H. Borse, and J. S. Lee, "Microwave synthesis of single-crystalline perovskite BiFeO₃ nanocubes for photoelectrode and photocatalytic applications," *Applied Physics Letters*, vol. 92, no. 24, Article ID 242106, 2008.
- [11] J. Chen, X. R. Xing, A. Watson et al., "Rapid synthesis of multiferroic BiFeO₃ single-crystalline nanostructures," *Chemistry of Materials*, vol. 19, no. 15, pp. 3598–3600, 2007.
- [12] J. Wei, D. S. Xue, and Y. Xu, "Photoabsorption characterization and magnetic property of multiferroic BiFeO₃ nanotubes synthesized by a facile sol-gel template process," *Scripta Materialia*, vol. 58, no. 1, pp. 45–48, 2008.
- [13] X. Y. Zhang, C. W. Lai, X. Zhao, D. Y. Wang, and J. Y. Dai, "Synthesis and ferroelectric properties of multiferroic BiFeO₃ nanotube arrays," *Applied Physics Letters*, vol. 87, no. 14, Article ID 143102, pp. 1–3, 2005.
- [14] X. Y. Zhang, J. Y. Dai, and C. W. Lai, "Synthesis and characterization of highly ordered BiFeO₃ multiferroic nanowire arrays," *Progress in Solid State Chemistry*, vol. 33, no. 2–4, pp. 147–151, 2005.
- [15] F. Gao, Y. Yuan, K. F. Wang et al., "Preparation and photoabsorption characterization BiFeO₃ nanowires," *Applied Physics Letters*, vol. 89, no. 10, Article ID 102506, 2006.
- [16] E. Zussman, A. Theron, and A. L. Yarin, "Formation of nanofiber crossbars in electrospinning," *Applied Physics Letters*, vol. 82, no. 6, pp. 973–975, 2003.
- [17] Y. Dzenis, "Spinning continuous fibers for nanotechnology," *Science*, vol. 304, no. 5679, pp. 1917–1919, 2004.
- [18] D. Li and Y. Xia, "Electrospinning of nanofibers: reinventing the wheel?" *Advanced Materials*, vol. 16, no. 14, pp. 1151–1170, 2004.
- [19] S. H. Xie, J. Y. Li, R. Proksch et al., "Nanocrystalline multiferroic BiFeO₃ ultrafine fibers by sol-gel based electrospinning," *Applied Physics Letters*, vol. 93, no. 22, Article ID 222904, 2008.
- [20] A. Baji, Y. Mai, Q. Li, S. Wong, Y. Liu, and Q. W. Yao, "One-dimensional multiferroic bismuth ferrite fibers obtained by electrospinning techniques," *Nanotechnology*, vol. 22, no. 23, Article ID 235702, 2011.
- [21] J. H. Song, J. H. Nam, J. H. Cho, B. Kim, M. Chun, and D. Choi, "Microstructures and multiferroic properties of electrospun BiFeO₃ nanofibers," *Journal of the Korean Physical Society*, vol. 59, no. 3, pp. 2308–2312, 2011.
- [22] N. L. Wei Wang, Y. Chi, Y. J. Li, W. F. Yan, X. T. Li, and C. L. Shao, "Electrospinning of magnetical bismuth ferrite nanofibers with photocatalytic activity," *Ceramics International*, vol. 39, no. 4, pp. 3511–3518, 2013.
- [23] P. M. Shaibani, K. Prashanthi, A. Sohrabi, and T. Thundat, "Photocatalytic BiFeO₃ nanofibrous mats for effective water treatment," *Journal of Nanotechnology*, vol. 2013, Article ID 939531, 6 pages, 2013.
- [24] Y. Wang, Q. Jiang, H. He, and C. Nan, "Multiferroic BiFeO₃ thin films prepared via a simple sol-gel method," *Applied Physics Letters*, vol. 88, no. 14, Article ID 142503, 2006.
- [25] S. Li, Y. Lin, B. Zhang, Y. Wang, and C. Nan, "Controlled fabrication of BiFeO₃ uniform microcrystals and their magnetic and photocatalytic behaviors," *Journal of Physical Chemistry C*, vol. 114, no. 7, pp. 2903–2908, 2010.
- [26] Y. Wang and C. Nan, "Site modification in BiFeO₃ thin films studied by Raman spectroscopy and piezoelectric force microscopy," *Journal of Applied Physics*, vol. 103, no. 11, Article ID 114104, 2008.
- [27] C.-W. Nan and Y. Wang, "Site modification in BiFeO₃ thin films studied by Raman spectroscopy and piezoelectric force microscopy," *Journal of Applied Physics*, vol. 103, no. 11, Article ID 114104, 2008.
- [28] S. V. Fridrikh, J. H. Yu, M. P. Brenner, and G. C. Rutledge, "Controlling the fiber diameter during electrospinning," *Physical Review Letters*, vol. 90, no. 14, Article ID 144502, pp. 1–4, 2003.
- [29] R. Guo, L. Fang, W. Dong, F. Zheng, and M. Shen, "Magnetically separable BiFeO₃ nanoparticles with a γ -Fe₂O₃ parasitic phase: controlled fabrication and enhanced visible-light photocatalytic activity," *Journal of Materials Chemistry*, vol. 21, no. 46, pp. 645–652, 2011.
- [30] V. I. Klimov, S. A. Ivanov, J. Nanda et al., "Single-exciton optical gain in semiconductor nanocrystals," *Nature*, vol. 447, no. 7143, pp. 441–446, 2007.
- [31] W. W.-F. Leung and C. C. Pei, "Enhanced photocatalytic activity of electrospun TiO₂/ZnO nanofibers with optimal anatase/rutile ratio," *Catalysis Communications*, vol. 37, pp. 100–104, 2013.
- [32] M. A. Butler, "Photoelectrolysis and physical properties of the semiconducting electrode WO₂," *Journal of Applied Physics*, vol. 48, no. 5, pp. 1914–1920, 1977.
- [33] A. J. Hauser, J. Zhang, L. Mier et al., "Characterization of electronic structure and defect states of thin epitaxial BiFeO₃ films by UV-visible absorption and cathodoluminescence spectroscopies," *Applied Physics Letters*, vol. 92, no. 22, Article ID 222901, 2008.
- [34] K. Takahashi, N. Kida, and M. Tonouchi, "Terahertz radiation by an ultrafast spontaneous polarization modulation of multiferroic BiFeO₃ thin films," *Physical Review Letters*, vol. 96, no. 11, Article ID 117402, 2006.
- [35] B. B. Kale, J. Baeg, S. M. Lee, H. Chang, S. Moon, and C. W. Lee, "CdIn₂S₄ nanotubes and "marigold" nanostructures: a visible-light photocatalyst," *Advanced Functional Materials*, vol. 16, no. 10, pp. 1349–1354, 2006.
- [36] Q. Liu, Y. Zhou, J. Kou et al., "High-yield synthesis of ultralong and ultrathin Zn₂GeO₄ nanoribbons toward improved photocatalytic reduction of CO₂ into renewable hydrocarbon fuel,"

Journal of the American Chemical Society, vol. 132, no. 41, pp. 14385–14387, 2010.

- [37] L. W. Martin, S. P. Crane, Y.-H. Chu et al., “Multiferroics and magnetoelectrics: thin films and nanostructures,” *Journal of Physics Condensed Matter*, vol. 20, no. 43, Article ID 434220, 2008.
- [38] F. Kubel and H. Schmid, “Structure of a ferroelectric and ferroelastic monodomain crystal of the perovskite BiFeO_3 ,” *Acta Crystallographica Section B*, vol. 46, no. 6, pp. 698–702, 1990.
- [39] A. V. Zaleskii, A. K. Zvezdin, A. A. Frolov, and A. A. Bush, “ ^{57}Fe NMR study of a spatially modulated magnetic structure in BiFeO_3 ,” *JETP Letters*, vol. 71, no. 11, pp. 465–468, 2000.

Research Article

Cobalt Xanthate Thin Film with Chemical Bath Deposition

İ. A. Kariper¹ and T. Özpozan²

¹ Erciyes University, Education Faculty, 38039 Kayseri, Turkey

² Erciyes University, Faculty of Art and Science, 38039 Kayseri, Turkey

Correspondence should be addressed to İ. A. Kariper; akariper@gmail.com

Received 15 March 2013; Accepted 8 May 2013

Academic Editor: Mengnan Qu

Copyright © 2013 İ. A. Kariper and T. Özpozan. This is an open access article distributed under the Creative Commons Attribution License, which permits unrestricted use, distribution, and reproduction in any medium, provided the original work is properly cited.

Cobalt xanthate thin films (CXTFs) were successfully deposited by chemical bath deposition, onto amorphous glass substrates, as well as on p- and n-silicon, indium tin oxide, and poly(methyl methacrylate). The structure of the films was analyzed by far-infrared spectrum (FIR), mid-infrared (MIR) spectrum, nuclear magnetic resonance (NMR), and scanning electron microscopy (SEM). These films were investigated from their structural, optical, and electrical properties point of view. Electrical properties were measured using four-point method, whereas optical properties were investigated via UV-VIS spectroscopic technique. Uniform distribution of grains was clearly observed from the photographs taken by scanning electron microscope (SEM). The transmittance was about 70–80% (4 hours, 50°C). The optical band gap of the CXTF was graphically estimated to be 3.99–4.02 eV. The resistivity of the films was calculated as 22.47–75.91 Ω ·cm on commercial glass depending on film thickness and 44.90–73.10 Ω ·cm on the other substrates. It has been observed that the relative resistivity changed with film thickness. The MIR and FIR spectra of the films were in agreement with the literature analogues. The expected peaks of cobalt xanthate were observed in NMR analysis on glass. The films were dipped in chloroform as organic solvent and were analyzed by NMR.

1. Introduction

Cobalt xanthates are similar to hybrid materials, because they have an organic sulfide part and inorganic metal part as iron xanthate. These organometallic compounds have wide ranging properties such as optical, electrical, and magnetic characteristics [1–4]. It has been shown that these thin films show different properties such as an antibacterial agent, magnetic and semiconductor material, which allowed them to be used for data storage, solar cell production, and water purification [5–10]. Neither cobalt isopropyl xanthate thin films production nor their optical, electrical properties and structural analysis have been studied yet. These thin films and their bulk compounds may be useful in many areas, especially in solar cells. Chemical vapor deposition and physical vapor deposition are included among thin film deposition methods used to produce metal sulfide thin films [5, 11]. These methods are expensive and need a variety of instruments unlike the chemical bath deposition method.

The aim of this paper was to produce cobalt xanthate thin film by chemical bath deposition method and to examine its structural, optical, and electrical properties. Metal xanthate

complexes rapidly occur when the precipitate rises to the surface in chemical bath deposition. Moreover, due to the nature of organometallic thin films, it is difficult to analyze them. The metal xanthates thin films were produced with difficulty.

2. Experimental

2.1. Reagents. Isopropyl xanthate was synthesized first as described in the literature, and the stock solution of 0.1 M was prepared. High purity reagents were used for all the prepared solutions. The stock solution was diluted each time when required. The other stock solution of iron nitrate salt was prepared from high purity compound (99.9%, E. Merck, Darmstadt, Sigma Aldrich). All laboratory glassware and substrates were cleaned by soaking in diluted nitric acid and rinsing with alcohol and deionized water prior to use.

2.2. Synthesis of Isopropyl Xanthate. Isopropyl xanthate was synthesized by dissolving 3.74 g of KOH (0.067 mol) in a mixture of 4.5 mL CS₂, 6 mL isopropyl alcohol and 9 mL benzene and heated under a reflux condenser. The mixture was mixed

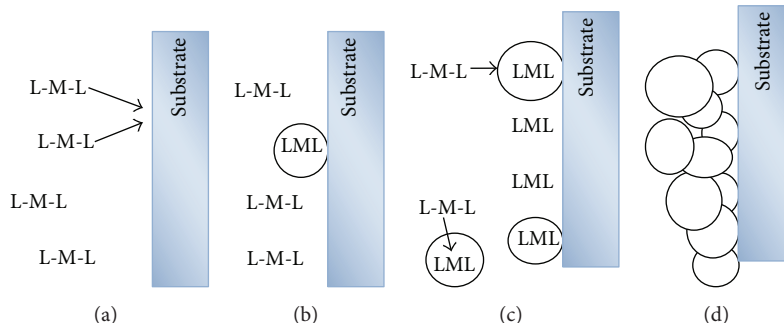


FIGURE 1: Probable steps related with complex formation (ion-ion mechanism). (a) Particles of L-M-L complexes are spread towards the substrate. (b) The complex is stuck to the substrate as an LML composite, still being in the solution. (c) LML grains grow with the formation of more complexes and absorption. (d) Grains form the film by sticking to each other (M: metal, L: ligand) [12].

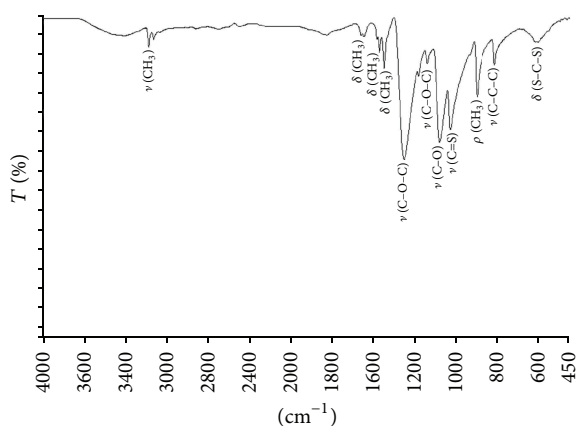


FIGURE 2: Cobalt xanthate thin film on glass substrate MIR spectrum.

for 20 minutes at 35°C and for 45 minutes at 45°C. Then, it was mixed for 1 hour at 60°C. Approximately 9 grams of the reaction product was then purified by rinsing with acetone and drying in the oven at 30°C for 48 hours [13–30].

2.3. Preparation of Films. Ten mL of 0.1 M cobalt nitrate and 10 mL of 0.1 M isopropyl xanthate were mixed in a beaker. The substrates were dipped into this chemical bath at required temperatures. As the result of ion-ion mechanism, CXTF was formed and was deposited on all the substrates. The films were deposited at different temperatures of 30, 40, and 50°C, whereas pH of the bath was maintained between 6.50. In addition, deposition time was changed from 4 to 7 hours at 40 and 50°C, 16–19 hours at 30°C. The thin films were cleaned in purified water and dried before their further examinations. The formation of the film is shown in detail in Figure 1.

2.4. Measurements. The vibrational spectrum of CXTF was recorded by Perkin Elmer Spectrum 400 spectrometer (TGS detector) with ATR. The scanning number was 10 and resolution was 4 cm⁻¹. The ¹H-NMR spectrum was measured by a Bruker (400 MHz) spectrometer. The surface properties of all films were examined using EVO40-LEO computer controlled digital scanning electron microscope (SEM) with seconder

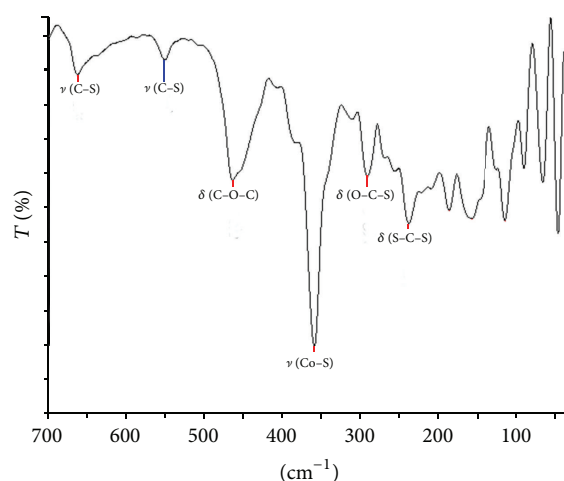


FIGURE 3: Cobalt xanthate thin film on glass substrate FIR spectrum.

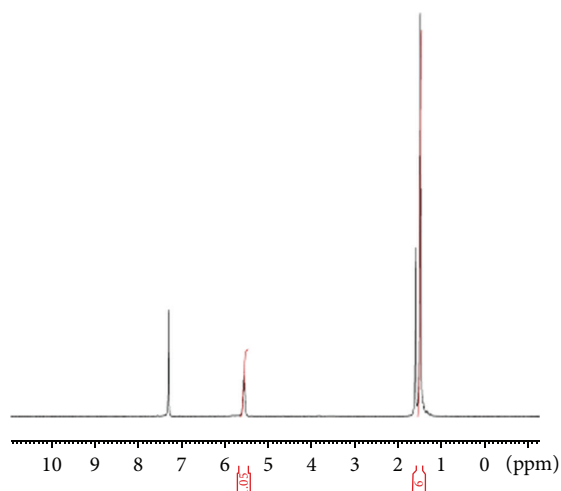
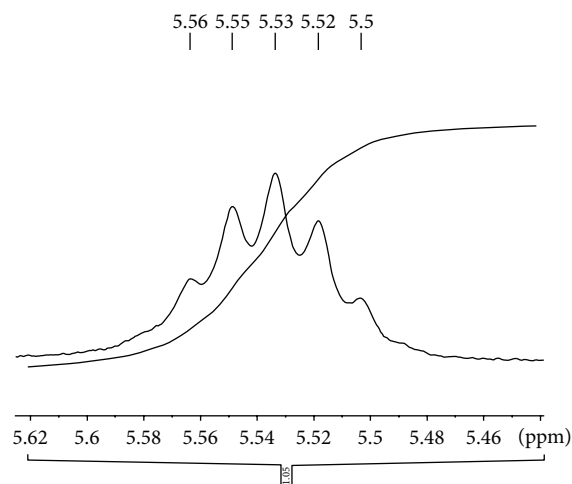
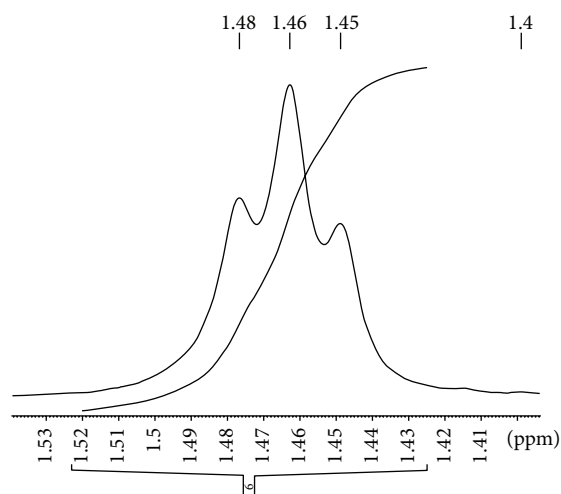
electron detector. Electrical properties were measured using four-point measurements technique, and accordingly the resistivity was calculated. The film thicknesses were measured with atomic force microscopy (AFM). The optical measurements were conducted by a Hach Lange DR 5000 spectrophotometer at room temperature by placing an uncoated identical glass substrate in the reference beam. The optical spectra of the thin films were recorded in the wavelength range of 250–700 nm.

3. Results and Discussion

We used the FIR, MIR, and ¹H-NMR spectra of cobalt xanthate thin film on glass. The spectra are shown in Figures 2, 3, 4, 5, and 6.

Figure 1 illustrates that in the cobalt xanthate thin film,

- (i) the –OH peak occurred at 3200–3600 cm⁻¹,
- (ii) the symmetric stretching vibration of the aliphatic groups (–CH₃) was seen at 2976–2932 cm⁻¹,
- (iii) the bending vibration of –CH₃ was seen at 1448–1373–1349 cm⁻¹,

FIGURE 4: Cobalt xanthate thin film $^1\text{H-NMR}$ at 0–10 ppm.FIGURE 6: Cobalt xanthate thin film $^1\text{H-NMR}$ at 5 ppm.FIGURE 5: Cobalt xanthate thin film $^1\text{H-NMR}$ at 1 ppm.

- (iv) the asymmetric stretching of C–O–C at $1253\text{--}1182\text{--}1141\text{ cm}^{-1}$,
- (v) the symmetric stretching vibration of –C–O at 1081 cm^{-1} ,
- (vi) the stretching vibration of –C=S at 1029 cm^{-1} ,
- (vii) rocking vibration of –CH₃ at 899 cm^{-1} ,
- (viii) symmetric vibration of –C–C–C at 811 cm^{-1} , and
- (ix) symmetric stretching vibration of S–C–S at 602 cm^{-1} .

In Figure 3, the stretching vibrations of Co–S were observed at 359 cm^{-1} , similar to the other functional groups of cobalt xanthate's organic parts [31–38]. We did not consider any measurements below 200 cm^{-1} . Figure 3 illustrates that in the cobalt xanthate thin film,

- (i) the vibration of –C–S at $662\text{--}521\text{ cm}^{-1}$,
- (ii) the bending vibration of –C–O–C at 463 cm^{-1} ,
- (iii) the stretching vibration of O–C–S at 291 cm^{-1} , and
- (iv) the bending vibration of S–C–S at 238 cm^{-1} .

In the $^1\text{H-NMR}$ spectrum (Figures 4–6), CXTF was dipped into a chloroform solution for spectrum analysis. The scanning number was 16 for all samples. The solvent peak (chloroform) was observed at 7.2 ppm, whereas trace concentration of the water peak was observed at 1.5 ppm when the triplet peak of the –CH₃ group occurred at 1.52 and 1.41 ppm. Since proton number was one, integration number was 1.05. The group of –CH NMR peaks was divided into five at between 5.50–5.60 due to neighboring –CH₃ groups, and the integration number was 1.05. The –CH group had an oxygen atom as a neighbor which caused a decreased electron shielding, so its peak was observed in the low area [39–41]. No impurities were observed in the spectra. The 1 ppm peak was expected to split into a double peak, but actually it was divided into triplet peak. This meant that

- (i) the rotation of the isopropyl groups can be obstructed, and the methyl groups give doublet-doublet resonance,
- (ii) the isopropyl groups can be bonded to different cobalt shapes, and the methyl groups give doublet-doublet resonance,
- (iii) magnetic properties of cobalt atom can also be affected by the NMR spectrum, which is come together doublet-doublet peak.

The doublet peaks can be combined with each other, thus we saw a triplet peak [42].

The transmittance (T) and absorbance (A) for CXTF can be used for the calculation of reflectance (R) from the following expression [43]:

$$T = (1 - R)^2 e^{-A}. \quad (1)$$

Transmittance and absorbance measurements were performed at room temperature in the range of 300–1100 nm. The films were deposited at different deposition temperatures and deposition times as shown in Figures 7, 8, and 9. The transmittance change with changing deposition times and deposition temperatures can be seen from the curves. The optimum

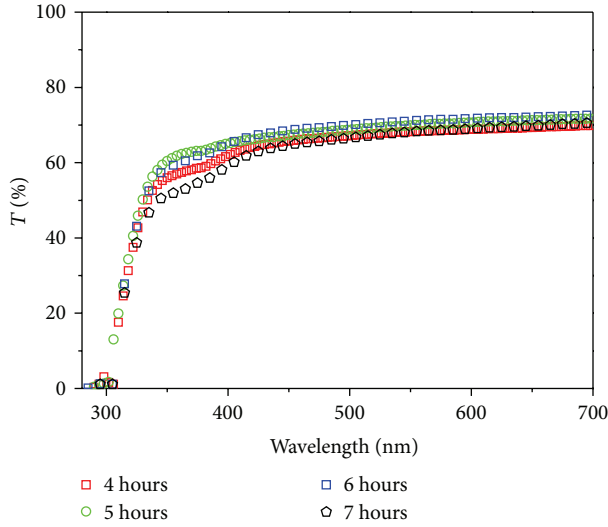


FIGURE 7: Change of % T and % R with wavelength at various deposition time ($t = 50^\circ\text{C}$).

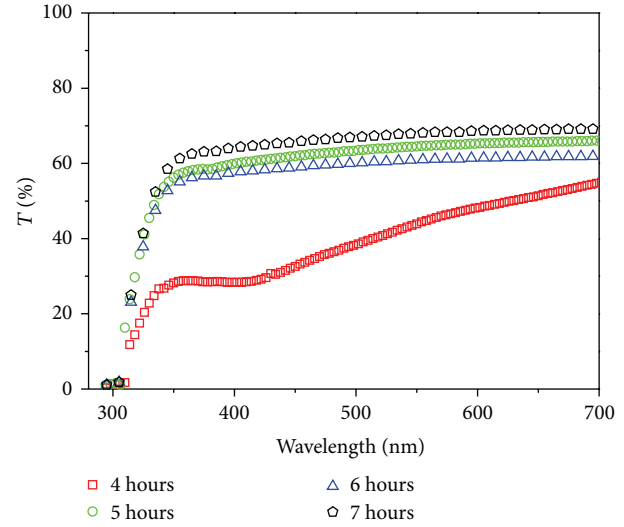


FIGURE 8: Change of % T and % R with wavelength at various deposition time ($t = 40^\circ\text{C}$).

values for deposition time and temperature were selected as 4 hours at 50°C , respectively ($\sim 70\%$ transmittance).

The highest deposition temperature and time were taken as 50°C and 19 hours (at 30°C) for upper limit of the parameters, respectively. Metal xanthates are known to decompose beyond these limits [36]. Cobalt xanthates, in a similar way, decomposed at 60°C and 21 hour of deposition time to give iron oxide, oxide chloride, or sulfide as decomposition product in this study. The cobalt xanthate decomposed into cobalt oxide or sulfide above 50°C and 19 hours.

The refractive index and extinction coefficient for the films are given by the following equations [43]:

$$n = \frac{(1+R)}{(1-R)} + \sqrt{\frac{4R}{(1-R)^2} - k^2}, \quad (2)$$

$$k = \frac{\alpha\lambda}{4\pi}.$$

The refractive index was not regularly affected by deposition temperatures at 30, 40, 50°C , and its values were reported as 1.80, 2.60, and 1.80 in Figure 10. The refractive index was sputtered at 40°C . Moreover, the extinction coefficients were, respectively, 0.023, 0.025, and 0.082 at 30, 40, 50°C (in 550 nm wavelength). The n - k graphic shows anomalous dispersion. According to literature, this anomalous behavior is due to the resonance effect between the incidental electromagnetic radiation and the electrons polarization, which leads to the electron coupling in the structure of the oscillating electric field [44]. The optic band gap energy (E_g) was determined from the absorption spectra of the films using the following relation [43–48]:

$$(\alpha h\nu) = A (h\nu - E_g)^n, \quad (3)$$

where A is a constant, α is the absorption coefficient, $h\nu$ is the photon energy, and n is a constant, which is equal to 1/2 for

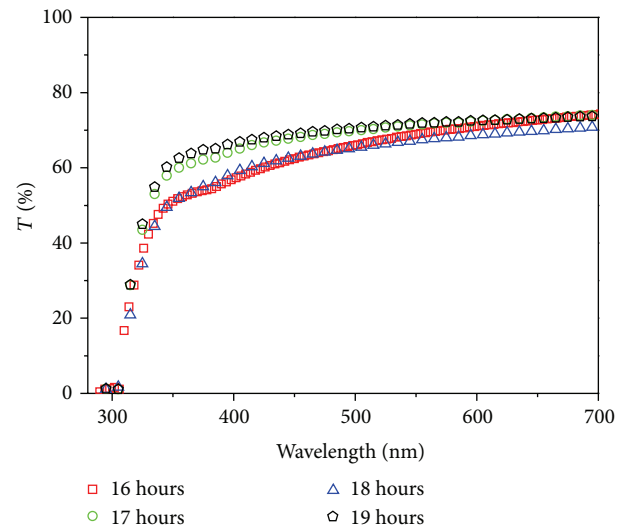


FIGURE 9: Change of % T and % R with wavelength at various deposition time ($t = 30^\circ\text{C}$).

the direct band gap semiconductor. The plot of $(\alpha h\nu)^2$ versus $h\nu$ is illustrated in Figure 11.

The band gaps (E_g) of the films changed as 3.98, 3.99, and 4.01 in Figure 11. Film thickness was increased with deposition temperature, whereas the band gap of the films was not decreased with film thickness. Both electrical and optical bandwidths of a material are correlated with the magnitude of columbic interactions. To be more precise, the size of atoms and electronegativity values are the two most important factors, affecting bandwidth. Bandwidth of a material is expected to get higher when the atoms get smaller, bonds getting stronger, and with higher electronegativity of the atoms. Although there are some exceptions, nitrides and oxides, which are the elements from III-V groups of periodic table, are generally known with their high optic band ranges.

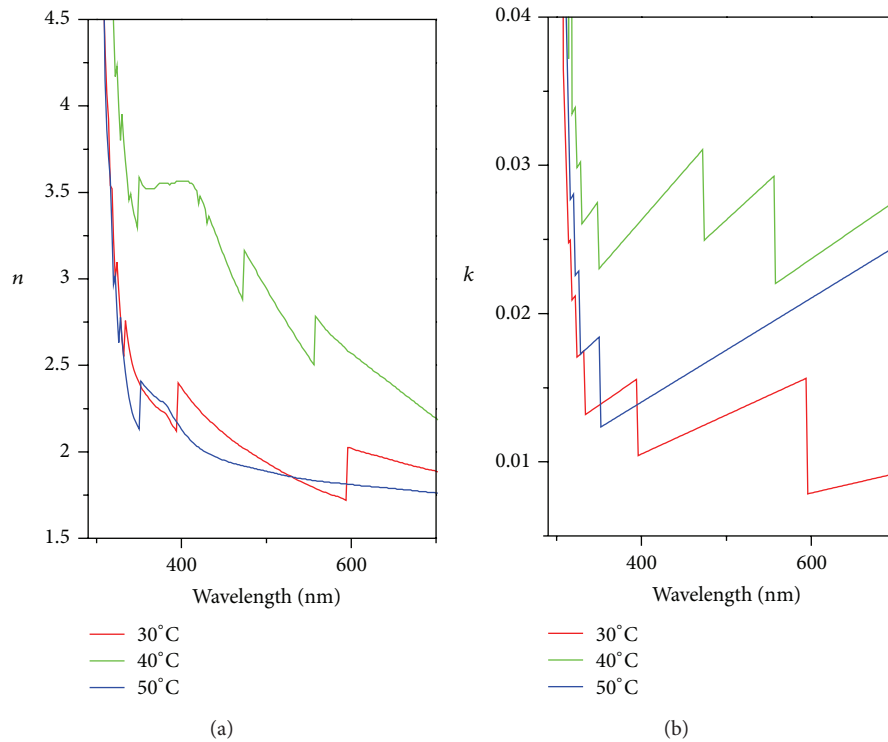


FIGURE 10: n - k graphic according to deposition temperature.

The high optic bandwidth of the organometallic compound used in our study is in line with the literature, since it is formed by small atoms with high electronegativity [49].

It was found that the film thicknesses were not increased nearly linearly with increasing deposition temperature whereas the band gap of the films decreased with increasing film thickness as expected. Similarly, resistivity increased with film thicknesses which was contradictory to the literature [50]. The film thickness of the films is shown at Figure 12, according to deposition time.

The resistivity of the films was determined by four-point measurements of the films using the following relation [51]:

$$\rho = \frac{\prod W V}{\ln 2 I} \quad (W \ll s), \quad (4)$$

where W is film thickness, V is the voltage, I is the current, and s is the distance between the probes. The resistivity was measured in dark, at room temperature. In the measurements, the distance of the probes was in millimeter, whereas the film thickness was in nanometer scale.

The resistivities of the films were measured as 22.47, 42.71, and 75.91 Ω -cm for the film thicknesses 198.14, 267.15, and 454.07 nm, respectively. The resistivity of the films deposited increased with the film thickness as can be seen from the plot of film thickness versus resistivity (Figure 13). Although Moualkia et al. and Kasap et al. found that the film thicknesses between 250–900 nm were slightly affected by the resistivity of the film, the resistivity of cobalt xanthate increased with the film thickness [48, 50]. It is a known fact that the aliphatic groups in the structure increase the resistance, they are not

conductive. Thus, they are causing an increase on the resistance with the increase of the film thickness.

Thin films were also produced on n-silicium, p-silicium, poly(methyl methacrylate), and indium tin oxide as different substrates in this work. The film resistivity on these substrates was found to be different than commercial glass studied previously. The resistivities of the poly(methyl methacrylate) (PMM), indium tin oxide (ITO), n-silicon (n-Si), and p-silicon (p-Si) substrates were measured as 67.15, 50.98, 44.90, and 73.10 Ω -cm at the optimized parameters of deposition time and temperature, respectively (Figure 14). It was found that CXTF on p-Si substrate had the highest resistivity, whereas the resistivity of the n-Si was the lowest [52–54]. It is a well-known fact that these kinds of materials are stuck to the surface with π -bonds or with idle electrons of electronegative atoms [6]. When such a material is deposited on n-Si, which is rich on electrons, the electron doublets of these bonds as well as idle doublets will apply a tension to the material; thus electron transmission between the substrate and thin film will be easier. So the resistance will decrease and the conductivity will increase. In the literature, there are examples about the impact of substrates on the resistance [55].

Figures 15(a) and 15(b) show SEM photos of cobalt xanthate thin film. It is given strange exposure. At 5 and 10 μ m, SEM photo of cobalt xanthate thin film was dispersed like biologic cells. The grains were resembling cancer cells in micron scale. It was assumed that the grains formed colonies. Spaces appeared very frequently at 10 μ m scale. The grains scattered very much. Any connection did not appear between the cells. These large spaces affect the homogeneity of the thin films,

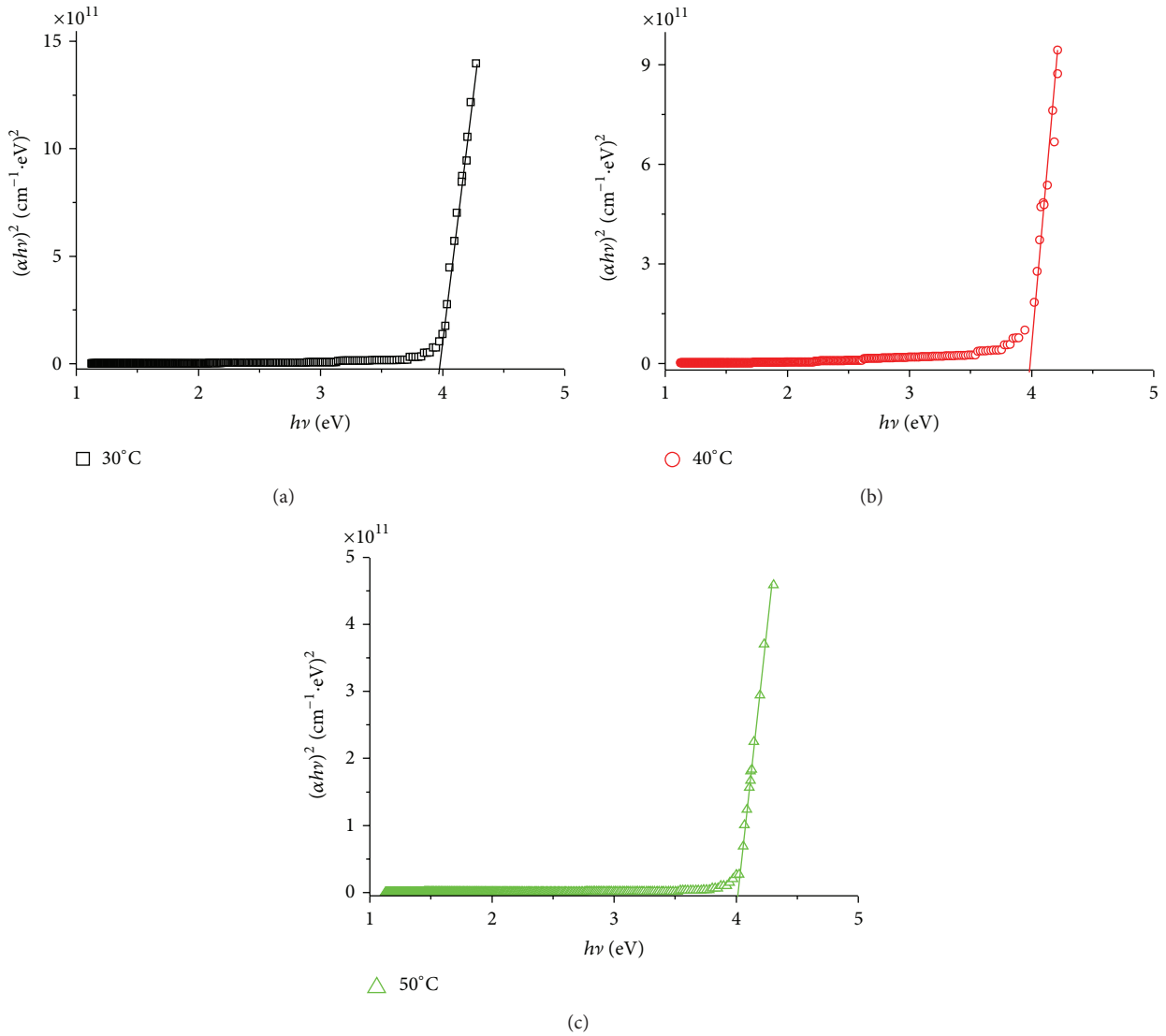


FIGURE 11: Plot of $(\alpha h\nu)^2$ versus $h\nu$ in different deposition temperatures.

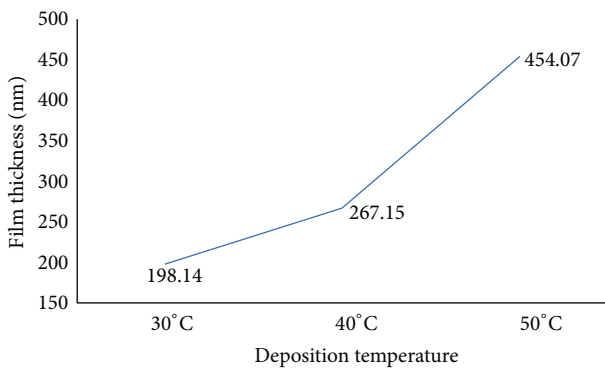


FIGURE 12: Film thickness—deposition temperature.

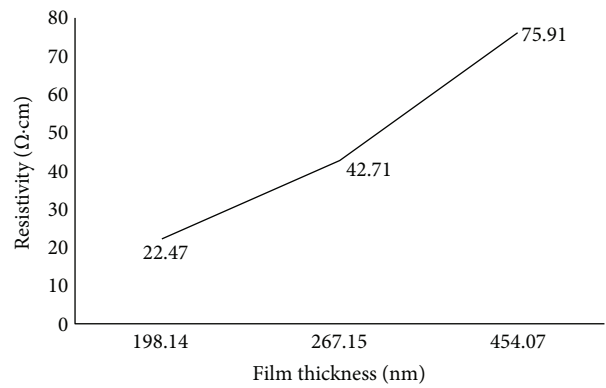


FIGURE 13: Resistivity—film thickness.

which might be the reason of their high resistivity. Also it may be the reason of anomalous behaviors of optical properties.

The elemental analysis results were calculated using the ratio of sulfide and cobalt according to EDX data in Figure 16.

The ratio of sulfide and cobalt changed with deposition temperature. The ratios of sulfide and cobalt in different deposition temperatures were 1.262, 1.776, and 2.112. In a cobalt

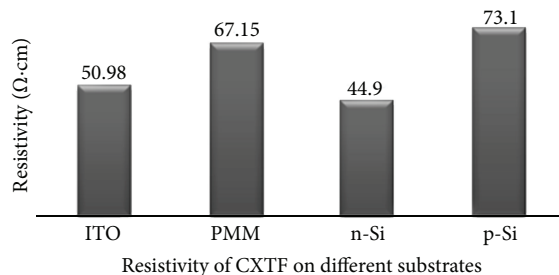


FIGURE 14: Resistivity of CXTF on different substrates.

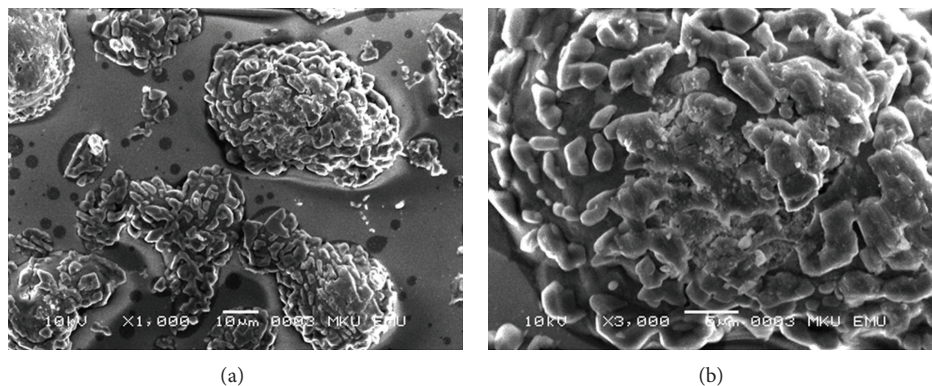


FIGURE 15: (a) Cobalt xanthate thin film on glass substrate (10 μm). (b) Cobalt xanthate thin film on glass substrate (5 μm).

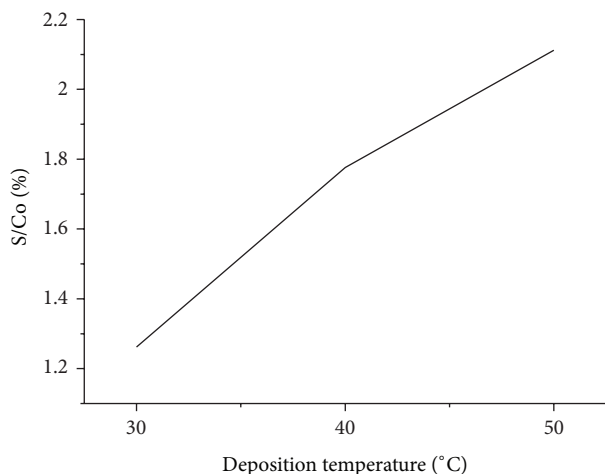


FIGURE 16: Sulfide and cobalt elemental ratio according to deposition temperature.

xanthate molecule, the theoretical ratio of the sulfide and cobalt is approximately 3.255. The elemental results were closer to the theoretical value at 50°C (Co-tris isopropyl xanthate). This shows that the cobalt cation bonds to the three xanthate molecule, as per the literature [37].

4. Conclusion

Cobalt isopropyl xanthate thin film was prepared first time on glass, poly(methyl methacrylate), indium tin oxide, n-silicon,

and p-silicon substrate via ion-ion mechanism. The optimum parameters were determined to be 4 hours and 50°C for the deposition time and the temperature. The variations of some chemical properties at different deposition temperatures, such as 30, 40, 50°C, were examined, and the following outputs have been obtained:

- (i) refractive indexes: 1.80, 2.60, and 1.80 (550 nm wavelength) at 30, 40, 50°C, respectively,
- (ii) extinction coefficients: 0.023, 0.025, and 0.082 at 30, 40, 50°C, respectively,
- (iii) band gaps (E_g) of the films: 4.01, 3.99, and 4.02 eV at 30, 40, 50°C, respectively,
- (iv) film thicknesses were changed between 198.14–454.07 nm when temperature has been increased from 30 to 50°C,
- (v) resistivities of the films: 22.47, 42.71, and 75.91 Ω-cm for the film thicknesses 198.14, 267.15, and 454.07 nm, respectively,
- (vi) the resistivities of the poly(methyl methacrylate) (PMM), indium tin oxide (ITO), n-silicium (n-Si) and p-silicium (p-Si), substrates were measured as 67.15, 50.98, 44.90, and 73.10 Ω-cm at the optimum deposition time and temperature.

SEM images of the thin films gave insight about their resistivity and refractive index. It can be seen that the film deposited on n-Si had lower resistivity than other ones. Although further investigation is needed for this new thin film, it seems to be a material which may be very useful for solar cells, dedectors, or sensors.

Acknowledgment

This study was extracted from Ph.D. thesis and was supported by Erciyes University. The authors are grateful for the technical and laboratory support of Erciyes University.

References

- [1] F. Lisdat, R. Dronov, H. Möhwald, F. W. Scheller, and D. G. Kurthw, "Self-assembly of electro-active protein architectures on electrodes for the construction of biomimetic signal chains," *Chemical Communications*, vol. 21, no. 3, pp. 274–283, 2009.
- [2] S. Liu, D. G. Kurth, and D. Volkmer, "Polyoxometalates as pH-sensitive probes in self-assembled multilayers," *Chemical Communications*, no. 9, pp. 976–977, 2002.
- [3] Z. Takáts, J. M. Wiseman, B. Gologan, and R. G. Cooks, "Electrosonic spray ionization. A gentle technique for generating folded proteins and protein complexes in the gas phase and for studying ion-molecule reactions at atmospheric pressure," *Analytical Chemistry*, vol. 76, no. 14, pp. 4050–4058, 2004.
- [4] G. Ramirez, M. C. Goya, L. Mendoza, B. Matsuhira, M. Isaacs, and Y. Y. Chen, "Iron porphyrin-modified electrodes: influence of the method of modification on the stability and electroactivity in oxidation of sulfite or hydrogensulfite in ethanol-water solutions," *Journal of Coordination Chemistry*, vol. 62, pp. 2782–2791, 2009.
- [5] H. J. Gao, Z. X. Bian, H. Y. Chen, Z. Q. Xue, and S. J. Pang, "A new type of organometallic system for high density data storage by scanning tunneling microscopy," *Chemical Physics Letters*, vol. 272, no. 5–6, pp. 459–462, 1997.
- [6] J. C. F. Rodríguez-Reyes and A. V. Teplyakov, "Chemistry of organometallic compounds on silicon: the first step in film growth," *Chemistry*, vol. 13, no. 33, pp. 9164–9176, 2007.
- [7] M. Grassi, D. A. W. Soares, A. A. A. De Queiroz, A. H. A. Bressiani, and J. C. Bressiani, "Organometallic chemical vapor deposition of compound semiconductors," *Materials Science and Engineering B*, vol. 112, no. 2–3, pp. 179–181, 2004.
- [8] R. A. Fischer, J. Weiß, and W. Rogge, "Organometallic chemical vapour deposition of cobalt/indium thin films using the single-molecule precursors $[(\text{CO})_4\text{Co}]_a\text{InR}_{3-a}$ ($\text{R} = \text{CH}_2\text{CH}_2\text{CH}_2\text{NMe}_2$; $a = 1-3$)," *Polyhedron*, vol. 17, no. 7, pp. 1203–1210, 1998.
- [9] Y. Jeong, J. Lee, S. Ha, and S. H. Kim, "Fabrication of cobalt-organic composite thin film via plasma-enhanced chemical vapor deposition for antibacterial applications," *Thin Solid Films*, vol. 517, no. 9, pp. 2855–2858, 2009.
- [10] P. L. Musetha, *The use of metal complexes to deposit metals calconide thin films and nanoparticles [Ph.D. thesis]*, University of Zululand, Richards Bay, South Africa, 2006.
- [11] M. L. Hitchman and K. H. Jensen, *Chemical Vapor Deposition: Principles and Applications*, Academic Press, San Diego, Calif, USA, 1993.
- [12] G. Hodes, *Chemical Solution Deposition of Semiconductor Films*, Merker Dekker, New York, NY, USA, 2003.
- [13] J. A. Ruffle, G. J. Knighton, and E. Y. Spencer, "Process for the production of sodium isopropyl xanthate," Canadian Intellectual Property Office, CA, 489807, 1953.
- [14] H. Wilhelm, "Process for preparing xanthates," United States Patent Office, 2024925, 1935.
- [15] H. Wilhelm, "Preparing of making xanthates," United States Patent Office, 2024924, 1935.
- [16] J. C. McCool, "Method of preparing alkali metal xanthates," United States Patent Office, 2678939, 1954.
- [17] H. Wilhelm, "Process of manufacturing sodium xanthates," United States Patent Office, 1701264, 1929.
- [18] A. López Valdivieso, A. A. Sánchez López, C. Ojeda Escamilla, and M. C. Fuerstenau, "Flotation and depression control of arsenopyrite through pH and pulp redox potential using xanthate as the collector," *International Journal of Mineral Processing*, vol. 81, no. 1, pp. 27–34, 2006.
- [19] J. D. Miller, J. Li, J. C. Davidtz, and F. Vos, "A review of pyrrhotite flotation chemistry in the processing of PGM ores," *Minerals Engineering*, vol. 18, no. 8, pp. 855–865, 2005.
- [20] J. Rubio, F. Capponi, R. T. Rodrigues, and E. Matiolo, "Enhanced flotation of sulfide fines using the emulsified oil extender technique," *International Journal of Mineral Processing*, vol. 84, no. 1–4, pp. 41–50, 2007.
- [21] A. Fehér, E. Urbán, I. Erős, P. Szabó-Révész, and E. Csányi, "Lyotropic liquid crystal preconcentrates for the treatment of periodontal disease," *International Journal of Pharmaceutics*, vol. 358, pp. 23–26, 2008.
- [22] G. C. Armitage, "Periodontal diagnoses and classification of periodontal diseases," *Periodontology 2000*, vol. 34, pp. 9–21, 2004.
- [23] U. Bertram and R. Bodmeier, "Parameters affecting the drug release from in situ gelling nasal inserts," *European Journal of Pharmaceutics and Biopharmaceutics*, vol. 63, no. 3, pp. 310–319, 2006.
- [24] E. Pellizzetti and E. Pramauro, "Analytical applications of organized molecular assemblies," *Analytica Chimica Acta*, vol. 169, pp. 1–29, 1985.
- [25] C. D. Stalikas, "Micelle-mediated extraction as a tool for separation and preconcentration in metal analysis," *Trends in Analytical Chemistry*, vol. 21, no. 5, pp. 343–355, 2002.
- [26] E. Pramauro and A. B. Prevot, "Solubilization in micellar systems. Analytical and environmental applications," *Pure and Applied Chemistry*, vol. 67, pp. 551–559, 1995.
- [27] J. L. Manzoori and A. Bavili-Tabrizi, "Cloud point preconcentration and flame atomic absorption spectrometric determination of Cd and Pb in human hair," *Analytica Chimica Acta*, vol. 470, no. 2, pp. 215–221, 2002.
- [28] M. E. F. Laespada and J. L. Perez, "Micelle-mediated methodology for the preconcentration of uranium prior to its determination by flow injection," *Analyst*, vol. 118, pp. 209–212, 1993.
- [29] M. Ghaedi, "Selective and sensitized spectrophotometric determination of trace amounts of Ni(II) ion using α -benzyl dioxime in surfactant media," *Spectrochimica Acta Part A*, vol. 66, pp. 295–301, 2007.
- [30] G. D. L. Paleologos, S. M. Tzouwara-Karayanni, and M. T. Karayanis, "Micelle mediated methodology for the determination of free and bound iron in wines by flame atomic absorption spectrometry," *Analytica Chimica Acta*, vol. 458, no. 1, pp. 241–248, 2002.
- [31] D. E. Zelmon, Z. Gebeyehu, D. Tomlin, and T. M. Cooper, "Investigation of transition metal-xanthate complexes for non-linear optical applications," in *Proceedings of the MRS Spring Symposium*, pp. 395–400, April 1998.
- [32] I. Haiduc, R. F. Semeniuc, M. Campian, V. C. Kravtsov, Y. A. Simonov, and J. Lipkowski, "The reaction of nickel(II) xanthates with tetraphenyldiphosphinoethane (dppe) revisited. Formation and crystal structures of $\text{Ni}_3\text{S}_2(\text{S}_2\text{COR})_2(\text{dppe})$ ($\text{R} = \text{Me}$, Et; dppe = $\text{Ph}_2\text{PCH}_2\text{CH}_2\text{PPh}_2$) at room temperature and of

- Ni(S₂CO)(dppe) at 150 K," *Polyhedron*, vol. 22, no. 21, pp. 2895–2900, 2003.
- [33] E. Erdik, M. Obalı, N. Yüksekşık, A. Öktemer, and T. Pekel, *Denel Organik Kimya. Gazi Kitabevi*, Ankara, Turkey, 4 edition, 2007.
- [34] N. Zohir, M. Bouhenguel, and A. E. Djebaili, "Synthesis and structural characterization of xanthate (KEX) in sight of their utilization in the processes of sulphides flotation," *Journal of Minerals and Materials Characterization and Engineering*, vol. 8, no. 6, pp. 469–477, 2009.
- [35] M. L. Shankaranarayana and C. C. Patel, "Infrared spectra and the structures of xanthates and dioxanthogens," *Canadian Journal of Chemistry*, vol. 39, no. 8, pp. 1633–1637, 1961.
- [36] D. Fornasiero, M. Montalti, and J. Ralston, "Kinetics of adsorption of ethyl xanthate on pyrrhotite: in situ UV and infrared spectroscopic studies," *Journal of Colloid And Interface Science*, vol. 172, no. 2, pp. 467–478, 1995.
- [37] G. W. Watt and B. J. McCormick, "The infrared spectra and structure of transition metal xanthates," *Spectrochimica Acta*, vol. 21, no. 4, pp. 753–761, 1965.
- [38] S. J. Cristol and D. G. Seapy, "New procedure for the transformation of alcohols to alkyl halides via xanthate esters and free-radical intermediates," *Journal of Organic Chemistry*, vol. 47, no. 1, pp. 132–136, 1982.
- [39] A. V. Ivanov, "Copper(II) and Nickel(II) alkylxanthate complexes (R = C₂H₅, i-C₃H₇, i-C₄H₉, s-C₄H₉, and C₅H₁₁): EPR and solid-State ¹³C CP/MAS NMR Studies," *Russian Journal of Coordination Chemistry*, vol. 30, no. 7, pp. 480–485, 2004.
- [40] H. Taş, *Coordination Polymerization of Cyclic Ethers by Metal Xanthates and Carbamates*, Yüksek Lisans Tezi, ODTU, Polimer Bilimi ve Teknolojisi Bölümü, Ankara, Turkey, 2003.
- [41] G. A. Soomro, G. A. Shar, and M. I. Bhangar, "Spectrophotometric determination of copper(II) and palladium(II) complexes with isoamylxanthate in micellar media of SDS/Tween 80," *Journal of the Chemical Society of Pakistan*, vol. 10, no. 2, pp. 143–147, 2004.
- [42] M. Balci, *Basic ¹H- and ¹³C- NMR Spectroscopy*, Elsevier, 2005.
- [43] N. Benramdane, W. A. Murad, R. H. Misho, M. Ziane, and Z. Kezzab, "A chemical method for the preparation of thin films of CdO and ZnO," *Materials Chemistry and Physics*, vol. 48, no. 2, pp. 119–123, 1997.
- [44] A. A. M. Farag, M. Cavas, F. Yakuphanoglu, and F. M. Amanullah, "Photoluminescence and optical properties of nanostructure Ni doped ZnO thin films prepared by sol-gel spin coating technique," *Journal of Alloys and Compounds*, vol. 509, no. 30, pp. 7900–7908, 2011.
- [45] J. Santos-Cruz, G. Torres-Delgado, R. Castaneda-Perez, C. I. Zúñiga-Romero, and O. Zelaya-Angel, "Optical and electrical characterization of fluorine doped cadmium oxide thin films prepared by the sol-gel method," *Thin Solid Films*, vol. 515, no. 13, pp. 5381–5385, 2007.
- [46] F. Liu, Y. Lai, J. Liu et al., "Characterization of chemical bath deposited CdS thin films at different deposition temperature," *Journal of Alloys and Compounds*, vol. 493, no. 1-2, pp. 305–308, 2010.
- [47] B. Pejova, I. Grozdanov, and A. Tanusevski, "Optical and thermal band gap energy of chemically deposited bismuth(III) selenide thin films," *Materials Chemistry and Physics*, vol. 83, no. 2-3, pp. 245–249, 2004.
- [48] H. Moualkia, S. Hariech, and M. S. Aida, "Structural and optical properties of CdS thin films grown by chemical bath deposition," *Thin Solid Films*, vol. 518, no. 4, pp. 1259–1262, 2009.
- [49] R. Kirschman, *High-Temperature Electronics*, IEEE Press, New York, NY, USA, 1999.
- [50] S. Kasap and P. Capper, *Springer Handbook of Electronic and Photonic Materials*, Springer, 2006.
- [51] P. Blood and J. W. Orton, *The Electrical Characterization of Semiconductors: Majority Carriers and Electron States*, Academic Press, London, UK, 1992.
- [52] P. Krulevitch, A. P. Lee, P. B. Ramsey, J. C. Trevino, J. Hamilton, and M. A. Northrup, "Thin film shape memory alloy microactuators," *Journal of Microelectromechanical Systems*, vol. 5, no. 4, pp. 270–282, 1996.
- [53] M. Singh, Y. K. Vijay, and I. P. Jain, "The effect of a sulfur layer on FeTi thin films obliquely deposited for hydrogen storage," *International Journal of Hydrogen Energy*, vol. 16, no. 2, pp. 101–104, 1991.
- [54] F. Bakkaloğlu, H. İ. Karahan, H. Efeoğlu, M. Yıldırım, U. Çevik, and Y. K. Yoğurtçu, "Magnetic studies on electrodeposited Cu_{1-x}Co_x alloy films," *Journal of Magnetism and Magnetic Materials*, vol. 190, no. 3, pp. 193–198, 1998.
- [55] Y. Shuai, X. Ou, C. Wu et al., "Substrate effect on the resistive switching in BiFeO₃ thin films," *Journal of Applied Physics*, vol. 111, Article ID 07D906, 2012.

Research Article

Nanocomposite Coatings Codeposited with Nanoparticles Using Aerosol-Assisted Chemical Vapour Deposition

Xianghui Hou,¹ Kwang-Leong Choy,¹ Nathalie Brun,² and Virginie Serin³

¹ Faculty of Engineering, Energy and Sustainability Research Division, The University of Nottingham, Nottingham NG7 2RD, UK

² Laboratoire de Physique des Solides, Université Paris-Sud, CNRS, UMR 8502, 91405 Orsay Cedex, France

³ CEMES Université Paul Sabatier, 29 rue Jeanne Marvig, BP 94347, 31055 Toulouse Cedex 4, France

Correspondence should be addressed to Kwang-Leong Choy; kwang-leong.choy@nottingham.ac.uk

Received 6 April 2013; Accepted 7 May 2013

Academic Editor: Jiamin Wu

Copyright © 2013 Xianghui Hou et al. This is an open access article distributed under the Creative Commons Attribution License, which permits unrestricted use, distribution, and reproduction in any medium, provided the original work is properly cited.

Incorporating nanoscale materials into suitable matrices is an effective route to produce nanocomposites with unique properties for practical applications. Due to the flexibility in precursor atomization and delivery, aerosol-assisted chemical vapour deposition (AACVD) process is a promising way to synthesize desired nanocomposite coatings incorporating with preformed nanoscale materials. The presence of nanoscale materials in AACVD process would significantly influence deposition mechanism and thus affect microstructure and properties of the nanocomposites. In the present work, inorganic fullerene-like tungsten disulfide (IF-WS₂) has been codeposited with Cr₂O₃ coatings using AACVD. In order to understand the codeposition process for the nanocomposite coatings, chemical reactions of the precursor and the deposition mechanism have been studied. The correlation between microstructure of the nanocomposite coatings and the codeposition mechanism in the AACVD process has been investigated. The heterogeneous reaction on the surface of IF-WS₂ nanoparticles, before reaching the substrate surface, is the key feature of the codeposition in the AACVD process. The agglomeration of nanoparticles in the nanocomposite coatings is also discussed.

1. Introduction

Nanotechnology is one of the most popular research areas in the last decade. Materials on nanoscale can exhibit unique properties as compared to those on a macroscale [1]. Various nanoscale materials have been developed, such as nanoparticles, nanotubes, nanofibers, nanowires, nanorods, nanobelts, and nanosheets, for promising applications in semiconductors, optics, mechanics, energy, catalysts, sensors and biology, and so forth [2–7]. Incorporating these nanoscale materials into suitable matrices to form nanocomposites, either in the form of bulk materials or coatings, is considered an important route to realise the unique properties of nanoscale materials for practical applications [8, 9]. However, nanoscale materials tend to be structurally sensitive and may lose their original properties during the incorporation into matrices to produce nanocomposites. Most studies on the use of nanoscale materials in nanocomposites or nanocomposite coatings are limited to inorganic filler and polymer matrix systems [10, 11],

in which the processing conditions are relatively mild in order to preserve the unique microstructures and properties of the nanoscale materials. It is a challenge to produce inorganic nanocomposite systems with the incorporation of the preformed nanoscale materials into ceramic matrices, due to a much higher processing temperature and critical processing environment which tend to be less favourable for the nanoscale materials.

Inorganic fullerene-like tungsten disulfide (IF-WS₂) nanoparticles are excellent solid lubricants under severe conditions [12]. It is reported that incorporation of IF-WS₂ nanoparticles into coatings would offer considerable improvements on tribological performance [13, 14] and adjust hydrophobic/hydrophilic behavior of the coating surface [15]. Recently, aerosol-assisted chemical vapor deposition (AACVD) has been adapted to synthesize inorganic nanocomposite coatings from the dispersion or colloid of nanoparticles [16, 17]. We have also incorporated IF-WS₂ nanoparticles into Cr₂O₃ coating using AACVD [18]. The atomization

of precursor dispersion or colloid in AACVD process allows the introduction of preformed nanoscale materials and codeposits them with matrix materials simultaneously, to form the desired nanocomposite coatings onto the substrate surface. These results demonstrated that AACVD is a promising method for the synthesis of nanocomposite coatings with the codeposition of preformed nanoscale materials. However, the codeposition mechanism in AACVD has yet to be investigated. The presence of the nanoparticles in the precursor aerosol would influence the chemical reactions and deposition process, and hence the microstructure of the nanocomposite coatings. The codeposition has significantly deviated from a standard CVD. For better understanding of the process, it is proposed to study the codeposition mechanism in AACVD and its correlation with the microstructure of the nanocomposite coatings. The results and conclusions may also be extended to other nanocomposite coating systems, consisting of other kinds of nanoscale materials and matrices.

2. Experimental

Chromium nitrate nonahydrate (Aldrich) was used as chemical precursor for the deposition of chromium oxide (Cr_2O_3), while IF- WS_2 nanoparticles ranging from 80 to 220 nm were supplied by NanoMaterials Ltd. The basic precursor solution was prepared by dissolving chromium nitrate nonahydrate in ethanol-based solvent to form 0.05 M solution. Then IF- WS_2 nanoparticles were added into the basic precursor solution (0.23 g/L) to obtain uniform suspension via an ultrasonic bath. Silicon wafers and stainless steel plates were used as substrates and cleaned in an ultrasonic bath with alcohol prior to the deposition.

The precursor suspension containing IF- WS_2 nanoparticles was then atomized to generate fine aerosol droplets using an ultrasonic generator, at a frequency of 1.7 MHz, with nitrogen as carrier gas. The droplets were subsequently directed towards a heated zone where they underwent evaporation, decomposition, and chemical reactions and deposited chromium oxide coatings with IF- WS_2 onto the substrates. The deposition temperatures were set in the range of 280–300°C. Post heat-treatment of the samples was carried out to obtain crystalline Cr_2O_3 and the desired microstructure of the nanocomposite coatings. The as-deposited coatings were annealed at 500°C in argon for 1 hour. For comparison, pure Cr_2O_3 coatings were also synthesized from precursor solution without adding IF- WS_2 nanoparticles. In order to study the intermediate reactions of the precursor in the deposition, dried precursor powder was prepared by removing the solvent from the precursor suspension at 50°C for 48 hours. The thermal decomposition behaviours of chromium nitrate nonahydrate and the dried precursor powder were determined separately by differential thermal analysis (DTA) using a Setaram Labsys 1600, from 30°C to 700°C, at 5°C/min in air. The structural changes of the dried precursor powder were also investigated by a Perkin Elmer Spectrum One Fourier transform infrared spectrometer (FTIR, attenuated total reflectance mode (ATR)).

The IF- $\text{WS}_2/\text{Cr}_2\text{O}_3$ coatings were characterized using a combination of scanning electron microscopy (SEM), X-ray photoelectron spectroscopy (XPS), atomic force microscope (AFM), transmission electron microscopy (TEM), and scanning transmission electron energy loss spectroscopy (EELS). A Philips XL30 scanning electron microscope equipped with an Oxford Instruments energy-dispersive X-ray spectrometry (EDX) was used to characterise the microstructure and composition of the nanocomposite coating. Surface chemical analysis of the coating was carried out using a VG ESCALab X-ray Photoelectron Spectrometer. A Veeco CP-Research Scanning Probe Microscope (contact AFM mode) was used to measure the roughness of the deposited coatings. For TEM (conventional and high resolution) imaging, an FEI TECNAI F20 was used. EELS analysis was performed with a 100-keV STEM instrument (VG HB 501) equipped with a field emission source and a parallel Gatan 666 EELS spectrometer.

3. Results

3.1. Differential Thermal Analysis (DTA). In AACVD process, the aerosol droplets of chemical precursor undergo evaporation and decomposition at elevated temperatures [19]. In order to study the intermediate reactions involved in the deposition, dried precursor powder was obtained by removing solvent from the precursor dispersion. Figure 1 shows DTA analysis of pure chromium nitrate nonahydrate and the dried precursor powder. As compared to the thermal behaviour of pure chromium nitrate nonahydrate, the main endothermic peak of the dried precursor powder shifts to 150–175°C, indicating significant changes in the chemical structure. A small exothermic peak around 425°C can be found, which corresponds to the oxidation of IF- WS_2 in the precursor powder. As reported [14], the oxidation of pure IF- WS_2 nanoparticles starts at 350°C and reaches its maximum at 400°C. While the oxidation of IF- WS_2 is significantly delayed in the DTA curve of dried precursor powder, indicating that IF- WS_2 nanoparticles are covered and protected by intermediates of the precursor from oxidation at elevated temperatures.

3.2. FTIR Spectra. Figure 2 shows the FTIR spectra of pure chromium nitrate nonahydrate and the dried precursor powder. In both spectra, the broad peak at circa 3060 cm^{-1} can be assigned to nondissociated water and it is confirmed by the peak at 1630 cm^{-1} . There are some new absorption peaks appearing in the FTIR spectrum of the dried precursor powder. The absorption bands centred at 1395, 1090, and 799 cm^{-1} could be assigned to CH_3 bend, C–O stretching, and CH_2 rock vibration, respectively [20, 21], which indicates that -OEt is introduced when chromium nitrate nonahydrate is dissolved in ethanol solvent. The new absorption band at 959 cm^{-1} can be assigned as antisymmetric O–Cr–O stretching vibration [22], while 892 cm^{-1} peak is associated with the symmetrical stretching mode of Cr–O bond [23]. There is another extra band at 1550 cm^{-1} , which may be due to the vibration of O–H stretching in short O–H–O bonds of $\text{Cr}(\text{OH})_3 \cdot 3\text{H}_2\text{O}$ [24, 25]. Further details on the

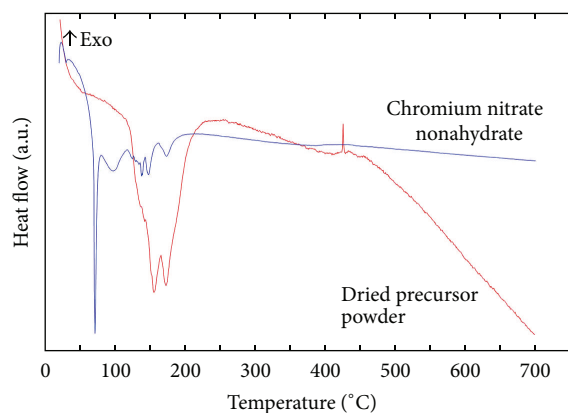


FIGURE 1: DTA analysis of chromium nitrate nonahydrate and the dried precursor powder.

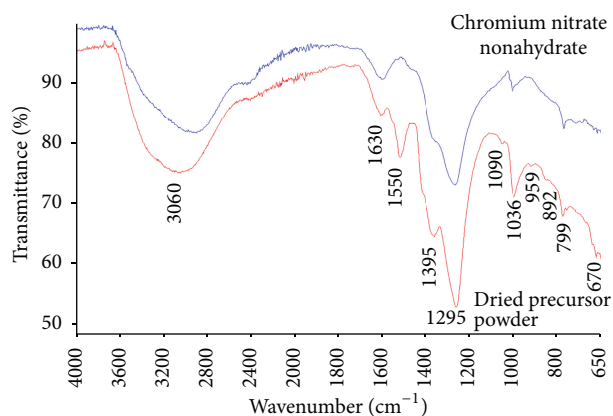


FIGURE 2: FTIR spectra of pure chromium nitrate nonahydrate and the dried precursor powder.

possible chemical structures and reactions will be discussed in Section 4.

3.3. EDX and XPS Analysis. Pure Cr_2O_3 coatings and $\text{IF-WS}_2/\text{Cr}_2\text{O}_3$ nanocomposite coatings were produced via AACVD and subsequent annealing at 500°C . EDX analysis of the nanocomposite coating is shown in Figure 3(a). The elements W and S can be clearly detected. Figure 3(b) presents XPS W(4f) line of nanocomposite coating, with the IF-WS_2 nanoparticles as reference. The presence of W could not be detected by XPS in the nanocomposite coating. Similarly, S element is also not detectable by XPS. As XPS has much smaller analysis depth than EDX, it reflects that the IF-WS_2 nanoparticles have been fully covered by the matrix. Thus, there is no naked IF nanoparticle on the surface of the coating.

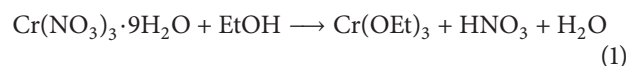
3.4. AFM Characterisation. The coatings were also characterised using AFM, to obtain further information on their surface morphology and roughness. As shown in Figure 4, the nanocomposite coating has a rough surface, with some peaks and valleys in microrange, while the pure Cr_2O_3

coating is smoother. There are some small grains appearing in the pure coating, several hundred nanometers in size. The average roughness (R_a) of the two coatings in Figures 4(a) and 4(b) are 16.9 nm and 62.6 nm, respectively.

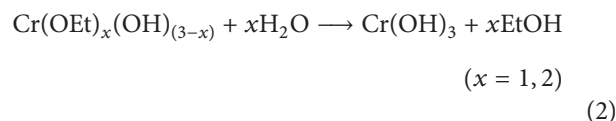
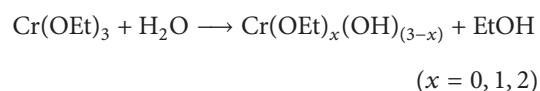
3.5. TEM and EELS Analysis. Figure 5(a) is an HREM image of IF nanoparticles incorporated in the nanocomposite coating. IF-WS_2 nanoparticles are confirmed to be incorporated into the coatings by TEM. The hollow onion structure of IF-WS_2 can be clearly observed in Figure 5(a). Several spectrum-lines were acquired across an IF-WS_2 particle (as shown in the inset of Figure 5(b)), in order to analyse the qualitative composition of the IF particle, matrix, and the interface [26]. Probe size is about 0.7 nm, and the step was 3 nm. Acquisition energy range was selected to analyse O K edge, S and Cr L edges, and W low energy edges (O and N). Figure 5(b) shows the intensity profiles for these edges. The resulting profiles clearly show the presence of Cr_2O_3 matrix on each side of the particle. It is noted that no O signal is detected in the IF-WS_2 nanoparticle, indicating that no oxidation of IF-WS_2 has occurred in the deposition process and the subsequent heat treatment. Thus, the results suggest that the hollow onion structure and chemical composition of IF-WS_2 nanoparticles are preserved without apparent modification; however, the agglomeration of IF-WS_2 has been observed.

4. Discussion

4.1. Chemical Reactions. In ethanol solution, nitrate group in $\text{Cr}(\text{NO}_3)_3 \cdot 9\text{H}_2\text{O}$ may be replaced by alkoxy group,

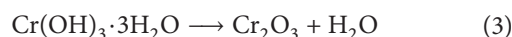


The intermediate $\text{Cr}(\text{OEt})_3$ is unstable with the existence of water molecule, and Cr-OEt bond would be hydrolysed to form Cr-OH bond:



Then $\text{Cr}(\text{OH})_3$ may absorb more water to form $\text{Cr}(\text{OH})_3 \cdot 3\text{H}_2\text{O}$. In Figure 2, the FTIR spectrum proves the presence of $\text{Cr}(\text{OH})_3 \cdot 3\text{H}_2\text{O}$ in the dried precursor powder. As the nitrate structure is still observed from FTIR, it is suggested that the dried precursor powder is a mixture of nitrate and hydroxide, and only part of nitrate has been converted in reaction (1).

At elevated temperature, chromium nitrate would directly decompose to Cr_2O_3 [27], and chromium hydroxide can form Cr_2O_3 via reaction (3) [28]:



In the real AACVD process, the chemical reactions and intermediates will be more complicated than the interpretation for the dried precursor powder. But it is suggested that

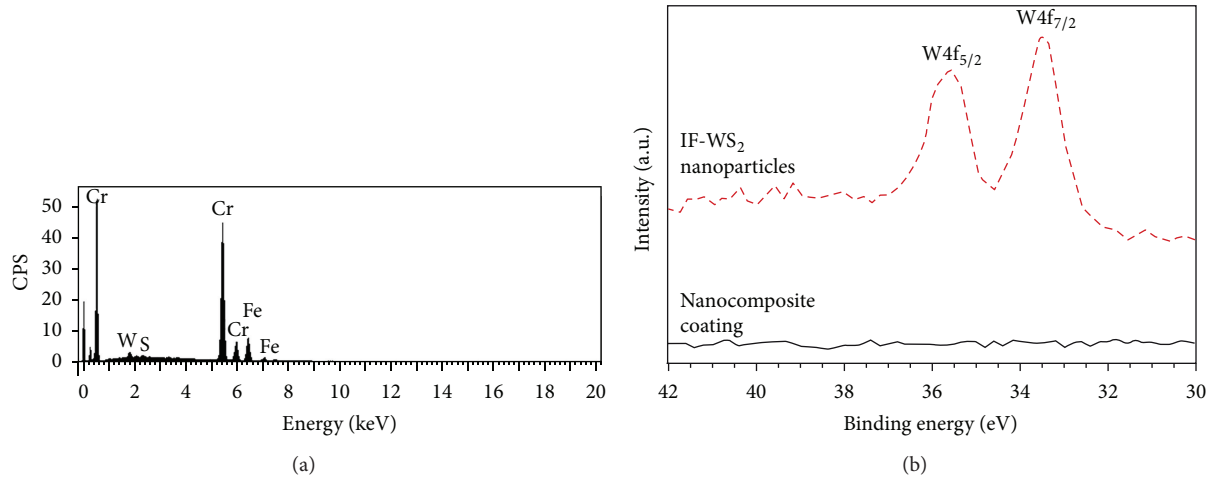


FIGURE 3: Analysis of the IF-WS₂/Cr₂O₃ nanocomposite coating. (a) EDX of nanocomposite coating and (b) XPS W(4f) line of IF-WS₂ nanoparticle and nanocomposite coating.

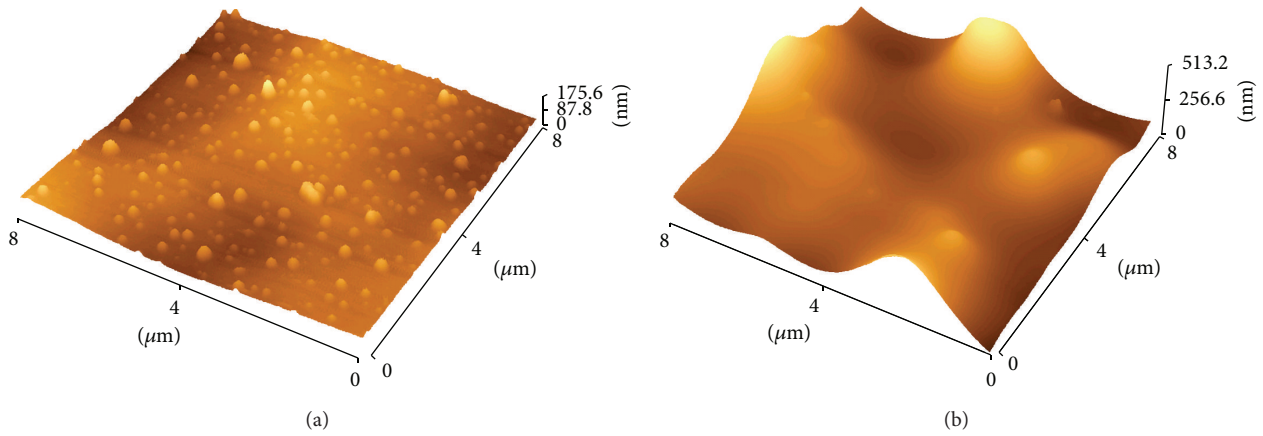


FIGURE 4: AFM images of the pure Cr₂O₃ (a) and the IF-WS₂/Cr₂O₃ nanocomposite coatings (b).

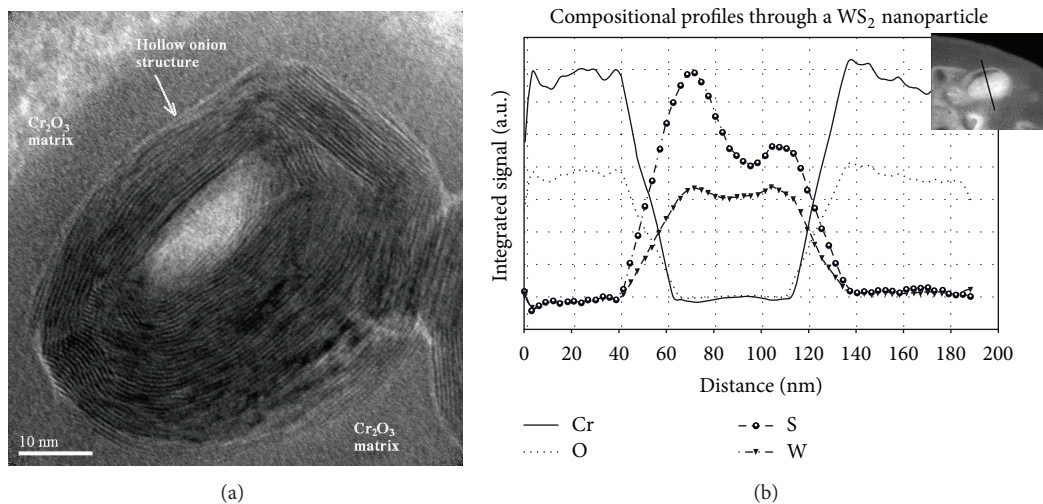


FIGURE 5: TEM imaging and EELS analysis of the IF-WS₂/Cr₂O₃ nanocomposite coatings. (a) HREM image of an IF-WS₂ particle showing typical layered structure formed by S-W-S sheets. (b) Qualitative compositional profiles after PCA analysis across an IFLM particle showing that no interdiffusion or oxidation of the particle takes place. The integrated signal has not been divided by the cross-section; the black line in the inset has the length of 130 nm.

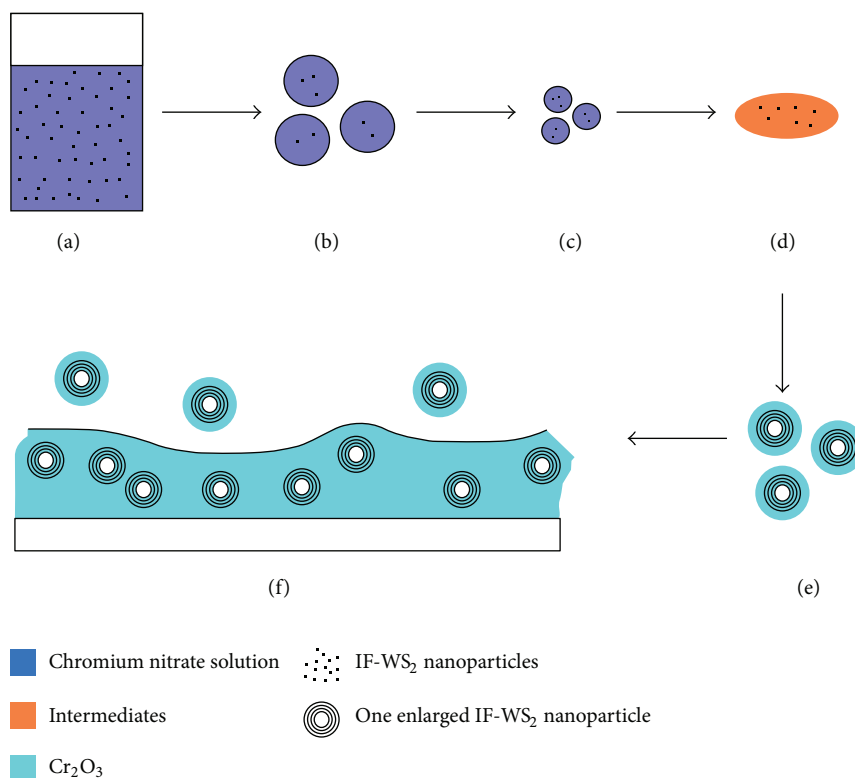


FIGURE 6: Deposition of nanocomposite coating using AACVD. (a) Formation of precursor dispersion consisting of chromium nitrate and IF-WS₂ nanoparticles, (b) atomization of precursor dispersion, (c) evaporation of solvent, (d) decomposition and chemical reactions of precursor intermediates in gas phase, (e) nucleation and growth on IF nanoparticle surface, and (f) deposition of IF-WS₂/Cr₂O₃ on the substrate surface.

alkoxy and hydroxide structure are involved in the reactions. At elevated temperature, it is a procedure of releasing N-containing groups and water, which corresponds to the main endothermic peak at 150–175°C in Figure 1.

4.2. Deposition Mechanism. To synthesize IF-WS₂/Cr₂O₃ nanocomposite coatings, the precursor dispersion consisting of IF nanoparticles was atomized to produce fine aerosol droplets. These aerosol droplets were subsequently directed towards a heated zone where they underwent evaporation, decomposition, chemical reactions, and deposition. In this process, IF nanoparticles were incorporated into the coating via “codeposition.” There are some studies on codeposition of particles via homogeneous nucleation using CVD process [29–32]. However, in the current study, the IF nanoparticles were obtained separately, instead of being formed *in situ* simultaneously with the matrix, which could provide independent control for both nanoparticles and matrix materials. IF nanoparticles might induce nucleation and growth of matrix on their surface in gas phase, prior to the deposition occurring on the substrate surface. The deposition mechanism of AACVD with IF nanoparticles is proposed in Figure 6 and described as follows.

(a) Formation of precursor dispersion consisting of chromium nitrate and IF-WS₂ nanoparticles: chromium nitrate is dissolved into ethanol-based solvent to form

homogeneous solution, and IF-WS₂ nanoparticles are distributed in the solution uniformly to obtain the desired dispersion.

(b) Atomization of precursor dispersion: the liquid dispersion is atomized to form fine aerosol droplets with diameter ranging from 1 to 10 microns. The size of the IF nanoparticles is circa 80–220 nm, so one droplet of dispersion, for example, may contain one or more nanoparticles. The aerosol droplets are delivered to the reaction area by carrier gas, together with the IF nanoparticles.

(c) Evaporation of solvent: when the aerosol droplets are being transported, they will undergo substantial evaporation, especially with increased environmental temperature. The small size and the large specific surface area of these droplets will accelerate the evaporation of solvent. The evaporation can cause rapid evaporative cooling effect and lead to decrease of surface temperature of droplets until heat transfer between the droplets and the environmental reaches a temporal balance [33]. Therefore, the fine aerosol droplets make it possible to achieve rapid removal of solvent when they are approaching the heated substrate.

(d) Decomposition and chemical reactions of precursor intermediates in gas phase: the decomposition and

chemical reactions of the precursor occur rapidly at the elevated temperatures. Some intermediates of precursor start to form in gas phase. From the TEM analysis, IF-WS₂ nanoparticles remain stable in the deposition. IF nanoparticles are always transported with the chemical precursor, when they are surrounded by the precursor intermediates, their surface can adsorb some intermediates or active species due to the high specific surface area.

- (e) Nucleation and growth on the IF nanoparticle surface: before reaching the substrate, IF nanoparticles play an important role as the “nucleation seeds” of Cr₂O₃ via heterogeneous reactions. Nucleation takes place from the adsorbed intermediates or active species on the surface of IF nanoparticles, where a thin layer of Cr₂O₃ is formed. Then a kind of spherical particles with Cr₂O₃ shell and IF core would be obtained. Via continuous heterogeneous reaction, these spherical particles grow bigger and bigger. Then all IF nanoparticles are covered by the Cr₂O₃ shell before they reach the substrate surface. The Cr₂O₃ shell can protect the IF nanoparticles from oxidation and other chemical reactions, so the unique hollow onion structure of IF can be preserved as shown in Figure 5(a). However, in the AACVD of pure Cr₂O₃ coating, there is no extra surface for heterogeneous reactions in the gas phase. Heterogeneous nucleation only happens on the surface of substrate. Thus, it is suggested that heterogeneous nucleation on the IF-WS₂ surface is one of the key features for the synthesis of nanocomposite coatings using AACVD process.
- (f) Cr₂O₃ can also directly deposit onto the substrate surface from the gas-phase species via heterogeneous reactions, similar to that of pure Cr₂O₃ coating in AACVD process, which is the major route for the formation of Cr₂O₃ matrix. Simultaneously, the IF-WS₂ nanoparticles with the Cr₂O₃ shells are delivered and deposited onto the substrate surface. The Cr₂O₃ shells outside the IF-WS₂ nanoparticles can be merged with the major Cr₂O₃ coating matrix in the subsequent deposition. As the deposition temperature is no more than 350°C, no oxidation of WS₂ occurs, and the IF-WS₂ nanoparticles remain stable.

In the deposition of pure Cr₂O₃ coating in AACVD, the heterogeneous nucleation of Cr₂O₃ only takes place at the substrate surface. Therefore, some small grain features on the coating surface can be observed from AFM image, and the coating is much smoother than that incorporated with IF nanoparticles, as seen in Figure 4. In the synthesis of nanocomposite coating, the heterogeneous nucleation of Cr₂O₃ also occurs on IF nanoparticles in the gas phase, so that the IF nanoparticles become bigger and bigger before they reach the substrate. After they have deposited onto the substrate and merge with the coating matrix, bigger peaks appear which significantly increases the surface roughness of the coatings. Thus, a much rougher surface is formed. As all IF nanoparticles are fully covered by Cr₂O₃ shell before they

reach the substrate surface, no naked IF nanoparticle can be detected by XPS on the surface of the nanocomposite coating.

In summary, as the nanoparticles have high specific surface area and they have close contact with the chemical reactants during the transport period, the heterogeneous reaction starts on the nanoparticles surface. It is suggested that the heterogeneous reaction on the surface of IF nanoparticles, before they reach the substrate, is the key point in the AACVD of nanocomposite coatings. The heterogeneous reaction would lead to the formation of a shelled layer on the nanoparticle surface, which greatly influences the microstructure and surface roughness of the coatings.

4.3. Agglomeration of IF Nanoparticles inside the Nanocomposite Coatings. Agglomeration is a general tendency of nanoscale materials. It is normally believed that nonagglomerated or less-agglomerated nanoscale materials could be beneficial to their unique properties. Ideally, it is desirable to have uniform and nonagglomerated distribution of nanoparticles inside the coating matrix. However, it is found that the agglomeration of IF nanoparticles occurred in the IF-WS₂/Cr₂O₃ nanocomposite coatings [18]. Thus, there is a need to minimize the agglomeration of IF nanoparticles inside the nanocomposite coating.

There are several possible sources and reasons of IF agglomeration in the final nanocomposite coatings produced by AACVD, as follows.

- (i) The supplied nanoparticles: if heavy agglomeration exists in the supplied nanoparticles, proper separation methods have to be applied to break up the agglomerates. Otherwise, the agglomeration will remain in the final nanocomposite coating. Therefore, less agglomerated nanoparticles would be favourable.
- (ii) Preparation of precursor dispersion consisting of nanoparticles: IF nanoparticles are required to be well dispersed in the precursor solution. Ultrasonic bath or other methods can be used to break up the agglomerates and obtain stable dispersion. Surfactant might be used in this stage to improve the stability of the dispersion.
- (iii) Atomization of precursor dispersion: in the atomization stage, nanoparticles will be loaded and carried by the aerosol droplets. If the droplet is big, it would carry more nanoparticles, which may have more chance for agglomeration in this droplet. Therefore, smaller size droplet is preferred. The same requirement can also be applied to the distribution of the droplets size. Thus, fine and uniform aerosol droplets are required for less-agglomeration in the AACVD process.
- (iv) Evaporation of solvent in the aerosol droplets: as discussed previously, evaporation of solvent takes place in the droplets transport period. If one droplet contains more nanoparticles, agglomeration of these nanoparticles may occur when the droplet shrinks, especially when all solvent has been evaporated from the droplet. It indicates that using finer aerosol

droplets or lowering the nanoparticle concentration in the dispersion may be helpful to reduce the possible agglomeration in this stage.

- (v) Heterogeneous reactions on the surface of IF nanoparticles during their transport period: before IF nanoparticles reaches the substrates, substantial heterogeneous reactions would occur on the surface of IF nanoparticles and form a layer of Cr_2O_3 . The Cr_2O_3 may act as connective materials between nanoparticles. This kind of agglomeration may be minimized by reducing the earlier heterogeneous reactions, via optimizing the processing parameters, such as deposition temperature and gas flow rate.

Therefore, it is suggested that the agglomeration of IF nanoparticles inside the nanocomposite coating is a combination of the physical and chemical properties of the nanoparticles and all the processing steps. Various measures can be applied to minimize the possible IF agglomeration at the different steps of the AACVD process. The results and conclusions would also be helpful for the fabrication of nanocomposite coatings using other processing techniques.

5. Conclusions

IF- WS_2 nanoparticles have been incorporated into Cr_2O_3 coating matrix to form nanocomposite coatings using AACVD. Hollow onion structure and chemical composition of IF- WS_2 nanoparticles are preserved inside the matrix. All IF nanoparticles are fully covered by the coating matrix and no naked IF nanoparticle can be detected. Individual IF nanoparticle in the coating can be clearly characterised by TEM analysis, but the agglomeration of the IF nanoparticles also exists. As compared to pure Cr_2O_3 coatings, the nanocomposite coatings have a much rougher surface.

The chemical reactions and intermediates in the AACVD process could be complex. From the thermal decomposition of the dried precursor powder, it is suggested that alkoxy and hydroxide structures are involved in the reactions.

A deposition mechanism has been proposed to discuss the codeposition of nanocomposite coating using AACVD. The heterogeneous reaction on the surface of IF nanoparticles, before they reach the substrate, is the key point in AACVD of nanocomposite coatings. The heterogeneous reaction would lead to the formation of a Cr_2O_3 shell on the nanoparticles surface, which greatly influences the microstructure and surface roughness of the coatings.

The agglomeration of IF nanoparticles inside the nanocomposite coatings might be attributed to the as-received nanoparticles and AACVD process. Various measures have been discussed for minimizing the possible IF agglomeration at different steps in the process. The results and conclusions would also be helpful for the fabrication of nanocomposite coatings using other processing techniques.

Acknowledgments

The authors would like to thank the European Union for financial support under the EU-Sixth Framework

FOREMOST project (Contract FP6-515840). They also would like to thank Mr. Martin Roe for performing XPS surface analysis and NanoMaterials Ltd. for kindly supplying IF- WS_2 nanoparticles for this research.

References

- [1] P. Dutta and S. Gupta, *Understanding of Nano Science and Technology*, Global Vision Publishing House, New Delhi, India, 2006.
- [2] J. Kong, N. R. Franklin, C. Zhou et al., "Nanotube molecular wires as chemical sensors," *Science*, vol. 287, no. 5453, pp. 622–625, 2000.
- [3] D. B. Kittelson, "Engines and nanoparticles: a review," *Journal of Aerosol Science*, vol. 29, no. 5-6, pp. 575–588, 1998.
- [4] R. H. Baughman, A. A. Zakhidov, and W. A. De Heer, "Carbon nanotubes—the route toward applications," *Science*, vol. 297, no. 5582, pp. 787–792, 2002.
- [5] J. Pérez-Juste, I. Pastoriza-Santos, L. M. Liz-Marzán, and P. Mulvaney, "Gold nanorods: synthesis, characterization and applications," *Coordination Chemistry Reviews*, vol. 249, pp. 1870–1901, 2005.
- [6] H. G. Yang, G. Liu, S. Z. Qiao et al., "Solvothermal synthesis and photoreactivity of anatase TiO_2 nanosheets with dominant 001 facets," *Journal of the American Chemical Society*, vol. 131, no. 11, pp. 4078–4083, 2009.
- [7] Z. L. Wang, "Functional oxide nanobelts: materials, properties and potential applications in nanosystems and biotechnology," *Annual Review of Physical Chemistry*, vol. 55, pp. 159–196, 2004.
- [8] G. Kickelbick, "Concepts for the incorporation of inorganic building blocks into organic polymers on a nanoscale," *Progress in Polymer Science*, vol. 28, pp. 83–114, 2003.
- [9] L. Rapoport, N. Fleischer, and R. Tenne, "Applications of WS_2 (MoS_2) inorganic nanotubes and fullerene-like nanoparticles for solid lubrication and for structural nanocomposites," *Journal of Materials Chemistry*, vol. 15, pp. 1782–1788, 2005.
- [10] C. Sanchez, B. Julián, P. Belleville, and M. Popall, "Applications of hybrid organic-inorganic nanocomposites," *Journal of Materials Chemistry*, vol. 15, no. 35-36, pp. 3559–3592, 2005.
- [11] D. R. Paul and L. M. Robeson, "Polymer nanotechnology: nanocomposites," *Polymer*, vol. 49, no. 15, pp. 3187–3204, 2008.
- [12] L. Rapoport, Y. Bilik, Y. Feldman, M. Homyonfer, S. R. Cohen, and R. Tenne, "Hollow nanoparticles of WS_2 as potential solid-state lubricants," *Nature*, vol. 387, no. 6635, pp. 791–793, 1997.
- [13] W. X. Chen, J. P. Tu, Z. D. Xu et al., "Wear and friction of Ni-P electroless composite coating including inorganic fullerene- WS_2 nanoparticles," *Advanced Engineering Materials*, vol. 4, pp. 686–690, 2002.
- [14] X. H. Hou, C. X. Shan, and K. L. Choy, "Microstructures and tribological properties of PEEK-based nanocomposite coatings incorporating inorganic fullerene-like nanoparticles," *Surface and Coatings Technology*, vol. 202, pp. 2287–2291, 2008.
- [15] X. H. Hou, P. T. Deem, and K. L. Choy, "Hydrophobicity study of polytetrafluoroethylene nanocomposite films," *Thin Solid Films*, vol. 520, pp. 4916–4920, 2012.
- [16] R. G. Palgrave and I. P. Parkin, "Aerosol assisted chemical vapor deposition using nanoparticle precursors: a route to nanocomposite thin films," *Journal of the American Chemical Society*, vol. 128, no. 5, pp. 1587–1597, 2006.

- [17] A. D. Ross and K. K. Gleason, "The CVD of nanocomposites fabricated via ultrasonic atomization," *Chemical Vapor Deposition*, vol. 12, pp. 225–230, 2006.
- [18] X. Hou and K. L. Choy, "Synthesis of Cr_2O_3 -based nanocomposite coatings with incorporation of inorganic fullerene-like nanoparticles," *Thin Solid Films*, vol. 516, no. 23, pp. 8620–8624, 2008.
- [19] X. H. Hou and K. L. Choy, "Processing and applications of aerosol-assisted chemical vapor deposition," *Chemical Vapor Deposition*, vol. 12, pp. 583–596, 2006.
- [20] R. A. Qyquist, *Interpreting Infrared, Raman and Nuclear Magnetic Resonance Spectra*, vol. 1, Academic press, London, UK, 2001.
- [21] J. M. Chalmers and P. R. Griffiths, *Handbook of Vibrational Spectroscopy*, vol. 3, John Wiley & Sons, Chichester, UK, 2001.
- [22] M. F. Zhou and L. Andrews, "Infrared spectra and density functional calculations of the CrO_2^- , MoO_2^- , and WO_2^- molecular anions in solid neon," *Journal of Chemical Physics*, vol. 111, p. 4230, 1999.
- [23] K. H. Xiang, R. Pandey, J. M. Recio, E. Francisco, and J. M. Newsam, "A theoretical study of the cluster vibrations in Cr_2O_2 , Cr_2O_3 , and Cr_2O_4 ," *Journal of Physical Chemistry A*, vol. 104, no. 5, pp. 990–994, 2000.
- [24] M. Schraml-Marth, A. Wokaun, H. E. Curry-Hyde, and A. Baiker, "Surface structure of crystalline and amorphous chromia catalysts for the selective catalytic reduction of nitric oxide II. Diffuse reflectance FTIR study of thermal treatment and oxygen adsorption," *Journal of Catalysis*, vol. 133, no. 2, pp. 415–430, 1992.
- [25] K. K. Singh, P. R. Sarode, and P. Ganguly, "Evolution of α - Cr_2O_2 from hydrous chromium oxides: magnetic susceptibility and extended X-ray absorption fine structure studies," *Journal of the Chemical Society, Dalton Transactions*, pp. 1895–1899, 1983.
- [26] M. Watanabe, E. Okunishi, and K. Ishizuka, "Analysis of spectrum-imaging datasets in atomic-resolution electron microscopy," *Microscopy and Analysis*, vol. 23, pp. 5–7, 2009.
- [27] M. García, M. Jergel, A. Conde-Gallardo, C. Falcony, and G. Plesch, "Optical properties of Co and Co-Fe-Cr thin films deposited from an aerosol on glass substrates," *Materials Chemistry and Physics*, vol. 56, no. 1, pp. 21–26, 1998.
- [28] Y. L. Bai, H. B. Xu, Y. Zhang, and Z. H. Li, "Reductive conversion of hexavalent chromium in the preparation of ultra-fine chromia powder," *Journal of Physics and Chemistry of Solids*, vol. 67, pp. 2589–2595, 2006.
- [29] R. H. Hurt and M. D. Allendorf, "Model of particle-vapor codeposition with application to ceramic materials synthesis," *AIChE Journal*, vol. 37, no. 10, pp. 1485–1496, 1991.
- [30] A. Gurav, T. Kodas, T. Pluym, and Y. Xiong, "Aerosol processing of materials," *Aerosol Science and Technology*, vol. 19, no. 4, pp. 411–452, 1993.
- [31] Y. Wang, M. Sasaki, and T. Hirai, "Thermal properties of chemical vapour-deposition SiC-C nanocomposites," *Journal of Materials Science*, vol. 26, pp. 5495–5501, 1991.
- [32] U. Backman, A. Auvinen, and J. K. Jokiniemi, "Deposition of nanostructured titania films by particle-assisted MOCVD," *Surface and Coatings Technology*, vol. 192, no. 1, pp. 81–87, 2005.
- [33] R. J. Hopkins and J. P. Reid, "Evaporation of ethanol/water droplets: examining the temporal evolution of droplet size, composition and temperature," *Journal of Physical Chemistry A*, vol. 109, pp. 7923–7931, 2005.